Experimental, Analytical and Numerical Analyses of Orthotropic Materials and Biomechanics Application

by

Abdulllah A. Alshaya

A dissertation submitted in partial fulfillment of

the requirements for the degree of

Doctor of Philosophy

(Mechanical Engineering)

at the

University of Wisconsin-Madison

2017

Date of final oral examination: 12/13/2016

The dissertation is approved by the following members of the Final Oral Committee:

Robert E. Rowlands, Professor, Mechanical Engineering
Roxann L. Engelstad, Professor, Mechanical Engineering
Tim Osswald, Professor, Mechanical Engineering
Heidi-Lynn Ploeg, Associate Professor, Mechanical Engineering
Robert J. Witt, Professor, Engineering Mechanics and Astronautics

Experimental, Analytical and Numerical Analyses of Orthotropic Materials and Biomechanics Application

Abdullah A. Alshaya

Under the supervision of Professor Robert E. Rowlands

at the University of Wisconsin-Madison

Abstract

The integrity assessment of an engineering structure or member, for instance criteria and fatigue-life predictions, necessitates the knowledge of the full-field individual components of stress, strain and/or displacement. Evaluating these using analytical or numerical techniques can be difficult or impossible for finite structures, contact problems, or if the material properties, loading or boundary conditions are unknown. Such information is often unavailable in practice so as to necessitate experimental approach to capture the exact boundary and loading conditions of the structure. However, extracting individual stress, strain and/or displacement information in the locality of geometric cutouts by purely experimental methods can be difficult and in most cases impossible and often suffer from bad, and in some cases, unavailable results at and close to the edges of cutouts. Combining (or hybridizing) experimental information with analytical and numerical tools enables one to solve aforementioned situations. For example, thermoelastic stress analysis (TSA) is combined with an Airy stress function to stress analyze an orthotropic composite containing an elliptical hole, a rectangular plate subjected to a concentrated edged-load with a near edge hole and a finite plate with a deep U-notch. Utilizing Digital Image Correlation (DIC), values of single displacement component are used here to determine full-field individual components of stresses and displacements in a notched orthotropic

composite without explicitly differentiating the measured displacements. The analytical ingredient of this hybrid approach consists of using the Airy stress function which is based on the mechanics foundations of compatibility and equilibrium. The study also emphasizes on reducing stress concentrations and on increasing strength in a side-notched finite-width orthotropic plate by reducing the adjacent structural stiffness through introducing nearby auxiliary notches. The stress and strain concentration factors for a thick plate with a circular hole were also investigated using three-dimensional finite element analysis. Bone surrogate which mimics the bone in strength and geometry were tested experimentally using 3- and 4-point bending and DIC.

The major contribution of this thesis is the demonstrated ability to combine experimental, numerical and analytical techniques for the full-field determination of the separate components of stress, strain, and displacement at and in the neighborhood of the cutouts in various loaded components and structures, with different boundary and loading conditions.

Acknowledgements

All praise goes to Allah Subhanahu wa Ta'Ala (God Almighty) without whose help this dissertation would not have come about. To say that is also to acknowledge the support and guidance of all those that Allah placed around me all along, from beginning to the end.

I count myself fortunate in having been blessed with a mentor and advisor as knowledgeable and as fatherly as Professor Robert E. Rowlands. I want to thank him for his constant encouragement, his technical and insightful guidance and his editorial meticulousness. It is rare to find a supervisor who would pore through the advisee's thesis drafts as carefully as if it were his own work. I thank him for keeping me sane and stable. Even when things were not perfect, I still felt encouraged and motivated every time we met and for that I will forever be grateful.

I am no less grateful to my committee members, Professors Roxann L. Engelstad, Ploeg Heidi, Tim Osswald and Robert J. Witt for their time and attention. I want to recognize all current and past student members of the UW applied mechanics lab for their support and collaboration both in and out of the lab. I especially want to thank Jacob Zeuske for his technical contribution and experimental advices.

Of course I cannot thank enough my immediate family, my parents, Ahmed Alshaya and Aisha Albatel, my brothers, Mohammed, Yousef, and Bader, my sisters Manal and Shahad, and last but not the least my wife, Fatima for motivating and supporting me. Needless to say that I take full responsibility for all the blemishes and mistakes herein. Finally, a special thanks to all my friends, Ayman Almuhanna, Fawaz Boodai, Bader Aldalali, Fahad Alkhayyat, Mohamed Abou Dbai, Abdulah Chehade, Sulaiman Alhammadi, Abdullah Alhajri, and Eissa Alnaserallah who made my stay in Madison an experience I will never forget!

Table of Contents

List of Figures

List of Tables

List of Symbols

a	Central circular radius of thick plate
a, b	major and axes of elliptical hole
A_j	Complex coefficients $A_j = a_j + ib_j$
$\bar{A}_j$	Complex conjugate of A_j
a_n, b_n, c_n, d_n a_n', b_n', c_n', d_n' A_0, B_0, C_0, D_0 A_1, A_1', B_1, B_1'	Airy coefficients
$[A]$	Airy Matrix
B, C	Complex material properties
c	Central notch diameter
$\{c\}$	Vector of Airy coefficients
C	Condition number
C_{ijkl}	4th order stiffness tensor
d_o	Optimum diameter of auxiliary notches
$\{d\}$	Vector of measured input data
$\{d'\}$	Vector of reconstructed data
D	Location of center of hole below top edge of the plate
D_k	Differential operator; $D_k = \frac{\partial}{\partial y} - \mu_k \frac{\partial}{\partial x}$, $k = 1,2,3,4$
E	Horizontal distance between center of hole and load or modulus of elasticity
E_{11}, E_{22}, E_{33}	Elastic moduli in material directions
f_x, f_y, f_z	Body forces in x-, y-, and z-directions
F	Applied load
$F_1(z_1), F_2(z_2)$	Arbitrary analytical functions

FWC	Finite width correlation
$\mathcal{F}$	Airy stress function
$\mathcal{F}(x,y)$	Airy stress function in rectangular coordinate
G_{12}, G_{13}, G_{23}	Shear moduli
h	Number of collocation positions on the edge of hole
H	Height of thick plate
Im	Imaginary part
k	Measure of number of Airy coefficients
K	Isotropic Thermomechanical coefficients (TSA calibration coefficients)
K_1, K_2	Orthotropic Thermomechanical coefficients (TSA calibration coefficients)
K^c	Compressive stress concentration factor
K_a^c	Compressive stress concentration factor at auxiliary holes and notches
K_c^c	Compressive stress concentration factor at central hole or notch
K^t	Tensile stress concentration factor
K_a^t	Tensile stress concentration factor at auxiliary holes and notches
K_c^t	Tensile stress concentration factor at central hole or notch
K^ε	Strain concentration factor
$K_{\max}^\varepsilon$	Maximum strain concentration factor along thickness of tip of hole for finite thickness plate
$K_{\mathrm{mp}}^\varepsilon$	Strain concentration factor on mid plane of a finite thickness plate
$K_{\mathrm{ps}}^\varepsilon$	Strain concentration factor for plane stress condition
$K_{\mathrm{sur}}^\varepsilon$	Strain concentration factor on the plate surface of finite thickness plate
K^σ	Stress concentration factor
$K_{\max}^\sigma$	Maximum stress concentration factor along thickness of tip of hole for finite thickness plate
K_{mp}^σ	Stress concentration factor on mid plane of a finite thickness plate
K_{ps}^σ	Stress concentration factor for plane stress condition

$K_{\mathrm{sur}}^{\sigma}$	Stress concentration factor on the plate surface of finite thickness plate
l_o	Optimum location of auxiliary notches
L	Thickness of thick plate
m	Number of measured input values
M	Magnification factor
$[M]$	Matrix consists of S^* input and other known boundary conditions
n, t	Elliptical coordinate; n and t are normal and tangent to edge of ellipse
N	Terminating integer of the summation series
p_1, p_2, q_1, q_2	Complex material properties
P	Load per thickness
P^*	Concentrated load
q	Number of known stress or displacement conditions
Q_{ij}	Reduced stiffness
$\boldsymbol{Q}$	Stiffness matrix, $\boldsymbol{Q} = \boldsymbol{S^{-1}}$
$\bar{Q}_{ij}$	Transformed reduced stiffness
$\overline{\boldsymbol{Q}}$	Transformed stiffness matrix, $\overline{\boldsymbol{Q}} = \overline{\boldsymbol{S}}^{\boldsymbol{-1}}$
r, θ	Polar coordinates
R	Radius of central circular hole or side circular notch
$\boldsymbol{R}$	Reuter matrix
R^*	Interested region in physical plane or rigid body rotations
Re	Real part
R_z	Region in the physical plane (x, y)
R_ζ	Mapped region of R_z in ζ-plane (ξ, η)
RMS	Root Mean Square
S	First stress invariant trace of stress tensor or isopachic stress $(= \sigma_1 + \sigma_2 = \sigma_{rr} + \sigma_{\theta\theta} = \sigma_{xx} + \sigma_{yy})$

S^*	Thermoelastic recorded signal (TSA raw data, uncalibrated)
S_{ij}	Reduced compliance
S_{ijkl}	4th order compliance tensor
S_1, S_2	Rigid body translations
$\boldsymbol{S}$	Compliance matrix, $\boldsymbol{S} = \boldsymbol{Q}^{-1}$
$\bar{S}_{ij}$	Transformed reduced compliance
$\overline{\boldsymbol{S}}$	Transformed compliance matrix, $\overline{\boldsymbol{S}} = \overline{\boldsymbol{Q}}^{-1}$
t	Thickness of plate or time coordinate
T_x	In-plane stress constraint factor
T_z	Out-of-plane stress constraint factor
$\boldsymbol{T}$	Transformation matrix
u, v, w	Cartesian displacements in x-, y-, and z-directions
u^*, v^*	Measured displacement values inside the region R^*
u_i	Displacement field
U	Strain Energy
$[U]$	Matrix consists of displacement input with other known boundary conditions
W	Width of plate
x, y	Cartesian (rectangular) coordinates
z_1, z_2	Complex variable; $z_j = x + \mu_j y$ for $j = 1,2$
z_c	Center of circular or elliptical holes
α	Angle to normal of a point on edge of hole
α and γ	Distinct real parts of complex parameters μ_k
β and δ	Distinct imaginary parts of complex parameters μ_k
Γ	Traction-free boundary in physical plane R_z
Γ_ζ	Mapped traction-free boundary, Γ, in ζ-plane R_ζ

Δ	Change
ε_{ij}	2nd order strain tensor
$\epsilon_{xx}, \epsilon_{yy}, \epsilon_{xy}$	Strains in Cartesian coordinate
ζ, ξ, η	Coordinates in the mapped plane, $\zeta = \xi + \mu_j \eta$
ζ	Normalized distance from hole tip by circular hole radius a i.e. $\zeta = x/a$
ζ_0	Some point on the traction-free boundary
θ_p	Principal stress direction
λ	Ratio of major to minor axes of ellipse a/b
μ_k	Roots of characteristic equation associated with the compatibility equation
$\nu_{12}, \nu_{13}, \nu_{23}$	Poisson's ratio
ξ	Normalized distance from mid-plane to surface by half thickness L i.e. $\xi = z/L$
ρ	Density or ratio of the radial coordinate to hole radius r/a
σ, σ_o	Far-field applied load and normal stresses
$\sigma_1, \sigma_2, \sigma_3$	Principal stresses
σ_{11}, σ_{22}	Normal stresses in the direction of material symmetry
σ_{ij}	2nd order stress tensor
σ_{max}	Maximum stress
σ_{net}	Nominal stress
$\sigma_{nn}, \sigma_{tt}, \sigma_{nt}$	Stresses in elliptical coordinate (normal, tangential, and shear stresses)
$\sigma_{rr}, \sigma_{\theta\theta}, \sigma_{r\theta}$	Stresses in polar coordinate (radial, tangential, and shear stresses)
$\sigma_{xx}, \sigma_{yy}, \sigma_{xy}$	Stresses in Cartesian coordinate
Σ	Summation
Φ	Airy stress function in real variable for isotropic material
$\Phi(z_1)$	Stress function $\Phi(z_1) = dF_1(z_1)/dz_1$
ψ	Angle between the normal of a point on hole and polar r-direction, $(\alpha - \theta)$

$\Psi(z_2)$	Stress function $\Psi(z_2) = dF_2(z_2)/dz_2$
$\omega(\zeta)$	Mapped function
∇^4	Biharmonic operator
\	Backslash operator (MATLAB)

Chapter 1: Introduction and Outline

1.1 Background

Engineering components often involve geometric discontinuities where the most serious stresses frequently occur so an assessment of the structural reliability necessitates knowing the stresses, strains, and displacements associated with such discontinuities. Such stress/strain risers can precipitate cracks, thereby aggravating the situation. Examples of such situation include bicycle sprockets, metal plate connector, internal cavities of solid rocket propellant materials, airplane and ship bulkheads, and fir-tree shaped anchoring used to connect turbine blades to their rotor. In addition to such cutouts not having a well-defined profile or any axes of symmetry, the actual and complete boundary conditions in practice are often unknown or at best difficult to simulate numerically using Finite Element Analysis (FEA) and virtually impossible to analyze analytically.

FEA is an attractive engineering tool designed within a computer aided design (CAD) for iterative optimizing design techniques. The advantages of the FEA are such as ease of performance, no need to carry out an experiment, and the results are generated rapidly. However, if the fatigue failure analysis of an existing structure is the main objective, the external boundary, material properties, and loading conditions that real structures experience in practice are often unknown, incomplete, and/or difficult to simulate numerically using finite element analysis (FEA). On the other hand, theoretical approaches which provide closed form and continuous solution tend to be limited to infinite structures of very simple geometry, whereas many practical problems involve complicated finite shapes, thus ruling out using analytical approaches to handle finite structures. An important aspect of experimental approaches is capturing the actual exact boundary and loading conditions of the structure. Moreover, traditional

experimental approaches such as thermoelastic stress analysis and photoelastic stress analysis do not provide the separate components of stress over the interested region and often suffer from bad, and in some cases, unavailable results at and close to the edges of cutouts. These locations are the highest interest due to stress concentration.

The deficiencies of FEA and analytical approaches when attempting to replicate the actual boundary and loading conditions motivated the use of full-field hybrid experimental-numerical-analytical approach for dealing with such perforated structures to determine the full-field stresses, strains, and displacements in continuous form and provide reliable results at the edges of the discontinuity.

1.2 Objective and Motivation

The objective of this research is to utilize contemporary experimental methods (optical techniques), such as Digital Image Correlation (DIC) and Thermoelastic Stress Analysis (TSA), and analytical and numerical tools to stress analyze finite structural members. In addition, the thesis presents a hybrid method for determining the full-field state of stress and displacement in structures with cutout geometries by combining measured experimental data with Airy stress function in real and complex variables. The major advantage of the presented methods is that they do not require knowing the external loading, boundary conditions, or distant geometry.

A simple general series solution of the bi-harmonic equation derived from the equilibrium and compatibility is available in (real) polar coordinates, such is not so in orthogonal curvilinear (rectangular) coordinates. However, the general bi-harmonic solution in real variable is only restricted to isotropic materials where the interested materials in this thesis are orthotropic. This necessitates using the solution of Airy stress function in complex variable for

orthotropic materials. The two stress analytical functions which satisfy the governing differential equation of Airy stress function can be related to each other in a region adjacent to traction-free condition using analytic continuation. Once the two equations are related, one of those stress function can be represented by a truncated series expansion whose coefficients can be determined using experimental data from TSA or DIC. The present hybrid technique combines discretely measured information with analytical representation of stress function while satisfying the traction-free boundary conditions analytically. The coefficients of the stress function were evaluated numerically using least-squares. The reliability of the present hybrid method results is supported by comparisons with FEA predictions, force equilibrium and strain gages.

The hybrid approach is applicable for different complicated shapes, various complex loading, and inverse problems. The present inverse technique does not presuppose knowledge of the external geometry or boundary conditions and overcomes the traditional difficulties of unreliable edge data. Particular attention is paid to determining a realistic value of the needed number of unknown coefficients. In the light of the above, this thesis also emphasizes reducing tensile stress concentration and the possible influence on strength at the geometric discontinuities by changing the neighboring structural compliance through introducing nearby auxiliary notches. The present research also considers the three-dimensional stress and strain concentrations, and in- and out-of-plane stress constraint factors, in a large, uniaxially-loaded, thick orthotropic plate containing a circular hole. This thesis also experimentally analyzes bone surrogates under 3- and 4-point bending tests using DIC.

1.3 Thermoelastic Stress Analysis (TSA)

Thermoelastic stress analysis (TSA) is a modern contemporary, non-contacting, non-destructive experimental technique for determining the full-field experimental surface stress

distribution in engineering components which deforms elastically from measured surface temperature changes induced by time-varying stress/strain distributions using a sensitive infrared detector [1–3]. Solids, like a confined gas, experience an increase in temperature when compressively loaded and a temperature decrease when stressed in tension. Thermoelastic stress analysis studies can be conducted on virtually any structure or material that is subjected to a sufficiently dynamic load. In the elastic, reversible and adiabatic process, the cyclic loading produces an in-phase temperature variation which is proportional linearly to local changes in stresses. Reference [1] contains a detailed derivation of thermal-mechanical response under isotropic and orthotropic responses. TSA uses a scanning infra-red (IR) radiometer system to record the local temperature fluctuation and relate these changes to the stress. The TSA systems are able to expeditiously record and process vast amounts of spatially-dense temperature information in only a few minutes contrasted with other alternative methods (e.g. strain gages, photoelasticity, moiré).

The technique enables the stress analysis of actual structures in their operating environment with a sensitivity equivalent to that of strain gages. TSA is an emerging technique which can be successfully used for the evaluation and validation of design concepts, fracture mechanics, damage detection, fatigue monitoring and residual stress analysis. No surface preparation is required other than perhaps applying a thin coat of flat black paint to provide an enhanced and uniform emissivity. While some experimental techniques are labor-intensive and time consuming, commercially available hardware and software renders TSA efficient. By cyclically loading the structure to satisfy adiabatic reversible conditions, the stresses at a location are related to the stress-induced temperature at that position. One typically records the temperature data with a sensitive infrared camera. The adiabatic conditions are achieved by cyclically loading the structure such that heat diffusion effects are negligible. If the load causing the volumetric change is removed and the material returns to its original temperature and shape, the process

is reversible. Figure 1-1 represents the thermoelastic effect and identifies the governing relationship between the change in the spectral radiant photon emittance derived from Planck's law and the temperature change under isotropic plane stress. At room temperature the peak photon emittance occurs at a wavelength of 12 μm and the photodetector is restricted to two discrete window of operations 3-5 μm and 8-13 μm. The TSA system used here, DeltaTherm, is that by Stress Photonics, Madison, WI, U.S.A. The sampling rate of the camera exceeds 1000 frames/sec and the loading frequency range is 0.6 – 1000 Hz. Commercial TSA systems (DeltaTherm) have temperature sensitivity in the 0.001^{o}C range and use array-based FPA (Focal Plane Array) infrared detectors to collect surface temperature perturbations so as to drastically decrease (compared with earlier systems) recording time to only a few minutes while still providing high quality stress data. The DeltaTherm TSA camera used either a liquid nitrogen or mechanical closed-cycle cooling system in order to achieve optimum sensitivity of FPA detectors when recording thermal data emitted from a stressed surface.

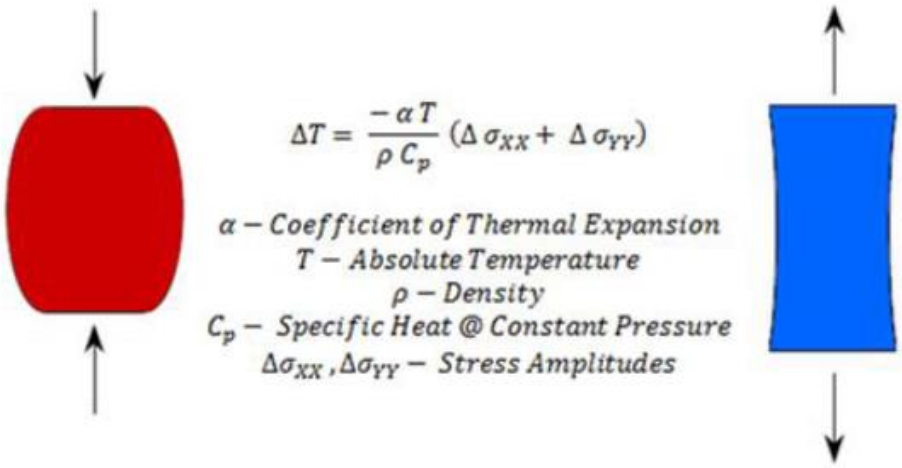

Figure 1-1: Thermoelastic effect on the specimen.

1.3.1 Induced-Stress-Temperature Relation

Under adiabatic reversible conditions, the stresses induce temperature change, S^*, (TSA recorded data) in an isotropic material is proportional to the changes in the sum of the normal

stresses, S, (sometimes it is called stress invariant; the trace of the stress tensor or the isopachic stress value), i.e.,

$$S^* = K\Delta S = K\Delta(\sigma_1 + \sigma_2) = K\Delta\left(\sigma_{xx} + \sigma_{yy}\right) = K\Delta(\sigma_{rr} + \sigma_{\theta\theta}) \tag{1-1}$$

where K is isotropic thermoelastic material (thermomechanical) coefficient (depends on physical material properties, surface conditions and TSA system parameters) sometimes called TSA calibration factor and can be determined experimentally, S is the isopachic value at each point, S^* is the raw TSA measured value at the same point, and σ_1, σ_2, σ_{rr}, $\sigma_{\theta\theta}$, σ_{xx} and σ_{yy}, are the normal stress components in the principal, polar and Cartesian rectangular coordinates, respectively. Under orthotropy, the thermoelastic measured information, S^*, is proportional to a linear combination of the changes in the normal stresses, σ_{11} and σ_{22}, in the direction of material symmetry, i.e.,

$$S^* = \Delta(K_1\sigma_{11} + K_2\sigma_{22}) \tag{1-2}$$

where K_1 and K_2 are orthotropic thermoelastic (or thermomechanical) material coefficients and can be determined experimentally. Although classical thermoelastic stress analysis (TSA) provides information on only a linear combination of the stresses, engineering applications such as fatigue or failure theories require knowing the magnitudes of the individual components of stress so it is necessary to "separate the stresses". The latter can be determined by hybridizing the stress-induced thermal data with some supplementary experimental methods or measured information. The need of using other experimental methods or information is circumvented here in that the individual stresses are evaluated by hybridizing the TSA information with an analytical and/or numerical tools (Airy stress function and some known boundary conditions). Although one could combine TSA with some other experimental method (such as photoelasticity) to separate the stresses, it is preferable to use only a single experimental process. TSA

benefits from available systems which are able to record and process the thermal data expeditiously. This general approach of combining thermal data with relevant mechanics-based equations was used to stress analyze finite engineering metal structures containing different geometric discontinuities [1,2,4–6].

1.3.2 History of TSA

The recognition of thermoelastic effect is attributed to Weber in 1830 when he observed a vibrating wire receives a sudden increase in tension when it experiences a delay in their change of its fundamental frequency. He hypothesized this delay due to the increased magnitude of stress causing a transient temperature change in the wire. William Thomson (i.e. Lord Kelvin) in 1853 established the theoretical foundation of the thermoelastic effect when he derived a linear relationship between the temperature change of a solid and the temperature in the sum of the principal stresses for isotropic materials. Compton and Webster in 1915 confirmed experimentally the equation derived by Thomson which regarded as the first theoretical themoelastic analysis. In 1967, Belgen accomplished the first non-contacting TSA measurements and used an infrared radiometer to measure temperature changes related to stress responses in a vibrating cantilevered beam. In 1982, a British company, Ometron Ltd. applied Belgen's technique to manufacture and market the first commercial TSA equipment, SPATE 8000 (Stress Pattern Analysis by measurement of Thermal Emission). This device and its improved system, SPATE 9000, were broadly used throughout the world during the past decades. Recently, thermoelastic stress analysis methods have been developed to obtain individual components of stress, determining reliable edge stresses, smooth measured temperature data, formulate approaches for three-dimensional components, and extend the general technique to cyclic plasticity, orthotropic materials, and mean and residual stresses, fatigue and fracture, address non-adiabaticity, and to illustrate a variety of mechanical and structural-type problems [7].

1.3.3 TSA Test Preparation

The quality of the TSA image data measured by infrared detectors depends on the efficiency of thermal radiation emission that is required to be high and uniform. Although some materials (for instance epoxy) have a natural capacity of high emissivity, most of metals do not. To enhance the magnitude and uniformity of a metal's emissivity and reduce the risk of spurious signal due to reflection when recording the thermal data, a metallic specimen is typically coated by flat black paint. From experience, Krylon Ultra-Flat black paint provides a suitable surface coating (has a surface emissivity of approximately 0.94). A high-emissivity coating is desirable for two reasons. First, the black coating more closely approximates a black body, which enhances the photodetector sensitivity by increasing the photon flux from the structure. Second, the coating provides the uniform surface emissivity necessary for quantitative stress analysis [7].

1.3.4 TSA Test Loading Requirement and Signal Processing

In a cyclically loaded component, the adiabatic and reversible conditions were achieved to obtain stress information from recorded temperature. The temperature change of a member will follow its mechanical cyclic loading. Therefore, as long as the specimen oscillates faster than heat transfer occurs, no heat flows from position to position during the test and the process can be regarded as adiabatic. An adiabatic response requires that a balance be maintained between the thermal and mechanical energy, that is, the process must be reversible so that there is no heat transfer from location to location. To achieve these conditions and accurate measurements, the temperature changes induced by the thermoelastic effect are repeated and time-averaged during a continuous dynamic loading, usually provided by a closed-loop hydraulic load frame. The minimum loading frequency to accomplish this can depend on the thermal

conductivity and stress gradients in the structure. Most metals can be safely considered adiabatic for frequencies above 2 Hz, but other factors such as the coating and system electronics might introduce concerns below 10 Hz. Also the minimum suitable frequency for a structure depends on the material properties, which affect heat transfer and the adiabatic loading requirements. Higher loading frequencies usually can improve the detail in the data since heat transfer is minimized.

Earlier TSA experiments indicate that approximately 20–25 Hz is a suitable loading frequency for aluminum and glass/epoxy and graphite/epoxy composites [1]. Materials having lower thermal conductivities tend to necessitate increased frequency to maintain adiabaticity. The adiabatic structural response is expected to be in phase with the reference loading frequency. If heat conduction occurs in regions of high stress gradients, or if the loading frequency is insufficient for an adiabatic response, a phase shift from the reference frequency will occur and will be apparent as an out-of-phase detector signal. A quick confirmation of adiabatic response is to check for the absence of any out-of-phase detector signal. Fortunately, the presence or absence of non-adiabatic response can be observed by checking the phase of the response signal with respect to the load signal. If heat conduction takes place within a component or coating, a detectable phase shift will occur between the reference and loading signals. Prior TSA experiments demonstrate that one can usually ignore any heat transfer between a structure and its surroundings.

Raw thermoelastic signals recorded by detectors include noise due to ambient effects. Since ambient temperature changes usually do not occur at the same frequency as a reference signal (which is in phase with cyclic loading), such ambient temperature changes can be rejected by a phase-lock amplifier when processing the TSA recorded signal. The recorded thermal images will therefore not be affected by environment; consequently, only by the applied periodic loading.

1.3.5 TSA Calibration

The thermoelastic coefficients (TSA calibration factor) K_1 and K_2 of orthotropic materials are determined in a component whose complete state of stress is known at a location far from any stress concentration and/or where there is uniform 1-D state of stress (no holes or irregular discontinuities) when the loads are applied parallel and perpendicular the material symmetry, respectively. The thermoelastic calibration was achieved from a tensile specimen of the same material and thickness and identical coating of the flat black paint and tested using the TSA recording characteristics. It is recommended to calibrate the TSA data on the same day as the component tested to reduce any environmental effects (temperature and humidity). The thermoelastic coefficients were determined from the averaging the recorded thermoelastic signal, S^*, along horizontal lines at different height of the strip and divided by the uniform stress. The calibration factors are related to the relevant physical properties of the material, surface condition and TSA system parameters as opposed to the thermoelastic constant of the material being tested which is solely a material property. Reference [8] provides a finite-element approach to estimate the calibration factors using the measured thermoelastic data, S^*, of the actual specimen.

1.3.6 TSA Limitations

TSA measured information can be noisy and involve some scatter. Recorded thermal information at and very close to an edge is typically unreliable because the pixels at an edge often see a spot which is partly on the stressed structure and partly on the stress-free background. The motion of the structure due to its cyclic loading also provides different data to the detector from different spatial positions. Therefore, even if one uses a high magnification and has a high spatial resolution, the quality of the data at and near an edge can be inadequate. Pixels at such locations are also susceptible to violating adiabaticity because of high stress

gradients. By using more values of S^* away from the edges than the number of Airy coefficients, plus perhaps some boundary conditions, the above described hybrid TSA scheme of processing measured thermal data with an Airy function overcomes these challenges. Such techniques simultaneously enhance reliability of thermoelastic edge information, smooth the interior measured information, separate the stresses into their three components and evaluate the non-zero stresses along a traction-free boundary (determining stress concentration) without knowing the loading, material constitutive properties, or boundary conditions beyond the traction-free conditions at the geometric discontinuity.

Because of the aforementioned scatter in recorded TSA data, it is customary to employ more known quantities (measured thermal data plus boundary conditions) than the number of unknown Airy coefficients, and to evaluate the latter using linear least-squares. Reference [9] provides helpful information on the amount and source locations of the TSA input data, and number of Airy coefficients, to employ.

1.3.7 General Comments

Advantages of the TSA-approach over many hybrid techniques for such situations include the following: (i) unnecessary to know far-field geometry or boundary conditions (unlike strictly numerical or theoretical approaches); (ii) suitable for finite (can be difficult theoretically) or infinite geometries; (iii) convenience of commercial hardware and software; (iv) able to rapidly record and process vast amounts of measured information; (v) no need to differentiate measured data; (vi) simultaneously smooths the original thermoelastic input data, satisfies the local boundary conditions, evaluates individual stresses, enhances the edge information, and separates the stresses; (vii) ability to obtain reliable stresses on the edge of the geometrical discontinuity despite unreliable measured data at such locations; (viii) virtually no component preparation needed; (ix) full-field capability (but digital information also available) and (x)

unlike isochromatic photoelasticity, the TSA approach involves only linear, not non-linear, least squares. That the hybrid-TSA method described does not necessitate any supplemental experimental information (such as measured displacements, isoclinics or ischromatics) is also desirable. Such inverse problems where the stresses on and in the neighborhood of the edge of a discontinuity are determined without explicit knowledge of the external loading or geometry can be very challenging. For thermodynamic reasons, thermoelastic stress analyses are usually conducted under cyclic loading. Motion and edge effects (pixels can straddle the boundary) result in recorded TSA data being unreliable at edges. The ability of the current technique to give accurate boundary stresses is therefore significant.

The idea of hybridizing thermal data and analysis is a significant ingredient in making TSA a quantitative, rather than just a qualitative, engineering tool. The hybrid-TSA approaches discussed enjoy the advantage of being based on strong mechanics foundations. They also do not require any numerically integrating or differentiating procedures. Future considerations might include the feasibility of functionally hybridizing TSA ideas for three-dimensional members, curved surfaces, inelastic behaviors (e.g., viscoelastic plastics), vibrations, boundary integral/boundary methods, and more complicated and practical applications beyond a laboratory environment.

1.3.8 Previous Research on Hybrid-TSA

There are a variety of other methods of experimental strain/stress analysis, e.g. moiré, holography, digital image correlation, and speckle which provide surface displacements. Spatially differentiating these displacements provides strains from which the stresses are available. However, differentiating measured data has its own perils, and it can be particularly challenging to obtain accurate strains on the edge of geometric cut-outs (often the locations of the great-

est interest) from measured displacements. Moiré has the additional inconvenience that it typically necessitates applying a grid or ruling to the surface to be analyzed. Optical requirements of these photomechanical displacement-measuring methods can hamper their application to practical engineering problems, in some cases essentially restricting their use to a laboratory environment. Traditional photoelasticity involves viewing a transparent loaded plastic model of the actual engineering problem in polarized light, while contemporary photoelasticity often strain analyses a birefringent coating which is bonded to the engineering component of interest. The three independent components of stress can then be determined by combining a series representation of the Airy stress function with measured isochromatics. However, whereas TSA analysis requires only linear least squares, photoelastic isochromatic analyses necessitate time-consuming iterative nonlinear least squares. Electrical strain gages find wide application, but they provide only point-by-point information. Moreover, mounting the many strain gages needed to analyze a region, and processing their outputs, can be onerous. Unlike all these displacement-based methods, TSA requires neither differentiation of the measured information nor knowledge of the constitutive material properties. Contrasted with the labor-intensive and time consuming techniques of moiré, holography, digital image correlation, speckle and strain gages, recent commercial hardware and software developments enable TSA results to be available within minutes.

This technique was utilized to evaluate the individual stresses in structures made of isotropic and orthotropic composite materials by recording the infrared radiation of a cyclically loaded structure to determine the temperature changes which accompany changes in stress. The Experimental Mechanics Research Laboratory at UW-Madison has considerable experience utilizing hybrid-TSA techniques. Table 1-1 summarizes some of the important research done in this area.

Table 1-1: Summary of some of the important research on TSA area carried out at Experimental Mechanics Research Laboratory at UW-Madison.

Topic	Corresponding Author	Year
Partially loaded aluminum half-plane [10]	Huang Y.M	1988
Symmetrical orthotropic plate with circular hole [11]	Feng	1992
Symmetrical orthotropic plate with side notch [12]	S.T. Lin	1995
Symmetrical orthotropic plate with circular hole and crack [13]	J. Rhee	1999
Mixed-mode thermoelastic fracture analysis of orthotropic composites [14]	S.H. Ju	2003
Stress intensity factors for inclined cracks in orthotropic plate [8]	S.H. Ju	2003
Diametrally-loaded disk [15]	B.E. Foust	2006
Plate with a near edge hole subjected to an offset concentrated load [16]	S.J. Lin	2007
Symmetrical plate with circular hole [17,18]	S.J. Lin	2007
Unsymmetrical loaded plate with central circular hole [16]	S.J. Lin	2007
Nonsymmetrical plate with circular hole [9]	N.S. Joglekar	2009
Plate with a near edge hole subjected to a concentrated load [19–22]	S.J. Lin	2011

Plate with two circular holes [23]	A.A. Khaja	2011
Symmetrical plate with elliptical hole [24,25]	A.A. Khaja	2013
Unsymmetrically-loaded plate with elliptical hole [26]	W.A. Samad	2013
Plate with bolted joint [27]	W.A. Samad	2014
Plate with irregularly-shaped hole [28,29]	W.A. Samad	2014
Unsymmetrically-loaded plate with irregularly-shaped hole [30]	W.A. Samad	2014
Finite structure with asymmetrical, arbitrarily-shaped cut-out [31]	S. Kurunthottikkal Philip	2015
Symmetrical orthotropic plate with elliptical hole [32–34]	**A.A Alshaya**	2016
Plate with a near edge hole subjected to a concentrated load using mapping-collocation technique	**A.A Alshaya**	2016
Plate with a U-notch subjected to a concentrated load	**A.A Alshaya**	2016

1.4 Digital Image Correlation (DIC)

Digital Image Correlation (DIC), also referred to digital image tracking (DIT), is a full-field computer-based image analysis technique for the non-contact measurement of displacements of a surface equipped with a speckle pattern. The method tracks the motion of the speckles by comparing the gray scale value at a point (subset) in a deformed and undeformed configuration, Figure 1-2. Two sets of images are recorded; the first image typically being at zero

load and the second image under load. A single camera setup can record both u and v in-plane full-field deformations. Out-of-plane motions can also be recorded if two cameras are employed. Digital image correlation (DIC) is a restively new and popular optical method that employs tracking and image registration techniques for accurate two dimensional (2D) or three dimensional (3D) measurements of changes in digital images. The achievable DIC resolution depends on a number of factors, including but not limited to, camera resolution, lens optical quality, and speckle size and quality. However, unlike electronic speckle, the surface of the structure under study has to have speckle pattern for tracking; but unlike TSA, DIC does not require cyclic loading. The latter makes DIC attractive as cycling can be inconvenient and particularly challenging for complicated boundary conditions. Advantages of DIC include full-field, non-contacting, non-destructive, static/dynamic measurements.

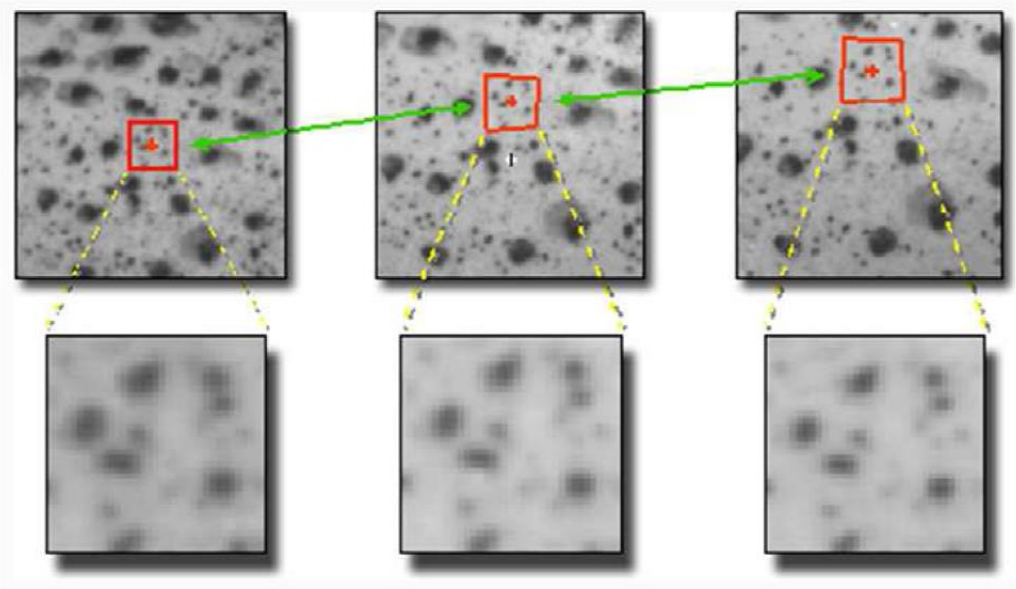

Figure 1-2: DIC algorithm tracking gray value pattern in small subsets [35].

1.4.1 History of DIC

The recognition of image correlation effect is attributed to Gilbert Hobrough (1919-2002) in the early 1950s who compared analog representation of photographs to register features from various views. Applications where DIC is currently being employed include biomedical testing, vibration analysis as well as tracking high speed impact deformations like that of a bullet hitting a Kevlar panel. In experimental solid mechanics, this technique is used to measure deformations; displacements and strains. Advantages of such technique are mainly that it is a full-field non-contacting displacement analysis technique. The only requirement is that the structure under study has to contain a random speckle pattern.

1.4.2 DIC Test Preparation

As mentioned earlier, a speckle pattern has to be applied to the structure of interest before performing a DIC test unlike electronic speckle. Ultra-Flat white paint (Krylon Ultra-Flat) is applied first to reduce the surface's reflectiveness and to create a good contrast for the speckle black dots applied later. The speckle (Krylon Ultra-Flat) coating should be applied after the base white paint has completely dried. If the undercoat is wet when applying the speckles, the paints could potentially blend and blur. The speckle is then applied using commercial Ultra-Flat black paint spray bottles, Figure 1-3.

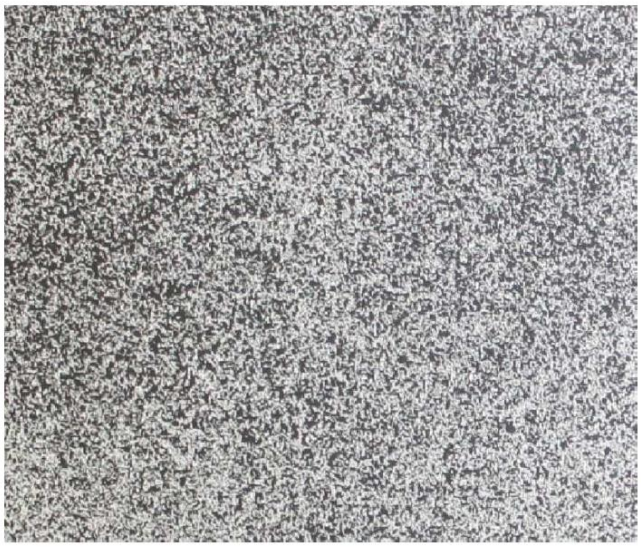

Figure 1-3: Speckle pattern for DIC test.

To achieve an effective correlation, the speckle pattern applied must be non-repetitive (random), isotropic (not exhibit a bias in any orientation) and high contrast (show dark blacks and bright whites) as shown in Figure 1-4. Note that while people refer to these patterns as speckle patterns, the DIC software only sees a contrasting field; the speckles themselves are not the analysis unit. Therefore, white speckles on black can work as well as black speckles on white, or a high-quality pattern may consist of neither.

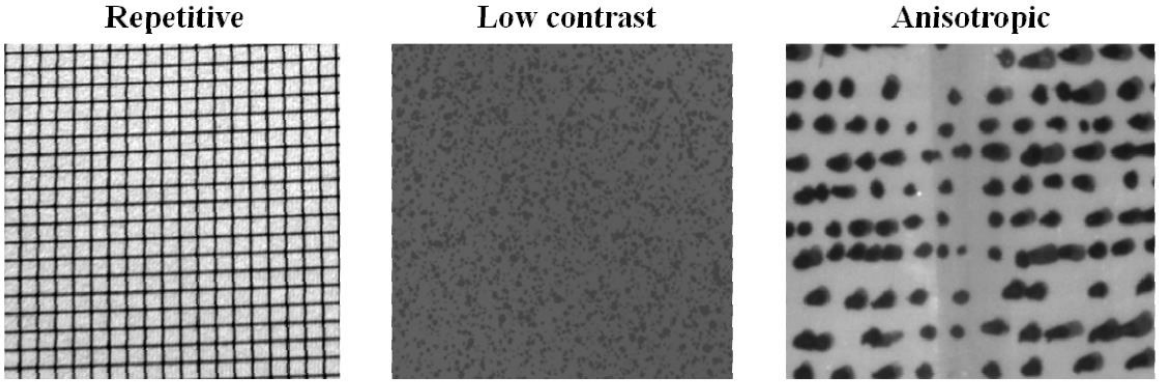

Figure 1-4: Examples illustrating repetitive, low contrast, and anisotropic speckle.

In addition to the above requirements, speckles should be neither too small nor too large. In practice, there is a very wide range in how large a speckle pattern may be, and still

achieve excellent results, but having an optimal pattern will give the best flexibility. To understand what makes an optimal pattern, a bit of background on the theory will be helpful. In DIC, a small subset of the image is tracked as the specimen moves and deforms, Figure 1-2. To perform the tracking, the subset is shifted until the pattern in the deformed image matches the pattern in the reference image as closely as possible; this match is calculated as the total difference in gray levels at each point. If the pattern is too large, one might find that certain subsets may be entirely on a black field or entirely on a white field. This does not allow making a good match, since one would have an exact match everywhere in the field. This can be compensated for this by increasing the subset size, but at the cost of spatial resolution. Conversely, if the pattern is too small, the resolution of the camera may not be enough to accurately represent the specimen; in information terms, this can be called aliasing. Instead of appearing to move smoothly as the specimen moves, the pattern will show jitter as it interacts with the sensor pixels; resulting images often show a pronounced moiré pattern in the results. Patterns which are too fine are also very sensitive to defocus – out of focus regions may simply become gray. In general, speckles should be at least 3-4 pixels in size to avoid these issues. Put another way, speckles should be visible as distinct features, as opposed to random 'salt and pepper' noise.

Vic-Snap software (by Correlated Solutions, Inc., Columbia, SC, USA, [35,36]) was used to record the images of the specimen in its loaded and unloaded conditions and employed for evaluating the displacements to post-process the results. When utilizing two cameras, a separate calibration grid (provided by Correlated Solution with the DIC package) was used to evaluate the displacement data in physical units rather than in pixels.

1.4.3 DIC Limitations

Displacement information at and near the geometrical discontinuity is unavailable because the DIC software's correlation algorithm is unable to track a group of pixels (subset)

which lack neighboring pixels. To perform the tracking, the subset is shifted until the pattern in the deformed image closely matches that of the reference image. Because of the aforementioned scatter in recorded DIC data, it is customary to employ more known quantities (measured displacement data plus boundary conditions) than the number of unknown Airy coefficients, and to evaluate the latter using linear least-squares.

1.4.4 General Comments

Advantages of the present DIC-approach over many hybrid techniques for such situations include the following: (i) unnecessary to know far-field geometry or boundary conditions (unlike strictly numerical or theoretical approaches); (ii) suitable for finite (can be difficult theoretically) or infinite geometries; (iii) convenience of commercial hardware and software; (iv) able to rapidly record and process vast amounts of measured information; (v) no need to differentiate measured data (differentiation based on mechanics foundation); (vi) simultaneously smooths the original displacement input data, satisfies the local boundary conditions, evaluates individual stresses, and enhances the edge information using only single displacement component; (vii) able to obtain reliable stresses on the edge of the geometrical discontinuity despite unreliable measured data at such locations; (viii) full-field capability (but digital information also available) and (ix) no cyclic loading is needed as in TSA. Such inverse problems where the stresses on and in the neighborhood of the edge of a discontinuity are determined without explicit knowledge of the external loading or geometry can be very challenging. The ability of the current technique to give accurate boundary stresses despite unreliable data at the edge of the discontinuity is also significant.

The idea of hybridizing displacement data and analysis is a significant ingredient in making DIC a quantitative, rather than just a qualitative, engineering tool. The hybrid-DIC approaches discussed enjoy the advantage of being based on strong mechanics foundations.

They also do not require any numerically integrating or differentiating procedures. Future considerations might include the feasibility of functionally hybridizing DIC ideas for three-dimensional members, curved surfaces, inelastic behaviors (e.g., viscoelastic plastics), vibrations, boundary integral/boundary methods, and more complicated and practical applications beyond a laboratory environment.

1.4.5 Previous Research on Hybrid-DIC

This hybrid technique was utilized to evaluate the individual stresses in structures made of isotropic and orthotropic composite materials by using a single displacement component from DIC. The Experimental Mechanics Research Laboratory at UW-Madison has considerable experience utilizing hybrid-DIC techniques. Table 1-2 summarizes some of the important research done in this area.

Table 1-2: Summary of some of the important research on DIC area carried out at Experimental Mechanics Research Laboratory at UW-Madison.

Topic	Corresponding author	Year
Symmetrical plate with circular hole [37]	A.A. Khaja	2012
Symmetrical plate with elliptical hole [38]	W.A. Samad	2012
Symmetrically loaded metal plate connecter in 3-point bending [26]	W.A. Samad	2013
Unsymmetrical structure subjected to a concentrated load [39]	S. Paneerselvam	2014
Symmetrical plate with side circular notches	**A.A Alshaya**	2016

1.5 Other Methods

Stress can be determined by conventional displacement measurement technique (strain gages, moiré, holography, and speckle) or reflective Photoelasticity stress analysis (PSA) when combining the measurements with Airy stress function. A strain gage is a discrete device used to measure the strain of an object when deformed. When an object is loaded/deformed, the foil of a bonded strain gage is deformed, causing a change in electrical resistance. This change in resistance, usually measured using a Wheatstone bridge, is related to the strain by the manufacturer's supplied gage factor [40]. Most applications of strain gages are point-wise measurements. Furthermore, capturing displacement at and very close to the edges of the holes and notches which is the location of interest is difficult and the measured data mostly are unreliable. Photoelastic Stress Analysis (PSA, or photoelasticity) which is optical method gives full-field non-contact stress information over a surface of interest. However, PSA like TSA suffers from the limitation that it records data about combinations of stress components rather than individual stresses and suffers from an inability to provide reliable edge data because of the machining and time-edge stresses. PSA gives the difference between the principal stress ($\sigma_1 - \sigma_2$) and the principal stress directions θ_p by counting isochromatic and icoclinic, respectively. Grey-field photoelasticity (GFP) conveniently and rapidly provides the in-plane shear stress and difference in in-plane normal stresses. References [16,41] combines TSA and PSA measurements to obtain surface stresses and stress expressions from Laplace's equation in terms of the first stress invariant and Beltrami-Michell's equations (i.e., stress compatibility equations) to nondestructively evaluate the six independent interior components in a loaded three dimensional component. The Experimental Mechanics Research Laboratory here at UW-Madison has considerable experience utilizing some hybrid techniques to determine the full-field stresses, strains, and displacement. Table 1-3 summarizes some of the important research done in this area.

Table 1-3: Summary of some of the important research on hybrid techniques area carried out at Experimental Mechanics Research Laboratory at UW-Madison.

Topic	Corresponding author	Year
Symmetrical composite plate with circular hole using moiré-measured displacement [42]	T.H. Baek	1999
Symmetrical plate with circular hole using biaxial strain gaga data [43]	T.H. Baek	2001
Pinned connection using reflective Photoelasticity [44]	B.E. Foust	2003
Symmetrical plate with circular hole using Laser Speckle Interferometry [45]	T.H. Baek	2010
Symmetrical plate with circular hole using 45 single-element strain gages [46]	A.A. Khaja	2012
Diametrically-loaded ring using 5 strain gages [46]	A.A. Khaja	2012

1.6 Outline

Chapter 2 discusses theoretical background in elasticity theory for isotropic and orthotropic materials. All the relevant equations of the Airy stress function in real and complex variables and other definitions are introduced in Chapter 2.

1.6.1 Thermoelastic Stress Analysis of a Finite Orthotropic Plate Containing an Elliptical Hole

Chapter 3 determines the individual stresses and displacements in a finite graphite/epoxy laminated composite containing an elliptical hole and loaded in the fiber direction

from recorded load-induced thermal information. In a cyclically loaded orthotropic composite, the temperature variation is proportional to a linear combination of the changes in the normal stresses in the direction of material symmetry. Equilibrium and compatibility conditions throughout the region are satisfied using complex variable formulation, conformal mappings and analytic continuation. Processing the measured thermal data with a stress function simultaneously smooths the measured data and evaluates the individual stress components, including on the edge of the hole. Reliability of experimental results is demonstrated by finite element method (FEM) and force equilibrium.

1.6.2 Hybrid Full-Field Stress Analysis of Finite Plate with Near Edge Hole Subjected to a Concentrated Load

Recognizing that the most serious structural stresses often occur at holes or notches, the ability to determine the stresses on and near the boundary of a near-edge circular hole in a finite plate subjected to a concentrated edge-load by combining recorded load-induced temperature with Airy stress function in complex variables is demonstrated in Chapter 4. Purely analytical or theoretical stress analyses tend to be available for only simple situations involving simple, infinite structures, whereas many practical problems involve complicated, finite shapes. Moreover, and like numerical (finite element method, finite different method) approaches, analytical/theoretical analyses depend on reliable knowledge of the boundary conditions. Experimental techniques are therefore important for determining the stresses associated with geometric discontinuities. Although it can sometimes be advantageous to combine measured information with that from other experimental or numerical techniques, it is convenient to acquire all the necessary data utilizing a single experimental method. The present approach combines data from thermoelastic stress analysis (TSA) and an applicable series representation of the Airy stress function in complex variables. The complex mapping-collocation method simultaneously smooths the measured input data, satisfies the local boundary conditions analytically

and evaluates individual stresses on, and in the neighborhood of, the edge of the hole. Using real variables is restricted to isotropic materials where the complex mapping-collocation technique is applicable for both isotropic and orthotropic materials.

1.6.3 Thermoelastically Determined Individual Stresses in a Deep-Notched Tensile Plate

Chapter 5 discusses determination of individual stresses are determined experimentally in a finite, tensile loaded aluminum plate containing a single-sided deep U-notch from recorded load-induced thermal information. Under elastic, reversible and adiabatic conditions, the cyclic loading produces an in-phase temperature variation which is proportional linearly to local changes in normal stresses. As engineering analyses often necessitate knowing the individual components of stress, supplementary experimental methods or information are frequently required to 'separate the stresses'. This need is circumvented here in that individual stresses are evaluated throughout the loaded plate without additional measured data. Processing the measured thermal data with an Airy stress function and some local known stress conditions simultaneously smooths the measured data, separates the stress components, and evaluates the individual stress components full-field, including at the root of the U-notch (location of highest tensile stress). The present hybrid technique does not presuppose knowledge of the external loading conditions and overcomes the traditional difficulties of unreliably edge data. Reliability of experimental results is demonstrated by comparison with those from finite elements and strain gages.

1.6.4 Experimental Stress Analysis of a Notched Finite Composite Tensile Plate

Chapter 6 determines the individual displacements and stresses in a vertically-loaded notched finite graphite/epoxy laminated composite by processing measured values of a single

component of displacement with an Airy stress function in complex variables. Displacements are recorded using digital image correlation. Traction-free conditions are imposed analytically at the notch using conformal mappings and analytic continuation, and discretely on the vertical free edge. Zero shear stress is also imposed on the horizontal line of symmetry. Consequences of employing different amounts and source locations of measured displacements and varying number of coefficients, as well as how displacements are differentiated to provide strains, are considered. Advantages of this method include ability to significantly simplify the experimental technique by needing only a single displacement component, provide reliable results both full-field and at the edge of geometric discontinuities, lack of need to differentiate the recorded data physically, and to simultaneously smooth the recorded data. Moreover, and compared against Correlated Solutions computed strains, the present hybrid-DIC technique offers the advantage of evaluating strains more accurate and without mathematically differentiating displacement experimental data. Reliability of experimental results is demonstrated by finite element and force equilibrium.

1.6.5 Stress Concentrations and Strengths in a Side Notched Finite-Width Composite Material

Chapter 7 emphasizes the ability to reduce the tensile stress concentration associated with a side notched orthotropic plate by introducing adjacent auxiliary notches, and the possible influence on strength, are investigated. A scheme for optimizing size and location of auxiliary notches of isotropic and three orthotropic composite materials, namely glass/epoxy (Gl/E) (E_{11}/E_{22} = 3), graphite/aluminum (Gr/Al) (E_{11}/E_{22} = 5), and boron/epoxy (B/E) (E_{11}/E_{22} = 10), to minimze stress concentration is included. Compared with reduction in stress concentration, results show that increases in strength when introducing auxiliary notches can be appreciable in highly orthotropic natural composites such as wood. This necessitate the importance of studying both the strength and stress concentration factor when dealing with failure criteria

since assuming that a specific value of a stress concentration factor necessarily leads to failure can be erroneous.

1.6.6 Studying the Effect of Thickness in Stress and Strain Concentration Factors

Chapter 8 determines stress and strain concentrations, and in-plane and out-of-plane stress constraint factors associated with a circular hole in thick, loaded orthotropic composite plates by three-dimensional finite element method. The plate has essentially infinite in-plane geometry but finite thickness. Results for Sitka Spruce wood are emphasized, although some for carbon-epoxy structural are included. While some results are similar to those for isotropy, there are significant consequences due to material orthotropy. Maximum stress and strain concentration factors occur at mid-plane for thin plates but closer to the external traction-free surfaces for thick plates. These factors decrease as the plate surface is approached and reach lower values unrepresentative of the maximum values. Differences between the mid-plane and/or maximum and surface stress or strain concentration factors in Sitka Spruce, range from 8% if the wood grain is parallel to the applied load to 15% when the grain is perpendicular to the load. These values exceed those typically reported for isotropic materials. Stress and strain concentration factors tend to differ in magnitude from each other. Moreover, this can occur in plates whose thickness is only twice as large as the hole radius, and is true irrespective of whether the plate's material is isotropic or orthotropic. The combination of high local stresses and directional strength dependency of orthotropic materials can be particular important. That maximum stress and/or strain concentrations in thick plates occur on other than the external plate surfaces where they are most readily measured is technically significant. The E_{11}/E_{22} ratio in Sitka Spruce exceeds that in the carbon composite by 60%. However, when loading parallel to the strong/stiff directions, the plane-stress tensile stress concentration factors of the two materials are comparable to each other.

1.6.7 Evaluation of Bone Surrogate Bending Stiffness using 3- and 4-Point Bending

Chapter 9 discusses testing a customizable surrogate bone analog composed of inexpensive materials and femur bone made of nylon material using 3D printer in order to mimic bone strength and geometry for testing validation of femoral bending. Such an analog reduces the costs of mechanical bone testing, and would allow for more consistent and reliable data acquisition utilized in predicting bone strength in patients suffering from osteoporosis. Manufactured testing apparatuses and performing appropriate testing on various bone samples.

Chapter 2: Theoretical Background

2.1 Theory of Elasticity

2.1.1 Hooke's Law – Constitutive Equation

For sufficiently small strains in nearly any elastic material, stresses are linearly related to strains.

$$\sigma_{ij} = C_{ijkl}\varepsilon_{kl} \tag{2-1}$$

$$\varepsilon_{ij} = S_{ijkl}\sigma_{kl} \tag{2-2}$$

Where σ_{ij} and ε_{ij} are 2nd order stress and strain tensors, respectively and C_{ijkl} and S_{ijkl} are 4th order stiffness and compliance tensors, respectively. There are 81 unknown elastic constants in the stiffness and compliance tensors but due to the symmetry of the stresses and strains $\sigma_{ij} = \sigma_{ji}$ and $\varepsilon_{ij} = \varepsilon_{ji}$ for $i \neq j$, then $C_{ijkl} = C_{ijlk}$ and $S_{ijkl} = S_{jikl}$ which reduce the 81 coefficients to 36 coefficients. Finally based on the energy consideration since the strain energy U_{ij} is related the stress to the strain by the following relation

$$\frac{\partial U_{ij}}{\partial \varepsilon_{ij}} = \sigma_{ij} \tag{2-3}$$

This will result another symmetric property $C_{ij} = C_{ji}$ and $S_{ij} = S_{ji}$. So any arbitrary anisotropic elastic material has 21 independent elastic constraints.

$$\sigma_{ij} = C_{ij}\varepsilon_{j} \tag{2-4}$$

$$\varepsilon_{ij} = S_{ij}\sigma_{j} \tag{2-5}$$

2.1.2 Strain and Displacement

Assuming a small displacements, the strains can be expressed as function of the displacements in $x = x_1, y = x_2$, and $z = x_3$ −directions

$$\varepsilon_{ij} = \frac{1}{2}\left(u_{i,j} + u_{j,i}\right) = \frac{1}{2}\left(\frac{\partial u_i}{\partial x_j} + \frac{\partial u_j}{\partial x_i}\right), \qquad i,j = 1,2,3 \tag{2-6}$$

Where $u = u_1, v = u_2,$ and $w = u_3$ are the displacements in x-, y-, and z-directions, respectively.

2.1.3 Equation of Motion

The equations of motion for a body of density ρ with arbitrary shape can be expressed as by summing the forces in all directions and summing moments at the center

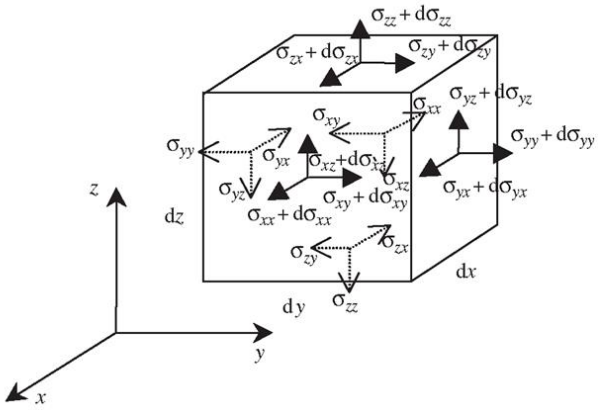

Figure 2-1: Stresses applied to an equilibrium body with arbitrary shape and volume.

$$\sigma_{ij,j} + f_i = \frac{\partial \sigma_{ij}}{\partial x_j} + f_i = \rho \frac{\partial^2 u_i}{\partial t^2}, \qquad i,j = 1,2,3 \tag{2-7}$$

Where $f_x, f_y,$ and f_z are the body forces in x-, y-, and z-directions, respectively. The classical analytical method of stress analyzing a loaded engineering component involves satisfying

stress equilibrium and strain compatibility throughout the entire component, subject to boundary conditions.

2.1.4 Orthotropic Material

For certain materials, some of the C_{ij} and S_{ij} remain invariant under certain coordinate transformations, i.e., there are certain degrees of elastic material symmetry or partial isotropy. If there are two perpendicular axes or planes of material symmetry, then there is also a third normal axis or plane of symmetry, such material is called orthotropic. Orthotropic materials are materials with three orthogonal planes of symmetry in material response.

$$\begin{Bmatrix}\sigma_{11}\\ \sigma_{22}\\ \sigma_{33}\\ \sigma_{23}\\ \sigma_{13}\\ \sigma_{12}\end{Bmatrix} = \begin{bmatrix}C_{11} & C_{12} & C_{13} & 0 & 0 & 0\\ C_{12} & C_{22} & C_{23} & 0 & 0 & 0\\ C_{13} & C_{23} & C_{33} & 0 & 0 & 0\\ 0 & 0 & 0 & C_{44} & 0 & 0\\ 0 & 0 & 0 & 0 & C_{55} & 0\\ 0 & 0 & 0 & 0 & 0 & C_{66}\end{bmatrix}\begin{Bmatrix}\varepsilon_{11}\\ \varepsilon_{22}\\ \varepsilon_{33}\\ \varepsilon_{23}\\ \varepsilon_{13}\\ \varepsilon_{12}\end{Bmatrix} \tag{2-8}$$

$$\begin{Bmatrix}\varepsilon_{11}\\ \varepsilon_{22}\\ \varepsilon_{33}\\ \varepsilon_{23}\\ \varepsilon_{13}\\ \varepsilon_{12}\end{Bmatrix} = \begin{bmatrix}S_{11} & S_{12} & S_{13} & 0 & 0 & 0\\ S_{12} & S_{22} & S_{23} & 0 & 0 & 0\\ S_{13} & S_{23} & S_{33} & 0 & 0 & 0\\ 0 & 0 & 0 & S_{44} & 0 & 0\\ 0 & 0 & 0 & 0 & S_{55} & 0\\ 0 & 0 & 0 & 0 & 0 & S_{66}\end{bmatrix}\begin{Bmatrix}\sigma_{11}\\ \sigma_{22}\\ \sigma_{33}\\ \sigma_{23}\\ \sigma_{13}\\ \sigma_{12}\end{Bmatrix} \tag{2-9}$$

There are 9 independent constants which are $E_{11}, E_{22}, E_{33}, G_{12}, G_{13}, G_{23}, \nu_{12}, \nu_{13}$ and ν_{23} that must be specified for any orthotropic material.

2.1.5 Plane Stress

When the stresses associated with 3-axis are zero ($\sigma_{13} = \sigma_{23} = \sigma_{33} = \varepsilon_{13} = \varepsilon_{23} = f_3 = 0$), the stress-strain relation becomes

$$\begin{Bmatrix} \varepsilon_{11} \\ \varepsilon_{22} \\ \varepsilon_{12} = \gamma_{12} \end{Bmatrix} = \begin{bmatrix} S_{11} & S_{12} & 0 \\ S_{12} & S_{22} & 0 \\ 0 & 0 & S_{66} \end{bmatrix} \begin{Bmatrix} \sigma_{11} \\ \sigma_{22} \\ \tau = \sigma_{12} \end{Bmatrix} \tag{2-10}$$

$$\begin{Bmatrix} \sigma_{11} \\ \sigma_{22} \\ \tau = \sigma_{12} \end{Bmatrix} = \begin{bmatrix} Q_{11} & Q_{12} & 0 \\ Q_{12} & Q_{22} & 0 \\ 0 & 0 & Q_{66} \end{bmatrix} \begin{Bmatrix} \varepsilon_{11} \\ \varepsilon_{22} \\ \varepsilon_{12} = \gamma_{12} \end{Bmatrix} \tag{2-11}$$

The strain out-of-plane

$$\varepsilon_{33} = S_{13}\sigma_{11} + S_{23}\sigma_{22} \tag{2-12}$$

For an orthotropic material under plane stress condition, 4 independent elastic constants are required to be specified and the stiffness matrix becomes

$$\boldsymbol{Q} = \begin{bmatrix} \dfrac{E_{11}}{1 - \nu_{12}\nu_{21}} & \dfrac{\nu_{12}E_{22}}{1 - \nu_{12}\nu_{21}} & 0 \\ \dfrac{\nu_{21}E_{11}}{1 - \nu_{12}\nu_{21}} & \dfrac{E_{22}}{1 - \nu_{12}\nu_{21}} & 0 \\ 0 & 0 & G_{12} \end{bmatrix} \tag{2-13}$$

Q_{ij} is the reduced stiffness such that $\boldsymbol{Q} = \boldsymbol{S^{-1}}$.

2.1.6 Stress and Strain Transformation

In plane stress, the stresses and strains in orthotropic materials are related using the transformed stiffness matrix $\overline{\boldsymbol{Q}}$

$$\begin{Bmatrix} \sigma_x \\ \sigma_y \\ \tau_{xy} \end{Bmatrix} = \begin{bmatrix} \bar{Q}_{11} & \bar{Q}_{12} & \bar{Q}_{16} \\ \bar{Q}_{12} & \bar{Q}_{22} & \bar{Q}_{26} \\ \bar{Q}_{16} & \bar{Q}_{26} & \bar{Q}_{66} \end{bmatrix} \begin{Bmatrix} \varepsilon_x \\ \varepsilon_y \\ \gamma_{xy} \end{Bmatrix} \tag{2-14}$$

Where $\overline{\boldsymbol{Q}} = \boldsymbol{T^{-1}QRTR^{-1}}$ is the transformed stiffness matrix and $\bar{Q}_{ij}$ is the transformed reduced stiffness. The transformation matrix $\boldsymbol{T}$ and Reuter matrix $\boldsymbol{R}$ are defined by

$$\boldsymbol{T} = \begin{bmatrix} \cos^2\theta & \sin^2\theta & 2\sin\theta\cos\theta \\ \sin^2\theta & \cos^2\theta & -2\sin\theta\cos\theta \\ -\sin\theta\cos\theta & \sin\theta\cos\theta & \cos^2\theta - \sin^2\theta \end{bmatrix} \tag{2-15}$$

$$\boldsymbol{R} = \begin{bmatrix} 1 & 0 & 0 \\ 0 & 1 & 0 \\ 0 & 0 & 2 \end{bmatrix} \tag{2-16}$$

The strains are defined in terms of plane stresses as following

$$\begin{Bmatrix} \varepsilon_x \\ \varepsilon_y \\ \gamma_{xy} \end{Bmatrix} = \begin{bmatrix} \bar{S}_{11} & \bar{S}_{12} & \bar{S}_{16} \\ \bar{S}_{12} & \bar{S}_{22} & \bar{S}_{26} \\ \bar{S}_{16} & \bar{S}_{26} & \bar{S}_{66} \end{bmatrix} \begin{Bmatrix} \sigma_x \\ \sigma_y \\ \sigma_{xy} \end{Bmatrix} \tag{2-17}$$

$$\overline{\boldsymbol{S}} = \boldsymbol{R}\boldsymbol{T}^{-1}\boldsymbol{R}^{-1}\boldsymbol{S}\boldsymbol{T} \tag{2-18}$$

Where $\overline{\boldsymbol{S}}$ is the transformed compliance matrix and $\bar{S}_{ij}$ is the transformed reduced compliance. So the strains and stresses for a homogeneous orthotropic plane-stress body should satisfy strain-displacement equations and the equations of motion.

2.1.7 Stresses in Polar and Elliptical Coordinates

The polar components of stresses are evaluated by converting the Cartesian stresses using standard transformation matrix, equation (2-15)

$$\begin{bmatrix} \sigma_{rr} \\ \sigma_{\theta\theta} \\ \sigma_{r\theta} \end{bmatrix} = \begin{bmatrix} \cos^2\theta & \sin^2\theta & 2\sin\theta\cos\theta \\ \sin^2\theta & \cos^2\theta & -2\sin\theta\cos\theta \\ -\sin\theta\cos\theta & \sin\theta\cos\theta & \cos^2\theta - \sin^2\theta \end{bmatrix} \begin{bmatrix} \sigma_{xx} \\ \sigma_{yy} \\ \sigma_{xy} \end{bmatrix} \tag{2-19}$$

Therefore, the Cartesian components of stresses are evaluated by converting the polar stresses using standard transformation matrix, equation (2-15)

$$\begin{bmatrix} \sigma_{xx} \\ \sigma_{yy} \\ \sigma_{xy} \end{bmatrix} = \begin{bmatrix} \cos^2\theta & \sin^2\theta & -2\sin\theta\cos\theta \\ \sin^2\theta & \cos^2\theta & 2\sin\theta\cos\theta \\ \sin\theta\cos\theta & -\sin\theta\cos\theta & \cos^2\theta - \sin^2\theta \end{bmatrix} \begin{bmatrix} \sigma_{rr} \\ \sigma_{\theta\theta} \\ \sigma_{r\theta} \end{bmatrix} \tag{2-20}$$

The stresses in elliptical coordinates, where n is the normal to the edge of the elliptical hole and t is the tangential to the edge of the hole, can then be obtained using the transformation matrix to convert polar coordinate to elliptical coordinates, Figure 2-2

$$\begin{bmatrix}\sigma_{nn}\\ \sigma_{tt}\\ \sigma_{nt}\end{bmatrix} = \begin{bmatrix}\cos^2\psi & \sin^2\psi & 2\sin\psi\cos\psi\\ \sin^2\psi & \cos^2\psi & -2\sin\psi\cos\psi\\ -\sin\psi\cos\psi & \sin\psi\cos\psi & \cos^2\psi-\sin^2\psi\end{bmatrix}\begin{bmatrix}\sigma_{rr}\\ \sigma_{\theta\theta}\\ \sigma_{r\theta}\end{bmatrix} \tag{2-21}$$

Where $\psi = \alpha - \theta$, as shown in Figure 2-2. Using elliptical geometry, the normal angle, α, is evaluated from

$$\alpha = \tan^{-1}\left(\frac{a^2\tan\theta}{b^2}\right) \tag{2-22}$$

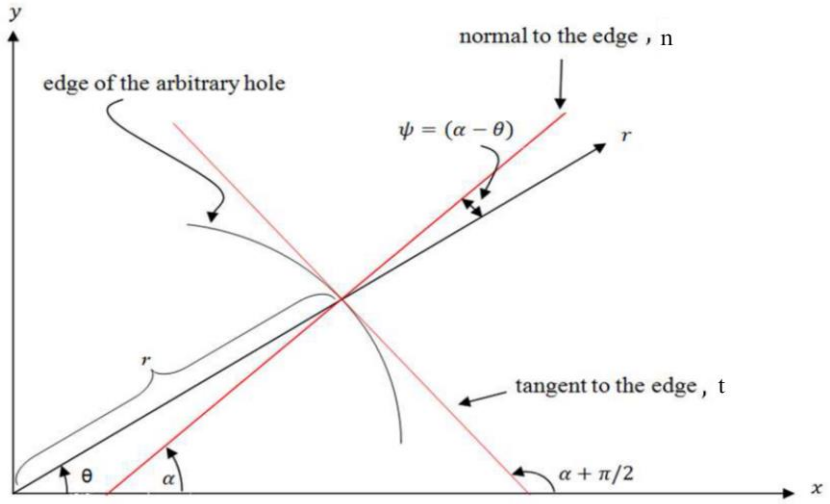

Figure 2-2: Representation of the elliptical coordinates.

From equation (2-21), the components of stress, σ_{tt} , tangential to the edge of the elliptical hole is given by

$$\sigma_{tt} = \sin^2\psi\,\sigma_{rr} + \cos^2\psi\,\sigma_{\theta\theta} - 2\sin\psi\cos\psi\,\sigma_{r\theta} \tag{2-23}$$

2.1.8 Airy Stress Function

By introducing a stress function $\mathcal{F}(x, y)$ in rectangular coordinates, the equilibrium equations are expressed in term of the stress function assuming no body forces

$$\sigma_{xx} = \frac{\partial^2 \mathcal{F}}{\partial y^2}, \qquad \sigma_{yy} = \frac{\partial^2 \mathcal{F}}{\partial x^2}, \qquad \sigma_{xy} = -\frac{\partial^2 \mathcal{F}}{\partial y \partial x} \tag{2-24}$$

The compatibility equation is

$$\frac{\partial^2 \varepsilon_{xx}}{\partial y^2} + \frac{\partial^2 \varepsilon_{yy}}{\partial x^2} - \frac{\partial^2 \gamma_{xy}}{\partial x \partial y} = 0 \tag{2-25}$$

Combining equations (2-17), (2-24), and (2-25), the following differential equation must be satisfied by the stress function

$$\frac{\partial^4 \mathcal{F}}{\partial x^4} - \frac{2S_{26}}{S_{22}} \frac{\partial^4 \mathcal{F}}{\partial x^3 \partial y} + \frac{2S_{12} + S_{66}}{S_{22}} \frac{\partial^4 \mathcal{F}}{\partial y^2 \partial x^2} - \frac{2S_{16}}{S_{22}} \frac{\partial^4 \mathcal{F}}{\partial x \partial y^3} + \frac{S_{11}}{S_{22}} \frac{\partial^4 \mathcal{F}}{\partial y^4} = 0 \tag{2-26}$$

For anisotropic materials, the equilibrium equations of stress and compatibility equation of strains can be represented in terms of Airy stress function, $\mathcal{F}$. Introduce the operator D_k, the previous equation can be written in operational equation

$$D_1 D_2 D_3 D_4 \mathcal{F} = 0 \tag{2-27}$$

where

$$D_k = \frac{\partial}{\partial y} - \mu_k \frac{\partial}{\partial x}, \qquad k = 1,2,3,4 \tag{2-28}$$

such that μ_k (complex material property) are the roots of the characteristic equation which are associated with the compatibility equation, i.e.,

$$S_{11}\mu^4 - 2S_{16}\mu^3 + (2S_{12} + S_{66})\mu^2 - 2S_{26}\mu + S_{22} = 0 \tag{2-29}$$

The $\mu's$ can be either complex or purely imaginary, but cannot be real numbers. The quantities $S_{11}, S_{12}, S_{16}, S_{22}, S_{26}$, and S_{66} are elastic compliances. The roots of the characteristic equation are

$$\mu_{1,3} = \alpha \pm i\beta, \qquad \mu_{2,4} = \gamma \pm i\delta \tag{2-30}$$

All the quantities α, β, γ, and δ are real numbers and both β and δ are positive. There are three cases; either the roots are purely imaginary and unequal, $\mu_1 = \beta i$ and $\mu_2 = \delta i$, purely imaginary and equal, $\mu_1 = \mu_2 = \beta i$, or distinct, $\mu_1 = \alpha \pm \beta i$ and $\mu_2 = -\alpha \pm \beta i$. For orthotropic material such that there are three orthogonal directions of material symmetry, the elastic compliances, S_{ij}, are related to engineering elastic quantities as follow

$$S_{11} = \frac{1}{E_{11}}, \qquad S_{22} = \frac{1}{E_{22}}, \qquad S_{12} = -\frac{\nu_{12}}{E_{11}}, \qquad S_{66} = \frac{1}{G_{12}} \tag{2-31}$$

where the other elastic compliances are zero and the 1- and 2-orientations are the directions of laminate material symmetry. The Airy stress equation then reduces to

$$\frac{1}{E_{22}}\frac{\partial^4 \mathcal{F}}{\partial x^4} + \left(\frac{1}{G_{12}} - \frac{2\nu_{12}}{E_{11}}\right)\frac{\partial^4 \mathcal{F}}{\partial x^2 \partial y^2} + \frac{1}{E_{11}}\frac{\partial^4 \mathcal{F}}{\partial y^4} = 0 \tag{2-32}$$

and the characteristic equation becomes

$$\mu^4 + \left(\frac{E_{11}}{G_{12}} - 2\nu_{12}\right)\mu^2 + \frac{E_{11}}{E_{22}} = 0 \tag{2-33}$$

The roots of the characteristic equation are purely imaginary ($\alpha = \gamma = 0$). For isotropic material, the elastic moduli are equal, $E_{11} = E_{22} = E$, and the shear modulus is related to elastic modulus and Poisson's ratio $G = \frac{E}{2(1+\nu)}$, the roots are $\mu_1 = \mu_2 = i$. The Airy's stress function will reduce to the isotropic case which is

$$\nabla^4 \mathcal{F} = \nabla^4 \Phi = 0 \tag{2-34}$$

and $\nabla^4 = \frac{\partial^4}{\partial x^4} + 2\frac{\partial^4}{\partial x^2 \partial y^2} + \frac{\partial^4}{\partial y^4}$. It is convenient to introduce the two constants

$$k = -\mu_1 \mu_2 = \sqrt{\frac{E_{11}}{E_{22}}}$$

$$n = -i(\mu_1 + \mu_2) = \sqrt{2\left(\sqrt{\frac{E_{11}}{E_{22}}} - \nu_{12}\right) + \frac{E_{11}}{G_{12}}}$$

For isotropic material, the constants are $k = 1$ and $n = 2$. For convenience, the Airy stress function for orthotropic material will be denoted by $\mathcal{F}$ and for isotropic material by Φ.

2.2 Airy Stress Function in Real Variable

The method behind determining the state of stress at and near the geometrical discontinuity lies in coupling the Airy stress function; a special case of the Maxwell stress function, with the measured data and imposing traction-free conditions either analytically or discretely, and hence the term *hybrid*. For elasto-static plane problems (plane-stress or plane-strain) in isotropic material with the absence of the body forces, the Airy stress function, Φ, satisfying stress equilibrium and strains compatibility condition, gives the biharmonic equation $\nabla^4 \Phi = 0$, equation (2-34), where ∇^2 is the Laplacian operator and $\nabla^2 = \frac{\partial}{\partial r^2} + \frac{1}{r}\frac{\partial}{\partial r} + \frac{1}{r^2}\frac{\partial}{\partial \theta^2}$. The general solution to $\nabla^4 \Phi = 0$ in polar coordinates is [47]

$$\begin{aligned}\Phi = {} & a_0 + b_0 \ln r + c_0 r^2 + d_0 r^2 \ln r + (A_0 + B_0 \ln r + C_0 r^2 + D_0 r^2 \ln r)\theta \\ & + \left(a_1 r + b_1 r \ln r + \frac{c_1}{r} + d_1 r^3\right) \sin\theta \\ & + \left(a_1' r + b_1' r \ln r + \frac{c_1'}{r} + d_1' r^3\right) \cos\theta + (A_1 r + B_1 r \ln r)\theta \sin\theta \\ & + (A_1' r + B_1' r \ln r)\theta \cos\theta \\ & + \sum_{n=2,3,..}^{\infty} \left(a_n r^n + b_n r^{n+2} + c_n r^{-n} + d_n r^{-(n-2)}\right) \sin n\theta \\ & + \sum_{n=2,3,..}^{\infty} \left(a_n' r^n + b_n' r^{n+2} + c_n' r^{-n} + d_n' r^{-(n-2)}\right) \cos n\theta\end{aligned} \tag{2-35}$$

Where r is the radial coordinate measured from the center and θ is measured counter-clockwise from the x-axis. The individual components of stresses in polar coordinate can be evaluated as

$$\sigma_{rr} = \frac{1}{r}\frac{\partial \Phi}{\partial r} + \frac{1}{r^2}\frac{\partial^2 \Phi}{\partial \theta^2} \tag{2-36}$$

$$\sigma_{\theta\theta} = \frac{\partial^2 \Phi}{\partial r^2} \tag{2-37}$$

$$\sigma_{r\theta} = -\frac{\partial}{\partial r}\left(\frac{1}{r}\frac{\partial \Phi}{\partial \theta}\right) \tag{2-38}$$

Therefore from equations (2-36), (2-37), and (2-38), the individual stresses are

$$\sigma_{rr} = \frac{b_0}{r^2} + 2c_0 + d_0(2\ln r + 1) + B_0\frac{\theta}{r^2} + 2C_0\theta + D_0(2\ln r + 1)\theta$$
$$+ \left(\frac{b_1}{r} - \frac{2c_1}{r^3} + 2rd_1\right)\sin\theta + \left(\frac{b'_1}{r} - \frac{2c'_1}{r^3} + 2rd'_1\right)\cos\theta$$
$$+ \frac{2A_1}{r}\cos\theta - \frac{2A'_1}{r}\sin\theta + \frac{B_1}{r}\theta\sin\theta + \frac{B'_1}{r}\theta\cos\theta$$
$$+ \left(\frac{2B_1}{r}\ln r\right)\cos\theta - \left(\frac{2B'_1}{r}\ln r\right)\sin\theta \qquad (2\text{-}39)$$
$$- \sum_{n=2,3,..}^{N}\begin{Bmatrix} a_n n(n-1)r^{n-2} + b_n(n+1)(n-2)r^n + \\ c_n n(n+1)r^{-(n+2)} + d_n(n-1)(n+2)r^{-n}\end{Bmatrix}\sin n\theta$$
$$- \sum_{n=2,3,..}^{N}\begin{Bmatrix} a'_n n(n-1)r^{n-2} + b'_n(n+1)(n-2)r^n + \\ c'_n n(n+1)r^{-(n+2)} + d'_n(n-1)(n+2)r^{-n}\end{Bmatrix}\cos n\theta$$

$$\sigma_{\theta\theta} = \frac{-b_0}{r^2} + 2c_0 + d_0(2\ln r + 3) - B_0\frac{\theta}{r^2} + 2C_0\theta + D_0(2\ln r + 3)\theta$$
$$+ \left(\frac{b_1}{r} + \frac{2c_1}{r^3} + 6rd_1\right)\sin\theta + \left(\frac{b'_1}{r} + \frac{2c'_1}{r^3} + 6rd'_1\right)\cos\theta$$
$$+ \frac{B_1}{r}\theta\sin\theta + \frac{B'_1}{r}\theta\cos\theta \qquad (2\text{-}40)$$
$$+ \sum_{n=2,3,..}^{N}\begin{Bmatrix} a_n n(n-1)r^{n-2} + b_n(n+1)(n+2)r^n + \\ c_n n(n+1)r^{-(n+2)} + d_n(n-1)(n-2)r^{-n}\end{Bmatrix}\sin n\theta$$
$$+ \sum_{n=2,3,..}^{N}\begin{Bmatrix} a'_n n(n-1)r^{n-2} + b'_n(n+1)(n+2)r^n + \\ c'_n n(n+1)r^{-(n+2)} + d'_n(n-1)(n-2)r^{-n}\end{Bmatrix}\cos n\theta$$

$$\begin{aligned}\sigma_{r\theta} = {} & \frac{A_0}{r^2} + B_0\frac{\ln r - 1}{r^2} - C_0 - D_0(\ln r + 1) + \left(-\frac{b_1}{r} + \frac{2c_1}{r^3} - 2rd_1\right)\cos\theta \\ & - \left(-\frac{b_1'}{r} + \frac{2c'_1}{r^3} - 2rd'_1\right)\sin\theta - \frac{B_1}{r}\sin\theta - \frac{B_1'}{r}\cos\theta - \frac{B_1}{r}\theta\cos\theta \\ & + \frac{B_1'}{r}\theta\sin\theta \\ & - \sum_{n=2,3,..}^{N}\begin{Bmatrix} a_n n(n-1)r^{n-2} + b_n n(n+1)r^n - \\ c_n n(n+1)r^{-(n+2)} - d_n n(n-1)r^{-n}\end{Bmatrix}\cos n\theta \\ & + \sum_{n=2,3,..}^{N}\begin{Bmatrix} a'_n n(n-1)r^{n-2} + b'_n n(n+1)r^n - \\ c'_n n(n+1)r^{-(n+2)} - d'_n n(n-1)r^{-n}\end{Bmatrix}\sin n\theta\end{aligned} \tag{2-41}$$

The radial and circumferential displacements derived using Hooke's law and integration from individual components of stresses are [39]

$$u_r = \frac{1}{E}\Bigg[\frac{-b_0(1+\nu)}{r} + 2c_0(1-\nu)r + d_0[(1-\nu)(2r\ln r - r) - 2\nu r]$$

$$- \frac{B_0(1+\nu)\theta}{r} + 2C_0(1-\nu)r\theta$$

$$+ D_0[(1-\nu)(2r\ln r - r) - 2\nu r]\theta$$

$$+ \left[(1-\nu)b_1\ln r + \frac{c_1(1+\nu)}{r^2} + d_1r^2(1-\nu) - 2d_1\nu r^2\right]\sin\theta$$

$$+ \left[(1-\nu)b_1'\ln r + \frac{c_1'(1+\nu)}{r^2} + d_1'r^2(1-\nu) - 2d_1'\nu r^2\right]\cos\theta$$

$$+ 2A_1\ln r\cos\theta - 2A_1'\ln r\sin\theta$$

$$+ B_1[(1-\nu)\ln r\,\theta\sin\theta + [\ln r]^2\cos\theta]$$

$$+ B_1'[(1-\nu)\ln r\,\theta\cos\theta - [\ln r]^2\sin\theta]$$

$$- \sum_{n=2,3,..}^{N}\begin{Bmatrix} a_n n(1+\nu)r^{n-1} + \\ b_n[(n-2)+\nu(n+2)]r^{n+1} \\ -c_n n(1+\nu)r^{-(n+1)} - \\ d_n[(n+2)+\nu(n-2)]r^{-n+1}\end{Bmatrix}\sin n\theta$$

$$- \sum_{n=2,3,..}^{N}\begin{Bmatrix} a_n' n(1+\nu)r^{n-1} + \\ b_n'[(n-2)+\nu(n+2)]r^{n+1} \\ -c_n' n(1+\nu)r^{-(n+1)} - \\ d_n'[(n+2)+\nu(n-2)]r^{-n+1}\end{Bmatrix}\cos n\theta + S_1\cos\theta$$

$$- S_2\sin\theta\Bigg] \qquad (2\text{-}42)$$

$$
\begin{aligned}
u_\theta = \frac{1}{E}\Bigg[& 4d_0 r\theta + 2D_0 r\theta^2 \\
& - \left[b_1(1-\nu)(1-\ln r) + \frac{c_1(1+\nu)}{r^2} + d_1(\nu+5)r^2\right]\cos\theta \\
& + \left[b_1'(1-\nu)(1-\ln r) + \frac{c_1'(1+\nu)}{r^2} + d_1'(\nu+5)r^2\right]\sin\theta \\
& - 2A_1(\ln r + \nu)\sin\theta - 2A_1'(\ln r + \nu)\cos\theta \\
& + B_1[1-\nu-(1+\nu)\ln r - [\ln r]^2]\sin\theta \\
& + B_1'[1-\nu-(1+\nu)\ln r - [\ln r]^2]\cos\theta \\
& - B_1(1-\nu)(1-\ln r)\theta\cos\theta + B_1'(1-\nu)(1-\ln r)\theta\sin\theta \\
& - \sum_{n=2,3,..}^{N} \begin{Bmatrix} a_n n(1+\nu)r^{n-1} + \\ b_n[n(\nu+1)+4]r^{n+1} \\ +c_n n(1+\nu)r^{-(n+1)} + \\ d_n[n(\nu+1)-4]r^{-n+1} \end{Bmatrix}\cos n\theta \\
& + \sum_{n=2,3,..}^{N} \begin{Bmatrix} a_n' n(1+\nu)r^{n-1} + \\ b_n'[n(\nu+1)+4]r^{n+1} \\ +c_n' n(1+\nu)r^{-(n+1)} + \\ d_n'[n(\nu+1)-4]r^{-n+1} \end{Bmatrix}\sin n\theta + S_1\cos\theta - S_2\sin\theta \Bigg]
\end{aligned}
\tag{2-43}
$$

Determination of individual stresses, strains, or displacements necessitates evaluating the unknown coefficients in Airy stress function (typically referred to as Airy coefficients). Coefficients a_0, a_1, and a_1' of equation (2-35) does not appear in the separate stress expressions of equations (2-39), (2-40), and (2-41) or displacement expressions of equations (2-42) and (2-43) due to differentiation in equations (2-36), (2-37), and (2-38). The specific form of the Airy stress function for a particular case can depend on conditions of symmetry, whether or not the coordinate origin is within the component, whether the component is finite or infinite in size (boundedness at origin or infinity), self-equilibrated at individual boundaries, and sin-

gle-valued stresses, strains and displacements. To ensure that the stresses, strains, and displacements are single-valued with respect to θ requires $d_0 = B_0 = C_0 = D_0 = B_1 = B_1' = 0$. For multi-connected structures whose individual boundaries are not self-equilibrated, $b_1' = 0.5(1-\nu)A_1$ and $b_1 = -0.5(1-\nu)A_1'$, where ν is Poisson's ratio. These four coefficients are otherwise zero. If there is symmetry about x-axis, then the stress function does not contain sine terms, and for symmetry about both the x- and y-axes, n includes only even numbers. If the coordinate origin is contained with the material or the structure is infinite in size, then appropriate coefficients must be equated to zero to prevent stress singularities when $r \to 0$ or $r \to \infty$, respectively.

It is often possible to reduce significantly the number of coefficients by satisfying the traction-free condition analytically for circular hole. To analyze a non-circular cutout, the traction-free conditions should be imposed discretely. Imposing traction-free conditions discretely requires more coefficients to be evaluated which requires more equations or more measured input values. Lin [16] demonstrated that imposing traction-free conditions discretely on the edge of a circular hole for varying number of locations gave identical results compared with imposing them analytically.

Although many stress analyses situations are really 3-D in nature, where possible it can be convenient to assume plane-stress or plane-strain. Moreover, in the absence of the body forces, $\nabla^4\Phi = 0$ prevails for plane-stress or plane-strain. Plane-stress corresponds to a plane-plate of small initial constant thickness, acted upon by forces only in the plane of the plate (but then typically has a displacement normal to the plane). Plane-strain, on the other hand, corresponds to the case of a theoretically infinite body acted upon by loads that are uniformly distributed in the infinite direction and have no forces (stresses) normal to the finite planes [47]. Plane-stress has been assumed throughout this research, however the hybrid techniques pre-

sented here can certainly be applied to structures under the plane-strain type of loading. Restating the above, with plane-strain, the displacement in the out-of-plane z-direction is constant, perhaps zero, and the other displacements are independent of the z-direction. As such, $\varepsilon_{xz} = \varepsilon_{yz} = \varepsilon_{zz} = 0$, all the stress, strain, and displacement expressions derived from the Airy stress function, the corresponding plane strain problems may be solved by replacing ν and E by ν^* and E^* according to the following equations

$$\nu^* = \frac{\nu}{1-\nu}, \qquad E^* = \frac{E}{1-E} \tag{2-44}$$

The above Airy stress function which is used in the different scenarios in this thesis was simplified based on the geometry for each structure being analyzed, whether or not there are any axes of symmetry, as well as the specific loading and boundary conditions for each experiment. Combining the simplified forms of the Airy stress function with measured data from the full-field experimental approaches provides the unknown Airy coefficients and consequently determines the full-field individual components of stress, strain and displacement data. The general concepts of the Airy stress function are applicable to multiple cutouts, photomechanical disciplines, and to complicated shaped holes, notches, or loading. Unlike the complex variable stress function technique, the current use of a stress function in terms of real variables enables application to loaded as well as traction-free boundaries.

2.2.1 Evaluating the Airy Coefficients

By gathering the measured data with the boundary conditions, the Airy coefficients can be solved by forming a linear system of equation represented in a matrix form as

$$[A]_{(m+h)\times k}\{c\}_{k\times 1} = \{d\}_{(m+h)\times 1} \tag{2-45}$$

where m is the total number of points, h is the number of the collocating boundary conditions, and k is number of unknown Airy coefficients. The matrix $[A]$ consists of the analytical expression of isopachics stress S $(= S^*/K)$ or the displacement in addition to h traction-free expressions as a function of polar coordinates (r, θ). The vector $\{c\}$ contains the k unknown Airy coefficients and vector $\{d\}$ contains m measured data with the h zeros from the right hand side of traction-free boundary conditions. Like most experimental data, the measured data incorporate some noise which necessitate collecting more measured input values than the number of unknown Airy coefficients. The number of equations, $m + h$, is larger than the number of coefficients, k, which produce an overdetermined system which can be solved using least-squares. The system was solved in MATLAB using the backslash '\' or pseudo inverse 'pinv' operator.

The locations of measured data, the number of measured data points, m, and the number of Airy coefficients, k, are all important parameters in solving the linear system equation. Unfortunately, there is no well-defined method that determines the best values and combination of the above parameters, however, the root mean square method can be utilized by comparing the reconstructed data with the measured one to help to determine the validity of a certain combination of the above parameters.

2.2.2 Data Reduction

If the Airy coefficients are too few, the produced results are inaccurate while if they are too many, the Airy matrix will become unstable or even singular due to computer round-off and quantization errors. The amount of measured input data needed can also depend on the choice of k, that is, more coefficients can necessitate more experimental values of S. The number of Airy coefficients to retain was assessed by monitoring the condition number of the respective Airy matrix, computing the Root Mean Square (RMS) for a series different number of

Airy coefficients and by comparing the reconstructed data with the measured one. The RMS, which represents the discrepancy between the reconstructed data, $\{d'\}$ and the measured data, d, in addition to the boundary conditions. Therefore, multiplying the original matrix $[A]$ by the least-squares evaluated values, $\{c\}$, gives the calculated vector $\{d'\}$, which is typically not exactly the same as $\{d\}$. The RMS is computed as

$$(\boldsymbol{d'} - \boldsymbol{d})_{rms} = \sqrt{\sum_{i=1}^{m+h} \frac{(d_i' - d_i)^2}{m+h}} \tag{2-46}$$

where $m + h$ is the number of points in vector $\{d\}$. It is desirable to use the smallest number of coefficients that gives sufficient accuracy since adding more coefficients than necessary could necessitate more measured input data and increase computational time and condition number of the Airy matrix which can increase the chances for the matrix to become singular. The condition number of a matrix with respect to an argument measures how much the output value of the matrix can change for a small change in the input argument. This is used to measure how sensitive a matrix is to changes or errors in the input, and how much error in the output results from an error in the input. A problem with a low condition number is said to be well-conditioned, while a problem with a high condition number is said to be ill-conditioned.

There are two methods which is commonly employed to solve matrix equations: the traditional linear least-squares method which involves taking matrix inverses and the method of singular value decomposition (SVD) which decomposes the original matrix into a set of matrices with special properties. The SVD approach has the advantage that it allows the condition number C of the matrix to be easily determined. With the value of C known, accuracy of the calculations can then be approximately determined by removing as many decimal places from the answer as are found in C. That is, if $C = 1 \times 10^9$ or $\log_{10} C = 9$, then nine digits of

accuracy are lost in the calculation. As the calculations in this thesis are all carried out in double precision format which generally gives an accuracy of about 12 digits, the above condition number would limit the accuracy of results to approximately three digits (12 − 9), which is a rough gauge of accuracy. Both of these methods, traditional linear least-squares and SVD, give equivalent values for the coefficients.

For a fixed number of equations, the matrix instability grows exponentially with the number of coefficients. It is therefore desirable to use the smallest number of coefficients that gives sufficient accuracy. Thus, some additional criterion is required to obtain accurate and reliable results. For this self-consistency of the Airy coefficients was used. There is no unique solution if there are more equations than unknown Airy coefficients. However, for an over-determined matrix equation of $[A]\{c\} = \{d\}$, solving $\{c\}$ and then using the now-known coefficient vector $\{c\}$ in the original matrix equation will give $[A]\{c\} = \{d'\}$, where in general $\{d'\}$ is not exactly the same as the input data $\{d\}$. The SVD method, as well as the traditional least-squares, gives a set of coefficients $\{c\}$ such that the RMS difference of the vector elements of $(\boldsymbol{d'} - \boldsymbol{d})$ is minimized. In the interest of self-consistency, it is desired that the RMS value, which represents the discrepancy between the reconstructed data $\{d'\}$ and actual measured $\{d\}$, and which will vary for each matrix having a different number of coefficients, be small. Larger values of k do not reduce the RMS value much further, would involve more calculations and a bigger condition number C, can increase the possibility of matrix $[A]$ becoming singular, as well as imply a potential need for more measured input data.

2.3 Literature Review in Real Variable Approach

Assuming coordinate origin at the center of a material and symmetry about x- and y-axes, each of the inner and outer boundaries is self-equilibrated, and the stresses, strains, and

displacements are single valued functions, the relevant Airy stress function, equation (2-35), reduces to

$$\Phi = a_0 + c_0 r^2 + \sum_{n=2,4,..}^{\infty} (a'_n r^n + b'_n r^{n+2}) \cos n\theta \qquad (2\text{-}47)$$

Foust and Rowlands (2011) stress analyzed a diametrally-loaded isotropic (aluminum) disk by using the Airy stress function of equation (2-47) and thermoelastic data [15]. A relevant Airy stress function satisfying the biharmonic equation, $\nabla^4\Phi = 0$, for a finite plate with geometric discontinuity which has mechanical and geometrical symmetry about x- and y-axes, each of the inner and outer boundaries is self-equilibrated, the stresses, strains, and displacements must be single valued functions of θ ($d_0, B_0, C_0, D_0, B_1, B'_1$ are all zero), and whose coordinate is not within the material of the structure (no resultant forces at the origin so the coefficients A_1, A'_1, b_1, b'_1 are all zero) is

$$\Phi = a_0 + b_0 \ln r + c_0 r^2 + \sum_{n=2,4,..}^{\infty} \left(a'_n r^n + b'_n r^{n+2} + c'_n r^{-n} + d'_n r^{-(n-2)}\right) \cos n\theta \qquad (2\text{-}48)$$

Lin et al. (2009) utilized equation (2-48) and evaluated the individual stresses reliably in a uniaxially loaded finite plate with a central circular hole from TSA-recorded information without supplementary experimental data, knowledge of constitutive information, or the distant external geometry or boundary conditions while imposing the boundary conditions analytically along the edge of the hole [18]. Khaja et al. (2014) analyzed the same finite plate but using single displacement component from Digital Image Correlation while also imposing the boundary conditions analytically along the edge of the hole [37]. Khaja (2014) evaluated the individual stresses of a symmetrical plate with circular hole using 45 single-element strain gages and diametrally-loaded ring using 5 strain gages [46]. Khaja and Rowlands (2013) and Samad and

Rowlands (2012) obtained the individual stresses in elliptically-perforated isotropic aluminum plates by processing the recorded temperature information and displacement from digital image correlation (DIC) with Airy stress function of equation (2-48), respectively [25,38]. Samad and Rowlands (2014) evaluated the individual stresses reliably in a uniaxially loaded finite plate with an irregularly-shaped hole from TSA-recorded information [28,29]. If the plate has only symmetry along the x-axis and whose coordinate is not within the material of the structure, the relevant Airy stress function becomes

$$\Phi = a_0 + b_0 \ln r + c_0 r^2 + \left(a_1' r + \frac{c_1'}{r} + d_1' r^3\right)\cos\theta + \sum_{n=2,3,..}^{\infty} \left(a_n' r^n + b_n' r^{n+2} + c_n' r^{-n} + d_n' r^{-(n-2)}\right)\cos n\theta \tag{2-49}$$

The stresses at and in the neighborhood of near-edge hole inside square plate subjected to a concentrated load were obtained using TSA and Airy stress function of equation (2-49) [20,22]. For the multiply-connected finite loaded plate of which possesses no conditions of regularity at either the origin or infinity, has symmetry about the vertical x-axis, whose stresses, strains and displacements are single-valued and whose inner and outer boundaries are not self-equilibrating, the Airy stress function, equation (2-35), reduces to

$$\Phi = a_0 + b_0 \ln r + c_0 r^2 + \left(a_1' r + b_1' r \ln r + \frac{c_1'}{r} + d_1' r^3\right)\cos\theta + A_1' r\theta\cos\theta + \sum_{n=2,3,..}^{\infty} \left(a_n' r^n + b_n' r^{n+2} + c_n' r^{-n} + d_n' r^{-(n-2)}\right)\cos n\theta \tag{2-50}$$

Samad et al. (2014) stress analyzed a plane-stressed pin-loaded plate using recorded load-induced temperature with an Airy stress function of (2-50), plus imposing the traction-free conditions on the non-contacting edge of the hole and on the external boundaries of the plate to

determine the individual components of the full-field stresses as well as on the pin-plate interface [27]. If plate does not have any mechanical and geometrical symmetry about x- and y-axes, and whose coordinate is not within the material of the structure, the relevant Airy stress function becomes

$$\begin{aligned}\Phi = a_0 + b_0 \ln r + c_0 r^2 + A_0\theta + \left(a_1 r + \frac{c_1}{r} + d_1 r^3\right)\sin\theta \\ + \left(a_1' r + \frac{c_1'}{r} + d_1' r^3\right)\cos\theta \\ + \sum_{n=2,3,..}^{\infty}\left(a_n r^n + b_n r^{n+2} + c_n r^{-n} + d_n r^{-(n-2)}\right)\sin n\theta \\ + \sum_{n=2,3,..}^{\infty}\left(a_n' r^n + b_n' r^{n+2} + c_n' r^{-n} + d_n' r^{-(n-2)}\right)\cos n\theta\end{aligned} \tag{2-51}$$

Lin et al. (2007) utilized equation (2-51) and evaluated the individual stresses reliably in an unsymmetrically loaded finite plate with a central circular hole from TSA-recorded information without supplementary experimental data, knowledge of constitutive properties, or the distant external geometry or boundary conditions while imposing the boundary conditions analytically along the edge of the hole [48]. The stresses at and in the neighborhood of near-edge hole inside square plate subjected to an offset load were obtained using TSA and Airy stress function of equation (2-51) [19,21,22] and DIC [39]. Samad and Rowlands (2014) evaluated the full-field state of stress in an unsymmetrical-loaded finite structure containing an arbitrarily-shaped hole and elliptical hole by processing the recorded load induced temperature information with an Airy stress function of equation (2-51) and imposing the local traction-free conditions discretely [26,30]. Paneerselvam (2014) determined the stresses at a hole in the junction region of the cooling module bracket of Hundai vehicle from only one measured components of displacement from DIC [39]. Sibin (2015) determined the full-field individual components of

stress in a compressively-loaded aluminum finite plate containing an asymmetrical arbitrarily shaped cutout [31,49]. Lin et al. (2015) summarizes extensive studies of hybridizing thermoelastic data with Airy stress function in the real variable using the general polar solution of the biharmonic equation [5].

2.4 Airy Stress Function in Complex Variables

For plane problems having rectilinear orthotropy and no body forces, the Airy stress function, $\mathcal{F}$, satisfying equation (2-32) can be expressed as a summation of two arbitrary analytical functions, $F_1(z_1)$ and $F_2(z_2)$, of the complex variables, z_1 and z_2, as [50–52]

$$\mathcal{F} = 2Re[F_1(z_1) + F_2(z_2)] \tag{2-52}$$

such that $z_j = x + \mu_j y$ for $j = 1,2$ and Re denotes the 'real part' of a complex number. The complex material properties μ_1 and μ_2 are two distinct roots of the equation (2-33) associated with the compatibility equation. The roots of this characteristic equation are complex with $\mu_1 = \alpha + i\beta$, $\mu_2 = \gamma + i\delta$, $\mu_3 = \bar{\mu}_1$, and $\mu_4 = \bar{\mu}_2$. Quantities α, β, γ, and δ are real numbers and both β and δ are positive. If $\mu_1 = \mu_2$ (pairwise equal complex roots), the stress function becomes

$$\mathcal{F} = 2Re[F_1(z_1) + \bar{z}_1 F_1(z_1)] \tag{2-53}$$

The stresses in rectangular coordinates (x, y) of the physical $z\ (= x + iy)$ plane can be expressed in terms of the stress functions. By introducing the new stress functions

$$\Phi(z_1) = \frac{dF_1(z_1)}{dz_1}, \qquad \text{and} \qquad \Psi(z_2) = \frac{dF_2(z_2)}{dz_2} \tag{2-54}$$

one can write the stresses as

$$\sigma_{xx} = 2Re[\mu_1^2 \Phi'(z_1) + \mu_2^2 \Psi'(z_2)] \tag{2-55}$$

$$\sigma_{yy} = 2Re[\Phi'(z_1) + \Psi'(z_2)] \tag{2-56}$$

$$\sigma_{xy} = -2Re[\mu_1\Phi'(z_1) + \mu_2\Psi'(z_2)] \tag{2-57}$$

where primes denote differentiation with respect to the argument. The stresses satisfy equilibrium and associated strains satisfy compatibility. The displacement can be written in terms of the stress functions as

$$u = 2Re[p_1\Phi(z_1) + p_2\Psi(z_2)] - w_o y + u_o \tag{2-58}$$

$$v = 2Re[q_1\Phi(z_1) + q_2\Psi(z_2)] + w_o y + v_o \tag{2-59}$$

where w_o, u_o, and v_o are constants of integration and characterize the rigid body translations (u_o and v_o) and rotation (w_o). The other quantities, which depend on material properties, are

$$p_1 = S_{11}\mu_1^2 + S_{12} - S_{16}\mu_1, \qquad p_2 = S_{11}\mu_2^2 + S_{12} - S_{16}\mu_2 \tag{2-60}$$

$$q_1 = S_{12}\mu_1 + \frac{S_{22}}{\mu_1} - S_{26}, \qquad q_2 = S_{12}\mu_2 + \frac{S_{22}}{\mu_2} - S_{26} \tag{2-61}$$

When the plate is loaded physically in a testing machine, the rigid body motions, u_o, v_o, and w_o are zero. Plane problems of elasticity classically involve determining the stress functions, $\Phi(z_1)$ and $\Psi(z_2)$, throughout a component and subject to the boundary conditions around its entire edge. For a region of a component adjacent to a traction free-edge, $\Phi(z_1)$ and $\Psi(z_2)$ can be related to each other by the conformal mapping and analytic continuation techniques. The stresses can then be expressed in terms of the single stress function, $\Phi(z_1)$. Moreover, $\Phi(z_1)$ will be represented by a truncated power-series expansion whose unknown complex coefficients can all be determined from experimental measured data. Once the $\Phi(z_1)$ and

$\Psi(z_2)$ are fully evaluated, the individual stresses and displacements are available from equations (2-55) through (2-59). For a significantly large region of interest in a finite structure, it may be necessary to satisfy other boundary conditions at discrete locations.

2.4.1 Conformal Mapping

Conformal mapping is introduced to simplify the plane problem by mapping the region R_z of a complicated physical $z = x + iy$ plane of a loaded component into a region R_ζ of a simpler shape in the $\zeta = \xi + i\eta$ plane, the latter being a half plane or unit circle [4,50,53–58]. The new coordinate system (and resulting geometry) is usually chosen to aid in solving the equations and the obtained solution from this simplified domain can then be mapped back to the original physical geometry for a valid solution. Assume that a mapping function of the form

$$z = \omega(\zeta) \tag{2-62}$$

exists and which maps R_ζ of the simpler plane into R_z of the more complicated physical plane. For orthotropy, auxiliary planes and their induced mapping functions are defined in terms of $\zeta_j = \xi + \mu_j\eta$ so by substituting $z_j = x + \mu_j y$ into equation (2-62) one obtains

$$z_j = \omega_j(\zeta_j), \qquad j = 1,2 \tag{2-63}$$

The induced conformal mapping functions are therefore one-to-one and invertible. The stress functions $\Phi(z_1)$ and $\Psi(z_2)$ can now be expressed as analytic functions of ζ_1 and ζ_2, respectively,

$$\Phi(z_1) = \Phi[\omega_1(\zeta_1)] \equiv \Phi(\zeta_1) \tag{2-64}$$

$$\Psi(z_2) = \Psi[\omega_2(\zeta_2)] \equiv \Psi(\zeta_2) \tag{2-65}$$

The derivatives of these stress functions with respect to their argument are

$$\Phi'(z_1) = \Phi'(\zeta_1)\frac{d\zeta_1}{dz_1} = \frac{\Phi'(\zeta_1)}{\omega_1'(\zeta_1)} \tag{2-66}$$

$$\Psi'(z_2) = \frac{\Psi'(\zeta_2)}{\omega_2'(\zeta_2)} \tag{2-67}$$

The analyticity of the mapping functions satisfies the equilibrium and compatibility equations throughout region R_z of the physical plane.

2.4.1.1 Traction-free boundary of the half-plane

Using the concept of analytic continuation, the stress functions for a region R_ζ adjacent to a traction-free boundary of the half-plane of an orthotropic material are related by

$$\Psi(\zeta_2) = B\overline{\Phi(\bar{\zeta}_2)} + C\Phi(\zeta_2) \tag{2-68}$$

where constants B and C are the following complex material properties and which depend on material properties, μ_i

$$B = \frac{\bar{\mu}_2 - \bar{\mu}_1}{\mu_2 - \bar{\mu}_2}, \qquad C = \frac{\bar{\mu}_2 - \mu_1}{\mu_2 - \bar{\mu}_2} \tag{2-69}$$

2.4.1.2 Traction-free boundary of the unit circle

Using the concept of analytic continuation, the stress functions for a region R_ζ adjacent to a traction-free boundary of the unit circle of an orthotropic material are related by

$$\Psi(\zeta_2) = B\overline{\Phi(1/\bar{\zeta}_2)} + C\Phi(\zeta_2) \tag{2-70}$$

where constants B and C are defined on equation (2-69). Equations (2-68) and (2-70) enable the elastic state of the structure to be expressed in terms of a single stress function, $\Phi(\zeta_1)$, the latter which can be represented by either a truncated Taylor series or Laurent series. Mapping

the boundary of the hole in the physical z-plane to the real axis ($\eta = 0$ surface) of the ζ-plane uses a truncated Taylor series expansion whereas mappings the boundary of the physical plane to the unit circle in the ζ-plane employs a Laurent series.

2.4.2 Mapping Formulation

The objective here is to apply the approach to any region R_z adjacent to a traction-free boundary of a physical member provided an appropriate mapping function to map the region R_ζ into region R_z.

2.4.2.1 Circular Cutouts, Fillets, or Notches

For a region adjacent to a circular cutout, fillet, or notch of radius R, the following function [12]

$$z = \omega(\zeta) = iRe^{-i\zeta} + z_c \tag{2-71}$$

maps the region of a half-plane, R_ζ, of the ζ-plane into the region R_z of the z-physical plane, where Γ_ζ, a section of the real axis in the ζ-plane, goes to the physical traction-free boundary, Γ and $z_c (= x_c + iy_c)$ is the center of the circular cutout, Figure 2-3. For convenience, the co-ordinate system is chosen here that the origin is at center of circle, i.e., z_c = 0. This conformal transformation can be applied to orthotropic materials by combining equation (2-71) with $z_j = x + \mu_j y$ produces

$$z_j = \omega_j(\zeta_j) = \frac{iR}{2}\left[(1 - i\mu_j)e^{-i\zeta_j} - (1 + i\mu_j)e^{i\zeta_j}\right], \qquad j = 1,2 \tag{2-72}$$

The derivative of the mapping function is

$$\omega_j'(\zeta_j) = \frac{R}{2}\left[(1 - i\mu_j)e^{-i\zeta_j} + (1 + i\mu_j)e^{i\zeta_j}\right], \qquad j = 1,2 \tag{2-73}$$

The inverse of the induced mapping functions is

$$\zeta_j = \omega_j^{-1}(z_j) = -i \ln\left(i\frac{z_j \pm \sqrt{z_j^2 - R^2(1 + \mu_j^2)}}{R(1 + i\mu_j)} \right), \qquad j = 1,2 \tag{2-74}$$

The branch of the square root in equation (2-74) is chosen such that $Im\ \zeta_j \geq 0$ for $j = 1,2$.

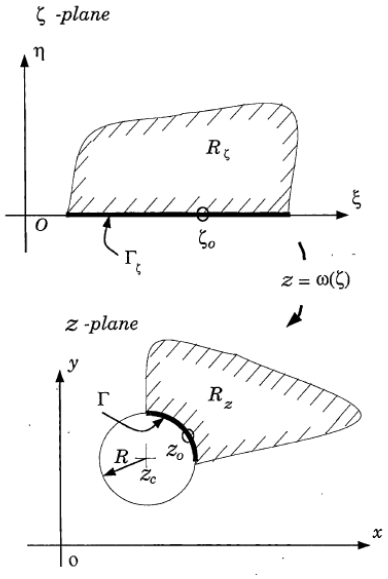

Figure 2-3: Conformal mapping for a circular boundary.

For a region adjacent to a circular cutout, fillet, or notch of radius R, the following function [50]

$$z_j = \omega_j(\zeta_j) = \frac{R}{2}\left[(1 - i\mu_j)\zeta_j + \frac{1 + i\mu_j}{\zeta_j}\right], \qquad j = 1,2 \tag{2-75}$$

maps the region of the exterior of a unit circle, R_ζ, of the ζ-plane into the region R_z of the z-physical plane, Figure 2-4. The derivative of the mapping function is

$$\omega_j'(\zeta_j) = \frac{R}{2}\left[(1 - i\mu_j) - \frac{1 + i\mu_j}{\zeta_j^2}\right], \qquad j = 1,2 \tag{2-76}$$

The inverse of the induced mapping functions is

$$\zeta_j = \omega_j^{-1}(z_j) = \frac{z_j \pm \sqrt{z_j^2 - R^2(1 + \mu_j^2)}}{R(1 - i\mu_j)}, \qquad j = 1,2 \tag{2-77}$$

The branch of the square root in equation (2-77) is chosen such that $|\zeta_j| \geq 1$ for $j = 1,2$.

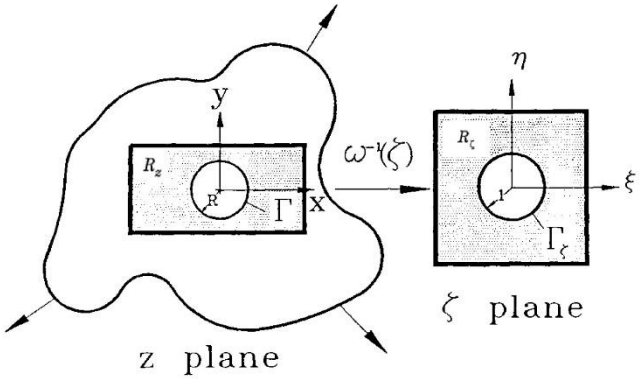

Figure 2-4: Mapping circular cutout in the physical z-plane into exteior region of a unit circle in ζ-plane.

2.4.2.2 Elliptical Shape

For a region adjacent to a traction-free elliptical edge, the following function maps the region R_ζ of the ζ-plane into region R_z of the z-physical plane where Γ_ζ is a section of the real axis of the ζ-plane, Figure 2-5. [12]

$$z = \omega(\zeta) = \frac{a + b}{2}\left(\frac{i - \zeta}{i + \zeta}\right) + \frac{a - b}{2}\left(\frac{i + \zeta}{i - \zeta}\right) + z_c \tag{2-78}$$

Quantities a and b are the lengths of major (parallel to x-direction) and minor (parallel to y-direction) axes of the ellipse, respectively, and z_c $(= x_c + iy_c)$ is the center of the ellipse. For

convenience, the origin of the coordinate system is chosen at the center of the ellipse, i.e., $z_c = 0$. Substituting equation (2-78) into $z_j = x + \mu_j y$ produces

$$z_j = \omega_j(\zeta_j) = \frac{a - ib\mu_j}{2}\left(\frac{i - \zeta_j}{i + \zeta_j}\right) + \frac{a + ib\mu_j}{2}\left(\frac{i + \zeta_j}{i - \zeta_j}\right), \qquad j = 1,2 \tag{2-79}$$

The derivative of the mapping function is

$$\omega_j'(\zeta_j) = -i\frac{a - ib\mu_j}{(i + \zeta_j)^2} + i\frac{a + ib\mu_j}{(i - \zeta_j)^2}, \qquad j = 1,2 \tag{2-80}$$

and the inverse of the induced mapping functions is

$$\zeta_j = \omega_j^{-1}(z_j) = i\frac{a - ib\mu_j - \left(z_j \pm \sqrt{z_j^2 - a^2 - b^2\mu_j^2}\right)}{a - ib\mu_j + \left(z_j \pm \sqrt{z_j^2 - a^2 - b^2\mu_j^2}\right)}, \qquad j = 1,2 \tag{2-81}$$

The branch of the square root in equation (2-81) is chosen such that $Im\ \zeta_j \leq 0$ for $j = 1,2$.

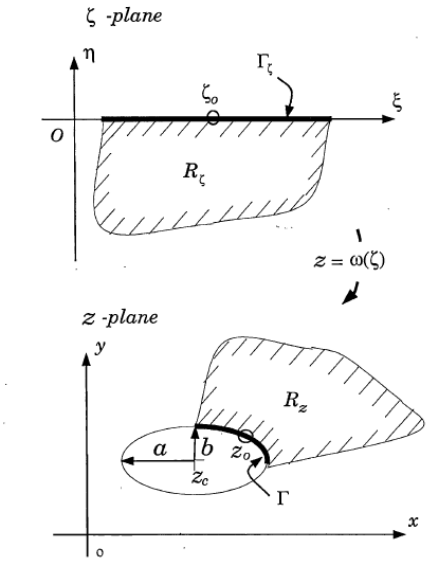

Figure 2-5: Conformal mapping for an elliptical boundary.

For a region adjacent to an elliptical boundary, the following function [50]

$$z = \omega(\zeta) = \frac{a-b}{2}\zeta + \frac{a+b}{2\zeta} + z_c \tag{2-82}$$

maps the unit circle and its exterior in region R_ζ of the ζ-plane into the corresponding elliptical hole and its exterior in region R_z of the z-physical plane. A physical elliptical hole has major and minor radii a and b in the x- and y-directions, respectively, and its center is located at $z_c\ (= x_c + iy_c)$. For orthotropic material such that a region adjacent to an elliptical hole of major radius a and minor radius b, the following function using $z_j = x + \mu_j y$ [50]

$$z_j = \omega_j(\zeta_j) = \frac{a + ib\mu_j}{2}\frac{1}{\zeta_j} + \frac{a - ib\mu_j}{2}\zeta_j, \qquad j = 1,2 \tag{2-83}$$

maps the region of a unit circle, R_ζ, in the ζ-plane into the region R_z in the z-physical plane. The derivative of the mapping function is

$$\omega_j'(\zeta_j) = \frac{a - ib\mu_j}{2} - \frac{a + ib\mu_j}{2}\frac{1}{\zeta_j^2}, \qquad j = 1,2 \tag{2-84}$$

The inverse of the induced mapping functions is

$$\zeta_j = \omega_j^{-1}(z_j) = \frac{z_j \pm \sqrt{z_j^2 - a^2 - \mu_j^2 b^2}}{a - ib\mu_j}, \qquad j = 1,2 \tag{2-85}$$

The branch of the square root in equation (2-85) is chosen such that $|\zeta_j| \geq 1$ for $j = 1,2$.

2.4.3 Mapping Collocation

Using the concept of analytic continuity, the finite Taylor series expansion of the stress function is

$$\Phi(\zeta_1) = \sum_{j=0}^{N} A_j(\zeta_1 - \zeta_0)^j \tag{2-86}$$

whereas the stress function expressed as Laurent series expansion is

$$\Phi(\zeta_1) = \sum_{\substack{j=-N \\ j\neq 0}}^{N} A_j \zeta_1^j \tag{2-87}$$

where $A_j = a_j + ib_j$ are the unknown complex coefficients (a_j and b_j are both real numbers) and ζ_0 is some point on the traction-free boundary. The $j = 0$ term in Laurent expansion contributes to rigid-body motion and can be omitted. For orthotropic composite whose complex parameters are purely imaginary when directions of material symmetry are parallel and perpendicular to the applied load, symmetry about horizontal and vertical directions require that only real and odd terms be retained in the Laurent expansions. Substituting equation (2-86) or (2-87) into (2-68) yields

$$\Psi(\zeta_2) = \sum_{j=0}^{N} \left(\bar{A}_j B + A_j C\right)(\zeta_2 - \zeta_0)^j \tag{2-88}$$

when using a Taylor series while for a Laurent expansion it is

$$\Psi(\zeta_2) = \sum_{\substack{j=-N \\ j\neq 0}}^{N} \left(\bar{A}_j B \zeta_2^{-j} + A_j C \zeta_2^j\right) \tag{2-89}$$

$\bar{A}_j$ is a complex conjugate of A_j. At least for a finite simply-connected region R_ζ, $\Phi(\zeta_1)$ is a single-valued analytic function. Upon combining equations (2-54) through (2-88), one obtains the following expressions for the stresses if using a Taylor series,

$$\sigma_{xx} = 2\sum_{j=1}^{N} Re\left\{\left[\frac{j\mu_1^2}{\omega_1'(\zeta_1)}(\zeta_1-\zeta_0)^{j-1} + \frac{j\mu_2^2 C}{\omega_2'(\zeta_2)}(\zeta_2-\zeta_0)^{j-1}\right]A_j + \left[\frac{j\mu_2^2 B}{\omega_2'(\zeta_2)}(\zeta_2-\zeta_0)^{j-1}\right]\bar{A}_j\right\} \tag{2-90}$$

$$\sigma_{yy} = 2\sum_{j=1}^{N} Re\left\{\left[\frac{j}{\omega_1'(\zeta_1)}(\zeta_1-\zeta_0)^{j-1} + \frac{jC}{\omega_2'(\zeta_2)}(\zeta_2-\zeta_0)^{j-1}\right]A_j + \left[\frac{jB}{\omega_2'(\zeta_2)}(\zeta_2-\zeta_0)^{j-1}\right]\bar{A}_j\right\} \tag{2-91}$$

$$\sigma_{xy} = -2\sum_{j=1}^{N} Re\left\{\left[\frac{j\mu_1}{\omega_1'(\zeta_1)}(\zeta_1-\zeta_0)^{j-1} + \frac{j\mu_2 C}{\omega_2'(\zeta_2)}(\zeta_2-\zeta_0)^{j-1}\right]A_j + \left[\frac{j\mu_2 B}{\omega_2'(\zeta_2)}(\zeta_2-\zeta_0)^{j-1}\right]\bar{A}_j\right\} \tag{2-92}$$

Introducing the Taylor series according to equation (2-86), the measured displacement data u and v can be expressed as

$$u = 2\sum_{j=0}^{N} Re\left\{\left[p_1(\zeta_1-\zeta_0)^j + p_2 C(\zeta_2-\zeta_0)^j\right]A_j + p_2 B(\zeta_2-\zeta_0)^j\bar{A}_j\right\} \tag{2-93}$$

$$v = 2\sum_{j=0}^{N} Re\left\{\left[q_1(\zeta_1-\zeta_0)^j + q_2 C(\zeta_2-\zeta_0)^j\right]A_j + q_2 B(\zeta_2-\zeta_0)^j\bar{A}_j\right\} \tag{2-94}$$

Upon combining equations (2-54) through (2-89) when using a Laurent series, the individual stresses can be expressed as

$$\sigma_{xx} = 2\sum_{\substack{j=-N,\dots \\ j\neq 0}}^{N} Re\left\{j\left[\frac{\mu_1^2{\zeta_1}^{j-1}}{\omega_1'(\zeta_1)} + \frac{C\mu_2^2{\zeta_2}^{j-1}}{\omega_2'(\zeta_2)}\right]A_j - j\mu_2^2 B\left[\frac{{\zeta_2}^{-j-1}}{\omega_2'(\zeta_2)}\right]\bar{A}_j\right\} \tag{2-95}$$

$$\sigma_{yy} = 2 \sum_{\substack{j=-N,\dots \\ j\neq 0}}^{N} Re\left\{ j\left[\frac{{\zeta_1}^{j-1}}{\omega_1'(\zeta_1)} + \frac{C{\zeta_2}^{j-1}}{\omega_2'(\zeta_2)}\right] A_j - jB\left[\frac{{\zeta_2}^{-j-1}}{\omega_2'(\zeta_2)}\right]\bar{A}_j \right\} \tag{2-96}$$

$$\sigma_{xy} = -2 \sum_{\substack{j=-N,,\dots \\ j\neq 0}}^{N} Re\left\{ j\left[\frac{\mu_1{\zeta_1}^{j-1}}{\omega_1'(\zeta_1)} + \frac{C\mu_2{\zeta_2}^{j-1}}{\omega_2'(\zeta_2)}\right] A_j - j\mu_2 B\left[\frac{{\zeta_2}^{-j-1}}{\omega_2'(\zeta_2)}\right]\bar{A}_j \right\} \tag{2-97}$$

Upon introducing the Laurent series according to equation (2-87), the measured displacement data u^* and v^* can be expressed as

$$u = 2 \sum_{\substack{j=-N,\dots \\ j\neq 0}}^{N} Re\left\{\left[p_1{\zeta_1}^{j} + p_2 C{\zeta_2}^{j}\right]A_j + p_2 B{\zeta_2}^{-j}\bar{A}_j\right\} \tag{2-98}$$

$$v = 2 \sum_{\substack{j=-N,\dots \\ j\neq 0}}^{N} Re\left\{\left[q_1{\zeta_1}^{j} + q_2 C{\zeta_2}^{j}\right]A_j + q_2 B{\zeta_2}^{-j}\bar{A}_j\right\} \tag{2-99}$$

The only unknowns in these expressions for the stresses and displacements are the complex coefficients $A_j = a_j + ib_j$, the other quantities involve geometry (location) or material properties. It should be noted that by using conformal mapping and analytic continuation techniques, equations (2-92) through (2-97) imply that the stresses satisfy equilibrium and traction-free conditions in the adjacent portion of the entire boundary. However, unlike a classical boundary-value problem where one would typically evaluate the unknown coefficients, A_j, by satisfying the boundary and conditions around the entire shape, one can use some combination of the measured stresses of equations (2-92) through (2-97) from the interior of the region R^* of interest to determine these unknown coefficients, A_j. Additional known boundary conditions can also be imposed at discrete locations. The concept of collecting measured data in a region R^* adjacent to an edge Γ, mapping R_z onto R_ζ such that Γ is mapped onto either $\eta = 0$ or the unit

circle in the ζ-plane whereby the traction-free conditions on Γ are satisfied continuously, relating the two complex stress functions to each other, plus satisfying other loading conditions discretely on the boundary of the component beyond Γ will be referred to as the mapping-collocation technique.

2.4.3.1 Determining Coefficients from Thermoelastic Data

The complex coefficients, A_j, can be determined by measured thermoelastic data. Choosing for example the y-axis parallel to the strongest, stiff direction, i.e., 1-direction of an orthotropic composite material and introducing the Taylor series according to equation (2-86), the TSA signal S^* can be expressed as

$$\begin{aligned} S^* &= K_1\sigma_{yy} + K_2\sigma_{xx} \\ &= 2\sum_{j=1}^{N} Re\left\{\left[\frac{j(K_1+K_2\mu_1^2)}{\omega_1'(\zeta_1)}(\zeta_1-\zeta_0)^{j-1}\right.\right. \\ &\left. + \frac{j(K_1+K_2\mu_2^2)C}{\omega_2'(\zeta_2)}(\zeta_2-\zeta_0)^{j-1}\right]A_j \\ &\left. + \left[\frac{j(K_1+K_2\mu_2^2)B}{\omega_2'(\zeta_2)}(\zeta_2-\zeta_0)^{j-1}\right]\bar{A}_j\right\} \end{aligned} \tag{2-100}$$

Upon introducing the Laurent series according to equation (2-87), the thermoelastic data S^* becomes

$$S^* = K_1\sigma_{yy} + K_2\sigma_{xx}$$

$$= 2\sum_{\substack{j=-N,-N+2,\dots \\ j\neq 0}}^{N} Re\left\{\left[\frac{j(K_1+K_2\mu_1^2)}{\omega_1'(\zeta_1)}{\zeta_1}^{j-1}\right.\right. \tag{2-101}$$

$$\left.\left.+\frac{j(K_1+K_2\mu_2^2)C}{\omega_2'(\zeta_2)}{\zeta_2}^{j-1}\right]A_j - \left[\frac{j(K_1+K_2\mu_2^2)B}{\omega_2'(\zeta_2)}{\zeta_2}^{-j-1}\right]\bar{A}_j\right\}$$

The interior thermoelastic data, S^*, at m different locations are chosen to be inside the region R^* with other q known stress or displacement conditions (in terms of σ_{xx}, σ_{yy}, σ_{xy}, u or v) at discrete points along the boundary. Equations (2-100) and (2-101) each forms a system of simultaneous linear equations, $[M]_{(m+q)\times 2N}\{c\}_{2N\times 1} = \{S^*\}_{(m+q)\times 1}$, where matrix $[M]$ consists of analytical expression of S^* and other expression of the known stress conditions, vector $\{c\} = \{a_1, b_1, a_2, b_2, \dots, a_N, b_N\}$ has $2N$ unknown real coefficients (a_j and b_j) and vector $\{S^*\}$ has m thermoelastic values and q discrete points with known stress conditions such that $m + q \gg 2N$. The best values of the coefficients A_j, in a least-squares numerical sense, can be determined from measured values of S^*.

2.4.3.2 Determining Coefficients from Displacement Data

The interior displacement data, u^* or v^*, at m different locations are chosen to be inside the region R^* with other q known stress or displacement conditions (in term of σ_{xx}, σ_{yy}, σ_{xy}, u or v) at discrete points along the boundary. Equations (2-93) through (2-99) each forms a system of simultaneous linear equations, $[U]_{(m+q)\times 2N}\{c\}_{2N\times 1} = \{U^*\}_{(m+q)\times 1}$, where matrix $[U]$ consists of analytical expression of displacement component u^* and/or v^* and other expression of the known stress conditions, vector $\{c\} = \{a_1, b_1, a_2, b_2, \dots, a_N, b_N\}$ has $2N$ unknown real coefficients (a_j and b_j) and vector $\{U^*\}$ includes m measured displacement values of u^* and/or v^* and q discretely imposed stress/displacement conditions such that $m + q \gg$

$2N$. The best values of the coefficients A_j, in a least-squares numerical sense, can then be determined.

The variables $\zeta_j = \xi + \mu_j\eta$, in equations (2-90) through (2-101) are related to the physical locations $z = x + iy$ through the inverse mapping function $z_j = \omega_j(\zeta_j)$. The individual stresses then are known throughout the region R_z, including on the traction-free edge Γ from equations (2-90) through (2-92) if using Taylor expansion or from equations (2-95) through (2-97) if using Laurent expansion. The number of term, N, to retain in the stress function was selected by evaluating the difference between the magnitude of experimentally based thermoelastic data or displacement data and those predicted by the present hybrid method by using root mean square approach. The technique is applicable for both isotropic and orthotropic materials, and simultaneously smooths the measured information and evaluates the stress along a traction-free boundary. The mapping-collocation method can be applied to isotropic material by letting $K_1 = K_2 = K$, $E = E_{11} \approx E_{22}$, $\nu_{12} = \nu$ and $G_{12} = G = E/2(1+\nu)$.

2.5 Literature Review in Complex Mapping Collocation Technique

Relatively little literature exists utilizing conformal mapping related to determining the full-field stresses from measured data and traction-free boundary. Lin and Rowlands (1995) evaluated the individual stress components on the edges of, and within, a notched orthotropic graphite/epoxy laminated plate in addition of applying other boundary conditions and axis of symmetry [12]. Lin mapped the free-traction boundary to the real axis of the ζ-plane and provided conformal mapping for a variety of geometries such as straight edges, circular openings, elliptical openings, and notches and used Taylor series expansion to represent the analytical stress functions. Their analysis suffered from not having a systematic means of determining how many Airy coefficients to retain. Rhee and Rowlands [13] evaluated the individual stress

components on the edge of a circular hole and determined stress intensity factors for plate with a crack. Huang and Rowlands (1991) provided a different coordinate system of the real z-plane and the mapped ζ-plane from Lin [59]. They studied a ring shape above a traction-free central hole in an infinite isotropic tensile plate and used theoretical trace of the stress tensor (isopachic) as input data superimposed with generated random noise.

Beak and Rowlands (1999, 2001, 2008) used conformal mapping with moiré input data [42] and biaxial strain gaga data [43] (4 single-element, 2 two-element, and 2 three-element strain gages) located within the region $2 \leq r/R \leq 2.9$ where r is the distance from the hole and R is the hole radius to determine full-field stresses by representing their functions explicitly by Laurent expansions [42,43,60]. They (2001) used 14 measured input data from strain gages in addition to other boundary condition and axis of material symmetry to evaluate the 18 coefficients of the stress function [43]. When the number of measured input strains is equal to approximately twice the number of unknown coefficients, all hybrid-computed stress concentration factors are within 5 percent of that measured directly using strain gage. Chen (1995) used conformal mapping technique to map an elliptical hole from real z axis to a unit circle of the ζ-plane and used a Laurent expansion to approximate stress functions [61]. Rhee and Rowlands (1996) solved for the full-field stress around a variety of geometries, including multiple elliptical holes, single holes, and individual cracks by mapping the boundary of the physical plane to the unit circle in the ζ-plane [62]. Lin, Feng, and Rowlands (1997) considered a loaded plate with a crack, using a J-integral method, and they mapped the boundary of the crack to the real axis and used a truncated Taylor series expansion to approximate the relevant stress functions [63]. Ju and Rowlands (2003) determined stress intensity factors for inclined cracks in a uniaxially-loaded orthotropic graphite epoxy composite using measured temperatures and least-squares [14,8]. Beak et al. (2008, 2010) used this approach to determine the full-field stress around a circular hole using only nine single component of displacement input from using laser

speckle to determine the unknown series coefficients of the stress functions (Laurent series) [45,60]. Their solution [60] contains some errors in their equations and this thesis provides a consistent set of equations free of errors.

Lin at al (1999) discusses the methods of combining experimental information with numerical and/or theoretical concepts to stress analyze isotropic and orthotropic components using mapping-collocation method approach [4].

2.6 Stress Concentrations

The stress concentration factor (SCF) is defined as the ratio of the maximum stress to the nominal stress in a net cross section of the part

$$K^t = \frac{\sigma_{max}}{\sigma_{net}} \tag{2-102}$$

The stress concentration factor for a circular hole in infinite isotropic plate is 3. The stress concentration factor for a free-load circular hole in anisotropic plate when the applied load is in the y-direction is

$$K_{oc}^t = \frac{\sigma_y(R,0)}{\sigma_0} = 1 + Re\left[\frac{i(\beta+\delta)}{\beta\delta}\right] \tag{2-103}$$

The SCF for an unidirectional fiber oriented plate with an elliptical hole and fiber orientation parallel to the loading direction as well as the minor axis is defined by

$$K_{oe}^t = 1 + \frac{a}{b} Re\left[\frac{\beta+\delta}{\beta\delta}\right] \tag{2-104}$$

The maximum stress location is at the base of the elliptical hole. For a finite width plate, the stress concentration factor can be calculated using finite-width correlation (FWC) factor. FWC factor is a scale factor defined as the stress concentration factor of infinite to a finite-width

plate with similar opening and material. FWC factor for isotropic materials is independent of material properties thus can be determined accurately by use of curve fitting technique. Whereas in orthotropic material, this factor must be obtained with stress analysis by use of elasticity equations or mainly using finite element methods. For an orthotropic and isotropic rectangular plate with length $2L$ and width $2W$ with elliptical opening of major radius a and minor radius b under action of unidirectional axial load (loading applied parallel to minor radius b and perpendicular to a and W), Figure 2-6, the FWC for $a/W \leq 0.9$ is [64,65]

$$FWC = \frac{K_\infty^t}{K^t} = \frac{\lambda^2}{(1-\lambda)^2} + \frac{1-2\lambda}{(1-\lambda)^2}\sqrt{1+(\lambda^2-1)\left(\frac{a}{W}M\right)^2} - \frac{\lambda^2}{1-\lambda}\frac{\left(\frac{a}{W}M\right)^2}{\sqrt{1+(\lambda^2-1)\left(\frac{a}{W}M\right)^2}} + \frac{\lambda^7}{2}\left(\frac{a}{W}M\right)^6\left(K_T^\infty - 1 - \frac{2}{\lambda}\right)\left[\frac{1+(\lambda^2-2)\left(\frac{a}{W}M\right)^2}{\sqrt{\left(1+(\lambda^2-1)\left(\frac{a}{W}M\right)^2\right)^7}}\right] \tag{2-105}$$

$$M^2 = \frac{\sqrt{1-8\left[\frac{3\left(1-\frac{a}{W}\right)}{2+\left(1-\frac{a}{W}\right)^3}-1\right]}-1}{2\left(\frac{a}{W}\right)^2}, \qquad \lambda = \frac{a}{b}$$

The magnification factor, M, is only function of a/W and is independent of material properties.

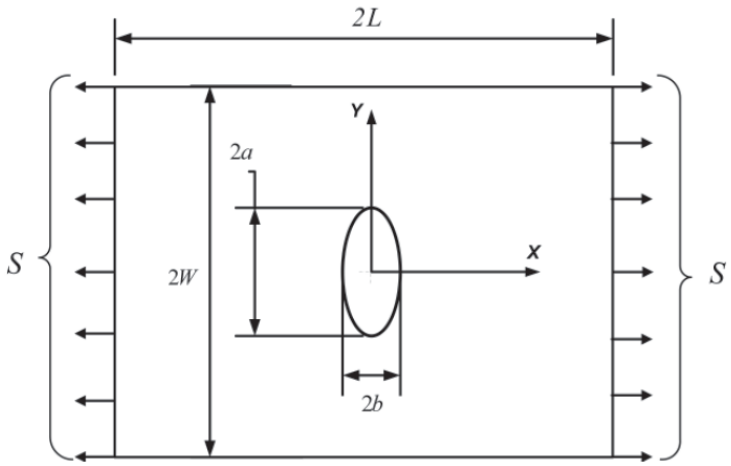

Figure 2-6: A finite-width plate with central elliptical opening.

Chapter 3: Thermoelastic Stress Analysis of a Finite Orthotropic Containing an Elliptical Hole

Individual stresses and displacements in a finite graphite/epoxy laminated composite containing an elliptical hole and loaded in the fiber direction are determined from recorded load-induced thermal information. In a cyclically loaded orthotropic composite, the temperature variation is proportional to a linear combination of the changes in the normal stresses in the direction of material symmetry. Equilibrium and compatibility conditions throughout the region are satisfied using complex variable formulation, conformal mappings and analytic continuation. Processing the measured thermal data with a stress function simultaneously smooths the measured data and evaluates the individual stress components, including on the edge of the hole. Reliability of experimental results is demonstrated by finite element method (FEM) and force equilibrium.

3.1 Introduction

Composite materials enjoy favorable specific strength and stiffness. Machine and structural members frequently contain holes or notches which produce stress concentrations. Purely analytical or theoretical stress analyses tend to be available for only simple situations involving infinite geometries, whereas many practical problems involve complicated, finite shapes. Moreover, and like numerical (finite element method, finite difference method) approaches, analytical/theoretical analyses depend on reliable knowledge of the boundary conditions. The latter are often unknown in practice. Recognizing these situations, it is advantageous to be able to stress analyze experimentally members made of orthotropic composite materials. The thermoelastic stress analysis (TSA) technique does not necessitate knowing the applied loads; in

fact, the loads can be determined. Such a feature suggests inverse capability. Candidate experimental approaches include moiré, speckle, holography, grids and digital image correlation. However, such displacement-based techniques necessitate differentiating the recorded data, something which can be unreliable. On the other hand, TSA provides the stresses directly, without having to differentiate the measured information.

Besides the fundamental interest in elliptical openings such that, when one axis collapses, the hole becomes a crack, windows in passenger aircrafts are often elliptical in shape, elliptical holes are employed to accommodate members having an elliptical cross section, elliptical access manholes and their covers are used in structures such as pressure vessels, and elliptical openings occur with nonperpendicular nozzles in pressure and nuclear vessels. That the external boundary conditions of these situations are often unknown virtually eliminates the prospects of determining the associated stresses theoretically or numerically. Acknowledging the prevalence of elliptical cutouts in structures such as aerospace and transportation vehicles, and pressure vessels, this chapter demonstrates the ability to determine the stresses in an elliptically perforated orthotropic composite member by TSA. The approach satisfies equilibrium and compatibility throughout the region using complex variable formulation. This mapping-collocation technique enhances reliability of thermoelastic edge information, smooths the interior thermoelastic data, and determines individual stresses throughout the composite structure. Experimental reliability is demonstrated by FEM and force equilibrium.

Having substantiated the numerical reliability and robustness of the least-squares method using ‘simulated’ thermoelastic input data, and assessed the influence of variations in the various parameters, the method was applied to an actual tensile composite containing elliptical hole using recorded load-induced temperature information. The author is unaware of prior utilization of mapping and complex variables to experimentally evaluate the stresses of a loaded composite material with elliptical hole using thermoelastic data.

3.2 Literature Review

Stanley and Chan [66] solved the restrictive case of a composite cylinder whose stresses are known from thin pressure-vessel theory, whereas Kageyama et al [67,68] analyzed a graphite/epoxy composite containing a circular hole. Their method, while adequate for determining the stresses transverse to the fibers, seems to be otherwise unrealistic. Some of their results are unreliable. Wong [69] proposed a non-adiabatic concept for stress analyzing orthotropic composites. The approach suffers from experimental scatter and fails to address the problem of unreliable edge information. Feng et al. [11] determined the stresses across the net section of a tensile composite strip containing a central circular hole. Although effective for this simple case, their approach is confined a long a line so the technique employed is not readily adaptable to general situations. Lin and Rowlands [12] evaluated the stresses in a notched laminate. Their analysis suffered from not having a systematic means of determining how many coefficients to retain. Khaja, Samad and Rowlands recently obtained the individual stresses in elliptically-perforated aluminum plates, but the their method is not applicable for orthotropy [25,38].

This study presents a nondestructive and non-contacting hybrid method for determining the full-field individual stresses in a finite orthotropic tensile plate containing an elliptical hole. This contribution extends the thermoelastic technique into a practical quantitative tool for stress analyzing actual orthotropic composite engineering structures in their operating environment. This is accomplished by combining traditional TSA with complex variable along with analytically imposing traction-free boundary conditions on the edge of the elliptical hole. In view of previously mentioned disadvantages of the FEA, analytical and some experimental approaches, this chapter demonstrate the ability to determine the separate components of stress in an elliptically-perforated finite orthotropic plate by hybridizing a TSA data with Airy stress function in complex variables and thus making use of TSA's advantage of providing the exact boundary and loading conditions.

3.3 General Comments

This chapter demonstrates the ability to determine the individual components of stresses and displacements by processing load-induced thermal information from TSA with a series representation of the Airy stress function in complex variables for orthotropic materials. The present case of a loaded plate containing an elliptical hole used firstly simulated experimental input from exact solution before employing actual thermoelastic data in order to substantiate the viability, robustness, and numerical stability of the desired numerical method. Once the reliability and robustness of the method were verified, it was used then to analyze the stresses in a finite orthotropic structure containing an elliptical hole using measured thermoelastic data. The method first assessed using exact theoretical input values of S^* which were obtained from the exact solution for an infinite orthotropic plate containing an elliptical hole. The stress function was represented by a Taylor series expansion and the elliptical hole in the physical plane was mapped into a real axis ($\eta = 0$) in the ζ-plane.

The measured TSA data, which are digitalized in a matrix form, were combined with the Airy stress function to determine the stress components in finite structures, whose distant geometry or loading is not well known. The unknown coefficients are determined using least-squares. Although the recorded thermoelastic data at, and adjacent to, an edge are unreliable and raw thermoelastic information in composites is inherently noisy, the present technique overcomes these challenges by avoiding the use of recorded data on and near edges and processing the measured interior data with a stress function employing complex variables, mapping and analytic continuation. A precaution should be taken in dealing with edge data to increase the results quality and determine the stress concentration. The resulting TSA-determined stresses are available on and in the neighborhood of the edge of the hole without knowing the

distant geometry or boundary conditions. The traction-free conditions on the boundary of the elliptical hole are satisfied analytically.

3.4 Numerical Experiment for Infinite Orthotropic Plate with Elliptical Hole

The mapping-collocation technique based on complex variables of Airy stress function was first assessed using exact theoretical input values of $S^* = K_1\Delta\sigma_{xx} + K_2\Delta\sigma_{yy}$ which were obtained from the exact solution [57]. The determined stresses from processing exact theoretical input values of S^* with mapping collocation technique will be compared subsequently with those evaluated directly by the exact solution and finite element from ANSYS to assess the validity of the described approach. A region R_z adjacent to the elliptical boundary Γ of Figure 3-1 is considered. The input thermoelastic data near the traction-free boundary were disregarded and only region R^* was used to simulate a situation in which the experimental boundary data are unreliable. To simulate a real situation when using actual measured data which tends to be noisy, a study was therefore conducted involving random noise superimposed on the exact theoretical solution as input S^*. The random noise which is ± 10 percent of the uniform far-field applied load, σ_0, was generated by random number generator in the computer complier. Once the reliability and robustness of the method was verified, it was used to stress analyze a finite orthotropic structure containing an elliptical hole using measured thermoelastic data.

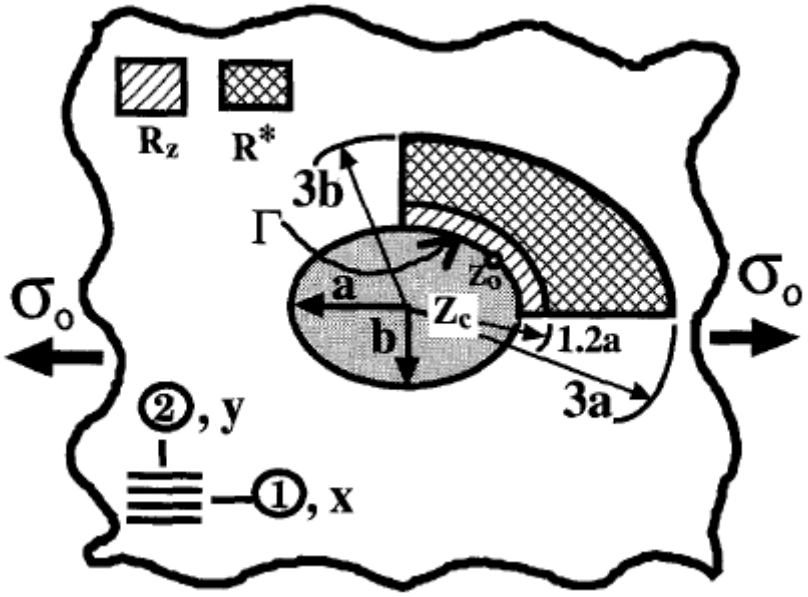

Figure 3-1: Infinite [0/90/0_{10}/90/0] glass/epoxy composite plate containing an elliptical hole loaded in x-direction.

3.4.1 Exact Solution

An infinite [0/90/0_{10}/90/0] glass/epoxy tensile orthotropic composite material with mechanical properties (E_{11} = 34.2 GPa, E_{22} = 14.1 GPa, G_{12} = 3.4 GPa, ν_{12} = 0.22; thermomechanical coefficients are K_1 = 1.17 mv/MPa and K_2 = 3.09 mv/MPa) containing an elliptical hole (a/b = 2) loaded in the fiber direction (1-direction) was employed in this example. The analytical stress functions for infinite homogeneous anisotropic linear elastic plate with an elliptical hole (major axis $2a$ parallel to x-axis and minor axis $2b$ parallel to y-axis) and subjected to a uniform far field stress of $\sigma_{xx} = \sigma_0$, $\sigma_{yy} = \sigma_{xy} = 0$ are [57]

$$\Phi_0(z_1) = -\frac{ib\sigma_0}{2(\mu_1 - \mu_2)} \cdot \frac{(a - i\mu_1 b)}{\left(z_1 + \sqrt{z_1^2 - a^2 - b^2\mu_1^2}\right)} \tag{3-1}$$

$$\Psi_0(z_2) = \frac{ib\sigma_0}{2(\mu_1 - \mu_2)} \cdot \frac{(a - i\mu_2 b)}{\left(z_2 + \sqrt{z_2^2 - a^2 - b^2\mu_2^2}\right)} \tag{3-2}$$

where $\mu_1 = \alpha + i\beta$, $\mu_2 = \gamma + i\delta$, $\mu_3 = \bar{\mu}_1$, and $\mu_4 = \bar{\mu}_2$. The individual stresses are obtained from

$$\sigma_{xx} = 2Re[\mu_1^2\Phi_0'(z_1) + \mu_2^2\Psi_0'(z_2)] + \sigma_0 \tag{3-3}$$

$$\sigma_{yy} = 2Re[\Phi_0'(z_1) + \Psi_0'(z_2)] \tag{3-4}$$

$$\sigma_{xy} = -2Re[\mu_1\Phi_0'(z_1) + \mu_2\Psi_0'(z_2)] \tag{3-5}$$

The $[0/90/0_{10}/90/0]$ glass/epoxy has purely imaginary and unequal roots of $\mu_1 = 3.059i$ and $\mu_2 = 0.509i$.

3.4.2 Evaluating Number of Coefficients to Employ

The induced mapping functions $\omega_j(\zeta_j)$ of equation (2-79) and its inverse of equation (2-81) are used to evaluate complex coefficients, A_j, using equation (2-100) from S^* defined on a region R^* (not including the free-traction boundary). Then the individual stresses throughout region R_z, including along edge Γ where no input data were employed, are evaluated using equations (2-90) through (2-92). The results of this numerical experiment, based on 150 input values of S^* distributed as shown in Figure 3-2, were used to evaluate 14 complex coefficients, A_j, (28 real coefficients) which can be chosen from plotting root mean square (RMS) values between the actual values of S^* and the reconstructed values of $\{S^*\} = [M]\{c\}$ versus N as shown in Figure 3-3. Values of N ranging from 2 to 20 were used to ascertain the effect of varying the number of terms of the power series representation of the stress function of equation (2-100). The maximum error of predicted values of maximum σ_{xx} agrees within one percent of the maximum theoretical value. The results for σ_{yy} and σ_{xy} are similarly excellent.

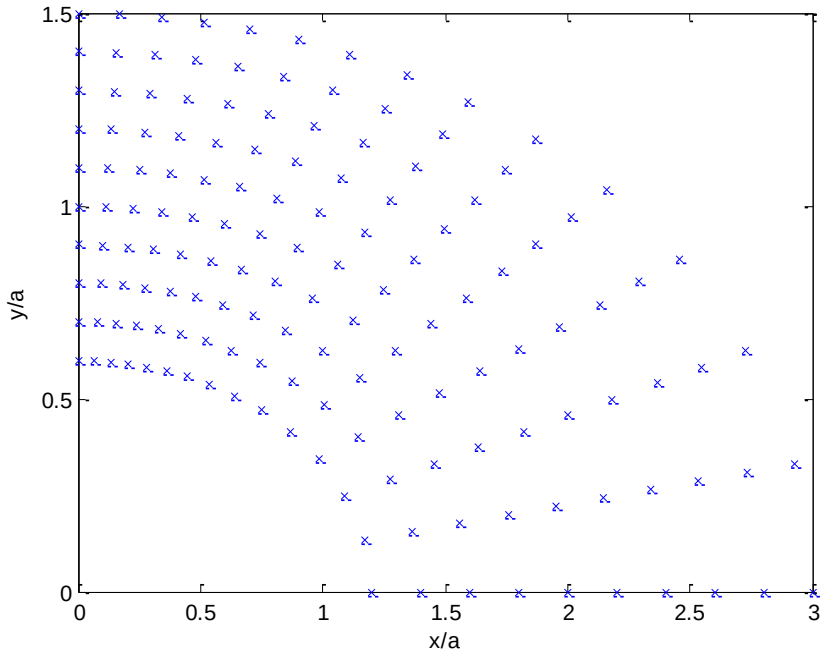

Figure 3-2: Locations of the 150 input values of S^*.

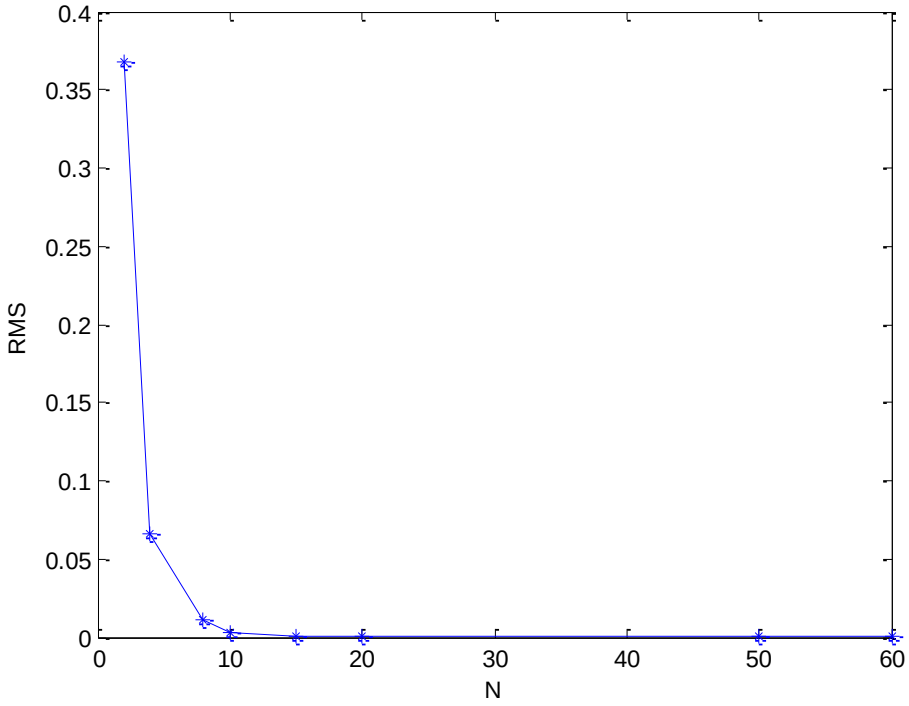

Figure 3-3: RMS versus the number of complex coefficients, N.

3.4.3 Stresses

The results shown in Figure 3-4 through Figure 3-11 demonstrate an excellent agreement with theory. The results of this numerical experiment based on discrete input values of S^* agree virtually exactly with theory throughout region R_z, including along edge Γ where no input values were employed. Figure 3-4 and Figure 3-5 illustrate the normalized longitudinal stress, σ_{xx}/σ_0, and σ_{yy}/σ_0 along the line $x = 0$ in Figure 3-1. Figure 3-6 demonstrates the normalized tangential stress along the traction-free elliptical hole which shows excellent agreement between the present method and exact theoretical solution and FE solution from ANSYS. Even for noisy input data, Figure 3-6 demonstrates that the scheme continues to provide very accurate edge stress around the elliptical boundary where no input S^* data were used. Contour plots of normalized longitudinal, transverse, and shear stresses in region adjacent to the elliptical hole are shown in Figure 3-9 through Figure 3-11, respectively. These results illustrate the ability of the method to provide reliable stresses even with such bad or noisy input data and/or no traction-free boundary data are included. Such numerical experiments employing simulated test data from exact solution help verifying that there are no algebraic errors and substantiate that the system is numerically robust.

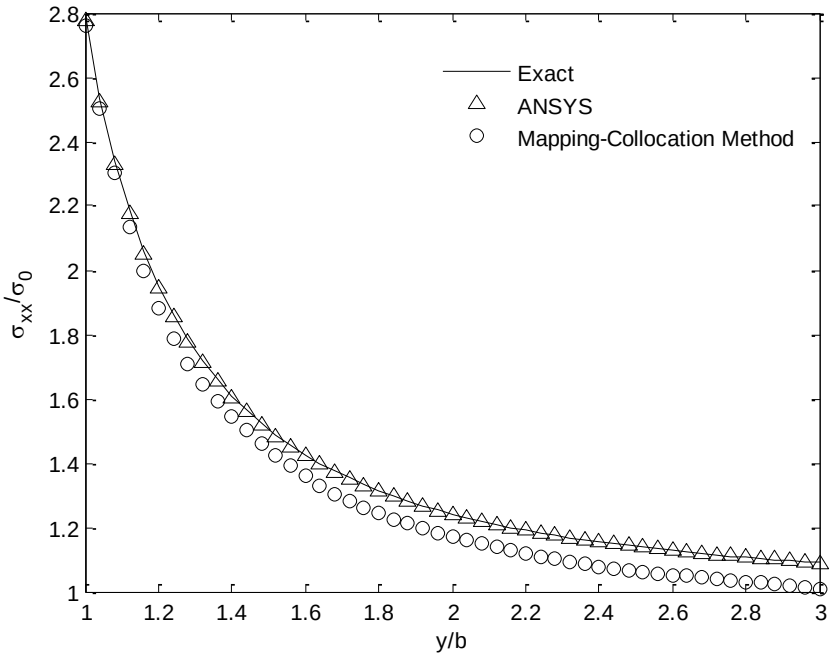

Figure 3-4: Variation of normalized longitudinal stress, σ_{xx}/σ_0, along the line $x = 0$ in Figure 3-1 from present method (28 real coefficients), ANSYS and Savin's exact theoretical solution.

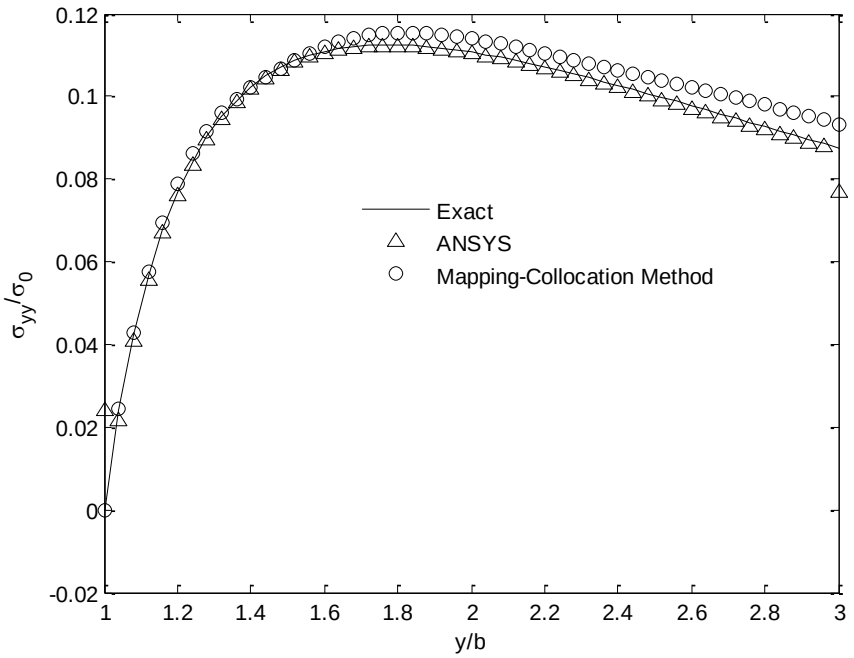

Figure 3-5: Variation of normalized stress σ_{yy}/σ_0 along the line $x = 0$ in Figure 3-1 from present method (28 real coefficients), ANSYS and Savin's exact theoretical solution.

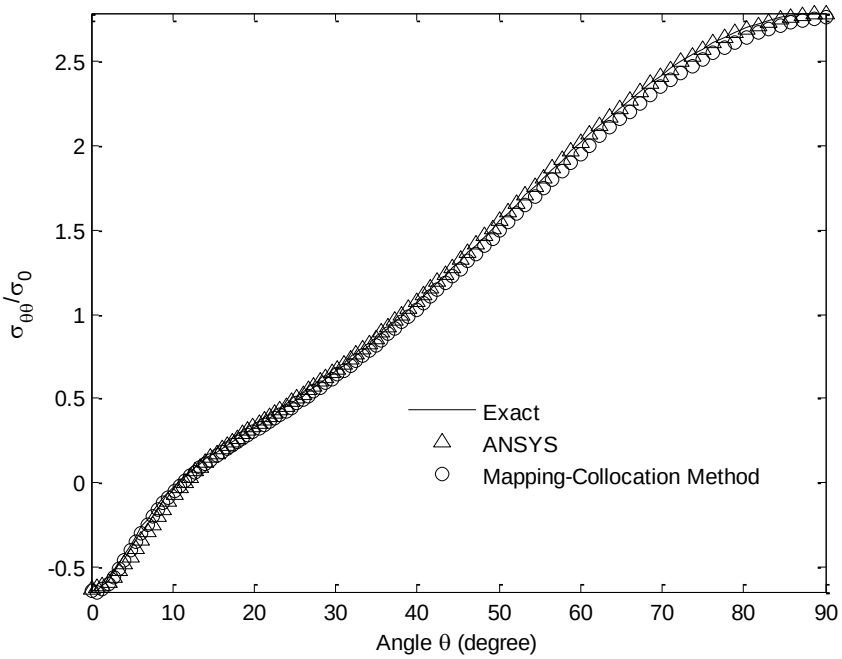

Figure 3-6: Variation of normalized tangential stress, $\sigma_{\theta\theta}/\sigma_0$, along the edge of the elliptical hole from present method (28 real coefficients), ANSYS and Savin's exact theoretical solution.

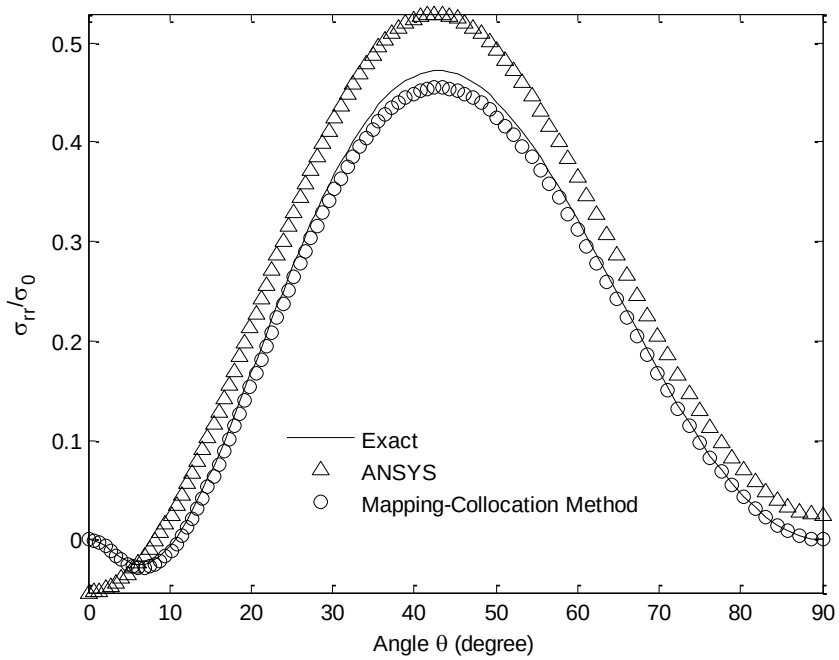

Figure 3-7: Variation of normalized radial stress, σ_{rr}/σ_0, along the edge of the elliptical hole from present method (28 real coefficients), ANSYS and Savin's exact theoretical solution.

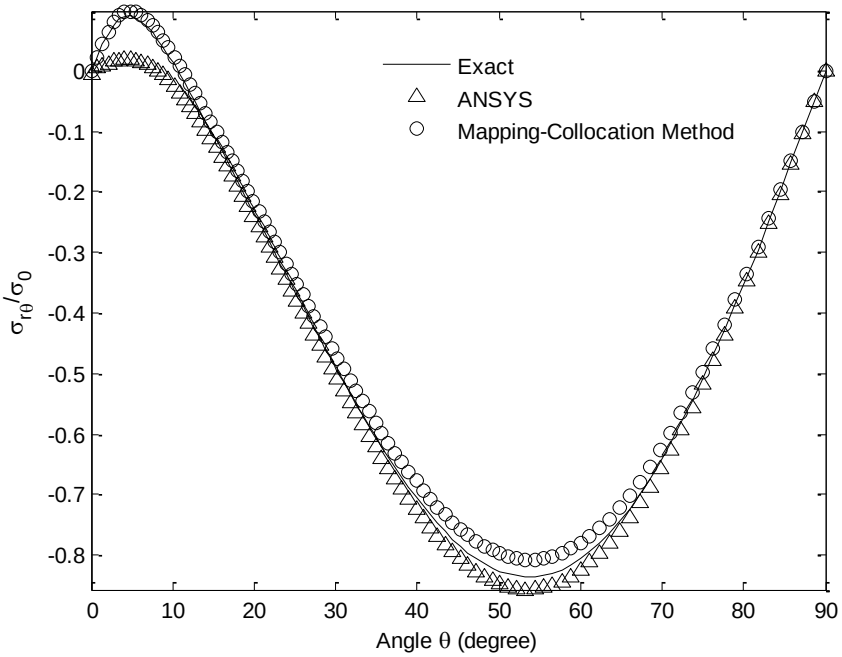

Figure 3-8: Variation of normalized shear stress, $\sigma_{r\theta}/\sigma_0$, in polar coordinate along the edge of the elliptical hole from present method (28 real coefficients), ANSYS and Savin's exact theoretical solution.

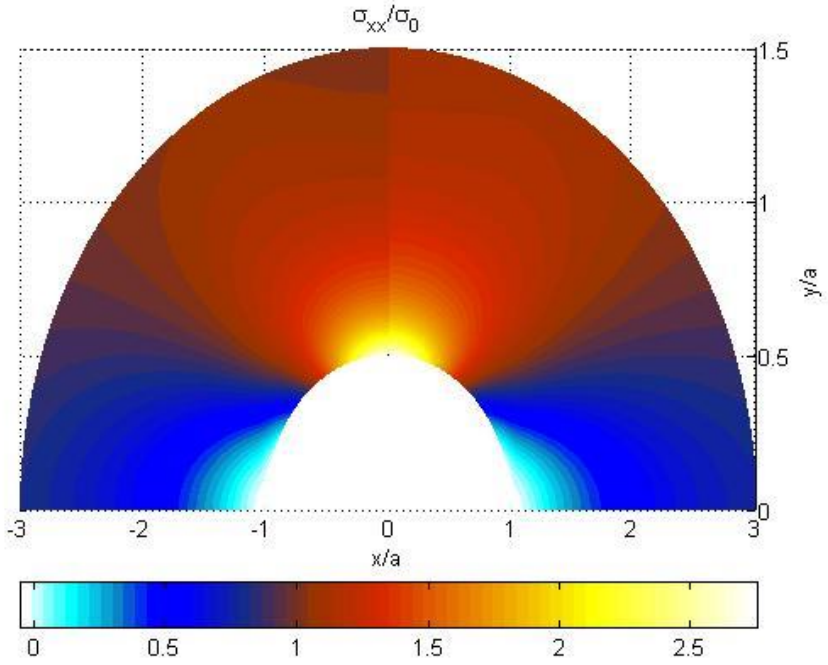

Figure 3-9: Contour plot of normalized stress σ_{xx}/σ_0 in region adjacent to the elliptical hole, Savin's exact theoretical solution (right) and present method using 28 real coefficients (left).

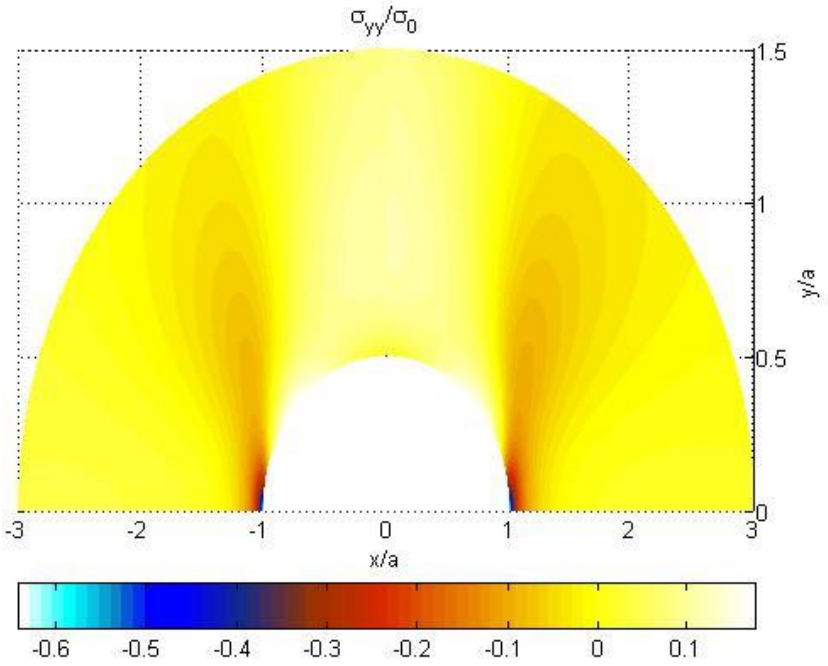

Figure 3-10: Contour plot of normalized stress, σ_{yy}/σ_0 in region adjacent to the elliptical hole, Savin's exact theoretical solution (right) and present method using 28 real coefficients (left).

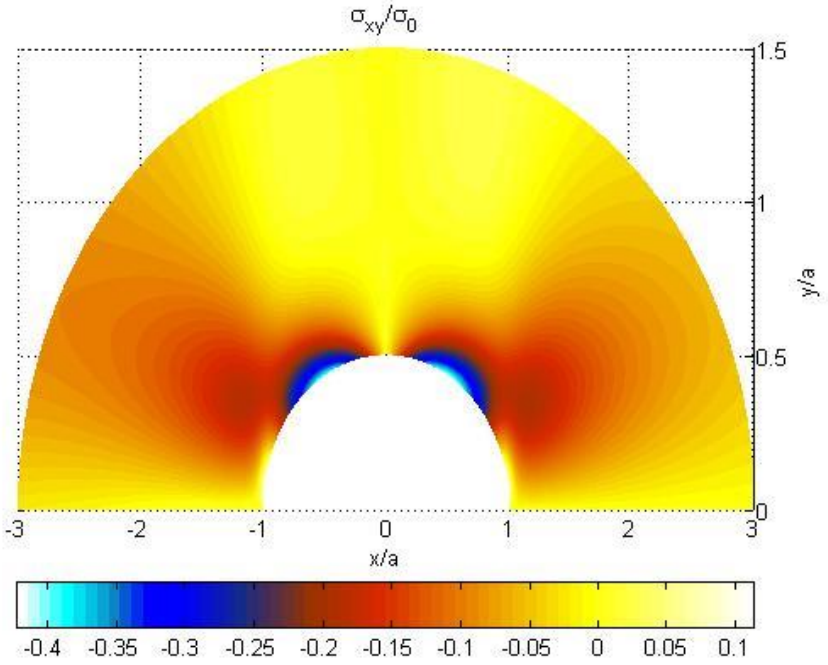

Figure 3-11: Contour plot of normalized shear stress, σ_{xy}/σ_0, in region adjacent to the elliptical hole, Savin's exact theoretical solution (right) and present method using 28 real coefficients (left).

3.4.4 Maximum Stress Concentration

Table 3-1 shows the obtained results when using exact input with and without the scatter. The least-squares results of Table 3-1, which are based on the exact input values, are more accurate than those obtained with scatter. However, results using very few values of N are always extremely reliable. Subsequent results substantiate this trend. Table 3-2 lists the values of $A_j = a_j + ib_j$ of equations (2-100) associated with the exact input data with scatter.

Table 3-1: Maximum tangential stress, σ_{tt}/σ_0, on the edge of the elliptical hole in the uniaxially loaded infinite [0/90/0_{10}/90/0] glass-epoxy composite plate of Figure 3-1.

		Least Squares method and Taylor series expansion	
$2N$ (number of real coefficients)	Theory (ANSYS)	'Exact' input data (Error)	Input with $\pm$10% scatter (Error)
2 (4)		2.888 (3.74 %)	2.983 (7.15 %)
4 (8)		2.587 (7.08 %)	3.362 (20.76 %)
8 (16)	2.784 (2.777)	2.760 (0.86 %)	2.710 (2.66 %)
14 (28)		2.776 (0.29 %)	2.783 (0.04 %)
20 (40)		2.782 (0.07 %)	2.733 (1.83 %)

Table 3-2: Magnitudes of the coefficients associated with the stress calculation in the uniaxially loaded, infinite [0/90/0_{10}/90/0] graphite/epoxy composite of Figure 3-1 using exact input data and Taylor series representation.

	Coefficients values using Taylor series expansion				
Coefficients	$N=1$	$N=2$	$N=3$	$N=4$	$N=5$
a_1	0.211	0.165	0.167	0.192	0.183
b_1	-0.002	0.029	0.018	0.012	0.023
a_2		-0.005	-0.109	-0.011	-0.048
b_2		0.035	-0.029	-0.011	-0.011
a_3			-.0.188	0.012	-0.022
b_3			-0.027	-0.040	-0.020
a_4				0.081	0.027
b_4				-0.042	0.004
a_5					-0.024
b_5					0.023

3.5 Experimental Setup

3.5.1 Constitutive Properties

The constitutive properties (E_{11}, E_{22}, G_{12} and ν_{12}) were obtained from two sets of uni-axial tests (of E_{11}, E_{22}, E_{45} and ν_{12}). One set of strain-gaged coupons was loaded and unloaded once using hydraulic grips in a MTS testing machine, whereas the other set of coupons was

loaded and unloaded several times using the same grips and MTS machine. The values obtained from the first set of tests are E_{11} = 15.65×10^6 psi = 107.9 GPa, E_{22}, = 4.41×10^6 psi = 30.4 GPa, G_{12} = 0.45×10^6 psi = 3.1 GPa and ν_{12} = 0.16. The averages of all the tests of the second set of tests are E_{11} = (14.63 $\pm$ 0.8) × 10^6 psi = 100.87 $\pm$ 5.5 GPa (Figure 3-12), E_{22}, = (3.61 $\pm$ 0.17) × 10^6 psi = 25.6 $\pm$ 1.17 GPa, G_{12} = 0.418×10^6 psi = 2.88 GPa and ν_{12} = 0.152 $\pm$ 0.020. The averages of these two sets of values are E_{11} = 104.4 GPa, E_{22}, = 28.0 GPa, G_{12} = 3.0 GPa and ν_{12} = 0.16 and they are used here.

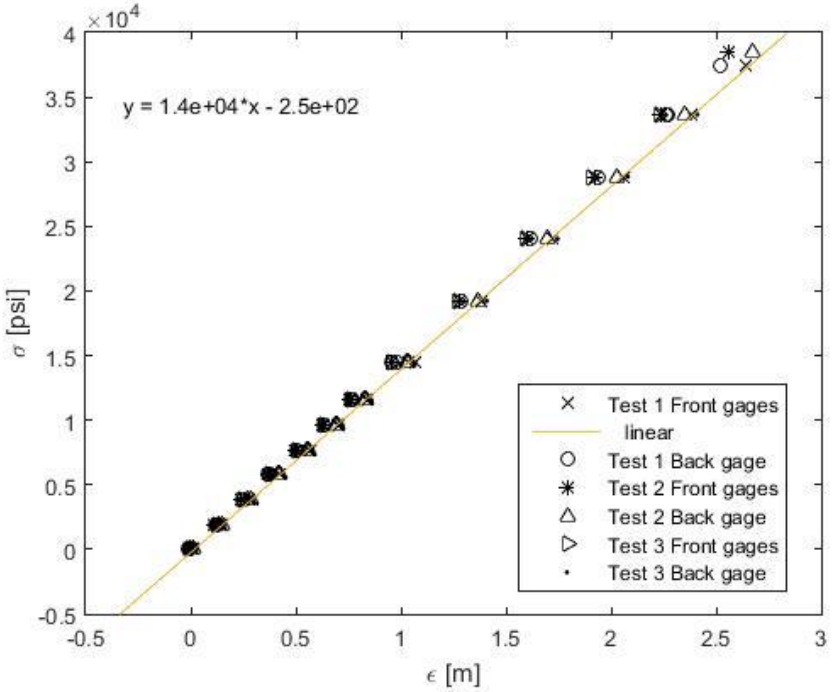

Figure 3-12: Tensile stress for determining modulus of elasticity in the strongest material direction for the second test.

However, results have shown that all of the material values and plots shown in this document are almost identical whether one uses the elastic properties based on the averaged values from the two sets of data (i.e., E_{11} = 104.4 GPa, E_{22}, = 28.0 GPa, G_{12} = 3.0 GPa and ν_{12} = 0.16) or the averages from just the second set of tests (i.e., E_{11} = 101.0 GPa, E_{22} = 25.6 GPa, G_{12} = 2.9 GPa and ν_{12} = 0.16). The maximum and minimum values from the second set of tests are E_{11} = 104.8 GPa and 97.2 GPa and E_{22} = 30.4 GPa and 23.3 GPa, respectively. The

range in measured values of each of E_{11} and E_{22} from the different set of specimens is therefore comparable to that from multiple testing of the same set of coupons.

3.5.2 Geometry and Mechanical Properties

The developed hybrid-TSA approach is utilized to stress analyze a finite-width tensile $[0_{13}/90_5/0_{13}]$ graphite/epoxy orthotropic plate (from Kinetic Composites, Inc., Oceanside, CA) containing a central elliptical hole, Figure 3-13. The 5.28 mm (0.21″) thick plate is 279.4 mm (11″) long and 76.2 mm (3″) wide. The tested perforated composite plate has an elliptical hole with semi-major axis a = 191. mm (0.75″) and a semi-minor axis b = 9.5 mm (0.375″), Figure 3-13 and Table 3-3. The coordinate origin is at the center of the elliptical hole and the response is symmetric about both x- and y-axes. The laminate elastic properties were obtained from conducting uniaxial tensile tests in the strong/stiff (y-direction), weak/compliant (x-direction) and 45-degee orientations, Table 3-3.

3.5.3 Plate Preparation

The plate was initially very lightly polished with 400 grit sand paper. TSA can be marginally conducted on graphite/epoxy composites directly. However, we prefer applying a coating of Krylon Ultra-Flat black paint to provide an enhanced and uniform emissivity. Recognizing Gr/E composite are black, one can record TSA images without applying a coating of black paint. However, our experience indicates is that superior TSA images are obtained by providing a coating of flat black paint. Precaution was taken when sanding the faces of the specimen to neither damage the fibers nor round-off the edge of the hole which could further erode the quality of the thermal information close to the edge of the elliptical hole.

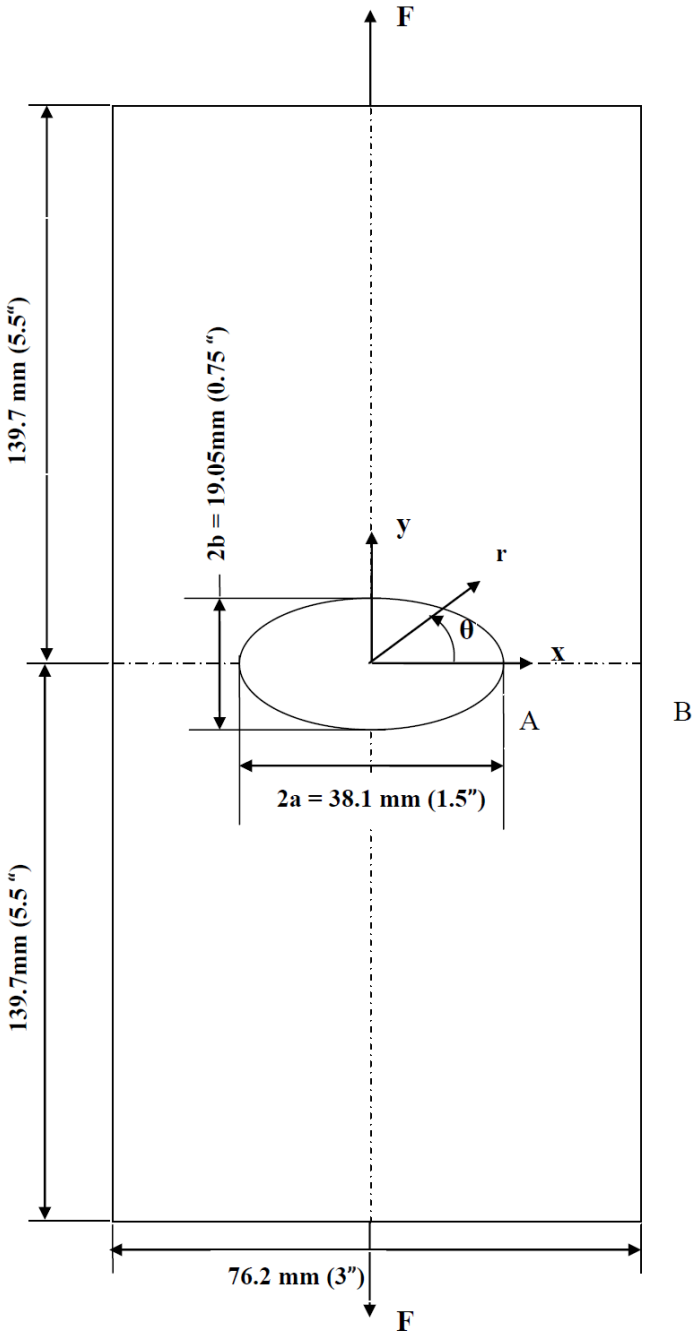

Figure 3-13: Loaded finite Gr/E [$0_{13}/90_5/0_{13}$] composite plate with central elliptical hole.

Table 3-3: Specimen specification and dimension and TSA experiment details.

Material	$[0_{13}/90_5/0_{13}]$ Graphite/Epoxy
Elastic Modulus, E_{11}	104.4 GPa = 15.0 × 10^6 psi
Elastic Modulus, E_{22}	28.0 GPa = 4.0 × 10^6 psi
Shear Modulus, G_{12}	3.0 GPa = 0.43 × 10^6 psi
Poisson's ratio, ν_{12}	0.16
Supplier	Kinetic Composites, Inc., Oceanside, CA
Thickness	5.28 mm (0.21″)
Length, L	279.4 mm (11″)
Width, W	76.2 mm (3″)
Ellipse major diameter, $2a$	38.1 mm (1.5″)
Ellipse minor diameter, $2b$	19.1 mm (0.75″)
Cyclic Loading	7117 ± 3559 N $= 1600 \pm 800$ lb
Loading Range	7117 N = 1600 lb

*The 1- and 2-orientations are directions of laminate material symmetry. They are in the longitudinal/vertical and transverse/horizontal directions, respectively, Figure 3-13.

3.5.4 Loading Condition

The plate was subjected to a cyclically varying sinusoidally load in a 20 kips capacity MTS hydraulic testing machine with a mean value of 7.1 kN (1600 lb.), maximum value of 10.7 kN (2400 lb.), and a minimum value of 3.6 kN (800 lb.) at a rate of 20 Hz. Our experience

indicates this is a suitable frequency to use with perforated graphite/epoxy composites. Phase information was also monitored to ensure that adiabatic conditions were maintained. The oscilloscope as shown in Figure 3-14 was employed to accurately monitor the applied load and frequency. The MTS machine employed hydraulic grips capable up to 18.5 kips. The machine can operate in either load or displacement control with any of four ranges (10%, 20%, 50%, and 100% of capacity). The plate was loaded at different cyclic rates while monitoring the phase information provided by the DeltaTherm Stress Photonics TSA system software in order to ensure that the adiabatic conditions were maintained at loading rate of 20 Hz. The hydraulic grips apply a uniform clamping pressure over both ends of the specimen. The corresponding load-induced TSA data were recorded using a TSA Delta Therm model DT1410 system having a sensor array of 256 horizontal by 256 vertical pixels which is cooled with liquid nitrogen to maintain the sensor at a very low temperature necessary for the accurate readings. The Delta Therm camera (Stress Photonics, Madison, WI) is aligned to be exactly perpendicular to the surface of the plate, Figure 3-15. The plate was carefully aligned between the top and bottom grips to produce a symmetrically loaded plate about y-axis.

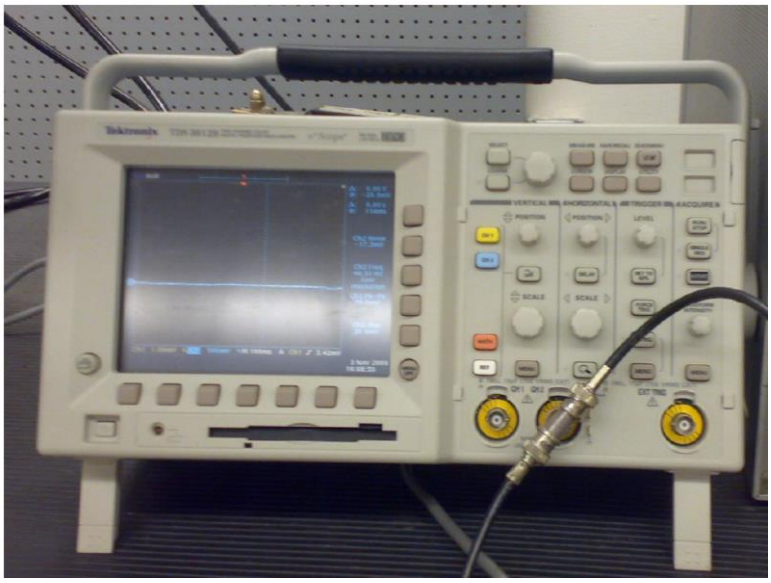

Figure 3-14: Oscilloscope for measuring the cyclic loads accurately.

Figure 3-15: Experimental test setup for recording temperature variations of finite plate with elliptical hole using Delta Therm model DT1410 infrared camera.

The present selected loading rate of 20 Hz was based on past experiences at UW with TSA on graphite/epoxy composites [8,12,63] and the desire to ensure adiabaticity. For example, reference [8,14] used 19 Hz, reference [12] used 13 Hz, reference [63] used 23 Hz and Dr. Kangyu He used 20 Hz in his thesis. The current situation was monitored to ensure adiabaticity prevailed. There is nothing to suggest any non-linear or inelastic behavior occurred. Although they were static, the coupon tests used to obtain constitutive and thermo-mechanical material properties behaved linearly elastically.

The reason of using high frequency is because under certain frequency, heat flow was observed in the TSA image at the high temperature gradient region, around the top edge of the hole. This violates the crucial requirement of adiabaticity for thermoelastic study. Conceptually, if the loading frequency is faster than the rate of heat flow, the adiabatic condition prevails. Therefore, increasing the loading frequency minimizes the any local heat transfer in the loaded body, thereby maintaining adiabaticity.

3.5.5 TSA Recording

The thermoelastic recorded signal, S^*, was recorded by the data acquisition system which is equipped with Delta Vision Software, Figure 3-16. TSA images were captured and averaged over two minutes durations, and then exported to Excel while converting each pixel into a data point, i.e., 256 by 256 matrix. Pixel size is 0.35 mm (0.014 inch). Since TSA data typically are unreliable on and near an edge, no recorded TSA information was used within at least six pixel positions ($0.1a$ = 1.9 mm = 0.075 inch) of the edge of the hole.

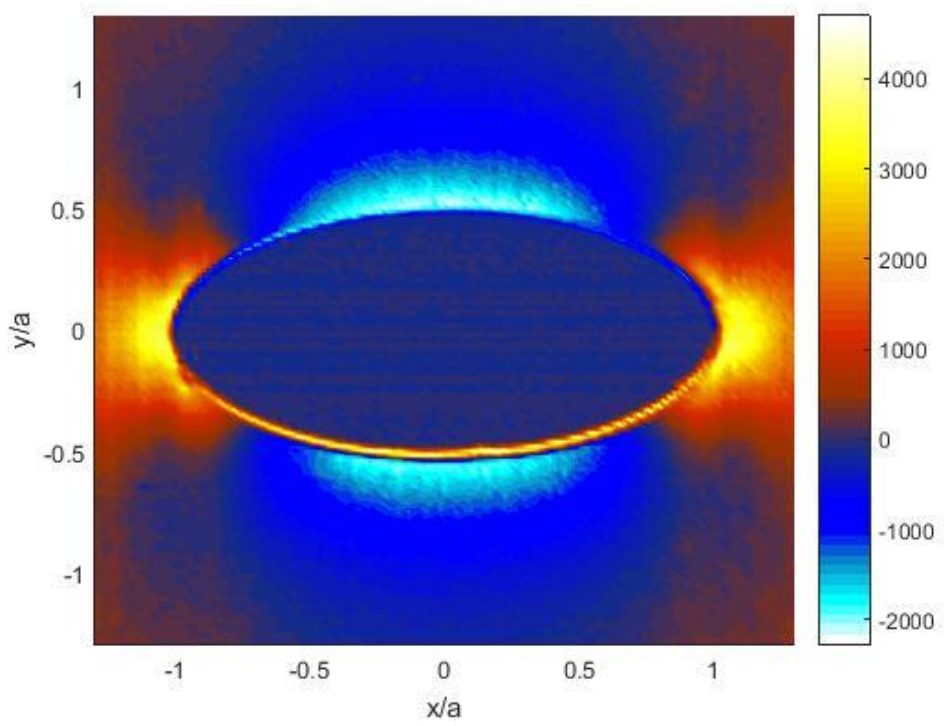

Figure 3-16: TSA image, S^*, of perforated orthotropic plate with elliptical hole loaded at a range of 7117 N (1600 lb).

3.5.6 TSA Calibration

The thermoelastic coefficients K_1 and K_2 were evaluated from uniaxial tensile coupons loaded in the strong/stiff (vertical, y-direction) and weak/compliant (horizontal, x-direction) laminate orientations of the orthotropic $[0_{13}/90_5/0_{13}]$ graphite/epoxy composite plate whose complete state of stress is known at a location far from any stress concentration and/or where

there is uniform 1-D state of stress (no holes or irregular discontinuities). These coupons were painted and tested at 20 Hz on the same day as the elliptically-perforated plate. The thermoelastic coefficients are K_1 = 1.80 mU/MPa (12.38 U/psi) in the vertical, y-direction of plate of Figure 3-13 and K_2 = 14.69 mU/MPa (101.25 U/psi). The unit U is used to signify the raw TSA output, in uncalibrated signal units. Another way to find the calibration factor is to scan a line of the actual perforated test sample far away from the discontinuity to insure uniform stress. The calibration factor was found to be K_2 = 105.6 U/psi.

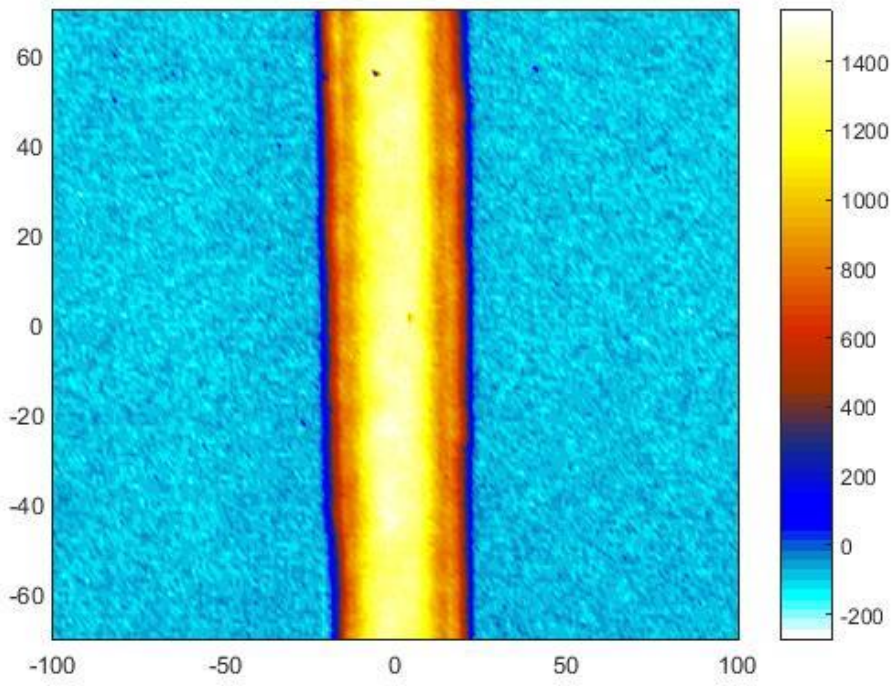

Figure 3-17: Thermoelastic data, S^*, for the calibration specimen when the applied load is parallel to the material symmetry.

3.5.7 Data Processing

Figure 3-16 is a contour plot of the raw measured thermoelastic data throughout a rectangular region containing the hole in the orthotropic composite (E_{yy}/E_{xx} = 3.7). The individual stresses throughout the region containing the elliptical hole were determined from such

thermoelastic data using the mapping-collocation technique. Since the plate behavior is symmetrical about the vertical y- and horizontal x-axes, the recorded thermoelastic data, S^*, of Figure 3-16 were averaged throughout the four quadrants to cancel any asymmetry. The resulting S^* information is plotted in the first quadrant in Figure 3-18. Due to unreliability, the recorded data along and near the edge of the hole were not used. Only the thermal information within the region covered by $1.1a$ (21.0 mm) and $1.1b$ (10.5 mm) to $1.85a$ (35.2 mm) and $1.85b$ (17.6 mm) was considered, as indicated by the source locations of the 2,558 values of S* shown in Figure 3-19. The region of Figure 3-19 is denoted as region R^*. Like most experimental data, the recorded S^* include some noise which necessitates collecting more measured input values than the number of unknown coefficients. The number of equations, m, will exceed the number of real coefficients, $2N$. The resulting overdetermined system of equations with which to evaluate the unknown coefficients was solved using least-squares. The system was solved in MATLAB using the backslash '\' or pseudo inverse 'pinv' operator. The subsequent analysis will demonstrate that the described approach is able to evaluate stresses reliably at the edge of the elliptical hole without using any thermoelastic data on, or very near, the edge. Recognizing the most important stresses occur on the edge of the hole, only a 'ring shaped' segment, rather than the entire quadrant, was considered.

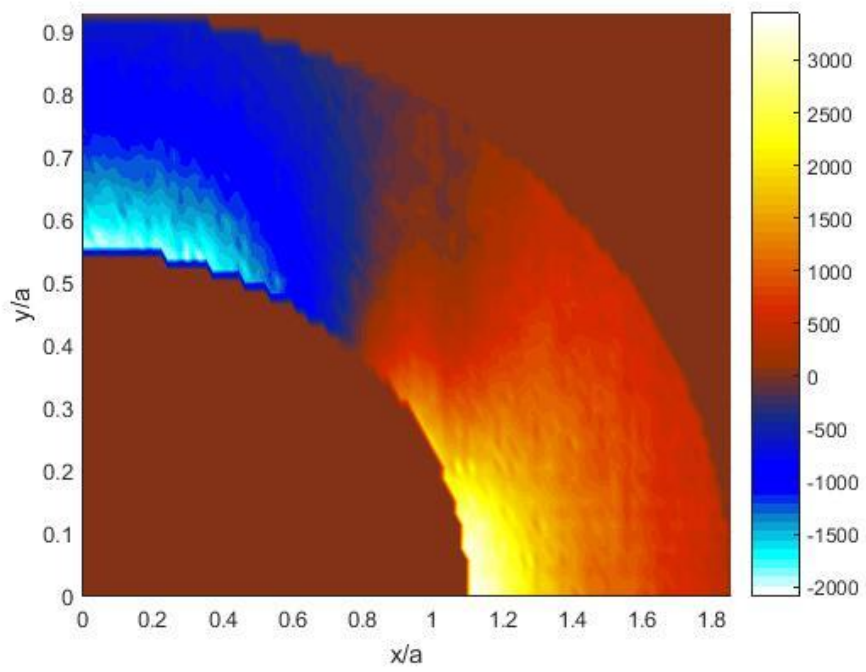

Figure 3-18: Averaged thermoelastic data S^*, throughout the four quadrants at a loading range of 7.12 kN (1600 lb).

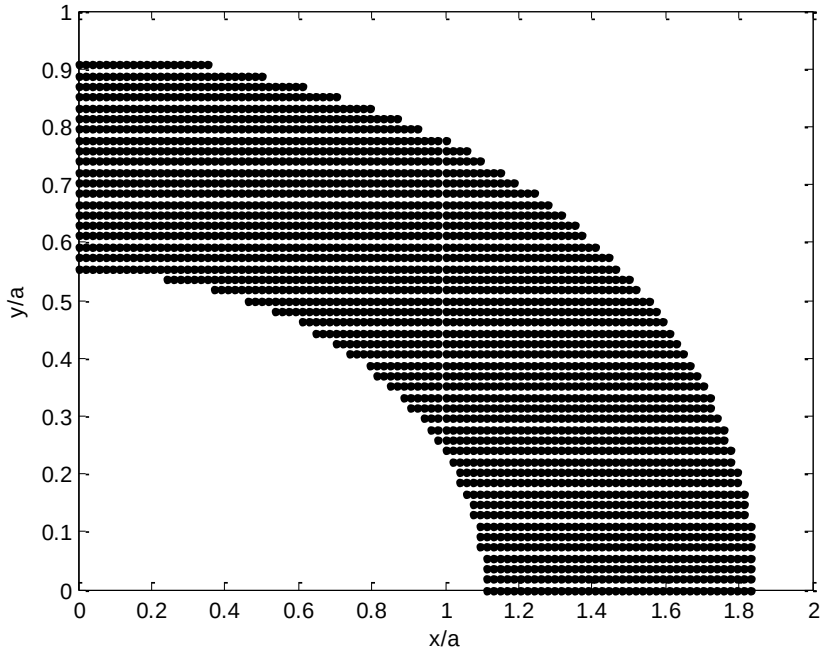

Figure 3-19: Source locations of employed S^* data (m = 2,558 data points).

3.6 Finite Element Analysis

For comparison with the TSA, a finite element analysis (FEA) using ANSYS prediction was prepared of the composite plate of Figure 3-13 and the elastic properties of Table 3-3. Due

to the symmetry, only the upper right quarter of the plate was modeled with symmetrical boundary condition applied at the bottom and left edges. Based on the static equivalent, a far-field stress of

$$\sigma_0 = \frac{F}{A} = \frac{1600 \text{ lb}}{0.208 \text{ in} \times 3 \text{ in}} = 2564 \text{ psi} = 17.68 \text{ MPa}$$

was applied numerically to the top edge of the plate, Figure 3-20. Plane 82 Isoparametric elements with eight nodes were employed. To obtain reliable data, a very fine mesh was used in the neighborhood of the elliptical hole as shown in Figure 3-20. A convergence test was applied until the change in results of maximum stress between two successive meshing was less than 2%. The FE model utilizes 67,500 elements and 68,101 nodes. The resultant radial, tangential, and shear stresses of the FE model are shown in Figure 3-21.

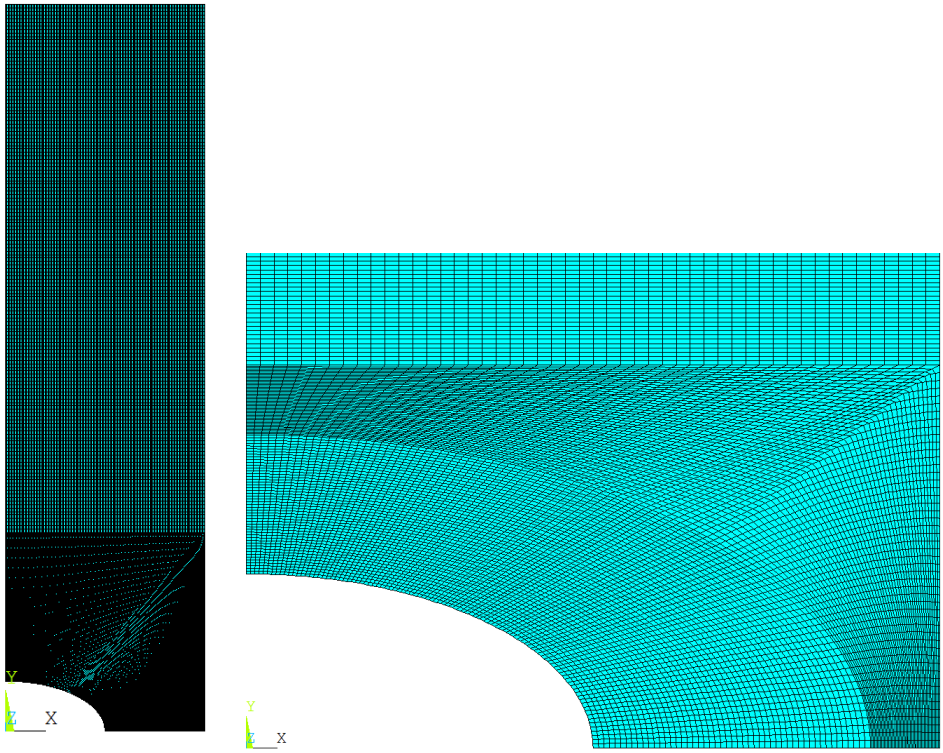

Figure 3-20: Meshed FE model with dense meshing adjacent the elliptical hole.

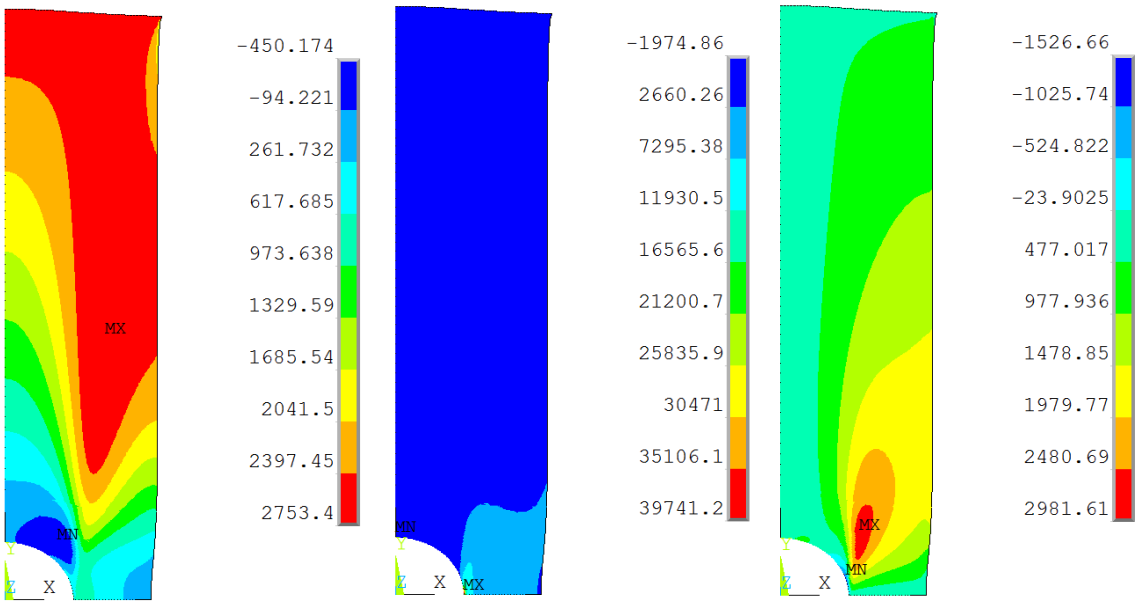

Figure 3-21: Contour plot for the radial, tangential and shear stresses from FEA in psi.

A stated motivation for developing the present ability is to enable stress analysis of orthotropic cases experimentally which cannot be analyzed numerically, although FEM is used here. The geometry and loading of the Figure 3-13 were deliberately selected so as one could obtain a reliable FEM result with which to validate the experimental results. The developed hybrid-TSA method is applicable to more complicated problems which are difficult for FEM. For example, while industry makes prevalent use of FEM, strain gages are often employed in that environment to obtain the boundary conditions for the FEA.

3.7 Results

3.7.1 Evaluating Number of Coefficients to Employ

The complex coefficients, $A_j = a_j + ib_j$, were evaluated by two approaches; the first approach used equations (2-79) through (2-81) and the Taylor representation of the stress function to map the physical plane to a half-plane ($\eta = 0$) in the ζ-plane; the second approach used equations (2-83) through (2-85) and the Laurent series expansion to map the physical plane to

the unit circle in the ζ-plane. The unreliable thermoelastic data on and near the elliptical boundary motivated only using thermoelastic data from $1.1a$ and $1.1b$ to $1.85a$ and $1.85b$. The complex coefficients, A_j, were evaluated individually from equations (2-100) or (2-101) employing the recorded thermoelastic data inside the region R^*, Figure 3-19, utilizing the Taylor and Laurent representations for the stress function, respectively. The individual stresses throughout region R_z, including on the edge Γ where no thermoelastic input data were employed, were evaluated using equations (2-90) through (2-92) for the Taylor expansion and (2-95) through (2-97) for the Laurent expansion. Among other techniques, the number of complex Airy coefficients, N, to retain in the stress function was selected by evaluating the difference between the magnitude of experimentally based thermoelastic data and those predicted by the present hybrid method by using root mean square approach, Figure 3-22 and condition number of matrix $\{M\}$, Figure 3-23. If many coefficients were used in this analysis which will reduce the RMS value, this will increase the condition number and the matrix $\{M\}$ becomes singular. This indicates that small number of coefficients should be used otherwise, the matrix $\{M\}$ will become singular (the solution will "blow-up"). By using small coefficients and observe both RMS and condition number, the first (Taylor expansion) and second (Laurent expansion) approaches both require 4 complex coefficients (8 real coefficients). The appropriateness of utilizing 4 complex coefficients is substantiated by comparing the reconstructed and experimentally-based, S^*, Figure 3-24.

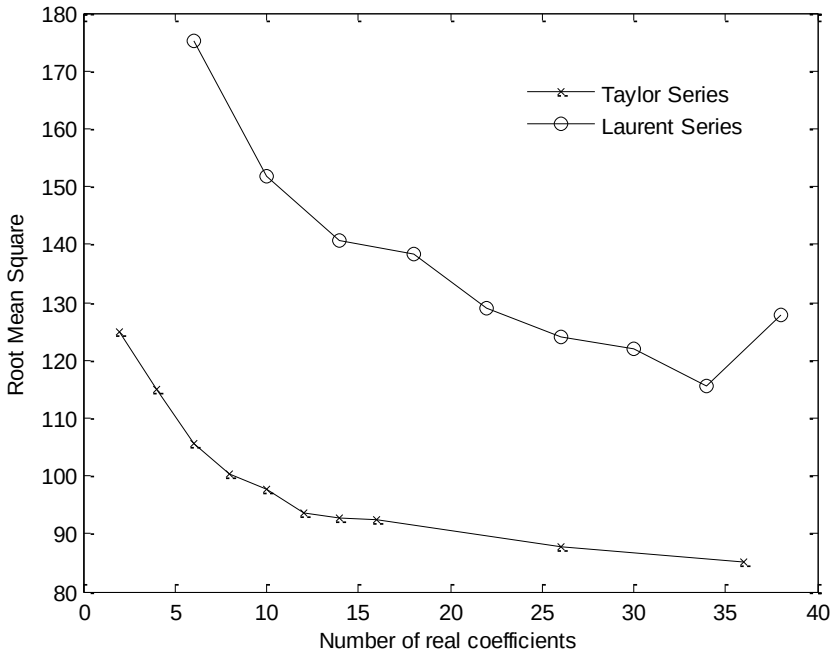

Figure 3-22: Root Mean Square value for different number of real coefficients for the first approach using Taylor series and second approach using Laurent series.

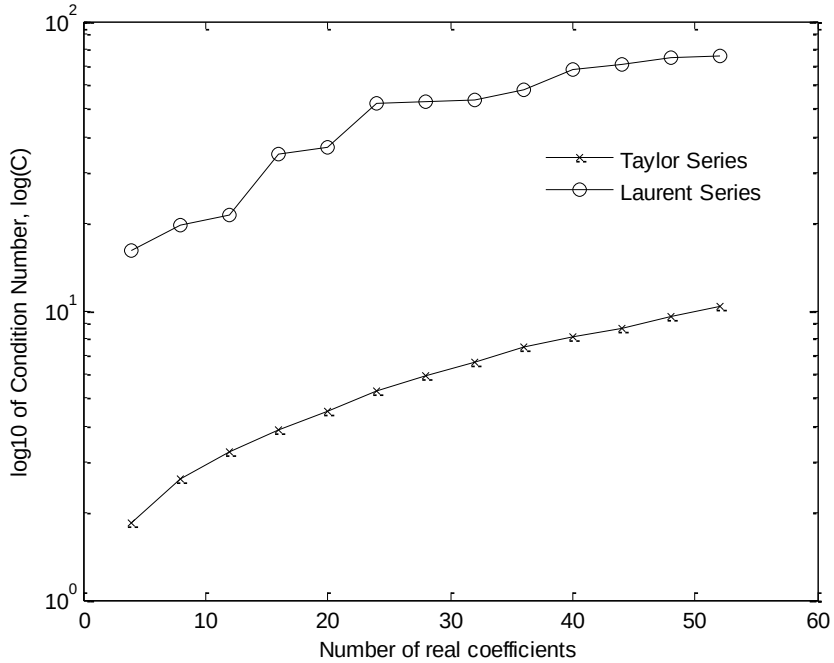

Figure 3-23: Condition number of matrix $[M]$ for different number of real coefficients for the first approach using Taylor series and second approach using Laurent series.

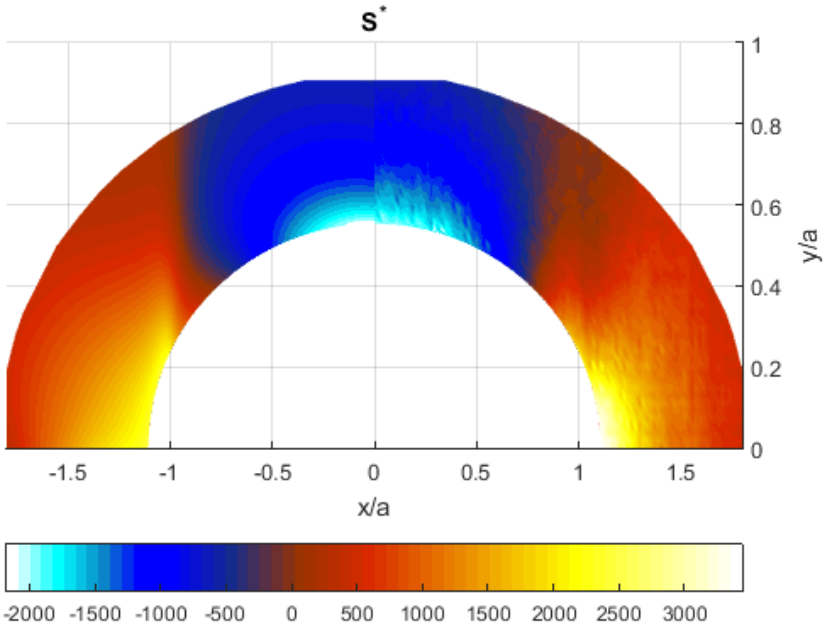

(a)

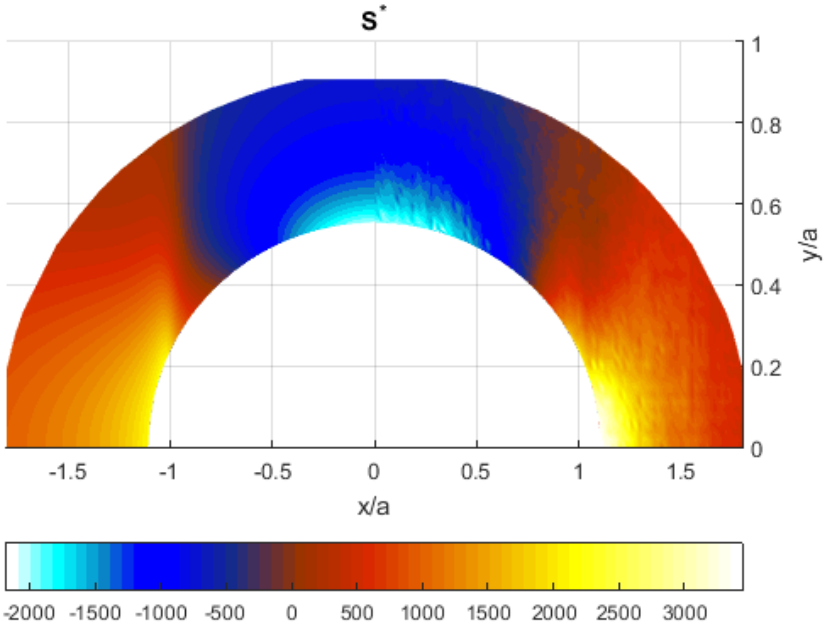

(b)

Figure 3-24: Contour plot of S^* of recorded (right) and reconstructed (left) throughout region adjacent to elliptical hole using (a) Taylor (b) Laurent series expansion (8 real coefficients).

3.7.2 Further Validation of Selected Number of Coefficients

In order to further assess the validity of using 8 real (4 complex) coefficients, Figure 3-25, Figure 3-27, and Figure 3-29 show prepared contour plots of S^* which corresponds to the comparison between recorded TSA image of Figure 3-18 in the right side and the reconstructed S^* stress patterns in the left sides based on the 4, 20, and 44 real TSA-determined coefficients using Taylor and Laurent series expansions in a segment of the perforated plate of Figure 3-1 extending $1.85a$ = 1.39 in = 3.52 cm on either side from the center of the hole and $1.85b$ = 0.69 in = 1.76 cm above the center of the hole.

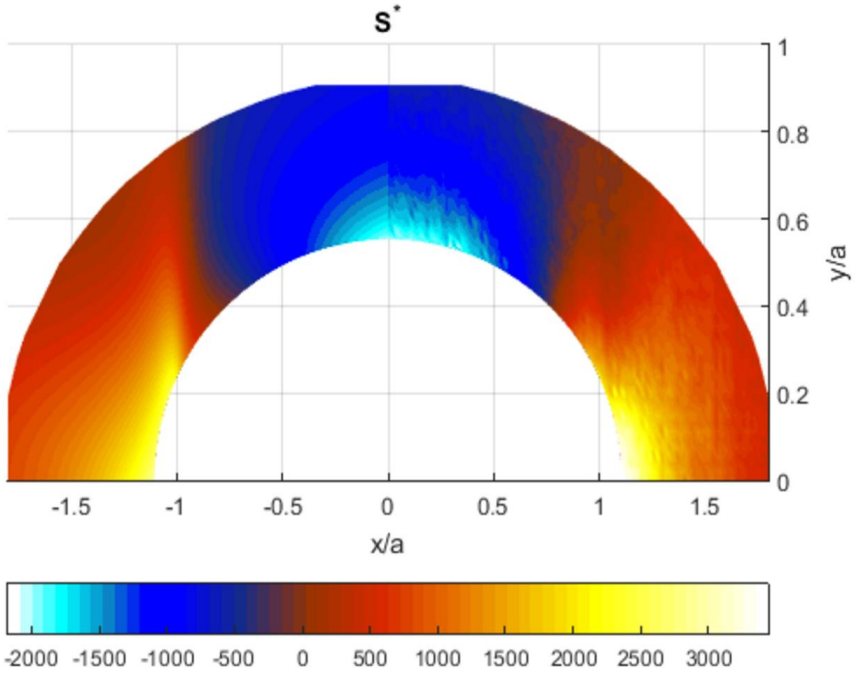

(a)

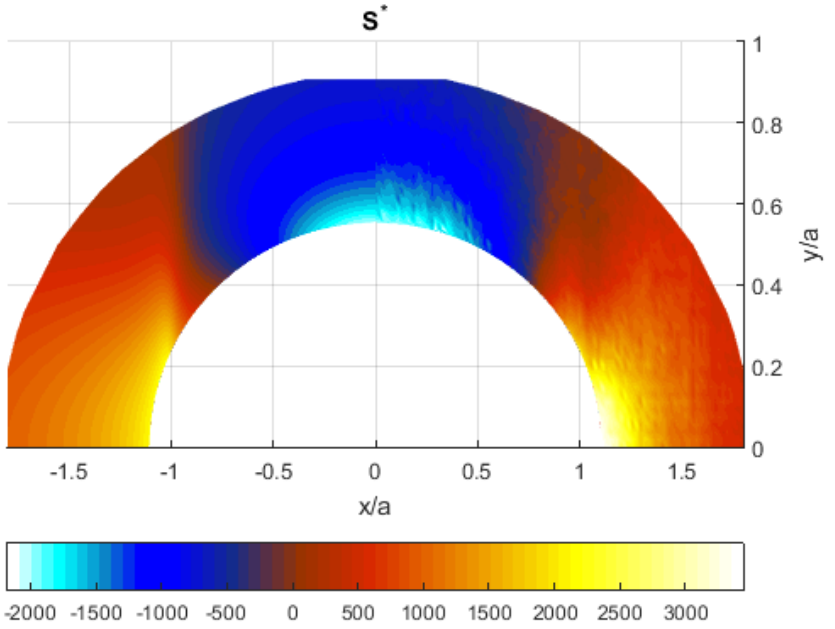

(b)

Figure 3-25: Contour plot of S^* of recorded (right) and reconstructed (left) throughout region adjacent to elliptical hole using (a) Taylor (b) Laurent series expansion (4 real coefficients).

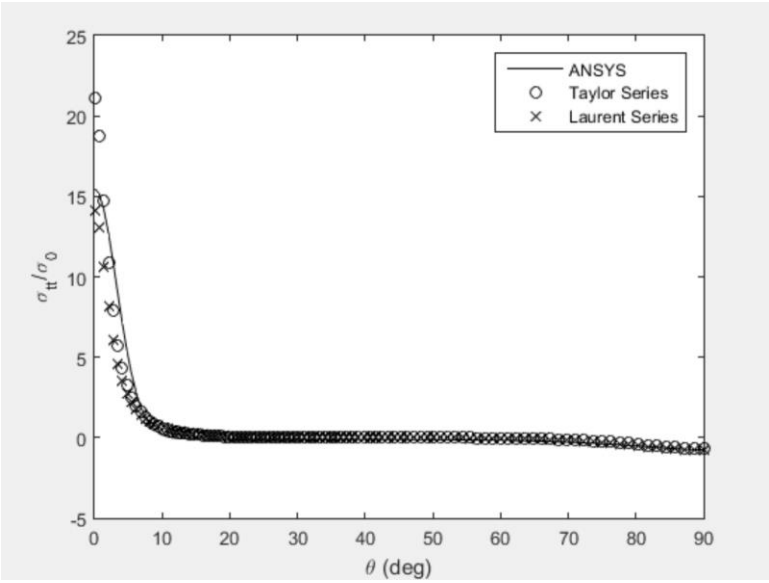

Figure 3-26: Variation of σ_{tt}/σ_0 along the boundary of the hole from FEA, hybrid-TSA using Taylor series (4 real coefficients), and hybrid-TSA using Laurent series (4 real coefficients).

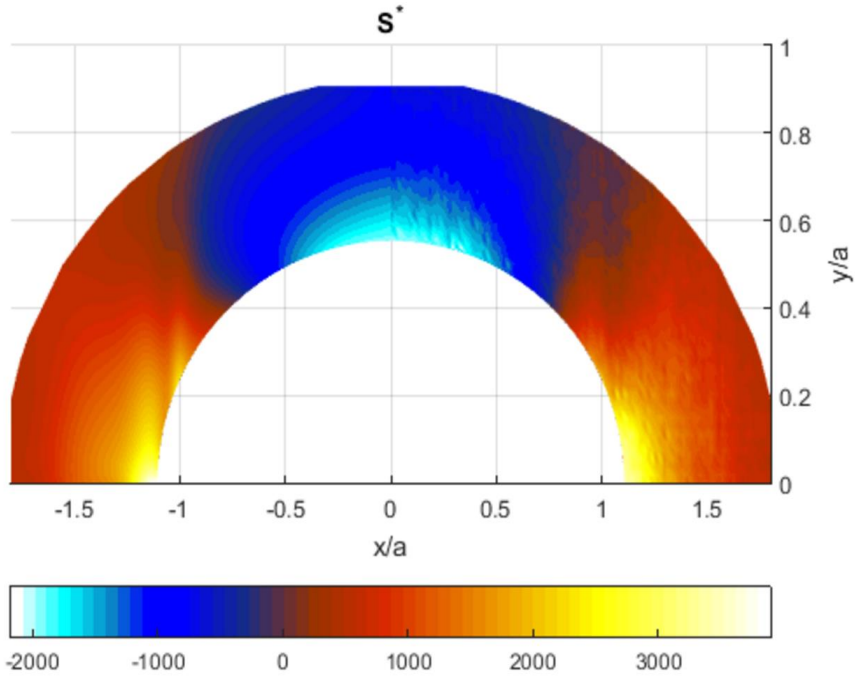

(a)

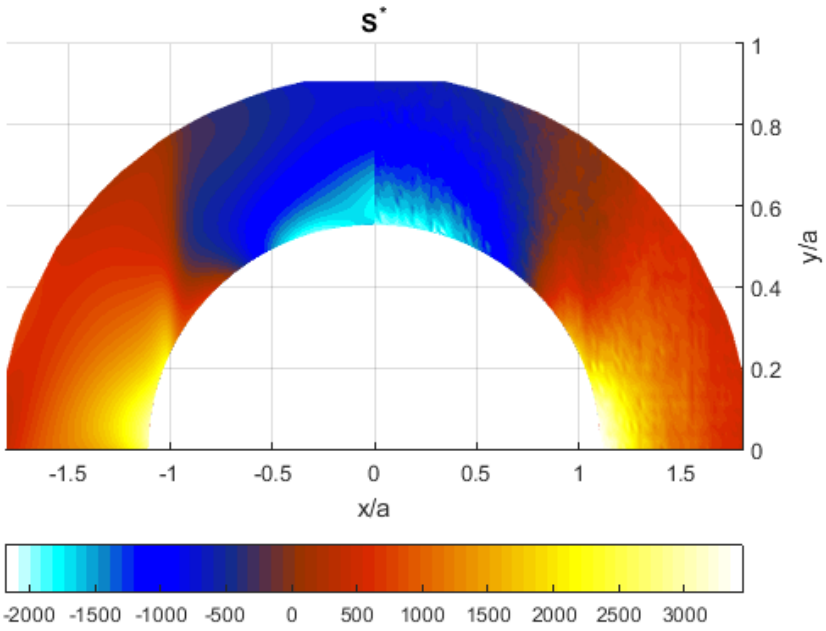

(b)

Figure 3-27: Contour plot of S^* of recorded (right) and reconstructed (left) throughout region adjacent to elliptical hole using (a) Taylor (b) Laurent series expansion (20 real coefficients).

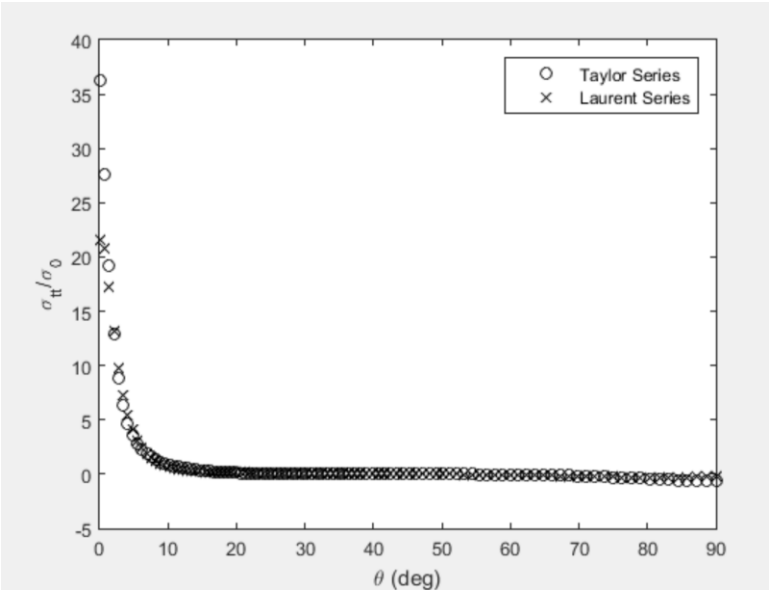

Figure 3-28: Variation of σ_{tt}/σ_0 along the boundary of the hole from hybrid-TSA using Taylor series (22 real coefficients) and hybrid-TSA using Laurent series (20 real coefficients).

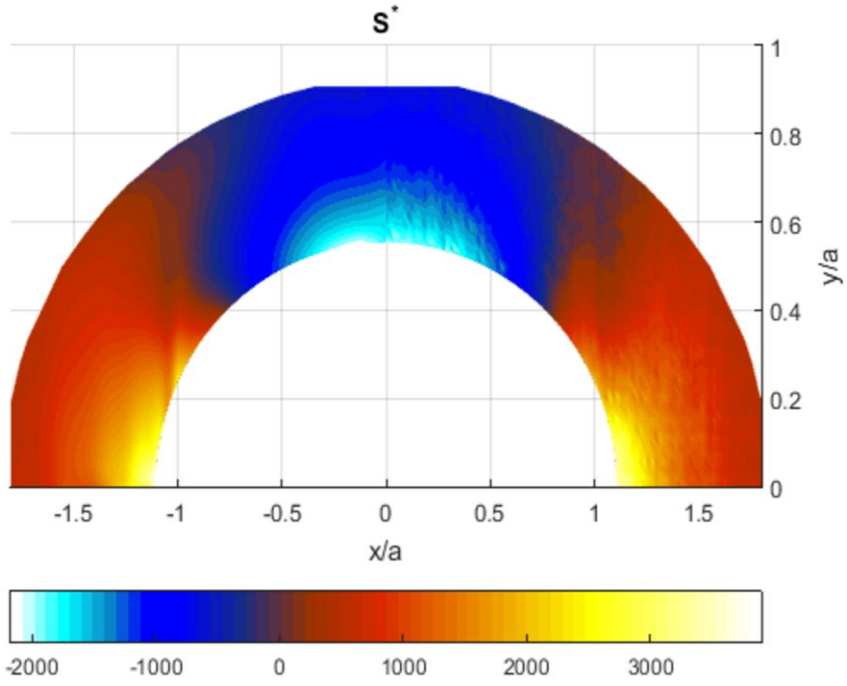

(a)

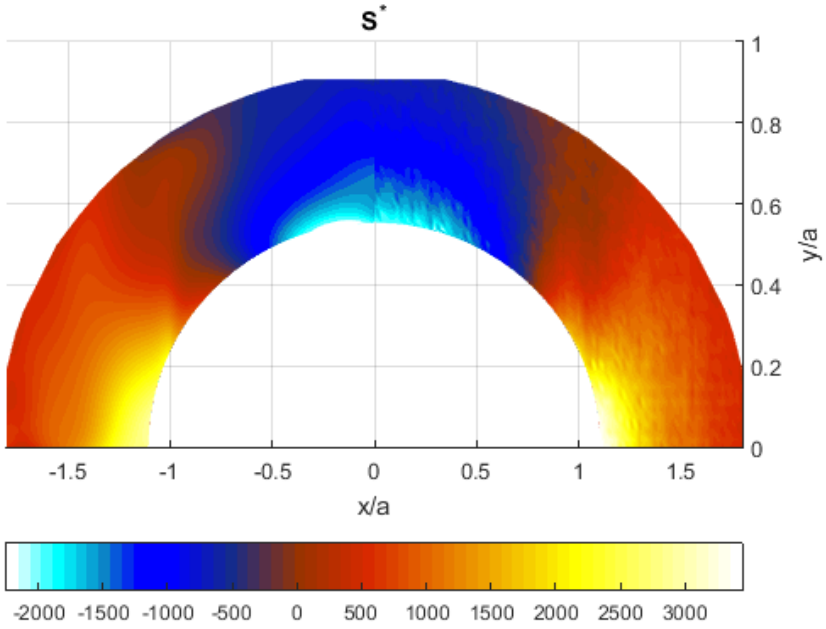

(b)

Figure 3-29: Contour plot of S^* of recorded (right) and reconstructed (left) throughout region adjacent to elliptical hole using (a) Taylor (b) Laurent series expansion (44 real coefficients).

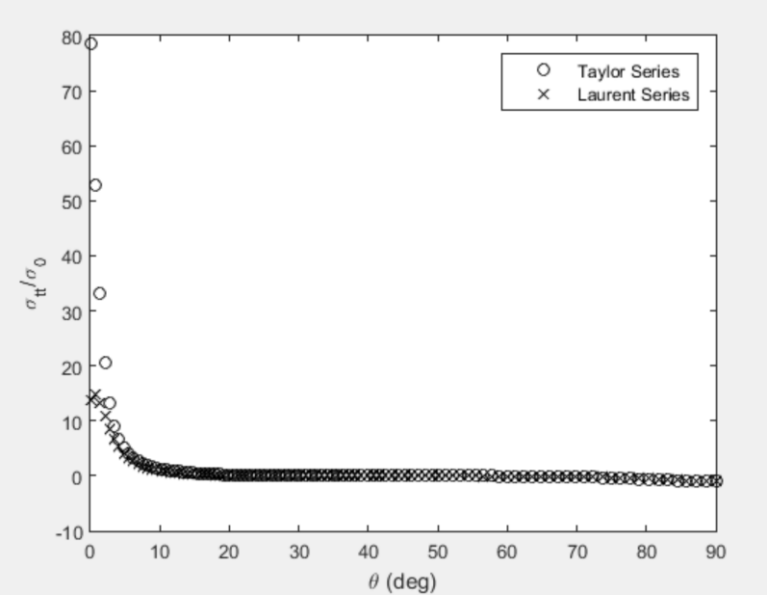

Figure 3-30: Plot of σ_{tt}/σ_0 along the edge of the hole from hybrid-TSA using Taylor series (44 real coefficients) and hybrid-TSA using Laurent series (44 real coefficients).

Note that even though the RMS plots of Figure 3-22 do not become a minimum or flatten out until about 34 real Airy coefficients, and respective experimentally-based and re-constructed plots of S^* (Figure 3-25, Figure 3-27, and Figure 3-29) are not too different, the stresses virtually 'blow up' as shown in Figure 3-26, Figure 3-28, and Figure 3-30 or become singular as one increases the number of coefficients. This information further justifies eight being a realistic number of real coefficients to retain. Although the stresses at the boundary from the Laurent series solution seem to be realistic, the stresses outside this region are unrealistic.

3.7.3 Stresses and Displacements

The tangential stress in the elliptical coordinate, σ_{tt}, from equation (2-23) and the polar components of stress from equation (2-19), normalized to the far-field stress, σ_0 = 17.68 MPa, are plotted on the edge of the hole in Figure 3-31 through Figure 3-34. These TSA-based results agree with the FEM predictions. Not surprising, the magnitudes of σ_{tt}/σ_0 and $\sigma_{\theta\theta}/\sigma_0$ are very similar to each other, and σ_{rr}/σ_0 and $\sigma_{r\theta}/\sigma_0$ are small, on the edges of the hole. Figure 3-31

and Figure 3-32 indicate the difference between these respective normalized stresses is measurable in the neighborhood of θ = 20^o (0.06/0.01) and θ = 60^o (-0.04/-0.38). The FEA and hybrid-TSA determined stress concentrations from Taylor and Laurent series expansion at the elliptical hole are 15.45, 15.37, and 16.16 respectively which agree with theoretical value 15.70 from equation (2-105).

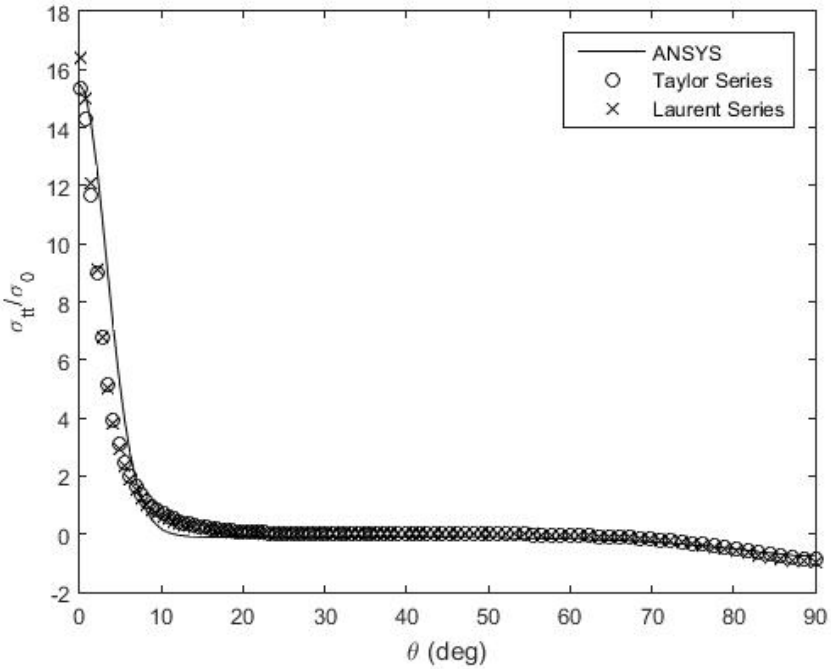

Figure 3-31: Plot of σ_{tt}/σ_0 along the edge of the hole from ANSYS, hybrid-TSA using Taylor series (8 real coefficients), and hybrid-TSA using Laurent series (8 real coefficients).

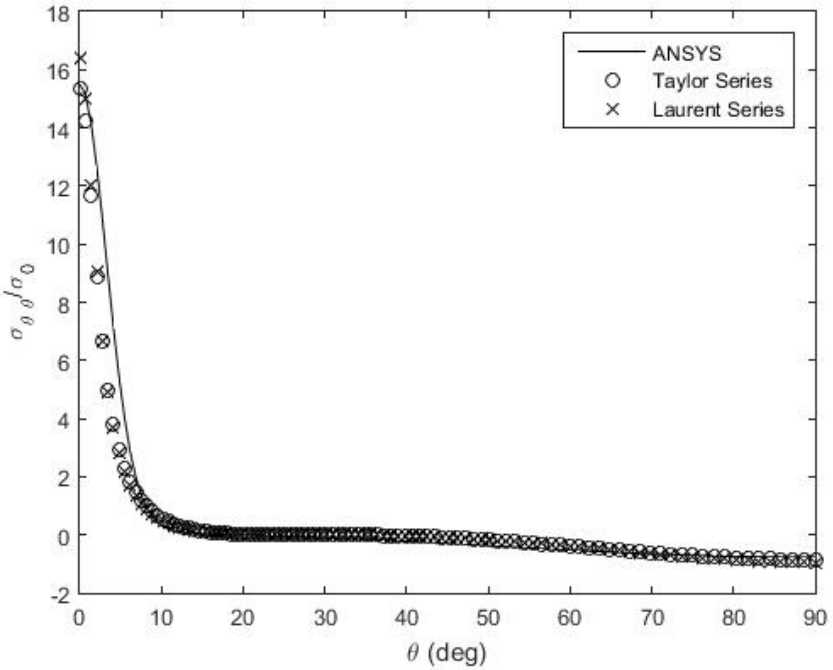

Figure 3-32: Plot of $\sigma_{\theta\theta}/\sigma_0$ along the edge of the hole from ANSYS, hybrid-TSA using Taylor series (8 real coefficients), and hybrid-TSA using Laurent series (8 real coefficients).

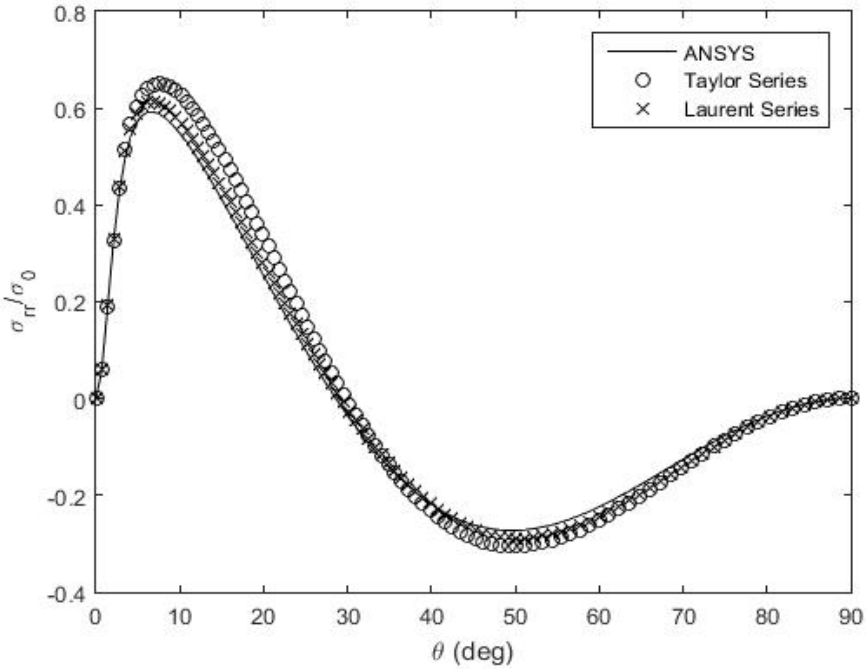

Figure 3-33: Plot of σ_{rr}/σ_0 along the edge of the hole from ANSYS, hybrid-TSA using Taylor series (8 real coefficients), and hybrid-TSA using Laurent series (8 real coefficients).

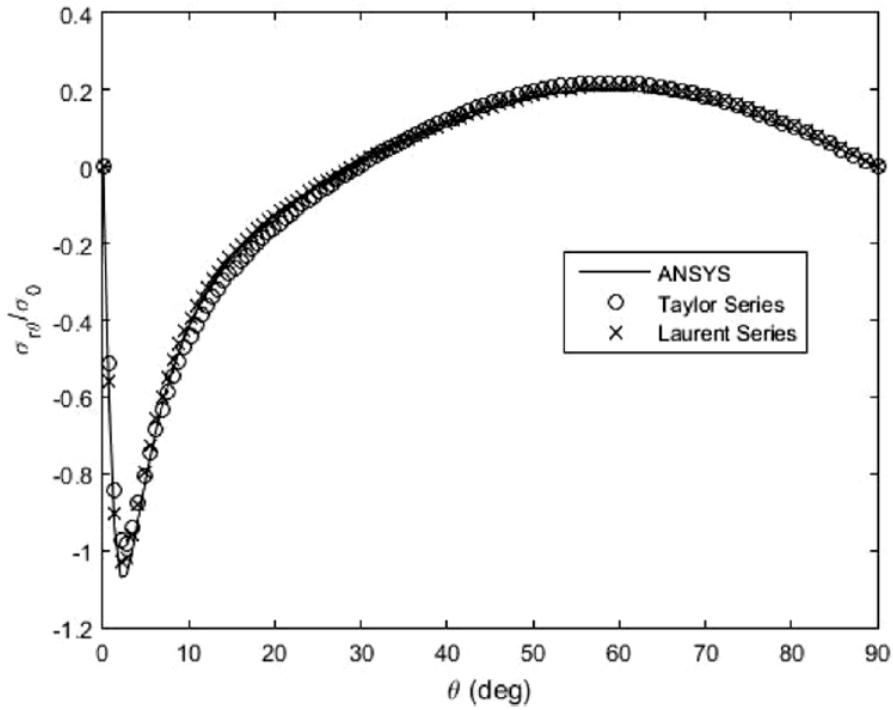

Figure 3-34: Plot of $\sigma_{r\theta}/\sigma_0$ along the edge of the hole from ANSYS, hybrid-TSA using Taylor series (8 real coefficients), and hybrid-TSA using Laurent series (8 real coefficients).

Contour plots of normalized Cartesian components of the stress and the displacement by the hybrid technique using the Taylor series and ANSYS are plotted in Figure 3-35 through Figure 3-39. The corresponding figures for Laurent series are plotted in Figure 3-40 through Figure 3-44. Those figures show an excellent agreement between the ANSYS-predicted values and the hybrid technique using thermoelastic data values for m = 2,558 data points.

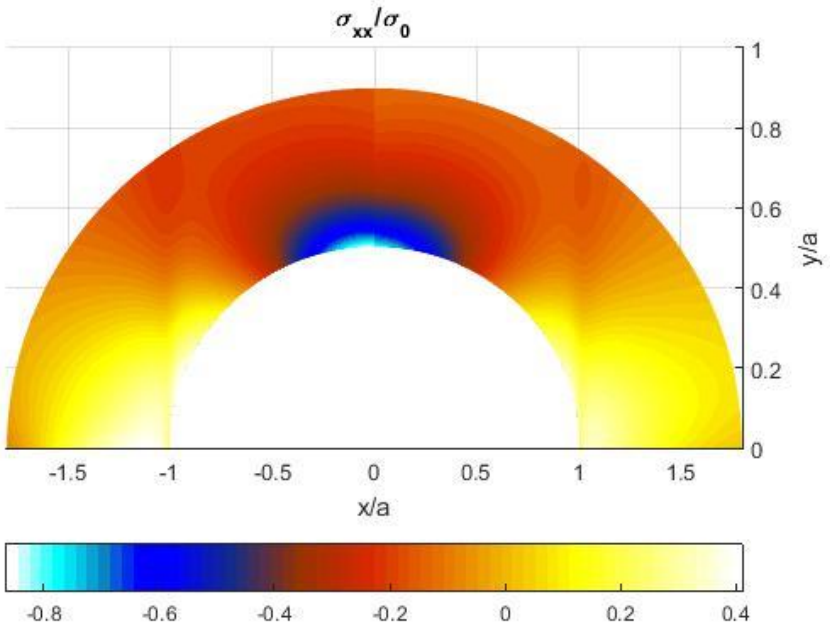

Figure 3-35: Contour plot of σ_{xx}/σ_0 throughout region adjacent to hole by FEA (right) and hybrid-TSA using the Taylor series and 8 real coefficients (left).

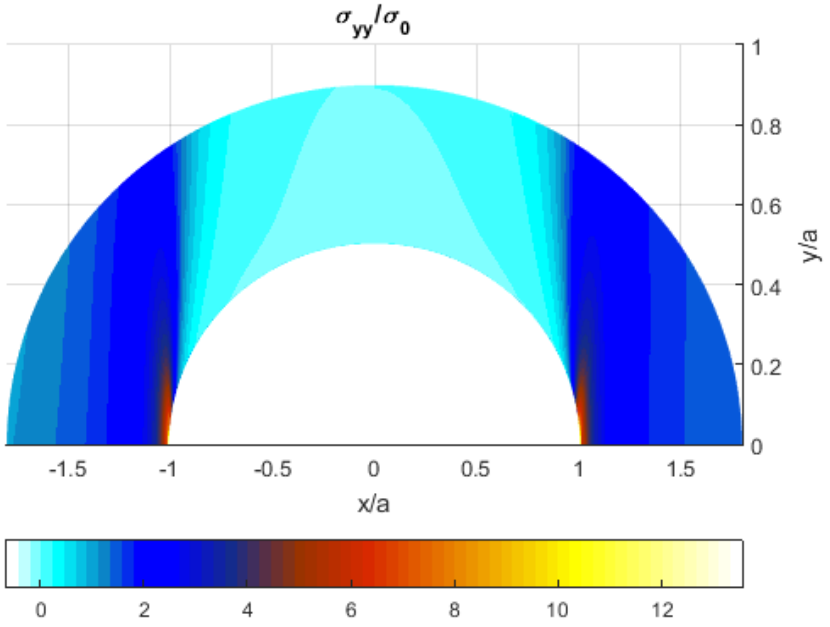

Figure 3-36: Contour plot of σ_{yy}/σ_0 throughout region adjacent to hole by FEA (right) and hybrid-TSA using the Taylor series and 8 real coefficients (left).

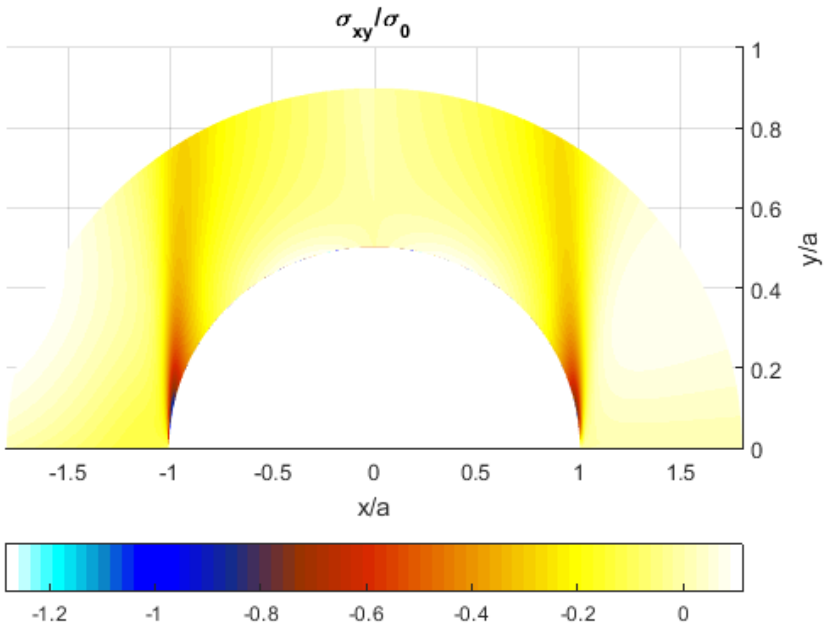

Figure 3-37: Contour plot of σ_{xy}/σ_0 throughout region adjacent to hole by FEA (right) and hybrid-TSA using the Taylor series and 8 real coefficients (left).

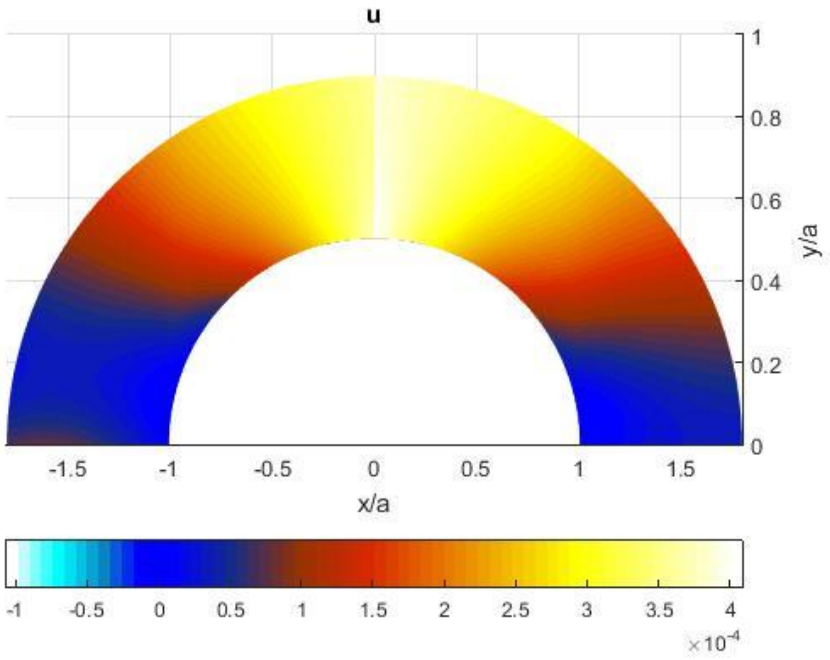

Figure 3-38: Contour plot of u throughout region adjacent to hole by FEA (right) and hybrid-TSA using the Taylor series and 8 real coefficients (left).

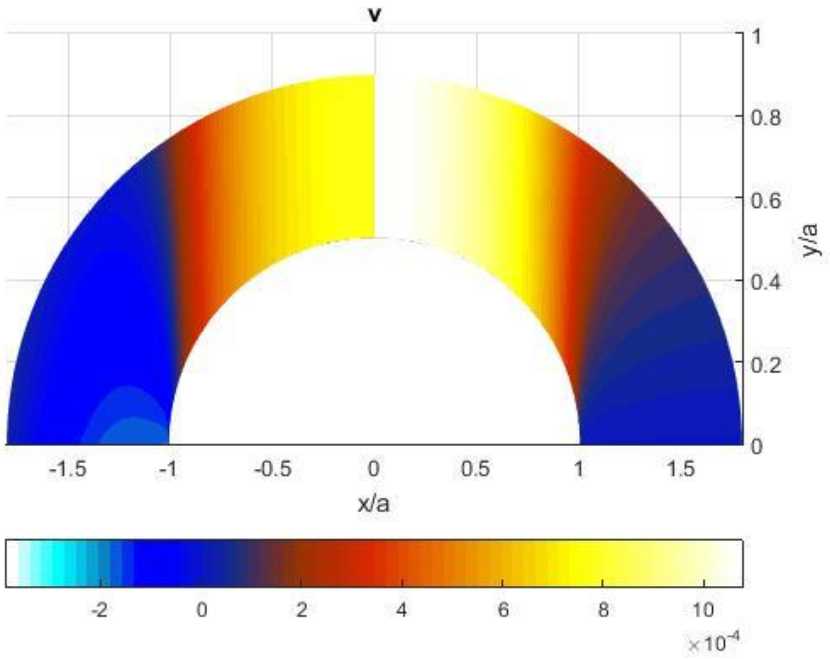

Figure 3-39: Contour plot of v throughout region adjacent to hole by FEA (right) and hybrid-TSA using the Taylor series and 8 real coefficients (left).

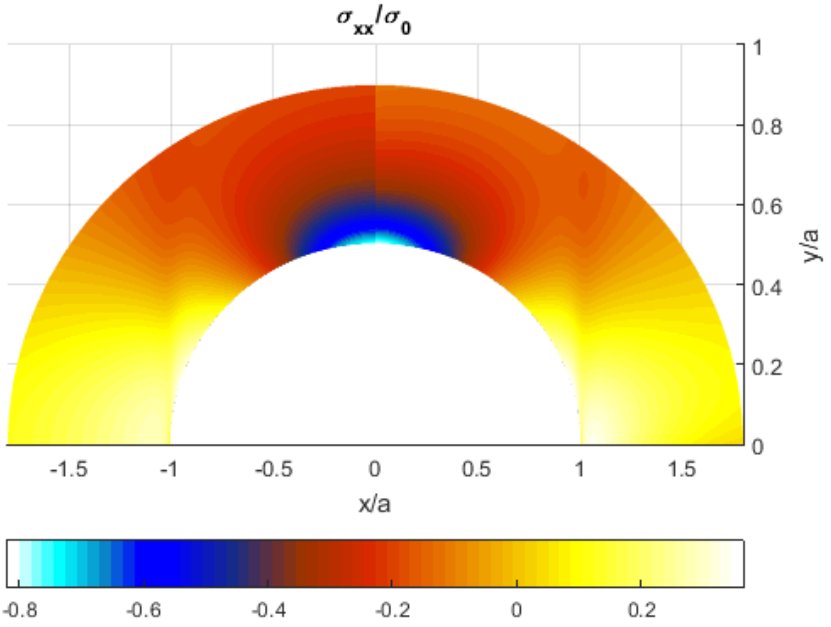

Figure 3-40: Contour plot of σ_{xx}/σ_0 throughout region adjacent to hole by FEA (right) and hybrid-TSA using the Laurent series and 8 real coefficients (left).

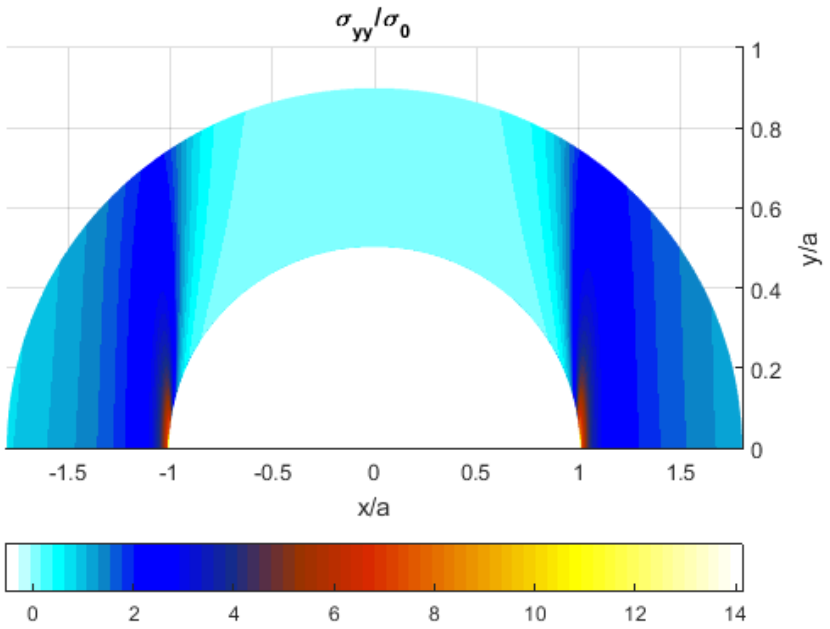

Figure 3-41: Contour plot of σ_{yy}/σ_0 throughout region adjacent to hole by FEA (right) and hybrid-TSA using the Laurent series and 8 real coefficients (left).

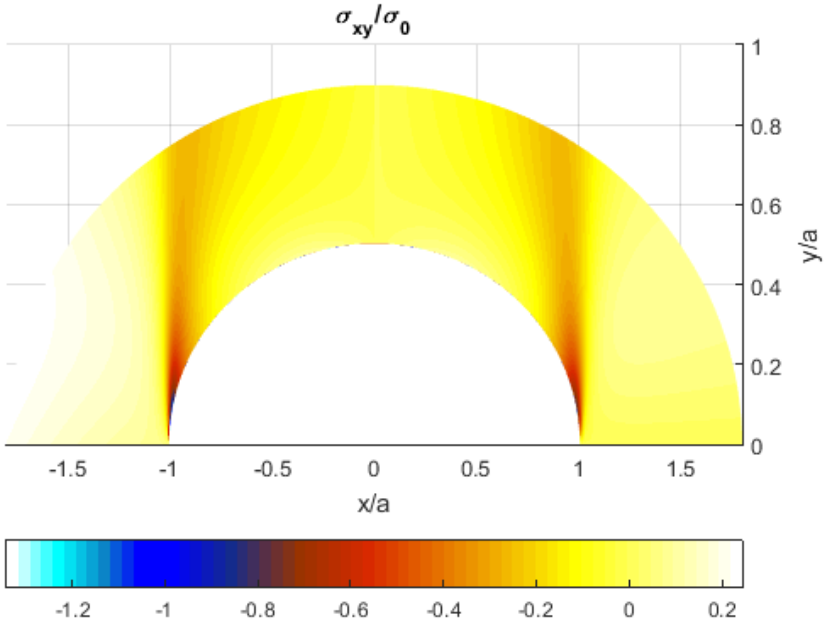

Figure 3-42: Contour plot of σ_{xy}/σ_0 throughout region adjacent to hole by FEA (right) and hybrid-TSA using the Laurent series and 8 real coefficients (left).

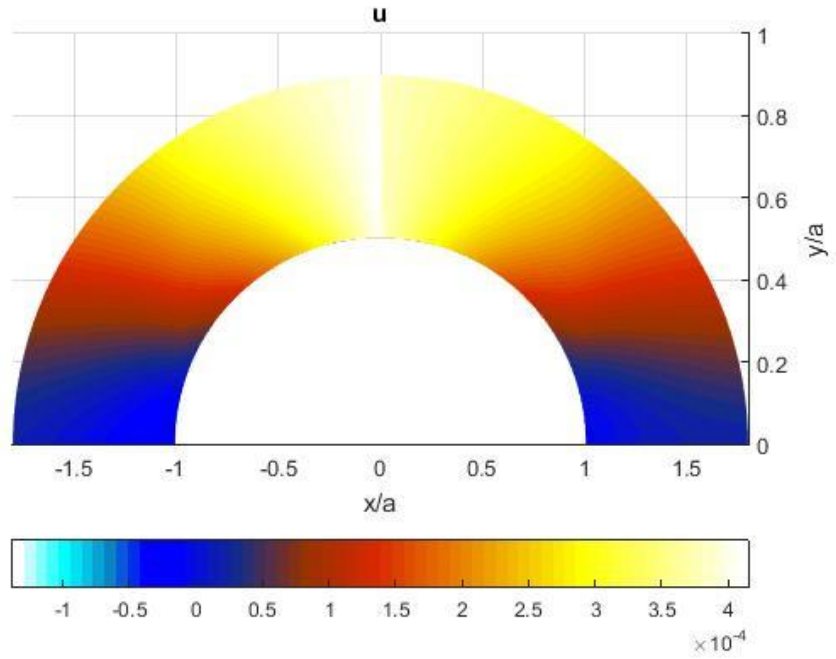

Figure 3-43: Contour plot of u throughout region adjacent to hole by FEA (right) and hybrid-TSA using the Laurent series and 8 real coefficients (left).

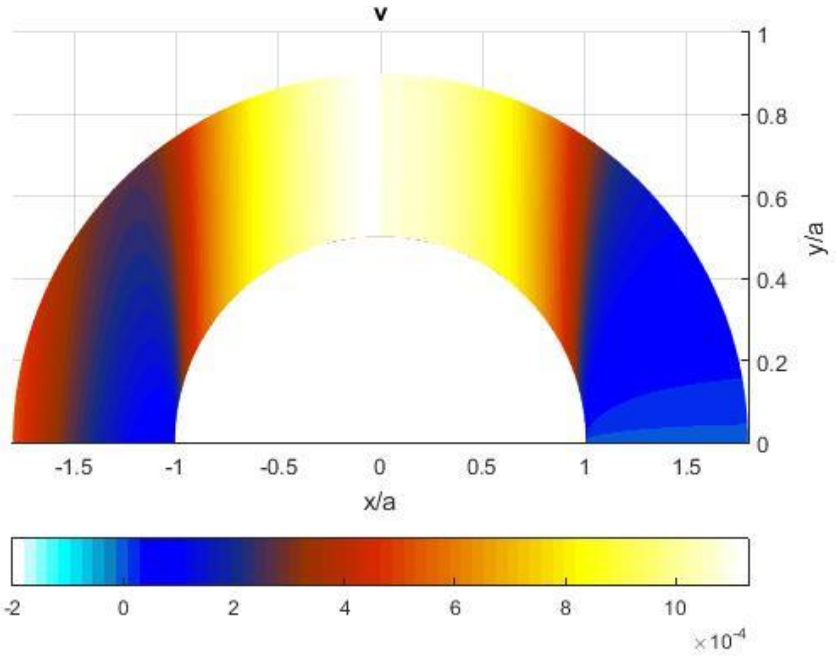

Figure 3-44: Contour plot of v throughout region adjacent to hole by FEA (right) and hybrid-TSA using the Laurent series and 8 real coefficients (left).

3.7.4 Load Equilibrium

Hybrid-TSA reliability was further assessed by checking load equilibrium. This was done by numerically integrating the TSA-determined vertical stress, σ_{yy}, along the line y = 0 (line AB in Figure 3-13) as shown in Figure 3-45.

$$F = \int \sigma_{yy} dA = 2 \int_{a}^{W/2} \sigma_{yy} t dx$$

where t and W are the plate thickness and width, respectively. Because of the symmetry the integration only covers the area from x = a to $W/2$. The integration of the TSA-determined stress was computed numerically using the trapezoidal rule in MATLAB to determine the area under the curve define by discrete values of $\sigma_{yy}(x, 0)$ along line AB as shown in Figure 3-45. Results based on the Taylor Laurent representations are 7.4 kN (1,658 lb) and 6.8 kN (1,529 lb), respectively, both of which are close to physically applied load of 7.12 kN (1,600 lb). The present equilibrium check supports the claim that the proposed method does not require knowing the applied load and in fact can handle inverse problems.

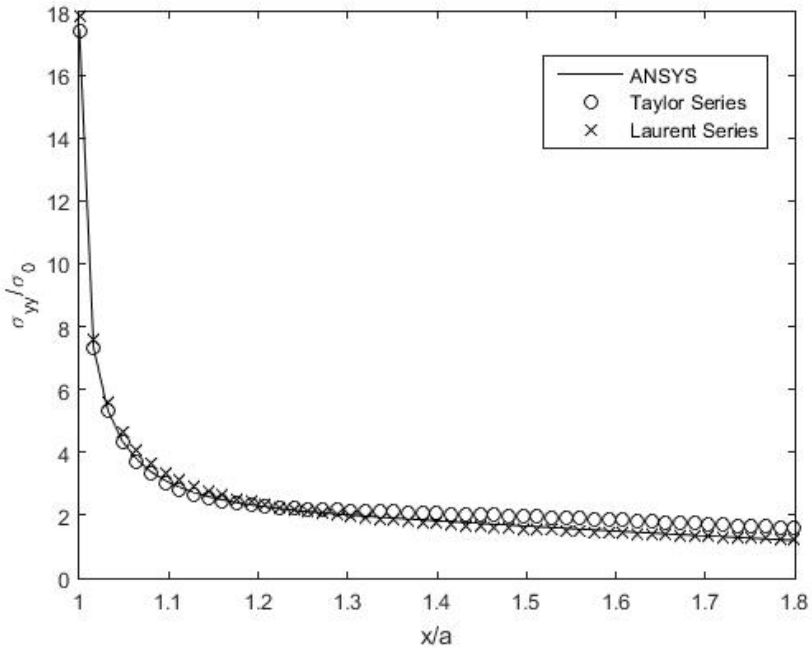

Figure 3-45: Variation σ_{yy}/σ_0 ahead of the hole along the line $y = 0$ in Figure 3-13 as function of x/a.

3.7.5 Effects of Variations in Number of Coefficients Employed

The maximum values of σ_{tt}/σ_0 where σ_{tt} is the tangential stress on the boundary of the hole from each of thermoelastic stress analysis, numerical hybrid finite element analyses, ANSYS, and Tan's approximation [64], equation (2-105), are compared in Table 3-4. Thermoelastic results of Table 3-4 agree within 4 percent of the average predicted value of 17.18 (average from ANSYS and Tan) when 8 real coefficients are used for both approaches.

Table 3-4: Stress concentration in the uniaxially loaded, finite-width $[0_{13}/90_5/0_{13}]$ graphite/epoxy tensile composite of Figure 3-13 containing an elliptical hole.

		Taylor series expansion		Laurent series expansion	
Theory (ANSYS)	Hybrid-ANSYS	N (number of real coefficients)	Hybrid-TSA method 1	N (number of real coefficients)	Hybrid-TSA method 2
	17.68	1 (2)	16.18	1 (4)	15.37
	20.56	2 (4)	23.04	3 (8)	16.16
15.7 (15.5)	15.82	3 (6)	17.18	5 (12)	19.79
	17.49	4 (8)	15.37	7 (16)	24.97
	17.48	5 (10)	20.23	9 (20)	26.65

3.7.6 Magnitudes of Coefficients, A_j

Table 3-5 and Table 3-6 list the values of $A_j = a_j + ib_j$ of equations (2-100) and (2-101) associated with thermoelastic data. Table 3-6 demonstrate the dominating influence of the early coefficients but the reduced consistency in magnitudes of the coefficients of larger N. On the other hand, in addition to the fact that lower-order a_j coefficients of equation (2-101) dominate, the values of these a_1 and a_{-1} tend to be very consistent for all values of N.

Table 3-5: Magnitudes of the coefficients associated with the stress calculation in the uniaxially loaded, finite-width [$0_{13}/90_5/0_{13}$] graphite/epoxy composite of Table 3-3 using thermoelastic data and Taylor series representation.

	Coefficients values using Taylor series expansion				
coefficients	$N = 1$	$N = 2$	$N = 3$	$N = 4$	$N = 5$
a_1	225.72	298.27	259.02	272.56	261.46
b_1	21.87	9.82	-0.27	-1.95	-6.40
a_2		66.28	-11.49	-86.21	49.02
b_2		-10.31	-12.51	-12.45	-9.51
a_3			-168.07	-42.56	-35.88
b_3			6.44	27.51	24.76
a_4				177.64	291.37
b_4				18.50	17.80
a_5					182.83
b_5					4.73

Table 3-6: Magnitudes of the coefficients associated with the stress calculation in the uniaxially loaded, finite-width [$0_{13}/90_5/0_{13}$] graphite/epoxy composite of Table 3-3 using thermoelastic data and Laurent series representation.

	Coefficients values using Laurent series expansion		
coefficients	$N = 1$	$N = 3$	$N = 5$
a_1	-93.4	-166	-85.5
b_1	0	0	0
a_{-1}	-106	-133	-104
b_{-1}	1.64	-0.99	12.2
a_3		-2.67	8.85
b_3		-3.36	-3.60
a_{-3}		-2.74	10.7
b_{-3}		3.93	4.18
a_5			0.406
b_5			0.764
a_{-5}			0.436
b_{-5}			-0.881

3.7.7 Effect of Input Data Location

Since recorded TSA data at, and close to, an edge are usually unreliable, one typically does not employ measured data within two or three pixels away from the edge of the hole. The previous results are based on the 2,558 recorded values of S^*, all of which originate 6 pixels ($0.1a$ = 2 mm) away from the edge of the hole. A small subroutine was subsequently prepared to assess the effect on the tangential stress, σ_{tt}, at the edge of the hole when employing S^* data at different minimum distances (number of pixels) from the hole, Figure 3-46 and Figure 3-47. These results demonstrate that neither the Taylor nor Laurent formulations are acceptable with thermal information collected up to one pixel away from the edge of the hole. Rather, one should use TSA data which originates at least 2 pixels away from the edge of the hole.

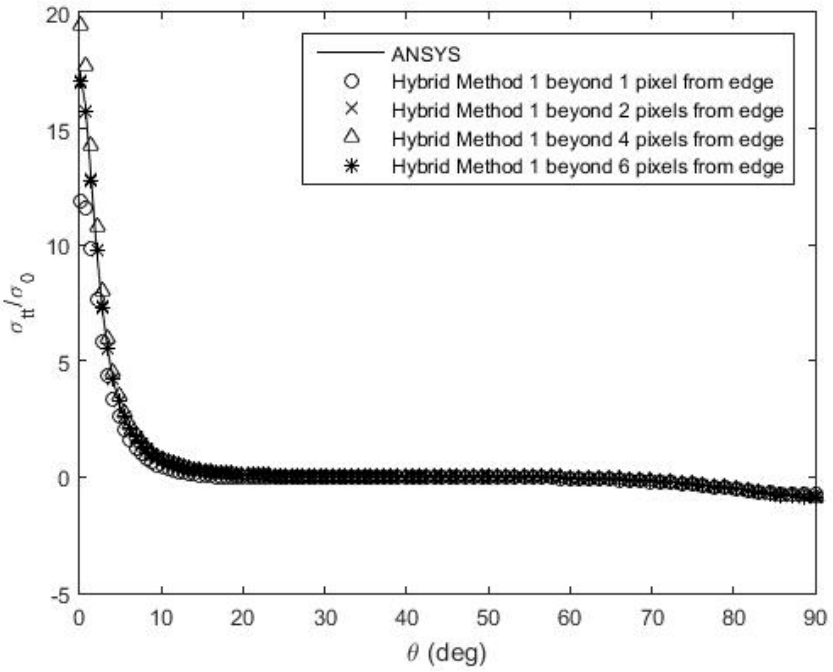

Figure 3-46: Effect of pixel location on TSA-determined σ_{tt}/σ_0 along edge of hole using hybrid first method-Taylor series (8 real coefficients).

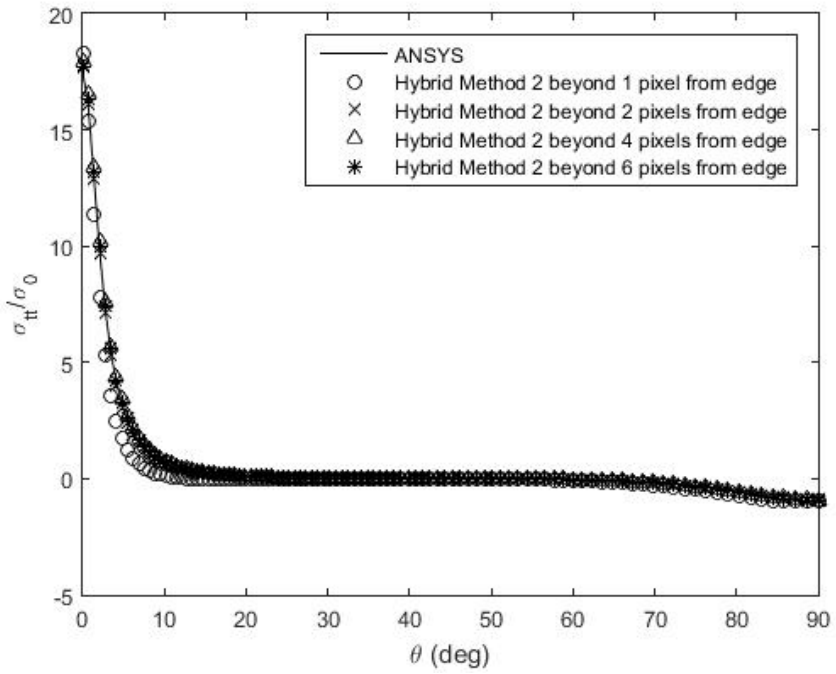

Figure 3-47: Effect of pixel location on TSA-determined σ_{tt}/σ_0 along edge of hole using hybrid second method-Laurent series (8 real coefficients).

3.8 Summary, Discussion and Conclusions

A hybrid method which processes the load-induced TSA signals with a stress function in complex variables, together with conformal mapping and analytic continuation concepts, provides the individual stresses on and in the neighborhood of an elliptical hole whose major axis is perpendicular to the direction of loading in a finite orthotropic composite plate. Both Laurent and Taylor series representations of the stress function are utilized with equal satisfaction. Unlike purely theoretical or numerical methods, knowledge of the external boundary or loading conditions is unnecessary. TSA results agree with those from FEM and force equilibrium. Results demonstrate the need to not employ recorded TSA data within at least two pixels of the edge of the hole. Unlike previous TSA approaches, rational means are provided with which to assess how many coefficients to retain and the suitability of employing either the Laurent or Taylor series representation is shown experimentally. More complicated shaped cutouts might necessitate the use of overlapping applications of the method.

Employing more measured input values than unknown coefficients filters out experimental noise/scatter and smooths the results. A method was developed to separate reliably the thermoelastic data into individual stresses throughout a region adjacent to a traction-free boundary as well as to evaluate accurate boundary information even though the recorded TSA data along, and adjacent to, an elliptical hole were not included.

Unlike a classical boundary value problem, the present approach does not guarantee the correct boundary conditions or the individual stresses on the rest of the boundary of the region R_z. The quality of the evaluated stresses could deteriorate as the dimension of the region R_z normal to its free edge becomes large (for plate with elliptical hole, the results are accurate up to at least x/b = 6). The objective of this approach is to determine reliable information along, and adjacent to, the edge of the component where the interested region is, rather than to evaluate the stresses necessarily throughout the entire structure. The size of region R_z over which the stress function is reliable can be increased by additional employing some boundary collocation. Least square method was used to evaluate unknown coefficients of overdetermined systems of equations. Experimental advantages of the method include the relatively small amount of measured data needed and such data can originate away from the discontinuity of concern.

Compared to finite-element analyses, the numerical computations of the present method are relatively simple and consume little computer time. In addition to satisfying force equilibrium, the thermoelastic determined stresses correlate well with finite-element results. A motivation for developing the present method is to enable stress analysis of orthotropic cases which cannot be analyzed numerically. The present geometry and loading were deliberately selected so as one could obtain a reliable FEA with which to compare the experimental results and thereby validate the presented experimental technique. The developed thermoelastic method is applicable to more complicated problems which are difficult for FEM.

A series representation of the stress function using either Taylor or Laurent series expansion is assumed and careful attention paid to determining an appropriate number of coefficients to retain (in this case, 8 real coefficients). The methods utilized here to ascertain how many coefficients to employ are general, not specific to the current data set or example. The successful outcome of these processes for choosing the appropriate number of coefficients to use indicates that they are reasonable and effective techniques, and probably useful in other situations.

Previous stress analyses whose measured data were processes by a stress function in complex variables are restricted to circular geometries [12,42,43,45,59,60,70–72]. A major contribution of this chapter is the demonstrated ability to determine the individual stresses in a finite engineering component by TSA, specifically on, and in the neighborhood of, the boundary of the elliptical hole. Such inverse problems where the stresses on and in the neighborhood of the edge of a hole are determined without explicit knowledge of the external loading or geometry can be very challenging. Symmetry about the x- and y-axes is not necessary, and stress function could handle finite and infinite geometry. Future consideration might also assess the best number of values of S^* (equivalent to choosing the number of equations) and their locations to provide reliable stresses.

The author is unaware of any previously published TSA technique capable of reliably stress analyzing general orthotropic composite structures or machine components. Aspects of this chapter were presented/published in Annual Technical Conference (ANTEC) [33], presented in annual Society of Experimental Mechanics conference [34] and published in Journal of Experimental Mechanics [32].

Chapter 4: Hybrid Full-Field Stress Analysis of Finite Plate with Near Edge Hole Subjected to a Concentrated Load

Recognizing that the most serious structural stresses often occur at holes or notches, the ability to determine the stresses on and near the boundary of a near-edge circular hole in a finite plate subjected to a concentrated edge-load by combining recorded load-induced temperature with Airy stress function in complex variables is demonstrated. Purely analytical or theoretical stress analyses tend to be available for only simple situations involving simple, infinite structures, whereas many practical problems involve complicated, finite shapes. Moreover, and like numerical (finite element method, finite different method) approaches, analytical/theoretical analyses depend on reliable knowledge of the boundary conditions. Experimental techniques are therefore important for determining the stresses associated with geometric discontinuities. Although it can sometimes be advantageous to combine measured information with that from other experimental or numerical techniques, it is convenient to acquire all the necessary data utilizing a single experimental method. The present approach combines data from thermoelastic stress analysis (TSA) and an applicable series representation of the Airy stress function in complex variables. The complex mapping-collocation method simultaneously smooths the measured input data, satisfies the local boundary conditions analytically and evaluates individual stresses on, and in the neighborhood of, the edge of the hole. Using real variables is restricted to isotropic materials where the complex mapping-collocation technique is applicable for both isotropic and orthotropic materials. The reliability of the present method is supported by comparing with finite element and previous results using the real variable approach.

4.1 Introduction

High stresses and stress gradients which occur at geometry discontinuities often lead to component failure. The stress distribution in such locations can be complicated and theoretical solutions are frequently unavailable, particularly for finite geometries. Moreover, like purely theoretical or numerical methods typically necessitates accurately knowing the far-field geometry and complete (distant) boundary conditions, information which can be unreliable or unavailable. On the other hand, although experimental techniques (for instance, TSA, PSA, moiré, speckle, digital image correlation, strain gages or holography) can be used to provide stress information in such cases, most experimental methods (except TSA) are tedious with respect to specimen preparation and/or quantitative measurements.

The load plate of Figure 4-1 and Figure 4-2 which supported along the bottom edge, CDC', and subjected to a concentrated edge-load directly above or away from the hole were previously stress analyzed from recorded temperature information by evaluating the coefficients of stress functions that accounted for the external loading [20,21] and by just using the simple Airy stress function in the real variables [22]. Those analyses utilized complicated, dedicated, and restrictive stress functions that were specifically developed by superposing to explicitly the applied load, P^* and/or just analytically imposing the boundary condition. The lacks of symmetry about either the x- or y- axis necessitates more coefficients which significantly complicated formulating the stress function. That approaches are not readily extendable to more complicated situations. The stresses at and in the neighborhood of hole are obtained here by processing measured data from thermoelastic stress analysis (TSA) using Airy stress function in complex variables. Superposing the general solution of biharmonic equation in real variable and the Flamant solution (1892) of a concentrated load on semi-infinite body [47,73]

where the boundary condition is imposed discretely is also introduced for comparison. A numerical method was firstly conducted by employing FE-simulated isopachic stress data from ANSYS in order to substantiate the viability, robustness, and numerical stability of the desired numerical method, then thermoelastic measured isopachic stress data will be utilized to investigate stress distributions in the actual plate. The results of the simulated numerical experiment are listed in Appendix A. The advantageous of using mapping-collocation technique is more general and substantially simpler formulation than the methods used previously.

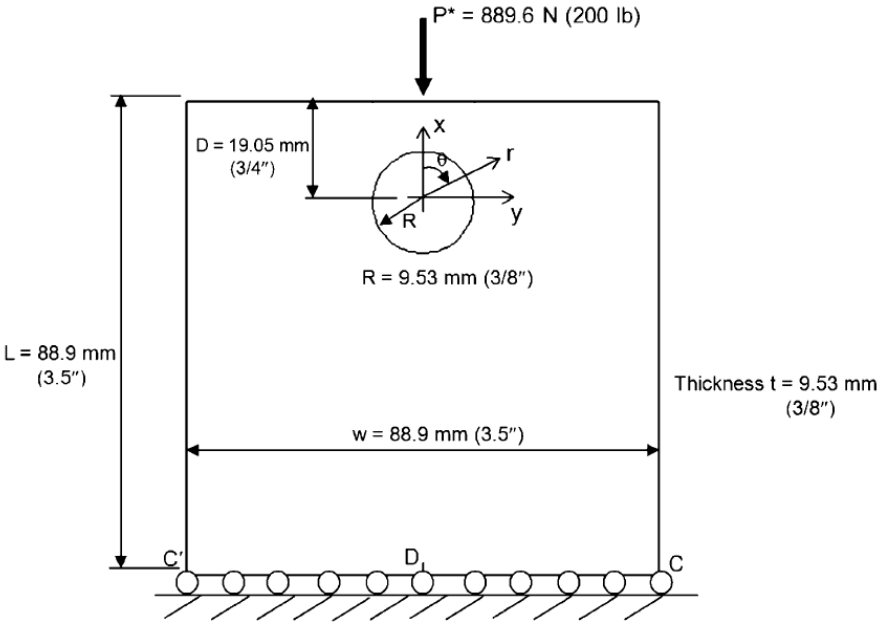

Figure 4-1: Schematic geometry of a plate containing a near-edge hole beneath a concentrated load.

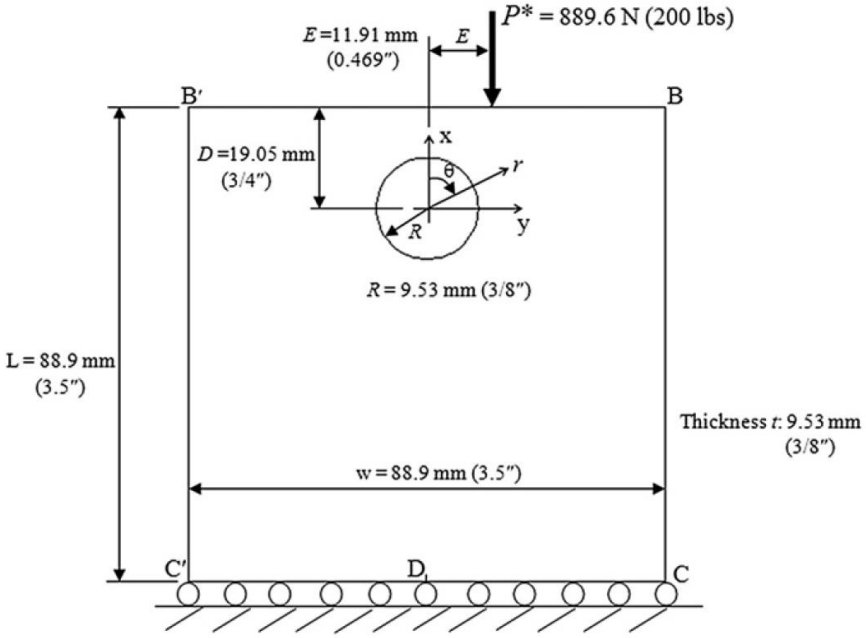

Figure 4-2: Schematic geometry of a plate containing a near-edge hole subjected to an offset concentrated load.

The stresses at, and in, the neighborhood of the edge of the geometrical discontinuity control the structural integrity so the present technique utilized complex variables and mapping, and satisfied the traction-free condition analytically at the circular hole to provide reliable stresses throughout the region without presupposing knowledge of the external boundary or loading conditions and material constitutive properties. This feature is important because the external loads are often poorly (if at all) known. The mapping-collocation technique is applicable for symmetrical or asymmetrical cases. Equilibrium and compatibility conditions throughout the region are satisfied using complex variable formulation involving conformal mappings and analytic continuation. Interest in the problem is motivated by applications to mechanical components and buries structures. The semi-infinite plate (half-plane) is approximated by a finite plate.

Thermoelastic Stress Analysis (TSA) only gives information related to the sum of the principal stress, it is generally difficult to ‘separate the stresses’ from temperature information alone. Since the region of interest is in the vicinity of the hole in the plate of Figure 4-1 and

Figure 4-2, the present hybrid-TSA method using complex mapping-collocation technique separates the stresses, provides reliable stress adjacent to the circular hole and satisfies the boundary conditions analytically. This approach is applicable irrespective of the form or magnitude of the loading and stresses are provided without the use of measured data on, or immediately near, the hole boundary. This is important since it is often difficult to obtain accurate measured information at the edge or the boundary of the discontinuity. The method is capable of solving inverse problem because the distant, geometry or external boundary conditions, including the concentrated load, are often unknown.

Wang et al. [74] investigated the state of stress around a near-surface circular hole in a semi-infinite plate under a concentrated load from photoelastic fringes and superposition between the classical solution of infinite plate with circular hole and Hertz contact. Unlike the photoelastic isochromatic method which requires non-linear least squares, the TSA-measured isopachics requires only linear least squares. Although applied here to a specific problem and recorded temperature, the current concepts are applicable to general situations involving more complicated geometry, different material response, and/or loading and other types of measured information, e.g., moiré, holography, speckle, digital image correlation, strain gages, or photoelasticity. Using real variables is limited to isotropic response where the complex mapping-collocation technique is applicable for both isotropic and orthotropic responses. A major contribution of this chapter is the ability to experimentally evaluate stresses associated with geometric discontinuities using stress function in complex variable essentially irrespective of the external boundary conditions and the consequently wide applicability of this approach.

Although the radius of the hole of Figure 4-1 is equal to the plate thickness, Lin et al. [20] substantiated the validity of assuming plane stress by using three-dimensional finite element method. This study presents a nondestructive and non-contacting hybrid method for determining the full-field individual stresses in a finite rectangular plate containing a near-edge

hole and subjected to a concentrated load. The present analysis of the plate of Figure 4-2 wherein the hole and load are offset both horizontally and vertically from each other significantly extends thermoelastic applicability beyond prior capabilities. The current study is the most complicated stress analysis formulation to date where temperature measurements (thermoelastic signals) are synergized with an Airy stress function in complex variables. The author is unaware of any previous use of measured temperature to evaluate the individual stresses on and in the neighborhood of a near-edge hole adjacent to an offset concentrated load using mapping-collocation technique.

4.2 Thermoelastic Stress Analysis

4.2.1 Experimental Details

The aluminum (6061 T6511, ultimate strength of 275 to 311 MPa (40 to 45 ksi) and yield point of 241 to 275 MPa (35 to 40 ksi)) plate of Figure 4-1 and Figure 4-2 was sprayed with Krylon flat black paint prior to testing to enhance and unify its surface emissivity. The coordinate origin lies at the center of the hole with radius R = 9.53 mm (0.375 inch). The plate is square with sides of 88.9 mm (3.5 inch) and thickness of 9.53 mm (0.375 inch). Figure 4-3 and Figure 4-4 are photographs of the experimental set-up. The specimen was mounted in a 88.96 kN (20,000 lbs) capacity MTS loading frame and loaded sinusoidally between 222.4 N (50 lb) and 1112 N (250 lb) at 20 Hz. Figure 4-3 and Figure 4-4 also show the liquid-nitrogen-cooled Stress Photonics DeltaTherm DT1410 infrared camera (sensor array of 256×256 pixels) used to record the load-induced temperature variations. The thermoelastic images of Figure 4-5 and Figure 4-6 were recorded/integrated over a duration of two minutes. The TSA pixel spacing of the images shown in Figure 4-5 and Figure 4-6 is approximately 0.73 mm (0.029″) and 0.72 mm (0.028″), so the entire plate contains approximately 14,500 and 15.000 discrete values, respectively. The specimen was prepared and the data were collected by Katherine Lin [16,21].

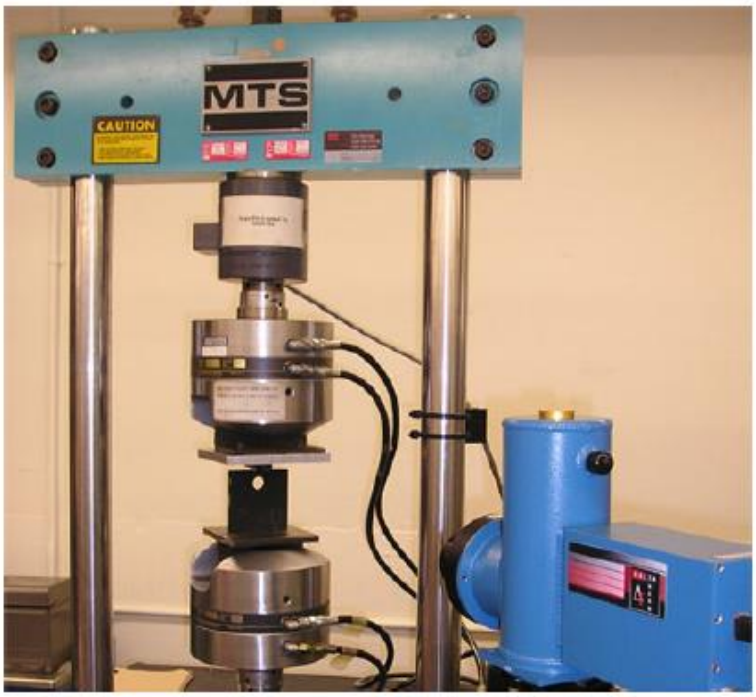

Figure 4-3: Photograph of the experimental set-up, with DeltaTerm DT1410 infrared camera at the bottom right [16].

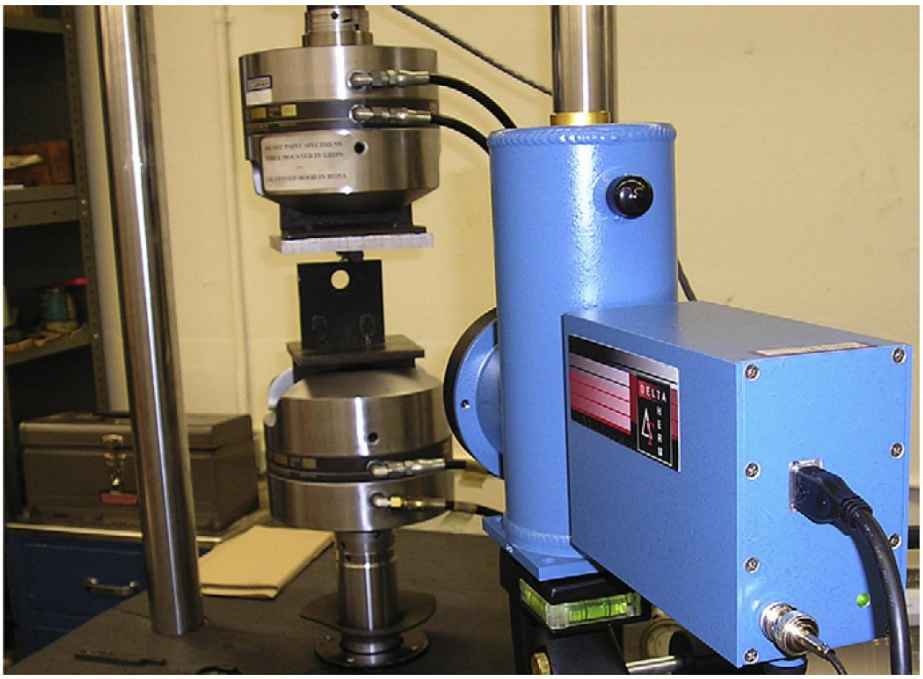

Figure 4-4: Photograph of the experimental set-up, with DeltaTerm DT1410 infrared camera at the bottom right [21].

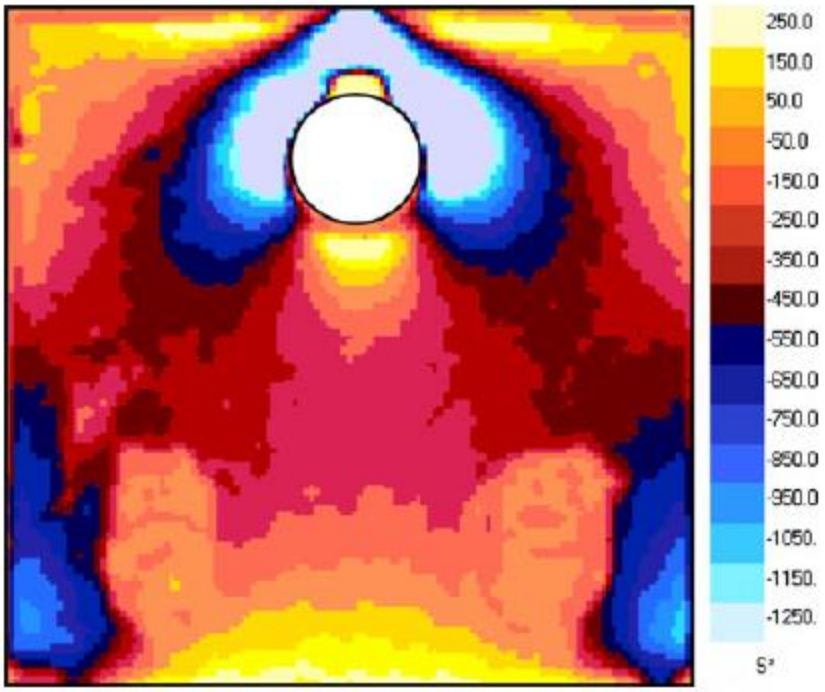

Figure 4-5: Thermoelastic image of loaded plate in Figure 4-1 at a frequency 20 Hz [16].

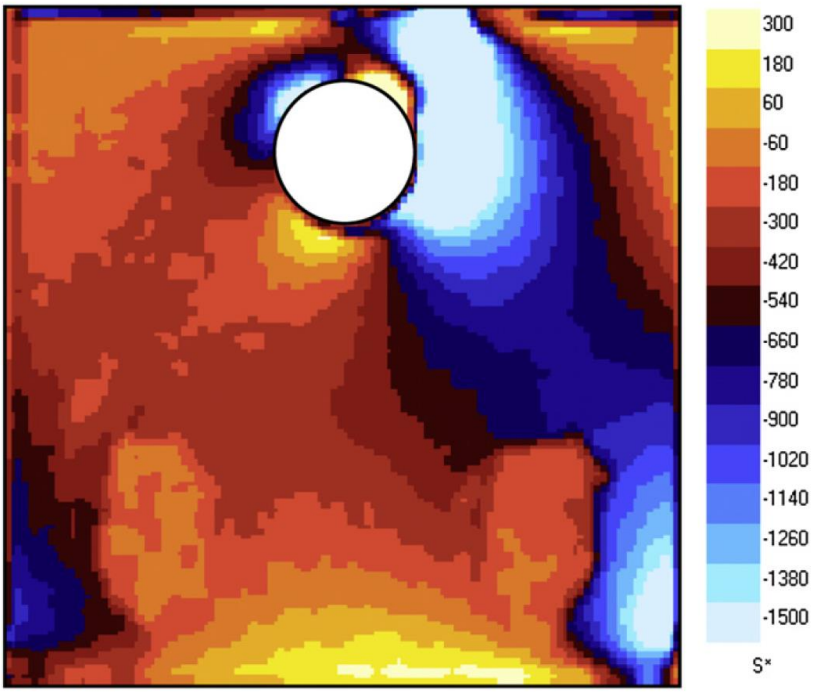

Figure 4-6: Thermoelastic image of loaded plate in Figure 4-2 at a frequency 20 Hz [21].

4.2.2 TSA Clabiration

Since the plate of Figure 4-1 and Figure 4-2 does not include any region of known uniform stress, calibration was obtained from a supplementary uniaxial tensile strip of the same

grade of aluminum. The calibration specimen was coated with the same paint, subjected to sinusoidal loading at the same frequency, 20 Hz, and monitored using the same TSA infrared system as the plate of Figure 4-1 and Figure 4-2. The thermomechanical coefficient, $K = S^*/(S = \sigma_{rr} + \sigma_{\theta\theta} = \sigma_{xx} + \sigma_{yy})$ was found to be equal to 319 U/MPa (2.21 U/psi) and this calibration factor was applied to the TSA data from the component of interest. The unit U is used to signify the raw TSA output, in uncalibrated signal units [16,21].

4.2.3 Data Collection

The unreliable thermoelastic data, S^*, on and near the circular boundary motivated only using thermoelastic data shown in Figure 4-7 for the plate in Figure 4-1 and thermoelastic data shown in Figure 4-8 for the plate in Figure 4-2 and those regions are denoted as region R^*. Figure 4-7 indicates the source locations of the 300 (of the approximately 14,500 available) thermoelastic input values of Figure 4-5 where Figure 4-8 indicates the source locations of the 849 (of the approximately 15,000 available) thermoelastic input values of Figure 4-6 used for the current stress analysis. As recorded TSA information within three or four pixels of an edge is usually unreliable, the TSA data of Figure 4-7 and Figure 4-8 originate at least 4 pixels (approximately 3 mm) away from the boundary of the hole and the top edge of Figure 4-1 and Figure 4-2, respectively.

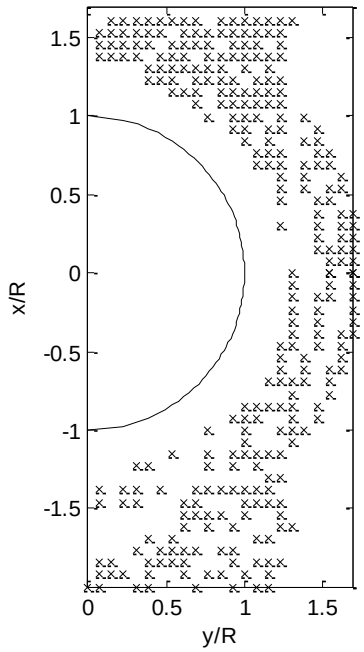

Figure 4-7: Thermoelastic data source location (m = 300 data points) for a plate in Figure 4-1.

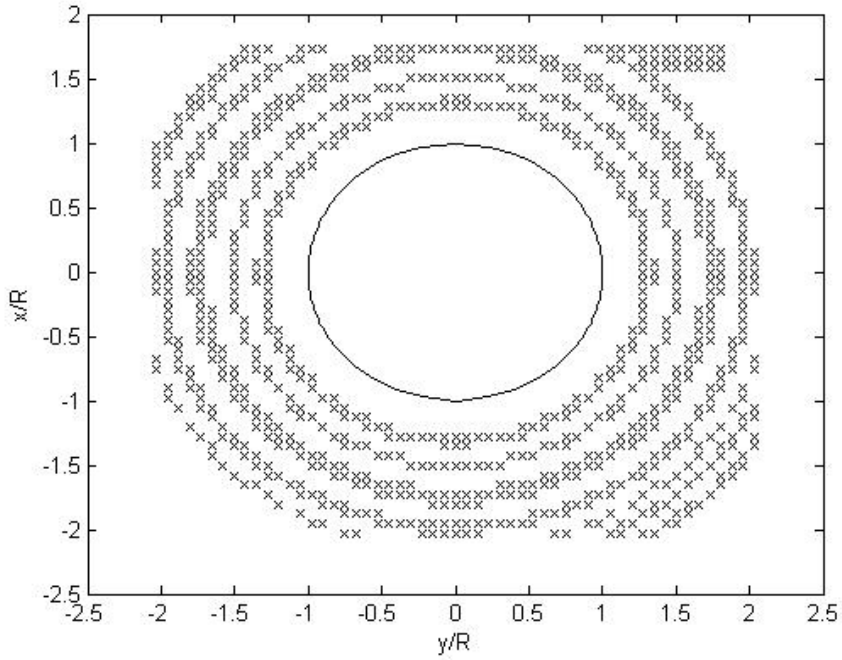

Figure 4-8: Thermoelastic data source location (m = 849 data points) for a plate in Figure 4-2.

Since this analysis determines the stresses on, and in the neighborhood of, the edge of the hole, only 300 and 849 measured values of S^* around the hole are used here. The source locations of these input values, which are indicated in Figure 4-7 and Figure 4-8, are largely

arbitrary, but based on experience and the high stresses between the top of the hole and the top concentrated load, P. If the intent were to stress analyze the entire plate, it would probably be necessary to include appreciably more Airy coefficients and perhaps thousands of measured TSA input values although the present model DT1410 staring-array camera records a full-field resolution. The unreliable temperatures at and near an edge (so-called 'edge effect') discussed in the preceding paragraph occurs because at a boundary, the detector "sees" a spot which is partly on the stressed specimen and partly on the stress-free background. The quality of an edge signal can be further reduced by the cyclic motion of the structure such that the detector receives different data from the different spatial positions.

4.2.4 Evaluating the Airy Coefficients

Thermoelastic stress analysis provides full-field stress information over the surface. If one records an appropriate amount of TSA measured data and employs a relevant Airy stress function in complex variable, it is possible to obtain the individual stress distributions in the plate, at least at and in the vicinity of geometric discontinuity, without any complex mathematical algebra or additional experimental and/or numerical techniques. Like most experimental data, the measured data incorporate some noise which necessitate collecting more measured input values than the number of unknown Airy coefficients. The number of equations are larger than the number of coefficients which produces an overdetermined system which can be solved using a least-square method. The system was solved in MATLAB using the backslash '\' or pseudo inverse 'pinv' operator.

4.3 Relevant Equations in Real Variables

4.3.1 Airy Stress Function

For plane-stress elasticity, the Airy stress function, Φ, satisfying the governing differential equation $\nabla^4\Phi = 0$ for isotropic is given by equation (2-35). The individual components of stress in polar coordinate can be evaluated using equations (2-36), (2-37), and (2-38) to give (2-39), (2-40), and (2-41), respectively. While a general expression for Φ might consist of numerous coefficients, many of these coefficients can often be eliminated by various conditions and/or arguments, e.g., symmetry, single-value stresses, strains, or displacements, whether or not the origin within the body, and whether the component is finite or infinite in size. Since the displacements, strains, and stresses cannot be multi-valued functions of θ, the coordinate origin is selected to be in the center of the hole. The symmetry of the specimen in Figure 4-1 about the vertical x-axis results in symmetrical stresses such that the Airy stress function is an even function, $\Phi(r,\theta) = \phi(r,-\theta)$. This means that all sine terms go to zero. Therefore, the Airy stress function, Φ_{sym}, in equation (2-35) satisfying the stress field in Figure 4-1 without considering the effect of the concentrated load becomes

$$\Phi_{\text{sym}} = a_0 + b_0 \ln r + c_0 r^2 + \left(a_1' r + \frac{c_1'}{r} + d_1' r^3\right)\cos\theta + \sum_{n=2,3,..}^{\infty} \left(a_n' r^n + b_n' r^{n+2} + c_n' r^{-n} + d_n' r^{-(n-2)}\right)\cos n\theta \tag{4-1}$$

The individual components of stresses in polar coordinate can be evaluated using equations (2-36), (2-37), and (2-38)

$$(\sigma_{rr})_{\text{sym}} = \frac{b_0}{r^2} + 2c_0 - \frac{2c_1'}{r^3}\cos\theta + 2d_1' r\cos\theta - \sum_{n=2,3,..}^{N} \begin{Bmatrix} a_n' n(n-1)r^{n-2} + b_n'(n+1)(n-2)r^n + \\ c_n' n(n+1)r^{-(n+2)} + d_n'(n-1)(n+2)r^{-n} \end{Bmatrix} \cos n\theta \tag{4-2}$$

$$(\sigma_{\theta\theta})_{\text{sym}} = \frac{-b_0}{r^2} + 2c_0 + \frac{2c_1'}{r^3}\cos\theta + 6d_1' r\cos\theta + \sum_{n=2,3,..}^{N} \begin{Bmatrix} a_n' n(n-1)r^{n-2} + b_n'(n+1)(n+2)r^n + \\ c_n' n(n+1)r^{-(n+2)} + d_n'(n-1)(n-2)r^{-n} \end{Bmatrix} \cos n\theta \tag{4-3}$$

$$(\sigma_{r\theta})_{\text{sym}} = -\frac{2c_1'}{r^3}\sin\theta + 2d_1' r\sin\theta + \sum_{n=2,3,..}^{N} \begin{Bmatrix} a_n' n(n-1)r^{n-2} + b_n' n(n+1)r^n - \\ c_n' n(n+1)r^{-(n+2)} - d_n' n(n-1)r^{-n} \end{Bmatrix} \sin n\theta \tag{4-4}$$

The first stress invariant for the resultant stresses is

$$\begin{aligned} S_{\text{sym}} &= (\sigma_{rr})_{\text{sym}} + (\sigma_{\theta\theta})_{\text{sym}} \\ &= 4c_0 + 8d_1' r\cos\theta \\ &\quad + \sum_{n=2,3,..}^{N} \{4b_n'(n+1)r^n - 4d_n'(n-1)r^{-n}\}\cos n\theta \end{aligned} \tag{4-5}$$

Notice that not all coefficients present in the individual stress equations are present in equation (4-5) above as S_{sym} is only function of (c_0, d_1', b_n', d_n') whereas the individual stresses being a function of $(b_0, c_0, c_1', d_1', a_n', b_n', c_n', d_n')$. In order to evaluate all Airy coefficients, traction-free boundary conditions must be imposed on the edge of the hole. The Airy stress function, Φ_{unsys}, in equation (2-35) for offset loaded plate in Figure 4-2 satisfying the stress field without considering the effect of the concentrated load becomes

$$\Phi_{\text{unsym}} = a_0 + b_0 \ln r + c_0 r^2 + A_0\theta + \left(a_1 r + \frac{c_1}{r} + d_1 r^3\right)\sin\theta + \left(a_1' r + \frac{c_1'}{r} + d_1' r^3\right)\cos\theta + \sum_{n=2,3,..}^{\infty}\left(a_n r^n + b_n r^{n+2} + c_n r^{-n} + d_n r^{-(n-2)}\right)\sin n\theta + \sum_{n=2,3,..}^{\infty}\left(a_n' r^n + b_n' r^{n+2} + c_n' r^{-n} + d_n' r^{-(n-2)}\right)\cos n\theta \quad (4\text{-}6)$$

The individual components of stresses in polar coordinate can be evaluated using equations (2-36), (2-37), and (2-38)

$$(\sigma_{rr})_{\text{unsym}} = \frac{b_0}{r^2} + 2c_0 - \frac{2c_1}{r^3}\sin\theta + 2d_1 r\sin\theta - \frac{2c_1'}{r^3}\cos\theta + 2d_1' r\cos\theta - \sum_{n=2,3,..}^{N}\left\{\begin{matrix} a_n n(n-1)r^{n-2} + b_n(n+1)(n-2)r^n + \\ c_n n(n+1)r^{-(n+2)} + d_n(n-1)(n+2)r^{-n}\end{matrix}\right\}\sin n\theta - \sum_{n=2,3,..}^{N}\left\{\begin{matrix} a_n' n(n-1)r^{n-2} + b_n'(n+1)(n-2)r^n + \\ c_n' n(n+1)r^{-(n+2)} + d_n'(n-1)(n+2)r^{-n}\end{matrix}\right\}\cos n\theta \quad (4\text{-}7)$$

$$(\sigma_{\theta\theta})_{\text{unsym}} = \frac{-b_0}{r^2} + 2c_0 + \frac{2c_1}{r^3}\sin\theta + 6d_1 r\sin\theta + \frac{2c_1'}{r^3}\cos\theta + 6d_1' r\cos\theta + \sum_{n=2,3,..}^{N}\left\{\begin{matrix} a_n n(n-1)r^{n-2} + b_n(n+1)(n+2)r^n + \\ c_n n(n+1)r^{-(n+2)} + d_n(n-1)(n-2)r^{-n}\end{matrix}\right\}\sin n\theta + \sum_{n=2,3,..}^{N}\left\{\begin{matrix} a_n' n(n-1)r^{n-2} + b_n'(n+1)(n+2)r^n + \\ c_n' n(n+1)r^{-(n+2)} + d_n'(n-1)(n-2)r^{-n}\end{matrix}\right\}\cos n\theta \quad (4\text{-}8)$$

$$(\sigma_{r\theta})_{\text{unsym}} = \frac{A_0}{r^2} + \frac{2c_1}{r^3}\cos\theta - 2d_1 r\cos\theta - \frac{2c_1'}{r^3}\sin\theta + 2d_1' r\sin\theta$$
$$- \sum_{n=2,3,..}^{N} \begin{Bmatrix} a_n n(n-1)r^{n-2} + b_n n(n+1)r^{n} - \\ c_n n(n+1)r^{-(n+2)} - d_n n(n-1)r^{-n} \end{Bmatrix} \cos n\theta \qquad (4\text{-}9)$$
$$+ \sum_{n=2,3,..}^{N} \begin{Bmatrix} a_n' n(n-1)r^{n-2} + b_n' n(n+1)r^{n} - \\ c_n' n(n+1)r^{-(n+2)} - d_n' n(n-1)r^{-n} \end{Bmatrix} \sin n\theta$$

The first stress invariant for the resultant stresses is

$$S_{\text{unsym}} = (\sigma_{rr})_{\text{unsym}} + (\sigma_{\theta\theta})_{\text{unsym}}$$
$$= 4c_0 + 8d_1 r\sin\theta + 8d_1' r\cos\theta$$
$$+ \sum_{n=2,3,..}^{N} \{4b_n(n+1)r^{n} - 4d_n(n-1)r^{-n}\}\sin n\theta \qquad (4\text{-}10)$$
$$+ \sum_{n=2,3,..}^{N} \{4b_n'(n+1)r^{n} - 4d_n'(n-1)r^{-n}\}\cos n\theta$$

Notice that not all coefficients present in the individual stress equations are present in equation (4-10) above as S_{unsym} is only function of $(c_0, d_1, d_1', b_n, b_n', d_n, d_n')$ whereas the individual stresses being a function of $(b_0, c_0, A_0, c_1, c_1', d_1, d_1', a_n, a_n', b_n, b_n', c_n, c_n', d_n, d_n')$. In order to evaluate all Airy coefficients, traction-free boundary conditions must be imposed on the edge of the hole either analytically or discretely.

Equation (4-2) through (4-4) and (4-7) through (4-9) account for a single-value stresses, strains, and displacements with respect to angle θ, and the stresses (loading) are self-equilibrating individually on each of the inner or external boundary, and the resultant forces at the origin are zero. They recognize that r = 0 is not within the physical compnonent and permit the plate to be large but do not assume/require it to be infinite (i.e., retain terms involving r^n). Equations (4-2) through (4-4) recognize symmetry about vertical x-axis. The stresses from

equations (4-7) through (4-9) are completely general as to the shape of any cutouts, the shape of and/or distance to the external edge and form of external loading.

4.3.2 Flamant Solution

By using the Flamant solution and shift the center from the location of concentrated load at the surface to the center of the hole located a distance D, Figure 4-1, the Airy stress function, $\Phi_{F,\text{sym}}$, due to the concentrated load is [20]

$$\Phi_{F,\text{sym}} = -\frac{P}{\pi} r \sin\theta \tan^{-1}\left(\frac{r\sin\theta}{D - r\cos\theta}\right) \tag{4-11}$$

The individual components of stresses in polar coordinate can be evaluated using equations (2-36), (2-37), and (2-38)

$$(\sigma_{rr})_{F,\text{sym}} = -\frac{2P(D - r\cos\theta)(r^2 + D^2\cos^2\theta - 2rD\cos\theta)}{\pi(r^2 + D^2 - 2Dr\cos\theta)^2} \tag{4-12}$$

$$(\sigma_{\theta\theta})_{F,\text{sym}} = -\frac{2PD^2\sin^2\theta\,(D - r\cos\theta)}{\pi(r^2 + D^2 - 2Dr\cos\theta)^2} \tag{4-13}$$

$$(\sigma_{r\theta})_{F,\text{sym}} = -\frac{2PD\sin\theta\,(D - r\cos\theta)(r - D\cos\theta)}{\pi(r^2 + D^2 - 2Dr\cos\theta)^2} \tag{4-14}$$

where P is the applied load per thickness and D is the respective vertical distance located from the origin of the coordinate axes (and ultimately the center of the circular hole of radius R) below the top of the plate as shown in Figure 4-1. The first stress invariant for the resultant stresses is

$$S_{F,\text{sym}} = (\sigma_{rr})_{F,\text{sym}} + (\sigma_{\theta\theta})_{F,\text{sym}} = -\frac{2P(D - r\cos\theta)}{\pi(r^2 + D^2 - 2Dr\cos\theta)} \tag{4-15}$$

For offset loaded plate in Figure 4-2, the corresponding equation of the Airy stress function, $\Phi_{F,\text{unsys}}$, due to the concentrated load in semi-infinite plate is obtained by shifting the center from the location of concentrated load at the surface to the center of the hole located a distance D below the top of the plate and horizontal distance E between the load and the center of the hole, [21]

$$\Phi_{F,\text{unsym}} = -\frac{P}{\pi}\tan^{-1}\left(\frac{E - r\sin\theta}{D - r\cos\theta}\right)(E - r\sin\theta) \tag{4-16}$$

The individual components of stresses in polar coordinate can be evaluated using equations (2-36), (2-37), and (2-38)

$$\begin{aligned}(\sigma_{rr})_{F,\text{unsym}} = \frac{2P(r - D\cos\theta - E\sin\theta)}{\pi(r^2 + D^2 + E^2 - 2Dr\cos\theta - 2Er\sin\theta)^2}\{r^2\cos\theta + D^2\cos\theta \\ - 2rD\cos^2\theta - rE\sin\theta\cos\theta + ED\sin\theta - rD\sin^2\theta\}\end{aligned} \tag{4-17}$$

$$(\sigma_{\theta\theta})_{F,\text{unsym}} = -\frac{2P(D\sin\theta - E\cos\theta)^2(D - r\cos\theta)}{\pi(r^2 + D^2 + E^2 - 2Dr\cos\theta - 2Er\sin\theta)^2} \tag{4-18}$$

$$(\sigma_{r\theta})_{F,\text{unsym}} = -\frac{2P(D\sin\theta - E\cos\theta)(D - r\cos\theta)(r - D\cos\theta - E\sin\theta)}{\pi(r^2 + D^2 + E^2 - 2Dr\cos\theta - 2Er\sin\theta)^2} \tag{4-19}$$

where P is the applied load per thickness and D and E are the respective vertical and horizontal distances located from the origin of the coordinate axes (and ultimately the center of the circular hole of radius R) below the top of the plate as shown in Figure 4-2. The first stress invariant for the resultant stresses is

$$S_{F,\text{unsym}} = (\sigma_{rr})_{F,\text{unsym}} + (\sigma_{\theta\theta})_{F,\text{unsym}} \tag{4-20}$$

As long as the external dimensions of the plates of Figure 4-1 and Figure 4-2 are reasonably large (compared to the size of the hole) or the hole is not too close to the concentrated load, P, it is believed reasonable to incorporate the Flamant solutions.

4.4 Superposition Principle

The effect of the concentrated load can be considered by superposition principle. The Airy stress functions employed here are assembled from two stress functions; one which can accommodate a hole in a plate (absent of the concentrated load) and one for a (theoretically semi-infinite) plate subjected to a concentrated edge load per thickness, P (Flamant solution). Superposing the two Airy stress function from Flamant solution, equation (4-11) or (4-16), and the general solution of the plane stress, equation (4-1) yields $\Phi = \Phi_{F,\text{sym}} + \Phi_{\text{sym}}$ for case in Figure 4-1, hence $S = S_F + S_{\text{syms}}$ and $\Phi = \Phi_{F,\text{unsym}} + \Phi_{\text{unsym}}$ for case in Figure 4-2, therefore $S = S_{F,\text{unsym}} + S_{\text{unsym}}$ where Φ_{sym} and Φ_{unsym} satisfy the stress field due to the hole. The stresses are

$$\sigma_{rr} = (\sigma_{rr})_i + (\sigma_{rr})_{F,i}, \qquad \sigma_{\theta\theta} = (\sigma_{\theta\theta})_i + (\sigma_{\theta\theta})_{F,i},$$
$$\sigma_{r\theta} = (\sigma_{r\theta})_i + (\sigma_{r\theta})_{F,i}, \qquad i = \text{syms}, \text{unsym} \tag{4-21}$$

By using the thermoelastic measured data, S^*, of region R^* in Figure 4-7 and Figure 4-8, the following condition should also be imposed

$$S = S_{F,i} + S_i = \frac{S^*}{K} \Rightarrow S_i = \frac{S^*}{K} - S_{F,i}, \qquad i = \text{syms}, \text{unsym} \tag{4-22}$$

The boundary conditions require that $\sigma_{rr}(R,\theta) = \sigma_{r\theta}(R,\theta) = 0$ at the boundary of the hole or

$$(\sigma_{rr})_i|_{r=R} = -(\sigma_{rr})_{F,i}\big|_{r=R}, \qquad (\sigma_{r\theta})_i|_{r=R} = -(\sigma_{r\theta})_{F,i}\big|_{r=R}, \qquad i = \text{sym, unsym} \tag{4-23}$$

By gathering the measured data with the boundary conditions, equations (4-22) and (4-23), the Airy coefficients can be solved by forming a linear system of equation represented in a matrix form as $[A]_{(m+h)\times k}\{c\}_{k\times 1} = \{d\}_{(m+h)\times 1}$ where m = 300 or 849 is the total number of measured input values, h is twice the number of the boundary points h = 300 (selected by a user) in both cases, and k is number of unknown Airy coefficients which is related to terminating index, N, as $k = 4(N-1)+4 = 4N$ for case in Figure 4-1 and $k = 8(N-1)+7 = 8N-1$ for the second case in Figure 4-2. The matrix $[A]$ consists of analytical expression of S_{sym}, equation (4-5), or S_{unsym}, equation (4-10), in addition to h traction-free expressions of the form of equations (4-2) and (4-4) or equations (4-7) and (4-9) for cases in Figure 4-1 and Figure 4-2, respectively. The vector $\{c\}$ contains the k unknown Airy coefficients and vector $\{d\}$ contains m thermoelastic measured data, S^*, subtracted by isopachic stress, S_F, of Flamant solution, equation (4-15) or equation (4-20), $(= S^*/K - S_F)$ with the h values of the radial, equation (4-12) or (4-17), and shear, equation (4-14) or (4-19), stresses from Flamant solution. Based on the condition number of Airy matrix relative to it becoming singular of Figure 4-9 and the RMS values of Figure 4-10, twenty-four coefficients, k = 24, are utilized here for the centrally loaded plate, Figure 4-1, and k = 31 for offset loaded plate, Figure 4-2. Once all the Airy coefficients of equations (4-1) and (4-6) have been evaluated from the thermoelastic measured data, S^*, the individual components of stress were obtained from equations (4-21), including those on the edge of the hole.

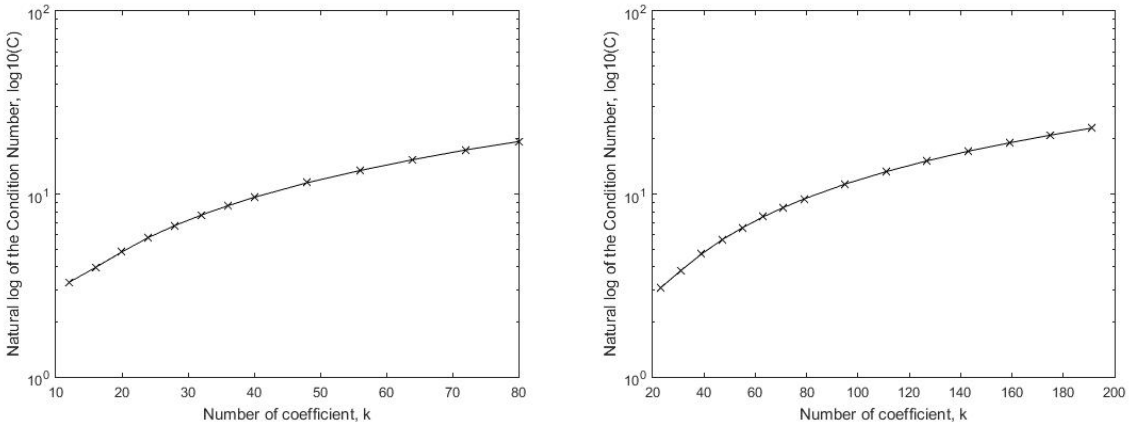

(a) (b)

Figure 4-9: Natural log of the condition number of Airy stress matrix, [A] using Airy stress function in real variables superposed with Flamant solution (a) Centrally loaded plate; (b) Offset loaded plate.

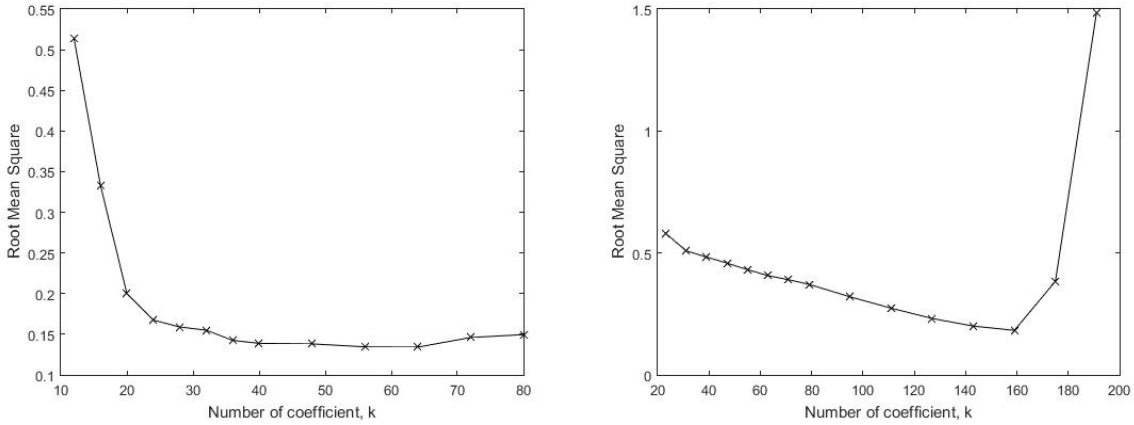

(a) (b)

Figure 4-10: Root mean square values between the reconstructed and thermoelastic measured data, S^*, using Airy stress function in real variables superposed with Flamant solution (a) Centrally loaded plate; (b) Offset loaded plate.

4.5 Simple Airy Stress Function

Reference [22] imposed the boundary conditions of the radial and shear stresses of equations (4-2) and (4-4) analytically on the edge of the hole without incorporating the effect of the concentrated load for both cases in Figure 4-1 and Figure 4-2. The individual stresses for the centrally loaded plate in Figure 4-1 are

$$
\begin{aligned}
(\sigma_{rr})_{\text{sym\_analy}} = &\left(\frac{1}{r^2}-\frac{3r}{2R^3}+\frac{r^3}{2R^5}\right)b_0+\left[2-\frac{3r}{R}+\left(\frac{r}{R}\right)^3\right]c_0\\
&+\left(-\frac{2R^4}{r^3}+2r\right)\cos\theta\, d_1'+3R^2(1-r^{-4}R^4)\cos 2\theta\, b_2'\\
&+(R^{-2}+3r^{-4}R^2-4r^{-2})\cos 2\theta\, d_2'\\
&+\left(\frac{24r}{R^6}-\frac{12r^3}{R^8}-\frac{12}{r^5}\right)\cos 3\theta\, c_3'+\left(\frac{18r}{R^4}-\frac{8r^3}{R^6}-\frac{10}{r^3}\right)\cos 3\theta\, d_3'\\
&+\sum_{n=4,5,..}^{N}\Big\{\big[(n^2-1)r^{n-2}R^2-(n+1)(n-2)r^n\\
&-(n+1)r^{-(n+2)}R^{2n+2}\big]b_n'\\
&+\big[(n-1)r^{n-2}R^{-2n+2}-(1-n^2)r^{-(n+2)}R^2\\
&-(n-1)(n+2)r^{-n}\big]d_n'\Big\}\cos n\theta
\end{aligned}
\tag{4-24}
$$

$$
\begin{aligned}
(\sigma_{\theta\theta})_{\text{sym\_analy}} = &\left(-\frac{1}{r^2}+\frac{3r}{2R^3}-\frac{5r^3}{2R^5}\right)b_0+\left[2+\frac{3r}{R}-5\left(\frac{r}{R}\right)^3\right]c_0\\
&+\left(\frac{2R^4}{r^3}+6r\right)\cos\theta\, d_1'+(-3R^2+12r^2+3r^{-4}R^6)\cos 2\theta\, b_2'\\
&-(R^{-2}+3r^{-4}R^2)\cos 2\theta\, d_2'+\left(\frac{-24r}{R^6}+\frac{60r^3}{R^8}+\frac{12}{r^5}\right)\cos 3\theta\, c_3'\\
&+\left(\frac{-18r}{R^4}+\frac{40r^3}{R^6}+\frac{2}{r^3}\right)\cos 3\theta\, d_3'\\
&+\sum_{n=4,5,..}^{N}\Big\{\big[-(n^2-1)r^{n-2}R^2+(n+1)(n+2)r^n\\
&+(n+1)r^{-(n+2)}R^{2n+2}\big]b_n'\\
&+\big[-(n-1)r^{n-2}R^{-2n+2}+(1-n^2)r^{-(n+2)}R^2\\
&+(n-2)(n-1)r^{-n}\big]d_n'\Big\}\cos n\theta
\end{aligned}
\tag{4-25}
$$

$$
\begin{aligned}
(\sigma_{r\theta})_{\text{sym\_analy}} = &\left(\frac{3r\tan 3\theta}{2R^3} - \frac{3r^3\tan 3\theta}{2R^5}\right) b_0 + \left[\frac{3r\tan 3\theta}{R} - \frac{3r^3\tan 3\theta}{R^3}\right] c_0 \\
&- \left(\frac{2R^4}{r^3} - 2r\right)\sin\theta\, d_1' - (3R^2 - 6r^2 + 3r^{-4}R^6)\sin 2\theta\, b_2' \\
&- (R^{-2} - 3r^{-4}R^2 + 2r^{-2})\sin 2\theta\, d_2' \\
&- \left(\frac{24r}{R^6} - \frac{36r^3}{R^8} + \frac{12}{r^5}\right)\sin 3\theta\, c_3' - \left(\frac{18r}{R^4} - \frac{24r^3}{R^6} + \frac{6}{r^3}\right)\sin 3\theta\, d_3' \\
&+ \sum_{n=4,5,..}^{N} \{\left[-(n^2-1)r^{n-2}R^2 + n(n+1)r^n\right. \\
&\left. - (n+1)r^{-(n+2)}R^{2n+2}\right] b_n' \\
&+ \left[-(n-1)r^{n-2}R^{-2n+2} - (1-n^2)r^{-(n+2)}R^2\right. \\
&\left. - n(n-1)r^{-n}\right] d_n'\} \sin n\theta
\end{aligned}
\tag{4-26}
$$

The isopachic stress (first stress invariant) for the resultant stresses is

$$
\begin{aligned}
S_{\text{sym\_analy}} = &-\frac{2r^3}{R^5} b_0 + \left[4 - 4\left(\frac{r}{R}\right)^3\right] c_0 + 8r\cos\theta\, d_1' + 12r^2\cos 2\theta\, b_2' \\
&- 4r^{-2}\cos 2\theta\, d_2' + \frac{48r^3}{R^8}\cos 3\theta\, c_3' + \left(\frac{32r^3}{R^6} - \frac{8}{r^3}\right)\cos 3\theta\, d_3' \\
&+ \sum_{n=4,5,..}^{N} \{4(n+1)r^n b_n' - 4(n-1)r^{-n} d_n'\} \cos n\theta
\end{aligned}
\tag{4-27}
$$

For the offset loaded plate of Figure 4-2, the individual stresses satisfying analytically the boundary conditions along the hole are

$$
\begin{aligned}
(\sigma_{rr})_{\text{unsys\_analy}} &= \left(\frac{1}{r^2}-\frac{3r}{2R^3}+\frac{r^3}{2R^5}\right)b_0+\left[2-\frac{3r}{R}+\left(\frac{r}{R}\right)^3\right]c_0 \\
&+\left(\frac{r\tan 3\theta}{2R^3}-\frac{r^3\tan 3\theta}{2R^5}\right)A_0+\left(2r-\frac{2R^4}{r^3}\right)\sin\theta\, d_1 \\
&+\left(2r-\frac{2R^4}{r^3}\right)\cos\theta\, d_1'+3R^2(1-r^{-4}R^4)\sin 2\theta\, b_2 \\
&+(R^{-2}+3r^{-4}R^2-4r^{-2})\sin 2\theta\, d_2 \\
&+\left(\frac{24r}{R^6}-\frac{12r^3}{R^8}-\frac{12}{r^5}\right)\sin 3\theta\, c_3+\left(\frac{18r}{R^4}-\frac{8r^3}{R^6}-\frac{10}{r^3}\right)\sin 3\theta\, d_3 \\
&+\sum_{n=4,5,..}^{N}\Big\{\Big[(n^2-1)r^{n-2}R^2-(n+1)(n-2)r^n \\
&-(n+1)r^{-(n+2)}R^{2n+2}\Big]b_n \\
&+\Big[(n-1)r^{n-2}R^{-2n+2}-(1-n^2)r^{-(n+2)}R^2 \\
&-(n-1)(n+2)r^{-n}\Big]d_n\Big\}\sin n\theta \\
&+\sum_{n=2,3,..}^{N}\Big\{\Big[(n^2-1)r^{n-2}R^2-(n+1)(n-2)r^n \\
&-(n+1)r^{-(n+2)}R^{2n+2}\Big]b_n' \\
&+\Big[(n-1)r^{n-2}R^{-2n+2}-(1-n^2)r^{-(n+2)}R^2 \\
&-(n-1)(n+2)r^{-n}\Big]d_n'\Big\}\cos n\theta
\end{aligned}
\tag{4-28}
$$

$$
\begin{aligned}
(\sigma_{\theta\theta})_{\text{unsys\_analy}} &= \left(-\frac{1}{r^2}+\frac{3r}{2R^3}-\frac{5r^3}{2R^5}\right)b_0+\left[2+\frac{3r}{R}-5\left(\frac{r}{R}\right)^3\right]c_0 \\
&+\left(-\frac{r\tan 3\theta}{2R^3}+\frac{5r^3\tan 3\theta}{2R^5}\right)A_0+\left(6r+\frac{2R^4}{r^3}\right)\sin\theta\, d_1 \\
&+\left(6r+\frac{2R^4}{r^3}\right)\cos\theta\, d_1'+(-3R^2+12r^2+3r^{-4}R^6)\sin 2\theta\, b_2 \\
&-(R^{-2}+3r^{-4}R^2)\sin 2\theta\, d_2+\left(-\frac{24r}{R^6}+\frac{60r^3}{R^8}+\frac{12}{r^5}\right)\sin 3\theta\, c_3 \\
&+\left(-\frac{18r}{R^4}+\frac{40r^3}{R^6}+\frac{2}{r^3}\right)\sin 3\theta\, d_3 \\
&+\sum_{n=4,5,..}^{N}\Big\{\Big[-(n^2-1)r^{n-2}R^2+(n+1)(n+2)r^n \\
&+(n+1)r^{-(n+2)}R^{2n+2}\Big]b_n \\
&+\Big[-(n-1)r^{n-2}R^{-2n+2}+(1-n^2)r^{-(n+2)}R^2 \\
&+(n-1)(n-2)r^{-n}\Big]d_n\Big\}\sin n\theta \\
&+\sum_{n=2,3,..}^{N}\Big\{\Big[-(n^2-1)r^{n-2}R^2+(n+1)(n+2)r^n \\
&+(n+1)r^{-(n+2)}R^{2n+2}\Big]b_n' \\
&+\Big[-(n-1)r^{n-2}R^{-2n+2}+(1-n^2)r^{-(n+2)}R^2 \\
&+(n-1)(n-2)r^{-n}\Big]d_n'\Big\}\cos n\theta
\end{aligned}
\tag{4-29}
$$

$$(\sigma_{r\theta})_{\text{unsys\_analy}}$$

$$
\begin{aligned}
&= \left(-\frac{3r\cot 3\theta}{2R^3} + \frac{3r^3\cot 3\theta}{2R^5}\right) b_0 + \left[-\frac{3r\cot 3\theta}{R} + \frac{3r^3\cot 3\theta}{R^3}\right] c_0 \\
&+ \left(\frac{r}{2R^3} - \frac{3r^3}{2R^5} + \frac{1}{r^2}\right) A_0 + \left(\frac{2R^4}{r^3} - 2r\right)\cos\theta\, d_1 \\
&- \left(\frac{2R^4}{r^3} - 2r\right)\sin\theta\, d_1' + (3R^2 - 6r^2 + 3r^{-4}R^6)\cos 2\theta\, b_2 \\
&+ (R^{-2} - 3r^{-4}R^2 + 2r^{-2})\cos 2\theta\, d_2 \\
&+ \left(\frac{24r}{R^6} - \frac{36r^3}{R^8} + \frac{12}{r^5}\right)\cos 3\theta\, c_3 + \left(\frac{18r}{R^4} - \frac{24r^3}{R^6} + \frac{6}{r^3}\right)\cos 3\theta\, d_3 \\
&+ \sum_{n=4,5,..}^{N} \Big\{\big[(n^2-1)r^{n-2}R^2 - n(n+1)r^n \\
&+ (n+1)r^{-(n+2)}R^{2n+2}\big] b_n \\
&+ \big[(n-1)r^{n-2}R^{-2n+2} + (1-n^2)r^{-(n+2)}R^2 \\
&+ n(n-1)r^{-n}\big] d_n\Big\}\cos n\theta \\
&+ \sum_{n=2,3,..}^{N} \Big\{\big[-(n^2-1)r^{n-2}R^2 + n(n+1)r^n \\
&- (n+1)r^{-(n+2)}R^{2n+2}\big] b_n' \\
&+ \big[-(n-1)r^{n-2}R^{-2n+2} - (1-n^2)r^{-(n+2)}R^2 \\
&- n(n-1)r^{-n}\big] d_n'\Big\}\sin n\theta
\end{aligned}
\tag{4-30}
$$

The isopachic stress (first stress invariant) for the resultant stresses is

$$
\begin{aligned}
S_{\text{unsys\_analy}} = &-\frac{2r^3}{R^5}b_0 + \left[4 - 4\left(\frac{r}{R}\right)^3\right]c_0 + \frac{2r^3\tan 3\theta}{R^5}A_0 + 8r\sin\theta\, d_1 \\
&+ 8r\cos\theta\, d_1' + 12r^2\sin 2\theta\, b_2 - 4r^{-2}\sin 2\theta\, d_2 + \frac{48r^3}{R^8}\sin 3\theta\, c_3 \\
&+ \left(\frac{32r^3}{R^6} - \frac{8}{r^3}\right)\sin 3\theta\, d_3 \\
&+ \sum_{n=4,5,..}^{N}\{4(n+1)r^n b_n - 4(n-1)r^{-n}d_n\}\sin n\theta \\
&+ \sum_{n=2,3,..}^{N}\{4(n+1)r^n b_n' - 4(n-1)r^{-n}d_n'\}\cos n\theta
\end{aligned}
\tag{4-31}
$$

Because all of the coefficients appearing in the individual stress components of equations (4-24) to (4-26) for the plate of Figure 4-1 and all the coefficients in the individual stress components of equations (4-28) to (4-30) for the plate of Figure 4-2 exist in the equation for isopachic stress of equation (4-27) and (4-31), respectively, the complete state of in-plane stress is available from the load induced temperature information. By gathering the measured data, the Airy coefficients can be solved by forming a linear system of equation represented in a matrix form as $[A]_{m\times k}\{c\}_{k\times 1} = \{d\}_{m\times 1}$ where m is the total number of measured input values (m = 300 or 849), and k is number of unknown Airy coefficients which is related to terminating index, N, as $k = 2(N-3)+7 = 2N+1$ for centrally loaded plate, Figure 4-1, and $k = 2(N-3)+2(N-1)+9 = 4N+1$. The matrix $[A]$ consists of analytical expression of S ($= S^*/K$), equation (4-27) or (4-31). The vector $\{c\}$ contains the k unknown Airy coefficients and vector $\{d\}$ contains m measured data, S^*/K. Based on the condition number of the Airy matrix relative to it becoming singular of Figure 4-11 and the RMS values of Figure 4-12, fifteen coefficients, k = 15, are utilized here for the centrally loaded plate, Figure 4-1, and k = 25 for offset loaded plate, Figure 4-2. Once all the Airy coefficients of equation (4-27) and (4-31) have been evaluated from the thermoelastic measured data, S^*, the individual components of

stress were obtained from equations (4-24) to (4-26) for the centrally loaded plate and from equations (4-28) to (4-30) for the offset loaded plate, including those on the edge of the hole.

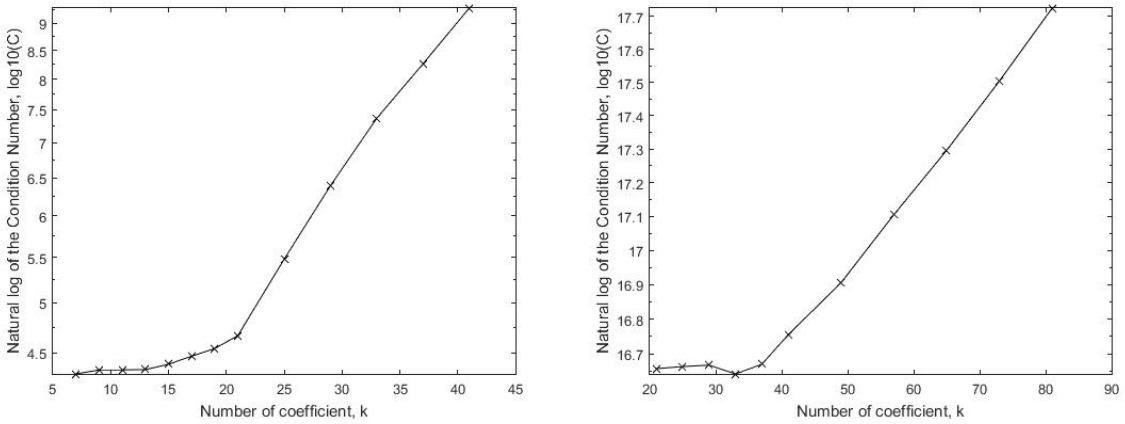

(a) (b)

Figure 4-11: Natural log of the condition number of simple Airy stress matrix (a) Centrally loaded plate; (b) Offset loaded plate.

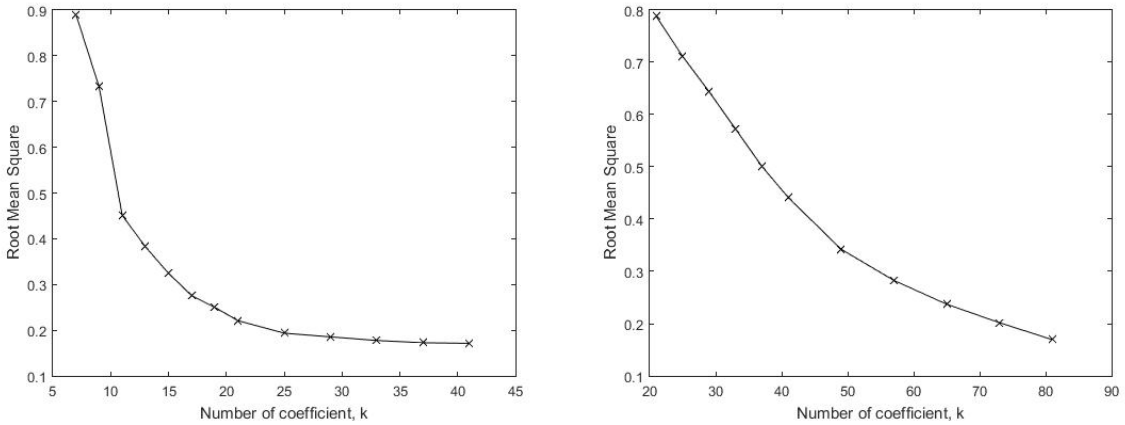

(a) (b)

Figure 4-12: Root mean square values between the reconstructed and thermoelastic measured data, S^*, using simple Airy stress function (a) Centrally loaded plate; (b) Offset loaded plate.

4.6 Airy Stress Function using Complex Variable (Complex Mapping-Collocation Method)

The complex coefficients, $A_j = a_j + ib_j$, were evaluated by using equations (2-83) through (2-85), and the Laurent series expansion to map the physical plane to the unit circle in the ζ-plane. The complex coefficients A_j were evaluated from equation (2-101) using the m =

300 or 849 thermoelastic data inside the region R^*, Figure 4-7 or Figure 4-8, utilizing the Laurent representations of the stress function. The individual full-field stresses throughout region R_z, including along edge Γ where no thermoelastic input data were employed, is evaluated using equations (2-95) through (2-97). The number of complex Airy coefficients, $2N$, to retain in the stress function was selected by evaluating the difference between the magnitude of experimentally based thermoelastic data and those predicted by the present hybrid-method by using root mean square approach, Figure 4-14 and observing the condition number of matrix $[M]$ relative to it becoming singular, Figure 4-13. The present method requires 12 complex coefficients (24 real coefficients) for centrally and offset loaded plate. The appropriateness of utilizing 12 complex coefficients is substantiated by comparing the reconstructed and measured experimental data using the hybrid methods with the TSA data, Figure 4-15.

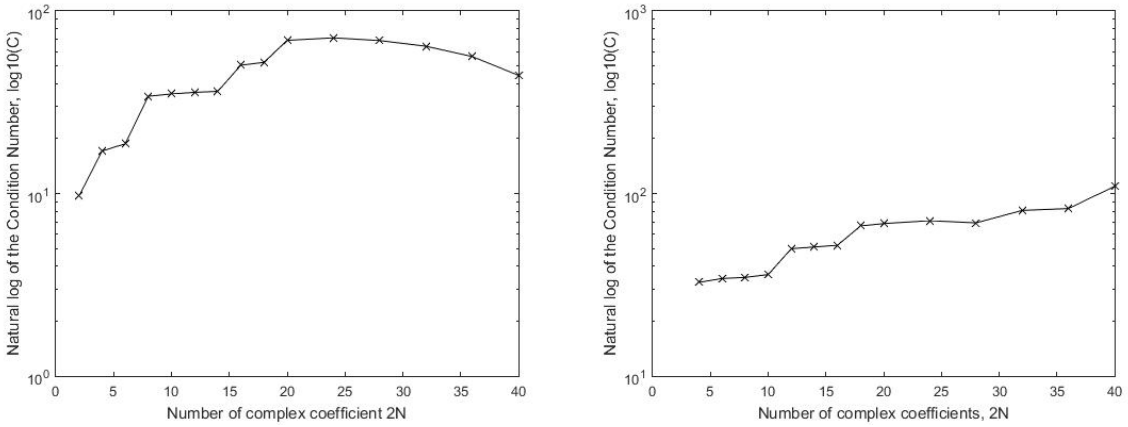

(a) (b)

Figure 4-13: Natural log of the condition number of matrix, $[M]$ (a) Centrally loaded plate; (b) Offset loaded plate.

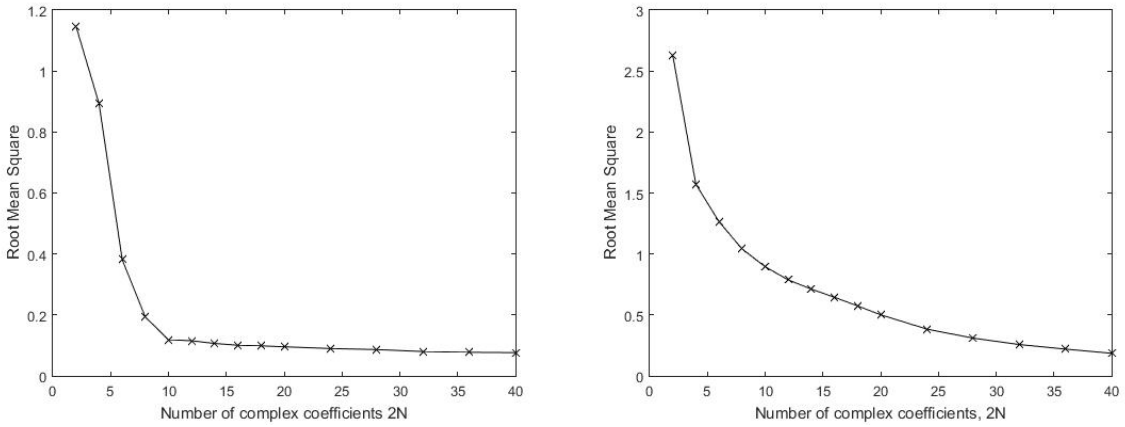

(a) (b)

Figure 4-14: Root mean square values between the reconstructed and thermoelastic measured data for Airy stress function in complex variables (a) Centrally loaded plate; (b) Offset loaded plate.

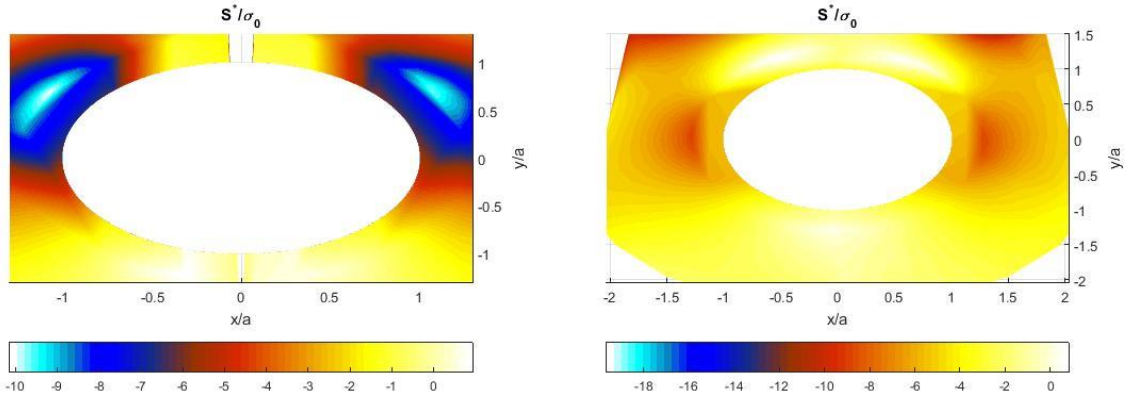

(a) (b)

Figure 4-15: Contour plot of S^*/σ_0 throughout the region adjacent to hole by TSA recorded data (right) and hybrid method using the complex mapping-collocation technique (left) (a) Centrally loaded plate; (b) Offset loaded plate.

4.7 Finite Element Analysis

In order to provide some results with which to compare those from TSA, a finite element analysis (FEA) using ANSYS prediction was prepared of the plate of Figure 4-1 and Figure 4-2. The Aluminum has elastic of modulus E = 68.95 GPa = 10×10^6 psi and Poisson's ratio ν = 0.33. Due to the symmetry in Figure 4-1, only one half of the plate is modeled with symmetrical boundary condition applied at the vertical line, $y = 0$. A roller constraint (assuming no vertical motion) was applied along the lower edge of the plate, C'DC of Figure 4-1 and

Figure 4-2. Isoparametric plane-82 elements which have eight nodes were employed. To obtain reliable data, a very fine mesh was used in the neighborhood of the circular hole as shown in Figure 4-16. A convergence test was applied until the change in results of maximum stress between two successive meshing is less than 2%. The resultant radial, tangential, and shear stresses of the FE model are shown in Figure 4-17.

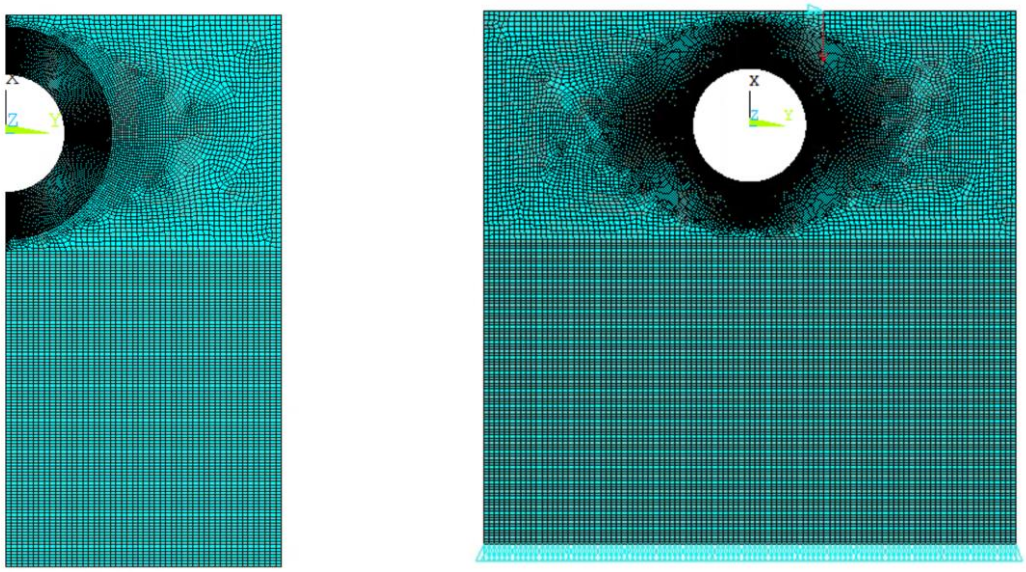

(a) (b)

Figure 4-16: Meshed FE model with dense meshing adjacent the circular hole (a) Centrally loaded plate; (b) Offset loaded plate.

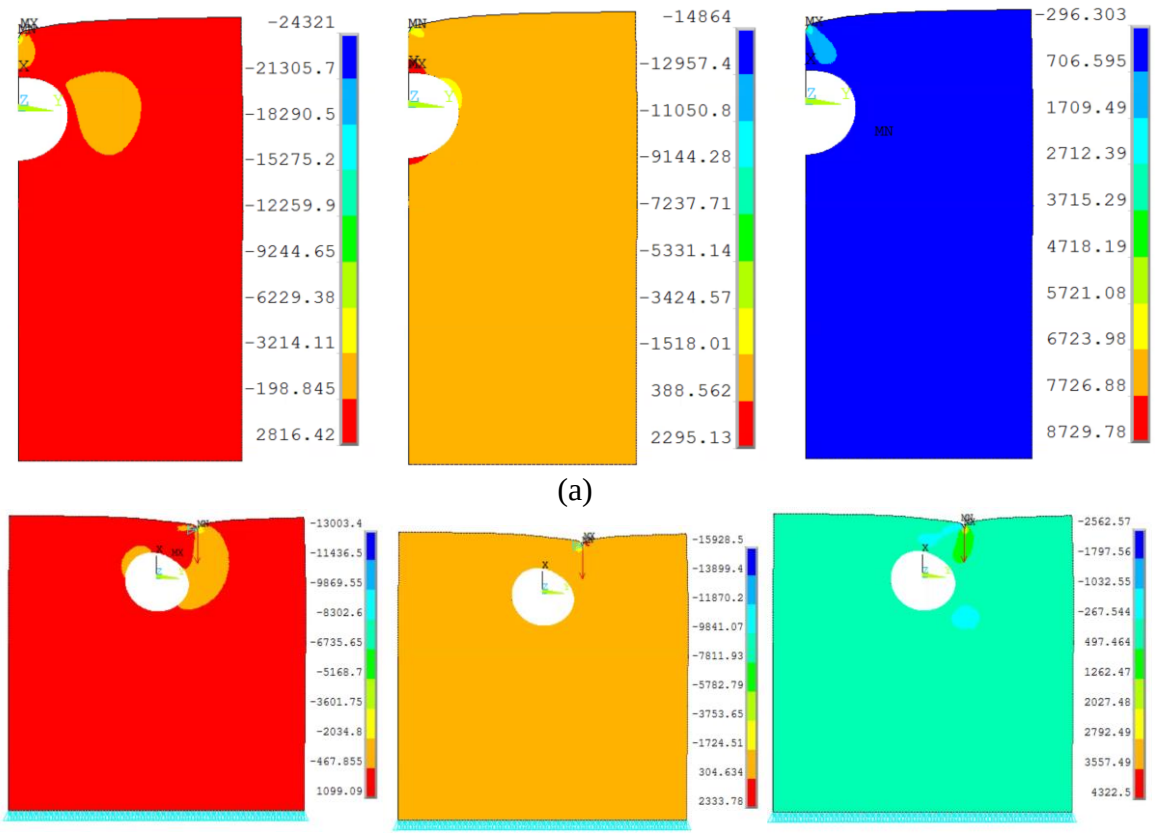

Figure 4-17: Contour plot for the radial, tangential and shear stresses from FEA in psi (a) Centrally loaded plate; (b) Offset loaded plate.

4.8 Results

For comparisons, the problem was solved using real variables with and without superposing the stress function from applied concentrated load and also by using mapping-collocation technique. Stresses are normalized with respect to σ_0 [concentrated edge load P^*/gross cross-sectional area = 200 lbs/(3.5 in. × 3/8 in.) = 1.05 MPa = 152.38 psi]. For the centrally loaded plate in Figure 4-1, the tangential stress, $\sigma_{\theta\theta}$, normalized by the far-field stress, σ_0, are plotted on the boundary of the circular hole as illustrated in Figure 4-18. These TSA-based results agree with the FEM predictions. The ANSYS and hybrid-TSA from simple Airy stress function (15 coefficients), Airy stress function superposed with Flamant solution (24 coefficients) and mapping-collocation technique (24 real coefficients) determine stress concentrations at the circular hole are 14.36, 13.63, 16.67, and 15.86 respectively. The variation of

σ_{xx}/σ_0 along the line y = 0 of Figure 4-1 from FEA, simple Airy stress function (15 coefficients), Airy stress function superposed with Flamant solution (24 coefficients) and mapping-collocation technique (24 real coefficients) are demonstrated in Figure 4-19. Figure 4-19 shows that Airy stress function superposed with the Flamant solution and the complex mapping-collocation technique predict the stresses beneath the concentrated load very well. In addition to the fact that $x/R \geq 1.5$ is approaching the location of the applied load, the reliability of the present TSA-determined σ_{xx} along the line y = 0 away from the hole might be influenced by the fact that the current complex mapping-collocation technique does not explicitly involve the contribution of the concentrated load, P^*, as does the Airy stress function in the real variable superposed with Flamant solution. Moreover, the load was applied physically through a piece of round drill rod while ANSYS modelled it as a top concentrated load.

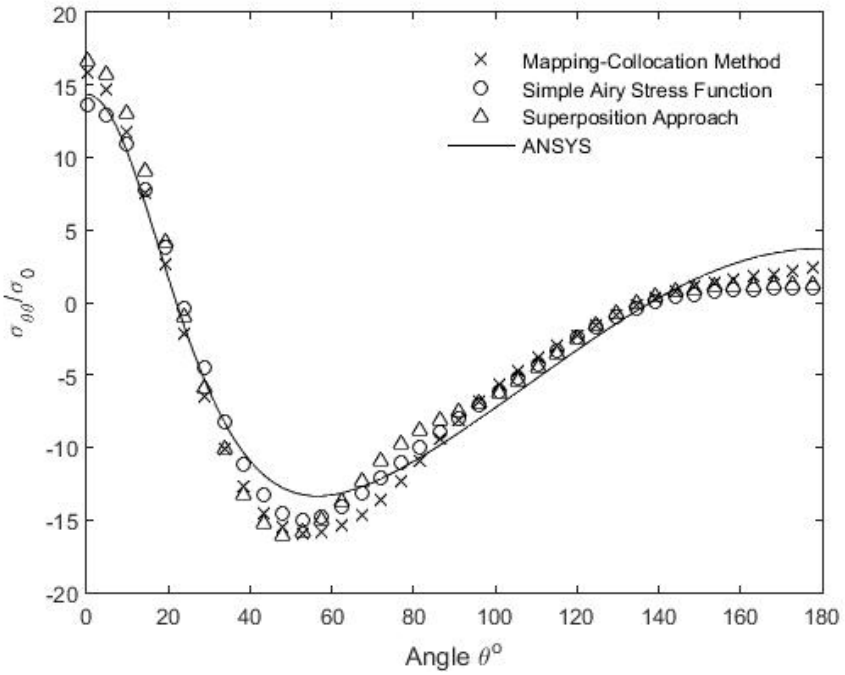

Figure 4-18: Variation of $\sigma_{\theta\theta}/\sigma_0$ along the boundary of the hole of Figure 4-1 from FEA, simple Airy stress function (15 coefficients), Airy stress function superposed with Flamant solution (24 coefficients) and complex mapping-collocation technique (16 real coefficients).

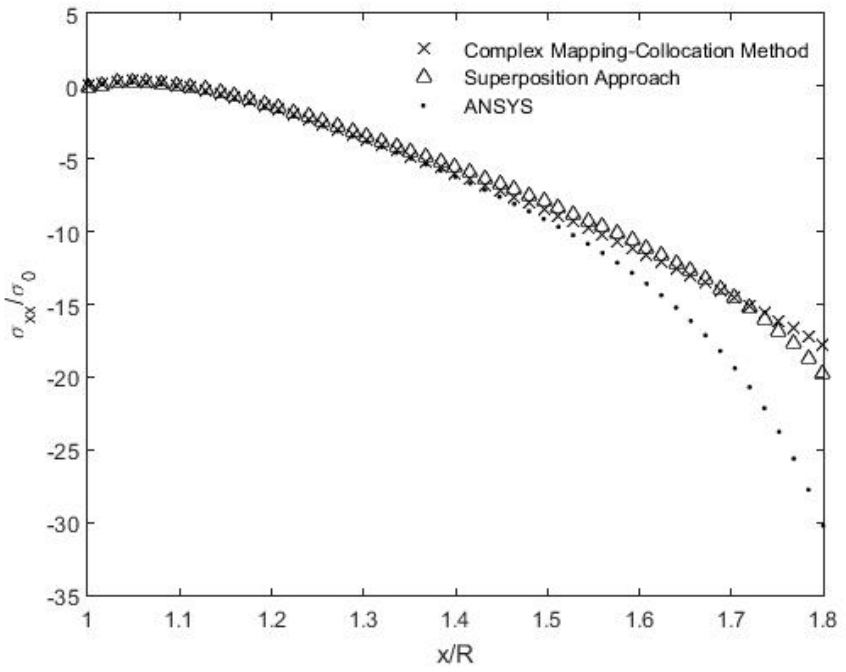

Figure 4-19: Variation of σ_{xx}/σ_0 along the line y = 0 of Figure 4-1 from FEA, Airy stress function superposed with Flamant solution (24 coefficients) and complex mapping-collocation technique (24 real coefficients).

Figure 4-20 through Figure 4-22 illustrate the variation of normalized radial, σ_{rr}/σ_0, tangential, $\sigma_{\theta\theta}/\sigma_0$, shear, $\sigma_{r\theta}/\sigma_0$, stress in the vicinity (rather than on the edge) of the hole, i.e., in the range of r/R = 1.24. The utilized location for r/R = 1.24 is not particularly significant, but was selected to illustrate the continuing reliability of the TSA upon moving away from the edge of the hole.

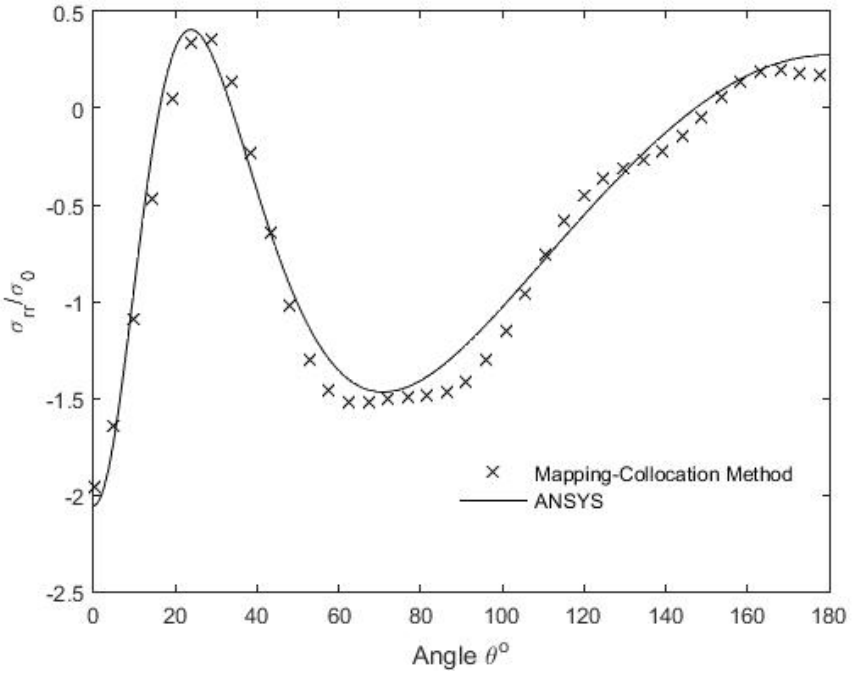

Figure 4-20: Variation of σ_{rr}/σ_0 along r/R = 1.24 from FEA and complex mapping-collocation technique (24 real coefficients).

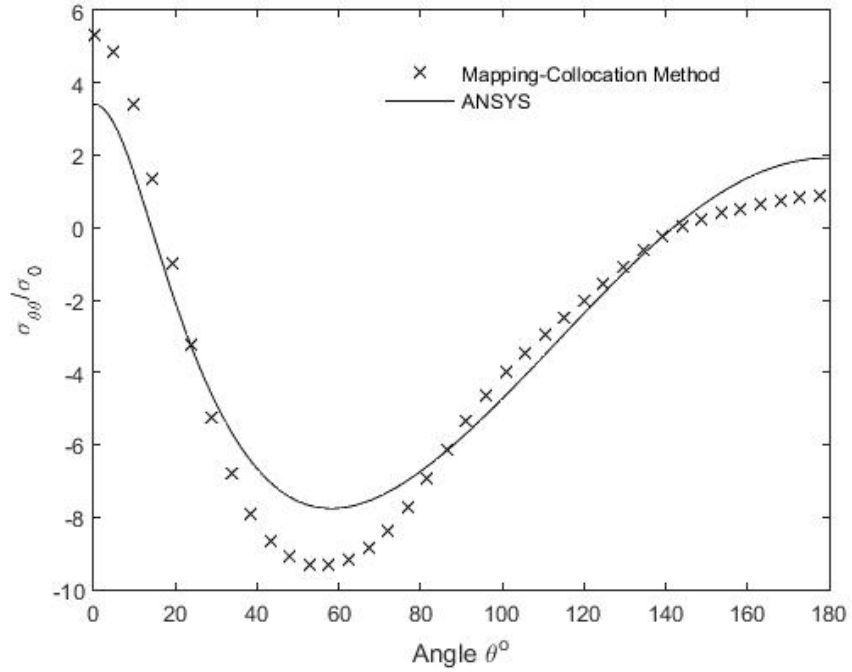

Figure 4-21: Variation of $\sigma_{\theta\theta}/\sigma_0$ along r/R = 1.24 from FEA and complex mapping-collocation technique (24 real coefficients).

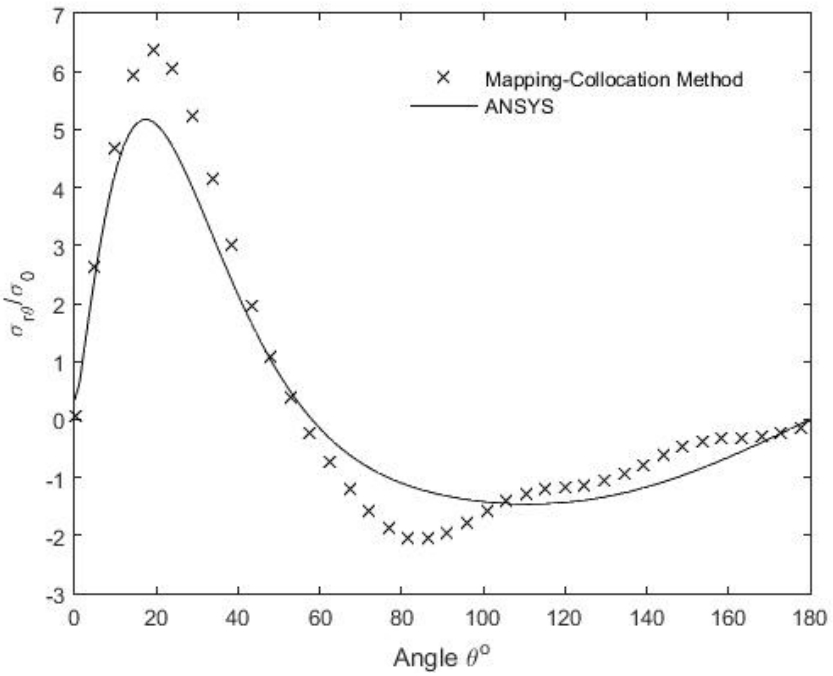

Figure 4-22: Variation of $\sigma_{r\theta}/\sigma_0$ along r/R = 1.24 from FEA and complex mapping-collocation technique (24 real coefficients).

The contour plots of normalized polar components of stress from the hybrid complex collocation technique and ANSYS are plotted in Figure 4-23 through Figure 4-25. Those figures show an excellent agreement between the ANSYS-predicted values and the hybrid technique using thermoelastic data values for m = 300 data points.

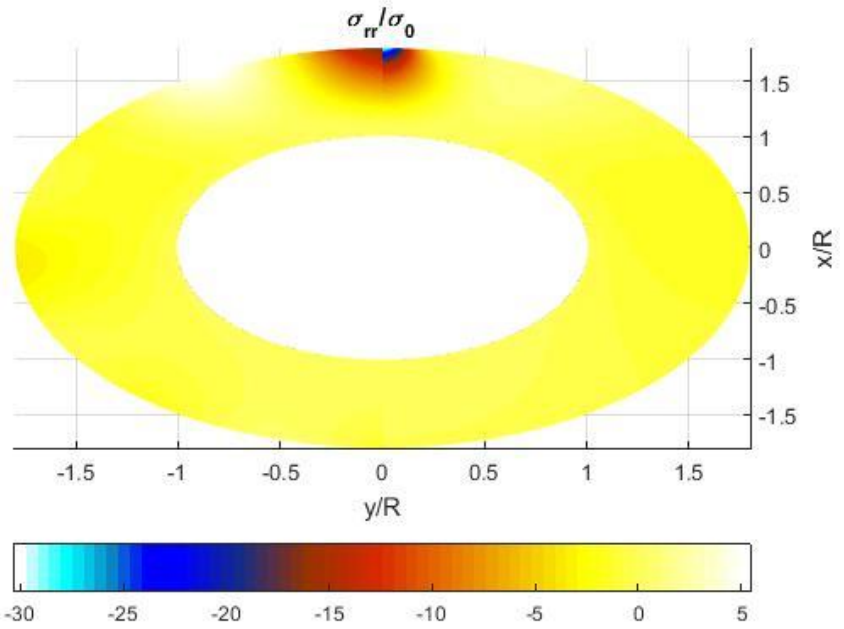

Figure 4-23: Contour plot of σ_{rr}/σ_0 throughout the region adjacent to hole by FEA (right) and hybrid-TSA using the complex mapping-collocation technique (left).

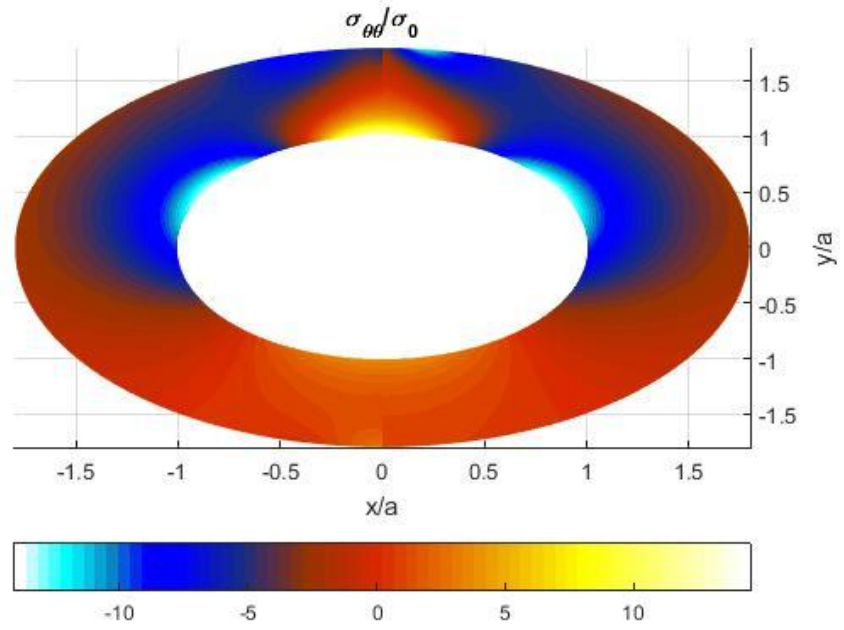

Figure 4-24: Contour plot of $\sigma_{\theta\theta}/\sigma_0$ throughout the region adjacent to hole by FEA (right) and hybrid-TSA using the complex mapping-collocation technique (left).

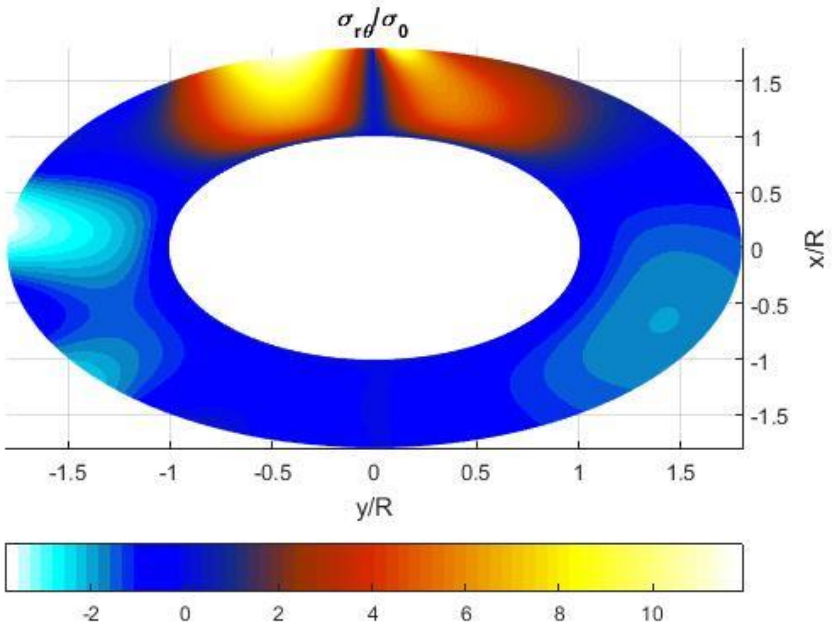

Figure 4-25: Contour plot of $\sigma_{r\theta}/\sigma_0$ throughout the region adjacent to hole by FEA (right) and hybrid-TSA using the complex mapping-collocation technique (left).

Normalized tangential stress, $\sigma_{\theta\theta}/\sigma_0$, along the boundary of the hole for the offset loaded plate of Figure 4-2 are depicted in Figure 4-26. Figure 4-27 and Figure 4-28 illustrate the variation of normalized tangential stress, $\sigma_{\theta\theta}/\sigma_0$, and normalized shear stress, $\sigma_{r\theta}/\sigma_0$, in the vicinity (rather than on the edge) of the hole, i.e., in the range of r/R = 1.24. The utilized location for r/R = 1.24 is not particularly significant, but was selected to illustrate the continuing reliability of the TSA upon moving away from the edge of the hole. As it was desired to compare these TSA-determined results with FEM predictions.

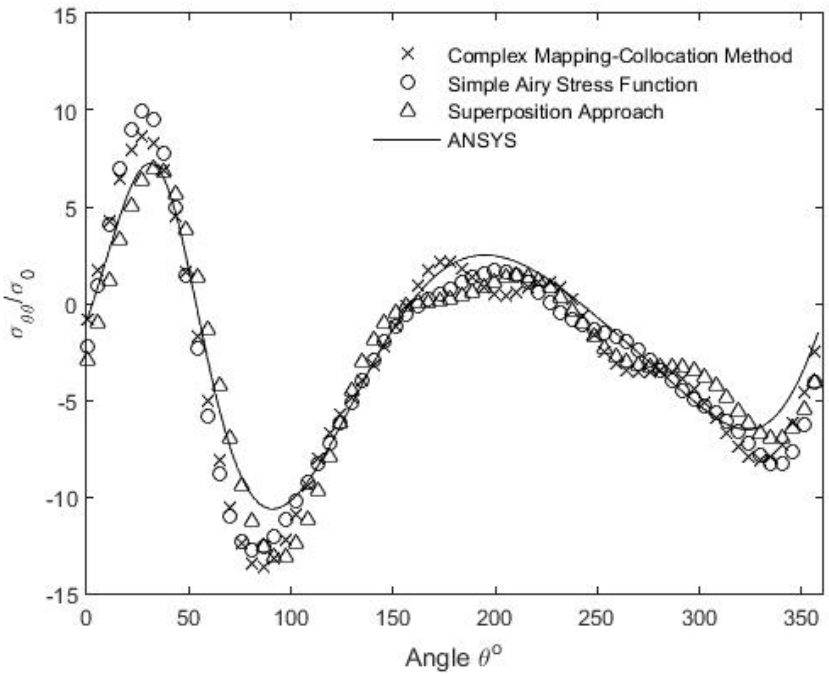

Figure 4-26: Variation of $\sigma_{\theta\theta}/\sigma_0$ along the boundary of the hole from FEA, simple Airy stress function (25 coefficients), Airy stress function superposed with Flamant solution (31 coefficients) and complex mapping-collocation technique (24 real coefficients).

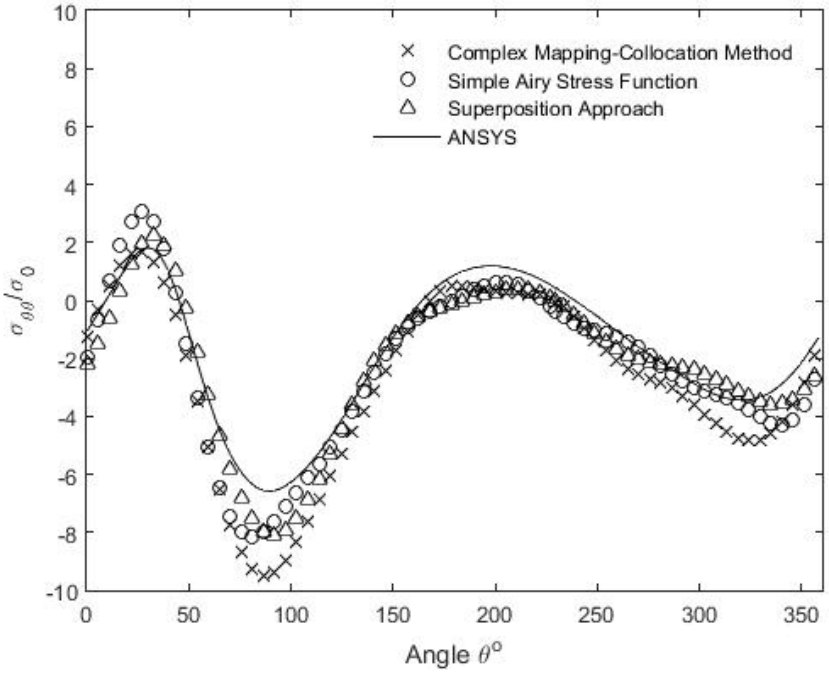

Figure 4-27: Variation of $\sigma_{\theta\theta}/\sigma_0$ along r/R = 1.24 from FEA, simple Airy stress function (25 coefficients), Airy stress function superposed with Flamant solution (31 coefficients) and complex mapping-collocation technique (24 real coefficients).

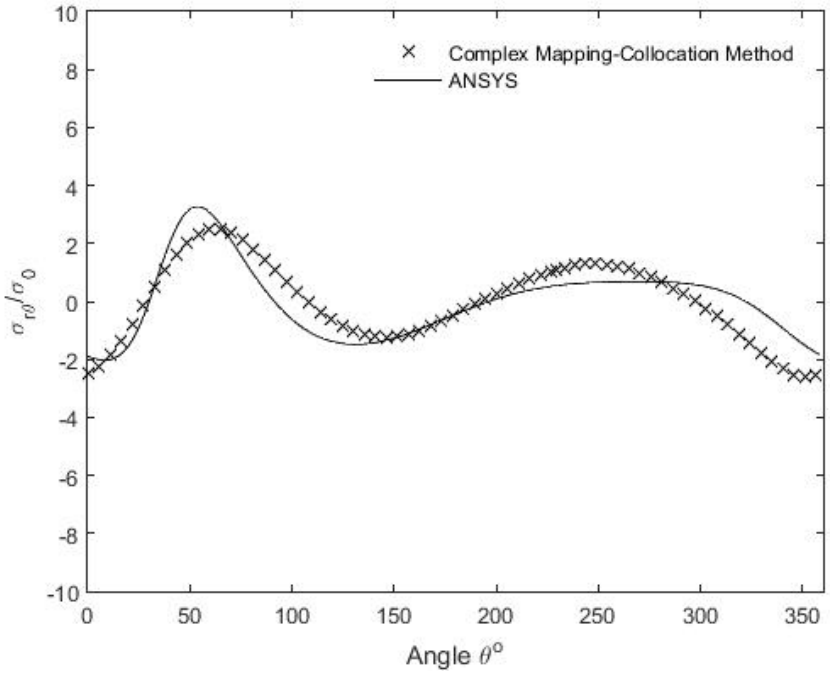

Figure 4-28: Variation of $\sigma_{r\theta}/\sigma_0$ along r/R = 1.24 from FEA and complex mapping-collocation technique (24 real coefficients).

The hybrid-TSA results based on the mapping-collocation technique agree with those from FEM, simple Airy stress function [22], and Lin [20,21]. The absence of P in the stress components indicates the mapping-collocation approach could handle inverse problem. For example, if the present analysis were extended to cover the entire width, w, of the plate of Figure 4-1 and Figure 4-2, the magnitude of P could be obtained by integrating the vertical stress, σ_{xx}, over the full horizontal cross-section of the plate at some value of x.

4.9 Summary, Discussion and Conclusions

A mapping-collocation technique which combines a stress function in the complex variables and conformal mapping and analytically satisfies equilibrium, compatibility and the traction-free conditions on the boundary of the circular hole was introduced to determine the state of stress on and near the edge of the circular hole in an edge-loaded perforated plate without the knowledge of the material constitutive properties, external geometry or loading and bound-

ary conditions. A method was developed to separate reliably the thermoelastic data into individual stresses throughout a region adjacent to a traction-free boundary as well as to evaluate accurate boundary information even though the recorded TSA data at, and very near to, circular edge were not included. Unlike earlier approaches that explicitly included the effects of the external load [20,21] and/or imposed analytically the traction-free boundary condition along the hole [22], thereby necessitating superposition and extensive algebra to from complicated stress function, excellent results are presently obtained using complex mapping-collocation technique. On the basis of the same number and source locations of the measured TSA input values, the mapping-collocation technique presented here were compared with those found using Airy stress function in real variable with and without considering the effect of the concentrated load and FE solution. The current concept is suitable for finite (which can be difficult theoretically) or infinite geometries and either symmetrical or asymmetrical cases. This chapter emphasizes a circular hole in a rectangular plate subjected to concentrated edge loads, but the concept is applicable to more complicated geometries and loading conditions. The general approach is valid for other types of measured data, e.g., moiré, holography, speckle, digital image correlation, strain gauges, or photoelasticity. Unlike other modes of stress (strain) analysis, the current technique dos not necessitate nonlinear least-squares, differentiating the measured information, or knowing the constitutive properties or external geometry.

One could conceptually evaluate the Airy coefficients, and hence the individual stresses throughout the full plate, by imposing the physical boundary conditions around the entire edge (inside and outside boundaries) of the plate and without involving any measured data. In addition to approximating the boundary conditions along the bottom edge of the plate, C’DC, such strict boundary collocation approach might well require hundreds of coefficients and thousands of equations. However, because the external boundary conditions of engineering situations are often insufficiently well known to apply pure boundary collocation (or theoretical) methods,

an objective of the present chapter is to determine the individual stresses at and near a cutout without knowledge of the far-field shape or boundary conditions.

Unlike a classical boundary value problem, the present approach does not guarantee the correct boundary conditions or the individual stresses on the rest of the boundary of the interest region, i.e., on and adjacent to the edge of the hole. The quality of the evaluated stresses would deteriorate as the dimension of the interest region normal to its free edge becomes large. The objective of this approach is to determine reliable information along, and adjacent to, the edge of the component where the interested region is, rather than to evaluate the stresses necessarily throughout the entire structure. The size of interest region over which the stress function is reliable can be increased by additionally employing some boundary collocation. Least square was used to evaluate unknown coefficients of overdetermined systems of equations.

Compared to finite-element analyses, the numerical computations of the present method are relatively simple and consume little computer time. The thermoelastic determined stresses agree very well with finite-element results. Although the agreement between the ANSYS and experimental thermoelastic results is good, the discrepancies between FEM and measured results might well represent a case where the assumed, versus actual, boundary conditions cause the ANSYS-predicted stresses not to represent exactly physical reality. Figure 4-5 and Figure 4-6 illustrate that the stress is not uniform along the bottom edge of the plate. The elastic modulus of the aluminum plate is one-third that of steel of the more massive supporting platen so there could be some nonuniformly distributed vertical displacement (and stresses) along the bottom edge of the plate. The ANSYS assumption of zero vertical motion of the bottom of the plate might therefore be incorrect. However, when a sheet of lead and a sheet of compliant paper were each separately inserted between the bottom surface of the vertically loaded plate and the supporting steel platen in attempts to assess any nonuniformity in the vertical motion

(or loading) along the bottom edge C'DC of the plate of Figure 4-1 and Figure 4-2, none was detected.

Other than having to approximate the boundary condition along the bottom edge of the plate, the external loading of the physical plate was known so FEM modeling was straight forward. However, engineering cases often involve unknown loads rendering it difficult to reliably model the situation numerically, thereby necessitating such experimental capabilities such as presented here. Stresses have been evaluated historically using boundary-collocation concepts involving a stress function and known boundary conditions. Insufficient knowledge of the externals acting on a structural member can preclude using boundary-collocation method.

A major contribution of this chapter is the demonstrated ability to determine the individual stresses in a finite engineering component by TSA, specifically on, and in the neighborhood of, the boundary of a near-edge circular hole in a rectangular plate subjected to a concentrated edge load. The author is unaware of any previous research in determining the stresses near-edge circular hole in a rectangular plate subjected to a concentrated edge load using mapping-collocation technique. Aspects of this chapter were presented in Midwest Experimental Mechanics Graduate Student Symposium in 2016.

Chapter 5: Thermoelastically Determined Individual Stresses in a Deep-Notched Tensile Plate

Individual stresses are determined experimentally in a finite, tensile loaded aluminum plate containing a single-sided deep U-notch from recorded load-induced thermal information. Under elastic, reversible and adiabatic conditions, the cyclic loading produces an in-phase temperature variation which is proportional linearly to local changes in normal stresses. As engineering analyses often necessitate knowing the individual components of stress, supplementary experimental methods or information are frequently required to 'separate the stresses'. This need is circumvented here in that individual stresses are evaluated throughout the loaded plate without additional measured data. Processing the measured thermal data with an Airy stress function and some local known stress conditions simultaneously smooths the measured data, separates the stress components, and evaluates the individual stress components full-field, including at the root of the U-notch (location of highest tensile stress). The present hybrid technique does not presuppose knowledge of the external loading conditions and overcomes the traditional difficulties of unreliably edge data. Reliability of experimental results is demonstrated by comparison with those from finite elements and strain gages.

5.1 Introduction

The high stresses associated with abrupt geometric discontinuities can significantly influence structural integrity. Traditional experimental approaches such as conventional thermoelastic stress analysis (TSA) do not provide the separate components of stress. Combining (or hybridizing) experimental information with analytical and numerical tools enables one to solve the aforementioned situations. The analytical ingredient of this hybrid approach consists of

using the Airy stress function which is based on the mechanic foundations of compatibility and equilibrium. The hybrid approach is applicable to different complicated shapes, various complex loading conditions and inverse problems. The present technique does not presuppose knowledge of the external loading conditions and overcomes the traditional difficulties of unreliable edge data. Particular attention is paid to determining a realistic number of unknown Airy coefficients. Other candidate experimental approaches include moiré, speckle, holography, grids and digital image correlation. However, such displacement-based techniques necessitate differentiating the recorded data (something which can be unreliable) and require knowledge of the constitutive material properties to get stresses. On the other hand, thermoelastic stress analysis (TSA) provides the stresses directly without having to differentiate the measured information. The deficiencies of FEA and analytical approaches when attempting to replicate the actual loading conditions motivate use of the present full-field hybrid experimental-numerical-analytical approach to determine the full-field stresses in continuous form and provide reliable results at the edges of the U-notch. Very few analytical solutions are available for finite geometries and both analytical and numerical techniques require knowing the external loading. The latter is often unknown in practice. The major contribution of this chapter is the demonstrated ability to combine experimental, numerical and analytical techniques for the full-field determination of the separate components of stresses at and in the neighborhood of the U-notch.

Having first substantiated the numerical stability, reliability and robustness of the least-squares hybrid method using ‘simulated’ thermoelastic input data from ANSYS, the method is then applied to an actual loaded finite aluminum plate having a single deep U-notch using measured thermal information, Figure 5-1. The author is unaware of prior utilization of Airy stress function to experimentally evaluate the stresses of a loaded material with U-notch using recorded load-induced thermal information.

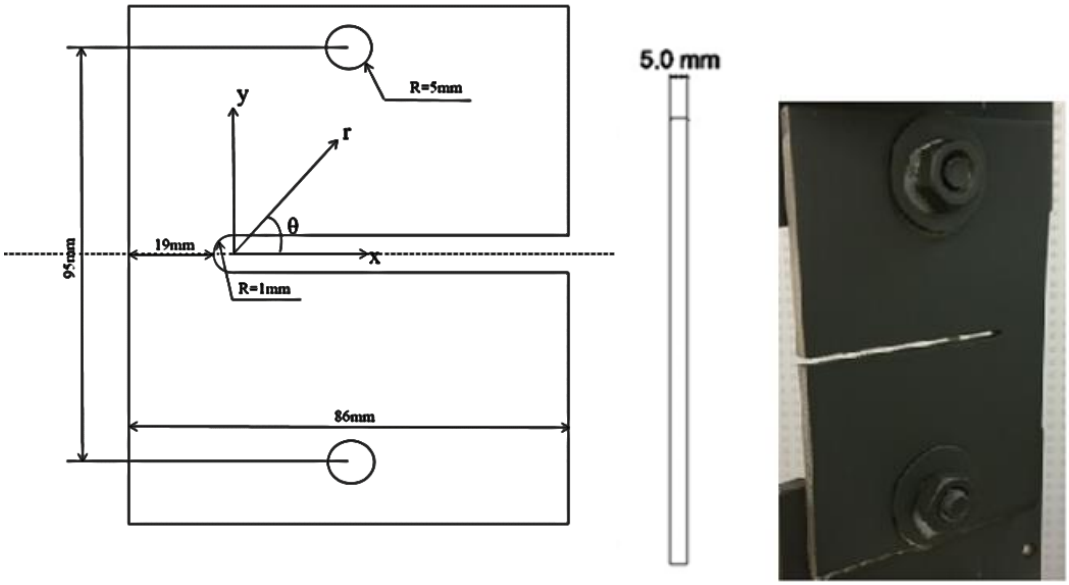

Figure 5-1: Plate geometry and dimension (with black paint for TSA).

5.2 Literature Review

The individual components of stress at and in the neighborhood of a deep side U-notch in an aluminum tensile plate are evaluated from the load-induced thermal data. The recorded temperature information is processed using an Airy stress function to provide individual components of stress and the results correlated with those from FEM and strain gages. While the literature contains information on double-edged deep notches, little appears to be available for single-edged deep notches.

This study presents a nondestructive and non-contacting hybrid method for determining the full-field individual stresses in a tensile loaded, finite plate containing a deep U-notch. This contribution extends the thermoelastic technique into a practical quantitative tool for stress analyzing actual complicated shaped engineering structures in their operating environment. This is accomplished by combining thermoelastic stress analysis (TSA) with an Airy stress function along with discretely imposing local traction-free boundary conditions on the edge of

the U-notch and outer free edges of the plate. In view of previously mentioned disadvantages of the FEA, analytical and most experimental approaches, this chapter demonstrate the ability to determine the separate components of stress in a finite plate by hybridizing recorded data with an Airy stress function.

5.3 General Comments

The measured TSA data were digitalized in a matrix form and combined with the Airy stress function to determine the stress components in the finite structure whose external loading need not be known. The unknown Airy coefficients are determined from recorded thermal information using least-squares. Although the recorded thermoelastic data at, and adjacent to, an edge are unreliable and raw thermoelastic information is inherently noisy, the present technique overcomes these challenges by avoiding the use of recorded data on and near edges and processing the measured interior data with an Airy stress function. Such a technique simultaneously enhances reliability of thermoelastic edge information, smooths the interior measured information, separates the stresses into their three components and evaluates the non-zero stresses along the traction-free boundary (determining stress concentration) without knowing the external loading or material constitutive properties. Because of the aforementioned scatter in recorded TSA data, it is customary to employ more known quantities (measured thermal data plus known local stresses) than the number of unknown Airy coefficients, and to evaluate the latter using linear least-squares. The resulting TSA-determined stresses are available here on and in the neighborhood of the edge of the notch without knowing the distant loading conditions.

5.4 Relevant Equations

The method behind determining the state of stress at and near the deep U-notch lies in coupling the Airy stress function, equation (2-35), with the measured theormoelastic stress data and imposing traction-free conditions. Determination of individual stresses, equations (2-39) through (2-41), necessitates evaluating the unknown coefficients in the Airy stress function (typically referred to as Airy coefficients). The specific form of the Airy stress function for a particular case can depend on conditions of symmetry, whether or not the coordinate origin is within the component, whether the component is finite or infinite in size (boundedness at origin or infinity), self-equilibrated at individual boundaries, and single-valued stresses, strains and displacements. Even though the plate geometry and loading are symmetric about the x-axis, all coefficients were retained here, i.e., utilized equation (2-35), because the coordinate origin is located outside the specimen boundary of the plate. The isopachis stress, $S = \sigma_{rr} + \sigma_{\theta\theta}$, is

$$
\begin{aligned}
S = {} & 4c_0 + 4d_0(\ln r + 1) + 4C_0\theta + 4D_0(\ln r + 1)\theta + \left(\frac{2b_1}{r} + 8rd_1\right)\sin\theta \\
& + \left(\frac{2b_1'}{r} + 8rd'_1\right)\cos\theta + \frac{2A_1}{r}\cos\theta \\
& + \frac{2B_1}{r}(\theta\sin\theta + \ln r\cos\theta) - \frac{2A_1'}{r}\sin\theta \\
& + \frac{2B_1'}{r}(\theta\cos\theta - \ln r\sin\theta) \\
& + 4\sum_{n=2,3,..}^{N}\{b_n(n+1)r^n - d_n(n-1)r^{-n}\}\sin n\theta \\
& + 4\sum_{n=2,3,..}^{N}\{b'_n(n+1)r^n - d'_n(n-1)r^{-n}\}\cos n\theta
\end{aligned}
\tag{5-1}
$$

Notice that S is a function of $(c_0, d_0, C_0, D_0, b_1, d_1, b_1', d_1', A_1, B_1, A_1', B_1', b_n, d_n, b_n', d_n')$ whereas the individual stresses are also functions of $(b_0, A_0, B_0, c_1, c_1', a_n, c_n, a_n', c_n')$. As a result, it is not sufficient to use only TSA signals, $S^* = K\Delta S$, to evaluate all the Airy coefficients and determine all the individual stresses. Therefore, some traction free boundary and symmetry conditions were also imposed to help evaluate all the coefficients. For this Cartesian components of stresses are necessary and they were evaluated by converting from the polar stresses using the standard transformation matrix.

5.4.1 Boundary Conditions

To help evaluate all of the Airy coefficients, boundary conditions in terms of stresses as shown in Figure 5-2 were imposed discretely (point-wise) at multiple locations on the traction-free surface of the U-notch and on the both outer vertical traction-free edges of the plate. Since no symmetry is assumed in the form of the Airy stress function, zero shear stress along the horizontal line of symmetry was also imposed. The nine conditions can be written as

$$\sigma_{rr}(R, \theta) = \sigma_{r\theta}(R, \theta) = 0, \qquad \pi/2 \leq \theta \leq \pi \tag{5-2}$$

$$\sigma_{yy}(x, R) = \sigma_{xy}(x, R) = 0, \qquad 0 \leq x/R \leq 66 \tag{5-3}$$

$$\sigma_{xy}(x, 0) = 0, \qquad -20 \leq x/R \leq -1 \tag{5-4}$$

$$\sigma_{xx}(-20R, y) = \sigma_{xy}(-20R, y) = 0, \qquad 0 \leq y/R \leq 20 \tag{5-5}$$

$$\sigma_{xx}(66R, y) = \sigma_{xy}(66R, y) = 0, \qquad 1 \leq y/R \leq 20 \tag{5-6}$$

where R is the radius of the notch.

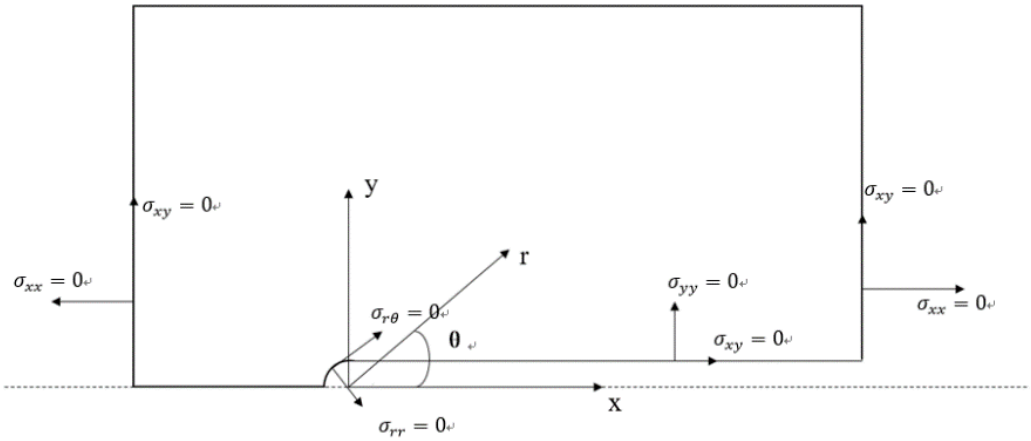

Figure 5-2: Imposing traction-free boundary conditions.

5.4.2 Coefficient Evaluation

From the recorded thermoelastic data and local boundary conditions, the Airy coefficients can be solved by forming a linear system of equation represented in matrix form as $[A]_{(m+h)\times k}\{c\}_{k\times 1} = \{d\}_{(m+h)\times 1}$ where m is the total number of measured values of S, h is the number of the imposed stress conditions, and k is the number of unknown Airy coefficients. The matrix $[A]$ consists of the analytical expression of isopachics stress S $(= S^*/K)$, equation (5-1), in addition to h known stress conditions, i.e., equations (5-2) through (5-6), as a function of polar coordinates (r, θ). The vector $\{c\}$ contains the k unknown Airy coefficients and vector $\{d\}$ contains the m measured TSA signal values with the h zeros from the right hand side known stress conditions. Like most experimental data, the measured data incorporate some noise which necessitate collecting more measured input values than the number of unknown Airy coefficients. The number of equations, $m + h$, is larger than the number of coefficients, k, which produces an overdetermined system which can be solved using least-squares. The system was solved in MATLAB using the backslash '\' operator.

The excellent agreement between the results from TSA and FEA will demonstrate the reliability with which one can evaluate the individual components of stress from thermoelastic

signals. Recognizing the unreliability of the measured data at any near edge, measured values of S originate at least three pixels away from the edge of the notch and vertical sides of the plate.

5.5 Finite Element Analysis

For comparison with the TSA, a finite element analysis (FEA) using ANSYS was prepared of the finite plate of Figure 5-1 using elastic properties of E = 70 GPa and ν = 0.33. Due to the symmetry, only the upper part of the plate was modeled with symmetrical boundary condition applied along the line of symmetry, y = 0. A concentrated load of 356 N was applied at the top hole in Figure 5-1. Plane 82 Isoparametric element with four nodes were employed. A convergence test was applied until the change in results of maximum stress between two successive meshing was less than 2%. This half FE model utilizes 25,000 elements and 25,351 nodes, Figure 5-3. The size of elements close to the notch is 0.016 mm, i.e., less than 2% of the radius of the groove.

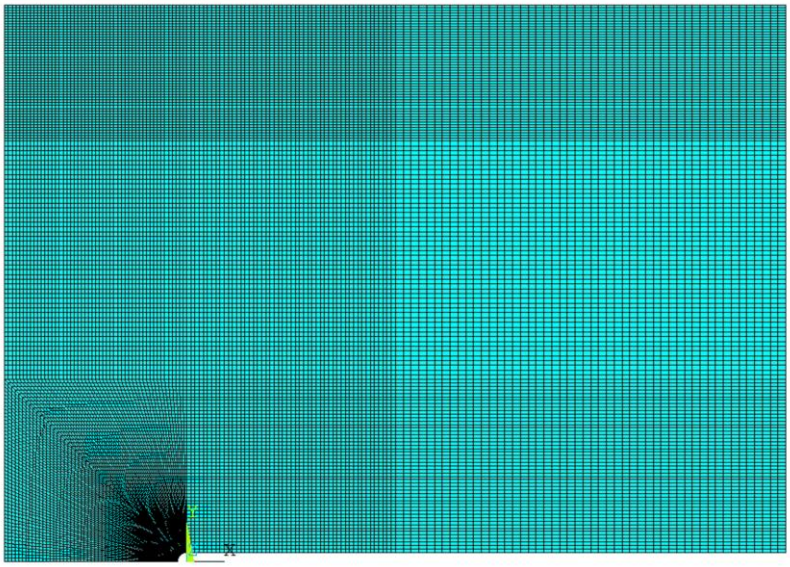

Figure 5-3: Mapped mesh FE model with dense meshing adjacent to the U-notch.

A motivation for developing the present ability is to enable stress analysis of cases experimentally which cannot be analyzed numerically; yet FEM is used here. The geometry and

loading of the Figure 5-1 were deliberately selected so as one could obtain a reliable FEM result with which to validate the experimental results. The developed hybrid-TSA method is applicable to more complicated problems which are difficult for FEM, e.g., do not know the external loading. For example, while industry makes prevalent use of FEM, strain gages are often employed in that environment to obtain the boundary conditions for the FEA.

5.6 Numerical Experiment

5.6.1 Evaluating Number of Coefficients to Employ

To help ensure the equations are all correct and check numerical reliability and robustness, a numerical-hybrid approach based on Airy stress function was first assessed using simulated input values of $S = \Delta\sigma_{xx} + \Delta\sigma_{yy}$ from ANSYS, Figure 5-4a. The source locations of the selected values of S are shown in Figure 5-4b and excluding at and near edges. The results of this numerical experiment, based on m = 6,300 input values of S distributed as shown in Figure 5-4b, and 50 equally-spaced points along the lines noted in Figure 5-2 (h = 50 × 9 = 450) were used to evaluate k = 49 coefficients (N = 5). The number of coefficients to employ was assessed by the plotting root mean square (RMS) values between the simulated values of S and the reconstructed values of $\{S\} = [A]\{c\}$ versus k and observing condition number of matrix $[A]$ as shown in Figure 5-5. Once the number of coefficients exceeds 49, Figure 5-5 shows the RMS increases dramatically which suggests choosing k = 49. The appropriateness of utilizing 49 coefficients is substantiated by comparing the reconstructed using the hybrid method and simulated S data from ANSYS as shown in Figure 5-4a.

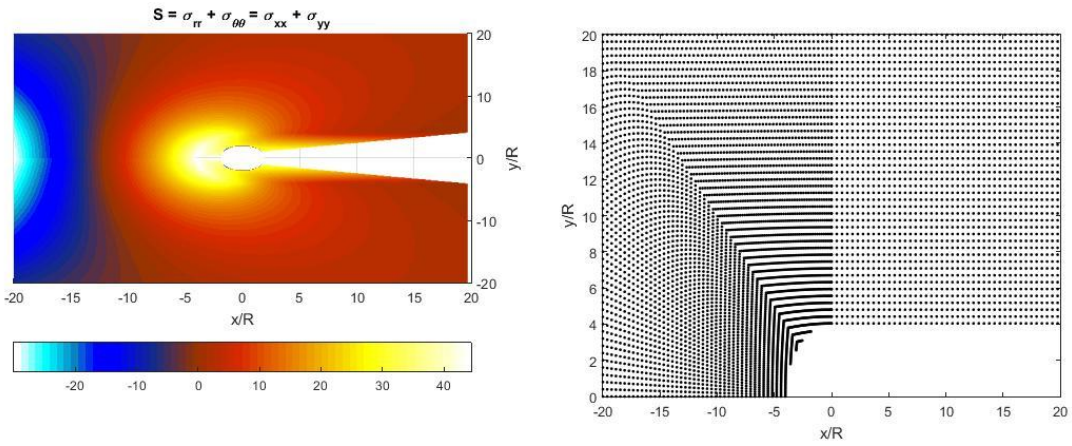

(a) (b)

Figure 5-4: (a) S values in MPa from ANSYS (upper) and reconstructed (k = 49) from hybrid method (lower) ans (b) Source locations of 6,300 simulated S values from ANSYS.

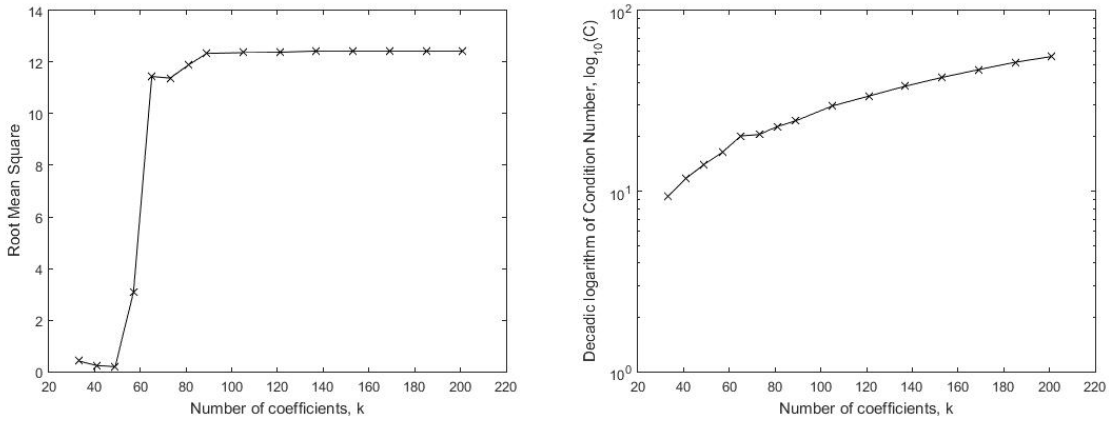

(a) (b)

Figure 5-5: (a) RMS and (b) condition number of matrix $[A]$ versus the number of coefficients, k ($m + h$ = 6,750).

5.6.2 Stresses

The determined stresses along the boundaries from processing the simulated input values of S by the hybrid technique are compared with those directly predicted by ANSYS to assess the validity of the described approach, Figure 5-6 through Figure 5-9. The maximum hybrid-determined value of $\sigma_{\theta\theta}$ agrees within one percent of that from ANSYS. Contour plots of polar stresses are shown in Figure 5-10 through Figure 5-12. The results of this numerical experiment based on discrete input values of S agree with ANSYS, including along edges where no input values were employed. Such numerical experiments employing simulated test

data help verifying that there are no algebraic errors and substantiate that the system is numerically robust. Having verified the reliability and robustness of the hybrid method, it was used then to stress analyze a finite aluminum plate containing a deep U-notch using actual measured thermoelastic data.

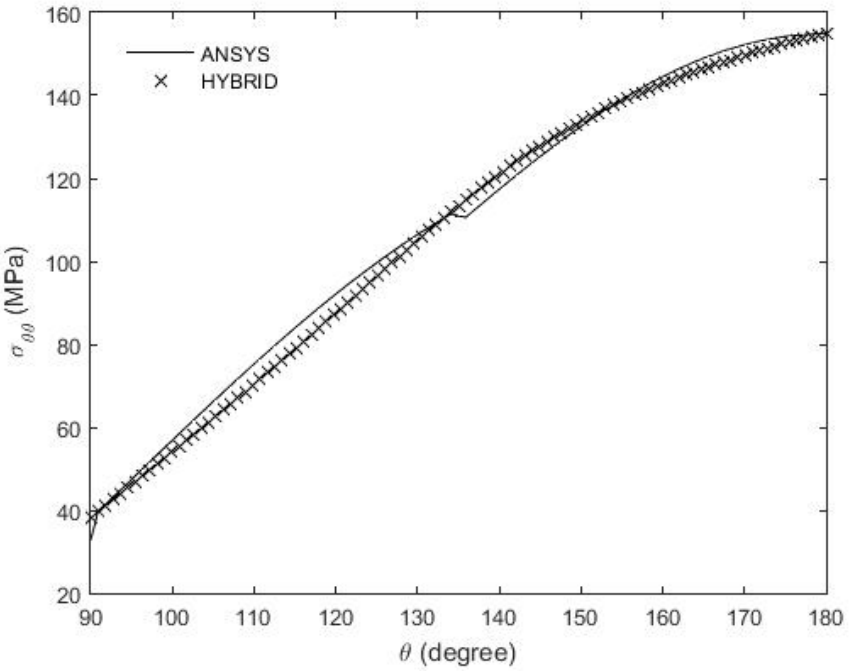

Figure 5-6: Tangential stress, $\sigma_{\theta\theta}$ along the curved edge of notch (k = 49, $m + h$ = 6,750).

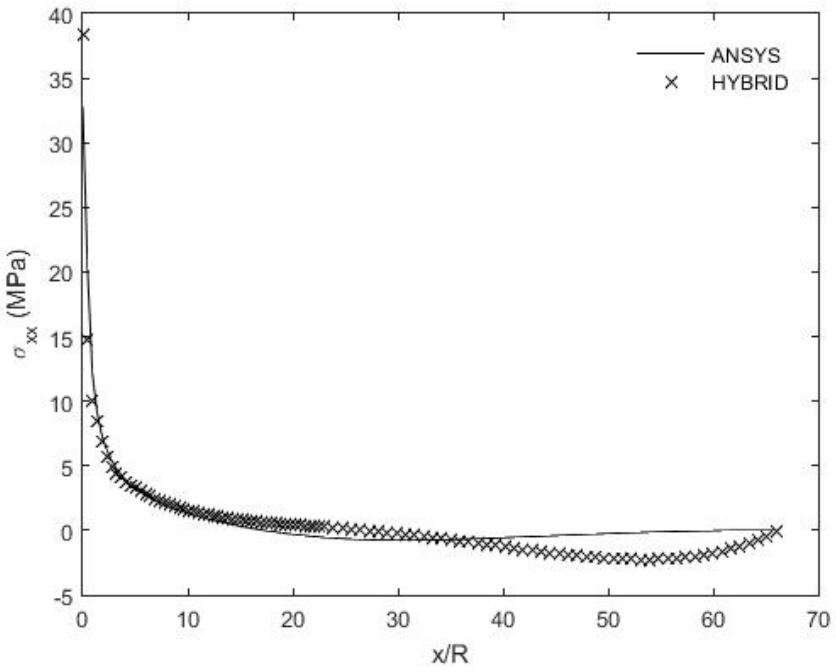

Figure 5-7: Stress σ_{xx} along the free edge of the notch, $x/R \geq 0$ and $y/R = 1$ (k = 49, $m + h$ = 6,750).

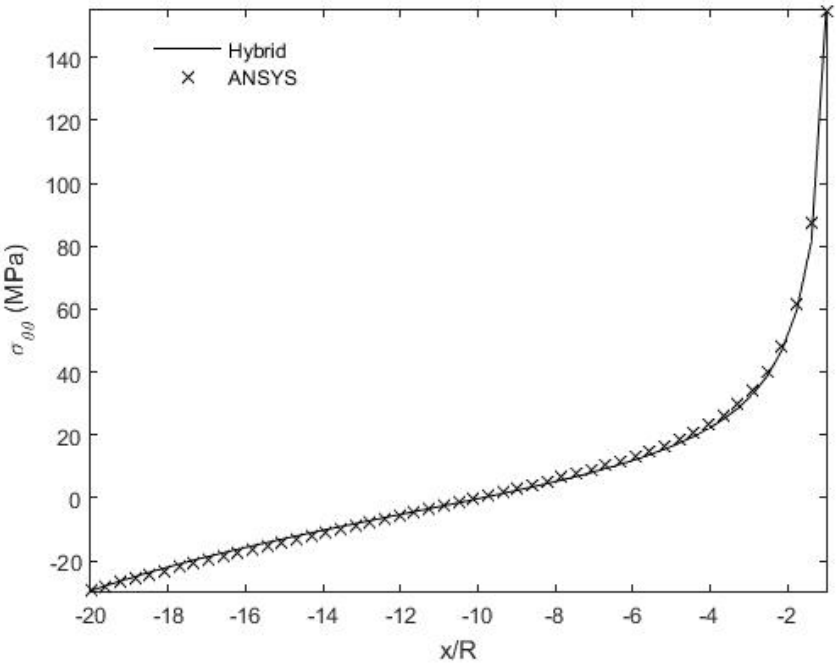

Figure 5-8: Stress $\sigma_{\theta\theta} = \sigma_{yy}$ along the line of symmetry, $x/R \leq -1$, $y/R = 0$ (k = 49, $m + h$ = 6,750).

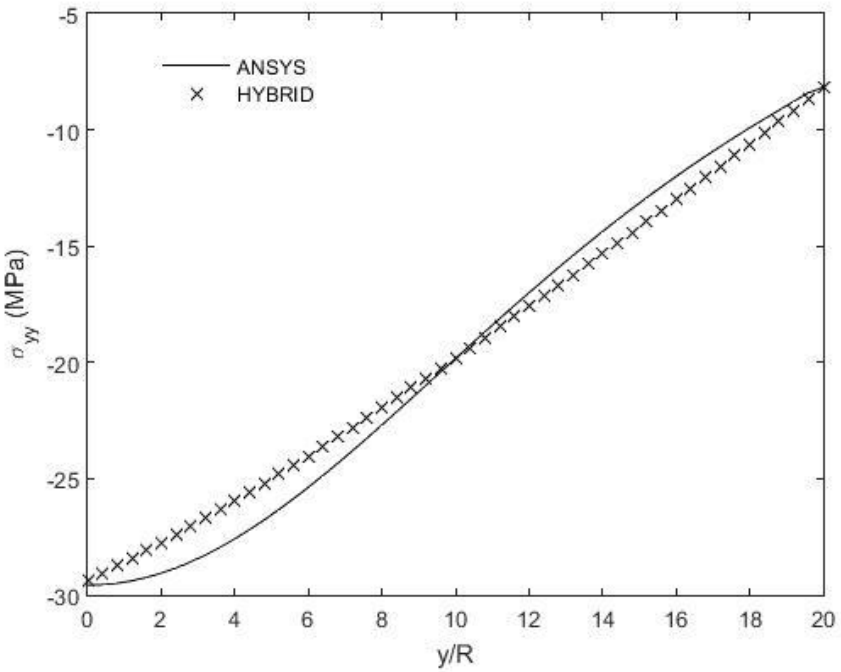

Figure 5-9: Stress σ_{yy} along left vertical left free-surface, x/R = -20 and $y/R \geq 0$ (k = 49, $m + h$ = 6,750).

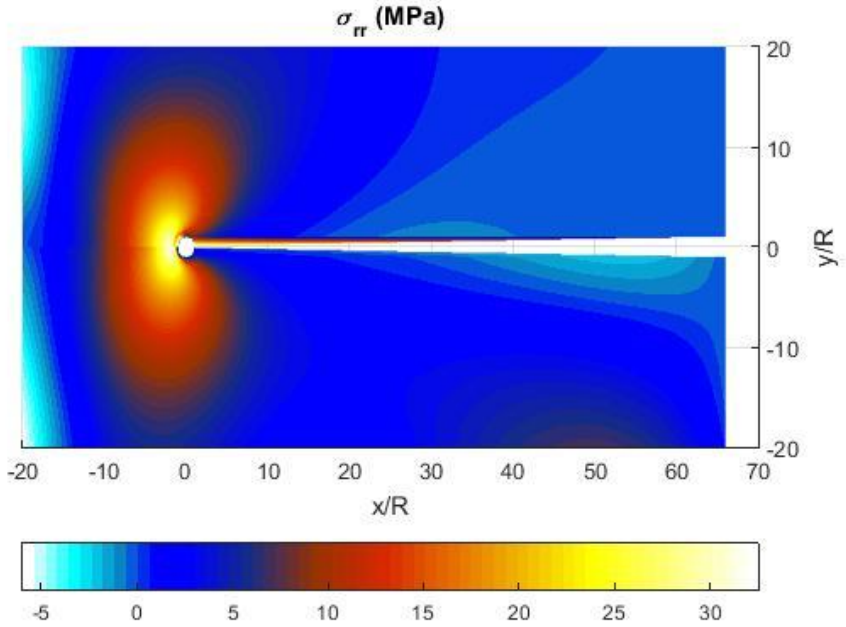

Figure 5-10: Contour plot of radial stress, σ_{rr}, from ANSYS (upper) and hybrid method (lower); k = 49, $m + h$ = 6,750.

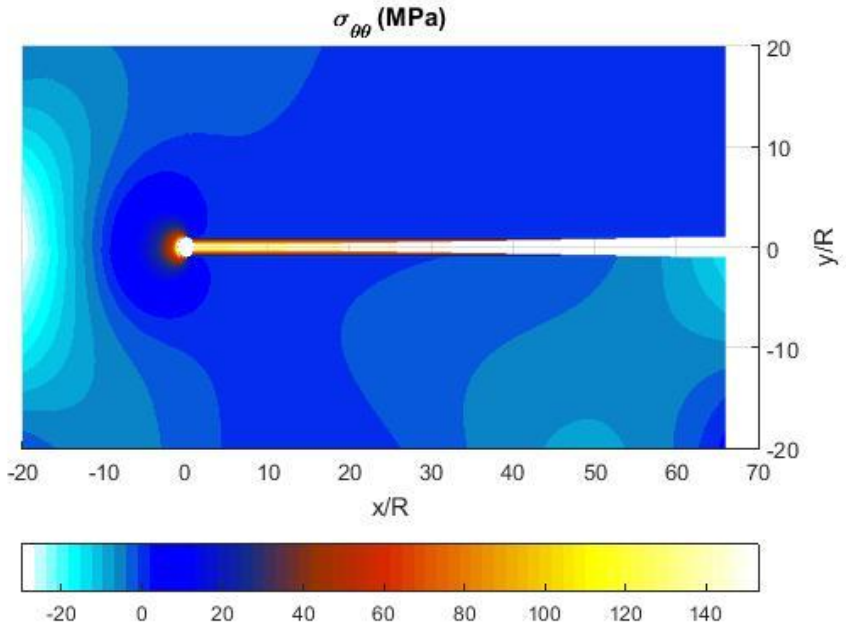

Figure 5-11: Contour plot of tangential stress, $\sigma_{\theta\theta}$, from ANSYS (upper) and and hybrid method (lower); k = 49, $m + h$ = 6,750.

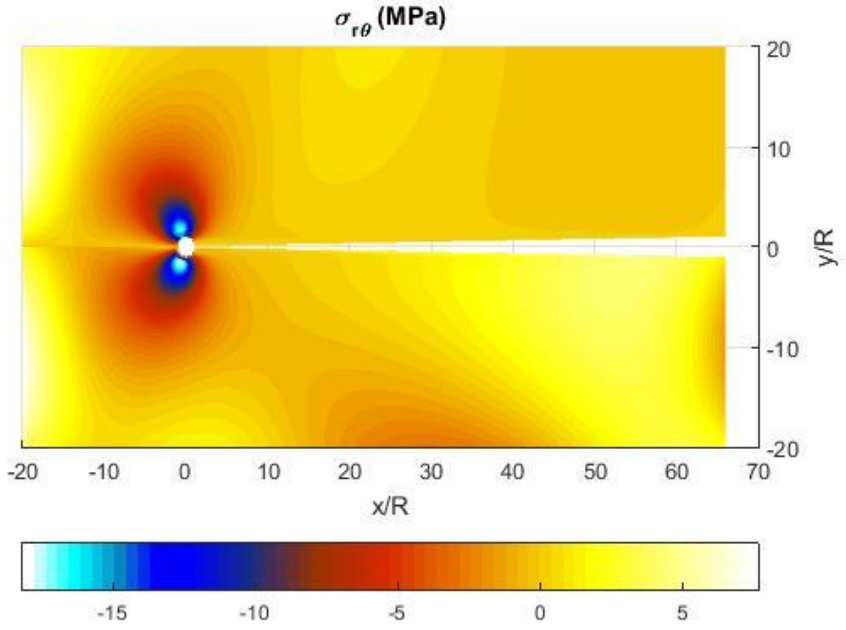

Figure 5-12: Contour plot of shear stress, $\sigma_{r\theta}$, from ANSYS (upper) and hybrid method (lower); k = 49, $m + h$ = 6,750.

5.6.3 Magnitudes of Airy Coefficients

Table 5-1 lists the values of the coefficients of equations (2-35). This information demonstrates that some coefficients, like $b_0, b_1, c_1, b_1', c_1', d_2, d_2'$, are identically zero and others are very small.

Table 5-1: Evaluated Airy coefficients using the simulated isopachic, S, from ANSYS.

Coefficient	Value	Coefficient	Value	Coefficient	Value
b_0	0	a_2	0.09195	b_4	-4.805× 10^{-7}
c_0	2.692	b_2	-40.16× 10^{-5}	c_4	2.543
d_0	-1.568	c_2	-8.044	d_4	-1.582
A_0	-5.692	d_2	0	a_4'	9.090× 10^{-5}
B_0	-15.94	a_2'	0.8392	b_4'	-1.607× 10^{-8}
C_0	4.399	b_2'	-26.58× 10^{-4}	c_4'	-0.9810
D_0	-0.6904	c_2'	1.008	d_4'	-0.8015
b_1	0	d_2'	0	a_5	-1.895× 10^{-6}
c_1	0	a_3	-20.63× 10^{-4}	b_5	2.811× 10^{-9}
d_1	−0.04444	b_3	2.966× 10^{-5}	c_5	0.5197
b_1'	0	c_3	0.08420	d_5	-0.4258
c_1'	0	d_3	-0.2787	a_5'	1.490× 10^{-6}
d_1'	0.1327	a_3'	-0.01245	b_5'	-2.793× 10^{-10}
A_1	-7.879	b_3'	3.125× 10^{-5}	c_5'	0.4595
A_1'	9.388	c_3'	-5.239	d_5'	-0.3147
B_1	6.649	d_3'	2.360		
B_1'	-13.58	a_4	-1.598× 10^{-6}		

5.7 Experimental Setup

5.7.1 Plate Preparation and Loading Condition

Having substantiated the numerical reliability, robustness, and stability of the present hybrid approach, it was then utilized to stress analyze a finite-width aluminum plate containing a deep U-notch and subjected to a concentrated load. The 5 mm thick aluminum plate is 86 mm wide and 125 mm long and has 2 mm wide deep U-notch, Figure 5-1. The coordinate origin is at the center of the end of the notch and the geometry and loading are symmetric about x-axes. The material properties are E = 70 GPa and ν = 0.33. The specimen was initially very lightly polished with 400 grit sand paper. A coating of Krylon Ultra-Flat black paint was then applied to provide an enhanced and uniform emissivity, Figure 5-1. Precaution was taken when sanding the faces of the specimen not to round-off the edges of the notch which could further erode the quality of the thermal information close to the edge of the U-notch. The plate was sinusoidally loaded in a 20 kips capacity MTS hydraulic testing machine at a load range of ΔF = 356 N (80 lb) at 30 Hz frequency, Figure 5-13. The plate was loaded at different cyclic rates while monitoring the phase information provided by the DeltaTherm Stress Photonics TSA system software (Madison, WI) in order to ensure that the adiabatic conditions prevailed at the employed loading frequency of 30 Hz. The corresponding load-induced TSA data were recorded using a TSA Delta Therm model DT1410 system (Stress Photonics, Madison, WI) having a sensor array of 256 horizontal by 256 vertical pixels which is cooled with liquid nitrogen to maintain the sensor at a very low temperature necessary for the accurate readings. The camera was aligned perpendicular to the surface of the plate, Figure 5-13.

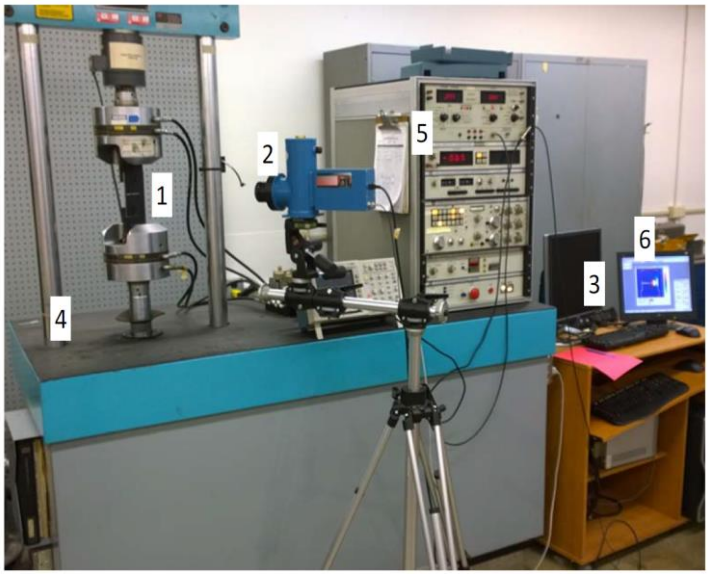

Figure 5-13: Experimental test setup for recording temperature variations of (1) finite plate with U-notch using (2) Delta Therm model DT1410 infrared camera, (3) computer to analyze image data, (4) load frame, (5) servo-hydraulic testing machine control panel, and (6) TSA image of loaded specimen.

5.7.2 TSA Recording and Calibration

The thermoelastic signal,S^*, was recorded by the data acquisition system which is equipped with Delta Vision Software, Figure 5-14. TSA images were captured and averaged over two minute durations, and then exported to Excel to convert each pixel into a data point, i.e., 256 by 256 matrix. Pixel size is 0.35 mm. Since TSA data typically are unreliable on and near an edge, no recorded TSA information was used within at least three to six pixel positions (1.1 to 2.1 mm) of the boundary edges, Figure 5-15. The thermoelastic coefficient K was evaluated from a separate uniaxial tensile coupon of the same material, thickness and coating of the flat black paint and tested on the same day at the same frequency using the same TSA arrangement as the notched plate. The thermoelastic coefficient was determined to be K = 212 U/MPa. The unit U is used to signify the raw TSA output, in uncalibrated signal units.

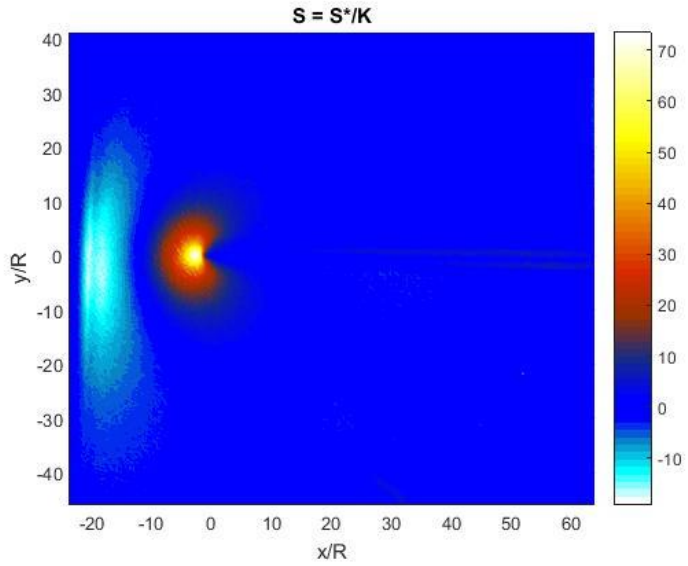

Figure 5-14: TSA image, S, of finite aluminum plate with deep U-notch loaded at a range of 356 N and frequency 30 Hz.

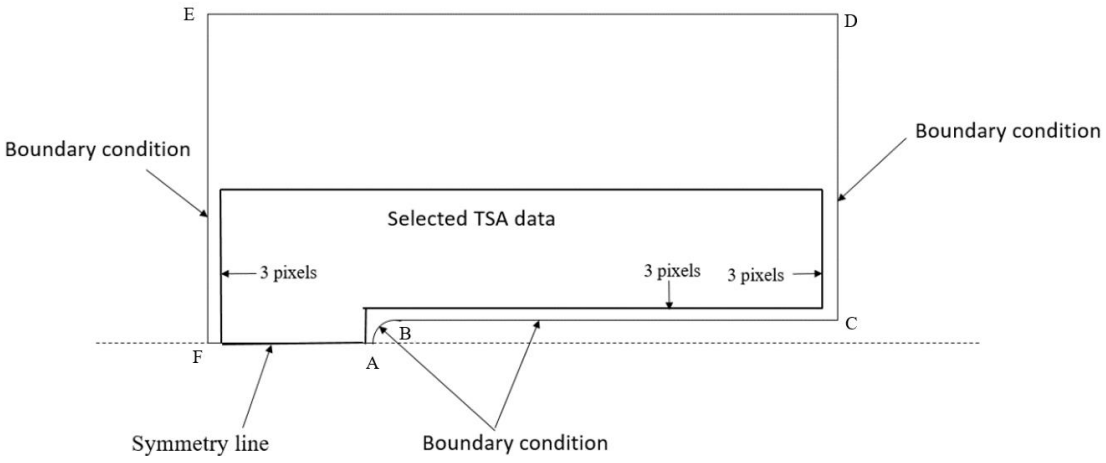

Figure 5-15: Source locations of the selected TSA data and the locations of the imposed boundary conditions and the line of symmetry.

5.7.3 Data Processing

The individual stresses throughout the region adjacent to the deep U-notch were determined from such thermoelastic data using an Airy stress function. Since the plate geometry and loading are symmetrical about the horizontal x-axes, the upper and lower recorded thermoelastic data, S^*, of Figure 5-14 were first averaged. Due to unreliability, the recorded data along and near the edge of the notch were not used. Only the 10,461 thermal values of S^* originated

at the locations shown in Figure 5-16 were utilized. Like most experimental data, the recorded S^* includes some noise which necessitates collecting more measured input values than the number of unknown coefficients. In addition to the employed 10,461 values of S^*, at total of h = 500 × 9 = 4500 boundary conditions were imposed at 500 equally-spaced discrete points on each of the nine relevant expression in equations (5-2) through (5-6) on the lines of Figure 5-2. The number of equations, $m + h$ = 14961, will exceed the number of coefficients, k. The resulting overdetermined system of equations with which to evaluate the unknown coefficients was solved using least-squares. The system was solved in MATLAB using the backslash '\'. The subsequent analysis will demonstrate that the described approach is able to evaluate stresses reliably at the edge of the U-notch without using any thermoelastic data on, or very near, the edges.

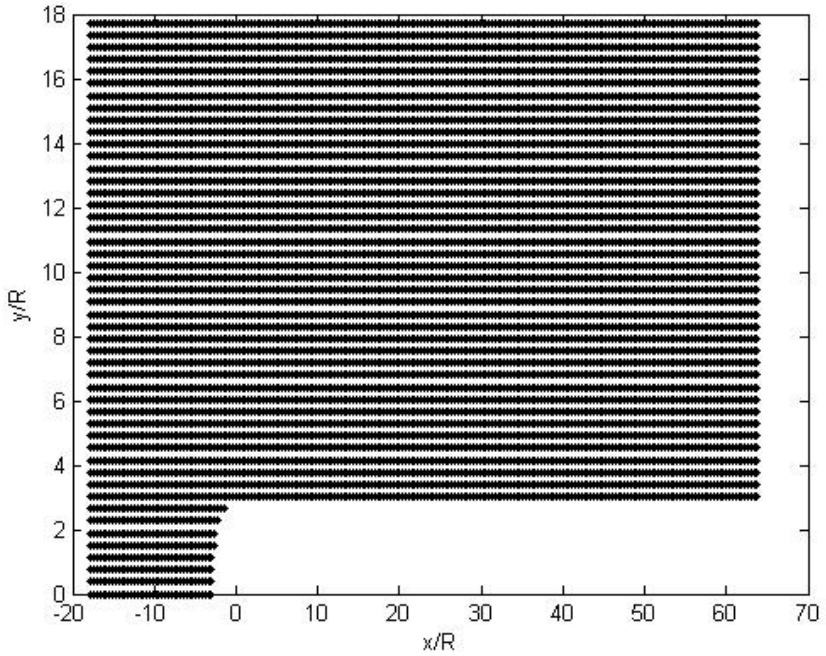

Figure 5-16: Source locations of employed S^* data (m = 10,461 data points).

5.8 Results

5.8.1 Evaluating Number of Coefficients to Employ

The results of this hybrid technique, based on m = 10,461 input values of S^* uniformly distributed as shown in Figure 5-16, and 500 equally-spaced points along the lines of Figure 5-2 (h = 4500) were used to evaluate the k = 49 coefficients (N = 5). The use of 49 Airy coefficients was again determined from plotting root mean square (RMS) values between $\{d\}$ which contains the recorded values of S^* plus h zeros from the boundary conditions and the reconstructed values of $\{d'\} = [A]\{c\}$ versus k, and observing condition number of matrix $[A]$, Figure 5-17. Once the number of coefficients exceeds 49, the RMS increases which suggests choosing k = 49. The appropriateness of utilizing 49 coefficients is substantiated by comparing the reconstructed (using the hybrid method) and recorded S^* data, Figure 5-18.

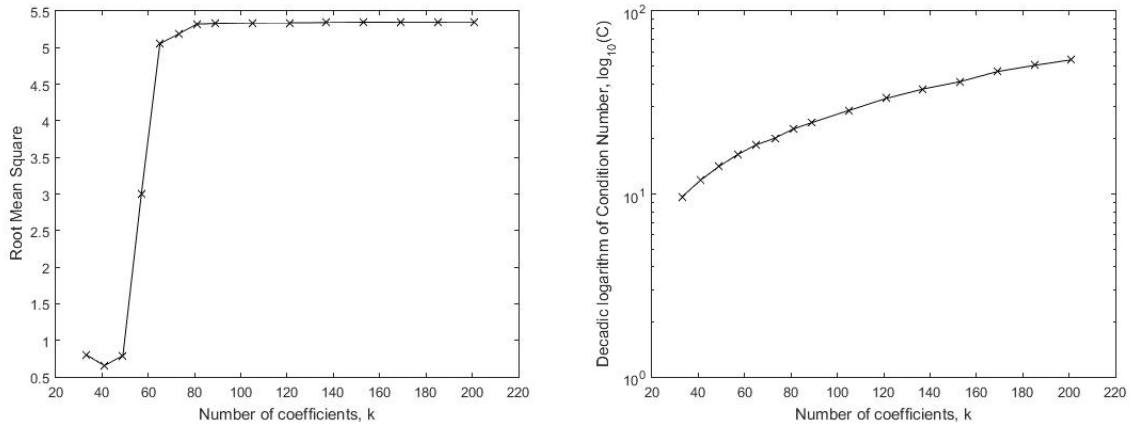

(a) (b)

Figure 5-17: (a) RMS and (b) condition number of matrix $[A]$ versus the number of coefficients, k ($m + h$ = 14,961).

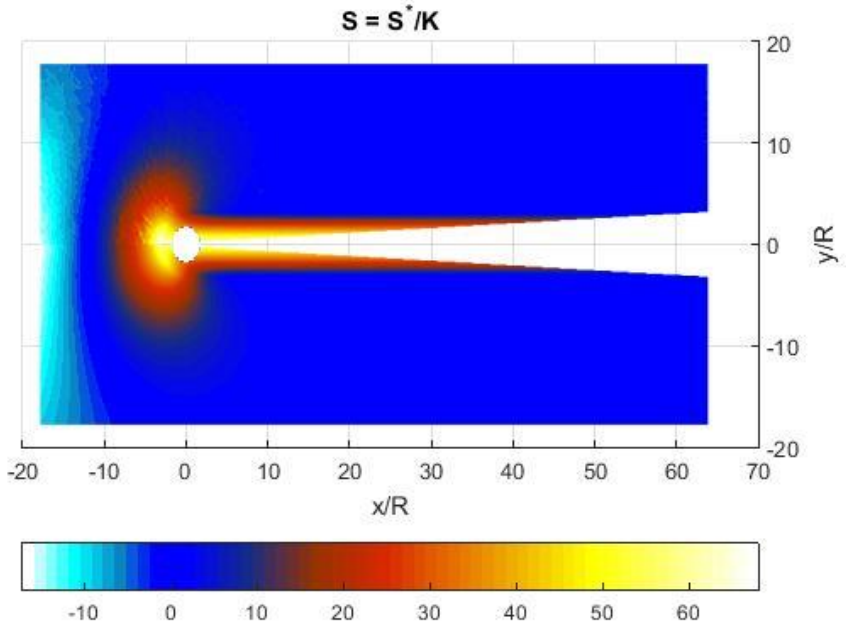

Figure 5-18: $S = S^*/K$ values in MPa from TSA (upper) and reconstructed from hybrid method (lower).

5.8.2 Stresses

The stresses determined along the edge of the notch and along $y = 0$ by processing the recorded TSA values of S^* with the Airy stress function, i.e., hybrid method, are compared with those from ANSYS in Figure 5-19 and Figure 5-20. The maximum values of $\sigma_{\theta\theta}$ from hybrid-TSA and ANSYS agree within one percent of each other. Contour plots of polar stresses are shown in Figure 5-21 through Figure 5-23. The results of this hybrid experiment based on discrete input values of S^* agree virtually exactly with ANSYS including along edges where no input values were employed.

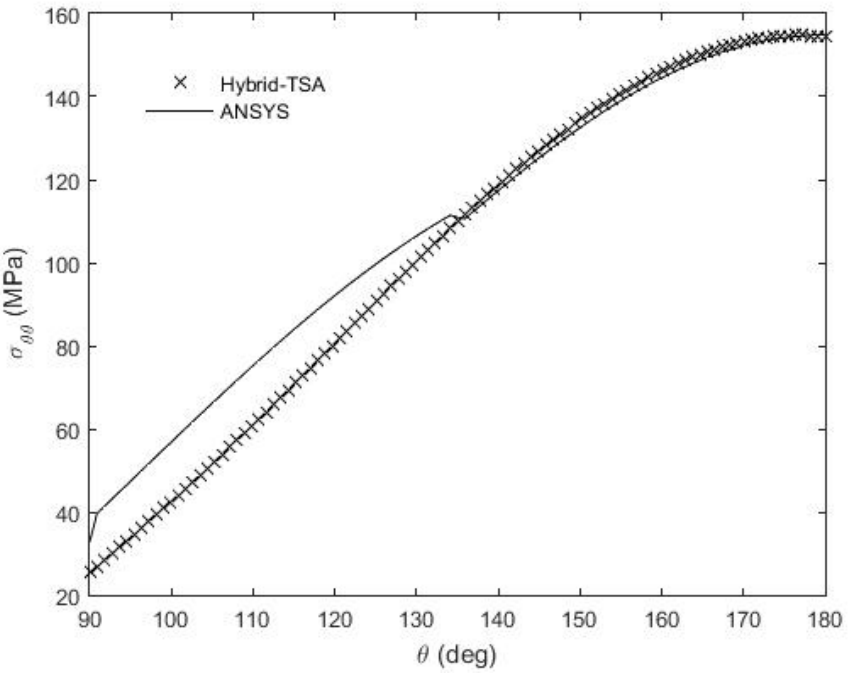

Figure 5-19: Tangential stress, $\sigma_{\theta\theta}$, along the edge of the notch (k = 49, $m + h$ = 14,961).

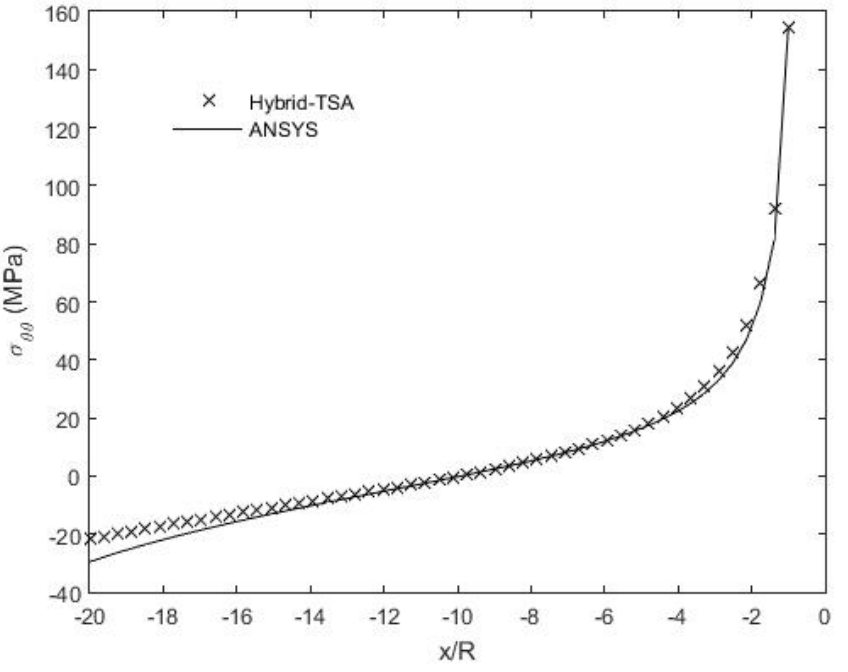

Figure 5-20: Stress $\sigma_{\theta\theta} = \sigma_{yy}$ along the line $y = 0$ and $x \leq -1$ (k = 49, $m + h$ = 14,961).

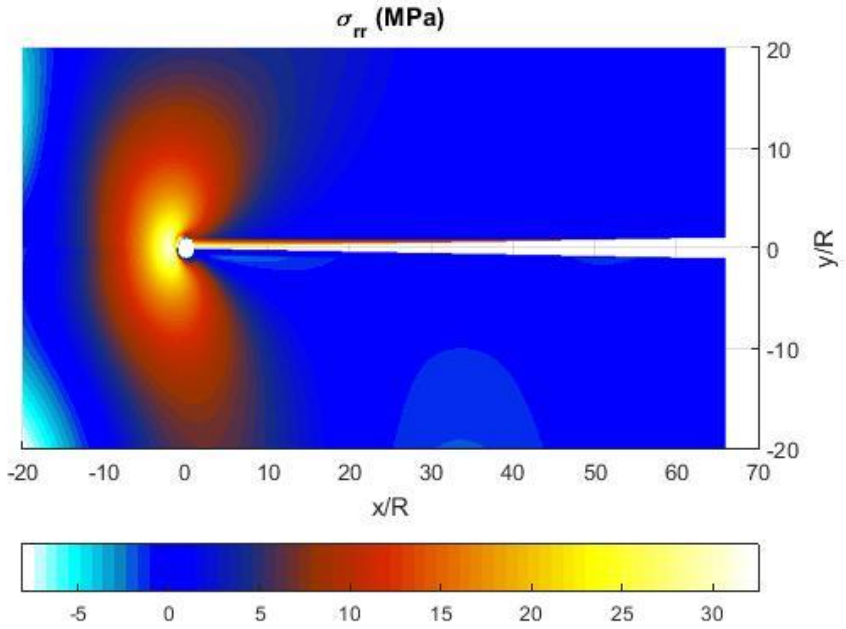

Figure 5-21: Contour plot of radial stress, σ_{rr}, from ANSYS (upper) and present hybrid method (lower); k = 49 $m + h$ = 14,961.

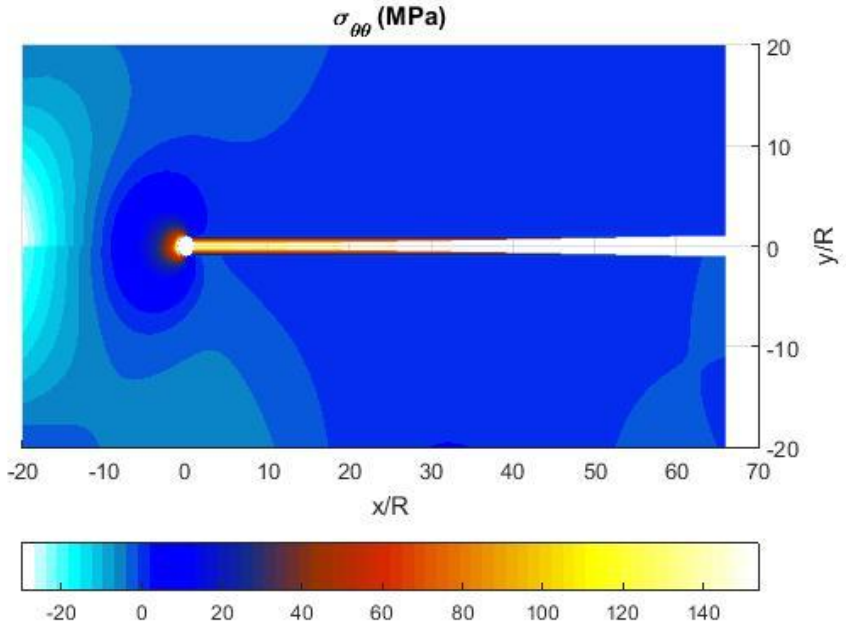

Figure 5-22: Contour plot of tangential stress, $\sigma_{\theta\theta}$, from ANSYS (upper) and present hybrid method (lower); k = 49 $m + h$ = 14,961.

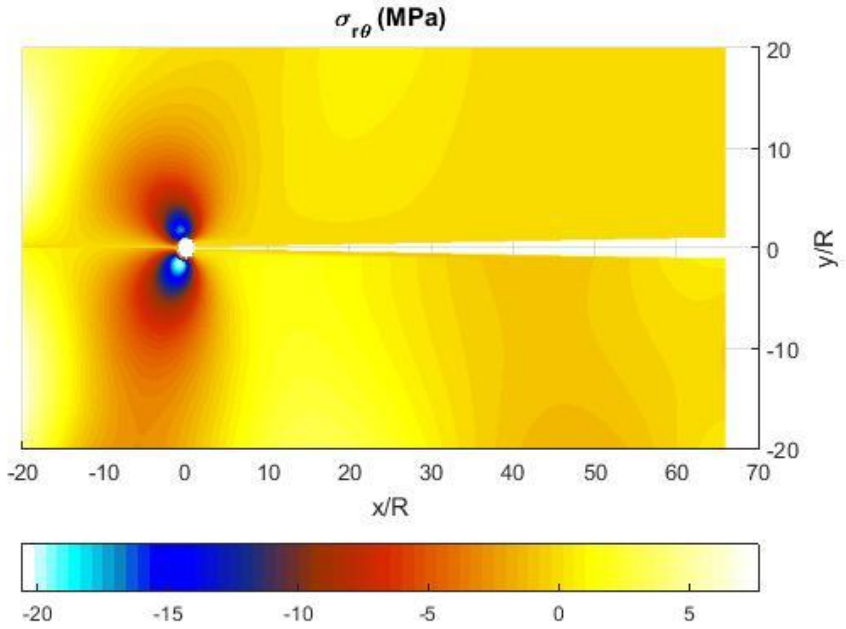

Figure 5-23: Contour plot of shear stress, $\sigma_{r\theta,}$ from ANSYS (upper) and present hybrid method (lower); k = 49 $m + h$ = 14,961.

5.8.3 Magnitudes of Airy Coefficients

Table 5-2 lists the values of coefficients of equations (2-35). Some of these coefficients, i.e., $b_0, A_0, b_1, c_1, b_1', c_1', A_1, A_1', c_2, d_2$ and d_2', are identically zero. However, while these coefficients are all zero in Table 5-1, not all of them are zero in Table 5-2. Since there are no resultant forces at the origin, reference [47] states that should have $b_1 = A_1 = b_1' = A_1' = 0$. Although this is true for the TSA case of Table 5-2, $A_1 \neq A_1' \neq 0$ for the ANSYS analyses of Table 5-1. Moreover, while $b_0 = b_1 = c_1 = b_1' = c_1' = d_2 = d_2' \equiv 0$ for both cases, $c_2 = 0$ in Table 5-2 but not in Table 5-1. Coefficients b_2, $b_2', a_3, b_3, b_3', a_4, b_4, a_4', b_4', a_5, b_5, a_5'$ and b_5' are very small by comparison in both Table 5-1 and Table 5-2. Associated with the geometric and loading symmetry about the x-axis, and no resultant force at the origin, reference [47] indicates that $b_1 = c_1 = d_1 = b_1' = A_1 = B_1 = A_1' = B_1' = a_n = b_n = c_n = d_n$ should be identically equal to zero in equation (2-35). Many of these coefficients are significantly non-

zero in Table 5-1 and/or Table 5-2. Note that neither a_0, a_1 nor a_1' appear in the expressions for the stresses.

Table 5-2: Evaluated Airy coefficients using the recorded TSA data of Figure 5-14.

Coefficient	Value	Coefficient	Value	Coefficient	Value
b_0	0	a_2	-0.512	b_4	-3.316×10^{-7}
c_0	-7.779	b_2	77.77×10^{-5}	c_4	1.060
d_0	2.311	c_2	0	d_4	-1.631
A_0	0	d_2	0	a_4'	-11.31×10^{-5}
B_0	-20.755	a_2'	1.141	b_4'	-1.995×10^{-7}
C_0	10.424	b_2'	-13.78×10^{-4}	c_4'	1.482
D_0	-3.100	c_2'	1.776	d_4'	-0.216
b_1	0	d_2'	0	a_5	-1.88×10^{-6}
c_1	0	a_3	-79.21×10^{-5}	b_5	1.827×10^{-9}
d_1	−0.016	b_3	1.261×10^{-5}	c_5	0.0241
b_1'	0	c_3	3.415	d_5	-0.365
c_1'	0	d_3	-2.751	a_5'	1.327×10^{-6}
d_1'	-0.02669	a_3'	-0.00566	b_5'	2.313×10^{-10}
A_1	0	b_3'	2.95×10^{-5}	c_5'	0.405
A_1'	0	c_3'	0.729	d_5'	-0.330
B_1	4.469	d_3'	1.188		
B_1'	-12.538	a_4	23.79×10^{-5}		

5.9 Strain Gage Analysis

Electrical resistance strain gages are probably the most widely used experimental technique available. Strain gages are fairly inexpensive and have good sensitivity. A wide range of associated instrumentation is available and can be utilized to monitor steady or transient phenomena, determine residual stresses, measure non-linear strain/stress response and are applicable for impact situations. However, the method requires some surface preparation and gage mounting, wiring and data processing, and can be arduous for a large number of gage locations as a gage does not (by itself) provide full-field data. Gage locations can be critical, particularly at steep strain gradients such as in the neighborhood of the root of the present notch. Strain gages measure the average strain over the gage length and might not capture the largest value. This can also be of concern in highly localized stress concentration regions having sharp strain gradients, implying the need to use small gages in such locations.

The present hybrid approach was further validated by comparing the hybrid-TSA obtained strains at a static load of 356 N (80 lb) with those from small commercial foil strain gages mounted away from the boundary of the U-notch by 2.5 mm on the front surface, Figure 5-24 (left), and 2.0 and 2.8 mm on the back surface, Figure 5-24 (right). Four single-element Micro-Measurements strain gages (EA-06-015DJ-120), each having gage resistance of 120.0 $\pm$ 0.3% Ω and gage factor of 2.05 ± 1.0%, were mounted along line $y = 0$ on the specimen (two gages on front face and two on the back face), Figure 5-24. One of the four gages mal-functioned. The present gages were mounted using standard strain gage procedures suggested by Vishay Micro-Measurements. The recommended conditioners and neutralizers were used on the aluminum before mounting the gages. M-Bond 610 adhesive (marketed by Vishay Micro-Measurements) was utilized in conjunction with a catalyst (200 Catalyst-C, recommended for use with M-Bond adhesive) for good adhesion and long-time stability. A protective air drying polyurethane coating, M-Coat, was applied over the

gages (and their wires) after the adhesive had dried. Although the gages were not ‘tuned’ for aluminum, they were mounted and the testing was conducted at room temperature so no dummy temperature compensating gages were employed.

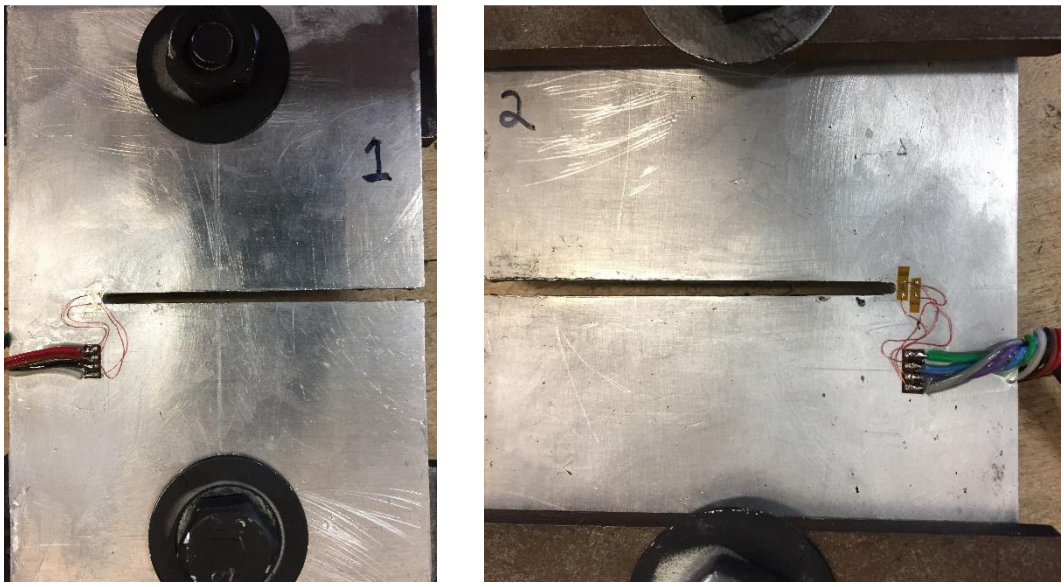

Figure 5-24: Specimen front and back surfaces with mounted strain gages.

Figure 5-25 contains strain-gage recorded strains for various levels of plate loading. The response is with load. All strain-gage results were recorded under both incremental increasing and decreasing static loading. The R-squared (which is a statistical measure of how well the regression line approximates the real data points) values for strain gages 1, 2 and 3 are 0.9737, 0.9972 and 0.9988, respectively. The strain gage tests were conducted under individual loading and after removing the black paint from the TSA-tested plate.

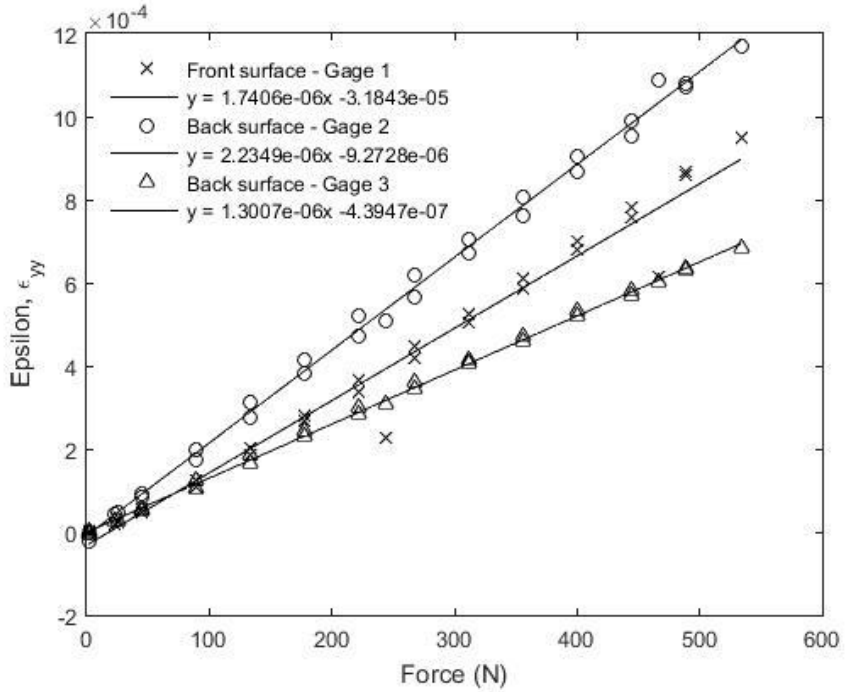

Figure 5-25: Recorded strains from the strain gages for different static loadings.

FEM-predicted strains and TSA-based strains evaluated from the TSA measured stresses were determined at the individual gage positions from Hooke's law (E = 70 GPa = 10×10^6 psi and ν = 0.33). Figure 5-26 shows the test arrangement for recording the strain gage data. This photograph includes the overall testing of the deeply grooved finite plate, and associated strain gage cables and instrumentation.

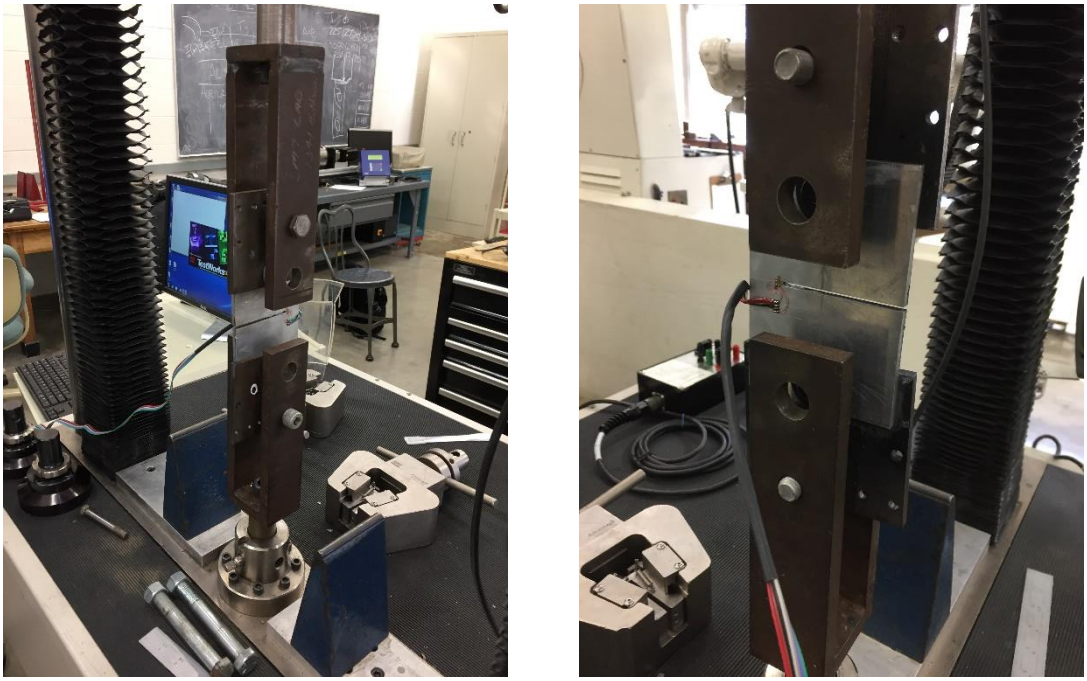

Figure 5-26: Experimental testing setup for measuring vertical strain of the deeply grooved finite plates using strain gages.

Figure 5-27 compares the strains (static equivalent specimen load of F = 356 N = 80 lb) along the line y = 0 obtained from hybrid-TSA with those from finite element analysis (ANSYS) and strain gages. Table 5-3 compares the strains from hybrid-TSA, FEA, and the strain gages. The good agreement between the current hybrid-TSA results and those from FEA and the strain gages provides strong confidence in the presently developed ability to obtain reliable stresses from recorded thermal information.

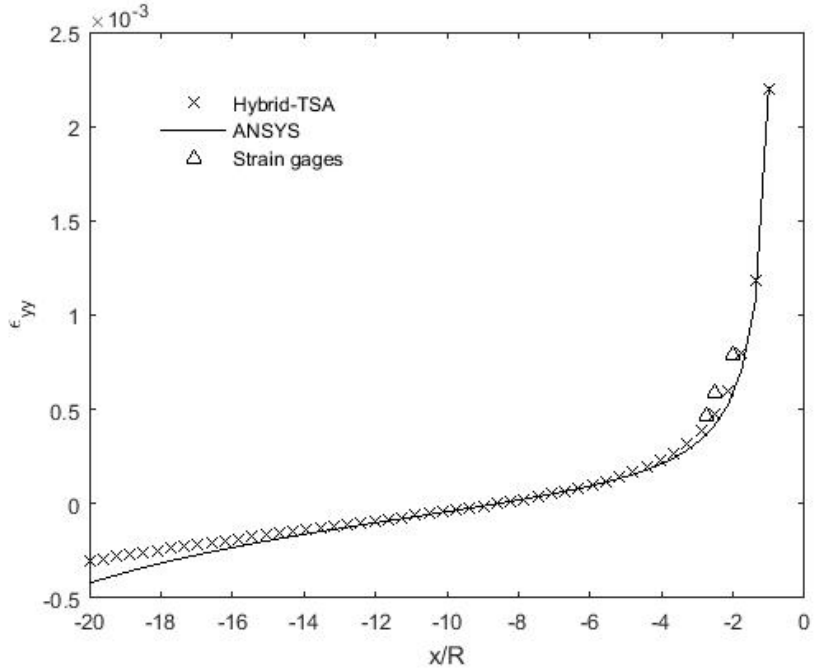

Figure 5-27: Strain ϵ_{yy} along line y = 0 of the deeply grooved finite aluminum plate of Figure 5-1 loaded by ΔF = 356 N from hybrid-TSA (k = 49 $m + h$ = 14,961), ANSYS, and strain gages.

Table 5-3: Strains ϵ_{yy} in $\mu\epsilon$ at locations in Figure 5-24 by each of hybrid-TSA, FEA (ANSYS), and strain gages for a static load of 356 N (80 lb) in the deeply grooved finite aluminum plate of Figure 5-1.

Strain Gage	Location, x/R	Strain value	Hybrid-TSA method	FEA (ANSYS)
1	-2.5	588	605	554
2	-2.0	786	888	831
3	-2.8	463	493	445

5.10 Summary, Discussion and Conclusions

A hybrid method which processes the load-induced TSA signals with an Airy stress function, together with applying local conditions discretely, provides the individual stresses at

and in the neighborhood of a deeply grooved finite plate. Unlike purely theoretical or numerical methods, knowledge of the external conditions is unnecessary. Employing more measured input values than unknown coefficients filters out experimental noise/scatter and smooths the results. A method was developed to separate reliably the recorded data into individual stresses and to evaluate accurate boundary information even though the recorded TSA data along, and adjacent to, the U-notch were not included. TSA results agree with those from FEA and strain gages.

A series representation of the stress function is assumed and careful attention paid to determining an appropriate number of coefficients to retain (in this case, 49 coefficients). The methods utilized here to ascertain how many coefficients to employ are general, not specific to the current data set or example. Least square method was used to evaluate unknown coefficients of overdetermined systems of equations.

A motivation for developing the present ability is to enable stress analysis of cases experimentally which cannot be analyzed numerically, although FEM is used here. The geometry and loading of the Figure 5-1 are sufficiently simple that one can obtain a reliable FEM result with which to validate the experimental results. However, the developed hybrid-TSA method is applicable to more complicated problems which are difficult for FEM, e.g., do not know the external loading. For example, while industry makes prevalent use of FEM, strain gages are often employed in that environment to obtain the boundary conditions for the FEA.

Reference [47] suggests that because of mechanical and geometric symmetry about the x-axis and no residual forces at the origin, $b_1, c_1, d_1, b_1', A_1, B_1, A_1', a_n, b_n, c_n, d_n$ can be assumed to be zero. The magnitudes of several of these coefficients in Tables 5-1 or 5-2 are significantly non-zero. Initial efforts to impose symmetry about y = 0 and assume the above coefficients to be zero produced totally incorrect results and led to using the entire Airy stress

function expression of equation (2-35). Reference [47] also indicates taking $d_0 = B_0 = C_0 = D_0 = B_1 = 0$ if the coordinate origin is within the body. Prior experience at UW-Madison demonstrates one needs to be careful in implementing this statement. Although one can correctly assume these coefficients to be zero for a plate with a hole and the coordinate origin within the hole, i.e., the origin is fully surrounded by structure, results here suggest that need not be valid if the origin is not fully enclosed by the structure. This is the present situation in that the coordinate origin of the singularly connected region (ignoring the area of the loading holes which was not involved in the analysis) of Figure 5-1 is outside of the plate. The suggestion in reference [47] to assume $A_0 = b_0 = A_1 = b_1 = A_1' = b_1' \equiv 0$ if there are no resultant forces at the origin is also not supported here.

A major contribution of this chapter is the demonstrated ability to determine the individual stresses in a finite engineering component by TSA using experimental-numerical-analytical hybrid technique, at, and in the neighborhood of, the boundary of the deep U-notch. The author is unaware of any previous research in determining the stresses near the boundary of the deep U-notch using thermal information and Airy stress function. Driven largely by the fact this situation involves a simply-connected body (the region analyzed omits the loading holes) and the coordinate origin is outside of the body, and not withstanding several of the Airy coefficients were subsequently determined to either be very small or identically zero, it was necessary to employ the entire stress function of equation (2-35). This is the first time known to the author when one has had to employ the entire form of the stress function when processing measured data, or perhaps even to stress analyze a structure by pure theory, i.e., analytically as a boundary-value problem. Having to use the full stress function of equation (2-35) was not expected here a priori. However, in retrospect, having to utilize the complete stress function is a significant contribution of this chapter as it expands the general hybrid concept of processing

measured information with a stress function to more complicate, but realistic, engineering problems.

Acknowledgement

S. Krunthottikkal Philip, J. L. Freire, B. Yang and J. Zeuske contributed to aspects of this chapter.

Chapter 6: Experimental Stress Analysis of a Notched Finite Orthotropic Composite Tensile Plate

Individual displacements and stresses in a vertically-loaded notched finite graphite/epoxy laminated composite are determined by processing measured values of a single component of displacement with an Airy stress function in complex variables. Displacements are recorded using digital image correlation. Traction-free conditions are imposed analytically at the notch using conformal mappings and analytic continuation, and discretely on the vertical free edge. Zero shear stress is also imposed on the horizontal line of symmetry. Consequences of employing different amounts and source locations of measured displacements and varying number of coefficients, as well as how displacements are differentiated to provide strains, are considered. Advantages of this method include ability to significantly simplify the experimental technique by needing only a single displacement component, provide reliable results both full-field and at the edge of geometric discontinuities, lack of need to differentiate the recorded data physically, and to simultaneously smooth the recorded data. Moreover, and compared against Correlated Solutions computed strains, the present hybrid-DIC technique offers the advantage of evaluating strains more accurate and without mathematically differentiating displacement experimental data. Reliability of experimental results is demonstrated by finite element and force equilibrium.

6.1 Introduction

Machine and structural members frequently contain holes or notches that produce stress concentrations and can consequently control component integrity. Although composite materials enjoy favorable specific strength and stiffness, their orthotropy influences the stress distributions. Purely analytical or theoretical stress analyses tend to be available for only simple situations involving infinite geometries, whereas most practical problems involve complicated, finite shapes. Moreover, and like numerical approaches such as the finite element method (FEM), analytical/theoretical analyses depend on reliable knowledge of the loading conditions. The latter are commonly unknown in practice. Classical experimental approaches suffer from poor results at the edges of cutouts, frequently locations of high mechanical interest. Recognizing these situations, it is advantageous to stress analyze composite structures experimentally by processing DIC-recorded displacement information with a stress function and evaluate reliable edge stresses utilizing analytic continuation.

For plane problems, strain, hence stress, determination from displacements typically necessitates knowing both in-plane components of displacements. However, individual components of displacement, strain, and stress are available here full-field by processing measured information of a single displacement component using a series representation of Airy stress function in complex variables. Needing only a single displacement field can be advantageous. For example, experimental techniques such as moiré, speckle, holography, grids or electronic speckle pattern interferometry (ESPI) necessitate additional rulings and/or optics to record two versus one in-plane component of displacement. Situations can also occur where there is a paucity or inferior quality of one or other of the in-plane displacements. Furthermore, such displacement-based techniques necessitate differentiating the recorded data, something which can be unreliable, especially on the edge of the geometric discontinuity (often location of great-

est interest) and may lead to highly inaccurate strains and stresses. This latter challenge is overcome here in that the stresses, strains, and displacements at, and in the neighborhood of the notch are obtained from measured information away from the edge of the notch. An additional strength of the present approach is the rigorous mechanics foundation (stress equilibrium and strain compatibility) by which strains are determined from measured displacement data.

6.2 Literature Review

Khaja, Samad and Rowlands [37,38] obtained the individual stresses in circularly- and elliptically-perforated isotropic plates by processing the recorded displacements with an Airy stress function in real variables using polar coordinates. Recognizing the general inability to analyze orthotropic materials using real variables, several stress analyses of orthotropic composites have utilized an Airy stress function in complex variables and conformal mapping. Lin and Rowlands [12] analyzed a notched orthotropic laminated plate thermoelastically, Hawong et. al. [76] combined measured isochromatic information and a complex stress function to study the stresses in a circularly-perforated composite whereas Rhee and Rowlands [13] thermoelasticaly determined the stresses at the edge of a circular hole and the stress intensity factors in a composite with a crack. Baek and Rowlands used conformal mapping with moiré [42] and strain gaga data [43] to determine the full-field stress around a circular hole in composite plate. Ju and Rowlands [14,8] determined stress intensity factors thermoelastically for inclined cracks in an orthotropic composite while Alshaya et al. [32] employed recorded temperature data to stress analyzed a finite orthotropic composite containing an elliptical hole. All the prior applications of the mapping technique either separated stresses from isopachic or isochromatic input information or evaluated the stresses using two components of displacement whereas the present approach only used one recorded displacement component to evaluates all the stresses.

Ashrafi and Tuttle [77] applied traditional DIC to circularly perforated orthotropic composites but experienced difficulties obtaining reliable results as one approached the edge of the hole.

A finite graphite/epoxy laminated composite plate containing symmetrically-located sided-notches and vertically loaded in the strong/stiff material direction is analyzed, Figure 6-1. The DIC-recorded displacement data employed are those in the loading direction. This hybrid method does not necessitate knowing the applied loads, smooths the measured displacement data and determines individual stresses throughout, including on the edge of the notch. Experimental reliability is demonstrated by FEM and force equilibrium. The authors are unaware of prior utilization of mapping and complex variables to experimentally evaluate the stresses in notched composites from displacement data, let alone using only a single measured displacement component.

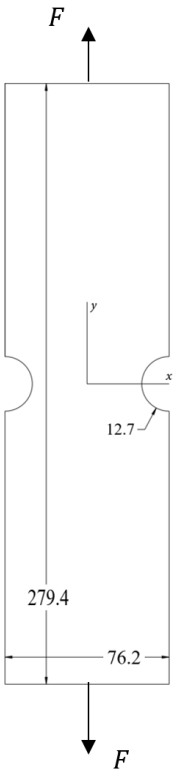

Figure 6-1: Vertically-loaded finite Gr/E [$0_{13}/90_5/0_{13}$] composite plate with circular side notches (units in mm).

6.3 General Comments

This chapter extends the DIC technique into a practical quantitative tool for stress analyzing actual orthotropic composite engineering structures in their operating environment. The concept is applied to the illustrative example of a loaded finite notched graphite/epoxy laminated composite plate in the fiber direction. The approach satisfies equilibrium and compatibility throughout the region using complex-variable formulation involving conformal mapping and analytic continuation. Firstly, simulated experimental input from FEM were used before employing actual displacement data from Digital Image Correlation (DIC) in order to substantiate the viability, robustness, and numerical stability of the numerical method. In view of previously mentioned disadvantages of the FEA, analytical and some experimental approaches, this chapter demonstrates the ability to determine the components of stress in a notched finite orthotropic plate by hybridizing a DIC data with Airy stress function in complex variables and thus making use of DIC's advantage of capturing the exact boundary and loading conditions. Advantages of this method include its ability to significantly simplify the experimental technique by measuring only a single displacement component, provide reliable results both full-field and at the edge of notch, and smooth the measured displacement data. The lack of need to differentiate the recorded data physically is also advantageous. The hybrid method does not necessitate knowing the applied loads; in fact, the loads can often be determined. Such a feature suggests inverse capability.

The excellent agreement between the results from hybrid-DIC and FEA demonstrates the reliability with which one can evaluate the individual components of displacement, strain and stress from a single measured component of displacement.

6.4 Numerical Experiment

The mapping-collocation technique based on complex variables of Airy stress function was first assessed using simulated displacement input values which were obtained from the ANSYS in order to substantiate the viability, robustness, and numerical stability of the technique. The determined stresses from processing simulated displacement with mapping collocation technique will be compared subsequently with those predicted directly by ANSYS to assess the validity of the described approach. A region R_z adjacent to the boundary Γ of side notch of Figure 6-1 is considered. The input displacement data near the traction-free boundaries were disregarded and only region R^* was used to simulate a situation in which the experimental boundaries data are unreliable. Once the reliability and robustness of the method were verified, it was used then to stress analyze a finite orthotropic structure containing a side circular notch using measured displacement data from DIC.

6.4.1 Geometry and Mechanical Properties

The finite-width tensile $[0_{13}/90_5/0_{13}]$ graphite/epoxy orthotropic plate (from Kinetic Composites, Inc., Oceanside, CA; E_{11} = 104 GPa = 15.1 × 10^6 psi, E_{22} = 28.0 GPa = 4.1 × 10^6 psi, G_{12} = 2.98 GPa = 0.43 × 10^6 psi, ν_{12} = 0.16) with side notches of radius R = 12.7 mm ($0.5''$) was loaded in the strong/stiff material direction (1-, y-direction), Figure 6-1. Over-all laminate dimensions are 279.4 mm ($11''$) long, 76.2 mm ($3''$) wide and 5.28 mm ($0.21''$) thick, Table 6-1. The side notches were machined with a water jet. The coordinate origin is at the center of the plate and the response is symmetric about x- and y-axes. The laminate elastic properties were obtained from conducting uniaxial tensile tests in the strong/stiff (y-direction), weak/compliant (x-direction) and 45-degee orientations.

Table 6-1: Specimen specification and dimension and TSA experiment details.

Material	$[0_{13}/90_5/0_{13}]$ Graphite/Epoxy
Elastic Modulus, E_{11}	104 GPa = 15.0 × 10^6 psi
Elastic Modulus, E_{22}	28.0 GPa = 4.0 × 10^6 psi
Shear Modulus, G_{12}	3.0 GPa = 0.43 × 10^6 psi
Poisson's ratio, ν_{12}	0.16
Supplier	Kinetic Composites, Inc., Oceanside, CA
Thickness	5.28 mm (0.208″)
Length, L	279.4 mm (11″)
Width, W	76.2 mm (3″)
Circular notch radius, R	12.7 mm (0.5″)
Static Loading	7117 N = 1600 lb

*The 1- and 2-orientations are directions of laminate material symmetry. They are in the longitudinal/vertical and transverse /horizontal directions, respectively, Figure 6-1.

6.4.2 Finite Element Analysis

In order to provide some results with which to compare those from DIC, a finite element analysis (FEA) using ANSYS (ANSYS, Inc, *Academic Research, Release 16.2*. 2015) was prepared of the composite plate of Figure 6-1 and elastic properties of Table 6-1. Due to symmetry, only one quarter of the plate was modeled with symmetrical boundary condition applied at the bottom and right edges. A far-field stress of

$$\sigma_0 = \frac{F}{A} = \frac{7117.2\ \text{N}}{0.52\ \text{cm} \times 7.62\ \text{cm}} = 17.96\ \text{MPa} = 2604\ \text{psi}$$

was applied numerically to the top edge, Figure 6-2. Eight-node isoparametric plane 82 elements were employed. A very fine mesh was used in the neighborhood of the circular notch as shown in Figure 6-2. A convergence test was applied until the change in magnitude of the maximum stress between two successive meshing was less than 2%. The FE quarter model utilizes 7,500 elements and 7701 nodes. The resultant radial, tangential, and shear stresses of the FE model are shown in Figure 6-3.

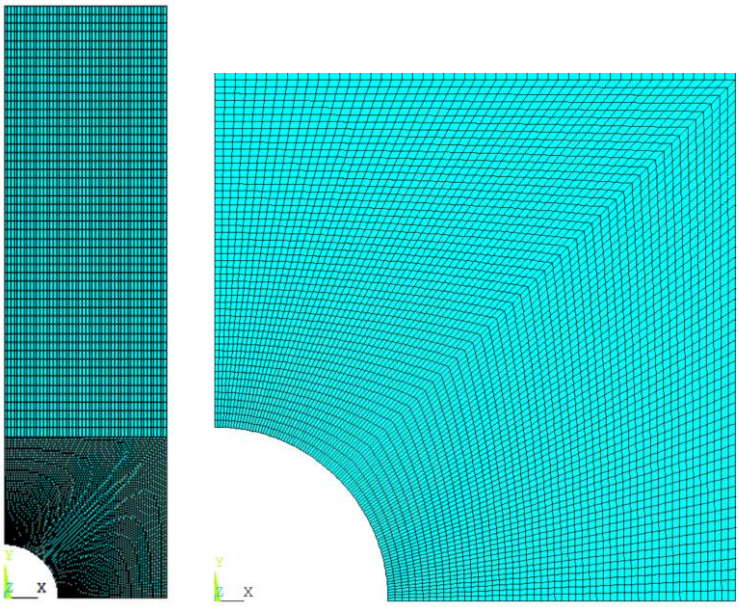

Figure 6-2: Meshed FE model with dense meshing adjacent the circular side notch.

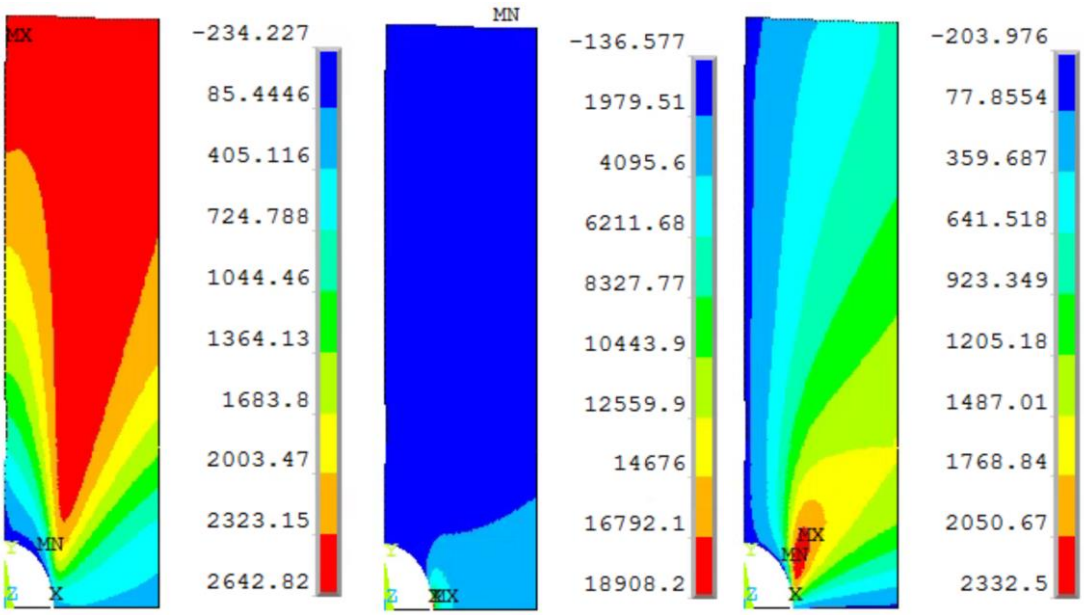

Figure 6-3: Contour plot for the radial, tangential and shear stresses from FEA in psi.

A stated motivation for developing the present ability is to enable stress analyze orthotropic cases experimentally which cannot be analyzed by numerically, yet FEM is used here. The geometry and loading of the Figure 6-1 were deliberately selected so as one could obtain a reliable FEM result. The developed hybrid-DIC method is applicable to more complicated problems which are difficult for FEM.

6.4.3 Evaluating Complex Coefficients

The $[0_{13}/90_5/0_{13}]$ graphite/epoxy has purely imaginary and unequal roots of μ_1 = $0.3423i$ and μ_2 = $5.8804i$. The induced mapping functions $\omega_j(\zeta_j)$ and its inverse of equations (2-75) and (2-77) are used to evaluate complex coefficients A_j using equations (2-99) for v^* defined on a region R^* (not including the free-traction boundaries) and imposing zero shear stress, σ_{xy} = 0 equation (2-97), on the outer free surface at 51 discrete locations and symmetry conditions at y = 0, i.e., σ_{xy} = 0 equation (2-97), at 51 discrete locations and at $x = W/2$, i.e., σ_{xy} = 0 equation (2-97), at 51 discrete locations. Then the individual stresses throughout region R_z, including along edge Γ where no input data were employed, are evaluated using equations

(2-95), (2-96), and (2-97). The results of this numerical experiment, based on m = 3,893 input values of v^* distributed as shown in Figure 6-4, in the region near the side notch and other boundary conditions, q = 153, were used to evaluate 6 complex coefficients, A_j, (12 real coefficients). The number of Airy coefficients to employ can be chosen from plotting root mean square (RMS) values between the actual values of $\{V^*\}$ and the reconstructed values of $\{V^*\} = [M]\{c\}$ versus $N + 1$ as shown in Figure 6-5 while observing the condition number of matrix $\{M\}$ as shown in Figure 6-6. Figure 6-5 and Figure 6-6 suggest using 6 complex coefficients. The maximum error of predicted values of maximum $\sigma_{\theta\theta}$ agrees within a few percent of the maximum numerical value from ANSYS. The results for σ_{rr} and $\sigma_{r\theta}$ are similarly excellent.

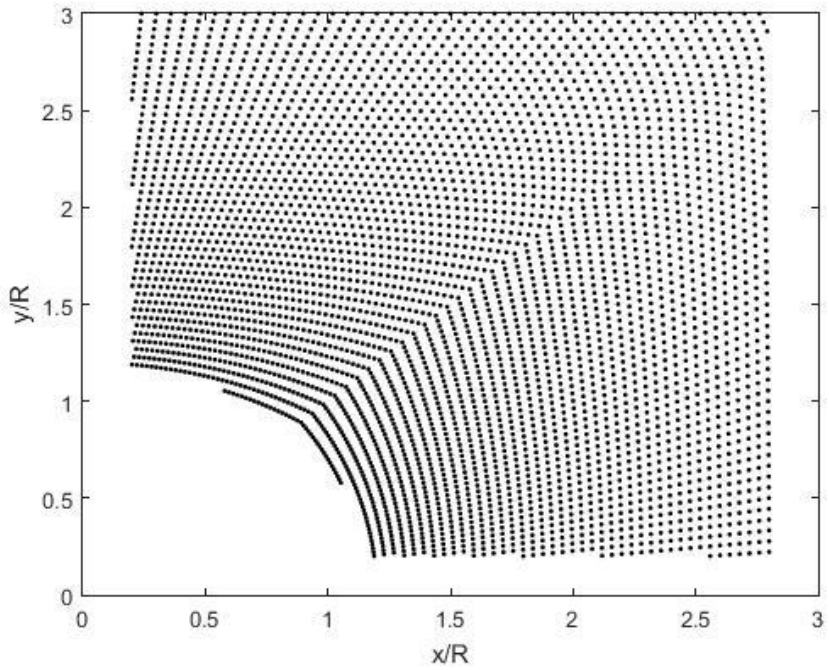

Figure 6-4: Locations of the m = 3,893 input values of v^*.

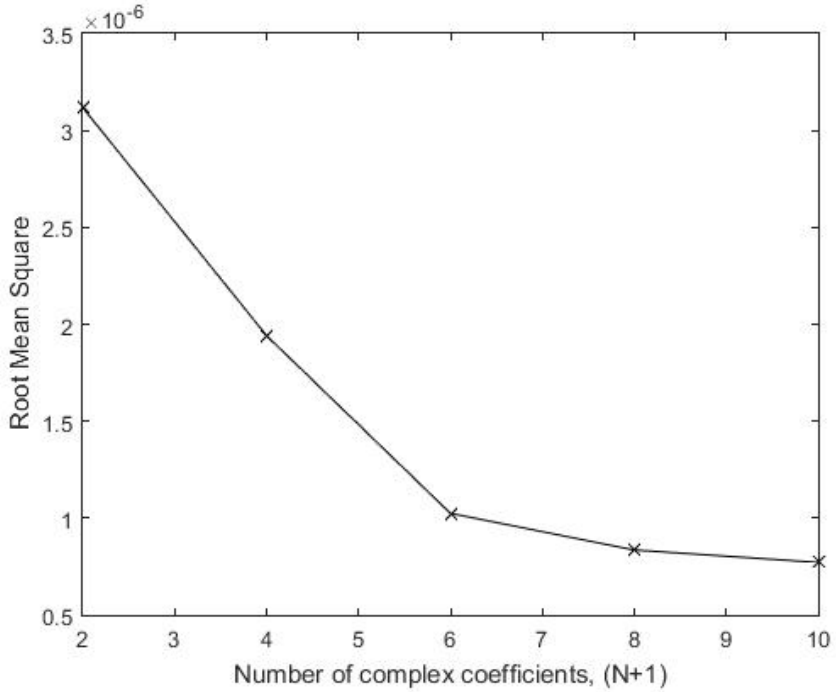

Figure 6-5: Root Mean Square (RMS) value for different number of complex coefficients, N+1.

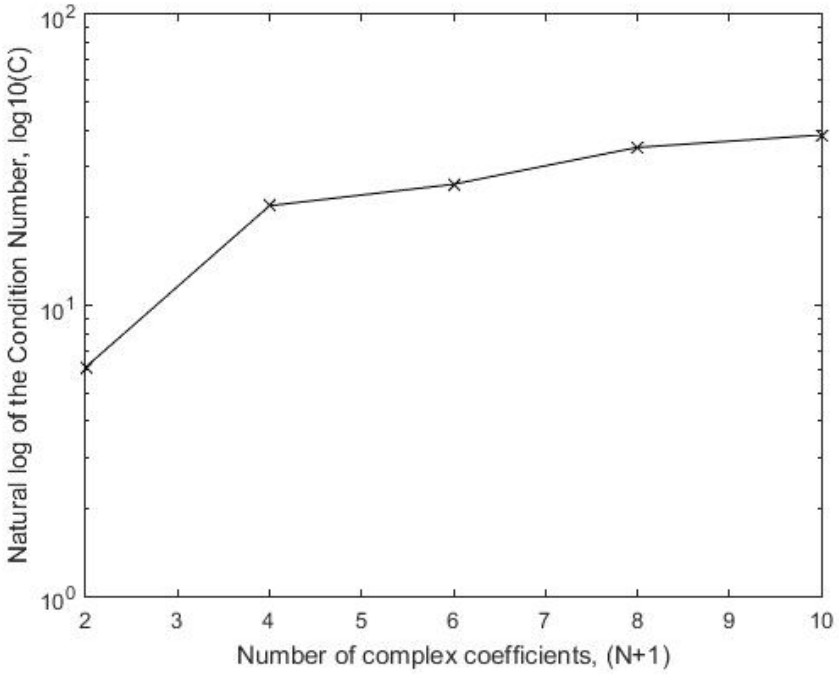

Figure 6-6: Condition number of matrix $[M]$ for different number of complex coefficients, $N+1$.

6.4.4 Results

The results shown in Figure 6-7 through Figure 6-10 demonstrate excellent agreement with finite element solution. The results of this numerical experiment based on discrete input

values of v^* agree virtually exactly with numerical solution throughout region R_z, including along edge Γ where no input values were employed. Figure 6-7 demonstrates the normalized tangential stress along the traction-free boundary of the side notch shows an excellent agreement between the present method and FE solution from ANSYS. Contour plots of normalized radial, tangential, and shear stresses in region adjacent to the side circular notch are shown in Figure 6-8 through Figure 6-10, respectively. These results illustrate the ability of the method to provide reliable stresses even with no traction-free boundary data are included. Such numerical experiments employing simulated displacement test data from ANSYS help verify that there are no algebraic errors and substantiate that the system is numerically robust.

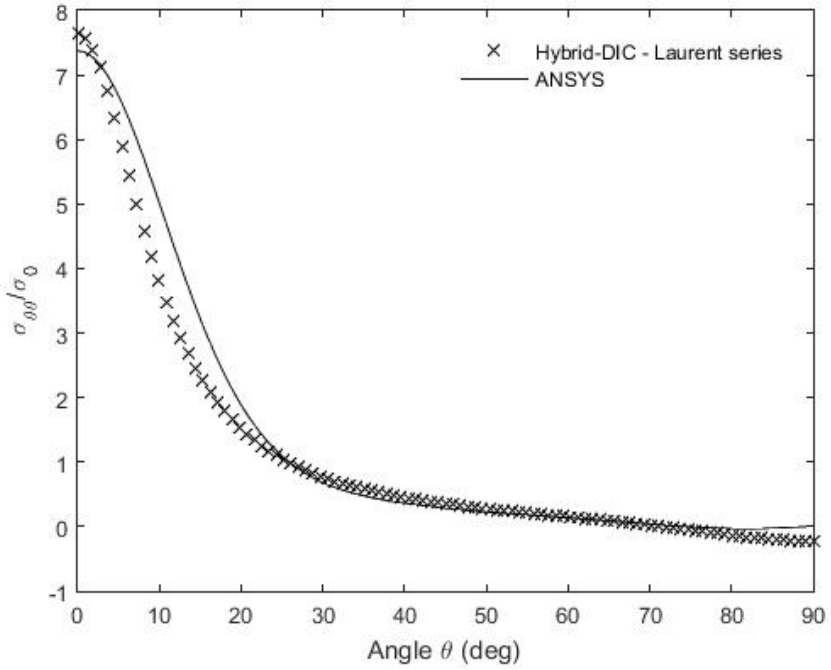

Figure 6-7: Normalized tangential stress, $\sigma_{\theta\theta}/\sigma_0$, along the edge of the side circular notch from present method (12 real coefficients) and ANSYS solution.

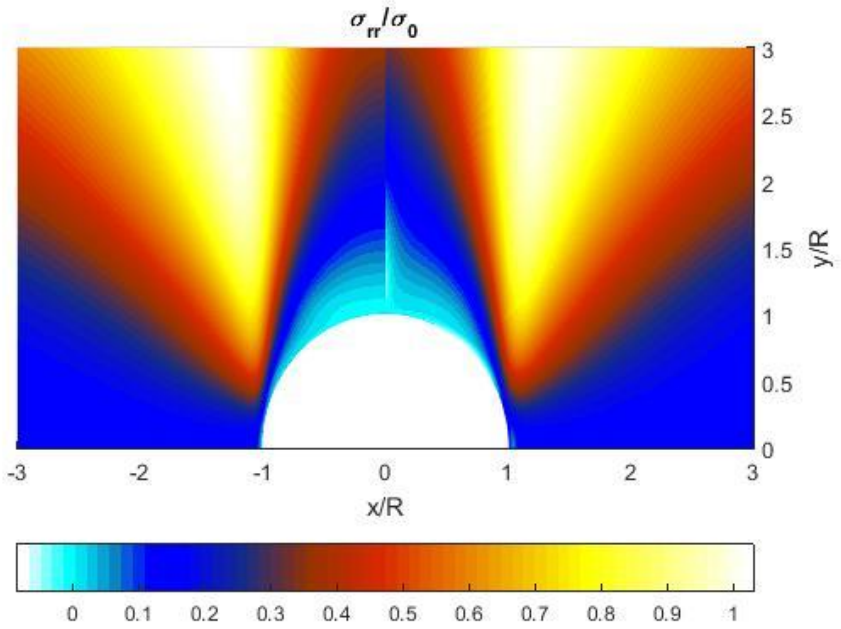

Figure 6-8: Normalized radial stress, σ_{rr}/σ_0, in region adjacent to the side notch from ANSYS (right) and present method and 12 real coefficients (left).

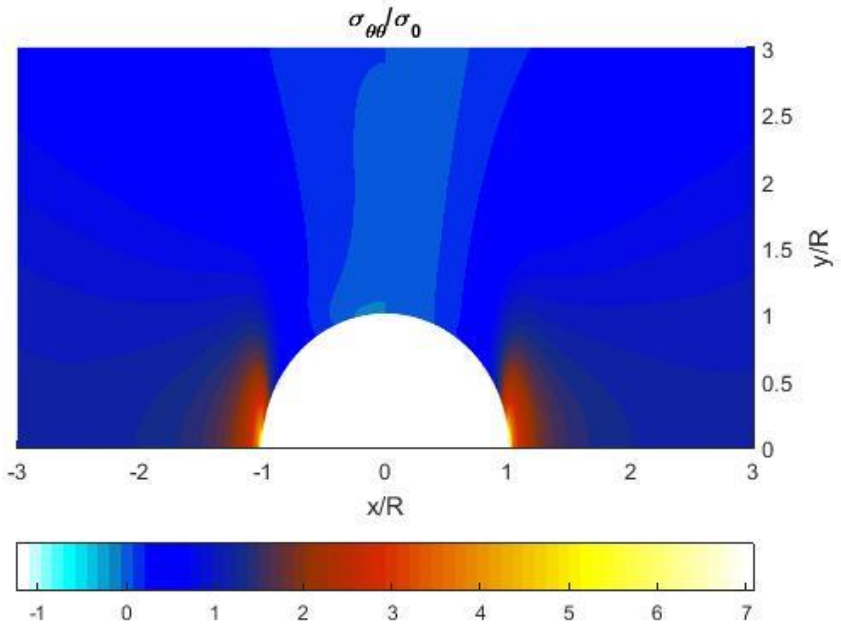

Figure 6-9: Normalized tangential stress, $\sigma_{\theta\theta}/\sigma_0$, in region adjacent to the side notch from ANSYS (right) and present method and 12 real coefficients (left).

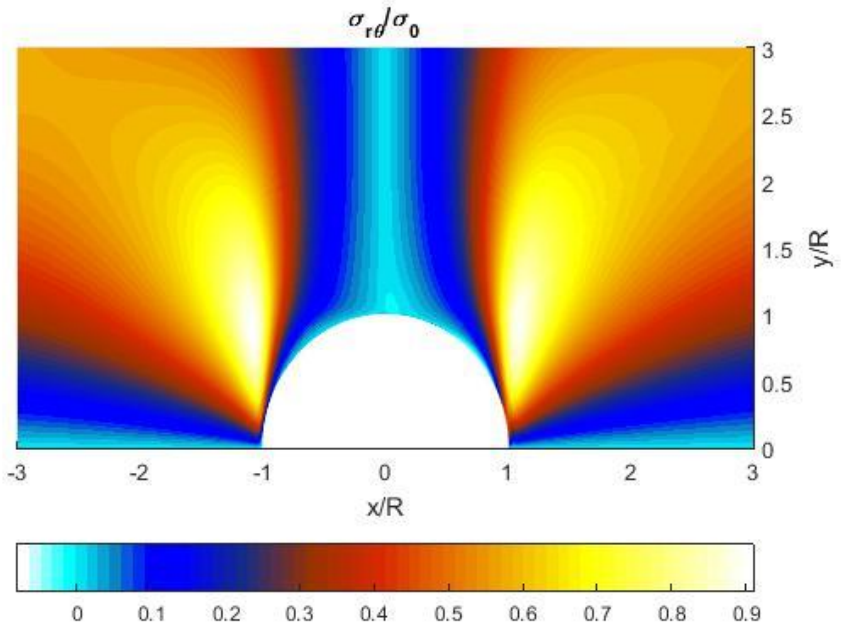

Figure 6-10: Normalized shear stress, $\sigma_{r\theta}/\sigma_0$, in region adjacent to the side notch from ANSYS (right) and present method and 12 real coefficients (left).

To further assess the reliability of the present method, load equilibrium was checked based on the present determined stresses from mapping-collocation technique with the actual applied load, 7117 N (1600 lb). This was done by numerically integrate the vertical stresses (based on simulated DIC input data) from σ_{yy} along the line y = 0 in Figure 6-1 as shown in Figure 6-11.

$$F = \int \sigma_{yy} dA = 2 \int_R^{W/2} \sigma_{yy} t dx$$

where t is the plate thickness and by symmetry the integration only covers the area from $x = a$ to $W/2$. The integration was computed numerically using the trapezoidal rule in MATLAB to determine the area under the curve define by discrete values of $\sigma_{yy}(x, 0)$ along line $y = 0$ as shown in Figure 6-1. The computed applied loads from the present determined stresses are 7.22 kN (1,624 lb), which is close to physically applied load, 7.12 kN (1,600 lb).

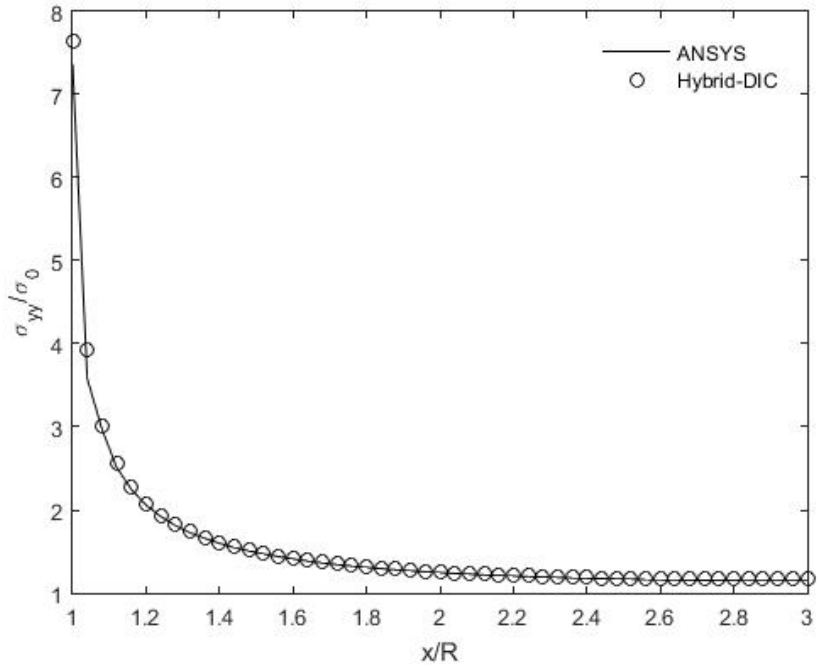

Figure 6-11: The variation σ_{yy}/σ_0 ahead of the notch along the line y = 0 in Figure 6-1 as function of x/R.

6.5 Experimental Setup

A DIC system (by Correlated Solutions, Inc., Columbia, SC, USA, [36]) was used to record the images of the plate in its loaded and unloaded conditions and employed for evaluating the displacements to post-process the results. When utilizing two cameras, a separate calibration grid (provided by Correlated Solution with the DIC package) was used to evaluate the displacement data in physical units rather than in pixels. Rather than using the Vic-Snap software to provided strains, the DIC-recorded v-displacement (vertical) data were processed using the Airy stress function. Displacement information at and near the edge of the notch and at (near) the longitudinal edge of the specimen is unavailable because the DIC software's correlation algorithm is unable to track a group of pixels (subset) which lack neighboring pixels. To perform the tracking, the subset was shifted until the pattern in the deformed image closely matched that of the reference image. Table 6-2 contains the DIC analysis details.

Table 6-2: Technical information about the DIC equipment, set-up, and system.

Parameter	Setting
Technique	Stereo Image Correlation
Cameras	The Grasshopper (Point Grey Research), Model GRAS-50S5M-C
Imaging sensor	Sony ICX625 CCD, 2/3'', 3.45 μm
Lens	CM120 BK 15 COMPACT-0901 (focal ratio: 1.9 and focal length: 35 mm)
Sensor/digitization	2448×2048 at 15 FPS
Lightening	Ambient white light
Pixel to inch conversion	1 pixel = 0.01 inch
Software	Vic-Snap software by Correlated Solutions, Inc.
Subset, step	17, 5
Strain Resolution	0.005% (50 microstrain)

The measured DIC data were digitalized in matrix form and combined with the Airy stress function to determine the stresses. Recognizing one has fewer complex coefficients to evaluate than amount of data from which to evaluate them, the coefficients were determined using least-squares. Although the recorded displacement data at, and adjacent to, an edge are unreliable and raw displacement information in composites is inherently noisy, the present technique overcomes these challenges by avoiding the use of recorded data on and near edges and by processing the measured interior data with a stress function, mapping and analytic con-

tinuation. The resulting reliable DIC-determined stresses are available on and in the neighborhood of the edge of the hole without knowing the distant geometry, loading or boundary conditions.

6.5.1 Plate Preparation

A speckle pattern has to be applied on the surface of the plate such that pixel locations of the unloaded plate can be correlated with those of the loaded plate. In order to achieve effective correlation, the provided speckle pattern must be random, should not exhibit bias in any one orientation, and should show dark black and white dots. The specimen was lightly polished with 320 grit sand paper and degreaser (CSM-2 by VISHAY) prior applying the speckle pattern. Then the specimen was sprayed with Ultra-Flat black paint to reduce the surface's reflectiveness. Precaution was taken when sanding the faces of the specimen to not round-off the edge of the side notch in order to record reliable displacements as close as possible to the edge of the side circular notch. The speckle coating should be applied after the base coat has dried. The paints will blend and blur if the undercoat is wet when applying the speckles. A speckle pattern was provided on the specimen using Ultra-Flat white paint, Figure 6-12.

Figure 6-12: Image of the tested specimen with speckle pattern.

While conducting the DIC experiment, a single camera was pointed straight onto the specimen. The room had enough light and therefore no extra lights were used to illuminate the specimen. The longest available lens was selected that allowed the camera to view the specimen normal to its line of sight and still image the entire area of interest of the specimen plate. Once

the camera (appropriate lens, etc.) were set-up, Vic-Snap software (Correlation Solutions, Inc.) was employed to preview the image.

6.5.2 Loading Condition

The plate was statically loaded in the hydraulic grips of a 20 kips capacity MTS hydraulic testing machine from 0 N to 7117 N (1600 lb) in 890 N (200 lb) load increments. At each load increment, digital images were recorded simultaneously by the DIC camera using Correlated Solution's Vic Snap software. The recorded digital images were subsequently processed and correlated using Correlated Solution's Vic 3D software. Two cameras were used to capture the three displacement components. The out-of-plane displacement component (w_{max} = 0.00585 mm) as shown in Figure 6-13 is relatively small comparing to the in-plane displacement (v_{max} = 0.02 mm). However, the 2D analysis was conducted here because the only required data for analysis are the in-plane displacements. For 3D analysis, the calibration was performed using the calibration scale from DIC equipment where in 2D analysis it was performed by selecting a known distance and enter that distance to Correlated solution Software. The loading was applied using MTS machine which has 20 kips capacity and hydraulic grip capable up to 18.5 kips and it can operate in either load or displacement control with any of four ranges (10%, 20%, 50%, and 100% of capacity). The hydraulic grips apply a uniform clamping pressure over bottom end of the specimen. The DIC camera was aligned to be exactly perpendicular to the flat front surface of the plate to record 2D images, Figure 6-14. The plate was carefully aligned between the top and bottom grips to produce a symmetrically loaded plate about y-axis.

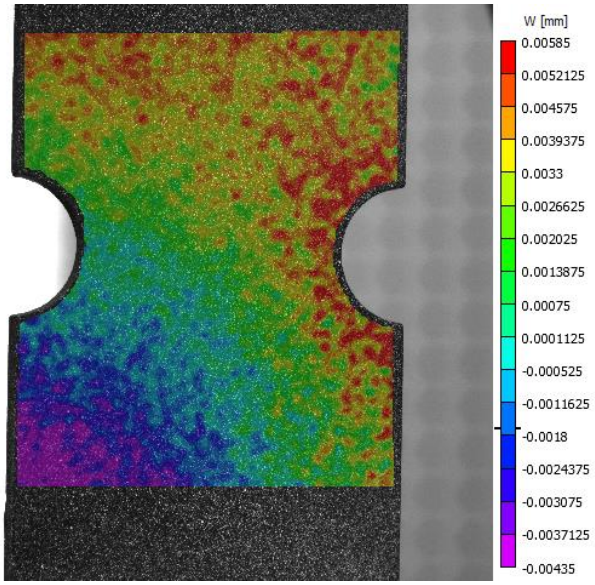

Figure 6-13: DIC recorded w-displacement data in mm at 7117 N (1600 lb).

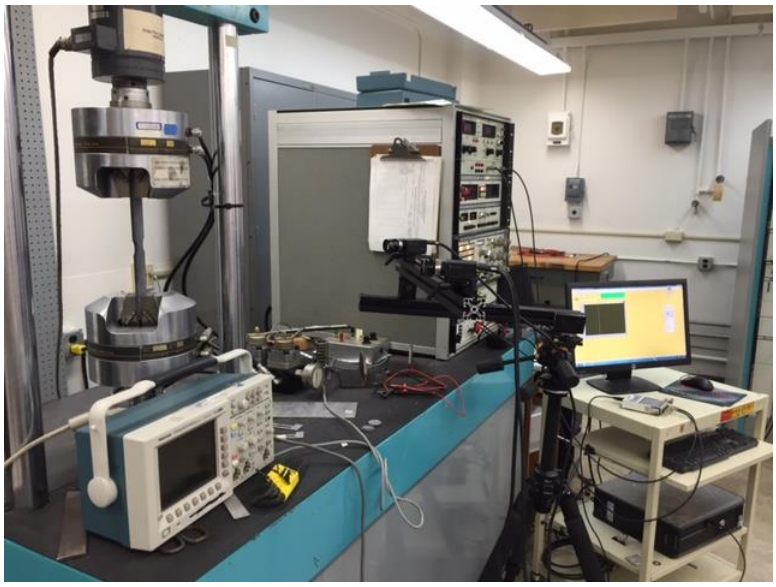

Figure 6-14: Experimental test setup for recording v-displacement data using two DIC cameras.

6.5.3 DIC Recording

The recorded v-displacment information, Figure 6-15, was exported to MATLAB (Mathworks, Inc., 2015) to convert each pixel into a data point. Since DIC data typically are unreliable on and near an edge, no recorded displacements were used within at least 2.95 mm = 0.12 inch of the boundary of the notch. The u-displacement are relatively small and their DIC-evaluated values are not as reliable as the v-displacements. Although not appreciated a

priori, this turned out to be an example where one of the two displacement fields is not highly reliable but by using the present hybrid technique, one could obtain displacement information in one direction from that in the other direction. One can moreover evaluate the full-field individual stresses and strains without physically differentiating the displacements.

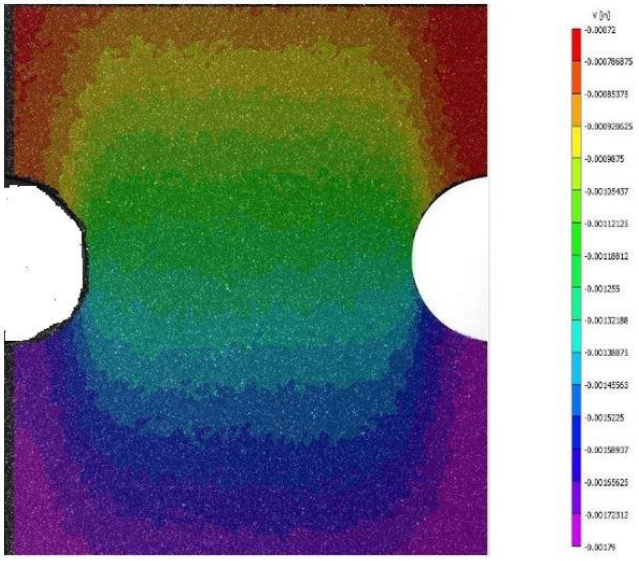

Figure 6-15: DIC recorded v-displacement data from Vic-snap software for notched finite orthotropic plate loaded at 7117 N (1600 lb).

6.5.4 Data Processing

The individual stresses were determined throughout the region containing the notch from the raw v-displacement data of Figure 6-15 using the mapping-collocation technique. The DIC correlated solution software provided approximately 102,200 values of v when the analysis was carried out for 17 subsets in 5 steps. The plate is geometrically and mechanically symmetrical about the vertical y-axes. Since the top end of the physically tested plate was fixed stationary while the bottom end moved vertically downward, Figure 6-14, the zero vertical displacement was shifted to be at the horizontal middle of the plate, Figure 6-16, to represent the case of the plate being extended at both top and bottom ends. The measured v-displacement data of Figure 6-16 were subsequently averaged about all quadrants to cancel any asymmetry and the resulting averaged measured of values of 17,666 v-displacement data are shown in the

second quadrant as shown in Figure 6-17. For the subsequently used mathematical mapping, the coordinate origin was also transferred to the center of the left notch. Due to the previously mentioned unreliability, recorded data on and near the edge of the notch were not employed. Only 2,200 of the available 17,666 v-displacements were selected randomly and used. Their source locations are shown in Figure 6-18. The region of Figure 6-18 is denoted as region R^*. Like most experimental data, the measured data incorporate some noise which necessitate collecting more measured input values than the number of unknown coefficients of a stress function. In addition to the selected v-displacements associated with Figure 6-17b, σ_{xy} = 0 of equation (2-97) was imposed at each of 12 equally-spaced discrete locations along the left vertical traction-free edge of the plate and along the horizontal line of symmetry, y = 0. The total number of equations (side conditions), $m + q$, where m = 2,200 and q = 24, exceeds the number of real coefficients, $2(N + 1)$, producing an overdetermined system which can be solved using a least-squares. The system was solved in MATLAB using the backslash '\' operator.

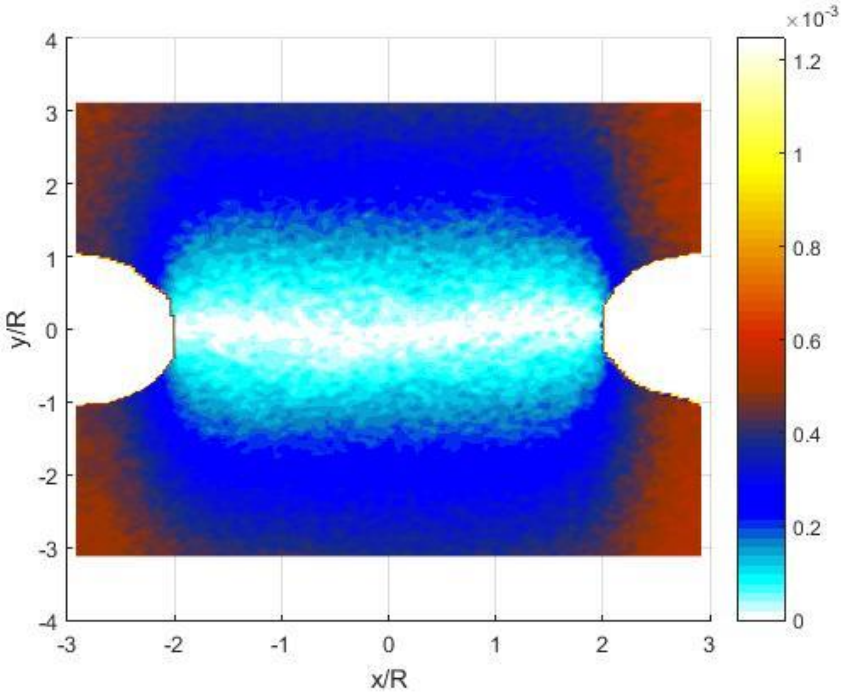

Figure 6-16: DIC recorded v-displacement data after shifting the zero displacement v to vertical middle of plate loaded at 7117 N (1600 lb).

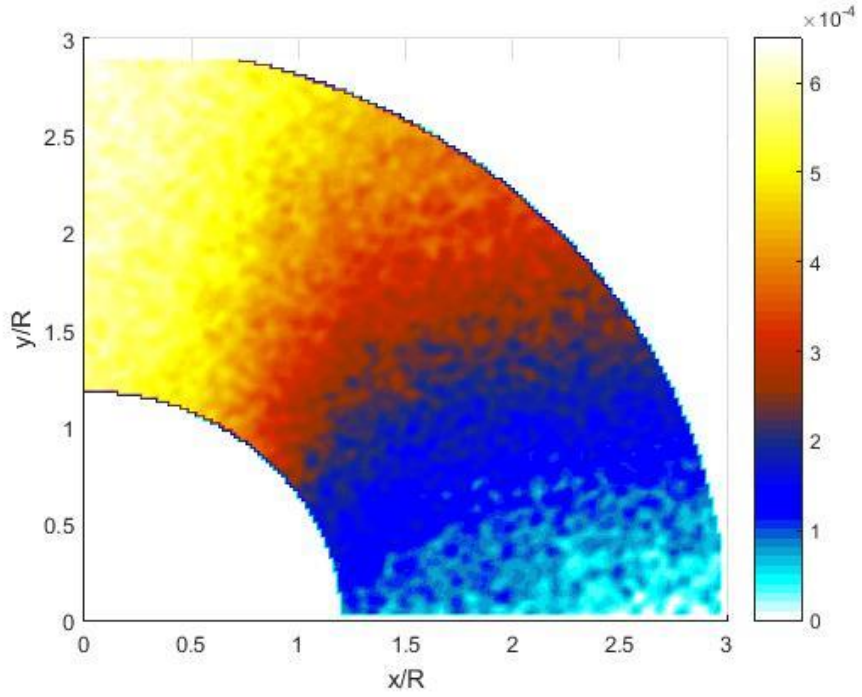

Figure 6-17: Averaged recorded v-displacement data from Vic-2D from all four quadrants.

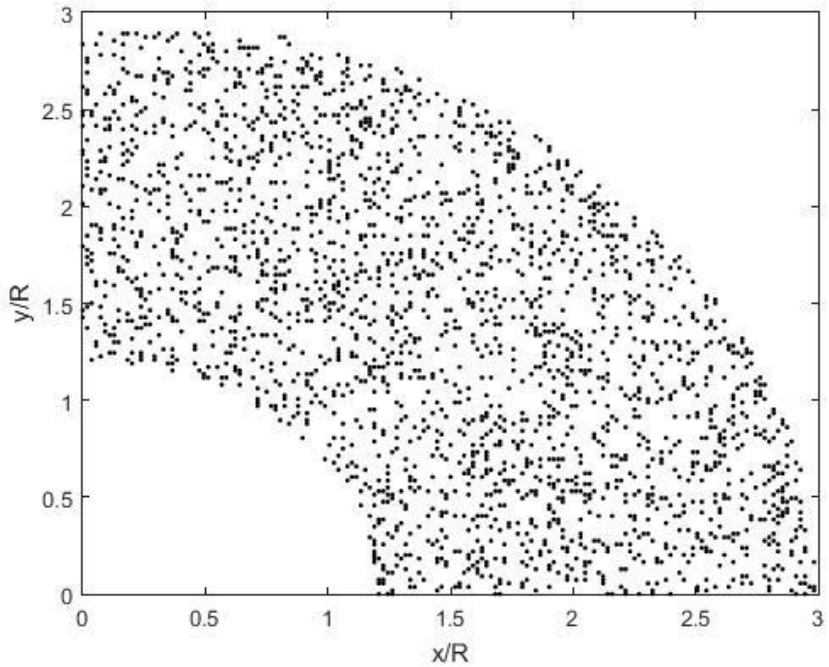

Figure 6-18: DIC source location (m = 2,200 data points).

6.6 Results

6.6.1 Evaluating Number of Coefficients to Employ

The coefficients, $A_j = a_j + ib_j$, were evaluated using equations (2-75) through (2-77) to map the physical plane into the unit circle in the ζ-plane. The unreliable v-displacement values on and near the boundary of the side notch motivated using only v-displacements originating at locations shown in Figure 6-18. The magnitude of the complex coefficients, A_j, were determined from equations (2-99) using the measured v-displacement data located inside the region R^*, Figure 6-18, and imposing zero shear stress discretely along the outer left vertical free surface and the line of symmetry, y = 0. The individual stresses were evaluated throughout region R_z using equations (2-95) through (2-97) including along edge Γ where no v-displacement input data were employed.

One must assess how many coefficients to employ in the stress function. Using too few coefficients gives inaccurate results, while too many can make the matrix, $[V]$, unstable or even singular due to computer round-off and quantization errors. The number of real coefficients, $2(N+1)$, to retain was selected by comparing, using the root mean square approach, the difference between the magnitudes of the DIC recorded v-displacements, with those predicted by least-square from equation (2-99) and the 24 zero shear conditions as a function of the number of evaluated coefficients, Figure 6-19, while observing the condition number of matrix $\{M\}$, Figure 6-20. These plots suggest using 6 complex (12 real) coefficients. The suitability of utilizing 12 real coefficients is supported by comparing the recorded v-displacement data with the reconstructed image based on equation (2-99) and 12 real coefficients, Figure 6-21 and Figure 6-22.

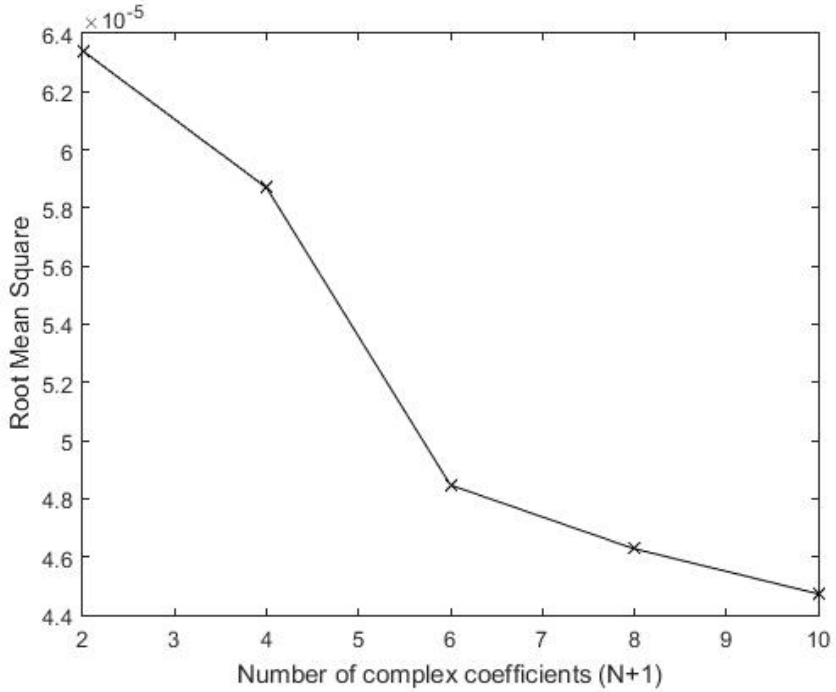

Figure 6-19: Root Mean Square value for different number of complex coefficients, N+1.

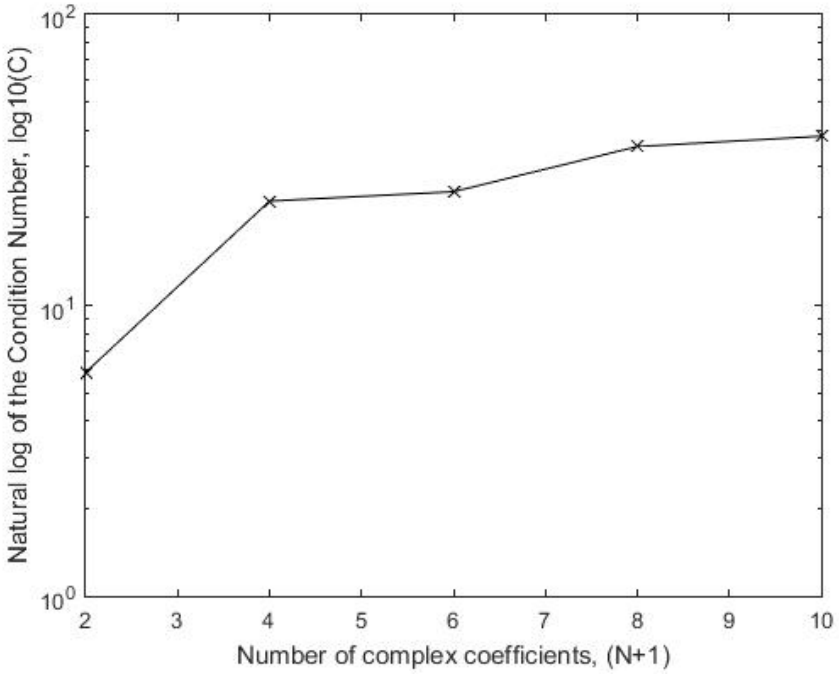

Figure 6-20: Condition number of matrix $[M]$ for different number of complex coefficients.

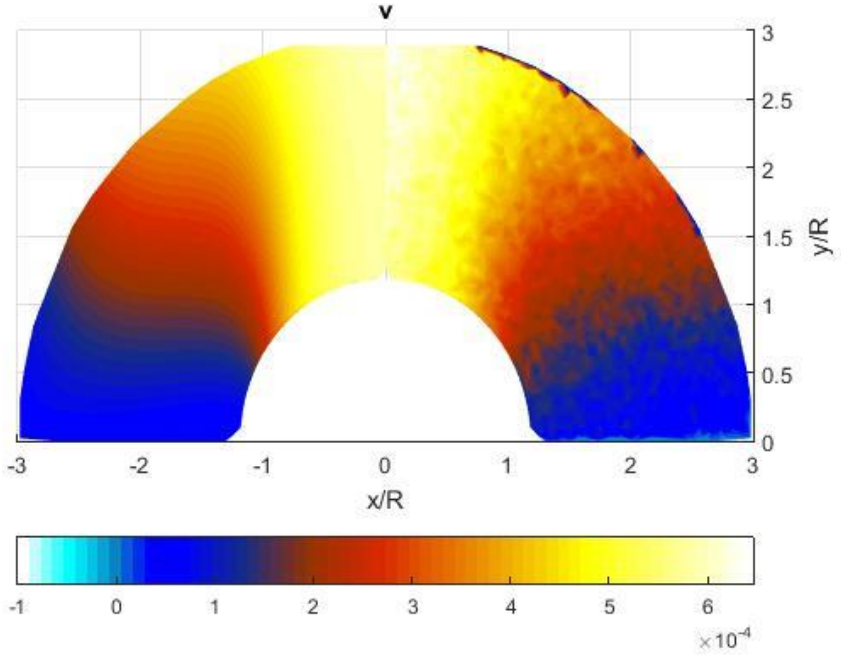

Figure 6-21: Comparison of v-displacement throughout region adjacent to hole from recorded DIC (right) and reconstructed; m = 2,200, q = 24 and 12 real coefficients (left).

6.6.2 Further Validation of Selected Number of Coefficients

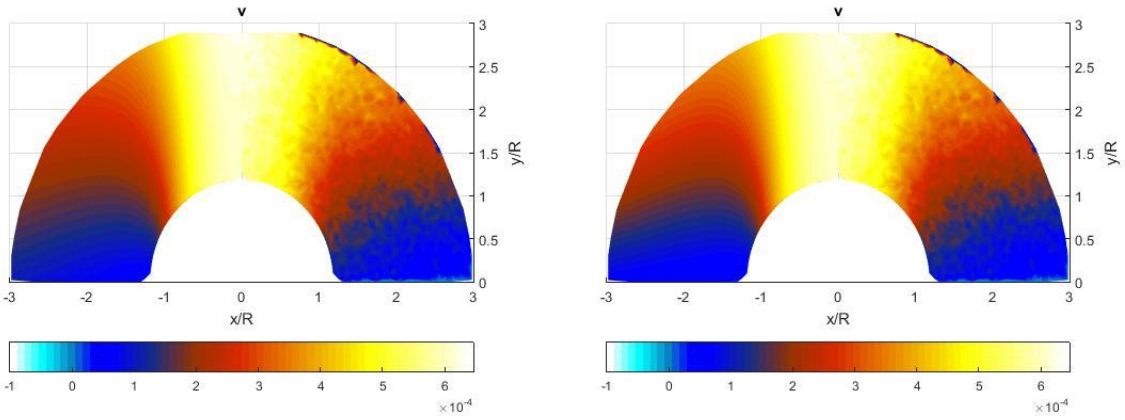

(a) (b)

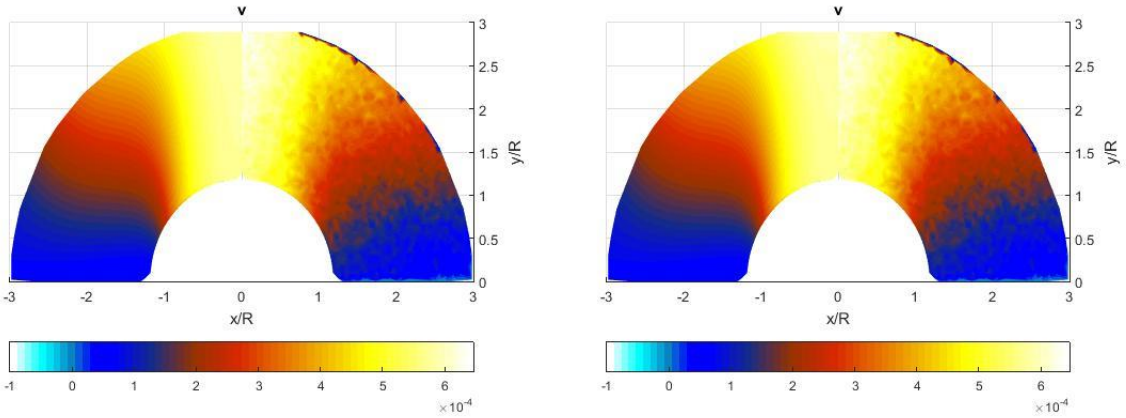

(c) (d)

Figure 6-22: Contour plot of reconstructed v-displacement for $N+1$ (number of real coefficients) (a) 2 (4); (b) 4 (8); (c) 8 (16); and (d) 10 (20) throughout the region adjacent to the notch by DIC (right) and hybrid-DIC using the Laurent series (left).

The number of complex coefficients, $N+1$, to retain was again determined from observing the RMS value between the experimental data $\{V^*\}$ and the recalculated one using the determined coefficients, $[V]\{c\}$, information of condition number, C, of the matrix $[V]$ and by comparing the experimental input from DIC and the reconstructed v-displacement data, Figure 6-21 and Figure 6-22. The reconstructed images of Figure 6-22 based on $N+1$ = 2, 4, 8, and 10 and reconstructed image of Figure 6-21 for $N+1$ = 6 are all fairy uniform with each other and with the experimental data. Since there is merit in employing no more coefficients than necessary and the RMS values for $N+1$ = 6 and 8 are close to each other, Figure 6-19 and Figure 6-22 support using $N+1$ = 6 complex coefficients (12 real coefficients).

6.6.3 Stresses and Displacements

The experimentally determined tangential stress, $\sigma_{\theta\theta}$, normalized to the far-field stress, σ_0 = 17.96 MPa, is plotted on the boundary of the notch in Figure 6-23. These hybid-DIC based results agree with the FEM predictions. The ANSYS and hybrid-DIC determined stress concentrations are 7.37, and 7.41 respectively.

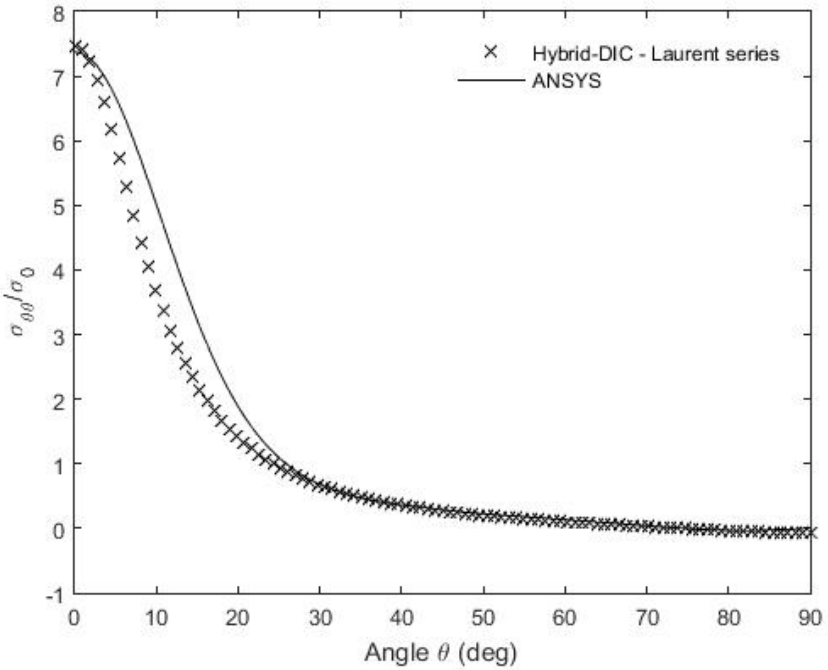

Figure 6-23: Variation of $\sigma_{\theta\theta}/\sigma_0$ along boundary of notch from FEA and DIC(m = 2,200, q = 24 and 12 real coefficients).

Contour plots of normalized polar components of stress and the displacement (u based on equation (2-98) and v from equation (2-99)) from hybrid-DIC and ANSYS are compared in Figure 6-24 through Figure 6-28. There is excellent agreement between the ANSYS-predicted values and the hybrid technique using m = 2,200 v-displacement values and q = 24.

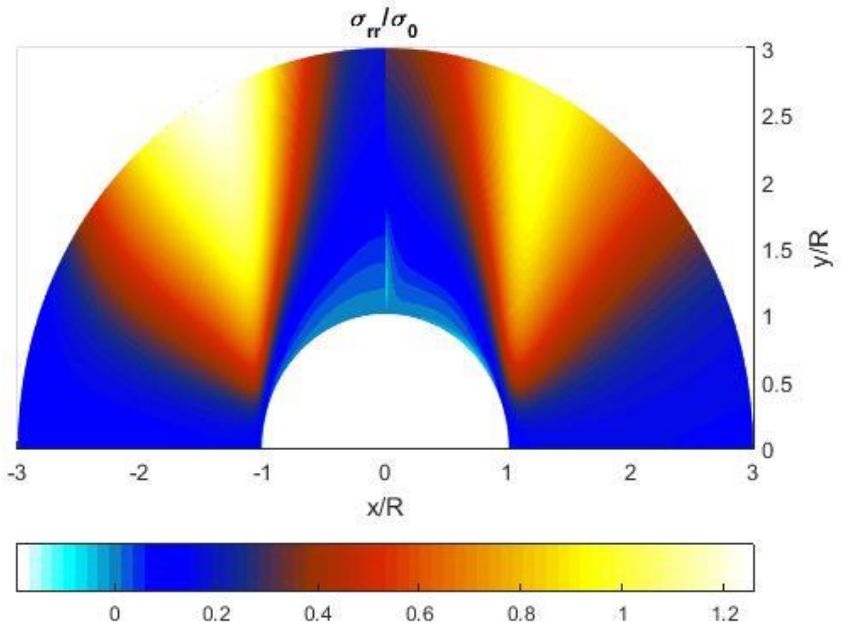

Figure 6-24: Contour plot of σ_{rr}/σ_0 throughout the region adjacent to the notch by FEA (right) and hybrid-DIC; m = 2,200, q = 24 and 12 real coefficients (left).

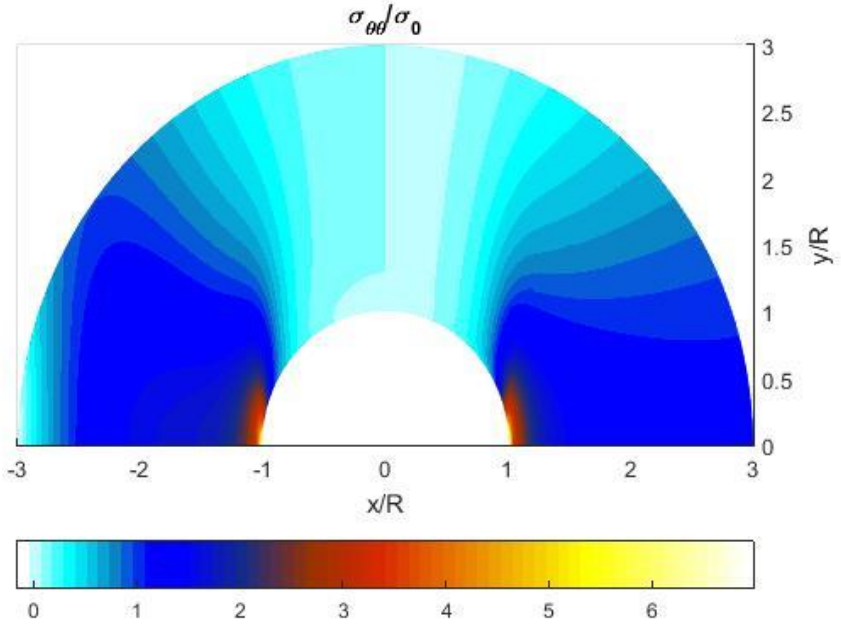

Figure 6-25: Contour plot of $\sigma_{\theta\theta}/\sigma_0$ throughout the region adjacent to the notch by FEA (right) and hybrid-DIC; m = 2,200, q = 24 and 12 real coefficients (left).

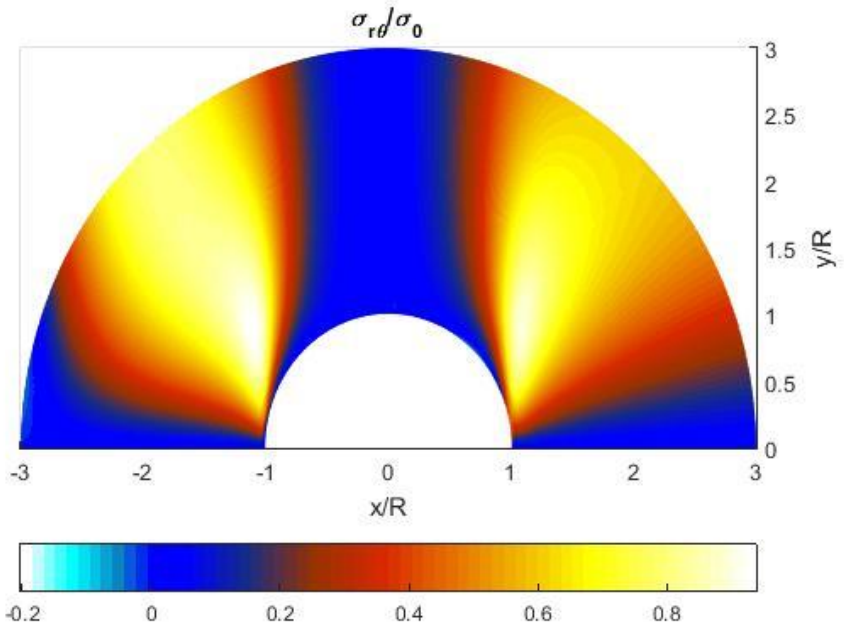

Figure 6-26: Contour plot of $\sigma_{r\theta}/\sigma_0$ throughout the region adjacent to the notch by FEA (right) and hybrid-DIC; m = 2,200, q = 24 and 12 real coefficients (left).

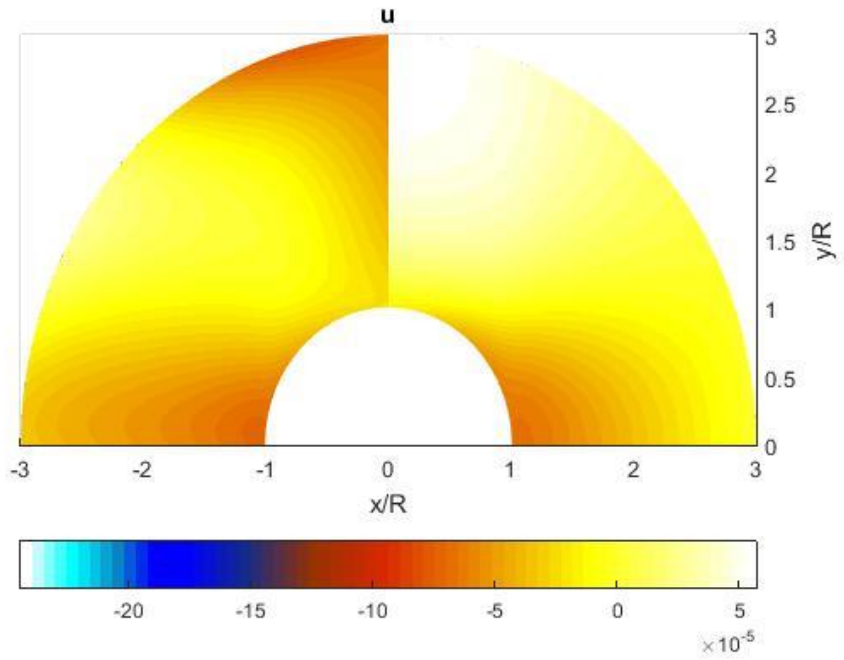

Figure 6-27: Contour plot of u throughout the region adjacent to the notch by FEA (right) and hybrid-DIC; m = 2,200, q = 24 and 12 real coefficients (left).

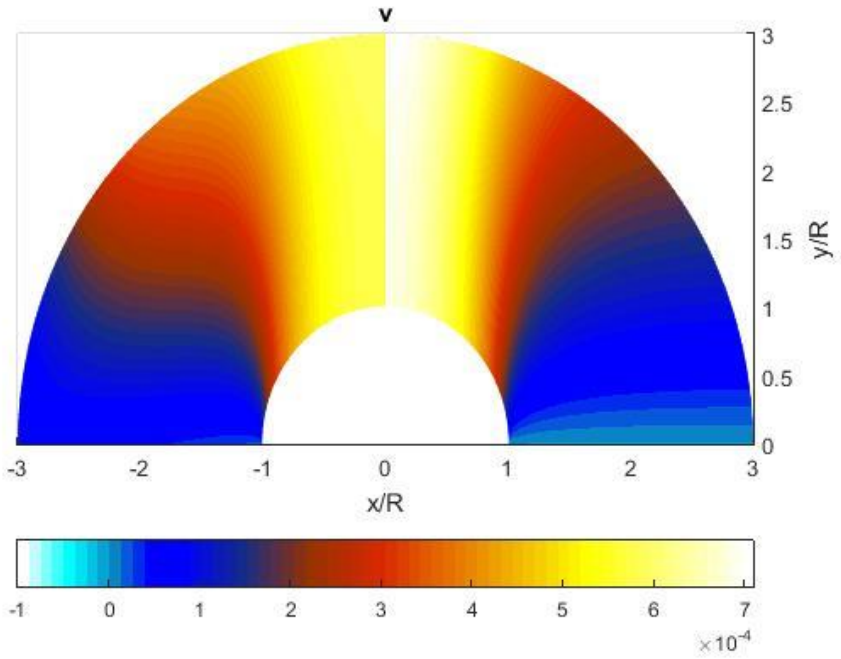

Figure 6-28: Contour plot of v throughout the region adjacent to the notch by FEA (right) and hybrid-DIC; m = 2,200, q = 24 and 12 real coefficients (left).

6.6.4 Load Equilibrium

To further assess reliability of the present hybrid-DIC method, load equilibrium based on DIC-determined stress was compared with the actual applied load. This was done by numerically integrating the vertical stress σ_{yy} along the line y = 0 in Figure 6-1.

$$F = \int \sigma_{yy} dA = 2 \int_{R}^{W/2} \sigma_{yy} t dx$$

where t is the plate thickness and by symmetry the integration only cover the area from R to $W/2$. The integration was computed numerically using the trapezoidal rule in MATLAB to determine the area under the curve define by discrete values of $\sigma_{yy}(x, 0)$ along line y = 0. The computed load based on hybrid-DIC stress is 7.10 kN (1,596 lb), which is 0.25% less than the physically applied load of 7.12 kN (1,600 lb). The present equilibrium check supports the claim that the proposed method does not require knowing the applied load and in fact can handle inverse problems.

6.6.5 Effect of Variations in Number of Coefficients Employed

Figure 6-19 through Figure 6-21 suggest using 6 complex (12 real) coefficients. Figure 6-23 through Figure 6-28 indicate these give accurate results. However, results of Table 6-3 demonstrate reliable DIC-determined values for the stress concentration factor at the notch when employing at least two to 10 complex coefficients.

Table 6-3: Stress concentration factor (maximum $\sigma_{\theta\theta}/\sigma_0$) at notch in finite-width $[0_{13}/90_5/0_{13}]$ plate for varying number of Airy coefficients (m = 2,200 and q = 24).

	Laurent series expansion (percentage difference with ANSYS)		
ANSYS	N (number of real co-efficient)	Hybrid-DIC	Hybrid-ANSYS
	1 (4)	6.88 (6.6 %)	7.69
	3 (8)	7.17 (2.7 %)	7.67
7.37	5 (12)	7.48 (1.5 %)	7.64
	7 (16)	7.59 (3.0 %)	7.63
	9 (20)	7.57 (2.7 %)	7.62

6.6.6 Magnitudes of Coefficients, A_j

Table 6-4 lists the magnitudes of experimentally-determined coefficients A_j of equations (2-99) associated with recorded v-displacement data. The data demonstrate the dominating influence of the early coefficients but the reduced consistency in magnitudes of the coefficients with increasing of N. On the other hand, in addition to the fact that lower-order a_j coefficients of equation (2-99) dominate, the values of these a_1 and a_{-1} tend to be very consistent for all values of N considered.

Table 6-4: Magnitudes of the coefficients associated with the stress calculation in the uniaxially loaded, finite-width [$0_{13}/90_5/0_{13}$] graphite/epoxy composite using DIC data and Laurent series representation.

	Coefficients values using Laurent series expansion		
coefficients	$N = 1$	$N = 3$	$N = 5$
a_1	-63.54	-63.93	-62.66
b_1	4.32	2.45	2.75
a_{-1}	-64.39	-65.15	-64.50
b_{-1}	-3.06	-1.74	-1.95
a_3		0.67	1.95
b_3		0	0
a_{-3}		0.76	2.25
b_{-3}		0	0
a_5			0.068
b_5			0
a_{-5}			0.075
b_{-5}			0

6.6.7 Amount of and Source Locations of Input Data

Results of Figure 6-23 and Table 6-3 demonstrate that the DIC-determined and ANSYS-predicted stress concentration factors agree. However, these results are based on the 2,200 recorded input v-displacements selected randomly from the available 17,666 values of region R^* in Figure 6-18. It is informative to consider how the magnitude of the stress concentration factor and predicted load depend on the amount and source locations of measured input data. A MATLAB subroutine was used to change randomly the amount of measured input v-displacement data employed in the region between $1.2R$ and $3R$ (retaining the same additional 24 conditions along the left vertical traction-free edge and the horizontal line of symmetry, $y = 0$). This routine was repeated 10 times and the resulting mean and standard deviation values for the stress concentration factor and calculated applied load are plotted in Figure 6-29 and Figure 6-30, respectively. The figures show that the results converge at approximately 1,000 recorded input data of the originally available 17,666 v-displacements. The plot of the calculated applied load is only used to show the reliability of the results for each input data. Reference [9] provides helpful information on the amount and source locations of the themoelastic stress (TSA) input data, and number of coefficients, to employ. However unlike reference [9], the present amount and source locations of the displacement input were generated and selected randomly and not necessarily uniformly. This assesses the effects on the reliability of such DIC techniques of varying the amount and source locations of the recorded input data.

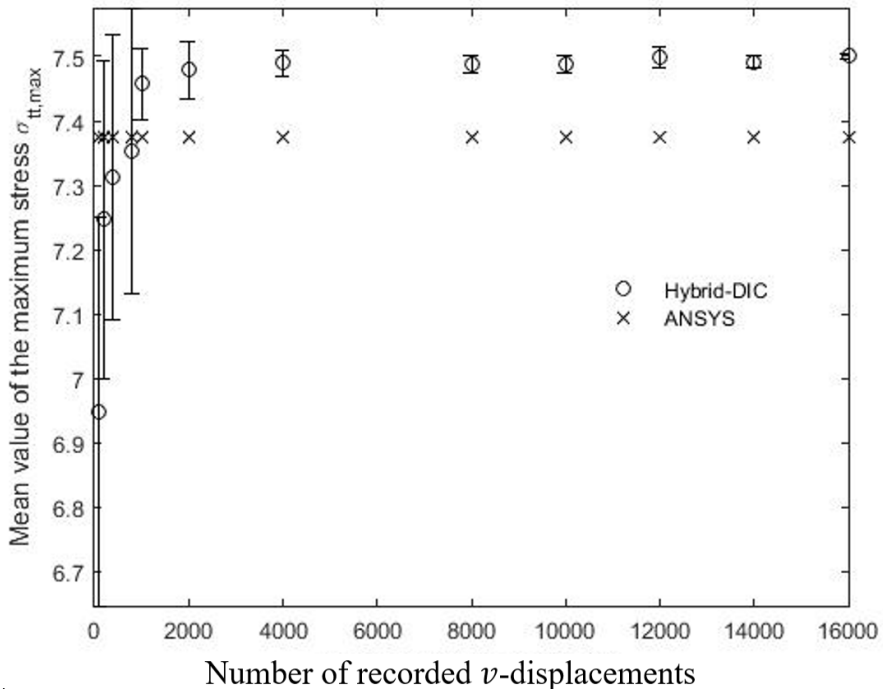

Figure 6-29: Mean and standard deviation of DIC-determined stress concentration factor at notch using different varying random amounts of DIC-recorded values of v (12 real coefficients; q = 24).

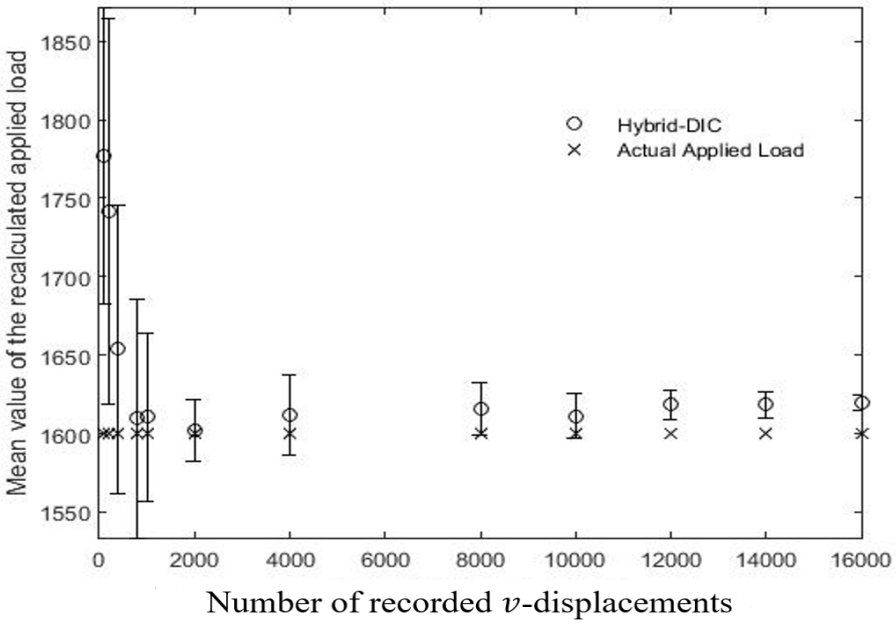

Figure 6-30: Mean and standard deviation of DIC-based load using different varying random amounts of DIC-recorded values of v (12 real coefficients; q = 24).

6.6.8 Comparison with Correlated Solutions

Recognizing recorded DIC data are unreliable at and close to an edge, there is merit in not employing such information along edges and it can be challenging to obtain reliable stress concentration factors. Strains in the vertical y-direction, ϵ_{yy}, along the line $y = 0$ in Figure 6-1 from FEA, hybrid-DIC, and Correlated Solution's commercial Vic snap software are compared in Figure 6-31. Unlike Correlated Solution's differentiation method for determining strains and without changing correlation parameters (subset, step, filter size) as in reference [77], the present DIC method determines the strains from measured displacements based on a rigorous mechanics foundation (Airy stress function, equilibrium and compatibility). Reference [38] reported similar discrepancy in strains computed using commercial DIC software and those from FEM and strain gages.

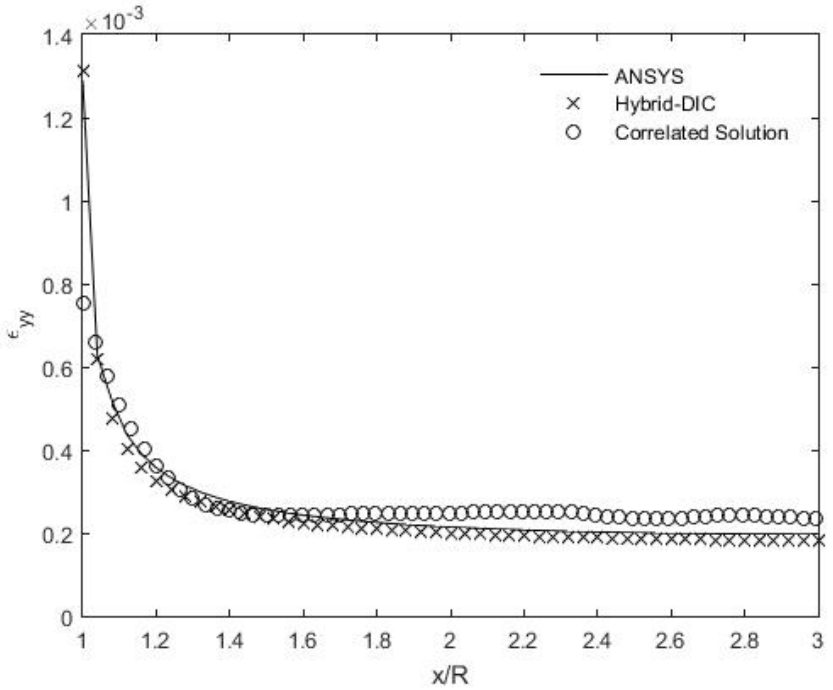

Figure 6-31: Strain ϵ_{yy} along the line $y = 0$ in Figure 6-1 from Hybrid-DIC, ANSYS, and Correlated Solutions as function of x/R.

6.7 Summary, Discussion and Conclusions

Stresses, strains, and displacements at and in the vicinity of the edge of a side notch in a uniaxially-loaded finite graphite/epoxy composite are determined by processing DIC-recorded values of a single component of displacement with an Airy stress function in complex variables. The equilibrium, compatibility and the traction-free conditions on the boundary of the side circular notch in finite-width orthotropic structure were satisfied using conformal mapping and analytic continuation. Reliability of experimental results is demonstrated by Finite Element and force equilibrium. The consequences of employing different random sets of measured input data, varying the number of coefficients and the manner in which displacements are differentiated to provide strains are considered. Most of the present results are based on 12 real coefficients and 2,200 measured input displacements, but information shows acceptable values of the stress concentration at the notch root when using between 8 and 20 real coefficients and 1000 or more measured input displacements. The dominating influence of the early coefficients and reduced consistency in magnitudes for subsequent coefficients is noted. Compared to the Correlated Solutions computed strains, the present hybrid-DIC technique offers the advantage of evaluating strains without mathematically differentiating displacement experimental data.

Strains (hence stresses) are often determined by evaluating the derivatives from the discretely measured displacement; a process which can be ill-conditioned and adversely influenced by data noise and quality. This shortcoming is overcome here as measured displacements are not differentiated numerically, but instead combined with an analytical formulations based on compatibility and equilibrium. However, unlike a classical boundary-value problem where one would typically evaluate the unknown coefficients, $A_j = a_j + ib_j$, by satisfying the boundary and loading conditions around the entire shape, the present hybrid method hybridize some

measured data and some known boundary conditions to determine the stresses adjacent to a traction-free boundary condition without the knowledge of the distant loading conditions.

Advantages of the present approach over many hybrid techniques for such situations include: (i) unnecessary to know far-field geometry or boundary conditions (unlike strictly numerical or theoretical approaches); (ii) suitable for finite (can be difficult theoretically) or infinite geometries; (iii) convenience of commercial hardware and software; (iv) able to rapidly record and process vast amounts of measured information; (v) evaluates individual stresses from single displacement component without differentiating measured data; (vi) smooths the original displacement input data; (vii) satisfies the local boundary conditions analytically; (viii) enhances the edge information; (ix) ability to obtain reliable stresses on the edge of the notch despite unreliable measured data at such locations; and (x) full-field capability (but digital information also available).

The objective of this approach is to determine reliable information along, and adjacent to, the edge of the component where the interested region is, rather than to evaluate the stresses necessarily throughout the entire structure. The size of interested region over which the stress function is reliable can be increased by employing additional boundary conditions. Least square method was used to evaluate unknown coefficients of overdetermined systems of equations. Such inverse problems where the stresses on and in the neighborhood of the edge of a notch are determined without explicit knowledge of the external loading or geometry can be very challenging. Symmetry about the x- and y-axes is not necessary, and concept of using a stress function could handle finite or infinite geometry. It is also notable that measuring a single component of displacement is advantageous, particularly in composite structures. This ability is significant since obtaining both displacement components can be non-trivial with moiré or speckle. Moreover, it is not uncommon in practice to find regions where one of the displace-

ment components is very small or is unreliable. Compared to finite-element analyses, the numerical computations of the present method are relatively simple and consume little computer time. The hybrid-DIC determined stresses agree with finite-element results. The idea of hybridizing DIC data and analysis is a significant ingredient in making DIC a quantitative, rather than just a qualitative, engineering tool. The hybrid-DIC approaches discussed enjoy the advantage of being based on strong mechanics foundations. They also do not require any numerically integrating or differentiating procedures.

The present paper demonstrates the ability to stress analyze orthotropic cases experimentally which cannot be analyzed numerically. However, the geometry and loading of the Figure 6-1 were selected so as to provide a reliable FEM prediction with which to validate the hybrid-experimental approach. Unlike here, it is not uncommon to have engineering structures whose external loads are unknown, thereby precluding using FEM. For example, ship or airplane members such as bulkheads and wing ribs and spars often contain cutouts and the external loads on such structures can be unknown. While DIC-recorded displacement data are utilized here, one could employ moiré, ESPI, or holographic techniques. Future considerations might include the feasibility of functionally hybridizing-DIC ideas for three-dimensional members, curved surfaces, inelastic behaviors (e.g., viscoelastic plastics), boundary integral/boundary methods, and more complicated and practical applications beyond a laboratory environment.

The author is unaware of any previously published determination of the individual stresses full-field in a side-notched orthotropic laminate from recorded information of a single displacement field. Aspects of this chapter were accepted for publication in Composite Science and Technology Journal and presented in the international Digital Image Correlation (iDIC) Conference in Philadelphia, November 2016.

Chapter 7: Stress Concentrations and Strengths in a Side Notched Finite-Width Composite Plate

The ability to reduce the tensile stress concentration associated with a side notched orthotropic plate by introducing adjacent auxiliary notches, and the possible influence on strength, are investigated. A scheme for optimizing size and location of auxiliary notches of isotropic and three orthotropic composite materials, namely glass/epoxy (Gl/E) (E_{11}/E_{22} = 3), graphite/aluminum (Gr/Al) (E_{11}/E_{22} = 5), and boron/epoxy (B/E) (E_{11}/E_{22} = 10), to minimze stress concentration is included. Compared with reduction in stress concentration, results show that increases in strength when introducing auxiliary notches can be appreciable in highly orthotropic natural composites such as wood. This necessitate the importance of studying both the strength and stress concentration factor when dealing with failure criteria since assuming that a specific value of a stress concentration factor necessarily leads to failure can be erroneous.

7.1 Introduction

Minimizing the stress concentrations of an engineering component involving geometric discontinuities can be important strength-wise. This study emphasizes reducing tensile stress concentration and the possible influence on strength at the geometric discontinuities by changing the neighboring structural compliance through introducing nearby auxiairy notches. Comparative effects of replacing a side notch, plus two adjacent auxiliary notches, by an oblong-shaped/elliptical/slotted notch are also considered. Results are included for a highly orthotropic natural composite, wood (Sitka Spruce). Unless otherwise stated, the strongest/stiffest material direction coincides here with that of the external loading. The material is assumed to behave

linearly elastic. Stresses are predicted numerically using ANSYS® 14. The tensile stress concentration for a finite-width side-notched plate (ratio of central notch diameter to width c/W = 0.5) made of orthotropic composite materials, namely glass/epoxy (Gl/E) (E_{11}/E_{22} = 3), graphite/aluminum (Gr/Al) (E_{11}/E_{22} = 5), and boron/epoxy (B/E) (E_{11}/E_{22} = 10), was reduced by optimizing the location and size of auxiliary notches. The effects of both replacing three adjacent notches by an elliptical notch and changing the direction of material symmetry when the fiber orientation is parallel and perpendicular to the applied load in the stress concentration reduction are included.

Under static loading, the local yielding in ductile isotropic material is often not catastrophic but when load is under cyclic conditions the reducing stress concentrations might be very important. Reducing stress concentration is particularly important in composites because such materials do not normally exhibit traditional yielding. Reducing stress concentration for isotropic materials by introducing two auxiliary holes or notches or elliptical shape has been studied by many researchers [57,73,78–81]. Howland [79] provided a solution for a single row of holes in an infinite isotropic plate. Schultz [81] obtained a solution for a uniaxially loaded finite-width plate containing single row of holes. Results for numerous geometric discontinuities in isotropic member were summarized by Paterson [80] and Savin [57]. In 1952, Heywood [82] reduced the stress concentration around a single circular hole in a loaded isotropic plate by introducing auxiliary holes.

The increased use of composites necessitates the need for stress and strength knowledge in orthotropic materials containing notches or holes. The orthotropic materials can produce extremely high stress concentrations compared with isotropic materials, and the possible influence on strength, motivates the need to know the stresses in composites structures containing geometric discontinuities such as holes and notches. Kosmodamiansky [83] studied the stresses in loaded infinite orthotropic laminate containing two holes of different size and provided the

first approximate stress distribution around the contour of the smaller hole. Lin and Ueng [84] subsequently evaluated the stresses in an infinite composite containing two identical elliptical holes. Fan and Wu [85] studied the stress concentration in an infinite anisotropic laminate containing multiple collinear holes. Interestingly, Considine et al [86] showed that the tensile paper ($2.13 \leq E_{11}/E_{22} \leq 3.05$) specimens loaded in 1-direction containing a single central circular hole plus symmetrically-located auxiliary holes were stronger than those having only single central hole. Assuming linear elastic constitutive paper response, the FEM-predicted tensile stress concentration at the auxiliary holes exceeded that at the central hole so failures occurred at the auxiliary holes and were longitudinal tensile along the ligament extending transversely from these auxiliary holes. The mean tensile strength decreases as the diameter of the central circular hole increases and when introducing two auxiliary holes it decreases with greater distance between the central and the auxiliary holes.

Many studies were conducted in optimizing many different geometrical discontinuity for isotropic material are available neverless prior investigations involving such optimization for orthotropic composites do not seem to be available. Rhee [87] reduces the tensile stresses in a finite-width plate containing three holes by optimizing the location and size of the two auxiliary holes. A similar approach has been followed here to minimize the tensile stress concentration for a finite-width plate containing a side and two auxiliary notches. The obtained results are also compared with effects of introducing two symmetrically auxiliary holes and replacing a central, plus two adjacent auxiliary holes by an oblong-shaped/elliptical/slotted opening found by Rhee [87].

7.2 Optimizing the Location and Size of Auxiliary Notches

The optimum diameter, d_o, of the auxiliary notches and the distance from the center of the auxiliary notches, l_o, to the center of the side notch as shown in Figure 7-1 were determined

for isotropic and the orthotropic materials glass/epoxy (Gl/E), graphite/aluminum (Gr/Al) and boron/epoxy (B/E) as listed in Table 7-1. The 66.04 cm long plate has a width, W = 5.08 cm, and a side notch diameter, c = 2.54 cm. The stiffest/strongest orientation of the material symmetry is parallel to the applied stress, σ_0. The maximum tensile stress occurring on the edge of the side or auxiliary notches is σ_{max} and the tensile stress concentration factors (TSCF) is defined as the ratio of the maximum tensile stress to the applied load on the boundary of a discontinuity which is based on gross area, $K^t = \sigma_{max}/\sigma_0$.

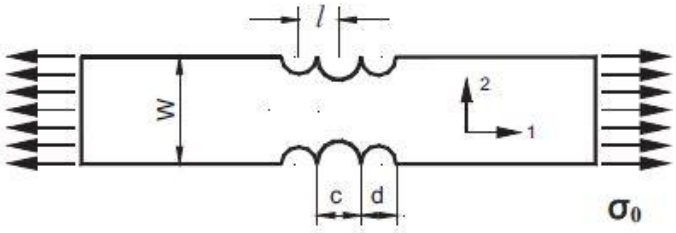

Figure 7-1: Finite-width uniaxially loaded tensile plate containing three circular notches located on the side of the plates.

Table 7-1: Orthotropic elastic properties.

	Glass/epoxy (Gl/E)	Graphite/aluminum (Gr/Al)	Boron/epoxy (B/E)
E_{11} (GPa)	53.78	124.11	206.85
E_{22} (GPa)	17.93	24.82	20.69
G_{12} (GPa)	8.96	22.06	6.9
ν_{12}	0.25	0.3	0.3

The analysis was carried out using ANSYS® 14 software package. The element type employed is PLANE 82, an 8-noded, quadrilateral shaped element which is used for two-dimensional analysis of solids under plain-stress or plane-strain conditions. Each of the eight nodes has two translation degrees of freedom, one degree in the x-direction and one in y-directions. The location and size of the two symmetrically-located side notches were determined

by fixing the location of the auxiliary notches, l, and changing their diameter, d. This diameter was increased until the maximum tensile stress at the auxiliary notches exceed the maximum tensile stress at the side notch. The results of the maximum stress on the boundary of the side or auxiliary notches are tabulated in Table 7-2. This table contains the FEA-predicted values of maximum stress on the boundary of the side and auxiliary notches for various combinations of dimensions, d and l. This procedure was done for isotopic material and composite materials listed in Table 7-1. Data of Table 7-2 are shown as a function of d/l for different user-selected locations of the auxiliary notches (l/W =0.1, 0.2, 0.35, 0.4, 0.5, 0.6, 0.7, 0.8, 0.9, and 1.0). Table 7-2 contains information for selected values of l/W.

For subsequent analyses, it is convenient to normalize the relevant value of the maximum tensile stress located on the boundary of the discontinuity, σ_{max}, by the maximum tensile stress on the boundary of single side notch, σ_c, if there were no auxiliary notches. The values of the maximum tensile stress concentration on the boundary of the side notch, σ_c/σ_o, if there were no auxiliary notches for isotropic, glass/epoxy (Gl/E), graphite/aluminum (Gr/Al), and boron/epoxy (B/E) materials are 3.25, 4.44, 4.54, and 7.66, respectively. The variation of σ_{max}/σ_c against the ratio d/l for various values of l/W were obtained and plotted for the four materials for a specified geometry (specific values of c and W). To demonstrate how the tensile stresses on the boundary discontinuity changes with the ratios d/l and l/W, ten values of the l/W were analyzed. For a fixed value of l/W, the tensile stresses on the side and auxiliary notches were plotted versus d/l by increasing the size of the auxiliary notches, d. The tensile stress on the boundary of side and auxiliary notches decreases and increases, respectively, with the increasing of d/l. A second-order polynomial curve was utilized to fit the data points for maximum stress values at the side and auxiliary notches. The minimum tensile stress in the plate occurs when the maximum tensile stress at the side notch coincides with that at the auxiliary notches. For a specific value of l/W, the intersection of a respective pair of curves (curve

defined by solid line for side notch and curve defined by dashed line for auxiliary notches) provides the optimum value of d/l for this particular value of l.

This interception point therefore represents the optimum condition stress-wise for the corresponding value of l/W. In order to illustrate how the trend of the σ_{max}/σ_c changes with d/l and l/W, the interception points were then plotted versus d/l and from which the location and size of the auxiliary notches can be obtained. A third-order polynomial fitting was utilized to fit the data of all interception points. As will be demonstrated graphically, the σ_{max}/σ_c decreases with increasing of d/l as well as l/W until reaching a minimum value which corresponds to the optimum tensile stress conditions in the plate. Such plots are used ultimately to determine the optimum individual values of d (i.e. d_o) and l (i.e. l_o) for each material. For a particular material and geometry (specific values of c and W), the optimum distance between the side and auxiliary notches, l_o, is determined by plotting l using a second-order least squares curve versus l/d for various values of l/W. The optimum values of $(d/l)_o$ and $(l/W)_o$ can be obtained so the corresponding values of d_o and $l_o$can then be calculated.

Table 7-2: Maximum tensile stress concentration factor at side and auxiliary notches in uniaxially loaded, finite width (c/W = 0.5) isotropic and orthotropic (Gl/E, Gr/A, and B/E properties of Table 7-1) tensile plates of Figure 7-1.

l/W	*d/l*	Isotropy ($E_{11}/E_{22} = 1$)		GL/E ($E_{11}/E_{22} = 3$)		Gr/Al ($E_{11}/E_{22} = 5$)		B/E ($E_{11}/E_{22} = 10$)	
W = 5.08 cm c = 2.54 cm		Side Notch	Aux. Notches	Side Notch	Aux. Notches	Side Notch	Aux. Notches	Side Notch	Aux. Notches
0.100	4.700	2.936	2.633	3.710	2.904	3.512	2.941	6.551	3.093
l = 0.508 cm	4.800	2.814	2.739	3.511	3.142	3.318	3.102	6.170	3.883
	4.900	2.639	2.843	3.216	3.355	3.038	3.266	5.491	4.768
0.200	2.400	2.703	2.857	3.218	3.241	3.004	3.247	5.386	4.151
l = 1.016 cm	2.600	2.262	3.132	2.400	3.761	2.241	3.640	2.940	5.718
	2.800	1.568	3.318	1.266	3.916	1.186	3.842	0.560	5.595
0.350	0.894	3.195	2.247	4.041	2.261	3.838	2.269	7.031	2.036
l = 1.778 cm	1.260	3.005	2.885	3.592	3.349	3.360	3.319	6.046	4.168
	1.596	2.539	3.372	2.511	4.095	2.336	4.000	2.451	6.079
0.400	1.200	2.965	3.076	3.395	3.652	3.181	3.600	5.199	4.994
l = 2.032 cm	1.500	2.519	3.579	2.320	4.327	2.183	4.241	1.647	6.061
	1.600	2.270	3.788	1.836	4.565	1.724	4.462	0.772	6.316
0.500	0.692	3.197	2.714	3.947	3.053	3.739	3.031	7.314	3.682
l = 2.54 cm	1.000	3.059	3.176	3.458	3.890	3.287	3.736	4.931	5.549
0.600	1.000	3.068	3.615	3.249	4.319	3.212	4.229	3.093	6.068
l = 3.048 cm	1.100	2.970	3.953	2.955	4.824	2.976	4.596	1.916	8.126
	1.200	2.839	4.464	2.598	5.356	2.664	5.045	0.489	8.211
0.700	0.238	3.250	2.651	4.117	2.814	3.930	2.746	7.615	2.802
l = 3.556 cm	0.523	3.257	2.815	3.967	3.470	3.808	3.445	7.038	4.445
	0.716	3.214	3.246	3.749	3.984	3.665	3.906	5.467	6.257
0.900	0.350	3.262	2.990	4.067	3.566	3.928	3.551	7.315	4.546
l = 4.572 cm	0.500	3.265	3.155	3.974	3.875	3.897	3.821	6.321	5.762
	0.650	3.259	3.512	3.841	4.296	3.853	4.213	4.732	6.208
1.000	0.300	3.262	3.011	4.091	3.639	3.954	3.618	7.724	4.288
l = 5.080 cm	0.450	3.269	3.168	4.020	3.930	3.950	3.853	7.044	5.280
	0.550	3.270	3.393	3.955	4.238	3.940	4.097	6.278	6.734

7.2.1 Results

7.2.1.1 Isotropic Case

In order to find the optimum location and size of the auxiliary notches for an isotropic material, the normalized σ_{max}/σ_c is plotted versus d/l for various values of l/W as illustrated in Figure 7-2. This figure demonstrates that the tensile stress at the central notch decreases with increasing of the ratio d/l whereas the tensile stress at the boundary of the auxiliary notches increases with the increasing of d/l. The optimum situation occurs when the respective lines for the stresses at the central and auxiliary notches intercept each other. Then the interception points versus $(d/l)_o$ were fitted with a 3rd order polynomial as shown in Figure 7-3. From Figure 7-3, the optimum value of $(d/l)_o$ which corresponds for a minimum σ_{max}/σ_c ratio is 3.2. The distance between the central and auxiliary notches l is plotted versus the reciprocal of d/l (i.e. l/d) as shown in Figure 7-4. Knowing that $(d/l)_o$ = 3.2 or $(l/d)_o$ = 0.3125, the corresponding value of optimum distance l_o is computed as 0.7376 cm from Figure 7-4. These values of d_o and l_o provide optimum/minimum equal σ_{max}/σ_c value at the central and auxiliary notches. Therefore, the optimum location l_o and size d_o of the auxiliary notches are 0.7376 and 2.36 cm, respectively. The optimum ratio of σ_{max}/σ_c is 0.8365 and the tensile stress concentration factor (TSCF) reduction is 16.35%. The maximum tensile stress if there were no auxiliary notches σ_c/σ_o is 3.25.

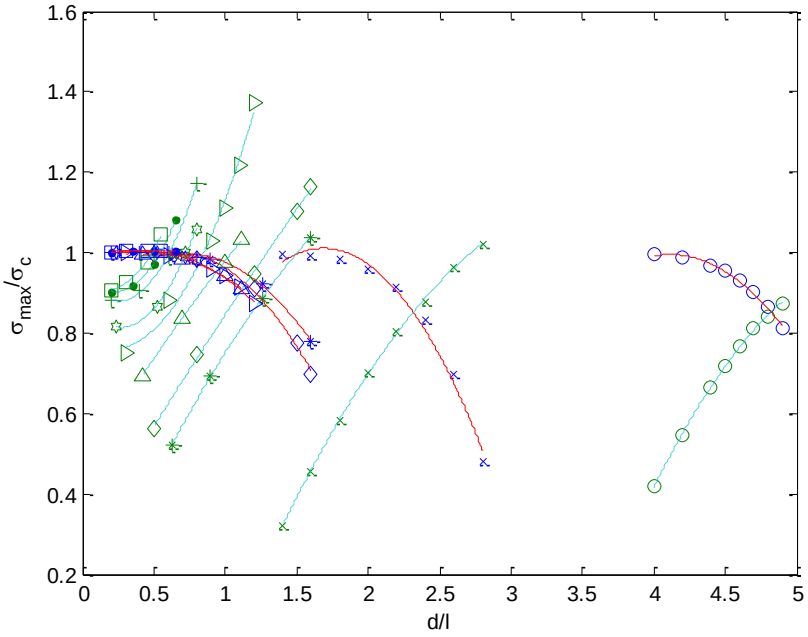

Figure 7-2: Maximum tangential stresses at central (solid line) and auxiliary (dashed line) notches σ_{max} divided by the maximum tangential stress at central notch without auxiliary notches σ_c in uniaxially loaded, finite-width (c/W = 0.5) plate for an isotropic material (E_{11}/E_{22} = 1) as a function of d/l.

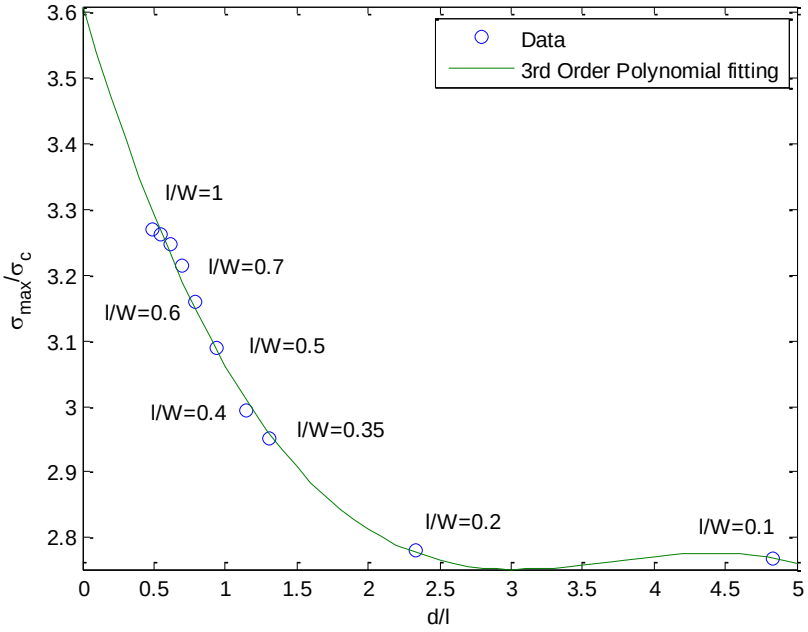

Figure 7-3: The interception points between the maximum tangential stresses at central and auxiliary notches $\sigma_{\max}$ divided by the maximum tangential stress around central notch without auxiliary notches σ_c in uniaxially loaded, finite-width (c/W = 0.5) plate for an isotropic material (E_{11}/E_{22} = 1) as a function of d/l.

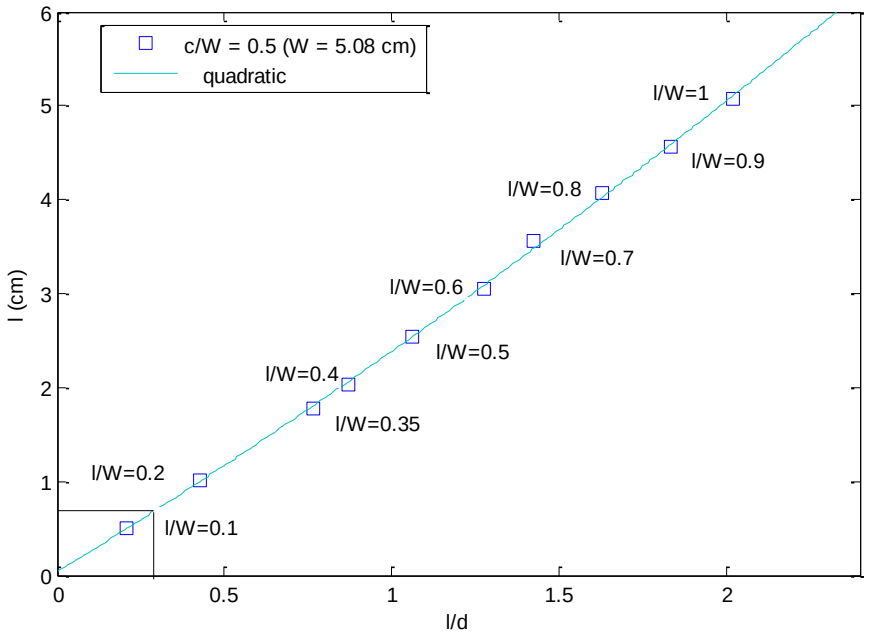

Figure 7-4: Determination of optimum distance between the central and auxiliary notches at optimum ratio d/l for an isotropic material in uniaxially loaded, finite-width (c/W = 0.5) tensile plate.

7.2.1.2 Glass/epoxy (Gl/E)

The above procedure was followed to find the optimum location and size of auxiliary notches for Glass/epoxy (Gl/E) (E_{11}/E_{22} = 3). Figure 7-5 and Figure 7-6 show how the σ_{max}/σ_c ratio varies with d/l. From Figure 7-7, the optimum value of l_o is 0.9544 cm corresponding for optimum $(d/l)_o$ which is 2.5. Then the optimum location l_o and size d_o of the auxiliary notches are 0.9544 and 2.386 cm, respectively. The optimum ratio of σ_{max}/σ_c is 0.717 and the TSCF reduction is 28.3%. The maximum tensile stress if there were no auxiliary notches σ_c/σ_o is 4.44.

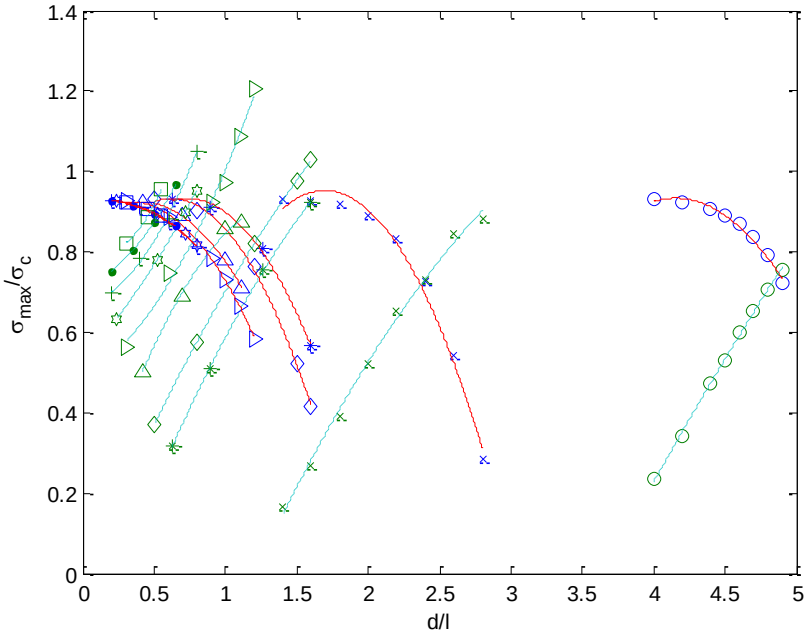

Figure 7-5: Maximum tangential stresses at side (solid line) and auxiliary (dashed line) notches σ_{max} divided by the maximum tangential stress at central notch without auxiliary notches σ_c in uniaxially loaded, finite-width (c/W = 0.5) plate for a glass/epoxy material (E_{11}/E_{22} = 3) as a function of d/l.

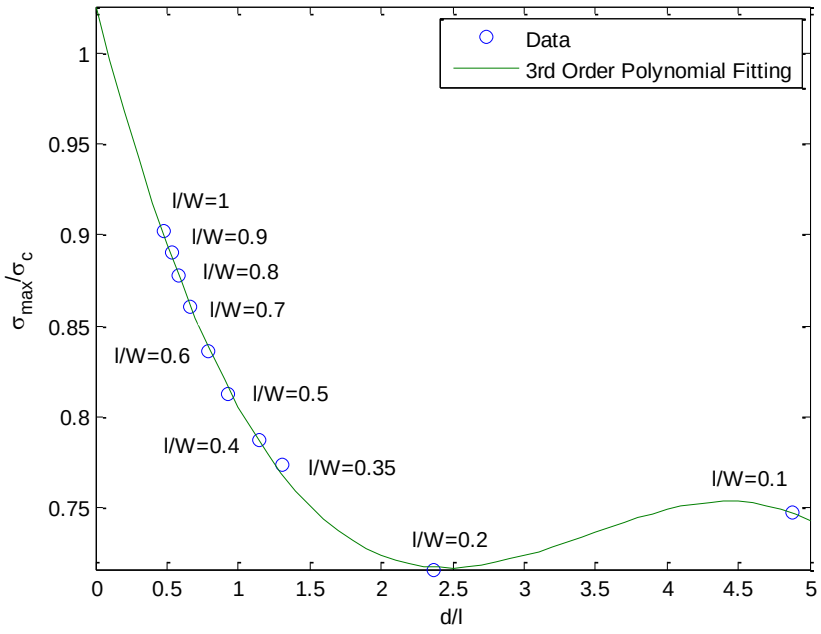

Figure 7-6: The interception points between the maximum tangential stresses around a side and auxiliary notches σ_{max} divided by the maximum tangential stress around central notch without auxiliary notches σ_c in uniaxially loaded, finite-width (c/W = 0.5) plate for a glass/epoxy material (E_{11}/E_{22} = 3) as a function of d/l.

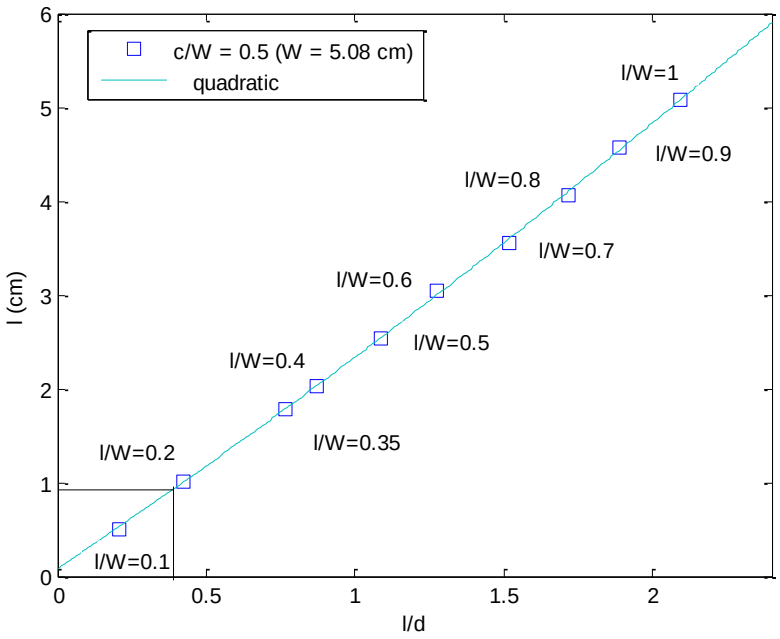

Figure 7-7: Determination of optimum distance between the side and auxiliary notches at optimum ratio d/l for a glass/epoxy material (E_{11}/E_{22} = 3) in uniaxially loaded, finite-width (c/W = 0.5) tensile plate.

7.2.1.3 Graphite/aluminum (Gr/Al)

The second orthotropic material used to optimum location and size of auxiliary notches is Graphite/aluminum (Gr/AL) (E_{11}/E_{22} = 5). Figure 7-8 and Figure 7-9 demonstrate how the σ_{max}/σ_c ratio varies with d/l. From Figure 7-10, the optimum value of l_o is 1.087 cm corresponding for optimum $(d/l)_o$ which is 2.1. Then the optimum location l_o and size d_o of the auxiliary notches are 1.087 and 2.2827 cm, respectively. The optimum ratio of σ_{max}/σ_c is 0.682 and the TSCF reduction is 31.8%. The maximum tensile stress if there were no auxiliary notches σ_c/σ_o is 4.54.

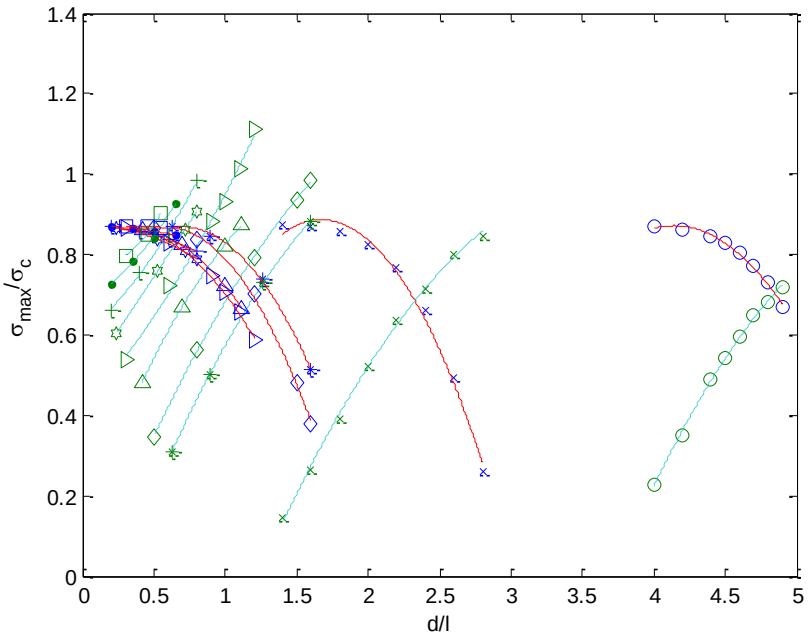

Figure 7-8: Maximum tangential stresses at central (solid line) and auxiliary (dashed line) notches σ_{max} divided by the maximum tangential stress at central notch without auxiliary notches σ_c in uniaxially loaded, finite-width (c/W = 0.5) plate for a Glass/epoxy material (E_{11}/E_{22} = 5) as a function of d/l.

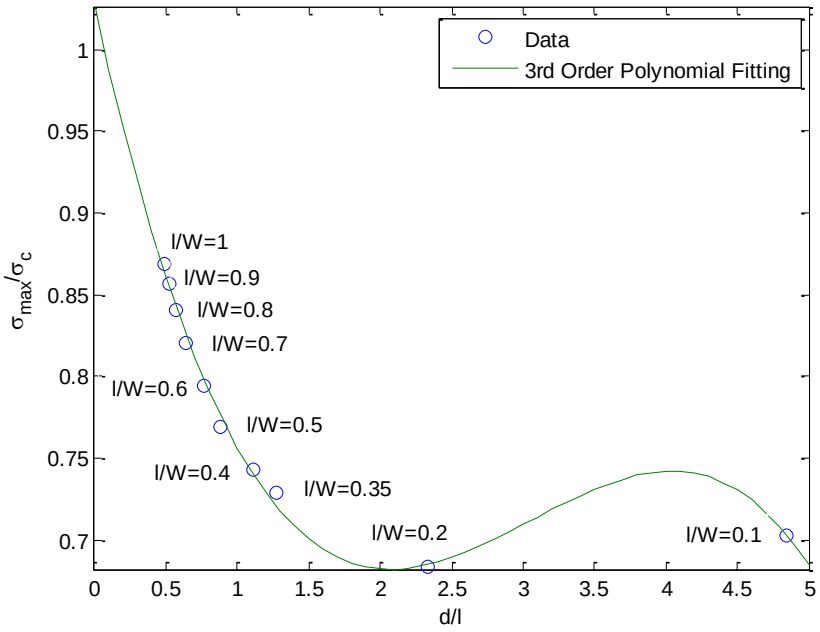

Figure 7-9: The interception points between the maximum tangential stresses around a central and auxiliary notches σ_{max} divided by the maximum tangential stress around central notch without auxiliary notches σ_c in uniaxially loaded, finite-width (c/W = 0.5) plate for a Graphite/aluminum material (E_{11}/E_{22} = 5) as a function of d/l.

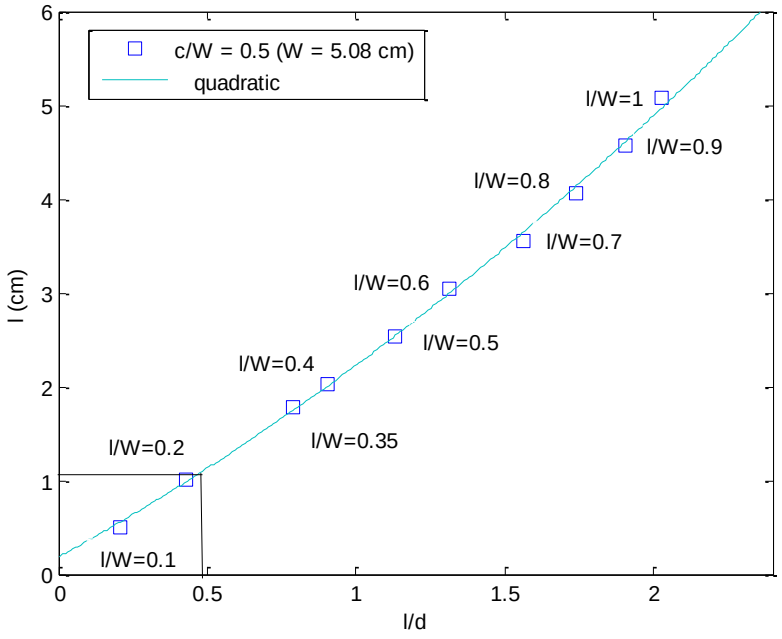

Figure 7-10: Determination of optimum distance between the central and auxiliary notches at optimum ratio d/l for a Graphite/aluminum material (E_{11}/E_{22} = 5) in uniaxially loaded, finite-width (c/W = 0.5) tensile plate.

7.2.1.4 Boron/epoxy (B/E)

Finally the optimum location and size of auxiliary notches were obtained for the Boron/epoxy (B/E) (E_{11}/E_{22} = 10) orthotropic material. Figure 7-11 and Figure 7-12 illustrate how the σ_{max}/σ_c ratio varies with d/l. From Figure 7-13, the optimum value of l_o is 1.167 cm corresponding for optimum $(d/l)_o$ which is 2.1. Then the optimum location l_o and size d_o of the auxiliary notches are 1.167 and 2.4507 cm, respectively. The optimum ratio of σ_{max}/σ_c is 0.5613 and the TSCF reduction is 43.87%. The maximum tensile stress if there were no auxiliary notches σ_c/σ_o is 7.66.

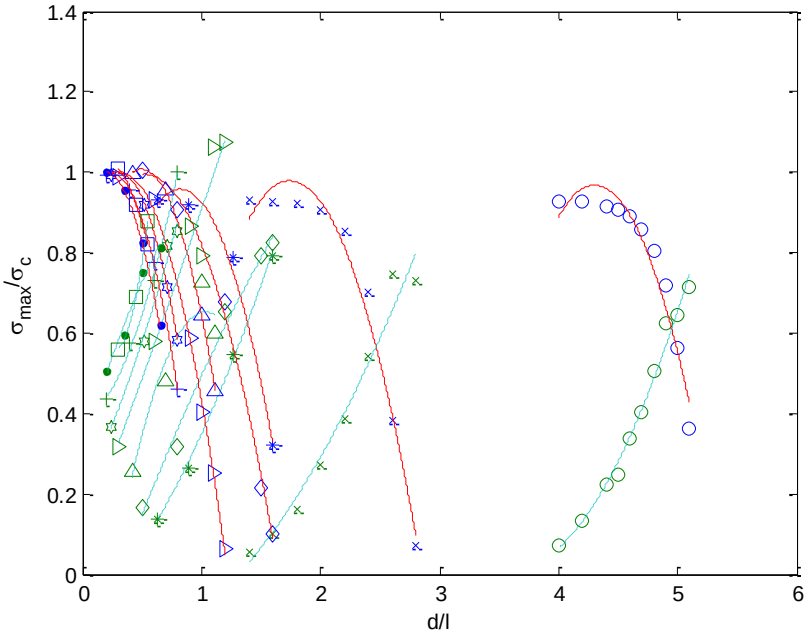

Figure 7-11: Maximum tangential stresses at central (solid line) and auxiliary (dashed line) notches σ_{max} divided by the maximum tangential stress around central notch without auxiliary notches σ_c in uniaxially loaded, finite-width (c/W = 0.5) plate for a Boron/epoxy material (E_{11}/E_{22} = 10) as a function of d/l.

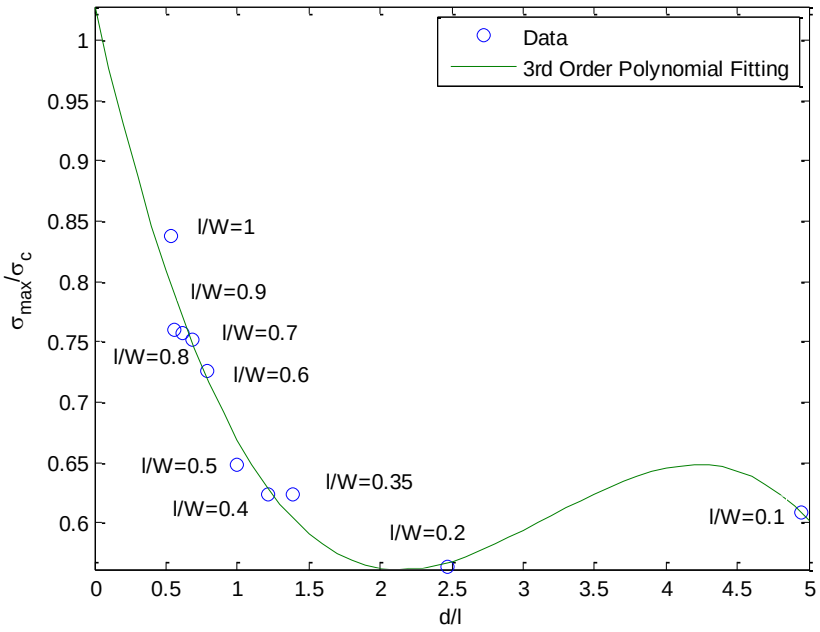

Figure 7-12: The interception points between the maximum tangential stresses around a central and auxiliary notches σ_{max} divided by the maximum tangential stress around central notch without auxiliary notches σ_c in uniaxially loaded, finite-width (c/W = 0.5) plate for a Boron/epoxy material (E_{11}/E_{22} = 10) as a function of d/l.

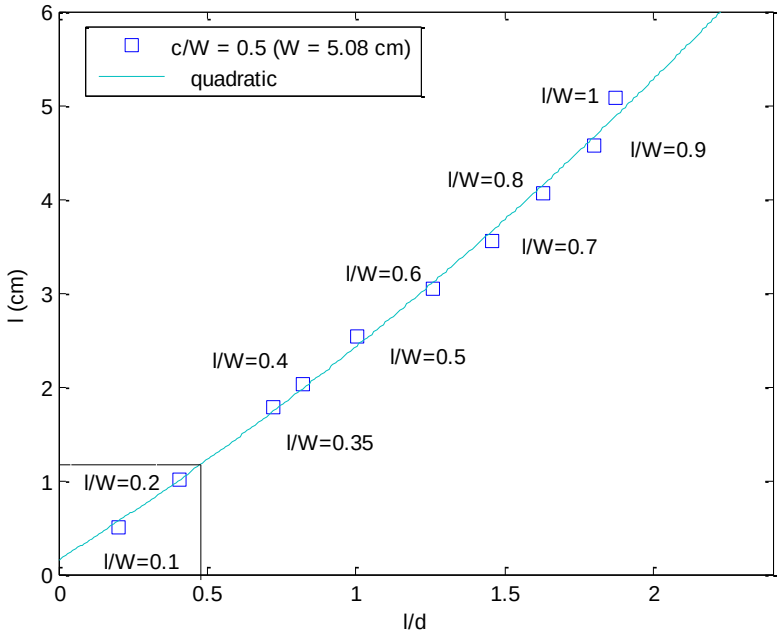

Figure 7-13: Determination of optimum distance between the central and auxiliary notches at optimum ratio d/l for a Boron/epoxy material (E_{11}/E_{22} = 10) in uniaxially loaded, finite-width (c/W = 0.5) tensile plate.

The trends of plotting σ_{max}/σ_c with d/l for isotropic and other composite orthotropic materials of Table 7-1 are similar to each other for a specified material and geometry (c/W = 0.5). Table summarizes the obtained results including the maximum tensile stress concentration reduction (TSCR) achieved. For a plate with a width W = 5.08 cm and a side notch diameter c = 2.54 cm, the optimum values of $(d/l)_o$ and the reduced TSC of these composite materials increase with the increasing of material orthotropy (E_{11}/E_{22} = 1,3,5 and 10) as do the optimum values of d_o and l_o. In all of these orthotropic cases, the values of d_o and l_o are slightly less than the central notch radius c = 2.54 cm so the auxiliary notches and central notch interact $l_o < (d_o + c_o)/2$. Optimizing the location and size of a pair of symmetrically-positioned auxiliary notches about a side notch reduces the TSCFs at the original side notch in the uniaxially loaded plated by 16.35% for isotropy,

28.3% for Glass/epoxy, 31.8% for Graphite/aluminum, and 43.9% for Boron/epoxy, respectively, compared to those without auxiliary notches.

For different values of c/W, different types of loading and/or different materials, the corresponding results of optimum values of d_o and l_o could change. Evaluation of the appropriate values of d_o and l_o to minimize/optimize the TSCFs as a function of W and/or c would necessitate repeating this approach for various values of W and/or c. Subsequent considerations include evaluating the consequences of such reductions in stress concentrations on the actual strength of side-notched orthotropic plates.

Table 7-3: Optimum values of l and d, and Tensile Stress Concentration Reduction (TSCR) in uniaxially loaded, finite-width (c/W = 0.5) tensile plates of Figure 7-1 and materials listed in Table 7-1.

	Isotropy	**(Gl/E)**	**(Gr/Al)**	**(B/E)**
Optimum d/l	0.465	0.470	0.449	0.482
Optimum l/W	0.145	0.189	0.214	0.230
Optimum l_o (cm)	0.738	0.954	1.087	1.167
Optimum d_o (cm)	2.36	2.386	2.283	2.451
σ_{max}/σ_c	0.837	0.717	0.682	0.561
TSCR	16.4%	28.3%	31.8%	43.9%

7.3 Introducing Elliptical Notches

For the optimum conditions, the side and auxiliary notches intersected with each other which raises the prospect of using elliptical or oval shaped notches instead of three circular notches located on the side of the plate. The minor radius of the elliptical notch is $b = c/2$ = 1.27 cm and

the major radius is $a = l + d/2$. The far filed load is applied parallel to the major axis of the elliptical notch. Using the values of the optimum distance, l_o, and diameter, d_o, of the auxiliary notches to calculate the major radius of the elliptical notch, the major radius of the elliptical notch (ratio of major to minor radius, a/b) for isotropic, glass/epoxy (Gl/E), graphite/aluminum (Gr/Al), and boron/epoxy (B/E) materials are 1.92 (1.51), 2.15 (1.69), 2.23 (1.75), and 2.39 cm (1.88), respectively. The corresponding values of TSCR for elliptical notch using the values of the optimum distance, l_o, and diameter, d_o, of the auxiliary notches are 20.5%, 29.9%, 32.2%, and 38.2% for isotropic, glass/epoxy (Gl/E), graphite/aluminum (Gr/Al), and boron/epoxy (B/E) materials, respectively, Table 7-4. These values show that the maximum TSCR for elliptical notch are slightly larger the optimum TSCR found from the optimum distance, l_o, and optimum diameter, d_o, except for boron/epoxy (B/E).

7.4 Comparing with Circular Holes

This study emphasizes side-notched composites. Nevertheless, Table 7-4 compares the reductions on ANSYS-predicted TSCFs in a sided-notched and centrally-perforated [87] composites (properties of Table 7-1) tensile member associated with introducing auxiliary notches or holes. The optimum diameters of the auxiliary side notches for the isotropic and orthotropic materials are relatively close to the optimum diameters for three central circular holes found by Rhee [87]. The TSCR for three side notches exceeds the TSCR for the three central circular holes for all the orthotropic materials and the difference increases with increasing of material orthotropy. For isotropic case, the TSCR for the three circular holes is greater than the TSCR for the three side notches.

Table 7-4: Reduction in Tensile Stress Concentration Factor (TSCF) relative to that for a three side notches, single elliptical notch, and three circular holes of c/W = 0.5 in uniaxially loaded, finite-width composite tensile plates of Figure 7-1 and materials listed in Table 7-1.

Stress Concentration	Isotropy	(Gl/E)	(Gr/Al)	(B/E)
Three Notches				
Optimum l_o (cm)	0.738	0.954	1.087	1.167
Optimum d_o (cm)	2.36	2.386	2.283	2.451
TSC reduction	16.4%	28.3%	31.8%	43.9%
Single elliptical notch				
Ratio a/b	1.51	1.69	1.75	1.88
TSC reduction	20.5%	29.9%	32.2%	38.2%
Three holes [5]				
Optimum l_o (cm)	2.152	2.225	2.283	1.955
Optimum d_o (cm)	2.373	2.387	2.401	2.475
TSC reduction	21.2%	22.1%	23.2%	30.9%

7.5 Effects of Material Direction in Stress Concentration Reduction

Unless stated otherwise, the strongest/stiffest direction of material symmetry coincides with direction of the external loading for all the results presented previously. The ANSYS-predicted tensile stress concentration factors, K^t, and their reductions, ΔK^t, associated with introducing auxiliary notches, in uniaxialy loaded, side-notched plate for specified materials listed in Table 7-1 and specific geometry (c/W = 0.5, d/W = 0.45, l/W = 0.2) when the strongest/stiffest 1-

direction of material symmetry is either parallel or perpendicular, respectively, to the applied loading were computed and tabulated in Table 7-5. The tensile stress concentration factors (TSCF) when the direction of material symmetry is parallel and perpendicular, respectively, to the applied loading for a plate with side notch are 4.436 and 3.072 for Gl/E, 4.537 and 2.696 for Gr/Al, and 7.756 and 3.347 for B/E, respectively. The TSCF when loading is parallel to material direction is larger than the TSCF when loading is perpendicular to material direction. For only a side notch when introducing auxiliary notches, the TSCFs at the central hole K_c^t are substantially less when the direction of symmetry is perpendicular to the direction of the applied loading for orthotropic materials (3.608 vs. 2.795 (Gl/E), 3.385 vs. 2.537 (Gr/Al), 6.394 vs. 3.017 (B/E)) so the corresponding reduction of TSCF at central notch $\Delta K_c^t = (K^t - K_c^t)/K^t$ are also less when the stiffest direction of material symmetry is perpendicular to the loading direction (18.7% vs. 9.0% (Gl/E), 25.4% vs. 5.9% (Gr/Al), 17.6% vs. 9.9% (B/E)). The composite would be weaker in the more-compliant 2-direction.

The relative size and locations of the auxiliary notches when the direction of symmetry is parallel or perpendicular to the applied loading for all the cases were not optimized, but rather motivated by previous experience for the corresponding values of c = 2.54 cm, d = 2.286 cm, and l = 1.016 cm. For specific geometry (fixed values of W and c) and material, the optimizations for the size and location of the auxiliary holes are needed for each of the two different material-directions. The TSCF at the side notch K_c^t and auxiliary notches K_a^t for Gl/E and Gr/Al when the weakest/most compliant material orientation coincide with the direction of the applied loading are close to each other which suggests the locations and sizes of the auxiliary notches are almost optimized.

Table 7-5: Effects of fiber orientation on tensile stress concentration factors, K^t, in uniaxially loaded, side-notched, plate and their reductions, ΔK^t, with auxiliary notches for specified materials listed in Table 7-1 and specific geometry (c/W = 0.5, d/W = 0.45, l/W = 0.2).

Stress Concentration	Isotropy	(Gl/E)	(Gr/Al)	(B/E)
The stiffest direction of material symmetry parallel to the direction of external loading				
K^t	3.249	4.436	4.537	7.756
K_c^t	2.915	3.608	3.385	6.394
K_a^t	2.694	3.044	3.029	3.784
ΔK_c^t	10.3%	18.7%	25.4%	17.6%
ΔK_a^t	17.1%	31.4%	33.2%	51.2%
The stiffest direction of material symmetry perpendicular to the direction of external loading				
K^t	3.249	3.072	2.696	3.347
K_c^t	2.915	2.795	2.537	3.017
K_a^t	2.694	2.543	2.368	2.624
ΔK_c^t	10.3%	9.0%	5.9%	9.9%
ΔK_a^t	17.1%	17.2%	12.1%	21.6%

7.6 Effect of Local Compliance Changes on Stresses and Strength

The effect of changing the neighboring structural compliance on stress concentration reduction and possibly increasing of strength were investigated. Rhee [87] investigates the increase of strength for two orthotropic man-made, aerospace typed composites, graphite/epoxy (Gr/E)(E_{11}/E_{22} = 14.6) and glass/epoxy (Gl/E)(E_{11}/E_{22} = 2.4), and one orthotropic natural composite, Sitka Spruce (E_{11}/E_{22} = 12.8), by decreasing the local stiffness through geometric changes.

For centrally-perforated, uniaxially loaded [0_5/90/0_5] Gr/E (loaded parallel to the ten 0-degree fiber piles), [0/90/0_{10}/90/0] Gl/E (load transversely to the twelve 0-degree fiber piles: parallel to the two 90-degree fiber piles), and wood (Sitka Spruce) (load parallel to strongest/stiffest direction) composites, despite the TSCFs predicted using ANSYS were reduced by adding two symmetrically holes to 18.3%, 16.2%, and 19.7% at the central hole and 37.5%, 19.7, and 30.9% at the auxiliary holes, their relative strength enhancements are unchanged, 11%, and 18.6% as summarized in Table 7-6, Table 7-7, and Table 7-8, respectively [87]. The values of K_c^t and K_a^t are different for three-hole geometry due to the lack of optimization. The difference response on strength of reducing the TSCF by adding auxiliary holes to these Gr/E and Gl/E laminated composites might reflect deficiencies in assuming plane-stress homogeneity and/or the complexity of the items influencing laminate strength, i.e. strength controlled by more than just the TSCF.

7.6.1 Graphite/epoxy

Specimens of uniaxially-loaded (in their strongest/stiffest direction) [0_{13}/90_5/0_{13}] Gr/E (E_{11} = 100.87 $\pm$ 5.51 GPa, E_{22} = 24.89 $\pm$ 1.17 GPa, G_{12} = 2.88 GPa and ν_{12} = 0.152 $\pm$ 0.020) composites prepared by electrical discharge machining EDM with three-notches were tested to measure the strengths. The TSCFs are reduced by decreasing the local stiffness through geometric changes. The stress concentration factors were predicted using ANSYS. The values of K_c^t and K_a^t are different for three-notches geometry due to the lack of optimization. The failure of specimens start at the edge of a hole, i.e. parallel to the dominant fiber direction. Two specimens of [0/90/0_{10}/90/0] Gl/E loaded perpendicular to the strongest/stiffest composite orientation were tested to measure the strengths. The fracture of specimens was located in tension across the transverse ligament adjacent to a hole.

Table 7-6: Stress concentrations and strengths in uniaxially-loaded [0_5/90/0_5] Gr/E tensile members with EDM[***]-prepared holes (E_{11} = 121 GPa, E_{11}/E_{22} = 14.6, E_{11}/G_{12} = 32 and ν_{12} = 0.34) [87].

	W (cm)	c/W	d/W	l/W	K^t	ΔK^t (%)	Strength[*] (MPa) (SD)[**]	Strength In-crease (%)	Number of specimens
None	0.95						1510 (250)		4
Central hole only	1.91	0.5			8.51		769 (70)		8
Central and auxiliary holes	1.91	0.5	0.42	0.7	K_c^t = 6.95 K_a^t = 5.32	ΔK_c^t = 18.3 ΔK_c^t = 37.5	768 (50)	0 %	8

[*] Based on gross area; ( )[**] standard deviation; [***] Electrical Discharge Machining

Table 7-7: Stress concentrations and strengths in uniaxially-loaded, perforated [0/90/0_{10}/90/0] Gl/E tensile members (E_{11} = 34.2 GPa, E_{22} = 14.1 GPa, G_{12} = 3.4 GPa and ν_{12} = 0.22) and length L = 34.53 cm and thickness = 0.32 cm [87].

	W (cm)	c/W	d/W	l/W	K^t	ΔK^t (%)	Strength[*] (N)	Strength Increase (%)
Central hole only	2.61	0.49			K^t = 4.57		4143	
Central and auxil-iary holes	2.61	0.49	0.43	0.68	K_c^t = 3.83 K_a^t = 3.67	ΔK_c^t = 16.2 ΔK_c^t = 19.7	4606	11 %

[*] Based on gross area;

7.6.2 Sitka Spruce

After evaluating the ability to reduce stress concentration, and thereby potentially increase strength, through controlling local compliance by introducing auxiliary holes in mane-made, aerospace-typed composites having fairly discrete fibers in matrix, a natural orthotropic material wood (Sitka Spruce) were also investigated. The Spruce specimens with 23 cm (9 inch) long by 0.5 cm (0.196 inch) thick are categorized into three groups based on the orientation of the growth rings, Figure 7-14 and Table 7-8. The orientation of the growth rings of the first group (G1) lie in the longitudinal-tangential plane where the tangential axis is parallel to the growth rings, Figure 7-14(a). The orientation of the growth rings of the second group (G2) lie in the longitudinal-radial plane where the radial direction is perpendicular to the growth rings, Figure 7-14(b). The orientation of the growth rings of the third group (G3) lies in a plane where the tangential and radial directions form 45^o with the growth rings, Figure 7-14(c). E_{11} is a measured value for the Spruce tested here, whereas the other independent properties E_{22}, G_{12}, ν_{12} (E_T/E_L = 0.043, E_R/E_L = 0.078, G_{LT}/E_L = 0.061, G_{LR}/E_L = 0.064, G_{RT}/E_L = 0.003, ν_{LT} = 0.467, ν_{LR} = 0.372, ν_{RT} = 0.435) are from the Wood Handbook [88]. The average measured values of E_{11} (and the corresponding standard deviation) for the 1st, 2nd, and 3rd groups are 11.70 (1.9), 10.58 (0.6), and 9.03 (1.0) GPa. The range of measured values of E_{11} for all the groups do not affect or change the ANSYS-predicted stresses.

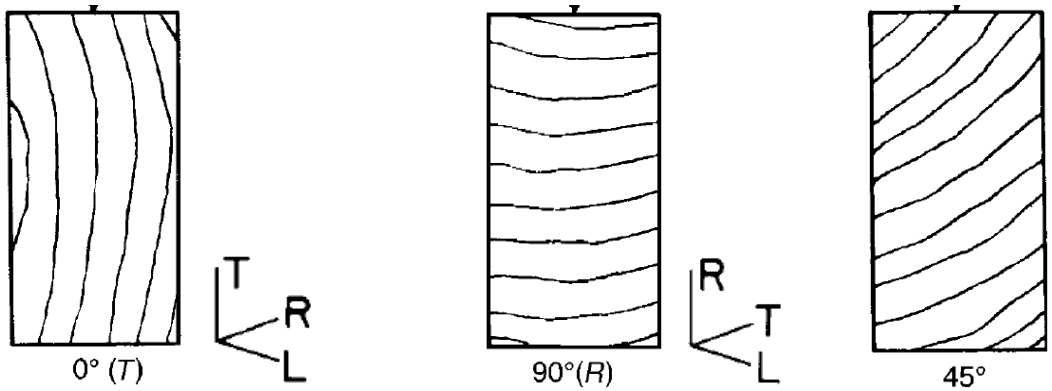

Figure 7-14: Direction of annual growth rings: 0º or parallel (T), 90º or perpendicular (R), and 45º.

The lack of available tooling sizes impede optimizing the size of the auxiliary notches. For instance, for spruce wood in longitudinal-tangential plane (E_{11}/E_{22} = 23.4, c/W = 0.5, W = 1.91 cm), the optimum diameter of the auxiliary notches, d_o, and their locations, l_o, are 0.927 and 0.386 cm (i.e., d/W = 0.49 and l/W = 0.20) found by similar procedure described early. The TSCR at this optimum case is 34.9% and this suggests that the auxiliary notches are intersected. Therefore, the location and size of the auxiliary notches, d/W and l/W, were selected depending on the experience of the other materials previously considered here, Figure 7-15. The moisture content of tested wood was pre-conditioned to 12% and sharp brad-point bits was used to fillet the notches, followed by reaming. All specimens were loaded parallel to the grain (longitudinal- or 1-direction) at 0.15 cm/minute using an Instron tensile machine, Figure 7-16. All measured strengths and the corresponding standard deviation for all the specimens are noted in Table 7-8. The average measured values of strength (and the corresponding standard deviation) for the 1st, 2nd, and 3rd groups for a single side notch are 23.3 (5.3), 26.5 (5.7), and 24.3 (2.2) MPa. The average measured values of strength (and the corresponding standard deviation) for the 1st, 2nd, and 3rd groups for three side notches are 29.8 (2.7), 34.3 (2.5), and 29.6 (3.2) MPa. The highest mechanical strength is when

the orientation of the growth rings lies in the longitudinal-radial plane and radial direction is perpendicular to the growth rings, group 2 of Figure 7-14(b). The increase in Spruce strength of specimens of Table 7-8 when introducing auxiliary notches are 27.9, 29.4, and 21.8% for the 1st, 2nd, and 3rd groups.

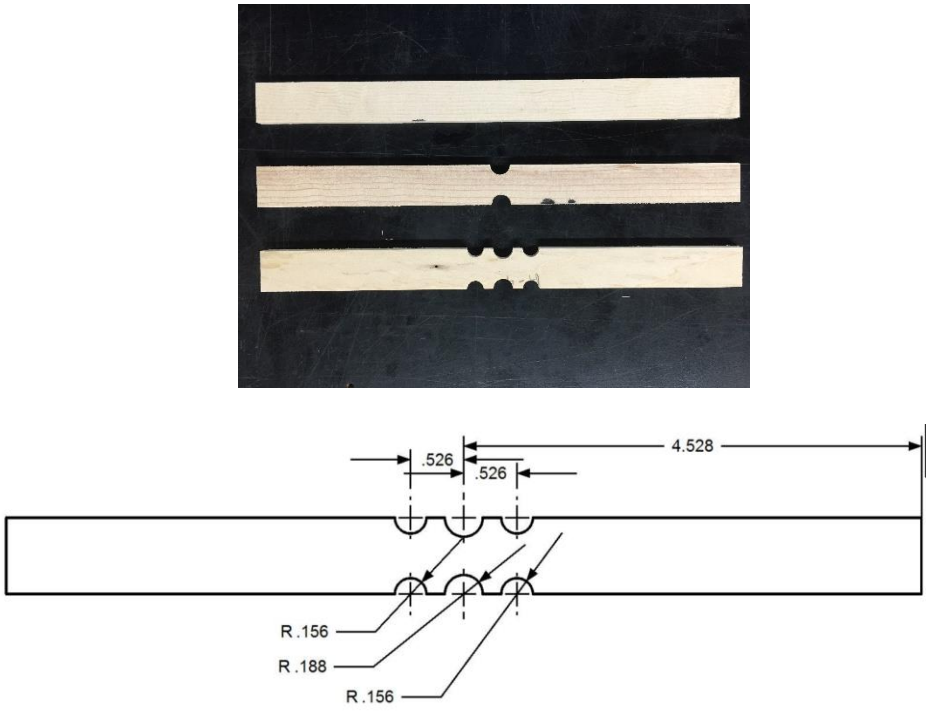

Figure 7-15: Sitka Spruce specimens of Table 7-8 (dimensions in inch).

Figure 7-16: Loaded specimen in Instron tensile machine at 0.15 cm/minute.

The reductions in TSCF, shown in Table 7-8, for 1st, 2nd, and 3rd groups at the notch, ΔK_c^t, associated with adding the auxiliary notches are ΔK_c^t = 15.0, 13.6, and 14.6%, respectively. The reductions ΔK_a^t = 23.5, 22.4, and 23.2% for 1st, 2nd, and 3rd groups of Table 7-8, respectively, are based on the values of TSCF at the notch without the auxiliary notches (K^t = 6.60, 6.25, and 6.43), and that at the auxiliary notches (K_a^t = 5.05, 4.85, and 4.95). The difference between the values of K_c^t and K_a^t for all cases for three sided-notches geometry of Table 7-8 reflects the lack of exact optimization. The increase in Spruce strength of specimens of Table 7-8 having auxiliary holes is 94% (18.6 of 19.7) of the concomitant reduction in TSCF at the central hole. Where the increase in Spruce strength of specimens of Table 7-8 having auxiliary notches are 186% (27.9 of 15.0),

216% (29.4 of 13.6), and 152% (21.8 of 14.3) for 1st, 2nd, and 3rd groups of the concomitant reduction in TSCF at the central hole. The reductions, ΔK_c^t and ΔK_a^t, for a spruce wood with circular hole and two symmetrically auxiliary holes [87] are larger than the reduction in a spruce wood with three sided notches, Table 7-8 where the increase in the strength is smaller with circular hole and two symmetrically auxiliary holes. Although the strength of the transversely-loaded $[0/90/0_{10}/90/0]$ Gl/E increases when auxiliary holes are added, its relative strength enhancements do not approach that achieved here for Spruce.

The stress concentrations of Table 7-8 demonstrates how the auxiliary notches soften the severity of the stresses surrounding the three notches combination, compared with the single side-notched plate. This raise the comparison of those situation with elliptical notch of a minor diameter equal to diameter of the notch, $b = c = 0.5W$, and a major diameter equal to $(a = 2l + d = 1.4W + 0.42W) = 1.82W$, Figure 7-17. The TSCF at the edge of this elliptical notches of the spruce specimens of Table 7-8 for 1st, 2nd, and 3rd groups are 2.69 (Figure 7-17), 2.65, and 2.67, respectively, compared with 5.61, 5.4, and 5.51, respectively, at the central notch of the three sided-notches geometry. Those reductions of the spruce specimens of Table 7-8 for 1st, 2nd, and 3rd groups are 59.2, 57.6, and 58.5%, respectively, comparing with the single side-notched tensile member (6.60, 6.25, and 6.43). The reductions of the spruce specimens of Table 7-8 with elliptical notch is greater than the reduction in spruce with elliptical hole 47% [87].

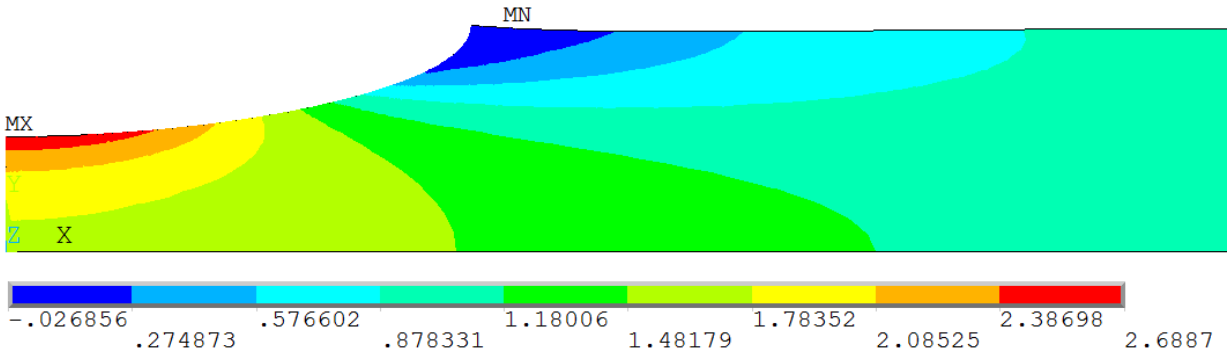

Figure 7-17: σ_{11}/σ_0 in Sitka Spruce (material properties of 1st group in Table 7-8) tensile member.

Like the tested [05/90/05] Gr/E, most Spruce specimens exhibited some early longitudinal failure starting at a hole, rather than in tension across the ligament extending transversely from a hole, Figure 7-18. However, Figure 7-18 also shows some transverse failures (including one extending from the edge of the notch). These data for Spruce might suggest that, even though increases in strength accompany reduced TSCFs, stress concentrations themselves are not the major (or only significant) issue controlling strength – and perhaps this demonstrates it would be better to apply a multiaxial strength/failure theory around (and in the neighborhood of) the boundary of the hole. Of course the behavior in materials like wood can be influenced by any grain deviations.

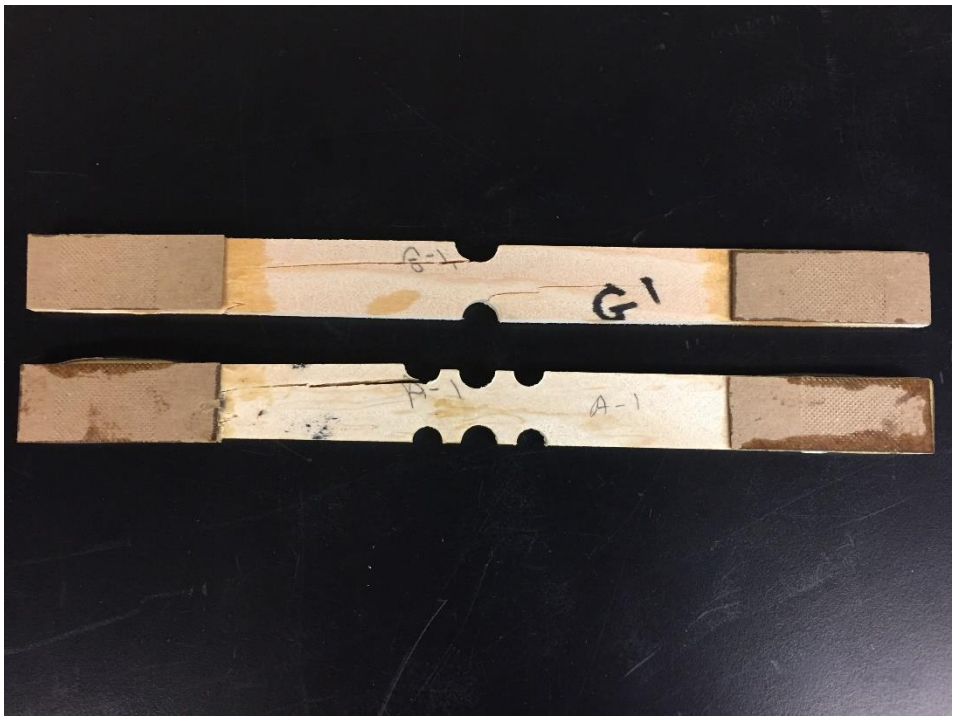

Figure 7-18: Failed Sitka Spruce specimens.

Table 7-8: Stress concentrations and strengths in uniaxially-loaded, side-notched and perforated Sitka Spruce tensile members.

Notches/holes	W (cm)	c/W	d/W	l/W	K^t	ΔK^t (%)	Strength* (MPa) (SD)**	Strength In-crease (%)	Number of specimens
G1 -Longitudinal-tangential plane in sided-notched tensile members (E_{11} = 11.7 $\pm$ 1.9 GPa, E_{22}/E_{11} = 0.043, G_{12}/E_{11} = 0.061 and ν_{12} = 0.467)									
None	0.98						75.1 (19.4)		8
Single notch	1.91	0.5			6.60		23.3 (5.3)		8
Auxiliary notches	1.91	0.5	0.42	0.7	K_c^t = 5.61 K_a^t = 5.05	ΔK_c^t = 15.0 ΔK_c^t = 23.5	29.8 (2.7)	27.9	9
G2 - Longitudinal-radial plane in sided-notched (E_{11} = 10.58 $\pm$ 0.6 GPa, E_{22}/E_{11} = 0.078, G_{12}/E_{11} = 0.064 and ν_{12} = 0.372)									
None	0.95						75.1 (10.3)		6
Single notch	1.91	0.5			6.25		26.5 (5.7)		8
Auxiliary notches	1.91	0.5	0.42	0.7	K_c^t = 5.40 K_a^t = 4.85	ΔK_c^t = 13.6 ΔK_c^t = 22.4	34.3 (2.5)	29.4	9
G3 - Longitudinal-45º plane in sided-notched (E_{11} = 9.03 $\pm$ 1.0 GPa, E_{22} = 0.103 GPa, G_{12} = 0.56 GPa and ν_{12} = 0.420)									
None	0.97						65.7 (8.9)		3
Single notch	1.91	0.5			6.43		24.3 (2.2)		7
Auxiliary notches	1.91	0.5	0.42	0.7	K_c^t = 5.51 K_a^t = 4.95	ΔK_c^t = 14.3 ΔK_c^t = 23.2	29.6 (3.2)	21.8	8

Longitudinal-radial plane in centrally-perforated tensile members [87] **(E_{11} = 11.45±0.25 GPa, E_{22}/E_{11} = 0.078, G_{12}/E_{11} = 0.064 and ν_{12} = 0.372)**

None	0.97						70.8 (1)		18
Central hole	1.91	0.5			7.11		33.3 (0.8)		18
Central and auxiliary holes	1.91	0.5	0.42	0.7	K_c^t = 5.70	ΔK_c^t = 19.7	39.5 (1.1)	18.6	18
					K_a^t = 4.91	ΔK_c^t = 30.9			

[*] Based on gross area; ( )[**] standard deviation.

7.7 Discussion and Conclusion

By altering locally the structural compliance of notched and perforated orthotropic plates, the ability to reduce tensile stress concentration and increase strength is studied. Being unaware of any commercial software for reducing stress concentration in notched or perforated anisotropic composite, a finite element based approach was developed in finding the optimum size and location of auxiliary notches or holes for a finite-width plate. Although the reduction in predicted TSCF tends to increases with increased orthotropy and can exceed 40% for highly orthotropic materials, the strength enhancement can be significantly less than the reduction in tensile stress concentration. Some issues considered here have been studied previously for isotropy, but prior investigation involving such optimization for sided-notched orthotropic composites do not seem to be available. The presently studied laminated composites have a relatively simple stacking sequence.

The present approach of utilizing auxiliary and/or non-circular notches to reduce local stresses is an alternative to providing a doubler by saving material and weight. Depending on the situation, adding additional notches around an existing notch might be unsuitable. However, the general concept of modifying the structure stiffness in the neighborhood of a cutout in a composite or locally controlling the fiber orientation/spacing can be helpful.

The maximum tensile stresses occurring on the boundary of the notches were evaluated numerically using finite elements, Table 7-2. Results show that the maximum tensile stresses occurring on the boundary of the central and auxiliary notches decreases and increases, respectively, with the increasing of size of the auxiliary notches for a fixed distance l between the centers of the auxiliary and central notches. The maximum tensile stress σ_{max} located on the boundary of the central and side notches are compared with the maximum tensile stress on the

boundary of a central notch if there were no auxiliary notches σ_c. The respective reductions in the tensile stress concentration (TSCR) factor $(\sigma_c - \sigma_{max})/\sigma_c$ for the isotropic material, Gl/E, Gr/Al and B/E are 16.35%, 28.3%, 31.8%, and 43.87%, respectively, Table 7-3. Moreover, the reduced tensile stress concentration increases with increasing of material orthotropy E_{11}/E_{22}. The trends of plotting σ_{max}/σ_c with d/l for isotropic and composite orthotropic materials of Table 7-1 are similar to each other for a specified material and geometry (c/W = 0.5). At least for the cases considered, the optimum geometry using auxiliary notches or holes typically involves the latter having a diameter which is approximately equal to the diameter of the original side notch or central hole.

The auxiliary notches intersect with the side notch which raise the concept of comparing the reduction in the optimum location and size of the auxiliary notches with side elliptical notch. The corresponding values of TSCR for elliptical notch using the values of the optimum distance l_o and diameter d_o of the auxiliary notches to compute the major and minor radii of the ellipse are 20.5%, 29.85%, 32.18%, and 38.2% for isotropic, Gl/E, Gr/Al, and B/E materials, respectively, Table 7-4. These values show that the maximum TSCR for elliptical notch are slightly larger than the maximum TSCR found from the optimum distance l_o and optimum diameter d_o except for B/E.

An elliptical notch whose major diameters has a length comparable to that of side notch and two symmetrically sided auxiliary notches results in a significantly large TSCR than for just the three symmetrically optimized notches whose diameter of the side notch equals that the minor diameter of the elliptical notch. This is due that the radius of the elliptical notch at the ends of the minor radius is greater than radius of the three notches. Therefore, composite plates with longitudinal elliptical sided notch is stronger than those with comparable circular sided notches. If the

diameter and locations of the auxiliary notches are optimized, then all three notches were intersected to each other. It is reasonable to consider the relative merits of an oval or slotted notch instead of a longitudinal elliptical notch relative to relieving stress concentrations. Furthermore, it is easy to machine slotted shapes than the elliptical notches. Adding auxiliary notches can be attractive to save weight and material and in addition reduce the local stress concentrations. The general concept of modifying the neighboring geometry and structural stiffness of a cutout in a composite can be useful.

The maximum TSCR has also been studied when the plane of symmetry is parallel or perpendicular to the applied loading. The reduction of tensile stress concentration factor TSCF when the plane of symmetry is parallel to the applied loading is larger than the reduction associated when the plane of symmetry is perpendicular to the applied loading, Table 7-5.

While changing the neighboring structure of the plate, the possibility to enhance the strength by reducing the TSCF in man-made aerospace-type composites and natural orthotropic composite is observed. While introducing auxiliary holes about a central hole in the Gr/E laminate, Gl/E laminate, and natural composite wood reduced the TSCF at central hole by 18.3%, 16.2%, and 19.7%, respectively, their strength enhancements are unchanged, 11%, and 18.6% as summarized in Table 7-6, Table 7-7, and Table 7-8 [87]. The increase in Spruce strength when introducing auxiliary notches are 27.9, 29.4, and 21.8% for the 1st, 2nd, and 3rd groups of specimens of Table 7-8. The reductions in TSCF, shown in Table 7-8, for 1st, 2nd, and 3rd groups at the notch, ΔK_c^t, associated with adding the auxiliary notches are ΔK_c^t = 15.0, 13.6, and 14.6%, respectively. The increase in Spruce strength of specimens of Table 7-8 having auxiliary holes is 94% (18.6 of 19.7) of the concomitant reduction in TSCF at the central hole. Where the increase in Spruce strength of specimens of Table 7-8 having auxiliary notches are 186% (27.9 of 15.0), 216% (29.4 of 13.6),

and 152% (21.8 of 14.3) for 1st, 2nd, and 3rd groups of the concomitant reduction in TSCF at the central hole. The reductions, ΔK_c^t and ΔK_a^t, for a spruce wood with circular hole and two symmetrically auxiliary holes [87] are larger than the reduction in a spruce wood with three sided notches, Table 7-8 where the increase in the strength is smaller with circular hole and two symmetrically auxiliary holes. The B/E composite of Rowlands [87] exhibited both a reduction in TSCF and increase in strength of approximately 27% upon replacing a circular hole by an elliptical hole. Unlike the Gr/E, the fact that the strength enhancement in the Sitka Spruce approaches the TSCF reduction suggests stress concentrations themselves might not be the critical issue. Rather, the competition between orthotropic strengths and stresses around (and beyond) the notch or hole could necessitate (among other consideration) at least a multiaxial strength/failure analysis.

There is no definite explanation as to why the natural composite, Sitka Spruce, exhibits such a greater strength enhancement comparing with discrete fiber-matrix aerospace-type composites. While the increase in strength of sided-notch and perforated tensile wood specimens when adding auxiliary notches or holes essentially equals or exceeds the associated reduction in the TSCF, introducing auxiliary holes in centrally-perforated Gr/E results in virtually no increase in strength, despite a reduced tensile stress concentration. The E_{11}/E_{22} ratios for tested $[0_5/90/0_5]$ Gr/E and wood are 14.6 and 12.8, respectively, so the two ratios are not highly different (both have also c/W = 0.5). The lack of meaningful strength enhancement accompanying the reduced TSCF in composites such as the Gr/E compared with that of wood might be at least partially associated with local or micro-mechanical effects due to the more discrete nature of the former man-made laminate compared with natural composites such as wood and in addition to the possible presence or absence of interlaminar stresses. The local or micro-mechanical effects associated with more highly discrete nature of the man-made composites compared with natural cellulosic composite

may play role in how stresses at and near a cutout influence strength. The relative ratios of fiber-to-matrix moduli could also contributes and the ratios of discrete artificially manufactured aero-space composite range between 20 and 150.

Assuming plane stress, linear elasticity and material homogeneity, stress concentration factors were predicted numerically using ANSYS finite element commercial software. Some of the composite materials exhibit an increased strength with the reduced tensile stress concentration when adding auxiliary notches or holes while some do not. Stress concentration might provide indicators of the strength degradation associated with a geometric discontinuity, and thus perhaps a measure of component integrity. This raises the question how strongly are the stress concentration factor related to the strength. Results suggest stress concentrations may be a reasonable predictor of relative strength for isotropic materials and macro-homogeneous composites such as wood and paper, but not necessarily for laminates consisting of stacked piles at several different orientations. As well as reducing a tensile stress concentration factor, adding angle-piles to a cross-ply type laminate could make the material more ductile and reduce the structural seriousness of the stress concentration factor. Even though the size and/or locations of the auxiliary holes or notches were not optimized due to the limitation of the size tooling to the Spruce and paper [86] specimens, their strengths were significantly enhanced. Some knowledge of the practical variations in size and/or locations of auxiliary holes and notches to provide approximate optimization and therefore enhancement in strength could be informative.

Future studies might consider (i) combining an extensive test program and 3-D stress analyses accounting for individual piles where applicable and possibly with a strength criterion applicable around/beyond the edge of discontinuities; (ii) other loading conditions (e.g. compression, in-plane bending, biaxial); (iii) different orthotropic and/or composite materials (involve more

complicated stacking sequence); (iv) different geometric conditions (different c/W, etc); (v) further investigation why reducing TSCFs in some situations (materials) show significant strength enhancement while not in others; (vi) applying current concepts to materials whose constitutive relations are nonlinear or inelastic; and (vii) developing a more direct method than utilized here for optimizing the size and locations of auxiliary notches and/or to otherwise minimize stress concentrations, e.g. use of genetic algorithm approaches [89,90].

Chapter 8: Studying the Effect of Thickness in Stress and Strain Concentration Factors

Stress and strain concentrations, and in-plane and out-of-plane stress constraint factors associated with a circular hole in thick, loaded orthotropic composite plates are determined by three-dimensional finite element method. The plate has essentially infinite in-plane geometry but finite thickness. Results for Sitka Spruce wood are emphasized, although some for carbon-epoxy are included. While some results are similar to those for isotropy, there are significant consequences due to material orthotropy. Maximum stress and strain concentration factors occur at mid-plane for thin plates but closer to the external traction-free surfaces for thick plates. These factors decrease as the plate surface is approached and reach lower values unrepresentative of the maximum values. Differences between the mid-plane and/or maximum and surface stress or strain concentration factors in Sitka Spruce, range from 8% if the wood grain is parallel to the applied load to 15% when the grain is perpendicular to the load. These values exceed those typically reported for isotropic materials. Stress and strain concentration factors tend to differ in magnitude from each other. Moreover, this can occur in plates whose thickness is only twice as large as the hole radius, and is true irrespective of whether the plate's material is isotropic or orthotropic. The combination of high local stresses and directional strength dependency of orthotropic materials can be particular important. That maximum stress and/or strain concentrations in thick plates occur on other than the external plate surfaces where they are most readily measured is technically significant. The

E_{11}/E_{22} ratio in Sitka Spruce exceeds that in the carbon composite by 60%. However, when loading parallel to the strong/stiff directions, the plane-stress tensile stress concentration factors of the two materials are comparable to each other.

8.1 Introduction

Engineering components often involve holes or notches and an assessment of the structural reliability necessitates knowing the stresses and the strains associated with such geometric discontinuities. Corner cracks at holes are among the most flaws in many applications such as aircraft structures. Cracks often originate and propagate from the location of the maximum stress and strain concentration so determining these locations are critical in designing the structural of engineering components. Round holes are common and their accompanying stresses and strains can reduce mechanical performance. For relatively thin plates, the crack either originates at the corner, where the holes meet the free surface of the plate, or at the center of the plate as proved by experimental evidence, and for thick plates the crack initiates in the vicinity of the corner. Such stress/strain risers can precipitate cracks, thereby aggravating the situation [91].

Stress concentration factors are available for many plane-stress isotropic cases [92,80,93]. Plane solutions are valid for plates having vanishing thickness (plane-stress) compared to the size of any cutouts or for infinite thickness (plain-strain). Notwithstanding the technical importance, few theoretical/analytical three-dimensional solutions exist for non-trivial geometries or loading conditions. Many of these theories based on an asymptotic expansion with respect to small parameter limit the validity of the obtained solutions to only small values of the chosen parameter which is usually the ratio of the thickness to a characteristic length of the problem. This explains the

slight difference between the in-plane stress obtained from plain-strain theory and the three-dimensional solution. On the other hand, stresses are practically determined through measuring strain or displacements on the plate surface. However, the strain concentration factor is different from the stress concentration factor in real structures which raises a potential risk in 3D stress concentrated structures. This increases the importance of modeling the structural components in a three-dimension. The complexity of the stress and strain fields near a curved boundary limits the existence of an analytical three-dimensional solution.

The previous discussed hybrid-TSA and DIC approaches are theoretically restricted to conditions of plane stress, i.e., the only non-zero stresses are those in the plane and they are uniform through the thickness of the member. The present research considers the 3D stress and strain concentrations, and the in- and out-of-plane stress constraint factors, in a large, uniaxially-loaded, thick orthotropic plate containing a circular hole. Although the behavior in Sitka Spruce wood is emphasized since this is a commonly employed and highly orthotropic (E_{11}/E_{22} = 23) structural material, some results for a unidirectional carbon/epoxy composite (E_{11}/E_{22} = 14) are included to illustrate the consequences of variations in orthotropy. Of structural relevance, Rhee et al (2012) showed that the effect of stress concentrations on strength in man-made (artificially) composites can be appreciably different than in natural orthotropic materials such as wood [87]. The situations at the edge of the hole are studied as a function of changes in plate thickness and orthotropic directions. Where possible, the present results are correlated with available information. The main purpose of this chapter is not primarily to provide numerical solutions for certain geometries but to highlight to the effect of thickness and material symmetry on stress and strain concentration factors for the three-dimensional stress or strain concentration problems and consequently to provide general advice used to investigate the fatigue strength of materials.

The plate material was assumed to behave homogeneously and linearly elastic. Stresses were predicted numerically using ANSYS® 14.5. The effect and influence of plate thickness, Poisson's ratio (isotropic plate), and grain orientation (orthotropic plate) in stress and strain concentration factors were studied.

8.2 Literature Review

Using a modified Ritz method, Sternberg and Sadowsky (1949) obtained an approximate solution for the three-dimensional stress distribution for a circular hole in a uniaxially-loaded, infinite isotropic plate having arbitrary thickness by using a series expansion and taking only finite terms [94]. They showed that for a plate thickness 0.7 times the radius of the hole, the maximum stress concentration at the traction-free surface is 7% less, whereas that at mid-plane is 3% higher, than the plane-stress value. Youngdal and Sternberg (1966) subsequently found that for an infinitely thick component subjected to shear, the maximum stress at the surface of the hole is 23% less, and that at the depth equal to the hole radius is 3% higher, than that for a thin component [95].

Folias (1975,1987,1989,1990) proposed a three-dimensional solution using Navier equation for an elastic plate with a circular hole and uniform thickness and demonstrated that the stress concentration factor in a circularly perforated three-dimensional elastic plate is sensitive to the plate thickness and Poisson's ratio. The condition starts to change from plane-stress to plane-strain when the ratio of hole radius to plate thickness is 0.5. When this ratio is less than 0.5, the maximum stress concentration factor occurs at the mid-plane and when this ratio exceeds 0.5, the maximum stress concentration factor occurs close to the external traction-free surfaces [96–99].

Based on the generalized plane-strain assumption that the out-of-plane strain is a constant in thickness direction, Kotousov et al. (2002) provided an analytical solution for the three-dimensional stress distribution in an isotropic perforated plate having arbitrary thickness. They considered the effects of Poisson's ratio and plate thickness on the in-plane stress concentration factor and the out-of-plane stress constraint factor [100–103].

Yang et al. (2008) studied the coupled influence of Poisson's ratio and plate thickness on the stress and strain concentration factors using finite element method (FEM). The magnitude of their stress and strain concentration factors differ which rise the importance of the strain concentration factor and the maximum strain concentration factor [104].

Dai and Gong (2013), by also assuming the out-of-plane strain in the thickness direction is a constant, obtained a theoretical solution for the three-dimensional stresses in an infinite isotropic elastic plate perforated with a circular hole. Their results show differences between the three-dimensional and plane-stress solutions, a significant effect of the Poisson's ratio on the tangential stress near the surface of the hole, and the effects of the plate thickness and Poisson's ratio on the stress concentration and the out-of-plane constraint factors [105].

The previously discussed analyses are for isotropic materials. While extensive acceptance and use of orthotropic composite structures require confidence in their load carrying capacity, the author is unaware of prior publications addressing the 3D stress or strain concentrations associated with circular cutouts in thick orthotropic plates. The fact that orthotropic materials can produce extremely high stress concentrations compared with isotropic materials motivates the need to know the stresses in orthotropic/composite structures containing holes or notches, including when the thickness is large compared with the size of the discontinuities.

Although Yang [104] has made extensive study of the effect of thickness and Poisson ratio in stress and strain concentration factors for a finite thickness elastic plate with a circular hole, rather less attention has been paid to case for orthotropic material. The purpose of the present work is to present a comprehensive analysis on the 3D stress and strain field of a thick infinite plate holding a circular cutout and subjected to remote uniaxial stress. The stress and the strain concentration factors on the discontinuity boundary were studied through the thickness with changing the plate thickness and fiber direction. These effects of these parameters on the in-plane and out-of-plane stress constraint factors were also investigated. The present numerical solutions are verified by comparing them with some related results in literature.

8.3 Problem Definition

8.3.1 Geometry and Loading

A large, finite thickness homogeneous elastic plate containing a hole of radius a is subjected to far-field vertical tensile stress, σ, has a height $2H$, width $2W$ and thickness $2L$ as shown in Figure 8-1. The origin of the xyz coordinate system is located at the middle of the plate (and center of the hole). The plane $z = 0$ is at the mid-plane of the plate and the plate has external traction-free surfaces at $z = \pm L$. The half-width, W, and half-height, H, of the plate are taken to be 100 times the radius of the hole, i.e, W/a = H/a =100. The normalized half-thickness of the plate $\Delta = L/a$ is varied from 0.1 (plane-stress condition) to 10.

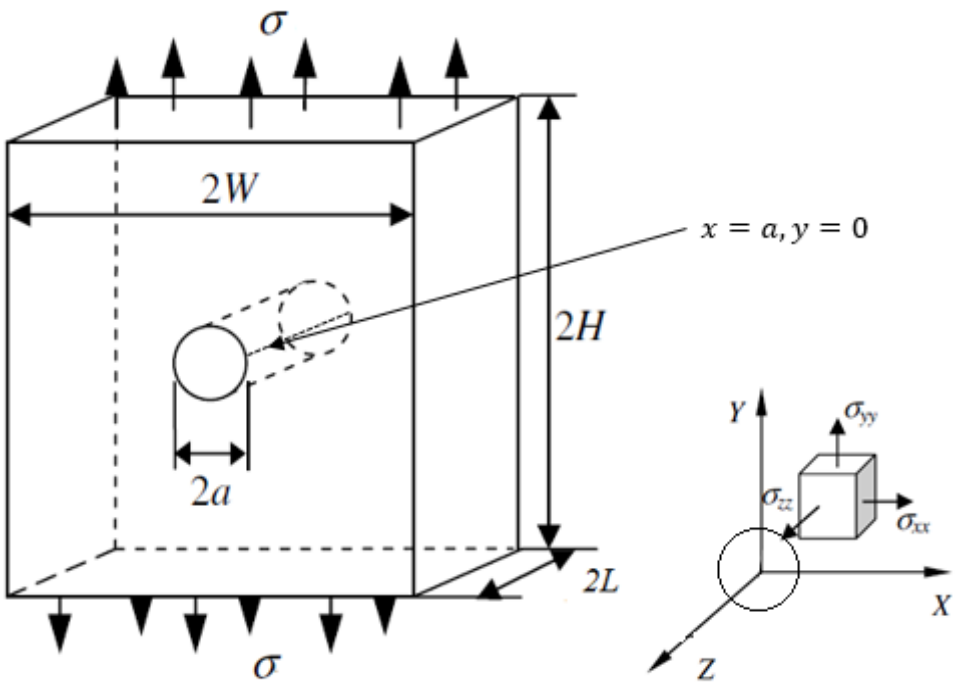

Figure 8-1: Plate geometry and coordinate system.

8.3.2 Stresses and Strains

The stress and strain concentration factors at the edge of the hole in vertical planes of $x = a,\ y = 0$ and $-L \le z \le L$ in Figure 8-1 are defined as

$$K^{\sigma} = \frac{\sigma_{yy}(a,0,z)}{\sigma_{net}}, \qquad K^{\varepsilon} = \frac{\varepsilon_{yy}(a,0,z)}{\varepsilon_{net}} \tag{8-1}$$

where $\sigma_{net} = \sigma A/A_{net}$ and $\varepsilon_{net} = \sigma A/EA_{net}$ are the nominal stress and strain at the net section of the plate, A is the gross area, i.e., $A = (2L)(2W)$ and the net area $A_{net} = (2W - 2a)(2L)$. The maximum stress, K^{σ}, and strain, K^{ε}, concentration factors occurring along the z-axis at $x = a$ and $y = 0$ are denoted by $K^{\sigma}_{\max}$ and $K^{\varepsilon}_{\max}$, respectively. The values of K^{σ} and K^{ε} at $x = a, y = 0$ and $z = 0$ (at the mid-plane) are denoted by K^{σ}_{mp} and $K^{\varepsilon}_{\mathrm{mp}}$. The corresponding values of K^{σ} and K^{ε} on the external traction-free surfaces of the plate ($x = a$, $y = 0$ and $z = \pm L$) are denoted by $K^{\sigma}_{\mathrm{sur}}$ and $K^{\varepsilon}_{\mathrm{sur}}$, i.e.

$$K^{\sigma}_{\max} = \max_{0\le z\le L} \frac{\sigma_{yy}(a,0,z)}{\sigma_{net}}, \qquad K^{\varepsilon}_{\max} = \max_{0\le z\le L} \frac{\varepsilon_{yy}(a,0,z)}{\varepsilon_{net}} \tag{8-2}$$

$$K^{\sigma}_{\mathrm{mp}} = \frac{\sigma_{yy}(a,0,0)}{\sigma_{net}}, \qquad K^{\varepsilon}_{\mathrm{mp}} = \frac{\varepsilon_{yy}(a,0,0)}{\varepsilon_{net}} \tag{8-3}$$

$$K^{\sigma}_{\mathrm{sur}} = \frac{\sigma_{yy}(a,0,\pm L)}{\sigma_{net}}. \; K^{\varepsilon}_{\mathrm{sur}} = \frac{\varepsilon_{yy}(a,0,\pm L)}{\varepsilon_{net}} \tag{8-4}$$

The stress and strain concentration factors for plane-stress condition (i.e., plate thin compared with size of geometric discontinuities) are independent of Poisson's ratio and modulus of elasticity for an isotropic material and are denoted by K^{σ}_{ps} and $K^{\varepsilon}_{\mathrm{ps}}$, respectively.

For a plane-stress state when the plate is only subjected to a stress in the y-direction, the stresses in x- and z-directions are zero ($\sigma_{xx} = \sigma_{zz} = 0$) so the strain concentration factor in plane-stress condition is $K^{\varepsilon}_{\mathrm{ps}} = \varepsilon_{yy}/\varepsilon_{net} = \sigma_{yy}/E\varepsilon_{net}$. For a plane-strain state when the plate is only subjected to a stress in the y-direction, the stresses in x- and z-directions are $\sigma_{xx} = 0$ and $\sigma_{zz} = \nu\sigma_{yy}$ so the plane strain concentration factor $K^{\varepsilon}_{\text{plane strain}} = \varepsilon_{yy}/\varepsilon_{net} = \sigma_{yy}(1-\nu^2)/E\varepsilon_{net}$. For an isotropic plate under plane stress condition with a circular hole and subjected to unidirectional tensile load σ in y-axis, the plane stress distribution solution in the plane $y = 0$ in the vicinity of a hole tip from the classical solution [92] is

$$\frac{\sigma_{xx}(x,0)}{\sigma} = \frac{3}{2\zeta^2}[1-\zeta^{-2}] \tag{8-5}$$

$$\frac{\sigma_{yy}(x,0)}{\sigma} = \frac{1}{2}[2+\zeta^{-2}+3\zeta^{-4}] \tag{8-6}$$

where $\zeta = x/a$ such that $\zeta \ge 1$.

For the three-dimensional state of stress around a circular hole of radius a in an isotropic plate of thickness $2L$ subjected to a unidirectional tensile stress σ parallel to the y-axis, Sternberg and Sadowsky (1949) determined the radial, σ_{rr}, tangential, $\sigma_{\theta\theta}$ and axial, σ_{zz} stresses in the vicinity of the edge of the hole to be [94]

$$\frac{\sigma_{rr}}{\sigma} = \frac{1}{2}\left(1 - \frac{1}{\rho^2}\right) + \frac{1}{2}\left(1 - \frac{4}{\rho^2} + \frac{3}{\rho^4}\right)\cos 2\theta + \frac{1}{2\Delta^2}\bar{Z}_n''\cos 2\theta \sum_{i=1}^{2} L\frac{\lambda_{1i}}{\rho^{q+i}} \tag{8-7}$$

$$\begin{aligned}\frac{\sigma_{\theta\theta}}{\sigma} = {} & \frac{1}{2}\left(1 + \frac{1}{\rho^2}\right) - \frac{1}{2}\left(1 + \frac{3}{\rho^4}\right)\cos 2\theta \\ & + \frac{1}{2\Delta^2}\bar{Z}_n''\cos 2\theta \sum_{i=1}^{2}\frac{1}{\rho^{q+i}}\{[-(q+i-1)L+1]\lambda_{1i} + L(\lambda_{2i} + 2\lambda_{3i})\}\end{aligned} \tag{8-8}$$

$$\begin{aligned}\frac{\sigma_{zz}}{\sigma\cos 2\theta} = {} & \frac{1}{2}\bar{Z}_n\sum_{i=1}^{2}\frac{1}{\rho^{q+i+2}}\{[4(q+i-1)L-4]\lambda_{1i} + [(q+i-4)L-1]\lambda_{2i} \\ & + [-2(q+i+2)L+2]\lambda_{3i}\}\end{aligned} \tag{8-9}$$

where $\rho = r/\mathrm{a}$ are dimensionless cylindrical coordinates, $\Delta = L/\mathrm{a}$ is normalized thickness ratio, $\bar{Z}_n = \bar{Z}_n(\xi) = \Delta^4(\xi^n - 1)^2$ and $\bar{Z}_n''$ are the second derivative with respect to $\xi = z/L$, $L(r) = \ln r$, and the exponents n, q as well as the values of $\lambda_{\alpha i}$ ($\alpha = 1,2,3$; $i = 1,2$) are parameters which depend on Δ and ν. The angle θ is measured counterclockwise from negative y-axis. When $\Delta \to 0$, the last term of equation diminishes to zero and the equations reduce to plane-stress. At the mid-plane, i.e., $\xi = 0$, the last term also vanishes and the equations reduce to plane-stress regardless of the value of thickness, Δ.

To study and describe the characteristic of the stress fields in a finite thickness plate, two constraint parameters namely out-of-plane T_z and in-plane T_x stress constraint factors are introduced and defined as follow

$$T_z = \frac{\sigma_{zz}}{\sigma_{xx} + \sigma_{yy}} \tag{8-10}$$

$$T_x = \frac{\sigma_{xx}}{\sigma_{yy}} \tag{8-11}$$

For plane stress, $\sigma_{zz} = 0$, and for plain-strain in an isotropic material, $\sigma_{zz} = \nu(\sigma_{xx} + \sigma_{yy})$, where ν is the Poisson's ratio, thus, T_z varies from 0 for plane-stress condition to a maximum value which is ν for plane-strain condition for an isotropic material. The T_z for a finite thickness plate of an elastic, isotropic, and homogeneous material is $0 \leq T_z \leq \nu$.

For an orthotropic material $\sigma_{zz} = \nu_{zx}\sigma_{xx} + \nu_{zy}\sigma_{yy}$ so $T_z = (\nu_{zx}\sigma_{xx} + \nu_{zy}\sigma_{yy})/(\sigma_{xx} + \sigma_{yy})$. For an elastic and isotropic material in three dimensional stress state, ε_{yy} can be evaluated from Hooke's law as

$$\varepsilon_{yy} = \frac{1}{E}[\sigma_{yy} - \nu(\sigma_{xx} + \sigma_{zz})] \tag{8-12}$$

Dividing equation (8-12) by ε_{net}, rearranging and setting $\sigma_{net} = E_y\varepsilon_{net}$, the following expression can be obtained

$$K^{\varepsilon} = K^{\sigma}[1 - \nu(T_x + T_z + T_x \cdot T_z)] \tag{8-13}$$

Where T_x and T_z are the in-plane and out-of-plane stress constraint factors, respectively. The in-plane stress constraint factor T_x and the ratio of the stress concentration factor K^{σ} to the stress

concentration K_{ps}^{σ} of the plane stress on different plane layer for different thickness can be derived from equations (8-5) and (8-6) for isotropic materials

$$T_x = \frac{\sigma_{xx}(x,0)}{\sigma_{yy}(x,0)} = \frac{3(1-\zeta^{-2})}{\zeta^2(2+\zeta^{-2}+3\zeta^{-4})} \tag{8-14}$$

$$\frac{K^{\sigma}(x,0)}{K_{\mathrm{ps}}^{\sigma}} = \frac{1}{6}(2+\zeta^{-2}+3\zeta^{-4}) \tag{8-15}$$

In elasticity state for a finite thickness plate, the strain concentration stress factor and stress concentration stress factor are different and a function of Poisson ratio and the distributions of in-plane and out-of-plane stress constraint factors.

For a plane-stress state in an orthotropic plate subjected to a stress in the y-direction, the stresses in x- and z-directions are zero ($\sigma_{xx} = \sigma_{zz} = 0$) so the strain concentration factor in plane-stress condition is $K_{\mathrm{ps}}^{\varepsilon} = \varepsilon_{yy}/\varepsilon_{net} = \sigma_{yy}/E_y\varepsilon_{net}$. For a plane-strain state when the plate is only subjected to a stress in the y-direction, the stresses in x- and z-directions are $\sigma_{xx} = 0$ and $\sigma_{zz} = \nu_{zy}\sigma_{yy}$ so the plane-strain concentration factor $K_{\text{plane strain}}^{\varepsilon} = \varepsilon_{yy}/\varepsilon_{net} = \sigma_{yy}\left(1-\nu_{\mathrm{yz}}\nu_{zy}\right)/E_y\varepsilon_{net}$.

For a plane-stress, perforated infinite orthotropic plate subjected to a unidirectional tensile stress σ parallel to the y-axis, the in-plane vertical stress distribution solution at $y = 0$ in the vicinity of the edge of the hole is [55]

$$\frac{\sigma_{yy}(x,0)}{\sigma} = 1 + Re\left\{\frac{1}{\beta-\delta}\left[\frac{-\delta(1-i\beta)}{\sqrt{\zeta^2-1-\beta^2}\left(\zeta+\sqrt{\zeta^2-1-\beta^2}\right)}\right.\right.$$
$$\left.\left. + \frac{-\beta(1-i\delta)}{\sqrt{\zeta^2-1-\delta^2}\left(\zeta+\sqrt{\zeta^2-1-\delta^2}\right)}\right]\right\} \tag{8-16}$$

where β and δ are the distinct imaginary parts of complex material properties, equation (2-29), and $\zeta = x/a$ such that $\zeta \geq 1$. For an elastic orthotropic material in three dimensions, the strains ε_{yy} can be evaluated from Hooke's law as [106]

$$\varepsilon_{yy} = \frac{\sigma_{yy}}{E_y} - \frac{\nu_{xy}}{E_x}\sigma_{xx} - \frac{\nu_{zy}}{E_z}\sigma_{zz} = \frac{\sigma_{yy}}{E_y}\left[1 - \frac{\nu_{yx}\sigma_{xx}}{\sigma_{yy}} - \frac{\nu_{yz}\sigma_{zz}}{\sigma_{yy}}\right] \tag{8-17}$$

Dividing equation (8-17) by ε_{net}, rearranging and setting $\sigma_{net} = E_y\varepsilon_{net}$, the following expression can be obtained

$$K^{\varepsilon} = K^{\sigma}\left[1 - \nu_{yx}T_x - \nu_{yz}T_z - \nu_{yz}T_x \cdot T_z\right] = K^{\sigma}\left[1 - \nu_{yx}T_x - \nu_{yz}T_z(T_x+1)\right] \tag{8-18}$$

For a finite thickness orthotropic plate, the ratio of stress and strain concentration factors, $K^{\varepsilon}/K^{\sigma}$, is a function of Poisson's ratios ν_{yx} and ν_{yz} and the in-plane, T_x, and out-of-plane, T_z, stress constraint factors, equation (8-18). Note that $T_x = \sigma_{xx}/\sigma_{yy} = 0$ at $(a, 0, z)$ for all values of z and $T_z = \sigma_{zz}/(\sigma_{xx} + \sigma_{yy}) = 0$ at the external traction-free surface $(x, 0, \pm L)$ so the stress and strain concentration factors are equal, $K^{\sigma} = K^{\varepsilon}$.

8.3.3 Material Properties

The analysis of studying the variation of the stress and strain concentration factors for varying plate thicknesses has been carried out for both isotropic and orthotropic cases. For the isotropic material, the Young's Modulus E is set to be 200 GPa and the analysis has been carried out for three values of Poisson's ratio ν which are 0.2, 0.3, and 0.4. By fixing the thickness, the Poisson's ratio has been changed from 0 (mathematically) to 0.45 to study the effect of Poisson's ratio on stress and strain concentration factor. Practically, the values of Poisson's ratio for actual isotropic materials are seldom less than approximately 0.3. For the orthotropic material, the constitutive properties of the Sitka Spruce Wood as tabulated in Table 8-1 were employed in this analysis. The xy-plane of the orthotropic wood plate is in longitudinal (grain orientation) and tangential plane of the wood and the axis of the hole is parallel to the radial direction of the wood or z-direction, Figure 8-1.

Table 8-1: Constitutive properties of the Sitka Spruce wood [88].

Moduli of Elasticity		Moduli of Rigidity		Poisson's ratio			
E_L (MPa)	11450	G_{LT} (MPa)	698	ν_{LT}	0.47	ν_{TL}	0.03
E_T (MPa)	492	G_{TR} (MPa)	34.4	ν_{TR}	0.25	ν_{RT}	0.46
E_R (MPa)	893	G_{RL} (MPa)	733	ν_{RL}	0.04	ν_{LR}	0.37

Note: L, T, and R denote longitudinal, tangential, and radial directions of the wood.

8.3.4 Validation of the Finite Element Model

Due to the symmetry and by applying appropriate boundary condition constraint at the plane of symmetry, only one-eighth of the plate was modeled and analyzed. Eight node solid linear elements (Solid185) element type was utilized in this model. The model has been meshed by two different approaches, one of this method is by using a mapped mesh and the other approach is by using finer mesh near to the discontinuity and applying constraint equations between the teo different meshes. Mapped meshing utilized 20 planar layers through the thickness of the plate, 15 layers through radial direction, and 45 layers through tangential direction of the plate. The distance between each successive layers of the 20 planar layers are kept fixed and the in-plane size of the element decreased gradually as one approached the hole as shown in Figure 8-2. The second approach is by using a finer mesh near the hole and coarse mesh otherwise. The interface of dissimilar meshes are linked together by developing degree of freedom (DOF) equations that connect the nodes of one mesh to the elements of the other. The finer and coarse region are meshed using mapped meshing where the finer meshing region are divided with 15 plane layers through its thickness and also along the radial and tangential direction. A mapped meshing for the coarse region has been utilized to mesh the model with 15 planar layers dividing the plate through its thickness, 20 layers through its radial direction, and 20 layers through its tangential direction as shown in Figure 8-3.

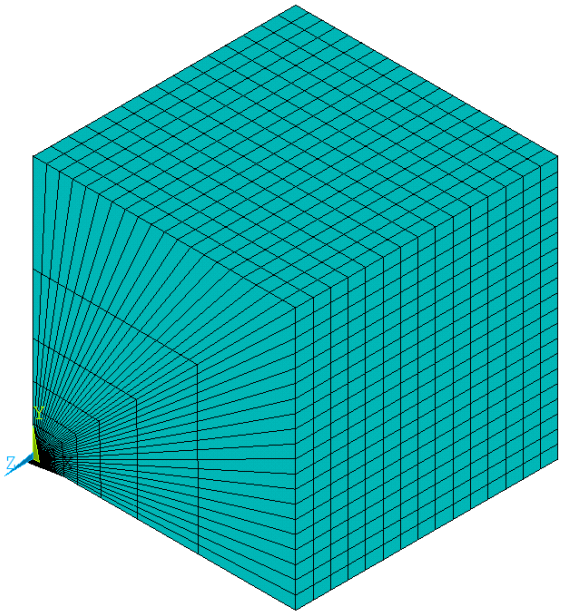

Figure 8-2: Mapped mesh used to mesh the plate.

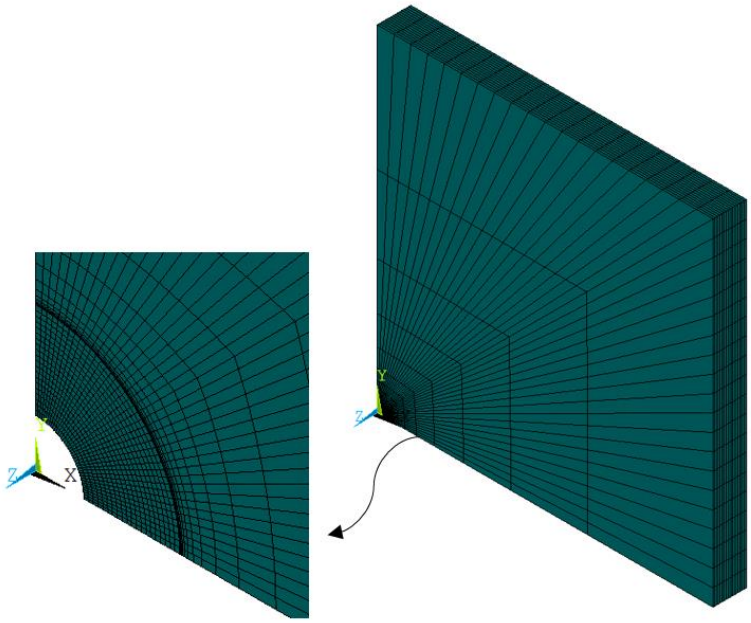

Figure 8-3: Finer mesh near the hole.

Because of the limited number of nodes allowed by ANSYS, this mesh was too coarse to produce satisfactory results in the region of the hole. For the mapped meshing model and model with finer mesh near to the hole, the number of elements and nodes are 2,700 and 29,946 and 2,800

and 31,857, respectively. A submodeling approach (also known as the cut-boundary displacement method) was subsequently employed. By creating a finer mesh near the hole and applying sub-modeling based on St. Venant's principle, more reliable results were obtained. However, accuracy necessitates the boundaries of the submodel be sufficiently far from the hole. This assumption is adequately validated by comparing it with 2D finite element analysis or any available analytical solution. The one-eighth submodel had 25,000 elements and 27,716 nodes. A coarse model or sometime called global model is firstly created and solved then the displacements of a cut through of this model will represent the specified boundary conditions of the new submodel. The required level of mesh refinement for this 3D model provides reasonable accurate results to solve the in-plane and through-thickness gradients of the stress and strain fields.

For an isotropic material, the stress solutions in x- and y- direction found from the plane stress conditions equations (8-5) and (8-6) have been plotted with the stresses found from the Finite Element solution in the front of the hole in order to validate the 3D Finite Element solution. The stresses, σ_{xx}, and, σ_{yy}, normalized to far-field stress, σ, in the front of the hole on different plane layers z/L are plotted versus $\zeta = x/a$ for three different values of thickness which are $\Delta = L/a = 1$ and 5 as shown in Figure 8-5 and Figure 8-7. The stresses on the mid plane ($z = 0$) for all the thickness values coincide with the plane stress solutions, equations (8-5) and (8-6), and deviate as the plane layer approaches the plate surface ($z = L$). The stress, σ_{yy}, on the plate surface is slightly less than the stress on the mid-plane or any different planes for all values of normalized thickness L/a. From this results for $L/a = 1$, almost all the solutions on any planes from 3D model coincide with the plane stress solutions, equations (8-5) and (8-6). This indicates that the Finite Element model provides reliable solutions as compared with the plane stress solution.

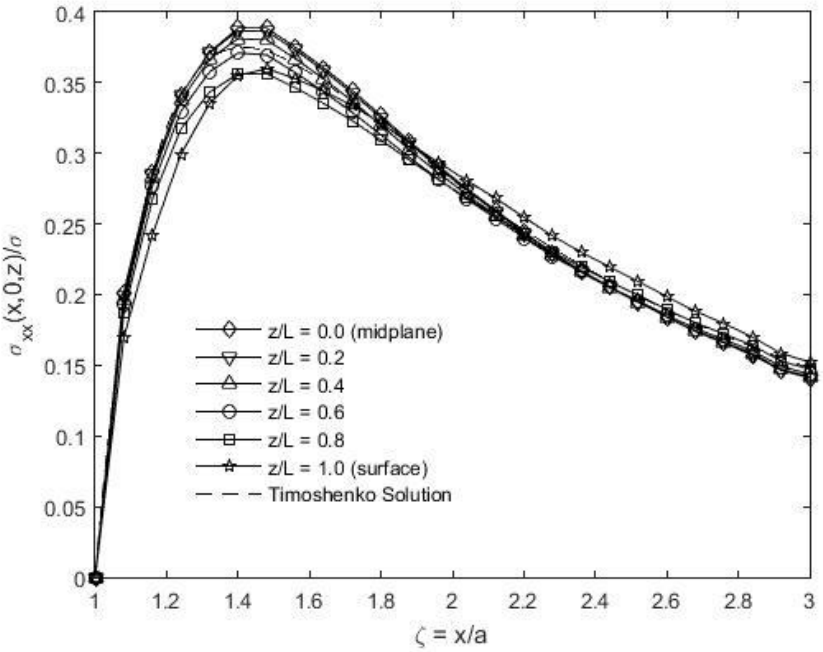

Figure 8-4: Normalized stresses distribution, σ_{xx}/σ, in $y = 0$ on different planes for thickness $\Delta = L/a$ = 1 and Poisson ratio ν = 0.3 in isotropic material from FE and equations (8-5).

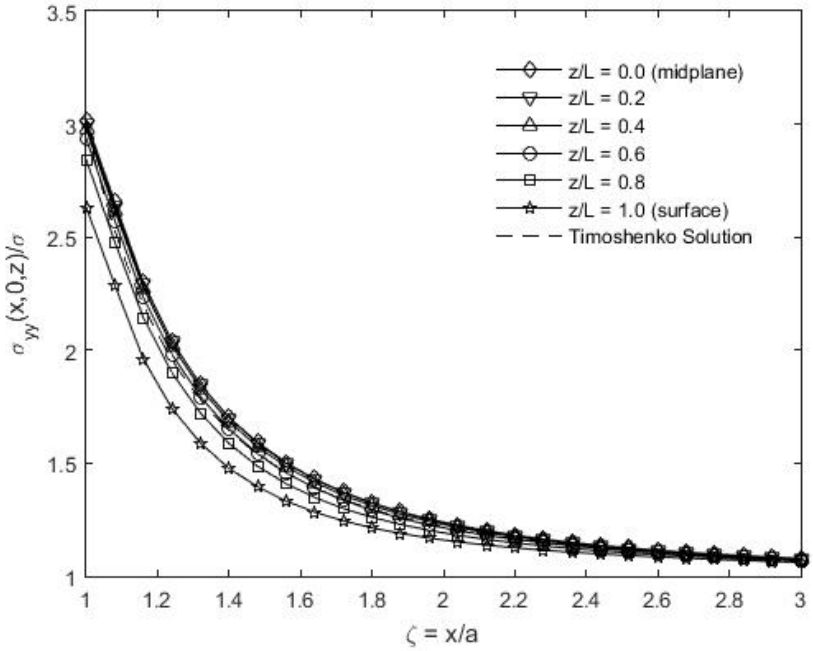

Figure 8-5: Normalized stresses distribution, σ_{yy}/σ, in $y = 0$ on different planes for thickness $\Delta = L/a$ = 1 and Poisson ratio ν = 0.3 in isotropic material from FE and equations (8-6).

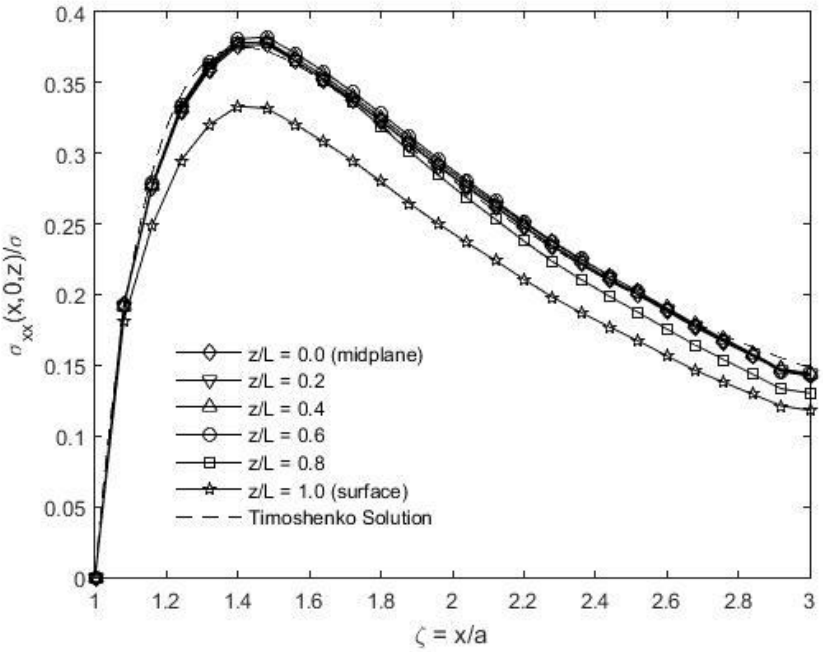

Figure 8-6: Normalized stresses distribution, σ_{xx}/σ, in $y = 0$ on different planes for thickness $\Delta = L/a$ = 5 and Poisson ratio ν = 0.3 in isotropic material from FE and equations (8-5).

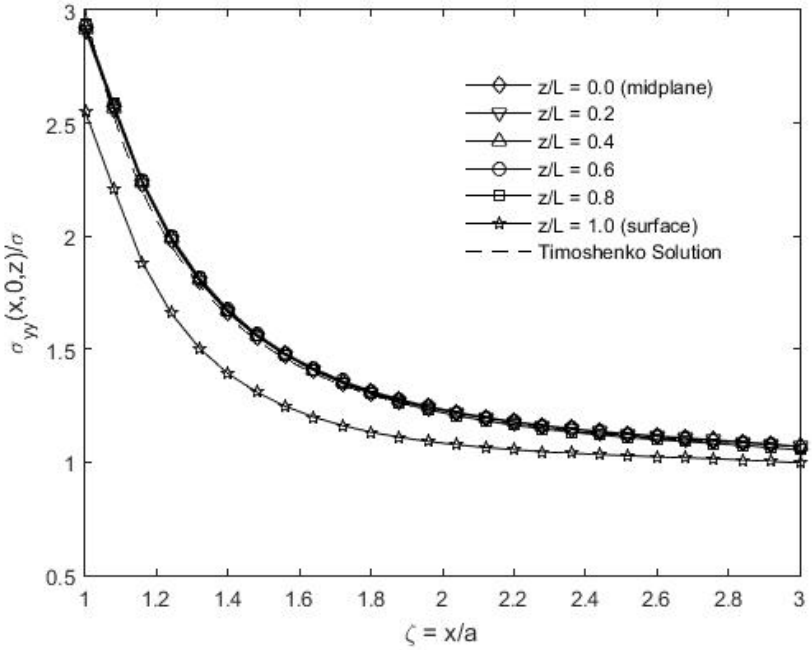

Figure 8-7: Normalized stresses distribution, σ_{yy}/σ, in $y = 0$ on different planes for thickness $\Delta = L/a$ = 5 and Poisson ratio ν = 0.3 in isotropic material from FE and equations (8-6).

Utilizing the 3D submodeling FEM approach described previously, Figure 8-8 compares the ANSYS result for the stress $\sigma_{zz,max}$, normalized by far-field stress, σ, with the analytical three-dimensional solution from Sternberq and Sadowsky, equation (8-9) [94] and Dai and Gong [105]. The agreement between these numerical and analytical results of Figure 8-8 further demonstrates the reliability of the present FEM model. The maximum value of the FE solution is in agreement with the exact plain-strain value $\sigma_{z,\max}/\sigma_0 = 2\nu$.

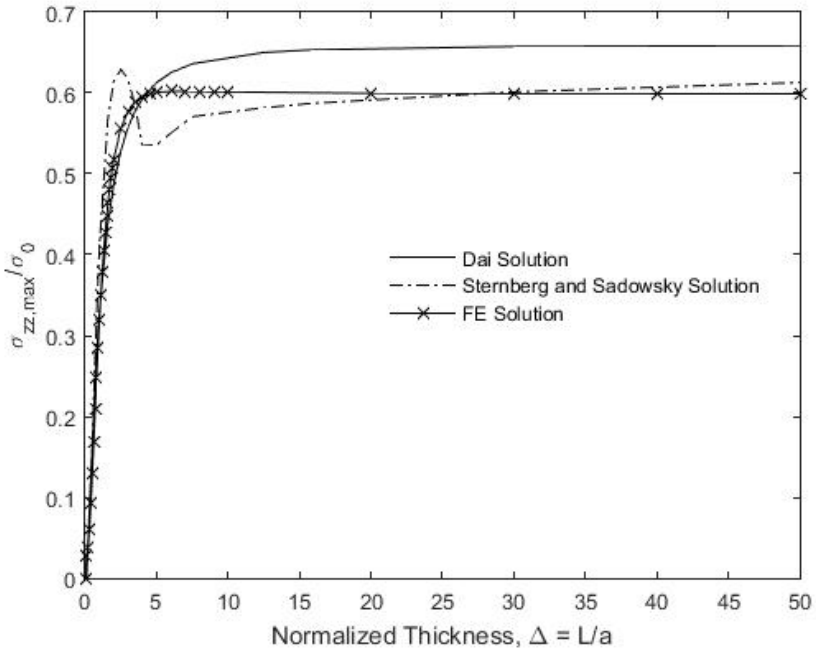

Figure 8-8: Analytical solutions from Sternberg and Sadowsky (1949) and Dai and Gong (2013) and FEM results for maximum normalized stress in the z-direction in a thick perforated isotropic plate and ν = 0.3.

For an orthotropic Sitka Spruce wood plate with properties listed in Table 8-1, the stress, σ_{yy}, normalized by far-field stress, σ, at the head of the hole tip on different plane layers z/L are plotted versus $\zeta = x/a$ for three different values of normalized thickness which are $\Delta = L/a = 1$ and 5 as shown in Figure 8-9 and Figure 8-10 when the grain orientation is parallel to the applied stress, σ, and the results are compared with plane stress solution, equation (8-16). As the thickness

of the plate is increased, the stress, σ_{yy}, does not change with ζ or the location of the planes z/L. These variation of the stress, σ_{yy}, on different planes parallel to the mid-plane shows that the Finite Element solution agrees with the solution of the plane-stress condition, equation (8-16). The distributions of the σ_{xx}/σ or σ_{yy}/σ for the isotropic and orthotropic materials on different planes for different thickness are similar.

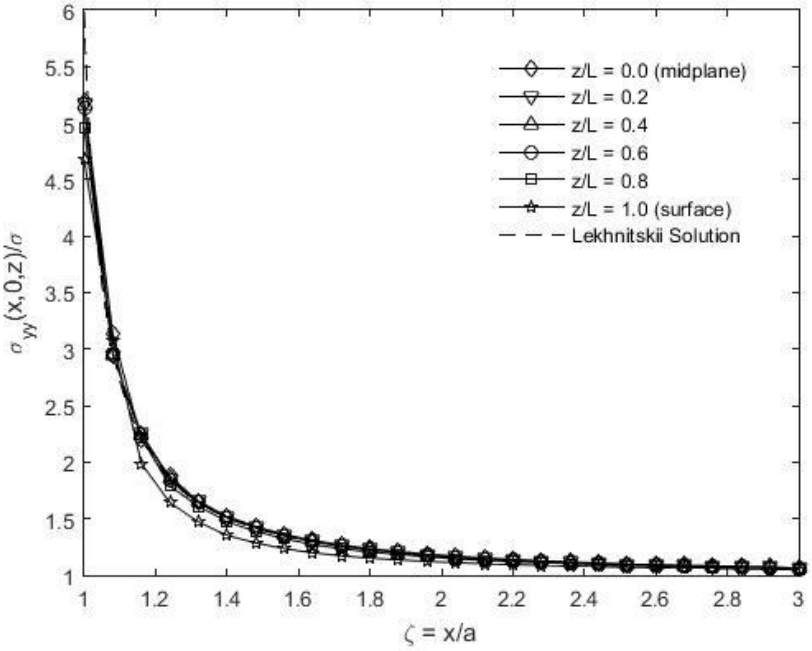

Figure 8-9: Stress distribution, $\sigma_{yy}(x,0,z)/\sigma$, in $y = 0$, $\zeta \geq 1$, and on different planes, z/L, for $\Delta = L/a$=1 in Sitka Spruce when grain orientation is parallel to the applied vertical stress, σ from FE and equation (8-16).

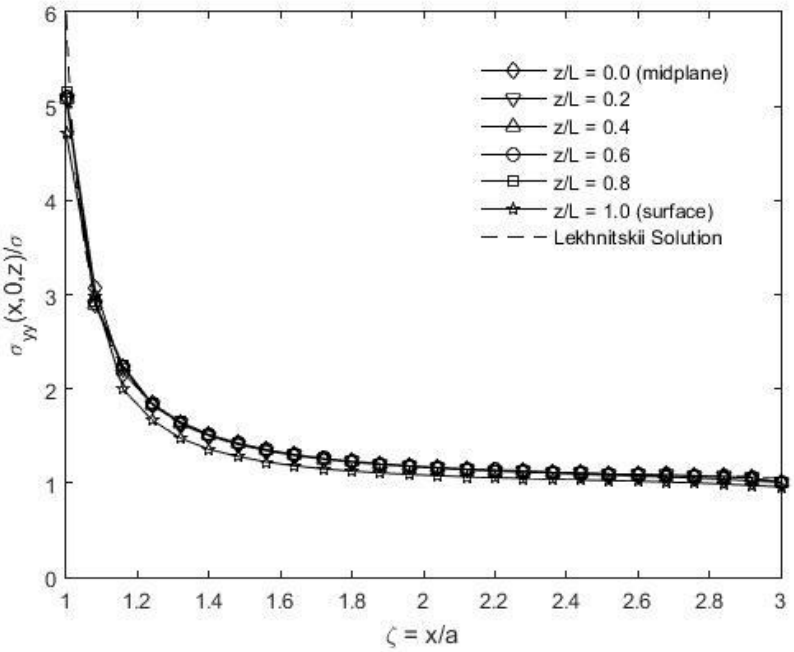

Figure 8-10: Stress distribution, $\sigma_{yy}(x,0,z)/\sigma$, in $y = 0$, $\zeta \geq 1$, and on different planes, z/L, for $\Delta = L/a$=5 in Sitka Spruce when grain orientation is parallel to the applied vertical stress, σ from FE and equation (8-16).

8.4 Results

8.4.1 In-plane Strees Distributation

The variations of $T_x = \sigma_{xx}/\sigma_{yy}$ and stress ratio $\sigma_{yy}(x,0,z)/\sigma_{yy}(a,0,z)$ predicted from the FE model versus $\zeta = x/a$ at $y = 0$ on different plane layers z/L and different normalized thicknesses ($\Delta = L/a$ = 1 and 5) are illustrated in Figure 8-11 through Figure 8-14 for an isotropic material and compared with equations (8-14) and (8-15). The distributions of T_x and $\sigma_{yy}(x,0,z)/\sigma_{yy}(a,0,z)$ for $\Delta = L/a$ = 1 agrees with the results found by Yang [104]. The distributions of T_x and $\sigma_{yy}(x,0,z)/\sigma_{yy}(a,0,z)$ with ζ on different plane layers are similar for all thickness values of L/a considered. The distributions of T_x with ζ on plane layers near the mid-plane almost coincide with each other but they change at end near the traction-free surface of the plate

where it changes with changing of normalized thickness L/a. The same observation for the distribution of $\sigma_{yy}(x,0,z)/\sigma_{yy}(a,0,z)$ with ζ except the distribution on the surface of the plate changes dramatically with the changing of normalized thickness L/a. These results show the distributions of T_x and $\sigma_{yy}(x,0,z)/\sigma_{yy}(a,0,z)$ are function of normalized thickness L/a, distance from the tip of the hole x/a, and location of the plane layer z/L. However, the effects of changes in z/L and L/a tend to be reasonable small. The equation of T_x, equation (8-14), could only describe the variation of T_x near the mid plane (i.e. small $\xi = z/L$) or near the tip of the hole (i.e. small $\zeta = x/a$).

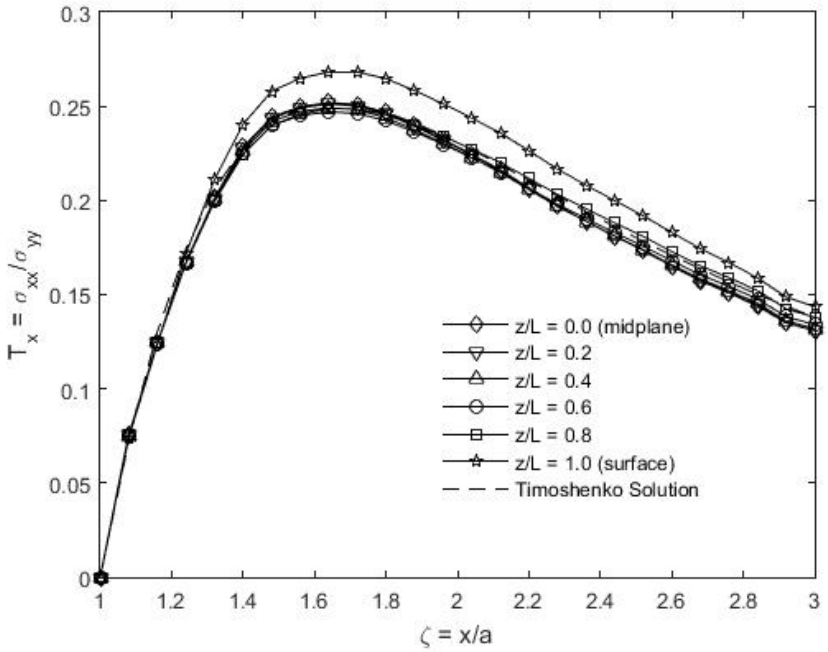

Figure 8-11: Variations of T_x in $y = 0$ and on different plane layers for thickness $\Delta = L/a$ = 1 in isotropic material with $\nu = 0.3$ from FE and equations (8-14).

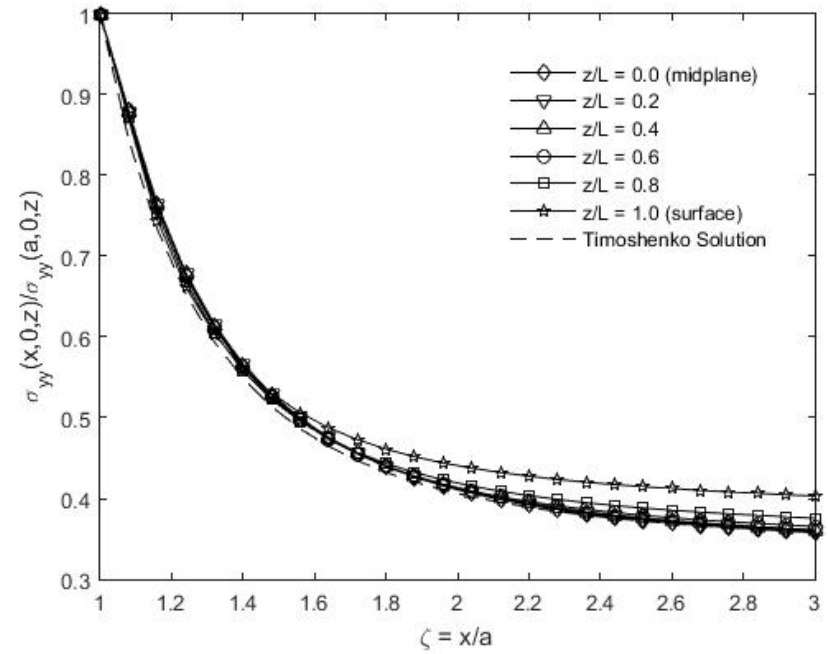

Figure 8-12: Variations of $\sigma_{yy}(x,0,z)/\ \sigma_{yy}(a,0,z)$ in $y = 0$ and on different plane layers for thickness $\Delta = L/a$ = 1 in isotropic material with $\nu = 0.3$ from FE and equations (8-15).

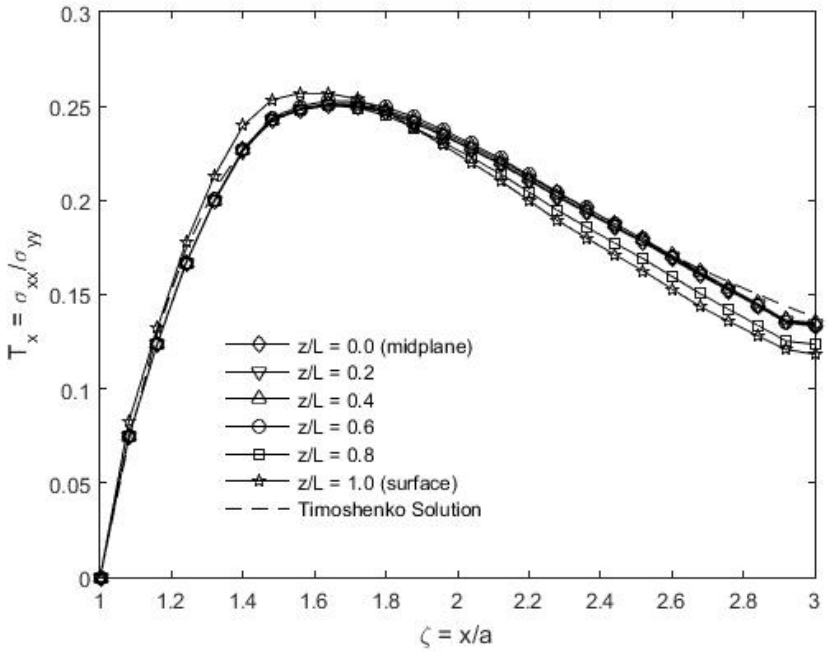

Figure 8-13: Variations of T_x in $y = 0$ and on different plane layers for thickness $\Delta = L/a$ = 5 in isotropic material with $\nu = 0.3$ from FE and equations (8-14).

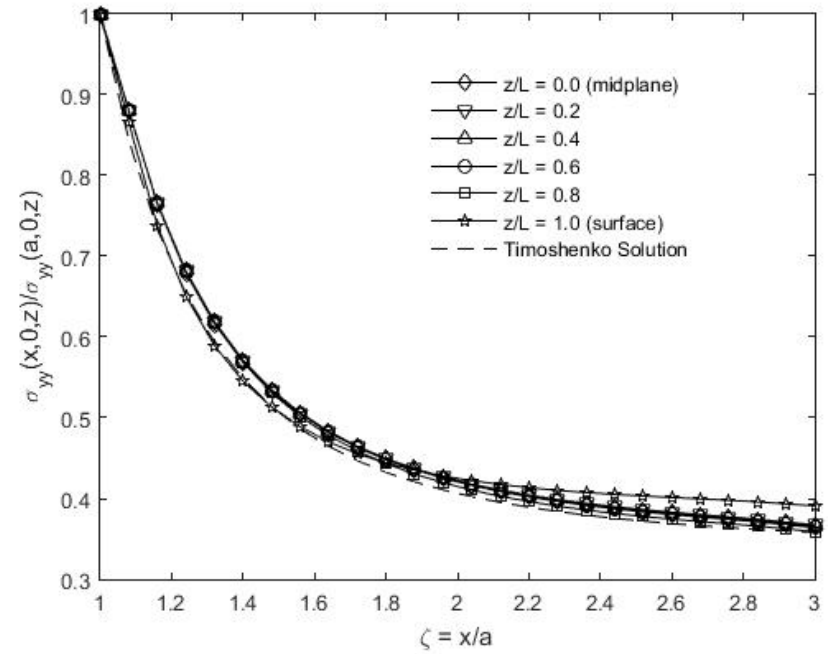

Figure 8-14: Variations of $\sigma_{yy}(x,0,z)/\ \sigma_{yy}(a,0,z)$, in $y = 0$ and on different plane layers for thickness $\Delta = L/a$ = 5 in isotropic material with $\nu = 0.3$ from FE and equations (8-15).

The variations of $T_x = \sigma_{xx}/\sigma_{yy}$ and stress ratio $\sigma_{yy}(x,0,z)/\sigma_{yy}(a,0,z)$ versus $\zeta = x/a$ at $y = 0$ on different vertical transverse planes $\xi = z/L$ for different normalized thicknesses $\Delta = L/a$ = 1 and 5 are illustrated in Figure 8-16 and Figure 8-18, respectively, when the grain direction is parallel to the applied stress, σ. These variations of T_x and $\sigma_{yy}(x,0,z)/\sigma_{yy}(a,0,z)$ in Sitka Spruce are similar to those for the isotropic case, although the present maximum value of T_x is considerably smaller. Values of T_{x} and $\sigma_{yy}(x,0,z)/\sigma_{yy}(a,0,z)$ at fixed $\zeta = x/a$ are virtually insensitive to the different layers, $\xi = z/L$.

If the wood grain orientation is perpendicular to the load, the variations of T_x and $\sigma_{yy}(x,0,z)/\sigma_{yy}(a,0,z)$ versus distances $\zeta = x/a$ away from the hole on different planes, $\xi = z/L$, for different normalized thicknesses $\Delta = L/a$ = 1 and 5 are illustrated in Figure 8-20 and Figure 8-22, respectively. The variations of T_x with ζ are now quite different than when the grain direction is parallel to the externally applied stress, σ, or for isotropy. Values of T_x increases monotonically to reach a relative maximum value. This response is also quite different than in Figure 8-16 and Figure 8-18 where values of T_x on the external traction-free surface in Figure 8-20 and Figure 8-22 are much higher than internal values.

The present numerically predicted variation of $\sigma_{yy}(x,0,z)/\sigma_{yy}(a,0,z)$ with ζ agrees reasonably well with the plane-stress solution of equation (8-16). The ratio $\sigma_{yy}(x,0,z)/\sigma_{yy}(a,0,z)$ decreased from 1 to 0.4 and 0.2 for isotropic and orthotropic materials, respectively, as ζ increases. Theoretically, $\sigma_{yy}(x,0,z)/\sigma_{yy}(a,0,z)$ approaches 0.33 and 0.17 as ζ reaches infinity for the isotropic and orthotropic cases, respectively. As the normalized thickness increases, the variation of T_x and $\sigma_{yy}(x,0,z)/\sigma_{yy}(a,0,z)$ with ζ on all the plane layers are the same.

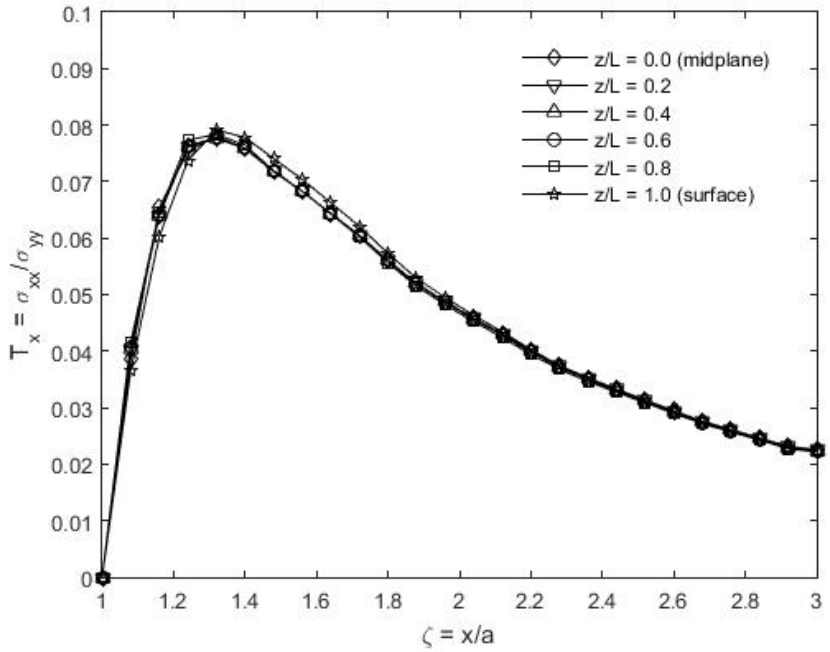

Figure 8-15: Variations of T_x in $y = 0$ and on different lateral plane layers for thickness $\Delta = L/a$ = 1 in Sitka Spruce when grain orientation is parallel to applied vertical stress, σ.

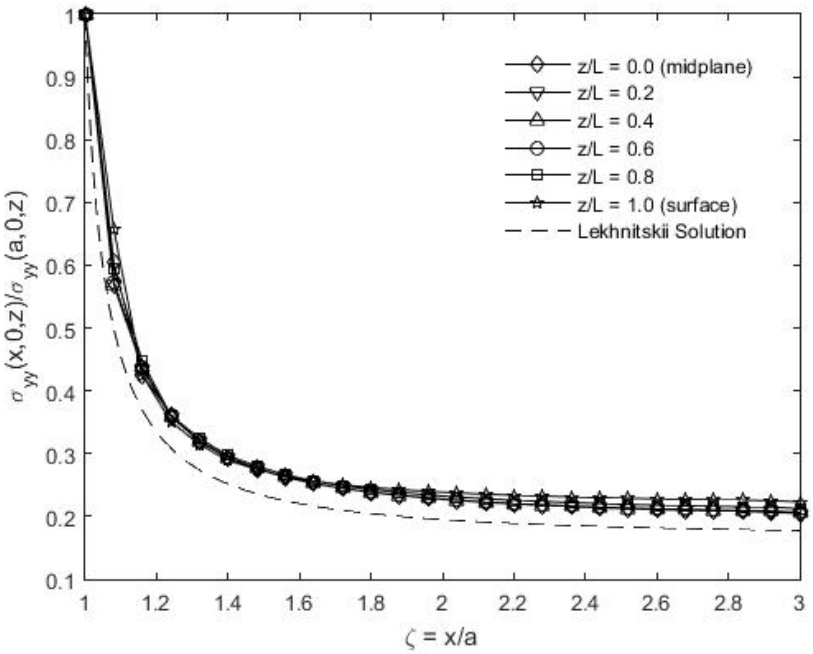

Figure 8-16: Variations of stress $\sigma_{yy}(x,0,z)/\sigma_{yy}(a,0,z)$ in $y = 0$ and on different lateral plane layers for thickness $\Delta = L/a$ = 1 in Sitka Spruce when grain orientation is parallel to applied vertical stress, σ.

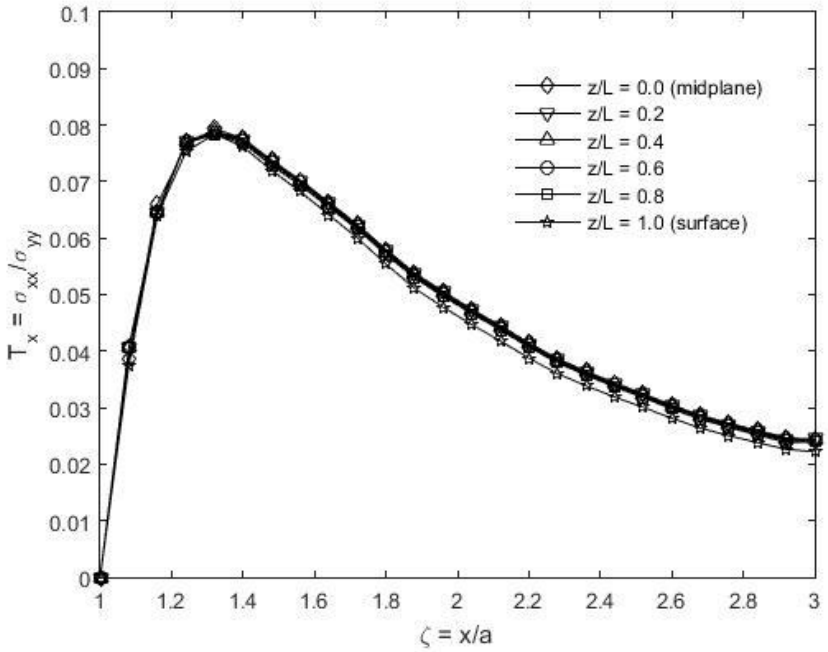

Figure 8-17: Variations of T_x in $y = 0$ and on different lateral plane layers for thickness $\Delta = L/a$ = 5 in Sitka Spruce when grain orientation is parallel to applied vertical stress, σ.

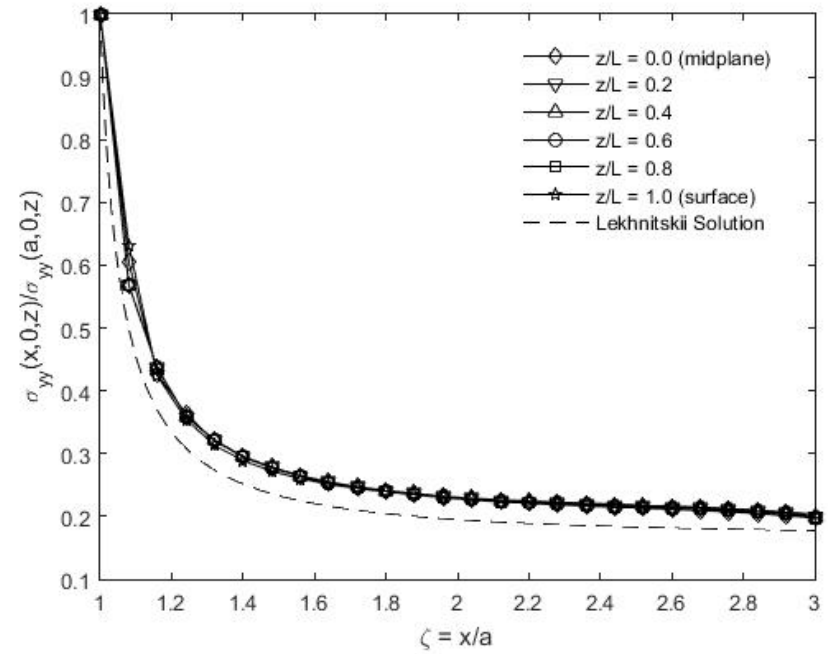

Figure 8-18: Variations of stress $\sigma_{yy}(x,0,z)/\sigma_{yy}(a,0,z)$ in $y = 0$ and on different lateral plane layers for thickness $\Delta = L/a$ = 5 in Sitka Spruce when grain orientation is parallel to applied vertical stress, σ.

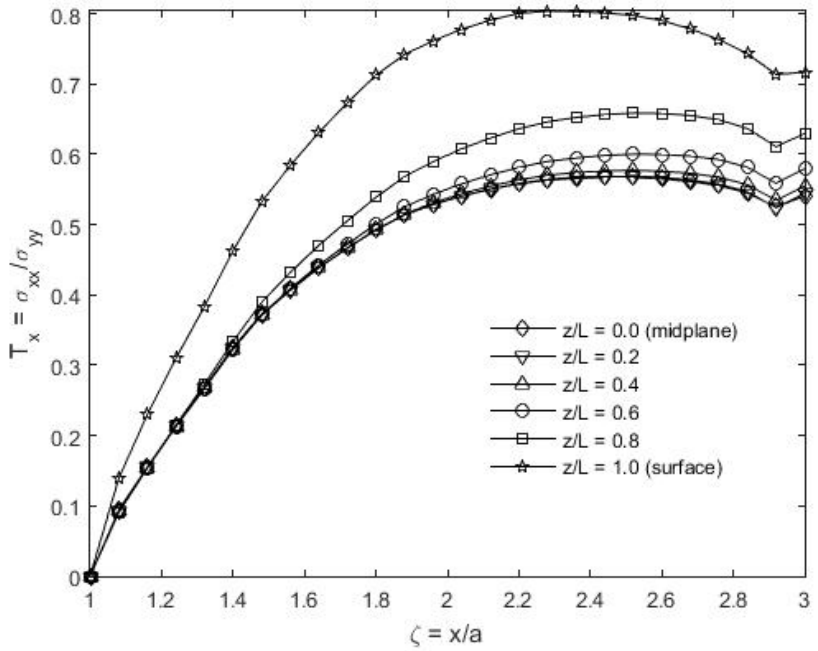

Figure 8-19: Variations of T_x at $y = 0$ and on different lateral plane layers for thickness L/a = 1 in Sitka Spruce when grain orientation is perpendicular to applied vertical stress, σ.

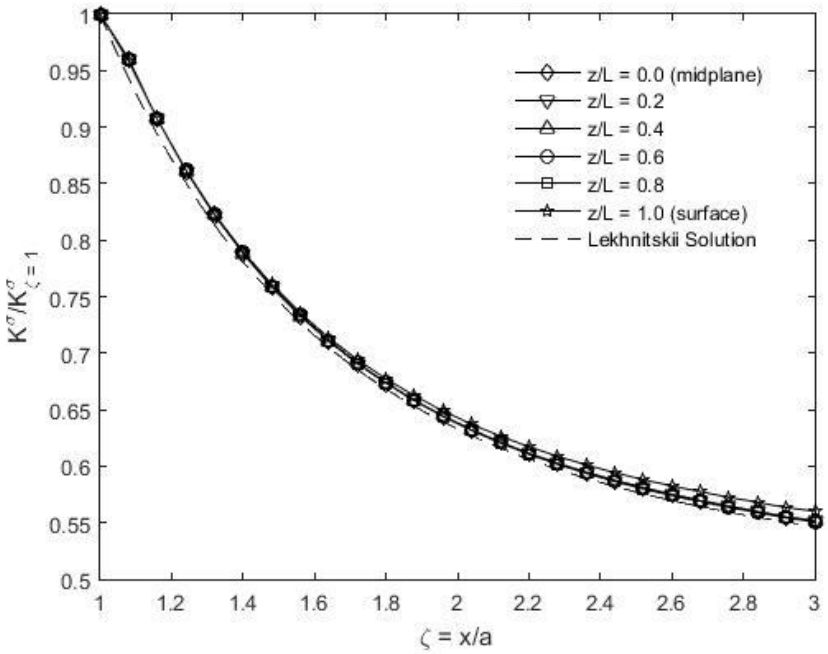

Figure 8-20: Variations of stress ratio $\sigma_{yy}(x,0,z)/\sigma_{yy}(a,0,z)$ at $y = 0$ and on different lateral plane layers for thickness L/a = 1 in Sitka Spruce when grain orientation is perpendicular to applied vertical stress, σ.

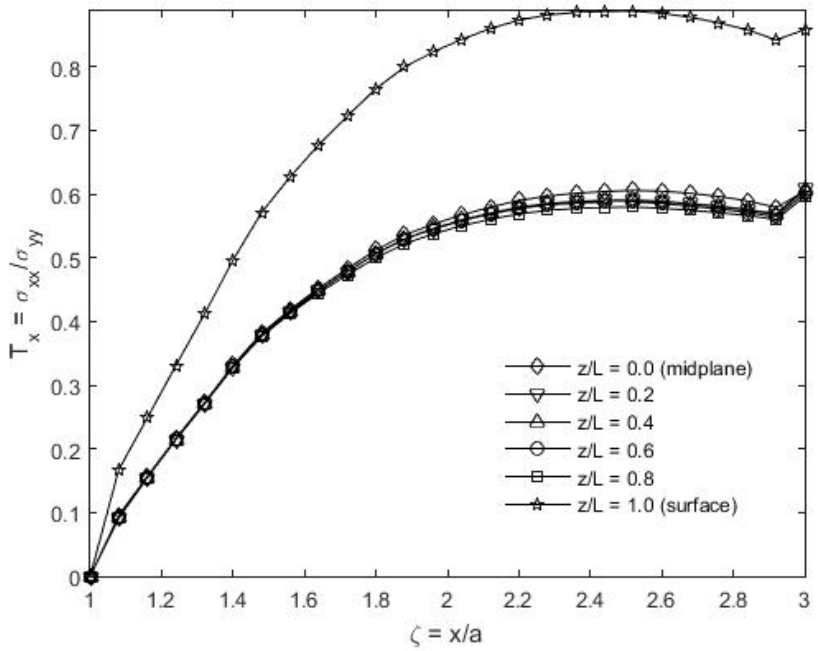

Figure 8-21: Variations of T_x at $y = 0$ and on different lateral plane layers for thickness L/a = 5 in Sitka Spruce when grain orientation is perpendicular to applied vertical stress, σ.

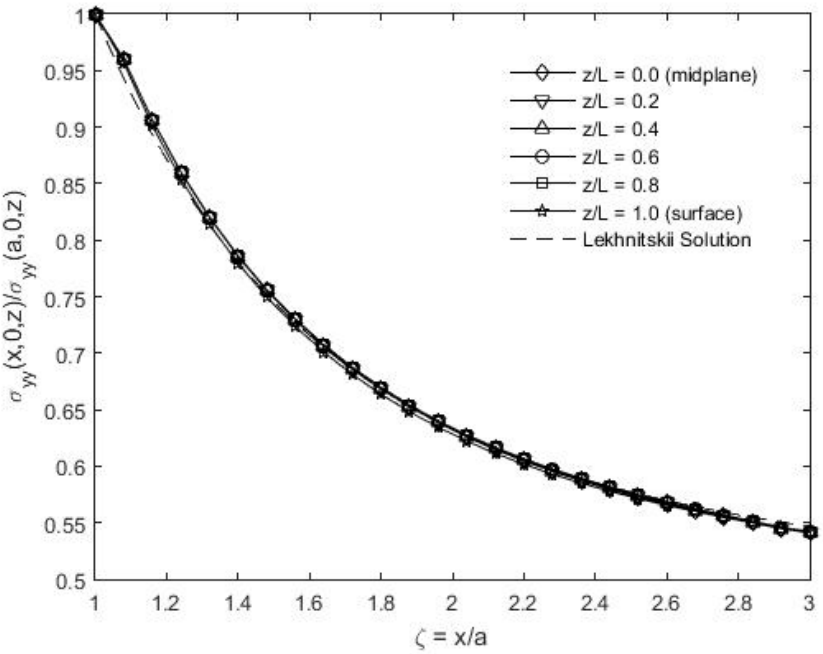

Figure 8-22: Variations of stress ratio, $\sigma_{yy}(x,0,z)/\sigma_{yy}(a,0,z)$, at $y = 0$ and on different lateral plane layers for thickness L/a = 5 in Sitka Spruce when grain orientation is perpendicular to applied vertical stress, σ.

8.4.2 Distributions of K^{σ} and K^{ε}

8.4.2.1 Distributions of K^{σ} and K^{ε} as Function of Plate Thickness

For the isotopic plate, the distributions of the stress, K^{σ}, and strain, K^{ε}, concentration factors normalized by the corresponding value of the mid-plane stress, K^{σ}_{mp}, and strain, $K^{\varepsilon}_{\mathrm{mp}}$, concentration factor for different normalized thickness L/a and for three values of Poisson's ratios ν = 0.2, 0.3, and 0.4 are illustrated in Figure 8-24 through Figure 8-28, respectively. The maximum ratio of the stress, $K^{\sigma}/K^{\sigma}_{\mathrm{mp}}$, or strain, $K^{\varepsilon}/K^{\varepsilon}_{\mathrm{mp}}$, concentration factor occurs on the mid-plane of the plate for small normalized thickness L/a (thin plates) and moves gradually with increasing normalized thickness L/a (thick plate) to the plane layer close to the plate surface. The distributions of $K^{\sigma}/K^{\sigma}_{\mathrm{mp}}$ and $K^{\varepsilon}/K^{\varepsilon}_{\mathrm{mp}}$ are weak at the middle region of the plate as the normalized thickness L/a is increasing. The corresponding thicknesses at which the maximum ratio of the stress, $K^{\sigma}/K^{\sigma}_{\mathrm{mp}}$, and strain, $K^{\varepsilon}/K^{\varepsilon}_{\mathrm{mp}}$, concentration factor shifts from mid-plane to a different plane layer are called transition thickness, L^{*}_{σ}, of the stress concentration factor and the transition thickness, L^{*}_{ε}, of the strain concentration factor, respectively. For all the values of the Poisson's ratio, the transition thickness, L^{*}_{σ}/a, of the stress concentration factor is approximately 3.5. The maximum value of $K^{\sigma}/K^{\sigma}_{\mathrm{mp}}$ increases slightly with increasing of Poisson's ratio, ν, and the normalized thickness L/a. The corresponding maximum values of $K^{\sigma}/K^{\sigma}_{\mathrm{mp}}$ for normalized thickness L/a = 10 and for Poisson's ratios ν = 0.2, 0.3, and 0.4 are 1.01, 1.02, and 1.03, respectively, and these values are located on plane layers at z/L = 0.84, 0.84, and 0.92, respectively.

For the values of the Poisson's ratios ν = 0.2, 0.3, and 0.4, the transition thicknesses, L^{*}_{ε}/a, of the strain concentration factors are approximately 1.9, 1.7, and 1.4, respectively. The maximum value of $K^{\varepsilon}/K^{\varepsilon}_{\mathrm{mp}}$ increases with increasing of Poisson's ratio, ν, and the normalized thickness,

L/a. The corresponding maximum values of $K^{\varepsilon}/K^{\varepsilon}_{\mathrm{mp}}$ for normalized thickness L/a = 10 and for Poisson's ratios ν = 0.2, 0.3, and 0.4 are 0.99, 0.98, and 0.96, respectively, and these values are located on plane layers at z/L = 0.92.

If the thickness of the plate or Poisson's ratio increases, the differences of K^{σ} and K^{ε} between the maximum value and the value of the mid-plane or surface increase. The maximum values of $K^{\sigma}/K^{\sigma}_{\mathrm{mp}}$ and $K^{\varepsilon}/K^{\varepsilon}_{\mathrm{mp}}$ do not always occur on the same plane layer, that is the transition thicknesses of the stress and strain concentration factor are not equal $L^{*}_{\sigma} \neq L^{*}_{\varepsilon}$. For a thick plate, the transition thickness L^{*}_{ε} of the strain concentration factor is smaller than the transition thickness L^{*}_{σ} of the stress concentration factor. The location of maximum $K^{\varepsilon}/K^{\varepsilon}_{\mathrm{mp}}$ on the corresponding plane layer is closer to the plate surface than the location of the plane layer of the maximum of $K^{\sigma}/K^{\sigma}_{\mathrm{mp}}$.

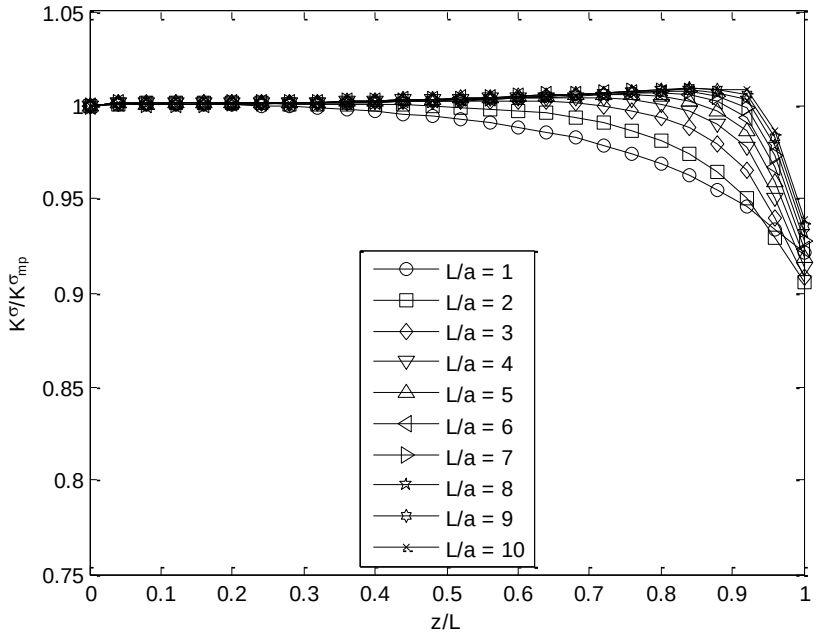

Figure 8-23: Distribution of stress concentration factors, K^{σ}, through thickness in isotropic plate for different normalized thicknesses and Poisson's ratio ν = 0.2.

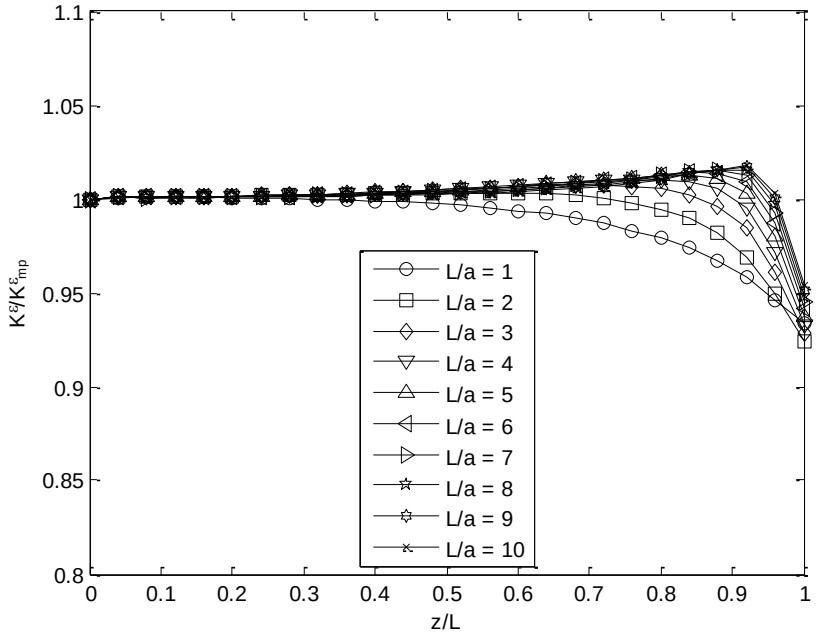

Figure 8-24: Distribution of strain concentration factors, K^{ε}, through thickness in isotropic plate for different normalized thicknesses and Poisson's ratio $\nu = 0.2$.

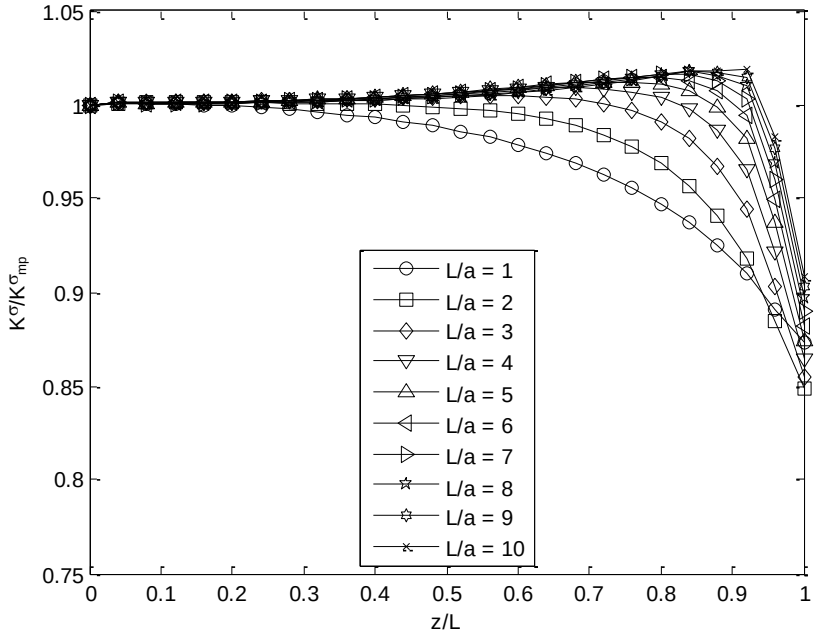

Figure 8-25: Distribution of stress concentration factors, K^{σ}, through thickness in isotropic plate for different normalized thicknesses and Poisson's ratio $\nu = 0.3$.

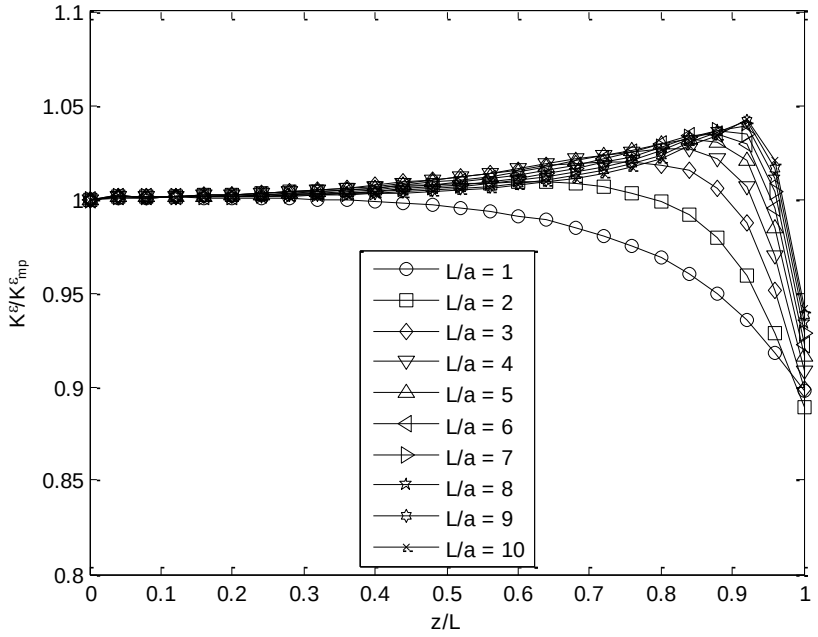

Figure 8-26: Distribution of strain concentration factors, K^{ε}, through thickness in isotropic plate for different normalized thicknesses and Poisson's ratio $\nu = 0.3$.

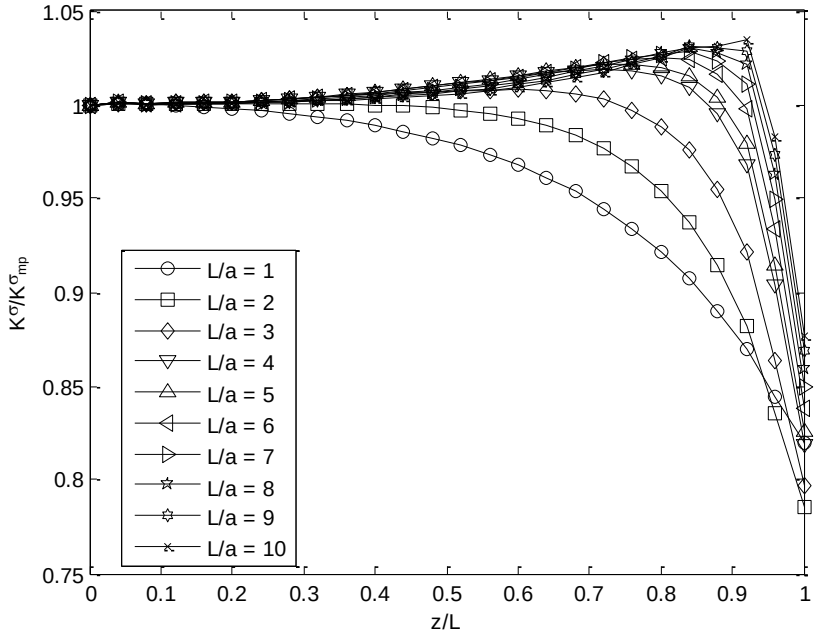

Figure 8-27: Distribution of stress concentration factors, K^{σ}, through thickness in isotropic plate for different normalized thicknesses and Poisson's ratio $\nu = 0.4$.

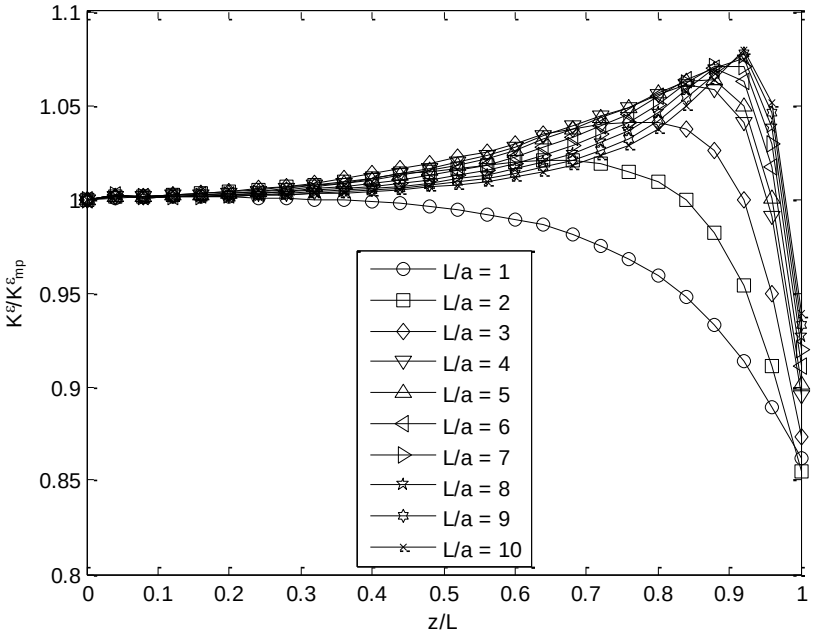

Figure 8-28: Distribution of strain concentration factors, K^{ε}, through thickness in isotropic plate for different normalized thicknesses with Poisson's ratio ν = 0.4.

For the orthotropic Sitka Spruce wood plate with properties listed in Table 8-1, the distributions of the stress, K^{σ}, and strain, K^{ε}, concentration factors normalized by the corresponding value of the mid-plane stress, K^{σ}_{mp}, and strain, $K^{\varepsilon}_{\mathrm{mp}}$, concentration factors with different normalized thicknesses L/a when the wood grain direction is parallel and perpendicular to the externally applied stress, σ, are illustrated in Figure 8-30 and Figure 8-32, respectively. As for the isotropic case, the maximum ratio of the stress, $K^{\sigma}/K^{\sigma}_{\mathrm{mp}}$, or strain, $K^{\varepsilon}/K^{\varepsilon}_{\mathrm{mp}}$, concentration factor occurs on the mid-plane of the plate for small normalized thicknesses L/a (thin plates) and moves gradually with increasing of the normalized thicknesses L/a (thick plate) to the plane layer close to the plate surface. The transition thicknesses L^{*}_{σ}/a of the stress concentration factor are approximately 7.0 in Figure 8-30 and 3.0 in Figure 8-32 when the grain direction is parallel and perpendicular to the vertical applied stress, σ, respectively. The stress concentration factors inside the wood plate can exceed those on the external traction-free surfaces by at least 8% (Figure 8-30) or 15% (Figure

8-32). The biggest differences occurs when $L/a = 1$. The plane layers when the maximum ratio of the stress concentration factor, $K^{\sigma}/K^{\sigma}_{\mathrm{mp}}$, starts shifting from the mid-plane are z/L = 0.92 and 0.36 when the grain direction is parallel and perpendicular to the vertical applied stress, σ, respectively. The maximum value of $K^{\sigma}/K^{\sigma}_{\mathrm{mp}}$ increases with increasing normalized thickness L/a. The corresponding maximum values of $K^{\sigma}/K^{\sigma}_{\mathrm{mp}}$ for normalized thickness L/a = 10 are 1.01 and 1.04 and these value are located on plane layers at z/L = 0.92 and 0.84 when the grain direction is parallel and perpendicular to the vertical applied stress, σ, respectively.

When the orientation of the wood grain is parallel to the applied stress, the variations of $K^{\varepsilon}/K^{\varepsilon}_{\mathrm{mp}}$, with respect to changes in thickness L/a, are relatively small in the middle region of the plate, Figure 8-30. However, when the wood grain orientation is perpendicular to the externally applied stress, Figure 8-32, the variation in $K^{\varepsilon}/K^{\varepsilon}_{\mathrm{mp}}$ increases with respect to changes in thickness. The transition thicknesses, L^{*}_{ε}/a, of the strain concentration factor are approximately 4.0 in Figure 8-30 and 1.7 in Figure 8-32 when the grain direction is parallel and perpendicular to the vertical applied stress, σ, respectively. The plane layers when the maximum ratio of the strain concentration factor, $K^{\varepsilon}/K^{\varepsilon}_{\mathrm{mp}}$, starts shifting from the mid-plane are z/L = 0.88 and 0.84. The maximum value of $K^{\varepsilon}/K^{\varepsilon}_{\mathrm{mp}}$ increases with increasing of the normalized thickness L/a. The corresponding maximum values of $K^{\varepsilon}/K^{\varepsilon}_{\mathrm{mp}}$ for normalized thickness L/a = 10 are 1.01 and 0.99 and these values are located on plane layers at z/L = 0.92 when the grain direction is parallel and perpendicular to the applied stress, σ, respectively. As the thickness of the plate increases, as the larger differences of K^{σ} and K^{ε} between the maximum value and the value of the mid-plane or surface are. The maximum values of $K^{\sigma}/K^{\sigma}_{\mathrm{mp}}$ and $K^{\varepsilon}/K^{\varepsilon}_{\mathrm{mp}}$ do not always occur on same plane layer, that is the transition thicknesses of the stress and the strain concentration factor are not equal $L^{*}_{\sigma} \neq L^{*}_{\varepsilon}$. For a

thick plate, the transition thickness L_{ε}^{*} of the strain concentration factor is smaller than the transition thickness L_{σ}^{*} of the stress concentration factor.

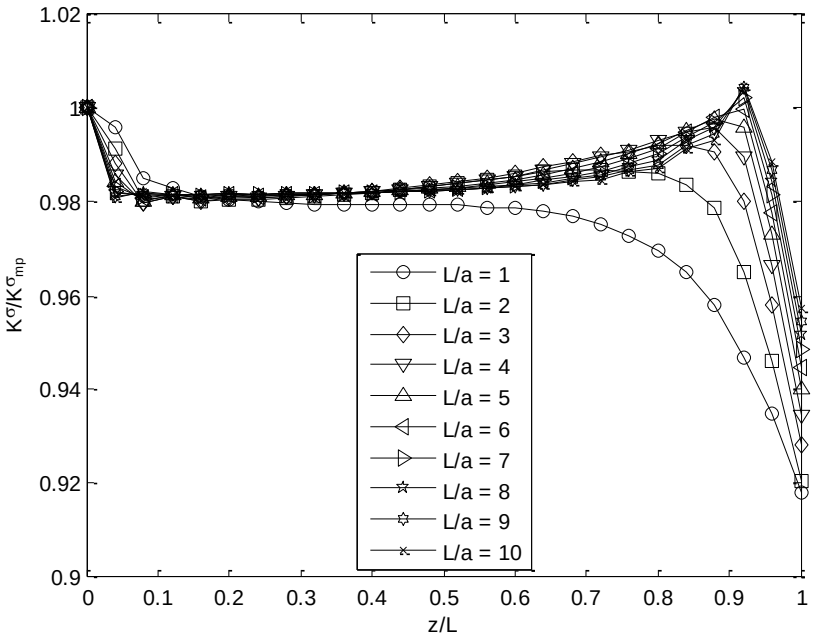

Figure 8-29: Distribution of normalized stress concentration factors, $K^{\sigma}/K^{\sigma}_{mp}$, through thickness in Sitka Spruce for different normalized thicknesses when longitudinal axis (grain orientation, L-direction) is parallel to applied vertical stress, σ.

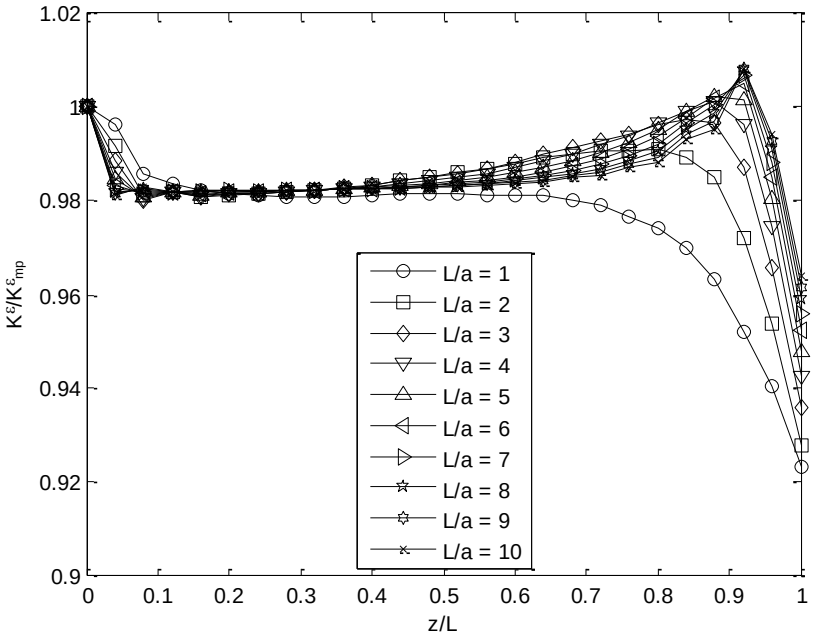

Figure 8-30: Distribution of normalized strain concentration factors, $K^{\varepsilon}/K^{\varepsilon}_{\text{mp}}$ through thickness in Sitka Spruce for different normalized thicknesses when longitudinal axis (grain orientation, *L*-direction) is parallel to applied vertical stress, σ.

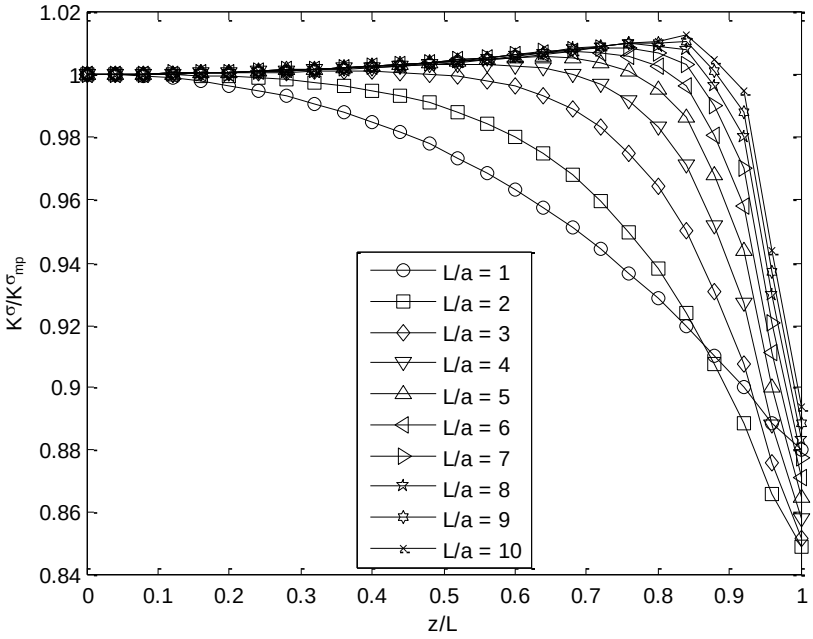

Figure 8-31: Distribution of normalized stress concentration factors, $K^{\sigma}/K^{\sigma}_{\text{mp}}$, through thickness in Sitka Spruce for different normalized thicknesses when longitudinal axis (grain orientation, *L*-direction) is perpendicular to applied vertical stress, σ.

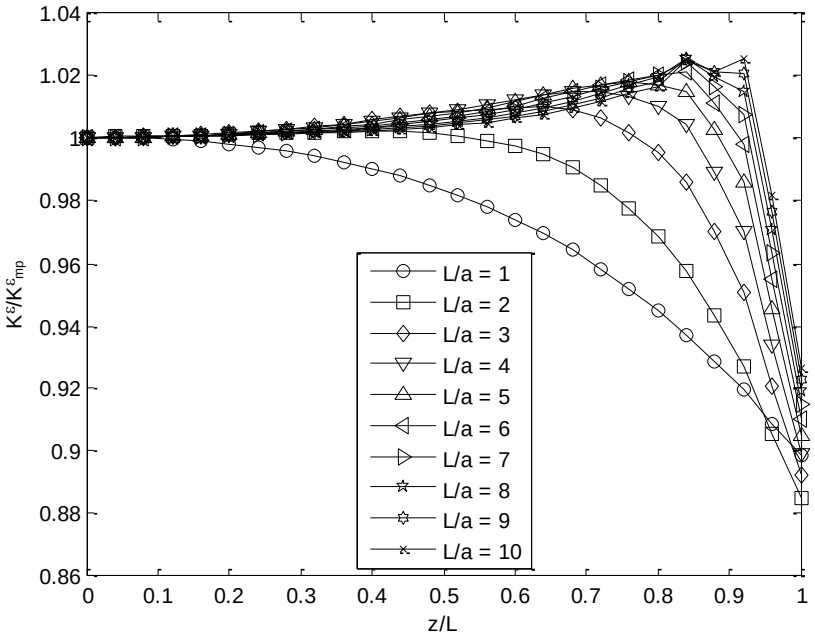

Figure 8-32: Distribution of normalized strain concentration factors, $K^{\varepsilon}/K^{\varepsilon}_{\text{mp}}$, through thickness in Sitka Spruce for different normalized thicknesses when longitudinal axis (grain orientation, L-direction) is perpendicular to applied vertical stress, σ.

8.4.2.2 Distributions of K^{σ} and K^{ε} as a Function of Poisson's Ratios

For the isotopic plate, the distributions of the stress, K^{σ}, and the strain, K^{ε}, concentration factor normalized by the corresponding value of the mid-plane stress, K^{σ}_{mp}, and strain, $K^{\varepsilon}_{\text{mp}}$, concentration factors with different Poisson's ratios for two values of normalized thickness $\Delta = L/a$ = 1 and 5 are illustrated in Figure 8-34 and Figure 8-36, respectively. When the Poisson's ratio is very small (mathematically approaching to zero), the variations of $K^{\sigma}/K^{\sigma}_{\text{mp}}$ and $K^{\varepsilon}/K^{\varepsilon}_{\text{mp}}$ does not change through the thickness. When the normalized thickness is less than the transition thickness of the stress and the strain, the maximum value of the stress or the strain concentration factors will always be on the mid-plane of the plate regardless the value of the Poisson's ratio, that is the Poisson's ratio does not change the distribution pattern of the curves as well as the location of the maximum stress or strain concentration factor. Variations of the Poisson's ratios will only change

the difference of the stress and strain concentration factor values between the mid-plane value and the maximum value as well as between the mid-plane value and the surface value. As the Poisson's ratio increases, the difference between the through thickness mid-plane value and the maximum value and the difference between the mid-plane value and the surface value of stress and strain concentration factor increase.

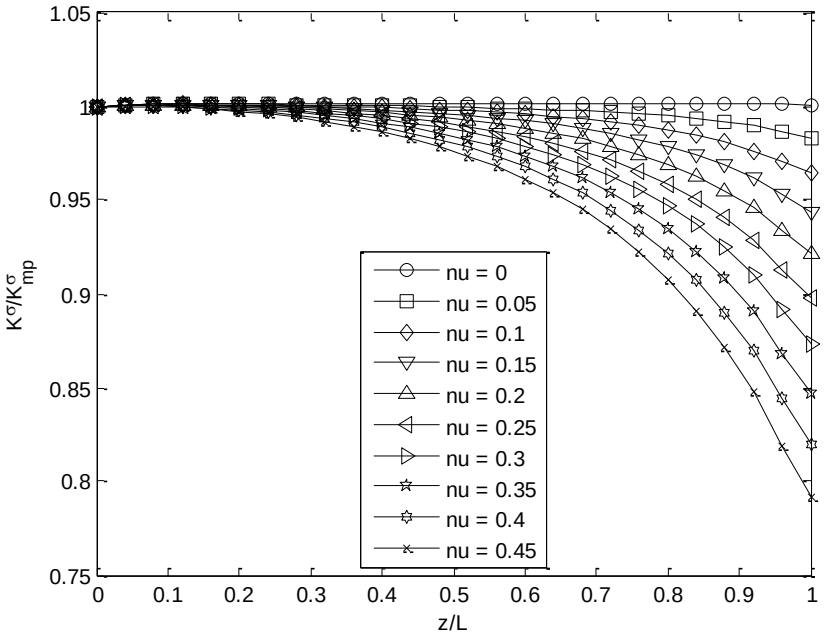

Figure 8-33: Distributions of the stress concentration factors, $K^{\sigma}/K^{\sigma}_{mp}$, through thickness in isotropic plate for different Poisson's ratios with normalized thickness $L/a = 1$.

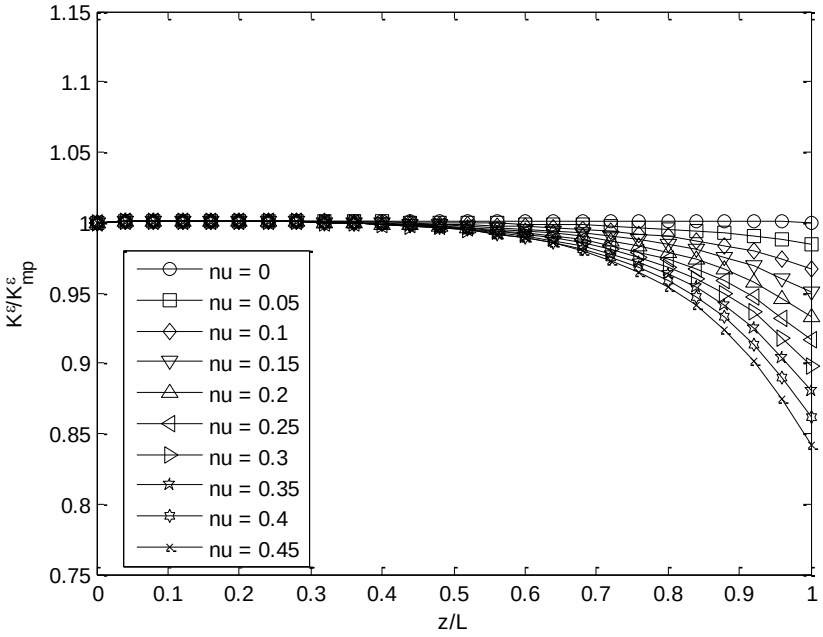

Figure 8-34: Distributions of the strain concentration factors, $K^{\varepsilon}/K^{\varepsilon}_{\mathrm{mp}}$, through thickness in isotropic plate for different Poisson's ratios with normalized thickness $L/a = 1$.

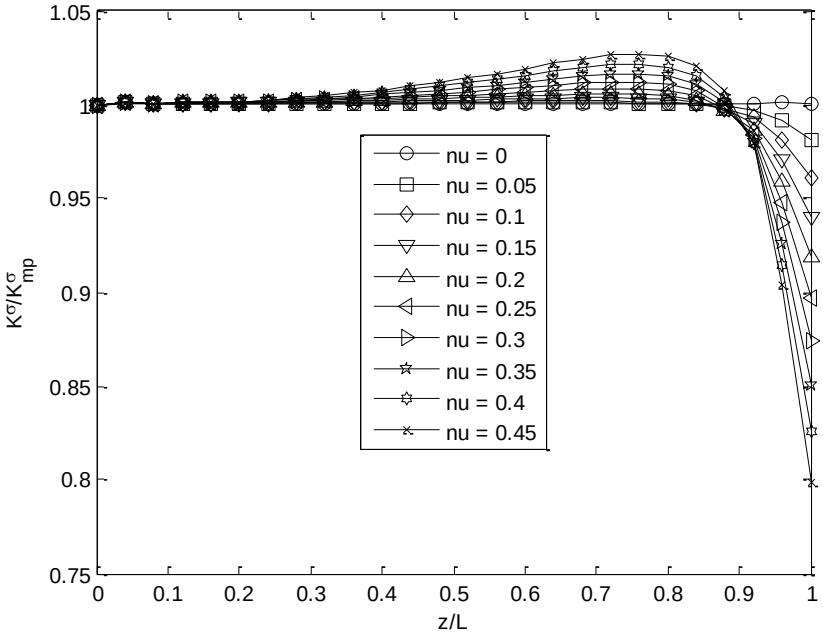

Figure 8-35: Distributions of the stress concentration factors, $K^{\sigma}/K^{\sigma}_{mp}$, through thickness in isotropic plate for different Poisson's ratios with normalized thickness $L/a = 5$.

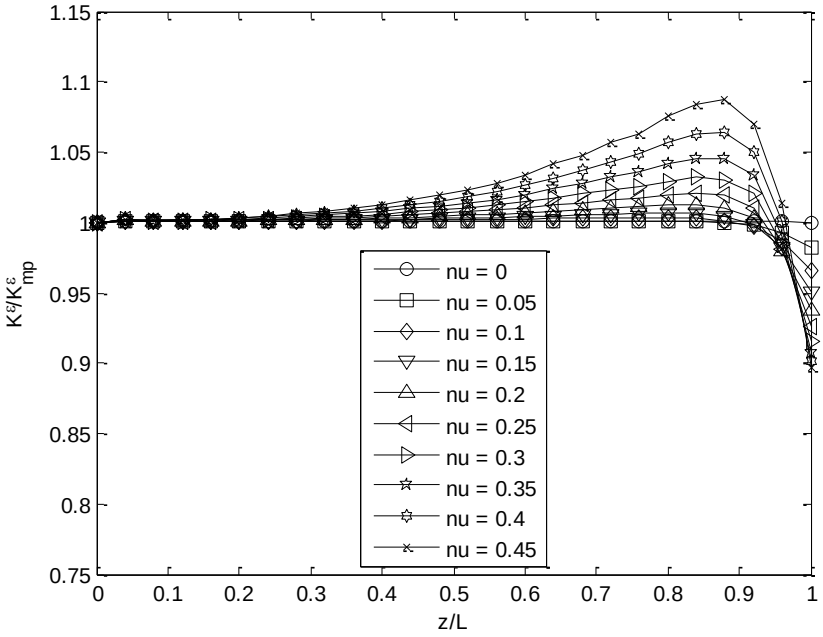

Figure 8-36: Distributions of the strain concentration factors, $K^{\varepsilon}/K^{\varepsilon}_{\mathrm{mp}}$, through thickness in isotropic plate for different Poisson's ratios with normalized thickness $L/a = 5$.

8.4.2.3 Distributions of K^{σ}_{mp}, $K^{\varepsilon}_{\mathrm{mp}}$, $K^{\sigma}_{\mathrm{max}}$, $K^{\varepsilon}_{\mathrm{max}}$, $K^{\sigma}_{\mathrm{sur}}$ and $K^{\varepsilon}_{\mathrm{sur}}$ as a Function of Plate Thickness

For isotropic materials, variations of the mid-plane (K^{σ}_{mp} and $K^{\varepsilon}_{\mathrm{mp}}$), maximum ($K^{\sigma}_{\mathrm{max}}$ and $K^{\varepsilon}_{\mathrm{max}}$), and the surface ($K^{\sigma}_{\mathrm{sur}}$ and $K^{\varepsilon}_{\mathrm{sur}}$) values of the stress and strain concentration factor normalized by the plane-stress (K^{σ}_{ps} and $K^{\varepsilon}_{\mathrm{ps}}$) as a function of normalized thickness L/a (from 0 to 10) for different Poisson's ratios ν = 0.2, 0.3, and 0.4 are demonstrated in Figure 8-37. For a finite thickness plate, the stress concentration factor at mid-plane, K^{σ}_{mp}, begins at value of plane-stress, K^{σ}_{ps}, ($K^{\sigma}_{\mathrm{mp}}/K^{\sigma}_{\mathrm{ps}}$ = 1) and increases gradually to reach a maximum value $\left(K^{\sigma}_{\mathrm{mp}}\right)_{\mathrm{max}}$ then decreases with the increasing of the normalized thickness L/a to reach the value of the plain-strain ($K^{\sigma}_{\mathrm{mp}}/K^{\sigma}_{\mathrm{plane\ strain}}$ = 1). The stress concentration factors of the plane-stress (L/a = 0) and plan-strain state (L/a = infinity) are equal. The maximum values of $K^{\sigma}_{\mathrm{mp}}/K^{\sigma}_{\mathrm{ps}}$ (and the corresponding

normalized thickness) for Poisson's ratios ν = 0.2, 0.3, and 0.4 are 1.023 (L/a = 1.1), 1.041 (L/a = 1.1), and 1.071 (L/a = 1.2), respectively. As shown in the Figure 8-37 when the $K^{\sigma}_{\max}/K^{\sigma}_{\mathrm{ps}}$ separates from $K^{\sigma}_{\mathrm{mp}}/K^{\sigma}_{\mathrm{ps}}$, the transition thickness L^{*}_{σ}/a of stress concentration factor is 3.5. As the Poisson ratio increases, the $K^{\sigma}_{\max}/K^{\sigma}_{\mathrm{ps}}$ value also increases when normalized thickness becomes large enough.

For a finite thickness plate, the strain concentration factor at mid-plane, $K^{\varepsilon}_{\mathrm{mp}}$, begins at value of plane-stress, $K^{\varepsilon}_{\mathrm{ps}}$, ($K^{\varepsilon}_{\mathrm{mp}}/K^{\varepsilon}_{\mathrm{ps}}$ = 1) and increases gradually to reach a maximum value $\left(K^{\varepsilon}_{\mathrm{mp}}\right)_{\max}$ then decreases as the increasing of the normalized thickness L/a to reach the value of the plain-strain ($K^{\varepsilon}_{\mathrm{mp}}/K^{\varepsilon}_{\text{plane strain}} = 1-\nu^2$). The curves of $K^{\sigma}_{\mathrm{mp}}/K^{\sigma}_{\mathrm{ps}}$ and $K^{\varepsilon}_{\mathrm{mp}}/K^{\varepsilon}_{\mathrm{ps}}$ versus L/a are different. The maximum values of $K^{\varepsilon}_{\mathrm{mp}}/K^{\varepsilon}_{\mathrm{ps}}$ (and the corresponding normalized thickness) for Poisson's ratios ν = 0.2, 0.3, and 0.4 are 1.012 (L/a = 0.6), 1.020 (L/a = 0.6), and 1.025 (L/a = 0.6), respectively. As shown in the Figure 8-37 when the $K^{\varepsilon}_{\max}/K^{\varepsilon}_{\mathrm{ps}}$ separates from $K^{\varepsilon}_{\mathrm{mp}}/K^{\varepsilon}_{\mathrm{ps}}$, the transition thickness L^{*}_{ε}/a of strain concentration factor are 1.9, 1.7, and 1.4 for Poisson's ratios ν = 0.2, 0.3, and 0.4, respectively. For L/a = 10, the values of $K^{\varepsilon}_{\mathrm{mp}}/K^{\varepsilon}_{\mathrm{ps}}$ for Poisson's ratios ν = 0.2, 0.3, and 0.4 are 0.975, 0.944, and 0.896, respectively, which these values are close to the theoretical values for plane-strain state $K^{\varepsilon}_{\mathrm{mp}}/K^{\varepsilon}_{\text{plane strain}} = 1-\nu^2$ which are 0.96, 0.91, and 0.84, respectively. The values of $K^{\varepsilon}_{\max}/K^{\varepsilon}_{\mathrm{ps}}$ after separating from the mid-plane values decrease monotonically and reach approximately constant values of 0.989, 0.981, and 0.963 at L/a = 10 for Poisson's ratios ν = 0.2, 0.3, and 0.4, respectively. All $K^{\varepsilon}_{\max}/K^{\varepsilon}_{\mathrm{ps}}$ values at L/a = 10 are greater than $1-\nu^2$, i.e., less than 1. As the Poisson's ratio increases, as the $K^{\varepsilon}_{\max}/K^{\varepsilon}_{\mathrm{ps}}$ value decreases and as the lower of $K^{\varepsilon}_{\mathrm{mp}}/K^{\varepsilon}_{\mathrm{ps}}$ value tends to when normalized thickness becomes large enough. The $K^{\sigma}_{\max}/K^{\sigma}_{\mathrm{ps}}$ value is greater than the $K^{\varepsilon}_{\max}/K^{\varepsilon}_{\mathrm{ps}}$ value for any specific Poisson's ratio.

The values of the stress, $K_{\mathrm{sur}}^{\sigma}$, and the strain, $K_{\mathrm{sur}}^{\varepsilon}$, concentration factors at the surface are coincided as shown in Figure 8-38. The curves of the stress, $K_{\mathrm{sur}}^{\sigma}$, and strain, $K_{\mathrm{sur}}^{\varepsilon}$, concentration factors versus the normalized thickness are monotonic descent curves except for large Poisson's ratio where the curve tends to increase with the increasing of normalized thickness. The values of the stress, $K_{\mathrm{sur}}^{\sigma}$, and strain, $K_{\mathrm{sur}}^{\varepsilon}$, concentration factors at the plate surface decrease rapidly from the plane-stress concentration factor value ($K_{\mathrm{sur}}^{\sigma}/K_{\mathrm{ps}}^{\sigma} = K_{\mathrm{sur}}^{\varepsilon}/K_{\mathrm{ps}}^{\varepsilon} = 1$) to reach values smaller than 1 for all values of normalized thickness. As the Poisson's ratio increases, as the decreasing rate of $K_{\mathrm{sur}}^{\sigma}/K_{\mathrm{ps}}^{\sigma}$ and $K_{\mathrm{sur}}^{\varepsilon}/K_{\mathrm{ps}}^{\varepsilon}$ curves is and as the lower $K_{\mathrm{sur}}^{\sigma}/K_{\mathrm{ps}}^{\sigma}$ and $K_{\mathrm{sur}}^{\varepsilon}/K_{\mathrm{ps}}^{\varepsilon}$ curves tend to when normalized thickness value becomes large enough. On the plate surface and along the line $x = a$ and $y = 0$, the stresses in x- and z-direction are zero, $\sigma_{xx} = \sigma_{zz} = 0$, so the in-plane and out-of-plane stress constraint factors are zero simultaneously, $T_x = T_z = 0$, which indicates that the stress and strain concentration factors are equal, $K^{\varepsilon} = K^{\sigma}$, from equation (8-13).

The difference between mid-plane (K_{mp}^{σ} and $K_{\mathrm{mp}}^{\varepsilon}$), or maximum ($K_{\mathrm{max}}^{\sigma}$ and $K_{\mathrm{max}}^{\varepsilon}$) and surface ($K_{\mathrm{sur}}^{\sigma}$ and $K_{\mathrm{sur}}^{\varepsilon}$) value of stress and strain concentration factor versus normalized thickness for different Poisson's ratios ν = 0.2, 0.3, and 0.4 is illustrated in Figure 8-40. The difference between mid-plane K_{mp}^{σ} (or the maximum $K_{\mathrm{max}}^{\sigma}$) and surface, $K_{\mathrm{sur}}^{\sigma}$, value of stress concentration factor increases with the increasing of the normalized thickness L/a until it reaches a maximum value around 10%, 16%, and 23% of the plane-stress for Poisson's ratios ν = 0.2, 0.3, and 0.4, respectively. The same behavior for the strain concentration factor is observed except that the maximum difference between the maximum and surface stress concentration factor is greater than the maximum difference between the maximum and surface strain concentration factor. The difference between mid-plane, $K_{\mathrm{mp}}^{\varepsilon}$, and surface, $K_{\mathrm{sur}}^{\varepsilon}$, values of strain concentration factor increases with the

increasing of the normalized thickness L/a until it reaches a maximum value around 8%, 11%, and 15% of the plane-stress for Poisson's ratios ν = 0.2, 0.3, and 0.4, respectively.

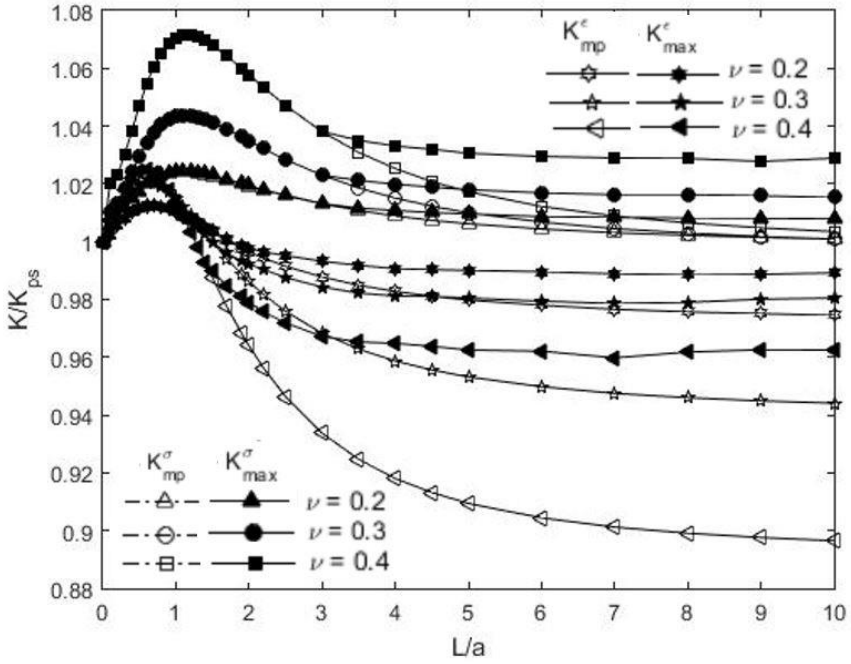

Figure 8-37: Distributions of normalized mid-plane ($K^{\sigma}_{mp}/K^{\sigma}_{ps}$ and $K^{\varepsilon}_{mp}/K^{\varepsilon}_{ps}$) and maximum ($K^{\sigma}_{max}/K^{\sigma}_{ps}$ and $K^{\varepsilon}_{max}/K^{\varepsilon}_{ps}$) stress and strain concentration factor in isotropic material as function of L/a for different Poisson's ratios.

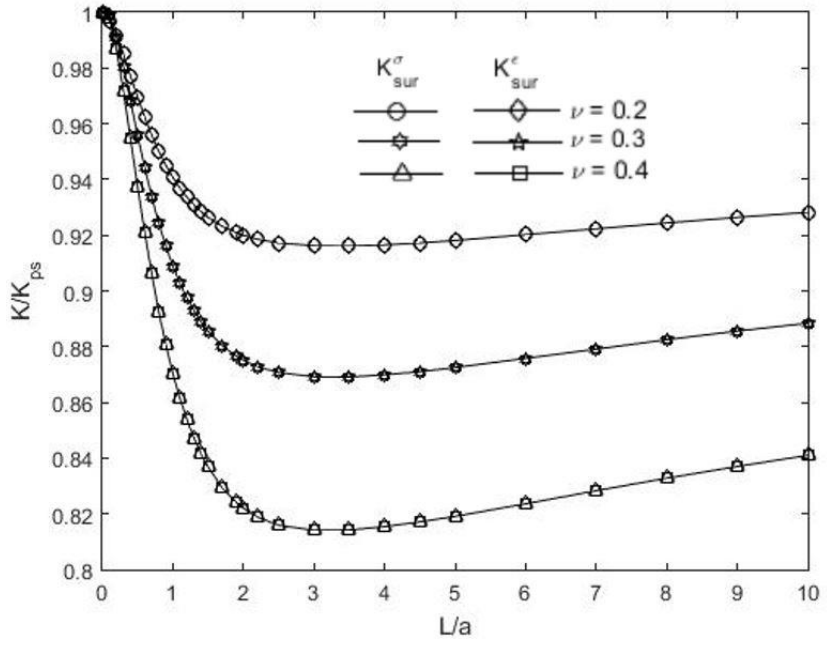

Figure 8-38: Distributions of normalized surface ($K^{\sigma}_{sur}/K^{\sigma}_{ps}$ and $K^{\varepsilon}_{sur}/K^{\varepsilon}_{ps}$) stress and strain concentration factor versus normalized thickness for different Poisson's ratios.

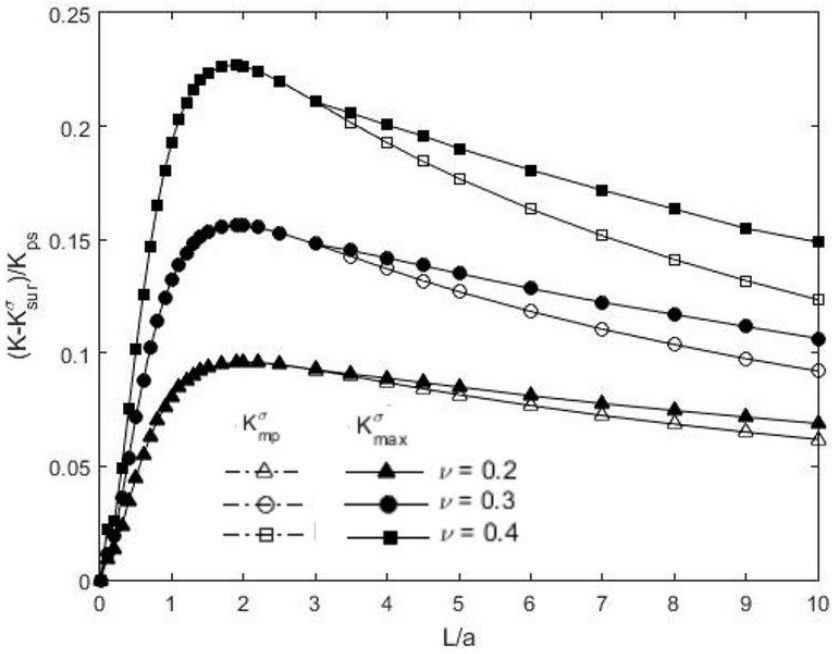

Figure 8-39: Distributions of normalized mid-plane ($K^{\sigma}_{mp}/K^{\sigma}_{ps}$ and $K^{\varepsilon}_{mp}/K^{\varepsilon}_{ps}$) and maximum ($K^{\sigma}_{max}/K^{\sigma}_{ps}$ and $K^{\varepsilon}_{max}/K^{\varepsilon}_{ps}$) stress and strain concentration factors in isotropic material as function of plate thickness L/a for different Poisson's ratios.

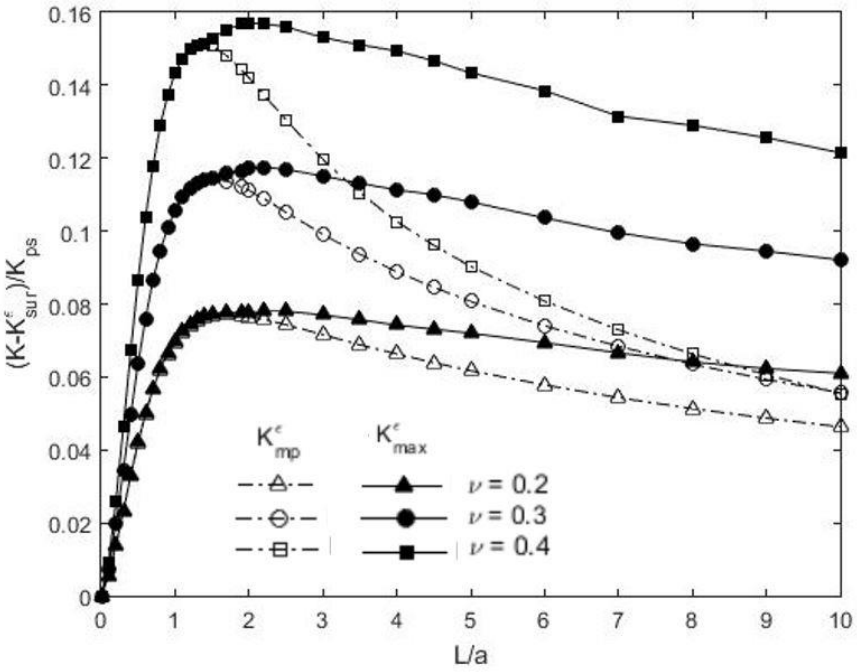

Figure 8-40: Distributions of surface stress, $K^{\sigma}_{sur}/K^{\sigma}_{ps}$, and strain, $K^{\varepsilon}_{sur}/K^{\varepsilon}_{ps}$, concentration factors in isotropic material as function of L/a for different Poisson's ratios.

For orthotropic Sitka Spruce wood plate with properties listed in Table 8-1, Figure 8-41 shows that the distributions of the mid-plane (K^{σ}_{mp} and $K^{\varepsilon}_{\mathrm{mp}}$) and maximum ($K^{\sigma}_{\mathrm{max}}$ and $K^{\varepsilon}_{\mathrm{max}}$) stress and the strain concentration factors normalized by the plane-stress values (K^{σ}_{ps} and $K^{\varepsilon}_{\mathrm{ps}}$) at the edge of the hole as a function of the Spruce plate thickness, L/a, for different grain orientations. Irrespective of the grain direction, all of these normalized quantities are equal to 1.0 for a very thin plate, i.e., $K^{\sigma}_{\mathrm{mp}}/K^{\sigma}_{\mathrm{ps}} = K^{\varepsilon}_{\mathrm{mp}}/K^{\epsilon}_{\mathrm{ps}} = K^{\sigma}_{\mathrm{max}}/K^{\sigma}_{\mathrm{ps}} = K^{\varepsilon}_{\mathrm{max}}/K^{\epsilon}_{\mathrm{ps}} = 1$. When the grain direction is perpendicular to the applied stress, σ, $K^{\sigma}_{\mathrm{max}}/K^{\sigma}_{\mathrm{ps}}$ (and $K^{\sigma}_{\mathrm{mp}}/K^{\sigma}_{\mathrm{ps}}$) and $K^{\varepsilon}_{\mathrm{max}}/K^{\varepsilon}_{\mathrm{ps}}$ (and $K^{\varepsilon}_{\mathrm{mp}}/K^{\varepsilon}_{\mathrm{ps}}$) increased to maximum values of 1.06 at $L/a \approx 1.5$ and 1.03 at $L/a \approx 1.0$, respectively. When the grain direction is parallel to the applied stress, the values of all of these ratios initially increased slightly and thereafter decreased to individual constant values as L/a increases.

Figure 8-41 also illustrates that when the $K^{\sigma}_{\mathrm{max}}/K^{\sigma}_{\mathrm{ps}}$ separates from $K^{\sigma}_{\mathrm{mp}}/K^{\sigma}_{\mathrm{ps}}$, the transition thicknesses, L^{*}_{σ}/a, of the stress concentration factor are located at L/a = 7.0 and 3.0, and when

the $K^{\varepsilon}_{\max}/K^{\varepsilon}_{\mathrm{ps}}$ separates from $K^{\varepsilon}_{\mathrm{mp}}/K^{\varepsilon}_{\mathrm{ps}}$, the transition thicknesses L^{*}_{ε}/a of strain concentration factor are located at L/a = 4.0 and 1.7 when the grain direction is parallel and perpendicular to the applied stress, σ, respectively. For L/a = 10, the values of $K^{\sigma}_{\mathrm{mp}}/K^{\sigma}_{\mathrm{ps}}$ and $K^{\sigma}_{\max}/K^{\sigma}_{\mathrm{ps}}$ when the load is parallel and perpendicular to the grain orientation are 0.97 and 1.02, and, 0.98 and 1.04, respectively. For L/a = 10, the values of $K^{\varepsilon}_{\mathrm{mp}}/K^{\varepsilon}_{\mathrm{ps}}$ and $K^{\varepsilon}_{\max}/K^{\varepsilon}_{\mathrm{ps}}$ when the grain direction is parallel and perpendicular to the vertical applied stress, σ, are 0.96 and 0.97, and, 0.97 and 0.99, respectively. The values of $K^{\sigma}_{\max}/K^{\sigma}_{\mathrm{ps}}$ exceed those for $K^{\varepsilon}_{\max}/K^{\varepsilon}_{\mathrm{ps}}$. The values of $K^{\sigma}_{\max}/K^{\sigma}_{\mathrm{ps}}$ and $K^{\varepsilon}_{\max}/K^{\varepsilon}_{\mathrm{ps}}$ are greater when the grain orientation is perpendicular to the load than if they were parallel to each other.

Figure 8-42 demonstrates that the values of stress $K^{\sigma}_{\mathrm{sur}}$ and strain $K^{\varepsilon}_{\mathrm{sur}}$ concentration factors at the traction-free surfaces of the plate are equal (although equal to different values depending whether the grain is parallel or perpendicular to the externally applied stress) for all the thicknesses. When the grain orientation parallels the applied stress, σ, the surface stress $K^{\sigma}_{\mathrm{sur}}$ and strain $K^{\varepsilon}_{\mathrm{sur}}$ concentration factors reached a minimum value of $\left(K^{\sigma}_{\mathrm{sur}}/K^{\sigma}_{\mathrm{ps}}\right)_{\min} \approx 0.9$ at L/a = 1.8, then increases gradually as the normalized thickness increased. The values of $K^{\sigma}_{\mathrm{sur}}/K^{\sigma}_{\mathrm{sur}}$ at L/a = 10 are 0.93 and 0.92 when the load is parallel and perpendicular to the grain orientation, respectively. The values of $K^{\varepsilon}_{\mathrm{sur}}/K^{\varepsilon}_{\mathrm{ps}}$ at L/a = 10 are 0.93 and 0.90 when the load is parallel and perpendicular to the grain orientation, respectively. On the plate surface and along the thickness of the hole tip, the stress and strain concentration factors are equal, $K^{\varepsilon} = K^{\sigma}$ ($T_x = T_z = 0$).

Figure 8-43 shows the differences between the mid-plane (K^{σ}_{mp} and $K^{\varepsilon}_{\mathrm{mp}}$) or the maximum ($K^{\sigma}_{\max}$ and $K^{\varepsilon}_{\max}$) stress and strain concentration factors and the plate's surface values ($K^{\sigma}_{\mathrm{sur}}$ and

$K_{\mathrm{sur}}^{\varepsilon}$) normalized by the plane stress-state values (K_{ps}^{σ} and $K_{\mathrm{ps}}^{\varepsilon}$) versus L/a for different grain orientations. The difference between mid-plan K_{mp}^{σ} (or maximum $K_{\mathrm{max}}^{\sigma}$) and surface $K_{\mathrm{sur}}^{\sigma}$ stress concentration factor increased with increasing thickness L/a until reaching a maximum value of approximately 8% and 16% of the plane-stress value when the grain orientation is parallel or perpendicular to the vertically applied stress, σ, respectively, Figure 8-43. After reaching their maximum values, these quantities decreased gradually as thickness, L/a, increased.

Figure 8-44 illustrates trends for strain concentration factors similar to those in Figure 8-43, although the largest difference between the maximum and surface stress concentration factors (Figure 8-43) exceeds the maximum difference between the mid-plane and surface strain concentration factors (Figure 8-44). The difference between mid-plane $K_{\mathrm{mp}}^{\varepsilon}$ and surface $K_{\mathrm{sur}}^{\varepsilon}$ strain concentration factor increased with increasing thickness L/a until reaching maximum values of approximately 8% and 12% of the plane-stress value when the grain orientation is parallel and perpendicular to the vertically applied stress, σ, respectively. After reaching their maximum values, all curves of Figure 8-43 and Figure 8-44 decreased gradually with increasing thickness, L/a. Figure 8-44 shows that measured strains on the plate surface can be 12% less than at mid-plane.

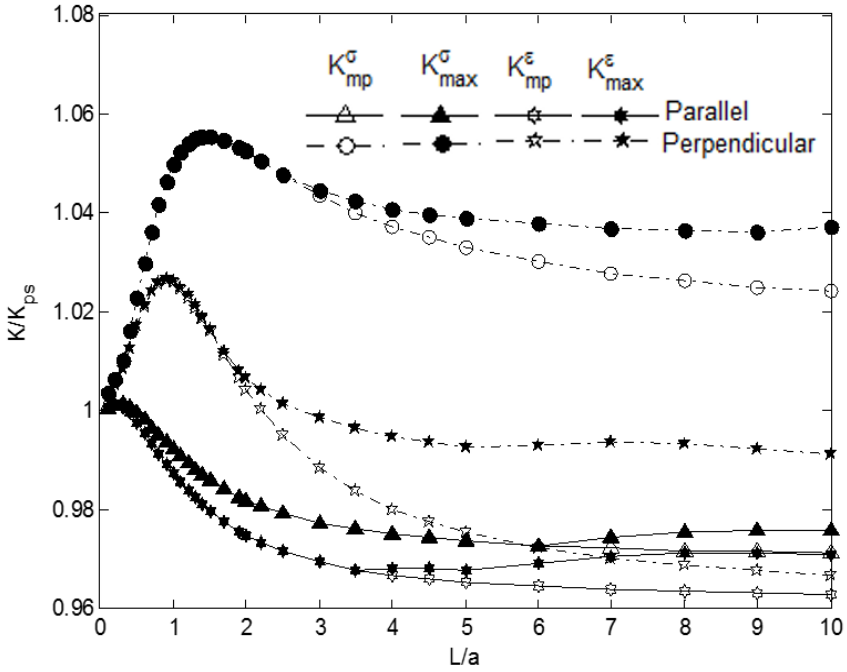

Figure 8-41: Distributions of normalized mid-plane ($K^{\sigma}_{mp}/K^{\sigma}_{ps}$ and $K^{\varepsilon}_{mp}/K^{\varepsilon}_{ps}$) and maximum ($K^{\sigma}_{max}/K^{\sigma}_{ps}$ and $K^{\varepsilon}_{max}/K^{\varepsilon}_{ps}$) stress and strain concentration factors in Sitka Spruce as function of plate thickness L/a for different grain orientations to applied vertical stress, σ.

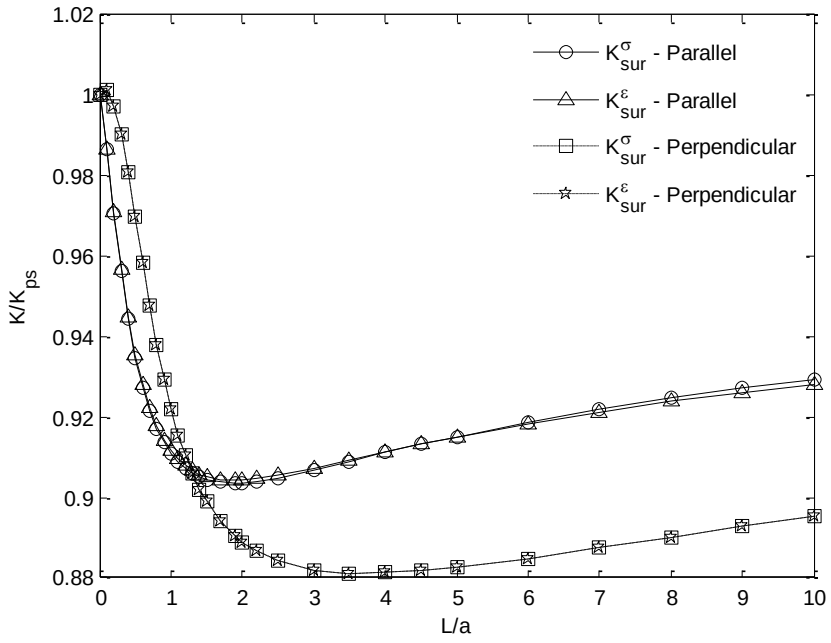

Figure 8-42: Distributions of normalized external traction-free surface stress, $K^{\varepsilon}_{sur}/K^{\varepsilon}_{ps}$, and strain, $K^{\sigma}_{sur}/K^{\sigma}_{ps}$, concentration factors in Sitka Spruce as function of L/a for different grain orientations to applied vertical stress, σ.

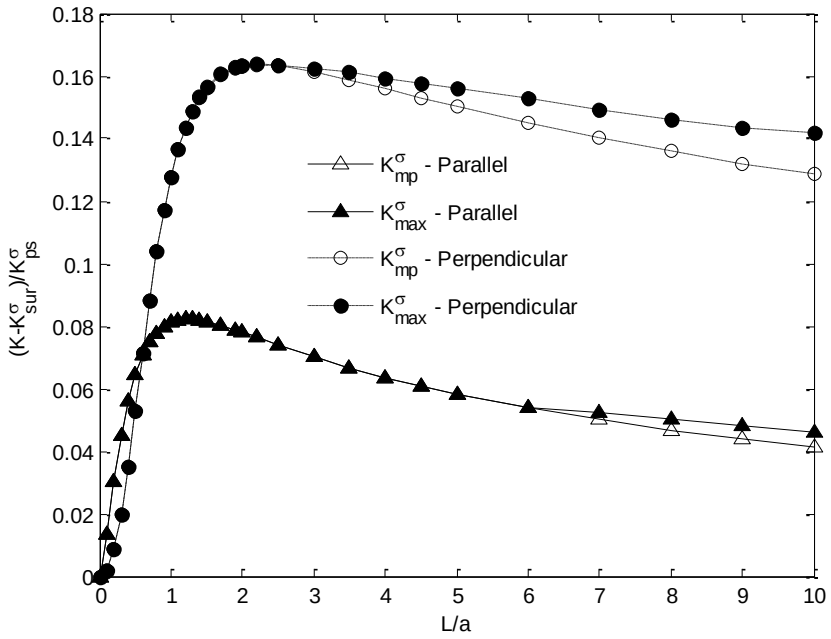

Figure 8-43: Differences between the normalized mid-plane, $(K^{\sigma}_{mp}-K^{\sigma}_{sur})/K^{\sigma}_{ps}$, and maximum, $(K^{\sigma}_{max}-K^{\sigma}_{sur})/K^{\sigma}_{ps}$, and surface stress concentration factors in Sitka Spruce as a function of L/a for different grain orientations to applied vertical stress, σ.

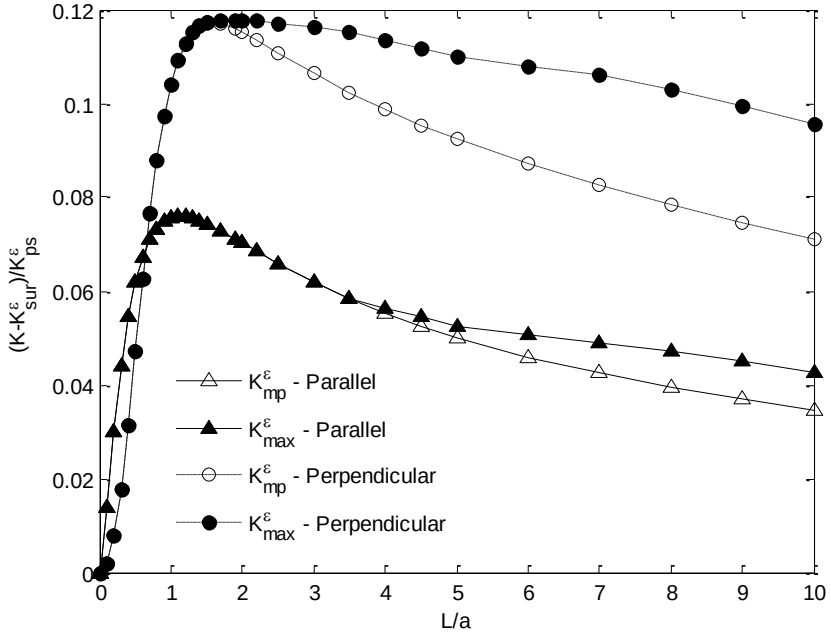

Figure 8-44: Differences between the normalized mid-plane, $(K^{\varepsilon}_{mp}-K^{\varepsilon}_{sur})/K^{\varepsilon}_{ps}$, and maximum, $(K^{\varepsilon}_{max}-K^{\varepsilon}_{sur})/K^{\varepsilon}_{ps}$, and surface strain concentration factors in Sitka Spruce as a function of L/a for different grain orientations to applied stress, σ.

8.4.1 The Relation of Stress and Strain Concentration Factor

The distribution of stress and strain concentration factor are different in elasticity state in the front of the hole tip and through the thickness. The distribution of stress and strain concentration factor are also different in orthotropic material in the front of the hole tip and along the thickness.

8.4.1.1 Distributions of $K^{\varepsilon}/K^{\sigma}$ Versus $\zeta = x/a$ for Different Plane Layers

The distributions of $K^{\varepsilon}/K^{\sigma}$ in the front of the hole for different plane layers parallel to the mid-plane of the plate with L/a = 1 and 5 are illustrated in Figure 8-45 and Figure 8-46, respectively. The distributions of $K^{\varepsilon}/K^{\sigma}$ in the front of the hole are different on different plane layers and each curve corresponding to its plane layer has a minimum which its value and location depends on Poisson's ratio, plane layer location, and the plate normalized thickness. When the distance x tends to infinity ($\zeta \to \infty$), the $K^{\varepsilon}/K^{\sigma}$ value approaches one since the stresses in x- and z-direction are zero $\sigma_{xx} = \sigma_{zz} = 0$ so the in-plane and out-of-plane stress constraint factors are zero simultaneously $T_x = T_z = 0$ which indicates that the stress and strain concentration factors are equal $K^{\varepsilon} = K^{\sigma}$. The value of $K^{\varepsilon}/K^{\sigma}$ is around one on the plate surface at the hole tip and less than one for all other plane layers. The distributions of $K^{\varepsilon}/K^{\sigma}$ in the plane layers paralleled to the mid-plane are close to each other for small normalized thickness and the distributions start to deviate from each other when normalized thickness becomes large enough. The minimum value of the most of the distributions of $K^{\varepsilon}/K^{\sigma}$ values occur around ζ = 1.5 and this minimum value decreases with the increasing of the normalized thickness (from around 0.93 for L/a = 1 to 0.88 for L/a = 5) for specified Poisson's ratio.

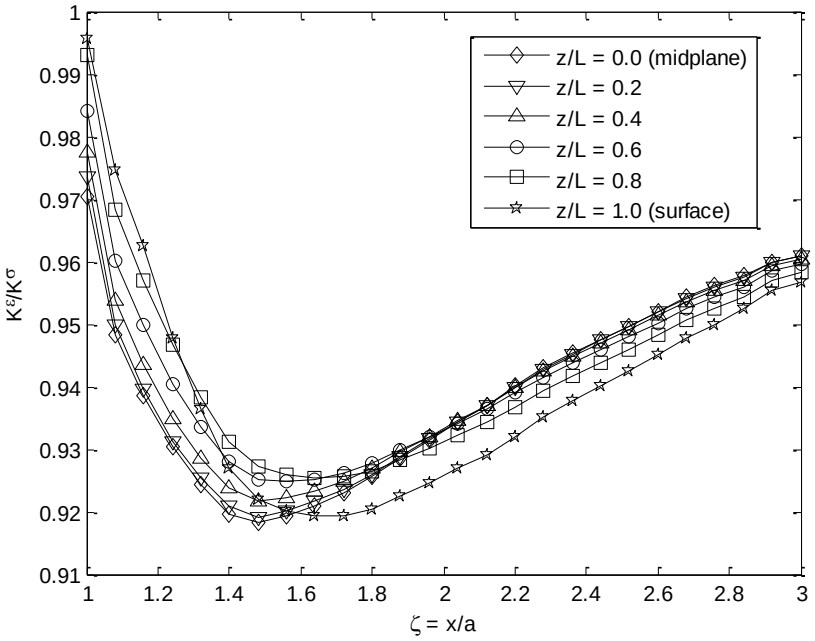

Figure 8-45: The distributions of K^{ϵ}/K^{σ} in the front of the hole for different plane layers with L/a = 1 for $\nu = 0.3$.

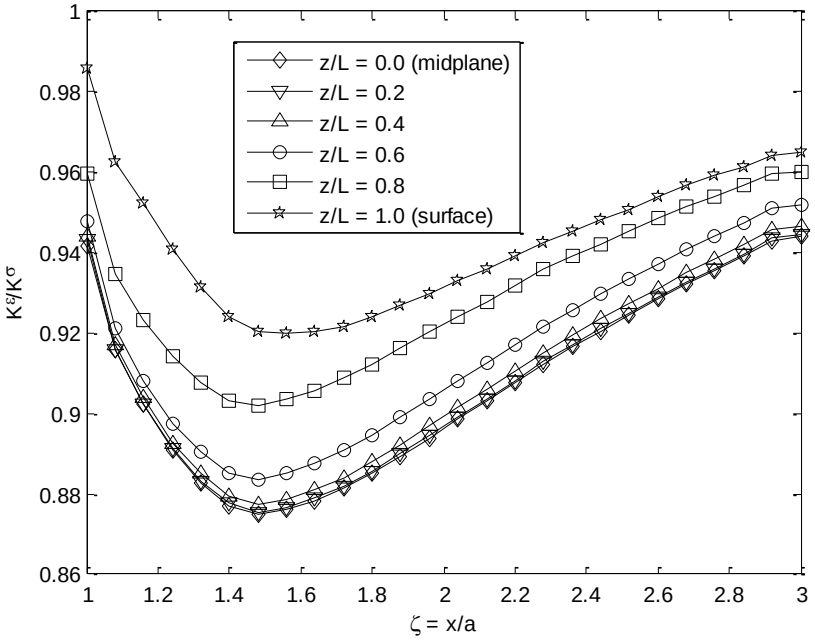

Figure 8-46: The distributions of K^{ϵ}/K^{σ} in the front of the hole for different plane layers with L/a = 5 for $\nu = 0.3$.

Figure 8-47 and Figure 8-48 show the distributions of $K^{\varepsilon}/K^{\sigma}$ at $\zeta = x/a \geq 1$ and $y = 0$ for different lateral planes parallel to the mid-plane of the plate for $\Delta = L/a$ = 1 and 5 when the grain orientation is parallel to the applied stress. These distributions are different on different planes. Each curve corresponding to its plane has a minimum value and location which depends on Poisson's ratios, the plane's location, and the thickness of the plate. All curves start at $K^{\varepsilon}/K^{\sigma}$ = 1.0 on the edge of the hole (ζ = 1.0), decrease for $\zeta \geq 0$ (i.e., $T_x \neq 0$) and pass through minimum values approximately at ζ = 1.3. These minimums values increase as one moves from the external surfaces ($z/L = \pm 1$) towards the center of the plate (z/L = 0). The distributions of $K^{\varepsilon}/K^{\sigma}$ in the plane layers paralleled to the mid-plane are close to each other for small normalized thickness and the distributions start to deviate from each other when normalized thickness becomes large enough. When the distance x tends to infinity ($\zeta \to \infty$), the $K^{\varepsilon}/K^{\sigma}$ value approaches one since $K^{\varepsilon} = K^{\sigma}$ ($T_x = T_z = 0$).

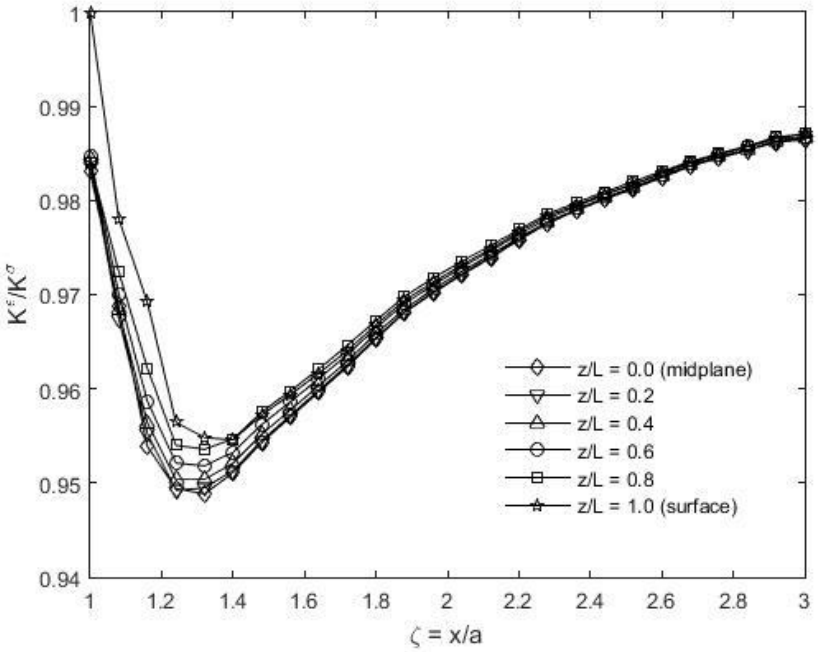

Figure 8-47: Distributions of K^{ϵ}/K^{σ} in Sitka Spruce on different plane layers for L/a = 1 when the grain orientation is parallel to the applied stress.

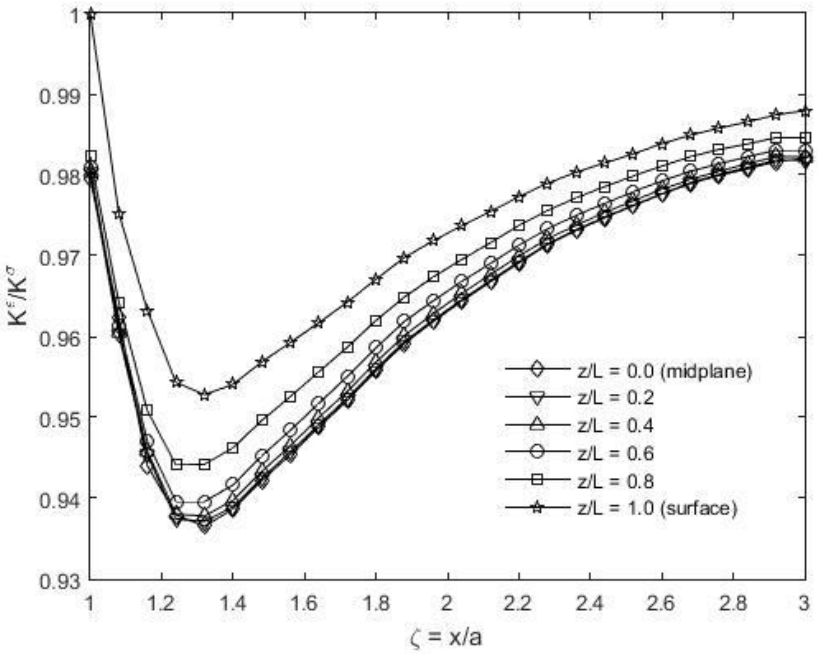

Figure 8-48: Distributions of K^{ϵ}/K^{σ} in Sitka Spruce on different plane layers for L/a = 5 when the grain orientation is parallel to the applied stress.

8.4.1.2 The Distribution of $K^{\varepsilon}/K^{\sigma}$ Along the Hole Tip for Different Poisson's Ratio

Along the thickness of the hole tip, the in-plane stress constraint factor T_x is zero so the ratio of strain to stress concentration factor, equation (8-13), along this line can be simplified as following

$$K^{\varepsilon}/K^{\sigma} = 1 - \nu T_z \tag{8-19}$$

The stress concentration factor and strain concentration factor are different along the hole tip for a finite thickness plate except on the plate surface where both stress and strain concentration factors are equal. The distributions of $K^{\varepsilon}/K^{\sigma}$ along the thickness at the hole tip is function of Poisson's ratio and out-of-plane stress constraint factor. Along the thickness of the hole tip, the out-of-plane stress constraint factor T_z is zero on free plate surface and its maximum value is on the mid-plane so the ratio of strain to stress concentration factor $K^{\varepsilon}/K^{\sigma}$ has a minimum value on the mid-plane where T_z is maximum and has a value of one where T_z is zero on plate surface. The distributions of $K^{\varepsilon}/K^{\sigma}$ along the hole tip for different Poisson's ratio and L/a = 1 and 5 are illustrated in Figure 8-49 and Figure 8-50, respectively. The changing of the normalized thickness does not change the curve pattern of the distributions of $K^{\varepsilon}/K^{\sigma}$ and it has been observed that the distribution is similar for large normalized thickness (L/a = 5). The minimum value along the thickness of the hole tip occurs on the mid plane layer and this minimum value decreases with the increasing value of the normalized thickness.

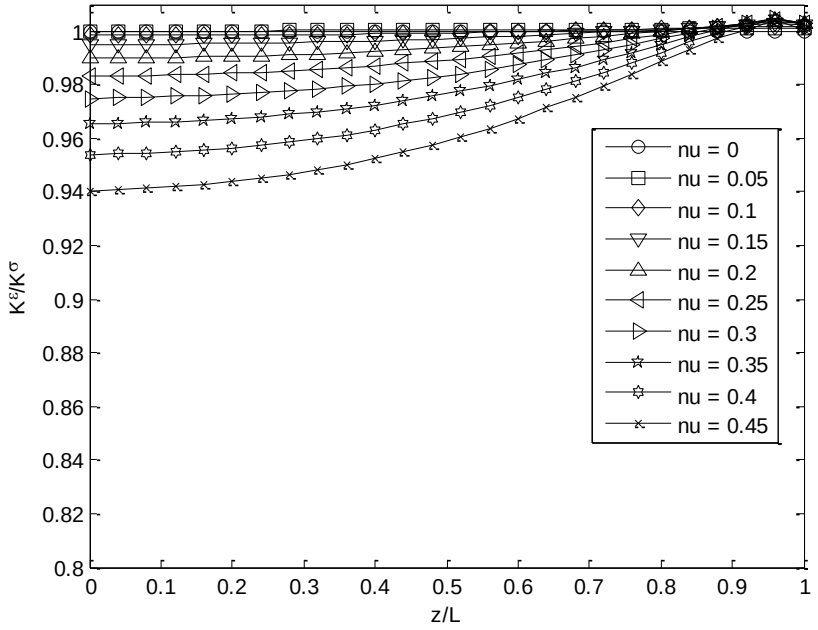

Figure 8-49: The distributions of K^{ϵ}/K^{σ} along the hole tip for different Poisson's ratio with L/a = 1.

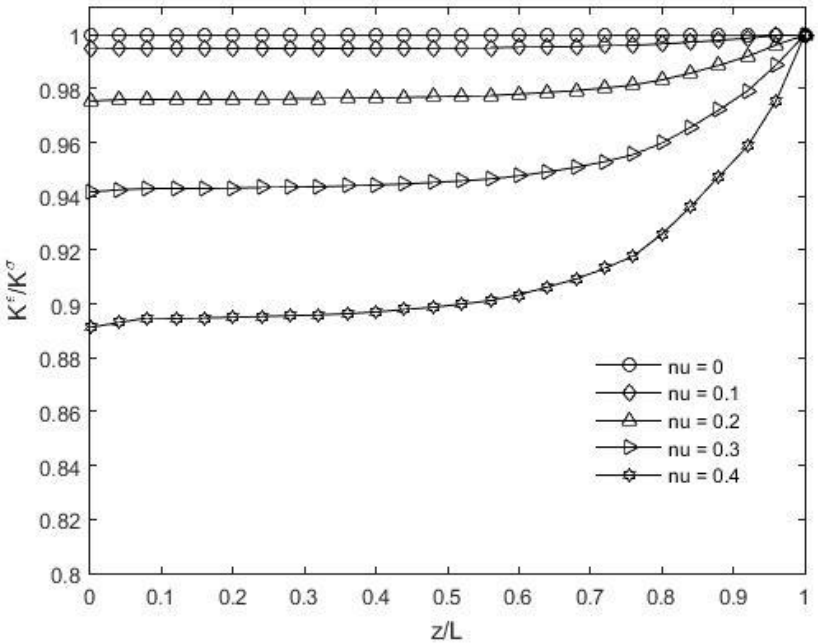

Figure 8-50: The distributions of K^{ϵ}/K^{σ} along the hole tip for different Poisson's ratio with L/a = 5.

8.4.1.3 The Distribution of Mid-Plane Values of $K^{\varepsilon}/K^{\sigma}$ as Function of Normalized Thickness and Poisson's Ratio

The distribution of mid-plane values of $K^{\varepsilon}_{\mathrm{mp}}/K^{\sigma}_{\mathrm{mp}}$ as a function of normalized thickness for three values of Poisson's ratio ν = 0.2, 0.3, and 0.4 is illustrated Figure 8-51. The $K^{\varepsilon}_{\mathrm{mp}}/K^{\sigma}_{\mathrm{mp}}$ curve versus the normalized thickness is a monotonic descent function. The $K^{\varepsilon}_{\mathrm{mp}}/K^{\sigma}_{\mathrm{mp}}$ starts from value of one in plane-stress. When the normalized thickness becomes large enough ($L/a > 4$), the $K^{\varepsilon}_{\mathrm{mp}}/K^{\sigma}_{\mathrm{mp}}$ value approaches constant values which are 0.9736, 0.9432, and 0.8933 for Poisson's ratio ν = 0.2, 0.3, and 0.4, respectively. The larger the Poisson's ratio is, the higher decreasing rate of the $K^{\varepsilon}_{\mathrm{mp}}/K^{\sigma}_{\mathrm{mp}}$ is and the lower the $K^{\varepsilon}_{\mathrm{mp}}/K^{\sigma}_{\mathrm{mp}}$ curve tends to when L/a becomes large enough. The distribution of mid-plane values of $K^{\varepsilon}_{\mathrm{mp}}/K^{\sigma}_{\mathrm{mp}}$ as a function of Poisson's ratio for three values of normalized thickness L/a = 1, 5, and 10 is illustrated Figure 8-52. The $K^{\varepsilon}_{\mathrm{mp}}/K^{\sigma}_{\mathrm{mp}}$ curve versus the Poisson's ratio is a monotonic descent function. All values of $K^{\varepsilon}_{\mathrm{mp}}$ are smaller than the values of K^{σ}_{mp} for all values of normalized thickness and Poisson's ratio. The $K^{\varepsilon}_{\mathrm{mp}}/K^{\sigma}_{\mathrm{mp}}$ starts from value of one at ν = 0. The curve of $K^{\varepsilon}_{\mathrm{mp}}/K^{\sigma}_{\mathrm{mp}}$ for normalized thickness L/a = 5 and 10 are coincided to each other which states that for large normalized thickness the variations of $K^{\varepsilon}_{\mathrm{mp}}/K^{\sigma}_{\mathrm{mp}}$ values with Poisson's ratio are the same regardless of the value of the normalized thickness.

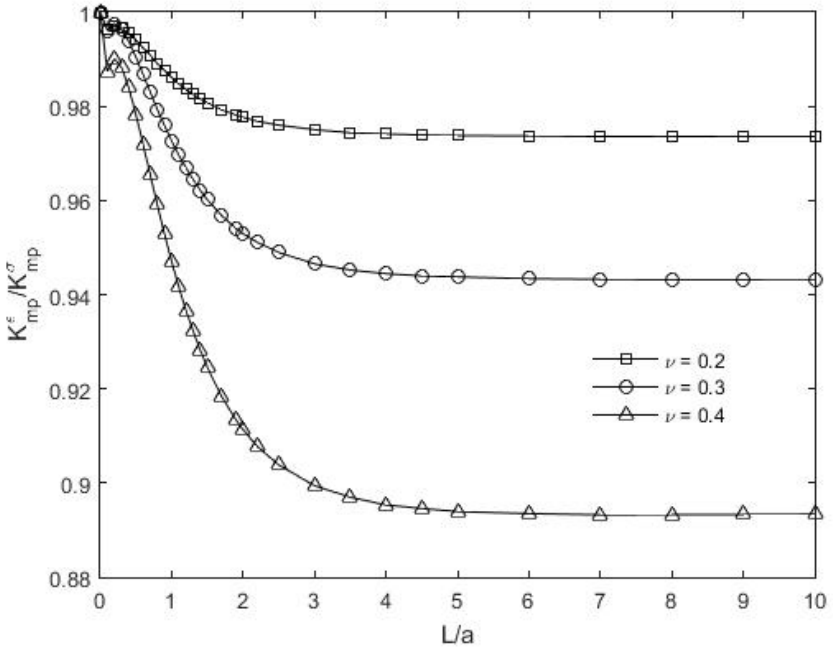

Figure 8-51: The distribution of $K^{\varepsilon}/K^{\sigma}$ at the hole tip of mid plane layer as function of normalized thickness for different Poisson's ratio.

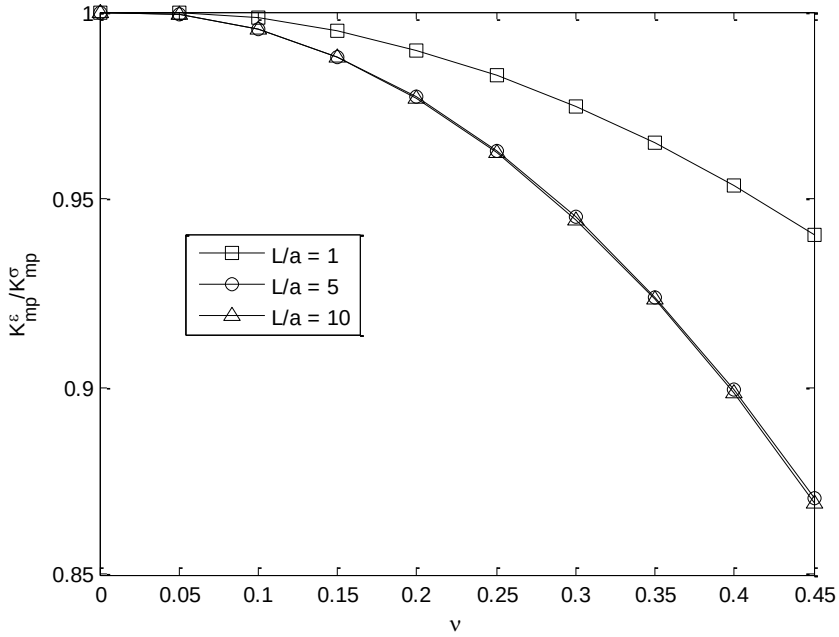

Figure 8-52: The distribution of $K^{\varepsilon}/K^{\sigma}$ at the hole tip of mid plane layer as function of Poisson's ratio for different normalized thickness.

Figure 8-53 shows the distribution of mid-plane values of $K^{\varepsilon}_{\mathrm{mp}}/K^{\sigma}_{\mathrm{mp}}$ as a function of plate thickness when the grain orientation is parallel or perpendicular to the applied stress, σ. Starting at K^{σ}_{mp} = 1, plane-stress (i.e., $L/a \sim 0$), these curves decreased monotonically with increasing thickness until $L/a > \sim 4$ where they approach constant (but different) values. The magnitudes of $K^{\varepsilon}_{\mathrm{mp}}/K^{\sigma}_{\mathrm{mp}}$ for very thick plates are substantially greater when the grain orientation of the wood is parallel, rather than perpendicular, to the externally applied stress, σ.

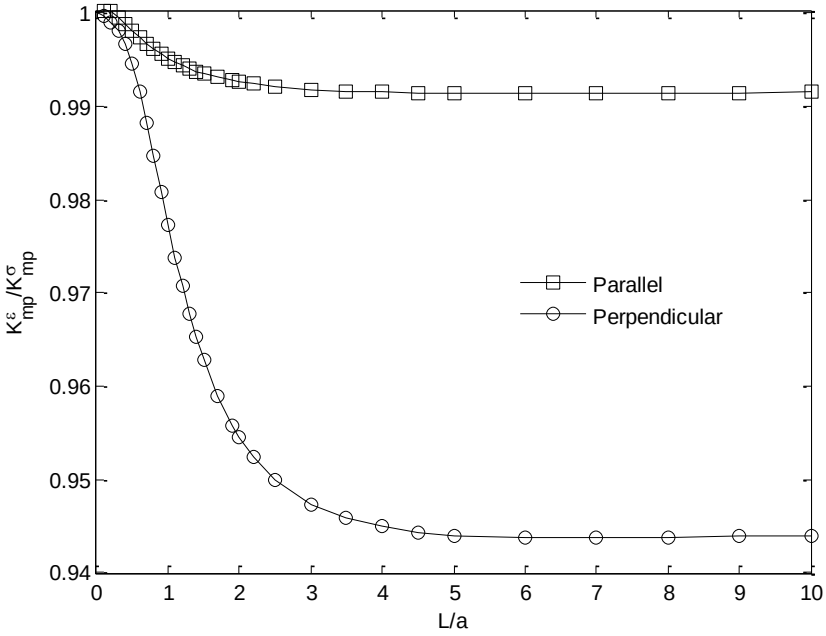

Figure 8-53: Distributions of $K^{\varepsilon}_{mp}/K^{\sigma}_{mp}$ as function of normalized thickness in Sitka Spruce for different grain orientations to the applied vertical stress.

8.4.1.4 The Distribution of $K^{\varepsilon}/K^{\sigma}$ in Front of the Hole Tip on Surface Plate for Different Normalized Thickness and Different Poisson's Ratio.

In the front of the hole tip on the plate surface, the out-of-plane stress constraint factor T_z is zero so the ratio of strain to stress concentration factor along this line can be simplified as following

$$K^{\varepsilon}/K^{\sigma} = 1 - \nu T_x \tag{8-20}$$

T_x is the in-plane stress constraint factor in the front of the hole tip on the plate surface. The distributions of $K^{\varepsilon}/K^{\sigma}$ in the front of the hole on the plate surface are functions of Poisson ratio and the in-plane stress constraint factor. There is no such expression for T_x in the front of the hole tip on the plate surface so the in-plane stress constraint factor for plane stress is used as an approximate expression for strain to stress concentration factor on the plate surface. By using the expression of T_x

$$K^{\varepsilon}/K^{\sigma} = 1 - \nu \frac{3(1-\xi^{-2})}{\zeta^2(2+\xi^{-2}+3\xi^{-4})} \tag{8-21}$$

The distributions of $K^{\varepsilon}/K^{\sigma}$ in the front of the hole on the plate surface for different normalized thickness and $\nu = 0.3$ is illustrated in Figure 8-54. The $K^{\varepsilon}/K^{\sigma}$ curves in the front of the hole on the plate surface have a minimum whose value depends on plate thickness and Poisson ratio and its location depends mainly on plate thickness. There are some differences between the approximate solution of $K^{\varepsilon}/K^{\sigma}$ on mid-plane layer with the values predicted from the FE solution on plate surface. The distributions of $K^{\varepsilon}/K^{\sigma}$ in the front of the hole on the plate surface for different Poisson's ratio and $L/a = 4.0$ is illustrated in Figure 8-55. For small values of Poisson's ratio ($\nu <$

0.3), the approximate solution provides a good agreement between the values of the approximate solution and the values of FE solutions. The difference between the FE results and the approximate solution increases with the increasing of Poisson's ratio and for large Poisson's ratio the approximate solution is not applicable to estimate the variation of $K^{\varepsilon}/K^{\sigma}$ on plate surface.

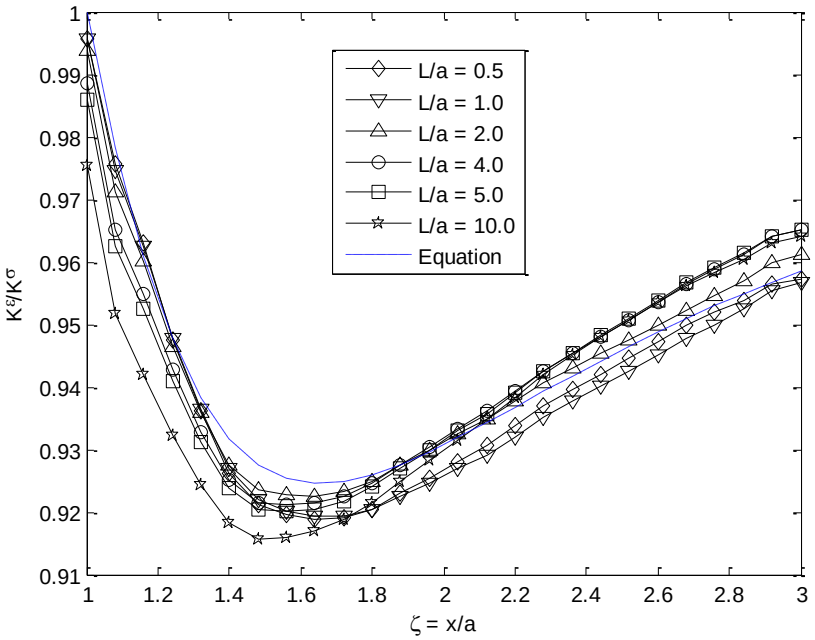

Figure 8-54: The distributions of $K^{\varepsilon}/K^{\sigma}$ in the front of the hole on the plate surface for different normalized thickness and ν = 0.3.

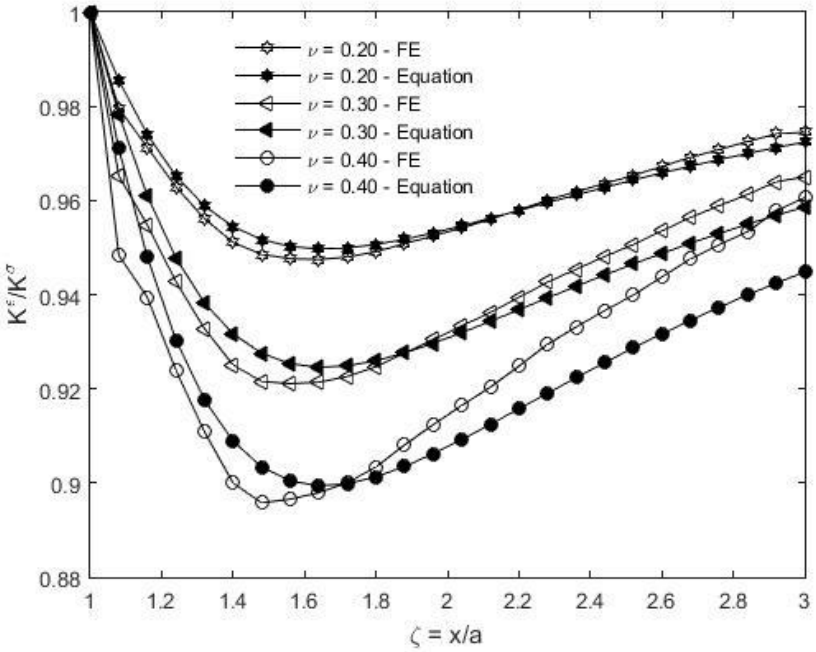

Figure 8-55: The distributions of $K^{\varepsilon}/K^{\sigma}$ in the front of the hole on the plate surface for different Poisson's Ratio and L/a = 4.0.

8.5 Discussion and Conclusions

The effect of thickness, Poisson's ratio for an isotropic plate, and grain orientation for orthotropic plates in stress and strain concentration factors in finite thickness plate were studied using 3D FE. The stress and strain concentration factors are different in elasticity and orthotropity state of a finite thickness plate in the front as well as along the thickness of the hole except on the plate surface. Not unlike in an isotropic plate, the stress and/or strain concentrations in perforated loaded orthotropic plates depend on the relative plate thickness. However, many results under orthotropy can be quite different from those in isotropic plates. In particular, they depend on whether the strongest/stiffest principal material direction is parallel or perpendicular to the direction of the external loading.

The distributions of $\sigma_{yy}(x,0,z)/\sigma_{yy}(a,0,z)$ are similar for isotropic and orthotropic Sitka Spruce plates when the vertical applied stress, σ, is either parallel or perpendicular to the grain

orientation. However, the distribution of T_x for an orthotropic plate when the applied stress, σ, is perpendicular to the grain can be different than when the applied stress, σ, is parallel to the grain or for an isotropic material. When the wood grain orientation is parallel to the applied loading, the maximum stress concentration factor occurs on the mid-plane and exceeds that on the external traction-free surface by ~8%. When the wood grain is perpendicular to the applied loading, the maximum stress concentration factor again occurs on the mid-plane and is ~15% higher than that on the external surface. By comparison, Sternberg and Sadowsky [94] showed that for an isotopic plate whose thickness is 0.7 that of the radius of the hole, the maximum stress concentration factor at the traction-free surface is 7% less, whereas that at the mid-plane is 3% higher, than the plane-stress value. Even when all other things are equal, unlike with isotropy, the stresses in orthotropic materials depend on the constitutive properties. Results show that the distributions of the in-plane stress constraint factor T_x and the values of stress concentration factor K^σ normalized by their values at the hole tip corresponding to each plane layer $K^\sigma_{\zeta=1}$, $K^\sigma/K^\sigma_{\zeta=1}$, are function of normalized thickness L/a, distance from the tip of the hole x/a, and location of the plane layer z/L for isotropic and orthotropic plates. The plane stress solution of T_x can only describe the variation of T_x near the mid-plane (i.e. small z/L) or near the tip of the hole (i.e. small ζ).

The through thickness distribution of the stress or strain concentration factor (K^σ and K^ε) normalized by value of the stress or strain concentration factor on the mid-plane ($K^\sigma/K^\sigma_{\mathrm{mp}}$ and $K^\varepsilon/K^\varepsilon_{\mathrm{mp}}$) depends on plate thickness. The maximum stress and strain concentration factors ($K^\sigma_{\max}$ and $K^\varepsilon_{\max}$) through the thickness at the hole occur at mid-plane for thin plates and occur on a different plane close to the plate surface for thick plates. The stress and strain concentration factors (K^σ and K^ε) decrease rapidly near the plate surface reach lower values which are not representative of the overall stress and strain concentration factors through the thickness as the thickness becomes

large enough for isotropic and orthotropic plates or for large Poisson's ratio for isotropic plate. For an isotropic plate, increasing the Poisson's ratio will increase the value of the maximum stress and strain concentration factor ($K^{\sigma}_{\max}$ and $K^{\varepsilon}_{\max}$) but has no effect on changing the location of the maximum stress or strain concentration factor. The increasing of Poisson's ratio will increase the difference between the through thickness mid-plane value and the maximum value ($K^{\sigma,\varepsilon}_{\max} - K^{\sigma,\varepsilon}_{\mathrm{mp}}$) and the difference between the mid-plane value and the surface value ($K^{\sigma,\varepsilon}_{\mathrm{mp}} - K^{\sigma,\varepsilon}_{\mathrm{sur}}$) of stress and strain concentration factor.

In a finite thickness plate, the stress concentration factor on mid-plane K^{σ}_{mp} is higher than the value in plane-stress, K^{σ}_{ps}, or plan-strain, $K^{\sigma}_{\text{plain strain}}$, where the strain concentration factor on mid-plane, $K^{\varepsilon}_{\mathrm{mp}}$, is lower than the value in plane-stress, $K^{\varepsilon}_{\mathrm{ps}}$, and greater than the value in plane-strain, $K^{\varepsilon}_{\text{plain strain}}$, for a finite thickness plate. The stress or strain concentrations on the mid-plane can increase from their plane-stress values when L/a = 1 to some relative maximum in a thicker plate and then decrease in much thicker plates. For isotropic and orthotropic finite thickness plate, the stress and strain concentration factors on the plate surface ($K^{\sigma}_{\mathrm{sur}}$ and $K^{\varepsilon}_{\mathrm{sur}}$) at hole tip are essentially equal to each other and lower than the values in plane-stress and plane-strain.

Since the tensile strength transverse to the wood grain or the fibers in structural orthotropic composites is usually appreciably less than that parallel to the grain or fibers, the present results can be particular significant. For a plate loaded in tension, the structural strength can be very low when the wood grain is transverse to the direction of externally applied stress. On the other hand, the low tensile strength transverse to the strong/stiff material direction in orthotropic composites can be particularly detrimental in tensile-loaded bolted joints involving such materials in that it often leads to splitting of the material supporting the bolt. Recognizing that the worst stresses in

thick plates frequently occur subsurface, such splitting could initiate below the surface and hence not be detected prior to catastrophic structural failure.

The distributions of $K^{\varepsilon}/K^{\sigma}$ for $\zeta \geq 1$ (away from the hole) are different on different planes and each curve corresponding to its plane has a minimum whose value depends on the Poisson's ratios, plane-location, and the plate thickness. Although the present minimums in the Sitka Spruce tend to occur at a common location away from the hole, the minimum locations might depend on material properties.

The directional strength dependency, combined with the fact that stresses σ_{xx}, σ_{yy} and σ_{zz} can all be nonzero on internal planes ahead of the hole (i.e., $x/a \geq 1$), can be a strength concern in orthotropic materials. That maximum stresses and/or strains associated with holes can occur other than on the external traction-free plate surfaces where measurements are most readily made is technically significant. The stress and strain concentrations factors are equal to each other only at the edge of the hole.

This chapter emphasizes the response in a highly orthotropic structural material, Sitka Spruce. However, the Appendix C contains some comparative results for a unidiretional carbon-epoxy composite. As with the Sitka Spruce, the maximum stress concentrations in such man-made composites can occur below the external surfaces. The principal material directions are aligned here with the plate geometry and loading. Consideration should be given to cases when the principal material directions are inclined to the plate geometry and direction of loading

The ratio of the strain to stress concentration factor $K^{\varepsilon}/K^{\sigma}$ for isotropic plate is function of Poisson's ratio and in-plane T_x and out-of-plane T_z stress constraint factors. This ratio $K^{\varepsilon}/K^{\sigma}$ has been studied in front and along the thickness of the hole tip. The distributions of $K^{\varepsilon}/K^{\sigma}$ in the

front of the hole are different on different plane layers and each curve corresponding to its plane layer has a minimum which its value and location depends on Poisson's ratio, plane layer location, and the plate thickness. The distributions of $K^{\varepsilon}/K^{\sigma}$ along the thickness at the hole tip is function of Poisson's ratio and out-of-plane stress constraint factor. The changing of the Poisson's ratio or thickness does not change the curve pattern of the distributions of $K^{\varepsilon}/K^{\sigma}$ along the thickness at the hole tip.

The $K^{\varepsilon}_{\mathrm{mp}}/K^{\sigma}_{\mathrm{mp}}$ curve versus the thickness or Poisson ratio is a monotonic descending function and reaches constant values when the thickness becomes large enough. The distributions of $K^{\varepsilon}/K^{\sigma}$ in the front of the hole on the plate surface is function of Poisson ratio and the in-plane stress constraint factor. The $K^{\varepsilon}/K^{\sigma}$ curves in the front of the hole on the plate surface have a minimum which its value and location depend on plate thickness and Poisson ratio.

The main purpose of this chapter is not primarily to give numerical solutions for certain geometries but to highlight the effects of thickness and material symmetry on stress and strain concentration factors for three-dimensional stress or strain concentration problems and consequently to provide guidance for static and cyclic (fatigue) situations. The author is unaware of any previous research in determining the stress and strain concentration factors for orthotropic materials. Aspects of this chapter were presented in Midwest Experimental Mechanics Graduate Student Symposium in 2015 and published in ASCE Journal of Engineering Mechanics [107].

Chapter 9: Evaluation of Bone Surrogate Bending Stiffness using 3- and 4-Point Bending

This chapter discusses testing a customizable surrogate bone analog composed of inexpensive materials and femur bone made of nylon material using 3D printer in order to mimic bone strength and geometry for testing validation of femoral bending. Such an analog reduces the costs of mechanical bone testing, and would allow for more consistent and reliable data acquisition utilized in predicting bone strength in patients suffering from osteoporosis. The surrogate bone was designed and manufactured by Caitlyn Collin [108]. Manufactured testing apparatuses and performing appropriate testing on various bone samples.

9.1 Introduction

Osteoporosis is generative bone disease which results in progressively compromised bone mechanical properties and causes a bone fracture. Over half of the total adult population of the United States over the age of 50 suffers from osteoporosis or low bone mass as reported by the National Osteoporosis Foundation in 2014 [109]. The number of adults over age 50 with osteoporosis or low bone mass will grow from approximately 54 million in 2014 to 64.4 million by 2020 and to 71.2 million by 2030 assuming osteoporosis or low bone mass prevalence remain unchanged. The increased risk of patient morbidity attributed to osteoporotic related fractures prioritizes early detection of a loss in bone mechanical properties. Methods used to evaluate bone mechanical properties vary widely depending on the motivation and environment which includes re-

search labs (biomechanics researcher), hospital and clinics (individual specialist such as orthopeadic surgeons), and industry (such as medical device companies). This necessitates the importance of developing new methods to evaluate mechanical properties. Reference [108] introduced the most common methods and evaluated methodological error between bone stiffness prediction methods and evaluated the ease of implementation of each method to predict long bone stiffness. A bi-material and CT scan compatible bone surrogate was designed and fabricated for quantification of methodological error between experimental, analytical, and computational bone bending stiffness prediction methods. These chapter discusses using 3- and 4-point bending method on the fabricated surrogate bone to predict the bone stiffness using digital image correlation (DIC).

Bone is a multiphase material characterized as heterogeneous, anisotropic, and viscoelastic. Mechanically, bone is responsible for maintaining the desired balance between the need for a certain degree of stiffness, to reduce strain on the body, as well as a high enough level of ductility to provide shock absorption, reducing the incidence of fracture. As a result, bone is a complex hierarchical composite comprised of a series of organic, inorganic, and cellular components [108].

The most common and reliable testing in determining bone mechanical properties (bone stiffness, strength, and/or flexural rigidity) in research and industrial labs is destructive mechanical testing. The accuracy of bone mechanical properties which depend on both geometry and strength of the material within is limited to the assumption of idealized cross-sectional geometries which typically only include macroscopic anatomical features and neglected trabecular architecture. Several researchers have found that apparent bone density and bone mineral content account for roughly 70-80% of the variation in experimentally determined stiffness and Young's modulus. Therefore, any

method implemented for clinically monitoring bone strength must be able to account for both the material properties of bone tissue as well as bone geometry [108,110]. On the other hand, analytical calculations based on physics principals provide a pragmatic solution for determining bone mechanical properties. The accuracy of this approach is limited by the geometrical and material information, the assumption of prismatic cross-sectional area, and the assumption of idealized isotropic linear elastic response to loading where bone behavior is anisotropic, nonlinear and viscoelastic.

Recently, the bone frailty and healing are evaluated using medical-image based analytical techniques which are capable of computing specimen specific cross-sectional geometries and heterogeneous material properties [111]. References [112–114] used micro-computed tomography (μCT) image-based analytical techniques in studies of murine fracture healing models and found significant correlations between callus tissue mineral content and mechanically determined strength and stiffness. These results further support that bone strength is dependent on both geometric and material properties and suggest that coupling medical-image based analysis with mechanical testing may lead to the determination of specific clinical parameters for evaluating bone integrity and refracture risk. As with the purely analytical method, accuracy of mechanical properties derived from medical-image based analytical methods is dependent on meeting the theoretical assumptions of the classical mechanics [108].

The most accurate and informative of the mechanical property characterization methods is medical Image-based finite element analysis. This considers as an alternative to destructive mechanical testing and capable of predicting the mechanical response of an object with complex geometry and material properties under a multifarious loading environment using computational modeling techniques. References [108,115–123] used image-based FEA to evaluate failure load

and fracture type of subject-specific proximal femur models under stance and fall loading conditions. The most disadvantages of image-based FEA are the complexity in designing the model, the considerable high computation time, the difficulties in validating the model, and the expertise of user.

The goal of this chapter is to test experimentally using DIC the surrogate bone using 3- and 4-point bending and femur bone made of Nylon 12 PA 360 using 3D printer in order to mimic the femur bone in terms of strength and geometry.

9.2 Literature Review

Volume kinematic measurements in composite materials can be investigated by association of X-ray micro-computed tomography acquisition and Digital Volume Correlation (DVC) techniques [124–126]. This study only considers using 2 cameras and study the deformation and strain of surrogate bone using Vic-2D and Vic-3D software. Reference [127] conducted an experimental on the bovine bone by carrying out the three-point bending test with 3D digital image correlation (DIC) method, which provides a noncontact and full field of displacement measurement in order to understand the fracture mechanisms of bone subjected to external force well. The local strain and damage evolution of the bone was recorded real time and the results show that the deflection measured by DIC agreed well with that obtained by the displacement sensor of the mechanical testing machine. The relationship between the deflection and the force is nearly linear prior to reaching the peak strength which is about 16 kN for the tested bovine tibia. The full-field strain contours of the bone show that the strain distribution depends on not only the force direction, but also the natural bone shape. The natural arched-shape bovine tibia bone could bear a large force,

due to the tissue structure with high strength, and the fracture propagation process of the sample initiates at the inner side of the bone first and propagates along the force direction.

Reference [128] carried out a microscale three-point bend experiment on wood and determined the full 3D strain field by use of digital volume correlation, based on reconstructed 3D image data acquired with synchrotron radiation micro-computed tomography. The correlation algorithm is based on a Chebyshev polynomial description of the displacements, which allows a continuous representation of the 3D deformation fields. 3D strain calculations based on the obtained displacement data shows a concentration of tensile strain in the region where the specimen eventually collapses. The experimental results show that the use of X-ray-based tomography with high spatial resolution in combination with digital volume correlation can successfully be used to perform 3D strain measurements on wood, at the microscale. References [108,115–123] used image-based FEA to evaluate failure load and fracture type of subject-specific proximal femur models under stance and fall loading conditions.

9.3 Testing Methods

Fracture healing is typically subjectively evaluated via radiographs or manual examination. Radiograph-based callus healing analysis uses visual markers, such as callus bridging and the disappearance of the fracture line, in order to track the state of fracture healing. Unfortunately, several studies on the efficacy of radiographic analysis have shown it to have a significant number of drawbacks: inaccuracy, poor to no correlation between the amount of callus and the stiffness of healed bone; and, an overall lack of relation between both the general fracture appearance and cortical bridging with physical bone healing results. From a mechanical perspective, fracture healing represents a gradual increase in strength and stiffness of the fractured bone. In the case of

secondary healing, the increase in strength and stiffness is directly associated with the change in mechanical properties of the initial provisional callus and the latter boney callus. From this perspective, obtaining information on the rate of increase of callus mechanical properties would be valuable in determining the rate of fracture healing as well as providing an objective quantitative definition of the completion of secondary fracture healing.

9.3.1 Mechanical Testing Methods

Mechanical testing methods such as bending (three- and four-point bending), compressive or tensile (uniaxial loading), or torsional (torsion testing) load-deformation tests can be used to determine bone mechanical properties [129]. The resultant force is recorded as a function of the applied deformation and analyzed to determine extrinsic and intrinsic parameters such as stiffness and strength, respectively. For characterization of whole bone mechanical properties, three- and four-point bending, Figure 9-1, require less sample preparation and less susceptible to misalignment during testing than both uniaxial and torsional loading methods.

Three-point bending test, Figure 9-1a, generates high shear stress at the midsection of the bone and the applied bending moment is non-uniform along the length of the bone. Whereas, four-point, Figure 9-1b, produces uniform bending moment region and zero shear force between the two upper supports giving that the forces at each loading point are equal (upper and lower supports are in contact with the bone throughout testing). The upper and lower supports used in both tests must be fairly smooth and rounded to minimize stress concentration factor at the point of contact.

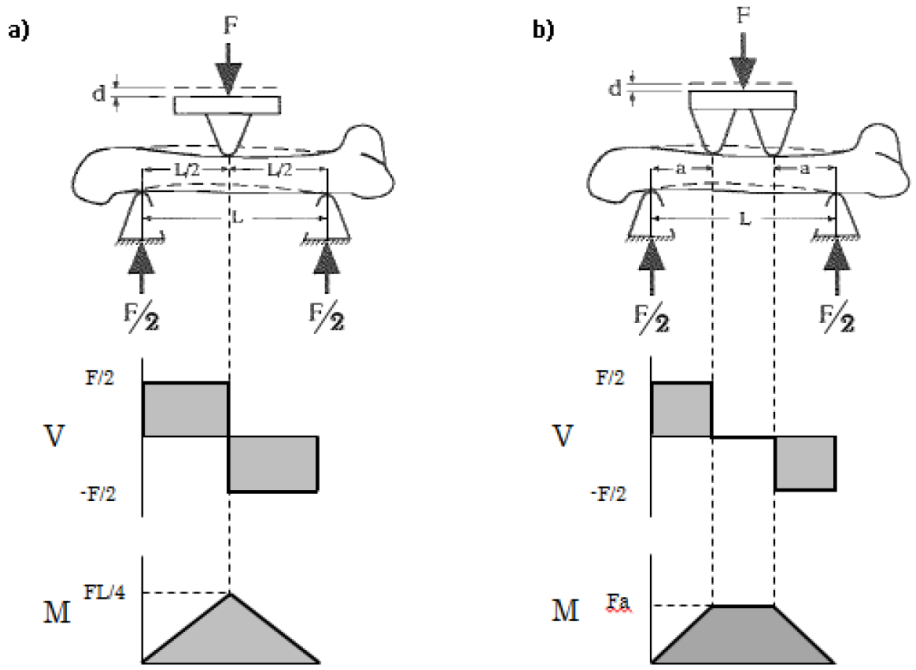

Figure 9-1: Shear (V) and bending moment diagrams of (a) three-point and (b) four-pint bending tests [108].

The accuracy of the bending tests is limited by a variety of factors such as; (a) the span length to bone diameter ratio is suggested to be L/D = 20 to prevent underestimation of the specimen's Young's modulus due to additional deformation from shear forces [73,130], (b) idealized the shape of the bone as cylindrical shape, (c) linear elastic material, and (d) plane sections remain plane and perpendicular the neutral axis throughout the bending test. The deflection, maximum deflection, stiffness and stress equations for 3-point and 4-point bending tests are given in Table 9-1. The equations derived using Euler-Bernoulli beam theory for prismatic, long beams in pure bending. The shape and cross-sectional area of whole bone specimens used to calculate the area moment of inertia are typically assumed to be hallow with constant elliptical or circular cross sections along their length [131–134].

Table 9-1: Deflection, maximum deflection, stiffness and stress equations for 3-point and 4-point bending tests.

	3-Point Bending	4-Point Bending
Deflection, $v(x)$	$-\frac{Fx}{48EI}(3L^2 - 4x^2)$	$-\frac{Fa}{12EI}(3Lx - 3x^2 - a^2)$
Maximum deflection	$\delta_{max} = \frac{FL^3}{48EI}$	$\delta_{max} = \frac{Fa}{48EI}(3L^2 - 4a^2)$
Rigidly, F/δ_{max}	$\frac{48EI}{L^3}$	$\frac{48EI}{a(3L^2 - 4a^2)}$
Flexural Rigidity, EI	$\frac{FL^3}{48\delta_{max}}$	$\frac{Fa(3L^2 - 4a^2)}{48\delta_{max}}$
Maximum stress, σ_{max}	$\frac{FLc}{4I}$	$\frac{Fac}{2I}$

E is elastic modulus, I is the area moment of intertia, L is the distance between the lower supports, F is the force applied, c is the maximum distance from the neutral axis to bone surface, and a is the distance between upper and lower supports.

9.4 Digital Image Correlation

Digital Image Correlation (DIC), also referred to digital image tracking (DIT), is a full-field computer-based image analysis technique for the non-contact measurement of displacements of a surface equipped with a speckle pattern. The method tracks the motion of the speckles by comparing the gray scale value at a point (subset) in a deformed and undeformed configuration. Two sets of images are recorded; the first image typically being at zero load and the second image under load. A single camera setup can record both u and v in-plane full-field deformations. Out-

of-plane motions can be recorded if two cameras are employed. Digital image correlation (DIC) is a restively new and popular optical method that employs tracking and image registration techniques for accurate two dimensional (2D) or three dimensional (3D) measurements of changes in digital images. The achievable DIC resolution depends on a number of factors, including but not limited to, camera resolution, lens optical quality, and speckle size and quality. However, unlike electronic speckle, the surface of the structure under study has to have speckle pattern for tracking; but unlike TSA, DIC does not require cyclic loading. The latter makes DIC attractive as cycling can be inconvenient and particularly challenging for complicated boundary conditions. Advantages of DIC include full-field, non-contacting, non-destructive, static/dynamic measurements. A DIC system (by Correlated Solutions, Inc., Columbia, SC, USA, [36]) was used to record the images of the tested specimens in its loaded and unloaded conditions and employed for evaluating the displacements and strains. To perform the tracking, the subset was shifted until the pattern in the deformed image closely matched that of the reference image.

9.4.1 Calibration

Calibration of the system was performed before taking the speckle images. For calibration the Vic-2D DIC system, only known distance should be entered to the system so the output of the DIC software is the physical units rather than in pixels. For calibrating the Vic-3D DIC system, a calibration grid of the appropriate size was selected and placed over the area of interest. When utilizing two cameras, a separate calibration grid (provided by Correlated Solution with the DIC package) was used to evaluate the displacement data in physical units rather than in pixels. Calibration of the DIC system creates a 3D-coordinate system on the specimen's surface and removes measurement bias. This is done by moving, imaging and analyzing a rigid calibration grid in front of the pair of stereo cameras. The calibration process also calculates the cameras' intrinsic and

extrinsic parameters, triangulates the cameras' position and removes lens distortions [36]. Images of the calibration grid in different orientations and different angles were captured and later these pictures were used to conduct the calibration analysis using the Correlation Solution supplied Vic snap software.

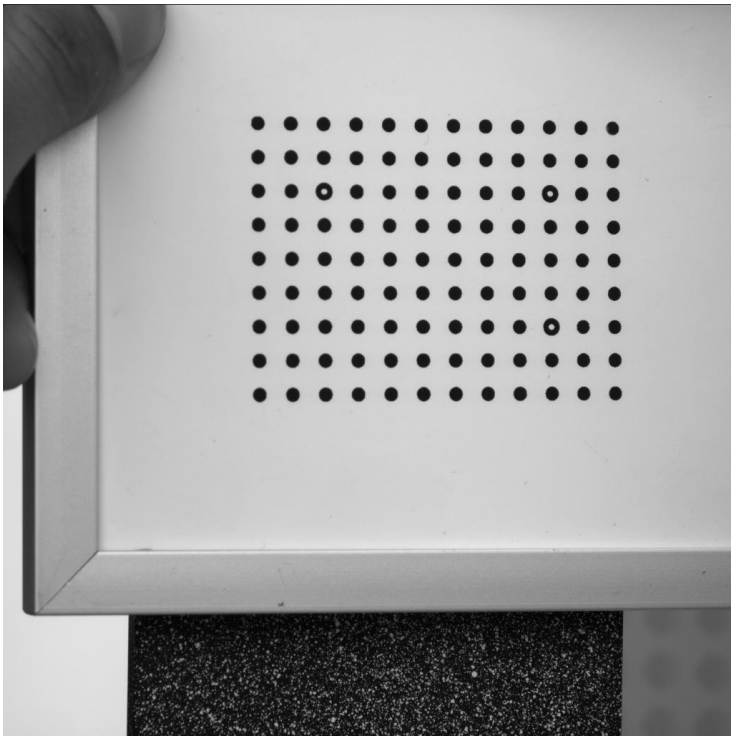

Figure 9-2: Using a Correlated Solution Inc.'s calibration grid in front of the specimen's area of interest to calibrate the system.

9.4.2 Subset and Step Size

The term subset in DIC, is the selection of an area of the speckle image over the area of interest that is used to track the displacement between images. DIC requires the use of a random and dense speckle pattern on the specimen that can provide unique markers to search for, between the unloaded and loaded images. The Vic-snap software assigns a predefined mesh of subsets or grids over the speckle image and from the random speckle pattern within each of the subsets DIC measures displacements by matching the reference subsets in the undeformed images with the

target subsets of the deformed images. The subset size is user defined and mostly depends on the quality of the speckle pattern. The accuracy of the measured displacement critically depends on the subset size. The subset size should be selected in such a way that each subset contains enough unique and identifiable speckles to achieve reliable displacements.

Step size defines the spacing of the points that are analyzed in DIC. A step size 1 means that the correlation analysis will be performed at every pixel in the area of interest. Analysis time is inversely proportional with the square of the step size.

9.4.3 Extra Light

While conducting the DIC experiment, two cameras were pointed onto the specimen with angle around 20^{o}. The room did not have enough light and therefore extra light was used to illuminate the specimen, Figure 9-3. The available lens of 1.9 focal ratio and 35 mm focal length was selected that allowed the camera to view the specimen normal to its line of sight and still image the entire area of interest (AOI) of the tested specimen. Once the camera (appropriate lens, etc.) were set-up, Vic-Snap software (Correlation Solutions, Inc.) was employed to preview the images.

Figure 9-3: Extra light was used to illuminate the specimen.

9.4.4 DIC Data Analysis

Using Correlated Solution's Vic Snap software, the captured images were processed and correlated. In DIC, a set of images for the specimen loaded at different loads need to be provided along with a reference image (digital image captured by the DIC system at zero load representing undeformed condition of the specimen). The correlation algorithm tracks a group of pixels known as subset and shifts the subset until the deformed image matches the reference image. Calibration scale is set using the Vic Snap software so that the subset shifting can be expressed as physical units such as displacements. Once the reference image, area of interest (AOI) and calibration scale are set, the software can perform the analysis and find the speckle displacements.

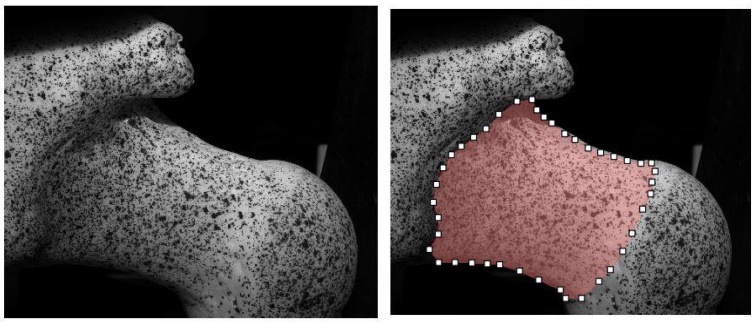

(a) (b)

Figure 9-4: Processing of the digital images using Vic snap software; (a) DIC image, (b) area of interest (AOI) selected using Vic snap software.

Figure 9-4, show how the analysis using the Vic Snap software is done. In Figure 9-4, (a) is an image of the loaded specimen captured by the DIC camera. The user needs to specify the area of interest and also subtract any discontinuity in the specimen manually as shown, Figure (b) the shaded area is the area of interest (AOI) on which the analysis will take place, Figure (c) indicate the analysis completed by the Vic snap software showing the displacement in the strong-stiff (vertical) direction.

9.5 Surrogate Bone

Reference [108] designed and developed a bi-material and CT scan compatible bone surrogate which provides consistent reproducible mechanical properties for methodological evaluation of experimental, analytical, and computational bone bending stiffness prediction methods. The bone surrogate has an outer shell made of stock acetyl co-polymer (AC) with rectangular cross sectional area of 25.0 ± 0.025 mm $\times$ 37.5 ± 0.025 mm and length of 102 ± 0.025 mm and a cylindrical core made of 40 pcf high-density polyurethane foam (HDPU), Figure 9-5. The tensile, compressive, and bending moduli are 384 ± 22.6, 2300 ± 115, and 2850 ± 82.0 MPa for AC and 212 ± 10.1, 342 ± 5.68, and 596 ± 49.1 MPa for HDPU, respectively [108]. Two bone surrogates

were considered; the first one with the core of the outer shell is filled by HDPU and the second one the outer shell is hollow. The flexural bending rigidity for bone surrogate is

$$EI = \left(E_{b,AC}\right)\left(\frac{bh^3}{12} - \frac{\pi D^4}{64}\right) + \left(E_{b,HDPU}\right)\left(\frac{\pi D^4}{64}\right)$$

$$= 2850\left(\frac{37.5 \times 25^3}{12} - \frac{\pi 14.68^4}{64}\right) + 596 \times \frac{\pi 14.68^4}{64} = 134.0 \times 10^6 \text{ N} \cdot \text{mm}^2$$

$$= 134 \text{ N} \cdot \text{m}^2$$

The 3- and 4-point bending tests were conducted using MTS Sintech 10/GL testing machine (MTS, Eden Prairie, MN) with displacement rate of 5.0 mm/min. The plane displacement field was captured using one camera of DIC and processed using Vic-2D correlated solution. The distance between the lower supports was fixed to be L = 2 in = 50.8 mm. The distance between the upper and lower supports in the 4-point bending test was a = 12.7 mm. The radii of the pin supports at each point of contact with the surrogates used in the 3- and 4-point bending apparatus were 2.5 mm. The maximum applied load was approximately F = 6,000 N, which is below the surrogate yield strength [108]. Incremental loads of approximately 1500 N, from 0 N to 6,000 N, were applied to the surrogate and images were captures at each increment using Grasshopper CRAS-50S5M camera with a 35 mm focal length lens and focal ratio of 1.9 (Point Grey Research, Richmond, BC, Canada).

The contour plot of DIC measured v-displacement in y direction at 6,000 N load increment on an image of the filled surrogate bone from 3-point bending test for the six trials are plotted in Figure 9-6 and Figure 9-7. The v-deflection at y = 0 is plotted as function of x-position in Figure 9-8a and Figure 9-9a. These figures were adjusted such that the v-deflection at support locations is shifted to zero and the corrosponding figures were plotted again in Figure 9-8b and Figure 9-9b.

The maximum deflection, δ_{max}, from these figures for the raw and adjusted data were used in the equation $EI = FL^3/48\delta_{max}$ from Table 9-1 to find the bending stiffness and the results were tabulated in Table 9-2.

The contour plot of DIC measured v-displacement in y direction at 6,000 N load increment on an image of the filled surrogate bone from 4-point bending test for the six trials are plotted in Figure 9-10 and Figure 9-11. The v-deflection at y = 0 is plotted as function of x-position in Figure 9-12a and Figure 9-13a. These figures were adjusted such that the v-deflection at support locations is shifted to zero and the corrosponding figures were plotted again in Figure 9-12b and Figure 9-13b. The maximum deflection, δ_{max}, from these figures for the raw and adjusted data were used in the equation $EI = Fa(3L^2 - 4a^2)/48\delta_{max}$ from Table 9-1 to find the bending stiffness and the results were tabulated in Table 9-2.

DIC flexural bending rigidity (EI_{DIC}) of the bone surrogate was calculated for 6,000 N at the maximum deflection located at (0,0) where the adjusted DIC flexural bending rigidity ($EI_{DIC,adj}$) were calculated based on the maximum deflection when the end deflections at $x = \pm$ 25 mm shifted to zero.

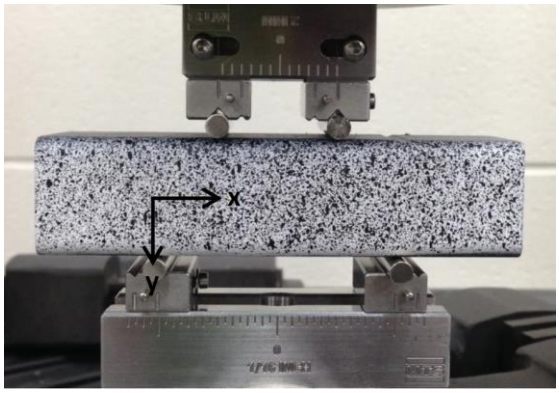

Figure 9-5: Black speckle pattern applied on the surrogate bone prior DIC testing.

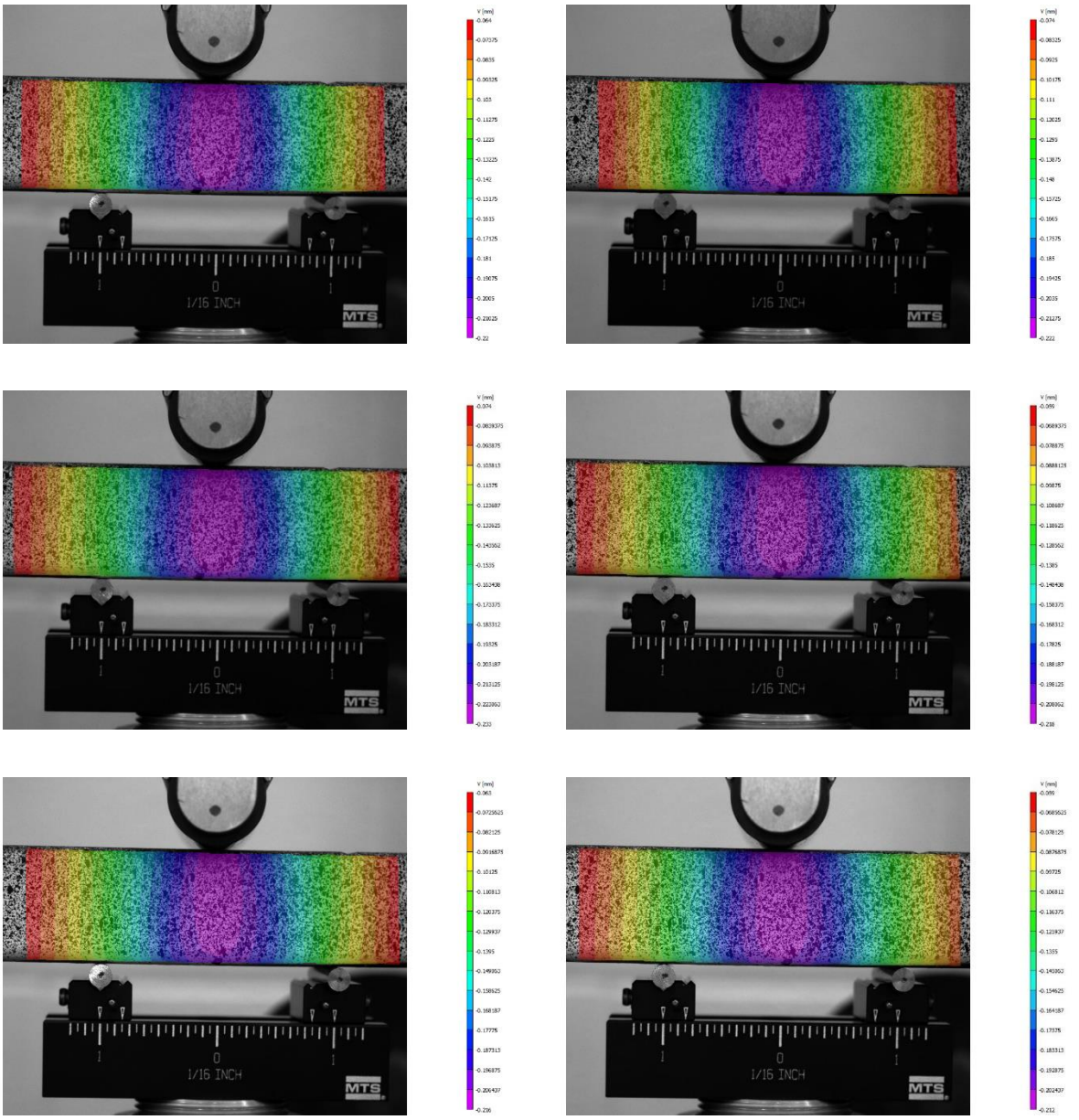

Figure 9-6: Contour plot of the calculated DIC v-displacement in y-direction at 6,000 N load increment on an image of the filled surrogate bone from 3-point bending test for the six trials.

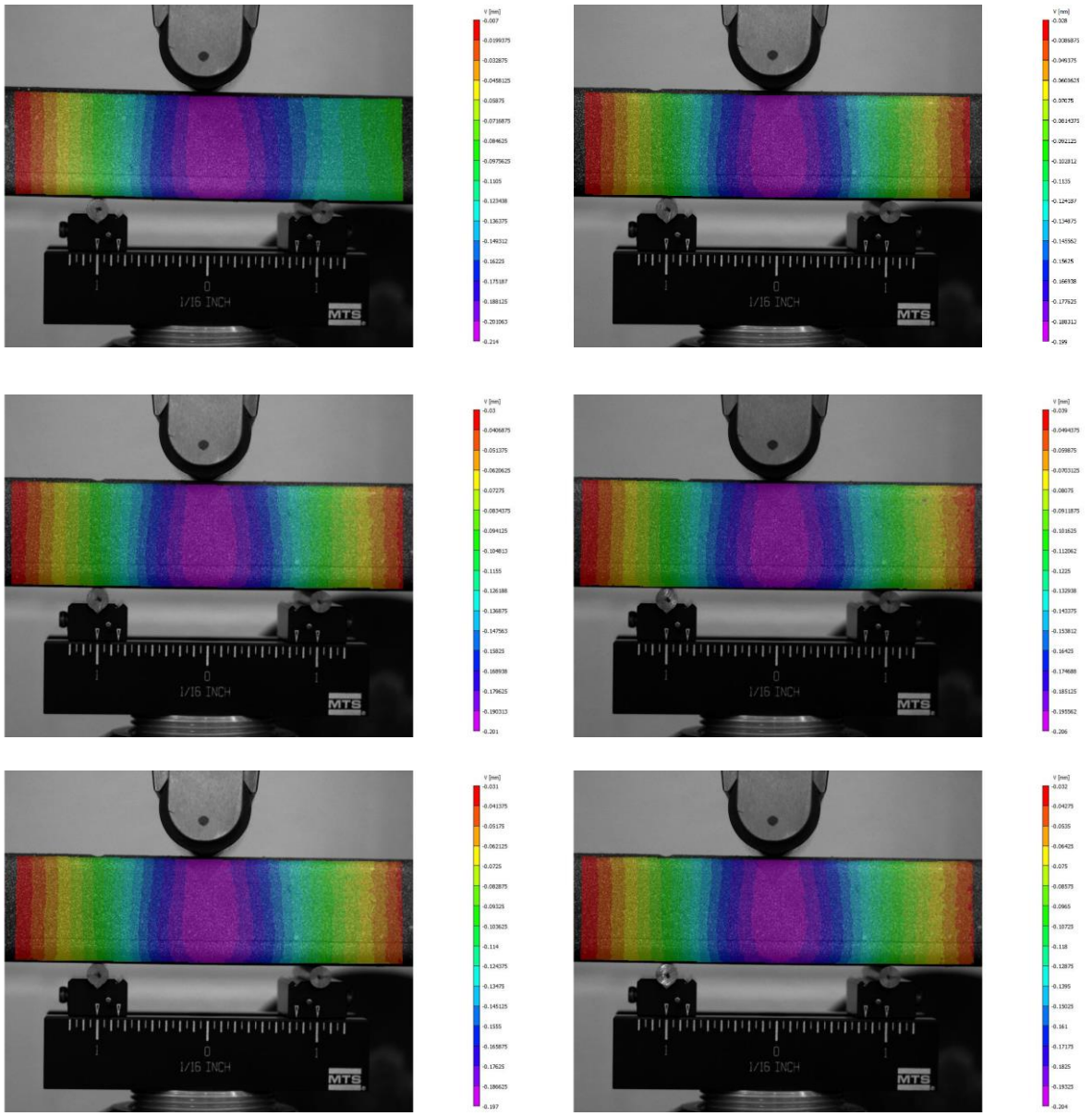

Figure 9-7: Contour plot of the calculated DIC v-displacement in y-direction at 6,000 N load increment on an image of the hollow surrogate bone from 3-point bending test for the six trials.

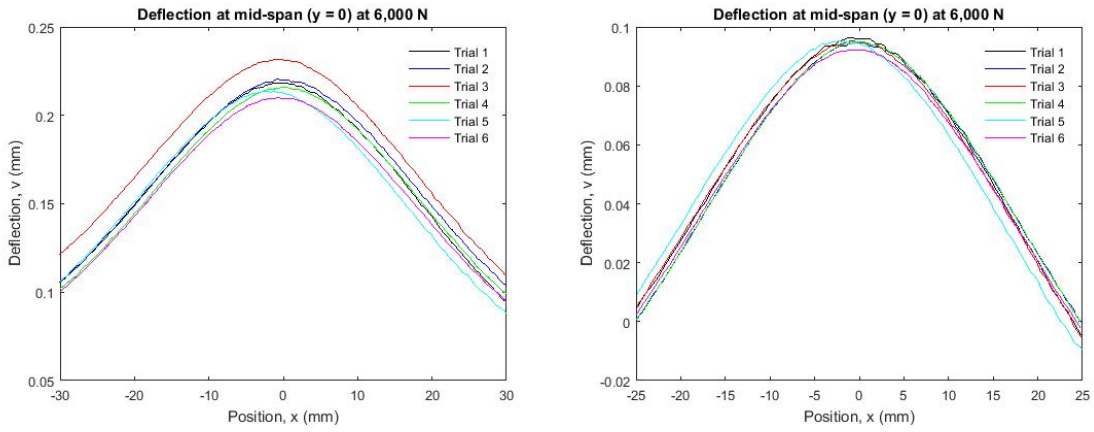

(a) (b)

Figure 9-8: DIC v-deflection at line y = 0 versus x-position at 6,000 N for the six trials from 3-point bending test for filled bone surrogate; (a) raw data and (b) adjusted data.

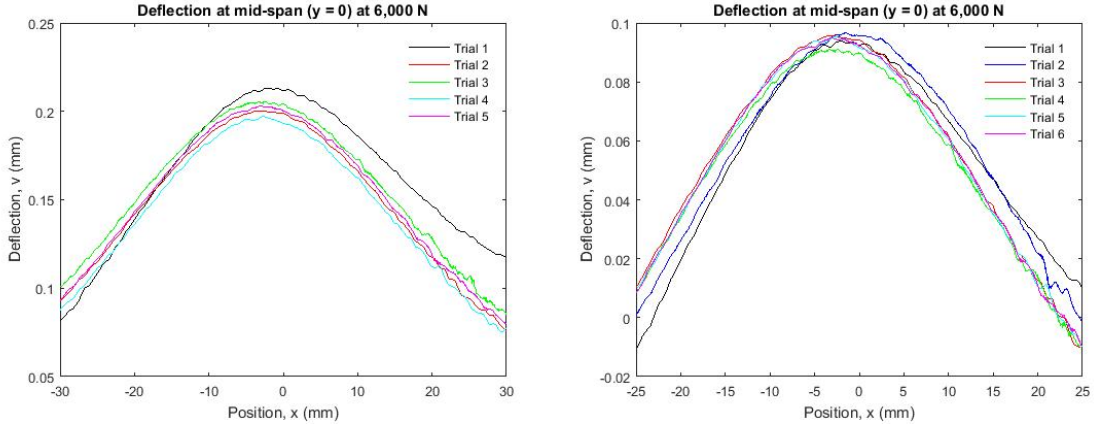

(a) (b)

Figure 9-9: DIC v-deflection at line y = 0 versus x-position at 6,000 N for the six trials from 3-point bending test for hollow bone surrogate; (a) raw data and (b) adjusted data.

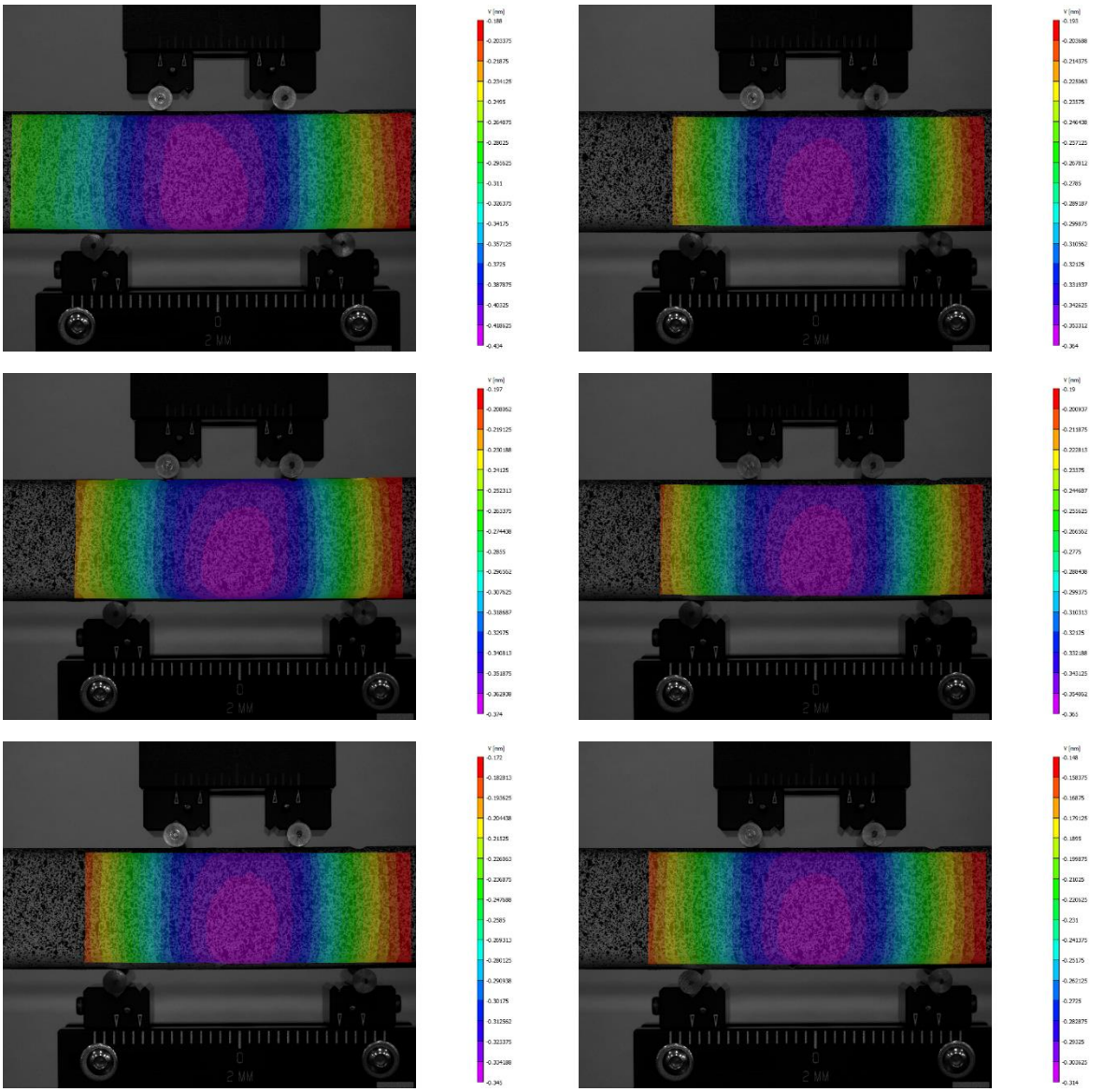

Figure 9-10: Contour plot of the calculated DIC v-displacement in y-direction at 6,000 N load increment on an image of the filled surrogate bone from 4-point bending test for the six trials.

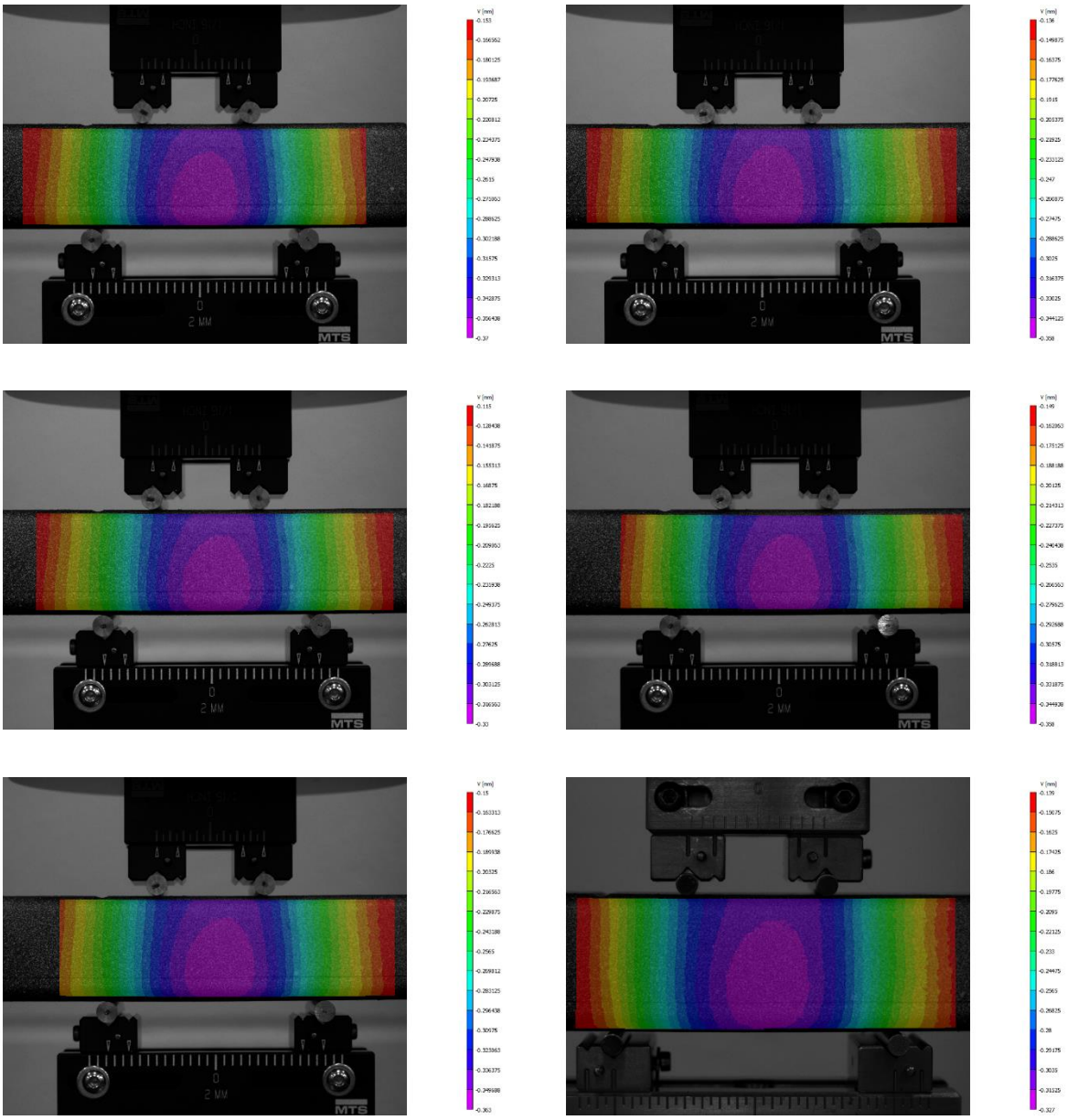

Figure 9-11: Contour plot of the calculated DIC v-displacement in y-direction at 6,000 N load increment on an image of the hollow surrogate bone from 4-point bending test for the six trials.

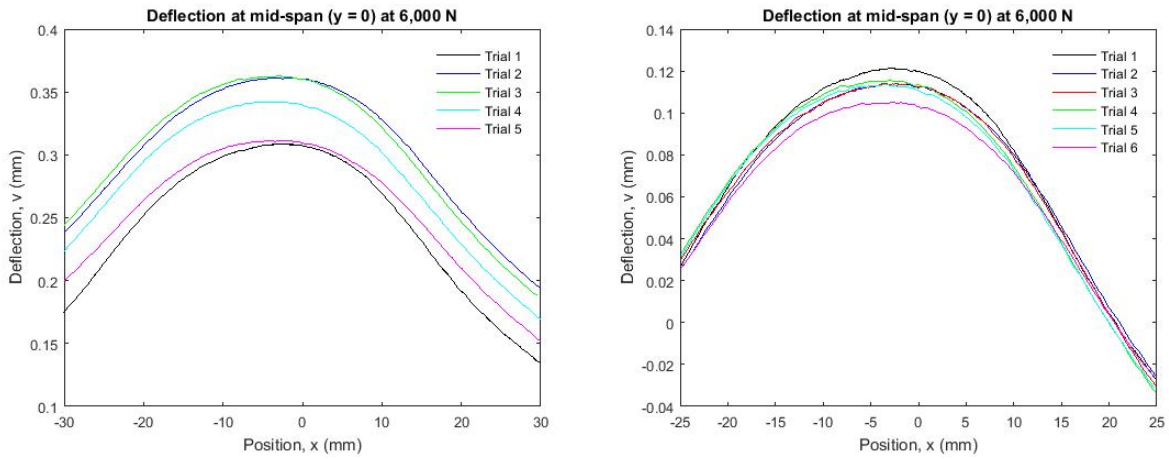

(a) (b)

Figure 9-12: DIC v-deflection at line $y = 0$ versus x-position at 6,000 N for the six trials from 4-point bending test for filled bone surrogate; (a) raw data and (b) adjusted data.

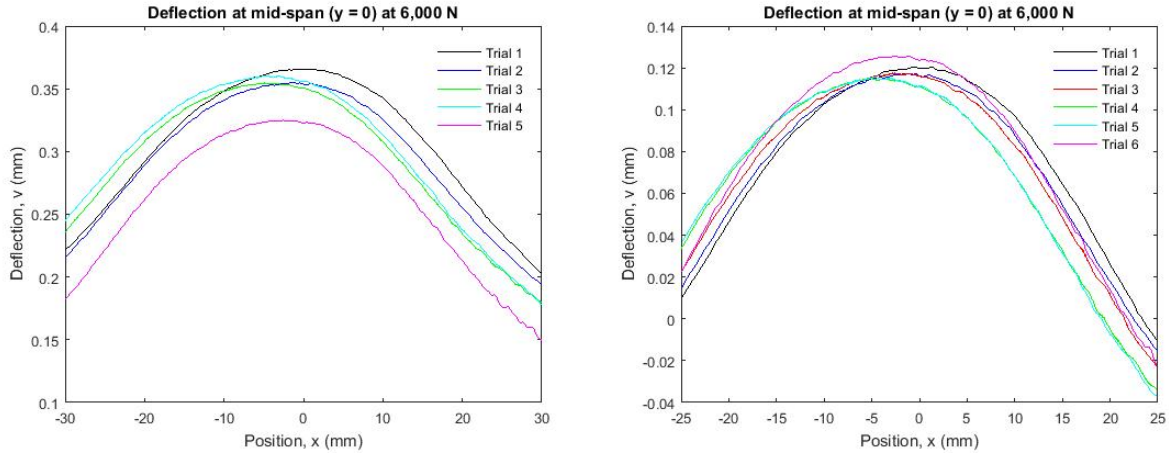

(a) (b)

Figure 9-13: DIC v-deflection at line $y = 0$ versus x-position at 6,000 N for the six trials from 4-point bending test for hollow bone surrogate; (a) raw data and (b) adjusted data.

Table 9-2: Flexural bending rigidity for filled and hollow bone surrogate using adjusted and (raw) DIC v-deflection, EI_{DIC} ($EI_{DIC,adj}$).

	Filled		Hollow	
Trial	3-Point	4-Point	3-Point	4-Point
1	169.9 (72.8)	92.5 (36.4)	174.6 (75.9)	93.7 (30.4)
2	172.4 (71.7)	99.2 (30.9)	169.4 (80.7)	95.9 (31.4)
3	172.1 (69.9)	98.8 (29.0)	171.2 (80.3)	95.8 (34.1)
4	172.2 (75.1)	97.6 (30.8)	179.6 (78.7)	97.9 (31.4)
5	172.2 (75.2)	99.4 (32.6)	171.7 (81.7)	97.5 (31.0)
6	177.7 (77.0)	107.1 (35.9)	172.4 (78.8)	89.6 (34.3)
Average	172.8 (73.6)	99.1 (32.6)	173.2 (79.4)	95.1 (32.1)
Std.	2.6 (2.6)	4.7 (3.0)	3.6 (2.0)	3.1 (1.7)

Adjusted value (Raw value)

9.6 Femur Bone

The tested specimen is made of Nylon 12 PA 650 with ultimate tensile strength of 48 MPa and modulus of elasticity of 1,700 MPa [135]. The specimen was made up using 3D printer, Figure 9-14a. Since the specimen is white in color, the speckle pattern was produced by spraying commercial Ultra-Flat black paint spray bottles over the structure of the specimen, Figure 9-14b. Table 9-3 contains the DIC analysis details.

(a) (b)

Figure 9-14: The femur bone specimen before and after applying the speckle pattern.

Table 9-3: Technical information about the DIC equipment, set-up, and system.

Parameter	Setting
Technique	Stereo Image Correlation
Cameras	The Grasshopper (Point Grey Research), Model GRAS-50S5M-C
Imaging sensor	Sony ICX625 CCD, 2/3'', 3.45 μm
Lens	CM120 BK 15 COMPACT-0901 (focal ratio: 1.9 and focal length: 35 mm)
Sensor/digitization	2448×2048 at 15 FPS
Lightening	Extra white light
Pixel to inch conversion	1 pixel = 0.01 inch
Calibration grid size	12×9 with 4 mm spacing
Software	Vic-Snap software by Correlated Solutions, Inc.
Subset, step	29, 7
Strain Resolution	0.005% (50 microstrain)

The specimen was tested using 3-point bending in MTS machine. Before conducting the experiment, a simple analytical calculation was carried out to estimate the maximum force that the specimen can handle. Assuming the femur bone has a cylindrical shape with diameter D and the moment of inertia is $I = \pi D^4/64$, the maximum force in term of maximum stress is

$$F = \frac{\pi D^3 \sigma}{8L}$$

The minimum diameter in the femur neck was measured to be D = 1.4 in = 35.56 mm. The 3-point bending span was taken to be L = 2.7 in = 68.58 mm. The applied force should be large enough so that DIC can capture displacement deformation (ϵ = 50 micostrain, Table 9-3) and produce stress less than the ultimate tensile strength, σ_{UT} = 48 MPa. Therefore, using the strain resolution of the DIC, ϵ = 50 micostrain from Table 9-3, the stress is $\sigma_{DIC} = E\epsilon$ = 1700 × 50 = 85 kPa. The applied force should produce stress larger than σ_{DIC} and less than σ_{UT}, that is; $20 < F < 12{,}000$ N.

Firstly, the specimen was mounted on the 3-point bending apparatus as shown in Figure 9-15. The load was applied from zero with 20 N increment till 800 N when the specimen fall down. The experiment was repeated and the same issue happened again. This suggest using different mounting configuration for the specimen as shown in Figure 9-16. This suggested configuration provides more stability and the applied force from MTS machine provides critical stress at the region of interest in bone neck.

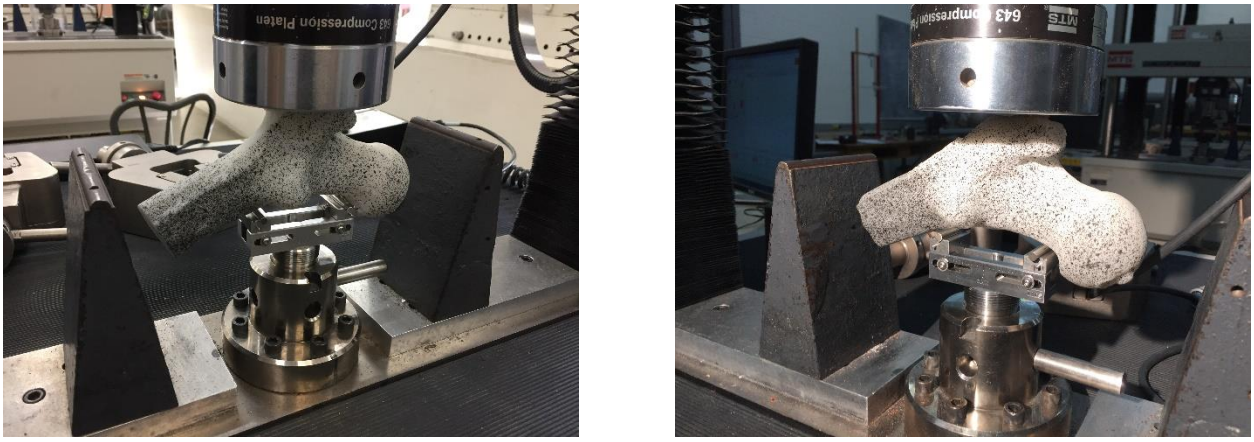

Figure 9-15: Experimental set-up of the femur bone using 3-point bending apparatus.

Figure 9-16: Experimental set-up for the second configuration.

The specimen was loaded and unloaded 8 times while capturing images using DIC correlated solution software at each 50 N increment. The specimen was tested to 6,000 N with factor of safety 2 for the first four tests and then to 8,000 N for remaining tests. The u, v, and w displacement in x, y, and z-directions, respectively, at 6,000 N for two different trials are shown in Figure 9-17. The results in Figure 9-17 show the consistency of the obtained displacement. The contour plot of the v-displacement is look similar to those obtained using standard 3-point bending test for surrogate bone. If the maximum displacement of v_{max} = -1.5 mm used in equation $\delta_{max} = FL^3/48EI$ with F = 6000 N, L = 114 mm, $I = \frac{\pi}{64}D^4$ and a mean diameter of D = 35.56 mm, the value of Young's117 modulus is E = 1.6 GPa which is close to the reported modulus of elasticity of 1,700 MPa [135]. The calculated strains from Correlated solution software using Lagrange differentiation method are shown in Figure 9-18.

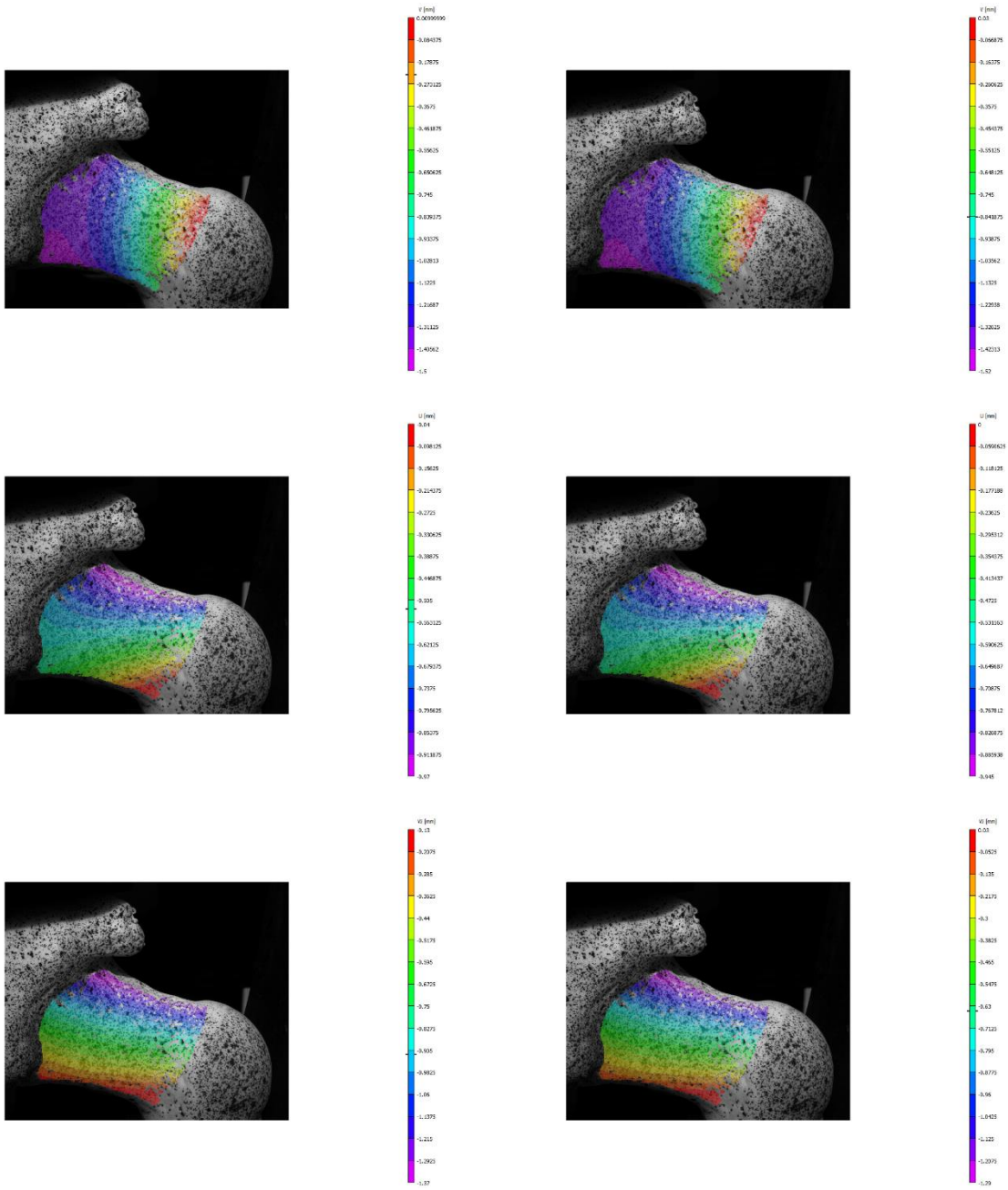

Figure 9-17: The DIC-measured displacements at 6,000 N from Correlated solution software for two different trials.

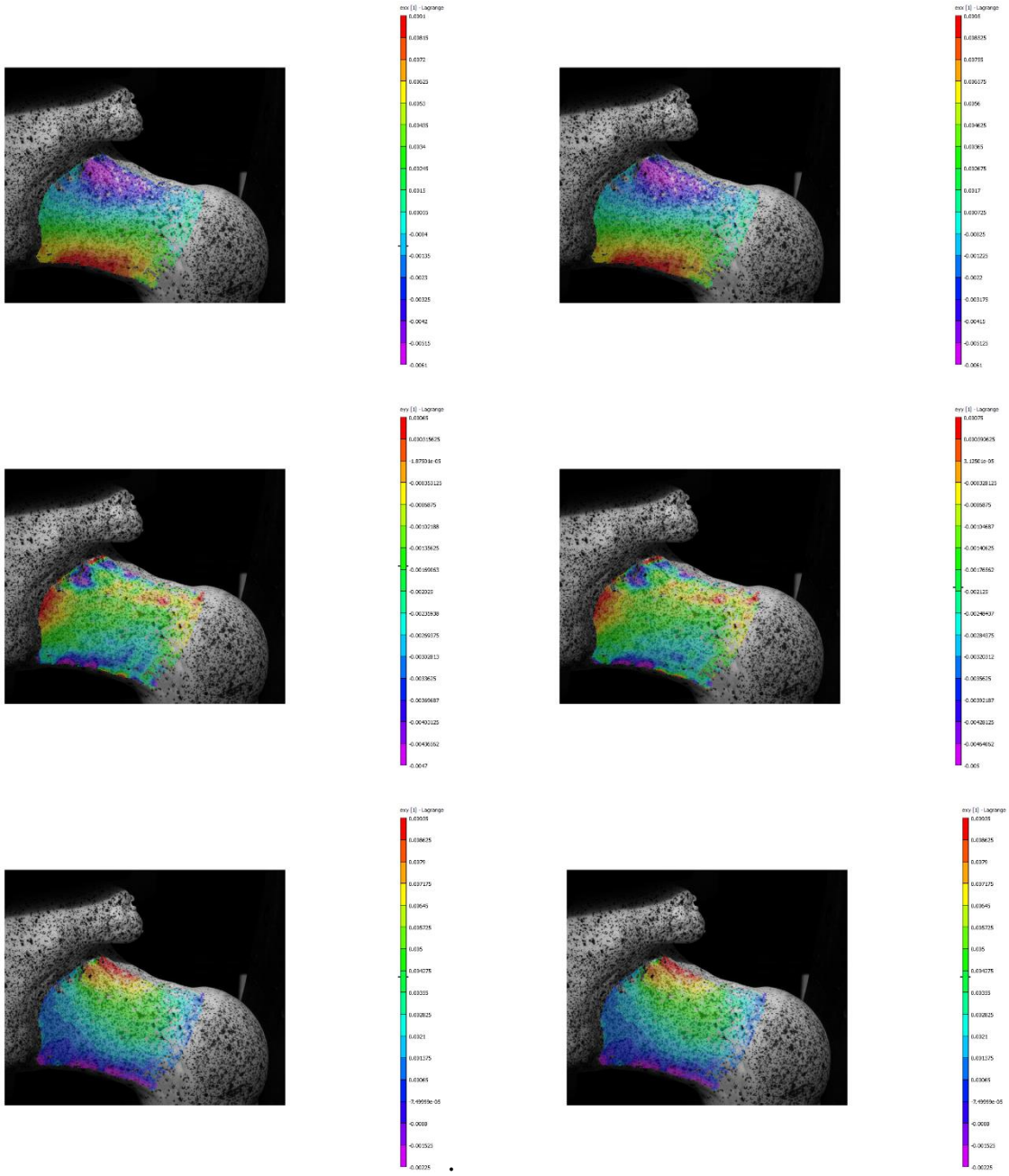

Figure 9-18: The DIC-calculated strains, ϵ_{xx}, ϵ_{yy} and ϵ_{xy}, at 6,000 N from Correlated solution software for two different trials.

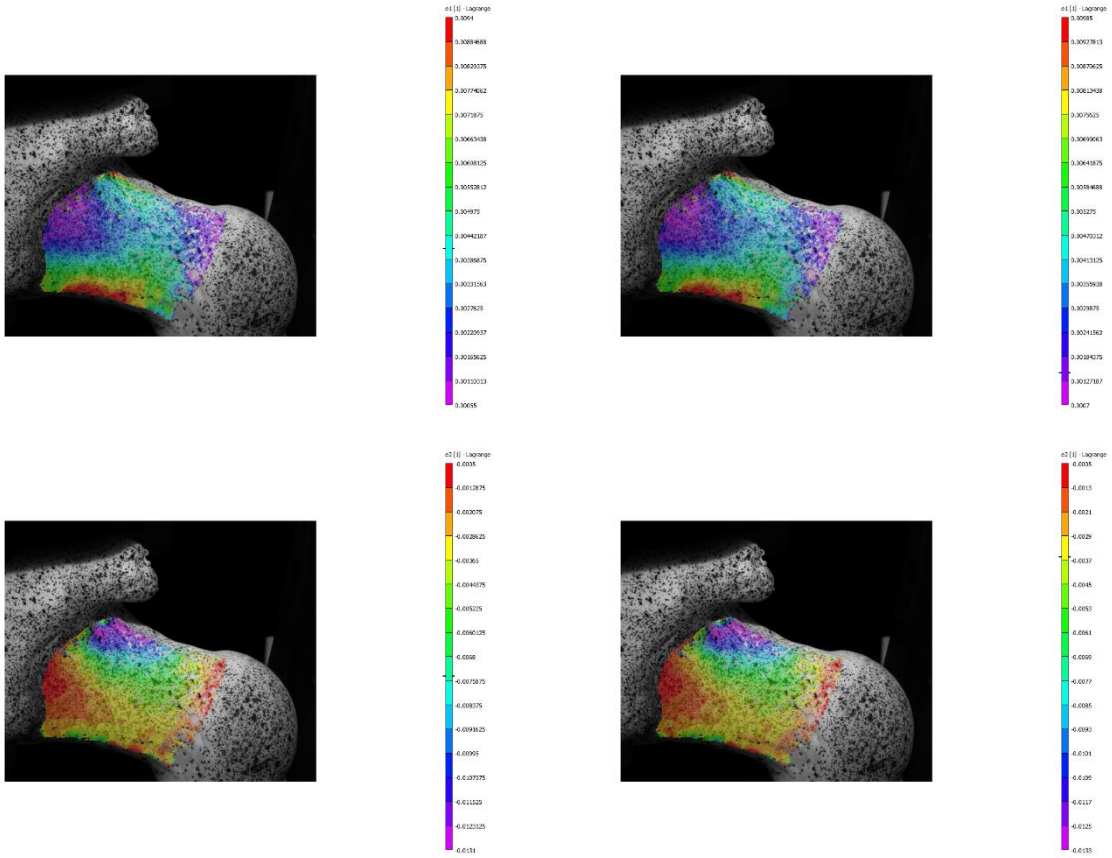

Figure 9-19: The DIC-calculated principal strains, ϵ_{11} and ϵ_{22}, at 6,000 N from Correlated solution software for two different trials.

Acknowledgement

The author thanks Jacob Zeuske, Carla Winsor, and Max Kahn for assisting with mechanical testing of the surrogates.

Chapter 10: Conclusion and Future Work

Recognizing challenges in determining stresses in finite shapes when complete boundary conditions are unknown using purely theoretical/analytical or numerical methods, contemporary techniques of thermoelasticity (TSA) and digital image correlation (DIC) are synergized with analytical and numerical concepts to stress analyze orthotropic composites. This thesis develops an experimental-analytical-numerical hybrid approach to stress analyze complex engineering problems involving near-edge hole, elliptical hole, deep U-notch, and side notches in finite geometries. Major contributions of this thesis include the following:

(i) Develop a hybrid full-field stress analysis technique to determine the structural integrity of finite structures containing different discontinuities (elliptical hole, deep U-notch, side notch) using thermoelastic stress analysis or digital image correlation.

(ii) Demonstrate the ability to stress analyze finite orthotropic and isotropic structures using complex mapping-collocation technique.

(iii) Incorporates the complex mapping-collocation technique with thermoelastic stress analysis and digital image correlation.

(iv) Demonstrate the ability to stress analyze a finite orthotropic composite containing an elliptical hole using a stress function in complex variable and a single experiment technique (TSA).

(v) Assess the effects of varying the source locations of measured TSA input data.

(vi) Determine accurate stresses on the boundary of a near-edge hole in aluminum finite plate without the knowledge of the far-field loading/boundary conditions using complex mapping-collocation technique.

(vii) Extend the applicability of the complex mapping-collocation technique to symmetrical and unsymmetrical cases.

(viii) Demonstrate the ability to separate the stress from recorded thermal information (TSA signals) for a finite isotropic component containing a deep U-notch using a complete stress function in real variable.

(ix) Full-field stress/strain determination without physically differentiating measured displacements (i.e., processed with a rigorous mechanic basis) for finite structures.

(x) Utilizing a single measured displacement component to determine the full-field individual components of stress, strain and displacement in finite loaded notched orthotropic composite.

(xi) Assess the effects of number of the measured DIC input data, generated randomly.

(xii) Analyze the stress and strain concentration factors of a composite plate with central hole using three dimensional finite element analysis.

(xiii) Employ DIC to record the displacements and strains in surrogate femur bone.

This research is believed to have made significant strides in hybridizing experimental techniques with analytical and numerical tools for the displacement, strain and stress analysis of engineering problems.

Future work and considerations might include the following:

(I) Assess the feasibility of extending TSA to curved/non-planner surfaces, loaded boundaries and nonlinear/inelastic behaviors (e.g., viscoelasticity; plasticity; biological, polymeric,

functionally-graded materials; metal-matrix composites; pultruded composites; cellulosic and materials).

(II) vibrations, and further pursuit of boundary integral/boundary methods.

(III) Extend TSA and DIC to three-dimensions (internal stresses) from surface recorded data.

(IV) Extend TSA to more complicated cutout geometries, possibly using more complicated coordinate systems, and more practical applications beyond a laboratory environment.

(V) DIC determination of stress intensity factors in orthotropic composites using concepts as J-integral or hybrid elements.

(VI) Assess the potential advantages of applying the concept of recording only one displacement component to moiré, holography, grids and electric speckle.

(VII) Combine current aspects with the XFEM concepts – the latter being a numerical method which enables local enrichment of the nodes.

(VIII) Combine current aspects with concepts such as radial basis functions, virtual field method, equilibrium equation and/or constitutive equation gap method.

(IX) Assess the feasibility of evaluating the constitutive properties of a composite material from DIC or TSA using inverse methods and Airy stress function.

(X) Assess the feasibility of extending aspects of rectangular isotropic plates subjected to a concentrated load to orthotropic composites.

(XI) Apply current concepts based on only one recorded displacement component or thermoelastic signals to situations involving totally unsymmetrically-shaped geometric discontinuity in mechanically or geometrically unsymmetrical member (i.e., unsymmetrical interior and exterior considerations). This could necessitate imposing the traction-free conditions discretely on the edge of the cutout and the external boundary.

(XII) Extend present concepts to stress analyze finite orthotropic plates containing holes, including inclined elliptical cutouts.

(XIII) Apply current concepts to more general bolt-loaded, finite-size isotropic and orthotropic members (bolt-hole clearance, multiple bolted-loaded holes, etc.).

(XIV) Feasibility of using Legendre polynomials to process TSA, DIC, vibrometry or measured strain data.

(XV) Hybrid full-field stress analysis of finite structures containing arbitrarily shaped (or square) holes using TSA and/or DIC. Arbitrarily shaped holes are architecturally common and plow bolts involve square holes.

(XVI) Apply the concept of mapping collocation technique in more complicated geometries using Schwarz-Christoffel mapping techniques.

(XVII) Use DIC or TSA to determine stresses in orthotropic materials involving a central plus auxiliary holes or notches. This could include pin/bolt loaded holes with all of the auxiliary holes at the weak side of the loaded hole.

(XVIII) Using either TSA or DIC, determine the feasibility of obtaining stresses in a region in a structure which is void of recorded input information.

(XIX) Consider developing approaches for optimizing the regions in a component from which one collects and uses the recorded/measured data.

(XX) Potential advantages of combining TSA or DIC measured data with the FEM-type scheme.

(XXI) Regarding the deep side-notched TSA analysis of Chapter 5, in view of some inconsistencies between reference [47] and present results relative to whether or not one can assume symmetry about x-axis and using the full stress function of equation (2-35)

warrant future attention. One might investigate correlating the present experience and results with those by M. Creager and P. Paris, Vieira et al. [75], Bowie and Neal, and the double edge-notch results in Peterson's Stress Concentration book [80]. Relative to a double-edge notched tensile plate, taking the origin of a new global coordinate system on $y = 0$ but at the mid-location between the notches, and denoting the distance from this global origin to the origin of the local polar coordinated system seen in Figure 5-1 by L, would provide symmetry about both the horizontal and vertical axes. One could represent the stress function in terms of the global set of polar coordinates relative to the local set of polar coordinates much as Professor Kathy Lin did in the case of an off-axis load on a perforated plate. Since the global origin would be within the material/structure, determine whether one can now realistically assume symmetry about the horizontal and vertical axes in disregarding the relevant coefficients in the stress function. Physically, one might load a 6061-T6 or 7075-T6 aluminum plate vertically in the hydraulic MTS grips rather than through pin-loaded holes, employ the TSA image averaged about both the horizontal and vertical axes of symmetry throughout the entire plate, impose the stress conditions of equations 5-2 through 5-6 of Chapter 5 at both $y > 0$ and $y < 0$, again analyze via each of FEA and TSA starting with the full Airy stress function of equation (2-35) of Chapter 5, stress analyze using each of the global and local coordinate systems and determine any consequence on the values of the resulting Airy coefficients. One could again compare TSA and strain gage results. Recognizing the size of the radius at the end of the present notch relative to the thickness of the plate, and since the concept of the Airy stress function assumes plane stress, consideration might be given to conducting a 3D FEA of the end of the notch region. Having said

that, previous UW-Madison results suggest plane stress remains a reasonable assumption provided a plate is not too thick compared to the diameter of the hole. The agreement between the present 2D FEM and strain gages and TSA results in Chapter 5 might suggest that the situation is reasonably plane stress. Future notches might be wider than in Figure 5-1 to minimize any possible 3D concerns at their ends, in fact they could be essentially semicircular in shape. If semi-circular, one could potentially then compare TSA results with some from Peterson's stress concentration book [80]. Edge notches having larger end radii would be beneficial in that one could bond strain gages on their curved surface at x/R = 1, i.e., at the immediate edge of the notch. One could stress analyze future double-notched plate with TSA and DIC. Subject to a suitable mapping function (maybe Schwarz-Christoffel mapping), one could consider using complex rather real variable technique.

Appendices

Appendix A: Simulated Input for a Rectangular Plate with edged-load for Isotropic Material

The unreliable thermoelastic simulated data, S, on and near the circular boundary motivated only using data shown in Figure A 1 and this region is denoted as region R^*.

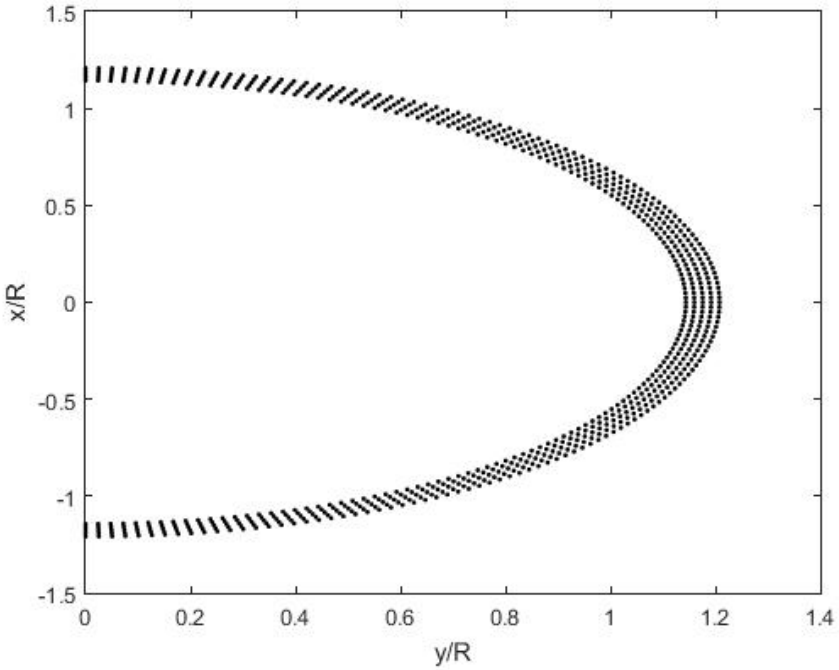

Figure A 1: Thermoelastic simulated data source location (m = 906 data points).

Simple Airy Stress Function in Real Analysis

By gathering the simulated data, the Airy coefficients can be solved by forming a linear system of equation represented in a matrix form as $[A]_{m\times k}\{c\}_{k\times 1} = \{d\}_{m\times 1}$ where m is the total number of measured points, and k is number of unknown Airy coefficients which is related to

terminating index, N, as $k = 2(N-3)+7 = 2N+1$. The matrix $[A]$ consists of analytical expression of S_S $(= S^*/K)$, equation (4-27). The vector $\{c\}$ contains the k unknown Airy coefficients and ordered as $\{c\} = \{b_0, c_0, d_1, b_2, d_2, c_3, d_3, b_4, d_4, \ldots, b_n, d_n\}$ and vector $\{d\}$ contains m = 906 simulated data, S^*/K. Based on the condition number of Airy matrix, $C = cond(A)$, of Figure A 2 and the RMS values of Figure A 3, k = 15 coefficients are utilized here. Once all the Airy coefficients of equation (4-27) have been evaluated from the thermoelastically simulated data, S^*, the individual components of stress were obtained from equations (4-24) to (4-26).

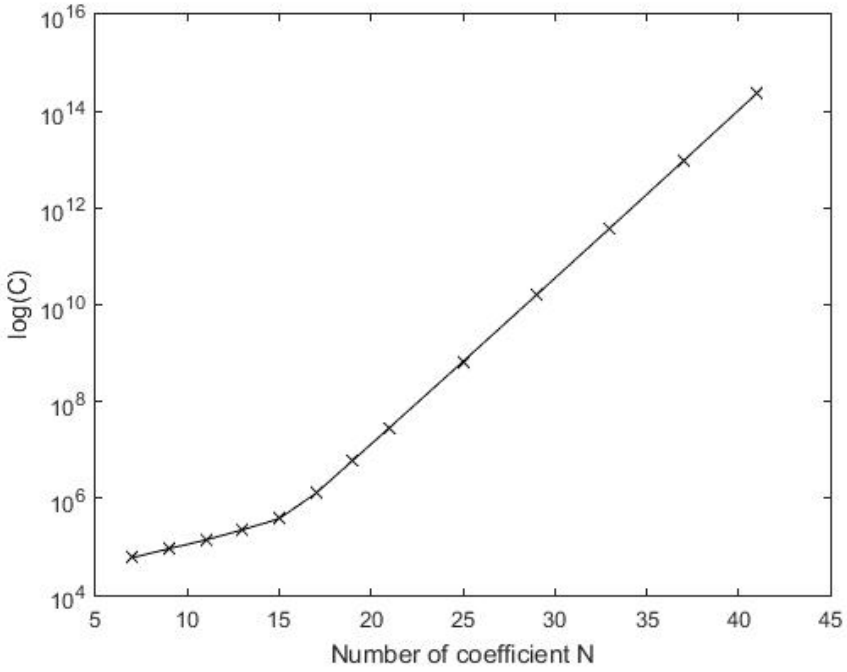

Figure A 2: Condition number of simple Airy stress matrix.

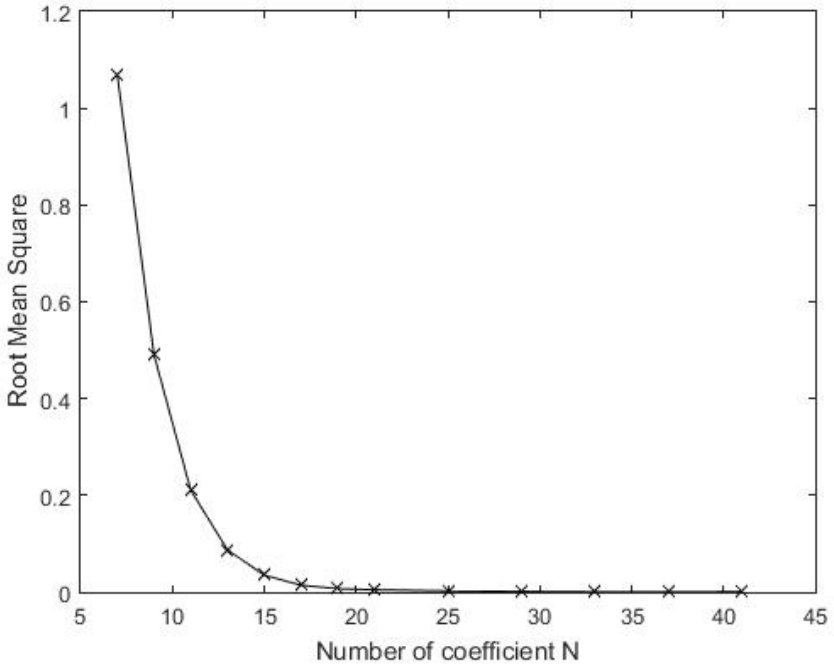

Figure A 3: Root mean square values between the reconstructed and thermoelastically measured data for simple Airy stress function in real analysis.

Airy Stress Function Superposed with Flamant Solution in Real Analysis

The effect of the concentrated load can be considered by superposition principle. By gathering the simulated data with the boundary conditions, equations (4-23) and (4-22), the Airy coefficients can be solved by forming a linear system of equation represented in a matrix form as $[A]_{(m+h)\times k}\{c\}_{k\times 1} = \{d\}_{(m+h)\times 1}$ where m is the total number of simulated points, h is twice the number of the boundary points, and k is number of unknown Airy coefficients which is related to terminating index, N, as $k = 4(N-1)+4 = 4N$. The matrix $[A]$ consists of analytical expression of S_C, equation (4-5), in addition to h traction-free expressions of the form of equations (4-2) and (4-4). The vector $\{c\}$ contains the k unknown Airy coefficients and ordered as $\{c\} = \{b_0, c_0, c_1, d_1, a_2, b_2, c_2, d_2, \dots, a_n, b_n, c_n, d_n\}$ and vector $\{d\}$ contains m = 906 simulated data, S, subtracted by isopachic stress, S_F, of Flamant solution, equation (4-15), $(= S - S_F)$ with the h values of the radial, equation (4-12), and shear, equation (4-14), stresses from Flamant solution.

Based on the condition number of Airy matrix of Figure A 4 and the RMS values of Figure A 5, k = 40 coefficients are utilized here. Once all the Airy coefficients of equation (4-5) have been evaluated from the simulated data, S, the individual components of stress were obtained from equations (4-21).

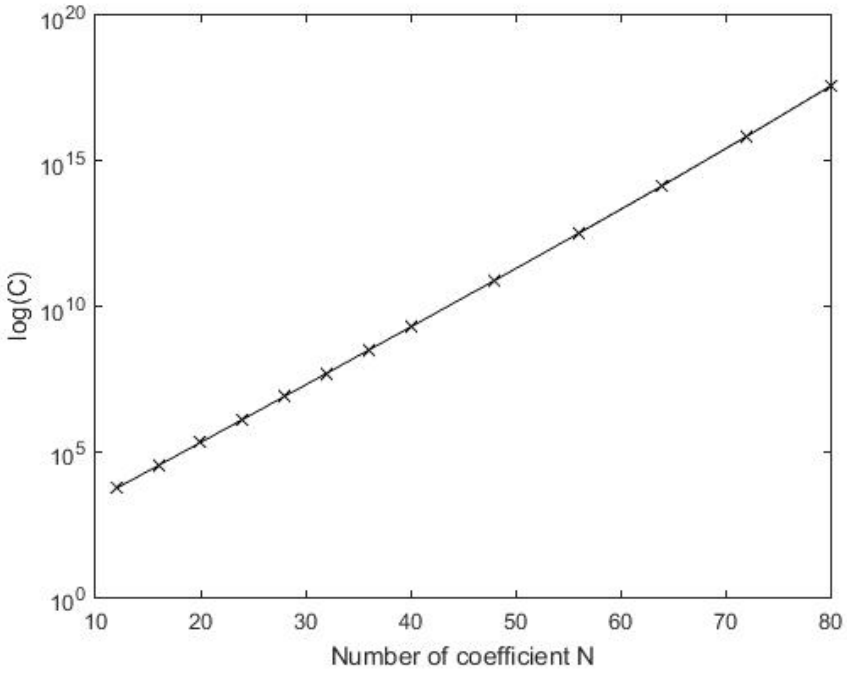

Figure A 4: Condition number of Airy stress matrix.

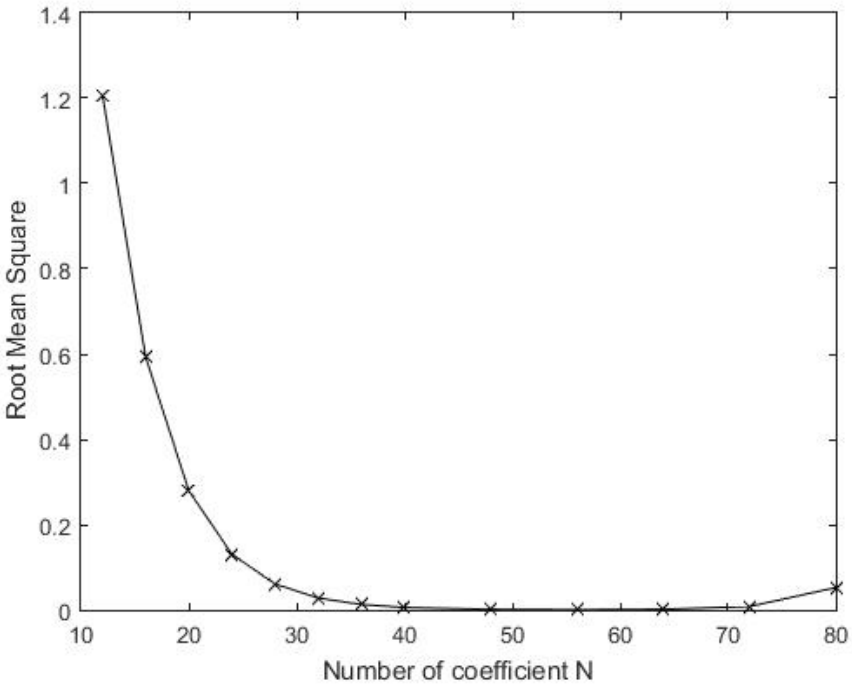

Figure A 5: Root mean square values between the reconstructed and thermoelastically measured data for Airy stress function in real analysis superposed with Flamant solution.

Stress Function in Complex Analysis (Complex Mapping Collocation Method)

The complex coefficients, $A_j = a_j + ib_j$, were evaluated by using equations (2-83) through (2-85), and the Laurent series expansion to map the physical plane to the unit circle in the ζ-plane. The complex coefficients A_j were evaluated from equation (2-101) using the simulated data inside the region R^*, Figure A 1, utilizing the Laurent representations of the stress function. The individual full-field stress throughout region R_z, including along edge Γ where no input data were employed, is evaluated using equations (2-95) through (2-97) for the Laurent expansion. The number of complex Airy coefficients, N, to retain in the stress function was selected by evaluating the difference between the magnitude of simulated based thermoelastic data and those predicted by the present hybrid method by using root mean square approach, Figure A 6. The present method

requires 20 complex coefficients (40 real coefficients). The appropriateness of utilizing 20 complex coefficients is substantiated by comparing the reconstructed and measured simulated data using the hybrid methods with the TSA data, Figure A 7.

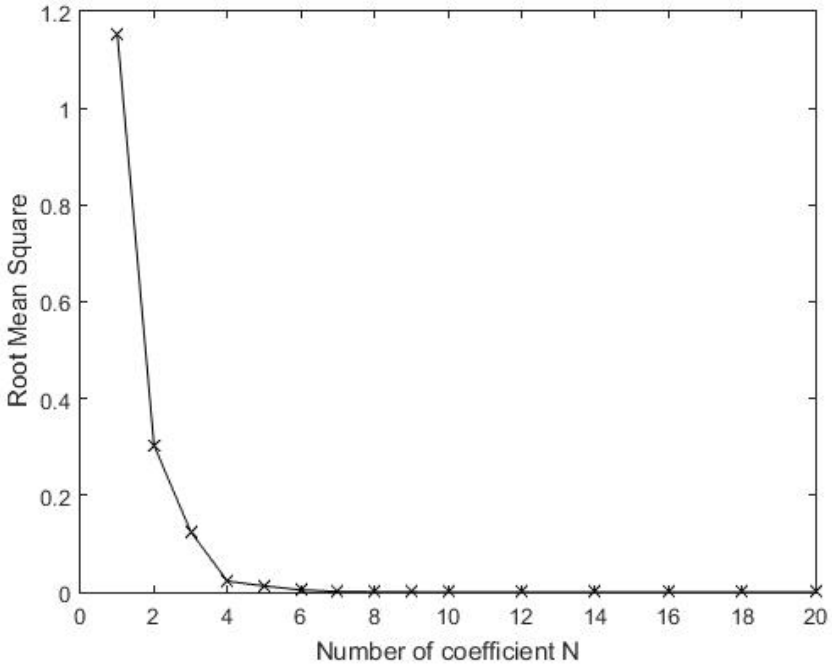

Figure A 6: Root mean square values between the reconstructed and simulated data for Airy stress function in complex analysis.

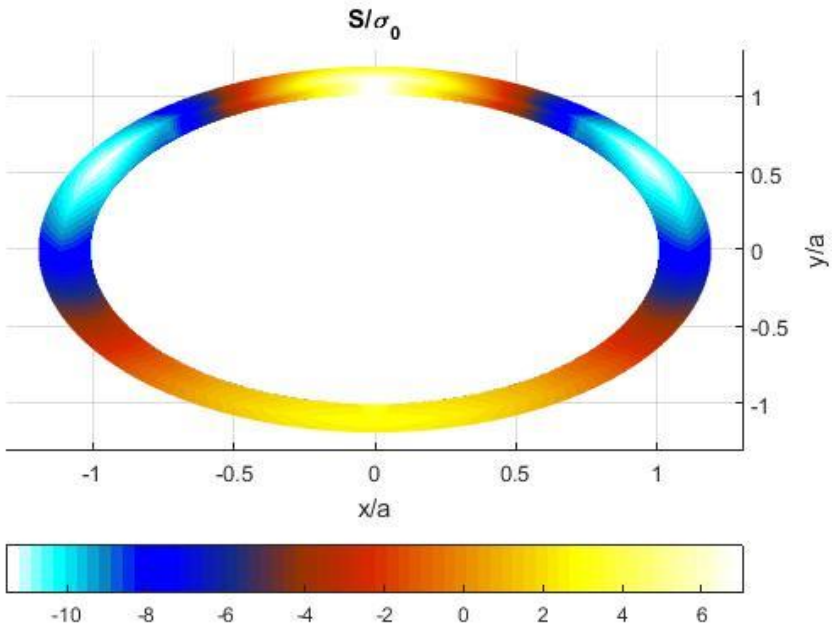

Figure A 7: Contour plot for S/σ_0 throughout the region adjacent to hole by simulated data (right) and hybrid method using the complex mapping collocation technique (left).

Results

For comparisons, the problem was solved using real variables with and without superposing the stress function from applied concentrated load, equation (4-11), and also by using complex mapping collocation technique. Stresses are normalized with respect to σ_0 [concentrated edge load P^*/gross cross-sectional are = 200 lbs/(3.5 in. × 3/8 in.) = 1.05 MPa = 152.38 psi]. The tangential stress, $\sigma_{\theta\theta}$, normalized to the far-field stress, σ_0, are plotted on the boundary of the circular hole as illustrated in Figure A 8. The variation of σ_{xx}/σ_0 along the line $y = 0$ and σ_{yy}/σ_0 along the line $x = 0$ of Figure 4-1 from FEA, simple Airy stress function (15 coefficients), and Airy stress function superposed with Flamant solution (40 coefficients) and complex mapping-collocation technique (40 real coefficients) are demonstrated in Figure A 9 and Figure A 10, respectively. The ANSYS and Hybrid methods from simple Airy stress function (15 coefficients), and Airy stress function superposed with Flamant solution (40 coefficients) and complex mapping-collocation

technique (40 real coefficients) determine stress concentrations at the circular hole to be 15.1, 14.26, 14.83, and 14.92 respectively. Figure A 9 shows that Airy stress function superposed with the Flamant solution and the complex mapping-collocation technique predict the stresses beneath the concentrated load very well comparing with the simple Airy stress function. In addition to he fact that $r/R \geq 1.5$ is approaching the location of the applied load, the reliability of the present determined σ_{xx} along the line $y = 0$ away from the hole might be influenced by the fact that the current complex mapping collocation technique does not explicitly involve the contribution of the concentrated load. P^*, as does the Airy stress function in the real analysis superposed with Flamant solution.

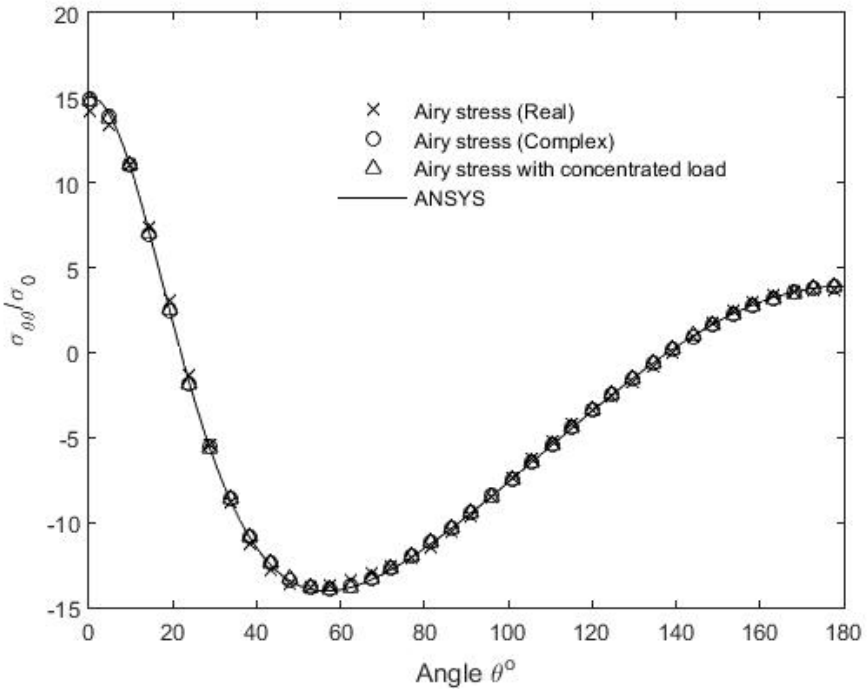

Figure A 8: The variation of $\sigma_{\theta\theta}/\sigma_0$ along the boundary of the hole from FEA, simple Airy stress function (15 coefficients), Airy stress function superposed with Flamant solution (40 coefficients) and complex mapping-collocation technique (40 real coefficients).

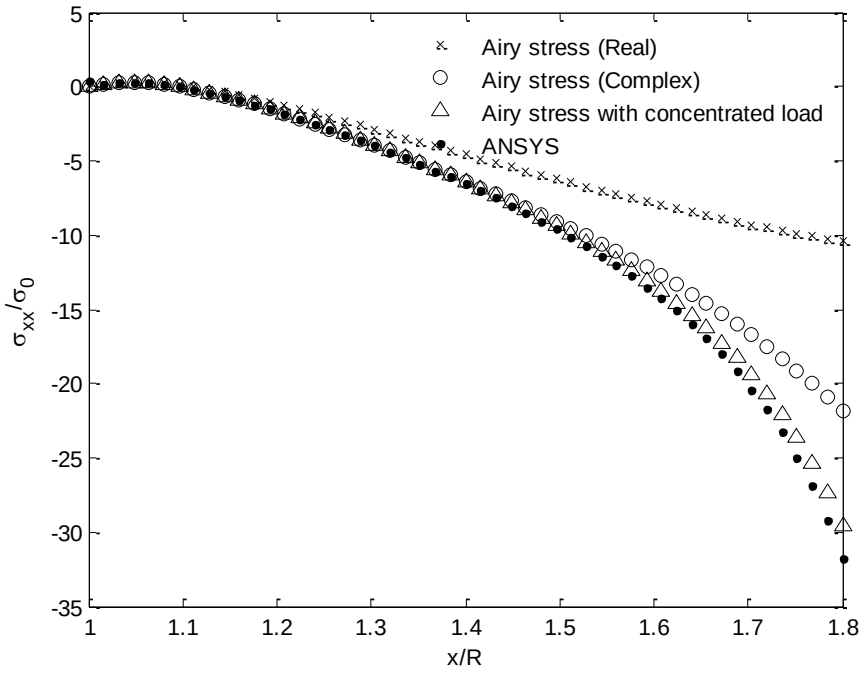

Figure A 9: The variation of σ_{xx}/σ_0 along the line y = 0 of Figure 4-1 from FEA, simple Airy stress function (15 coefficients), Airy stress function superposed with Flamant solution (40 coefficients) and complex mapping collocation technique (40 real coefficients).

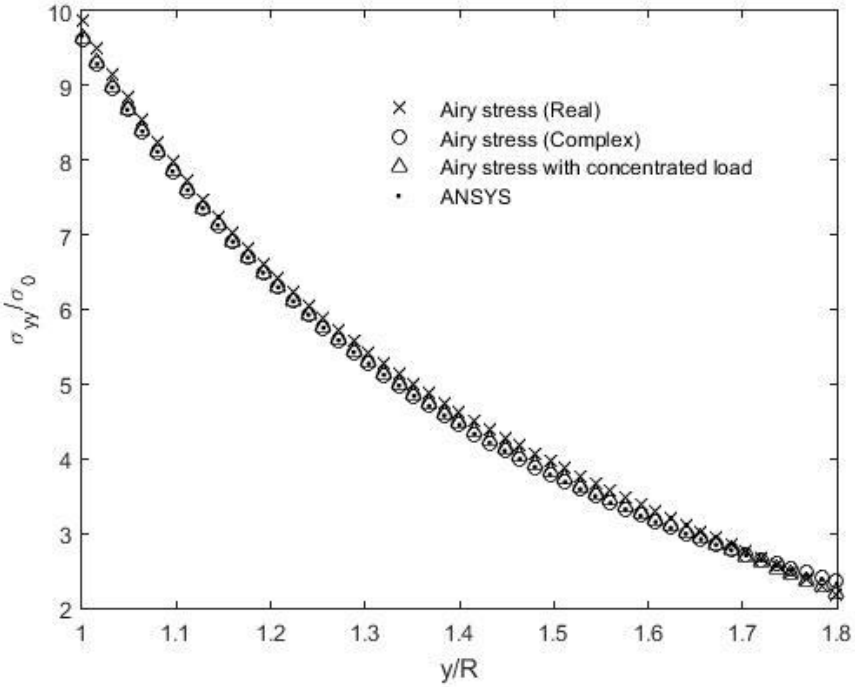

Figure A 10: The variation of σ_{yy}/σ_0 along the line x = 0 of Figure 4-1 from FEA, simple Airy stress function (15 coefficients), Airy stress function superposed with Flamant solution (40 coefficients) and complex mapping-collocation technique (40 real coefficients).

The contour plots of normalized polar components of stress from the hybrid complex collocation technique and ANSYS are plotted in Figure A 11 through Figure A 13. Those figures show an excellent agreement between the ANSYS-predicted values and the hybrid technique using thermoelastic data values for m = 906 data points.

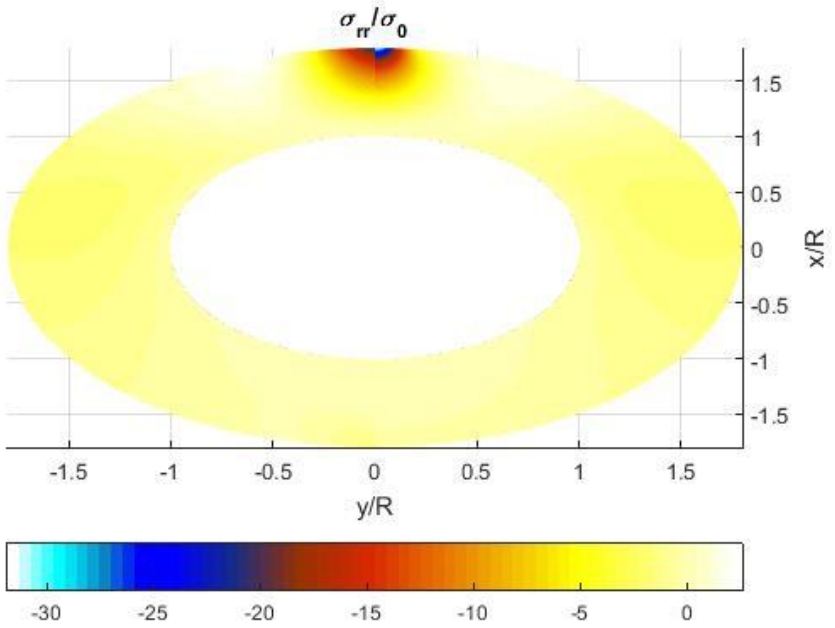

Figure A 11: Contour plot for σ_{rr}/σ_0 throughout the region adjacent to hole by FEA (right) and hybrid-TSA using the complex mapping-collocation technique (left).

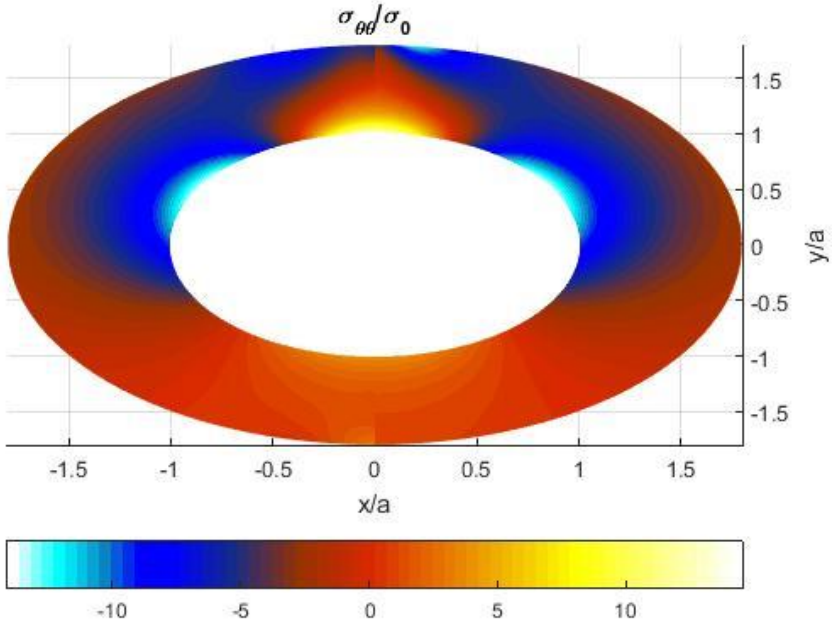

Figure A 12: Contour plot for $\sigma_{\theta\theta}/\sigma_0$ throughout the region adjacent to hole by FEA (right) and hybrid-TSA using the complex mapping collocation technique (left).

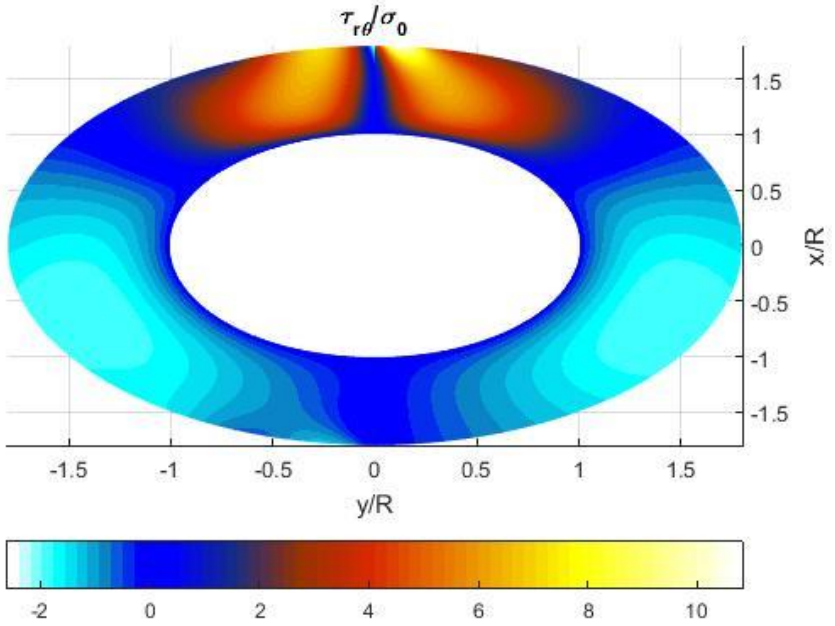

Figure A 13: Contour plot for $\sigma_{r\theta}/\sigma_0$ throughout the region adjacent to hole by FEA (right) and hybrid-TSA using the complex mapping collocation technique (left).

Appendix B: Simulated Input for a Rectangular Plate with edged-load for Orthotropic Material

To illustrate the applicability of the mapping-collocation technique on orthotropic materials, a simulated displacement input from ANSYS was utilized. A Graphite/epoxy material was used here with properties listed in Table 3-3. For plane problems having rectilinear orthotropy and no body forces, the Airy stress function, F, satisfying equation (2-32) can be expressed as a summation of two arbitrary analytical functions, $F_1(z_1)$ and $F_2(z_2)$, of the complex variables, z_1 and z_2, as giving in equation (2-52) such that $z_j = x + \mu_j y$ for $j = 1,2$ and Re denotes the 'real part' of a complex number. The complex material properties μ_1 and μ_2 are two distinct roots of the equation (2-33) associated with the compatibility equation. The roots of this characteristic equation

are complex so $\mu_1 = \alpha + i\beta$, $\mu_2 = \gamma + i\delta$, $\mu_3 = \bar{\mu}_1$, and $\mu_4 = \bar{\mu}_2$. The stresses in rectangular co-ordinates (x, y) of the physical $z(= x + iy)$ plane can now be expressed in terms of the well-known Airy stress function, $\Phi(z_1)$ and $\Psi(z_2)$. The stresses can be written as shown in equations (2-55) to (2-57). The stresses satisfy equilibrium and associated strains satisfy compatibility. The displacement can be written in term of the stress functions as shown in equation (2-58).

Boundary Conditions

The boundary condition along the boundary of the circular hole is traction-free so for a region of a component adjacent to a traction free-edge, Φ and Ψ can be related to each other by the conformal mapping and analytic continuation techniques.

Evaluating the Airy Coefficients

The unreliable displacement information, u^*, on and near the circular boundary motivated only using displacement information from $1.1R$ to $1.8R$. The region of Figure B 1 is denoted as region R^* where the displacement data was chosen.

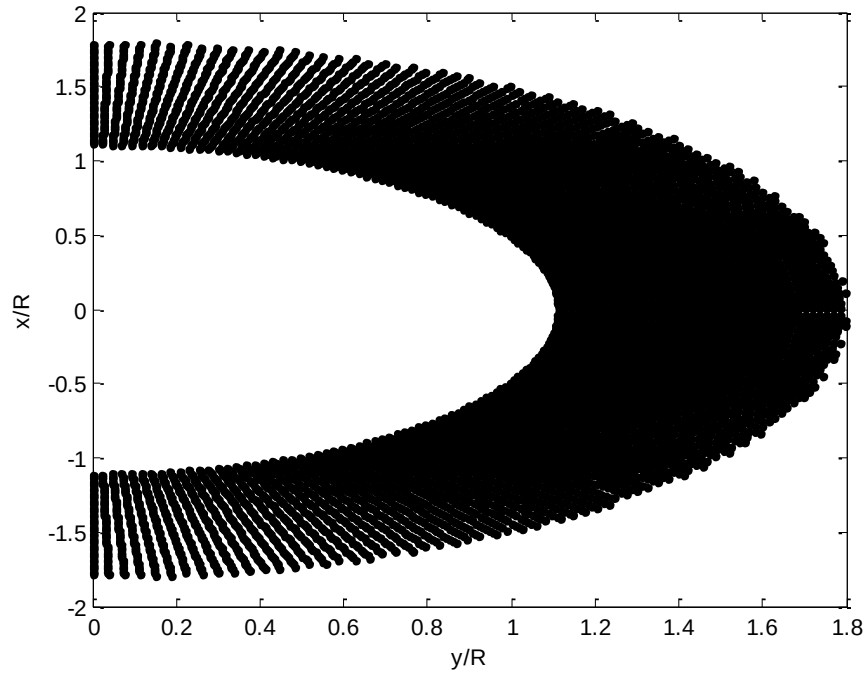

Figure B 1: Simulated displacement data source location (m = 6,557 data points).

The complex coefficients, $A_j = a_j + ib_j$, were evaluated by using equations (2-83) through (2-85), and the Laurent series expansion to map the physical plane to the unit circle in the ζ-plane. The complex coefficients A_j were evaluated from equation (2-98) using the displacement data inside the region R^*, Figure B 1. The individual full-field stress throughout region R_z, including along edge Γ where no displacement input data were employed, is evaluated using equations (2-95) through (2-97). The number of complex Airy coefficients, N, to retain in the stress function was selected by evaluating the difference between the magnitude of simulated based thermoelastic data and those predicted by the present hybrid method by using root mean square approach, Figure B 2. The present method requires 15 complex coefficients (30 real coefficients). The appropriateness of utilizing 15 complex coefficients is substantiated by comparing the reconstructed and simulated experimental displacement data, Figure B 3.

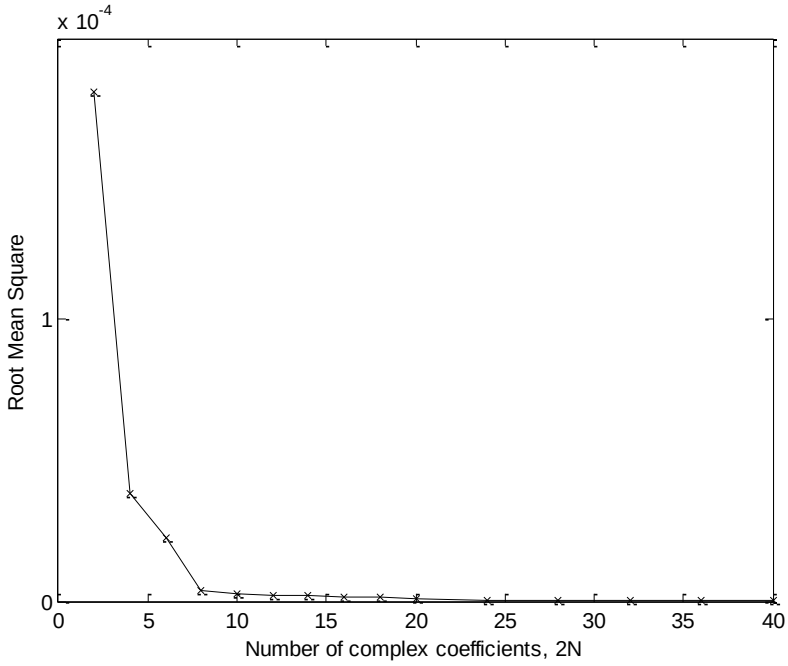

Figure B 2: Root mean square values between the reconstructed and thermoelastically simulated data for Airy stress function in complex analysis.

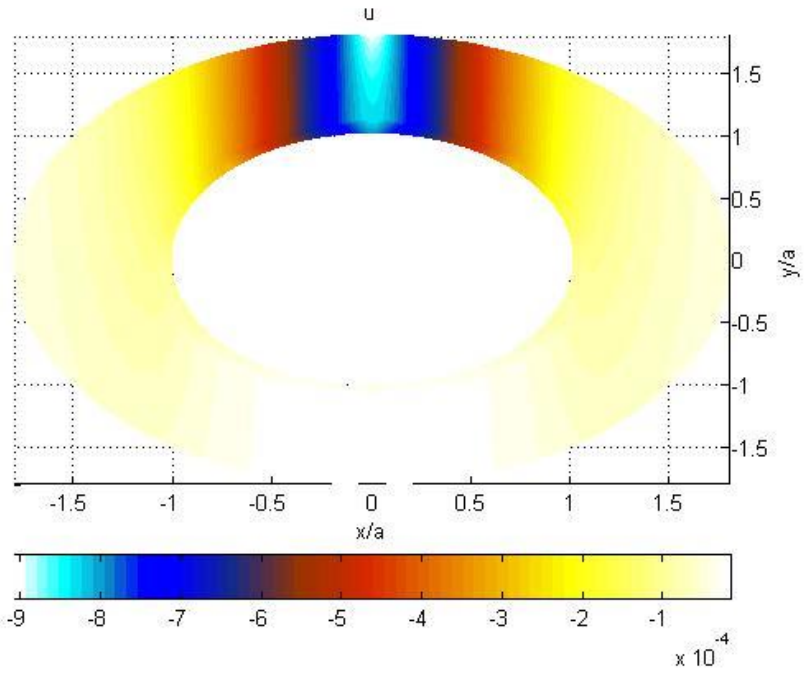

Figure B 3: Contour plot for u throughout the region adjacent to hole by simulated displacement data (right) and hybrid method using the complex mapping collocation technique (left).

The tangential stress, $\sigma_{\theta\theta}$, normalized to the far-field stress, σ_0, are plotted on the boundary of the circular hole as illustrated in Figure B 4. The variation of σ_{xx}/σ_0 along the line y = 0 and σ_{yy}/σ_0 along the line x = 0 of Figure 4-1 from FEA and mapping-collocation technique (30 real coefficients) are demonstrated in Figure B 5 and Figure B 6, respectively. Figure B 5 shows that the mapping-collocation technique predicts the stresses beneath the concentrated load very well.

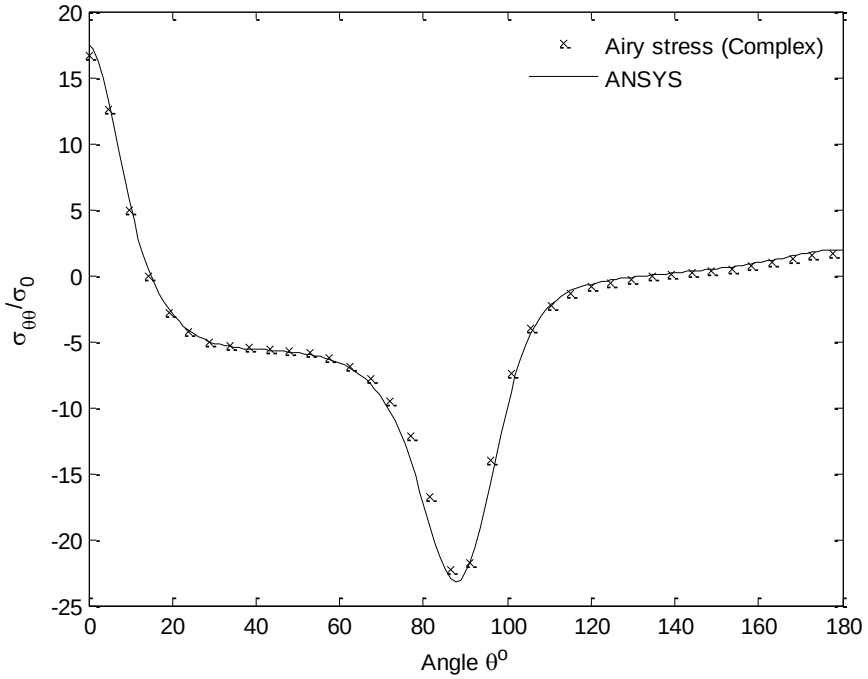

Figure B 4: The variation of $\sigma_{\theta\theta}/\sigma_0$ along the boundary of the hole from FEA using complex mapping-collocation technique (30 real coefficients).

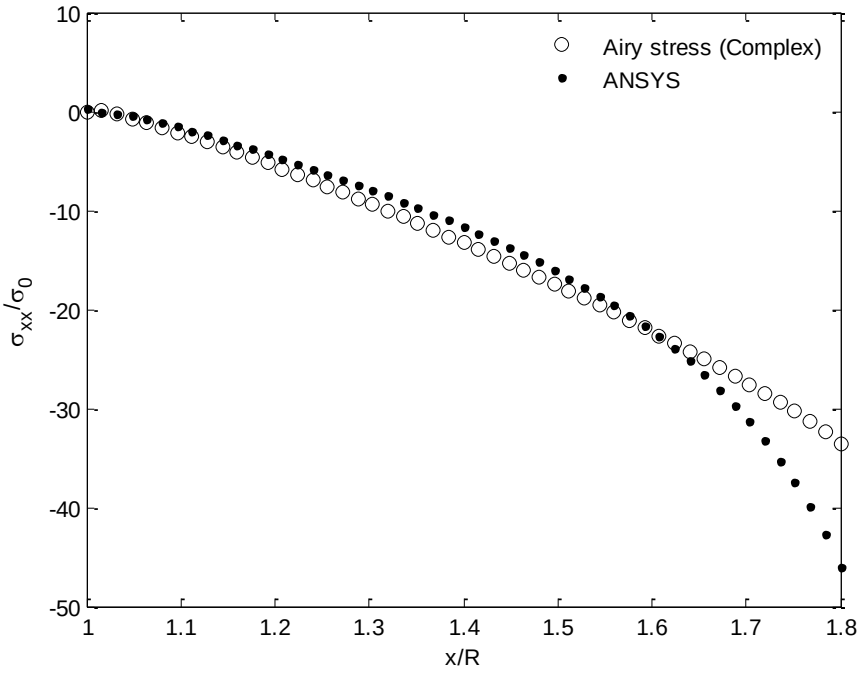

Figure B 5: The variation of σ_{xx}/σ_0 along the line y = 0 of Figure 4-1 from FEA using complex mapping-collocation technique (30 real coefficients).

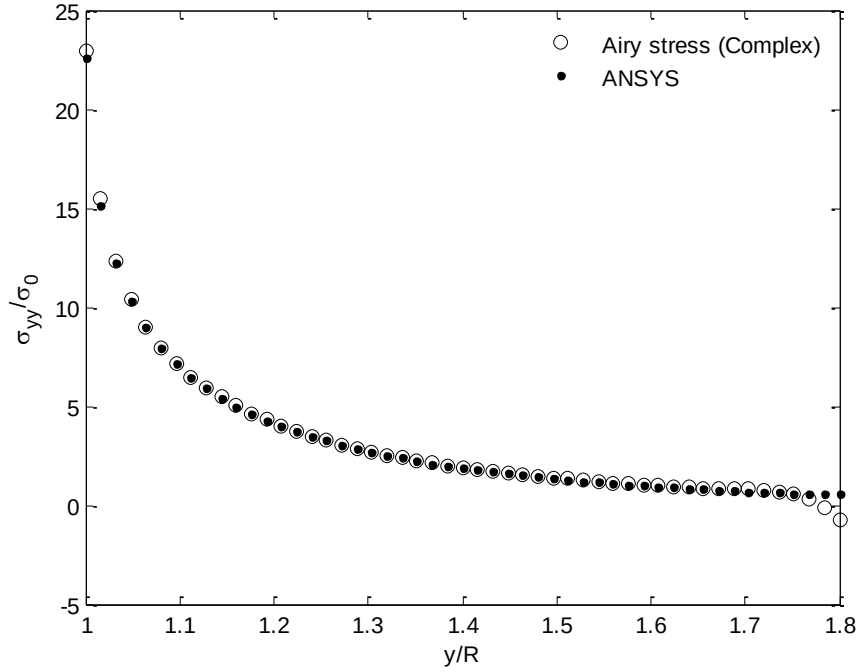

Figure B 6: The variation of σ_{yy}/σ_0 along the line x = 0 of Figure 4-1 from FEA using complex mapping-collocation technique (30 real coefficients).

The contour plots of normalized polar components of stress from the hybrid complex collocation technique and ANSYS are plotted in Figure B 7 through Figure B 9. Those figures show an excellent agreement between the ANSYS-predicted values and the hybrid technique using displacement data values for m = 6,557 data points.

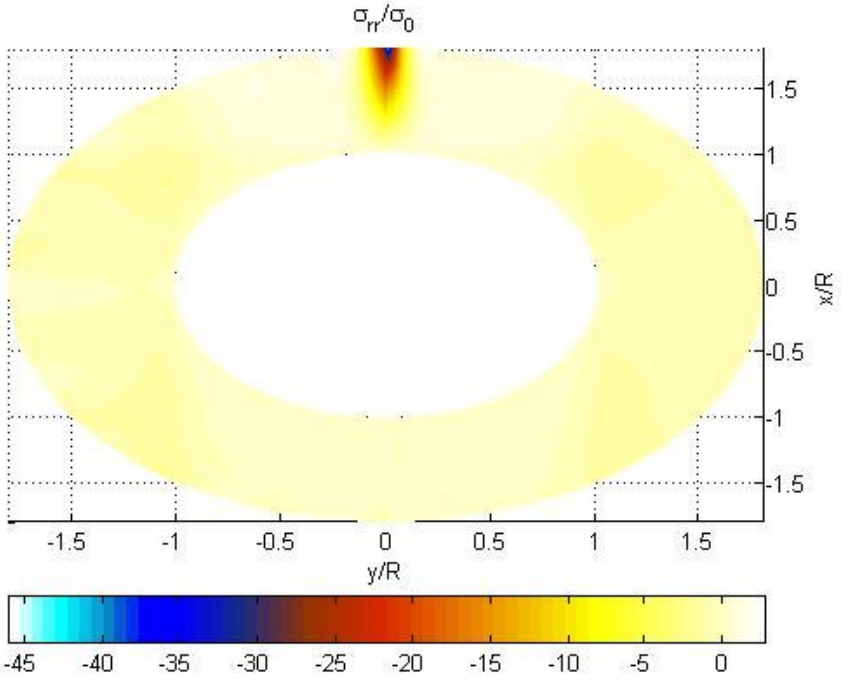

Figure B 7: Contour plot of σ_{rr}/σ_0 throughout the region adjacent to hole by FEA (right) and the complex mapping-collocation technique (left).

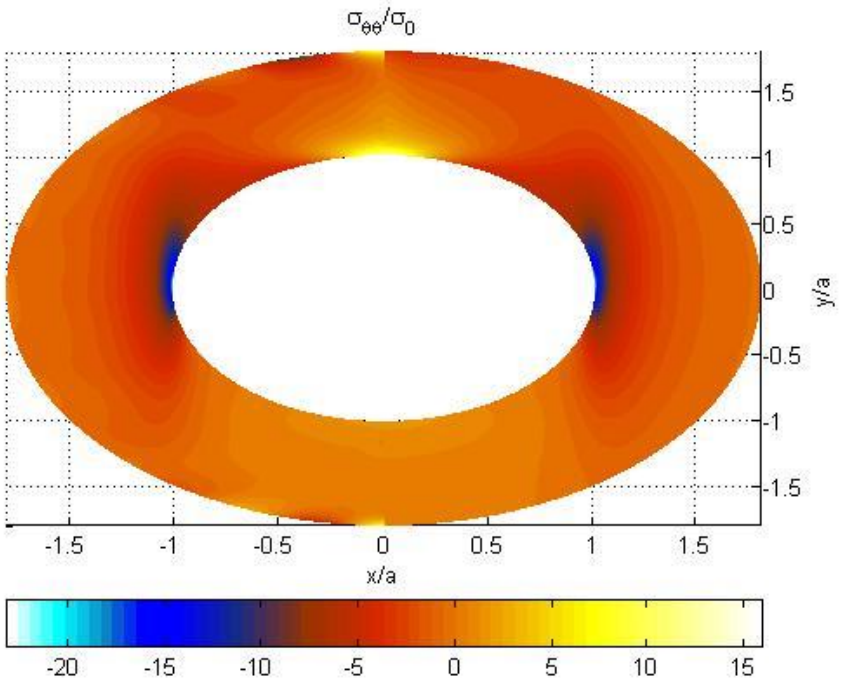

Figure B 8: Contour plot of $\sigma_{\theta\theta}/\sigma_0$ throughout the region adjacent to hole by FEA (right) and the complex mapping-collocation technique (left).

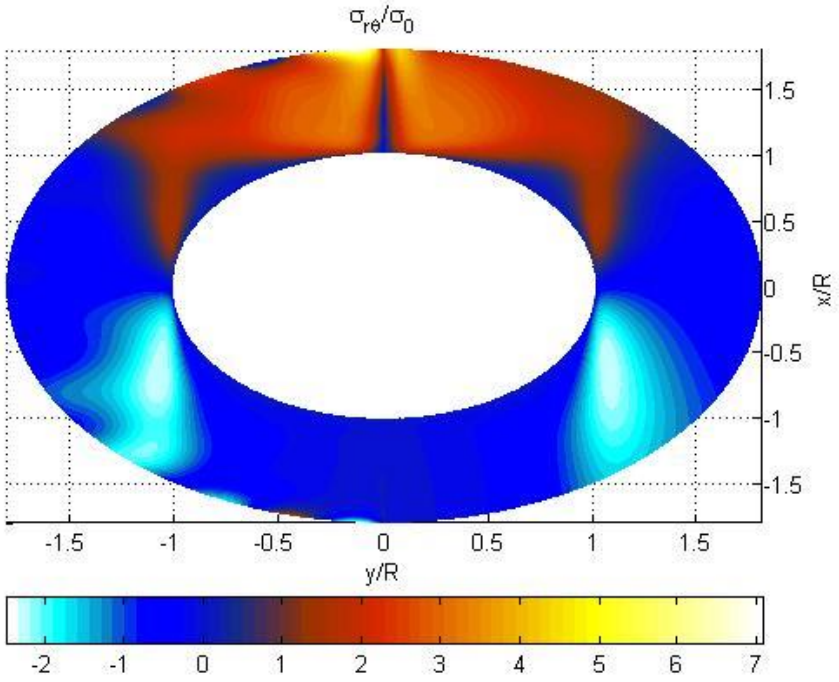

Figure B 9: Contour plot of $\sigma_{r\theta}/\sigma_0$ throughout the region adjacent to hole by FEA (right) and hybrid-TSA using the complex mapping-collocation technique (left).

Appendix C: Additional Results for Carbon/Epoxy in Finite Thickness Plate

Chapter 8 emphasizes the response in a highly orthotropic structural material, Sitka Spruce. However, this Appendix contains some comparative results for a unidiretional carbon-epoxy composite. As with the Sitka Spruce, the maximum stress concentrations in such man-made composites can occur below the external surfaces. For the geometry and loading of Figure 8-1, and elastic properties of Table C 1, Figure C 1 and Figure C 2 show the distributions of the stress concentration factors, K^{σ}, as a function of plate thicknesses in a carbon/epoxy plate when the strong/stiff orientation (1-direction) is parallel or perpendicular to the externally applied stress. These results were obtained using the same ANSYS modeling as for wood. The present trends are not unlike those for the Sitka Spruce. For the carbon/epoxy, equation (2-104) gives 5.57 and 2.40 for the load parallel and perpendicular to strong/stiff orientation, whereas Figure C 1 and Figure C 2 give 5.5 and 2.56 at L/a = 1, respectively. When the longitudinal axis (grain orientation, L-direction) in the Sitka Spruce is parallel and perpendicular to the applied vertical stress, σ , equation (2-104) gives 5.99 and 2.0, respectively. For a thin plate (plane stress), FE solutions give 5.35 and 2.08, respectively, at L/a = 1.

Table C 1: Constitutive properties of unidirectional carbon/epoxy composite.

Elastic Moduli (GPa)		Shear Moduli (GPa)		Poisson's ratio	
E_{11}	147	G_{12}	7	ν_{12}	0.27
E_{22}	10.3	G_{23}	3.7	ν_{23}	0.54
E_{33}	10.3	G_{13}	7	ν_{13}	0.27

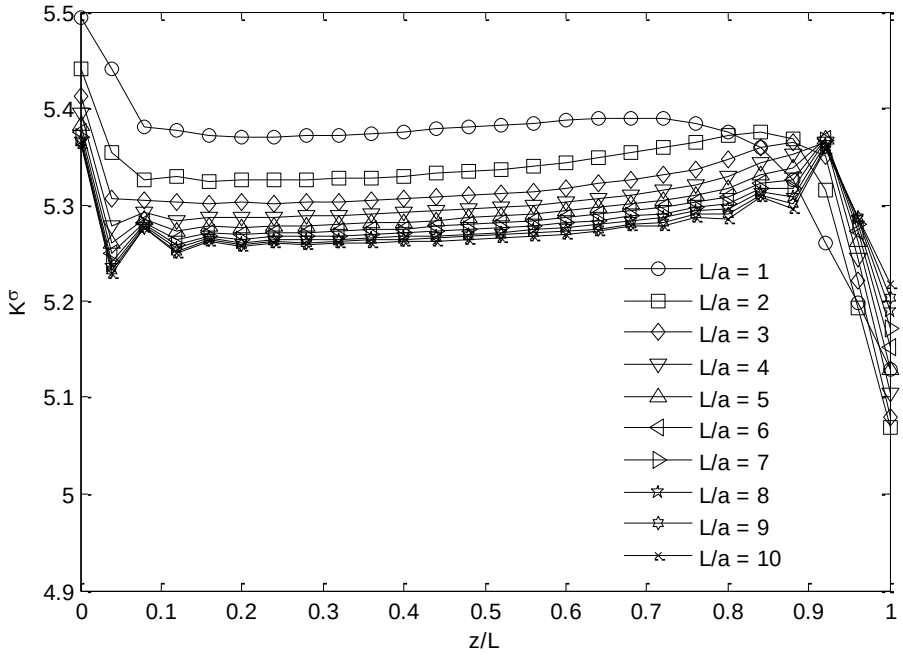

Figure C 1: Distribution of normalized stress concentration factors, K^{σ}, through the thickness in carbon/epoxy for different thicknesses when the 1-direction is parallel to applied stress, σ.

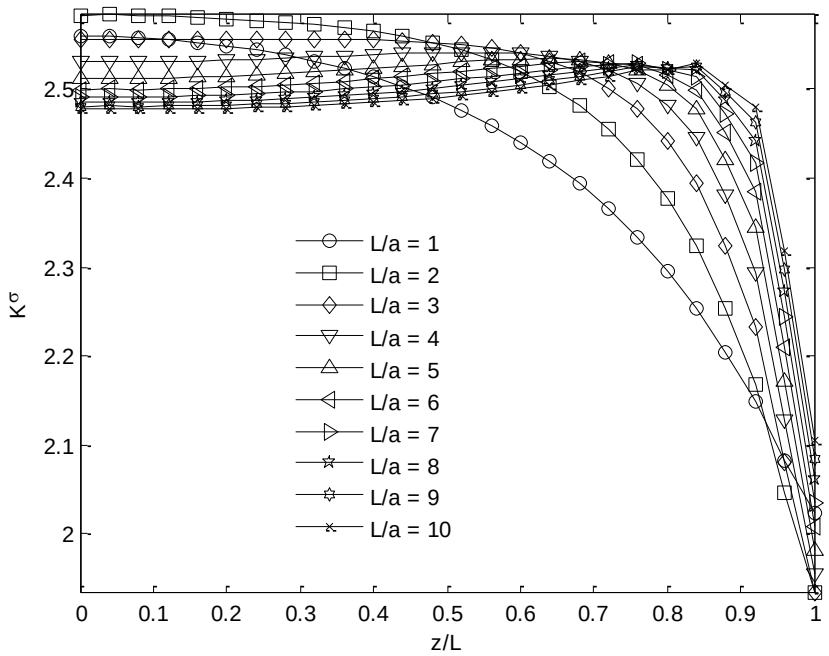

Figure C 2: Distribution of normalized stress concentration factors, K^{σ}, through the thickness in carbon/epoxy for different thicknesses when 2-direction is parallel to applied stress, σ.

References

[1] Greene, R., Patterson, E., and Rowlands, R., 2008, "Thermoelastic Stress Analysis," Springer Handbook of Experimental Solid Mechanics, J. Sharpe William N., ed., Springer US, pp. 743–768.

[2] Patterson, E. A., and Rowlands, R. E., 2008, "Determining individual stresses thermoelastically," J. Strain Anal. Eng. Des., **43**(6), pp. 519–527.

[3] Shukla, A., and Dally, J., 2010, Experimental Solid Mechanics, College House Enterprise, LLC, Knoxville.

[4] Lin, S. T., and Rowlands, R. E., 1999, "Hybrid stress analysis," Opt. Lasers Eng., **32**(3), pp. 257–298.

[5] Lin, S. J., Samad, W. A., Khaja, A. A., and Rowlands, R. E., 2015, "Hybrid thermoelastic stress analysis," Exp. Mech., **55**(4), pp. 653–665.

[6] Quinn, S., Sambasivam, S., and Dulieu-Barton, J. M., 2009, "Derivation of the stress concentrations at holes in orthotropic plates using thermoelastic stress analysis," SEM Annual Conference & Exposition on Experimental and Applied Mechanics - Experimental Mechanics of High Performance Systems, Society for Experimental Mechanics, Albuquerque, USA.

[7] Rauch, B. J., and Rowlands, R. E., 1993, Thermoelastic Stress Analysis, VCH Publishers, New York.

[8] Ju, S. H., and Rowlands, R. E., 2003, "Thermoelastic determination of KI and KII in an orthotropic graphite–epoxy composite," J. Compos. Mater., **37**(22), pp. 2011–2025.

[9] Joglekar, N. S., 2009, "Separating stresses using airy's stress function and TSA, effects of varying the amount and source locations of the input measured TSA data and the number of airy coefficients to use," Master Thesis, University of Wisconsin-Madison.

[10] Huang, Y. M., AbdelMohsen, H. H., and Rowlands, R. E., 1990, "Determination of individual stresses thermoelastically," Exp. Mech., **30**(1), pp. 88–94.

[11] Feng, Z., Zhang, D., Rowlands, R. E., and Sandor, B. I., 1992, "Thermoelastic determination of individual stress components in loaded composites," Exp. Mech., **32**(2), pp. 89–95.

[12] Lin, S. T., and Rowlands, R. E., 1995, "Thermoelastic stress analysis of orthotropic composites," Exp. Mech., **35**(3), pp. 257–265.

[13] Rhee, J., and Rowlands, R. E., 1999, "Thermoelastic-numerical hybrid analysis of holes and cracks in composites," Exp. Mech., **39**(4), pp. 349–355.

[14] Ju, S. H., and Rowlands, R. E., 2003, "Mixed-mode thermoelastic fracture analysis of orthtropic composites," Int. J. Fract., **120**(4), pp. 601–621.

[15] Foust, B. E., and Rowlands, R. E., 2011, "Thermoelastic determination of individual stresses in a diametrally loaded disk," Strain, **47**(2), pp. 146–153.

[16] Lin, S.-J. K., 2007, "Two-and three-dimensional hybrid photomechanical-numerical stress analysis," PhD Thesis, University of Wisconsin-Madison.

[17] Lin, S. J., Matthys, D. R., and Rowlands, R. E., 2007, "Using Airy Function to Thermoelastically Separate Stresses in a Central Circularly Perforated Plate," Applied Mechanics and Materials, Trans Tech Publ, pp. 63–72.

[18] Lin, S.-J., Matthys, D. R., and Rowlands, R. E., 2009, "Separating stresses thermoelastically in a central circularly perforated plate using an airy stress function," Strain, **45**(6), pp. 516–526.

[19] Lin, S. J., Matthys, D. R., Quinn, S., Davidson, J. P., Boyce, B. R., and Rowlands, R. E., 2007, "Determining Individual Stresses around a Near-Edge Hole in a Plate Subjected to an Offset Load using Thermoelasticity," Springer.

[20] Lin, S.-J., Quinn, S., Matthys, D. R., New, A. M., Kincaid, I. M., Boyce, B. R., Khaja, A. A., and Rowlands, R. E., 2011, "Thermoelastic determination of individual stresses in vicinity of a near-edge hole beneath a concentrated load," Exp. Mech., **51**(6), pp. 797–814.

[21] Lin, S. J., Matthys, D. R., Quinn, S., Davidson, J. P., Boyce, B. R., Khaja, A. A., and Rowlands, R. E., 2013, "Stresses at and in the neighborhood of a near-edge hole in a plate subjected to an offset load from measured temperatures," Eur. J. Mech. - ASolids, **39**, pp. 209–217.

[22] Khaja, A. A., and Rowlands, R. E., 2015, "Experimentally determined stresses at geometric discontinuities using simple stress functions," J. Eng. Mech., p. 4015042.

[23] Khaja, A. A., and Rowlands, R. E., 2011, "TSA analysis of vertically- and incline-loaded plates containing neighboring holes," Thermomechanics and Infra-Red Imaging, Volume 7, Springer New York, pp. 117–122.

[24] Khaja, A. A., and Rowlands, R. E., 2011, "Extending TSA with a Polar Stress Function to Non-Circular Cutouts," Experimental and Applied Mechanics, Volume 6: Proceedings of the 2010 Annual Conference on Experimental and Applied Mechanics, T. Proulx, ed., Springer New York, New York, NY, pp. 279–288.

[25] Khaja, A. A., and Rowlands, R. E., 2013, "Experimentally determined stresses associated with elliptical holes using polar coordinates," Strain, **49**(2), pp. 116–124.

[26] Abdel Samad, W., 2013, "Hybrid full-field stress analysis of structures containing irregularly-shaped cutouts," PhD Thesis, University of Wisconsin-Madison.

[27] Samad, W. A., Khaja, A. A., Kaliyanda, A. R., and Rowlands, R. E., 2014, "Hybrid thermoelastic stress analysis of a pinned joint," Exp. Mech., **54**(4), pp. 515–525.

[28] Samad, W. A., and Rowlands, R. E., 2014, "Full-field thermoelastic stress analysis of a finite structure containing an irregularly-shaped hole," Exp. Mech., **54**(3), pp. 457–469.

[29] Samad, W. A., and Rowlands, R. E., 2015, "On improving thermoelastic stress analysis data near edges of discontinuities," Experimental and Applied Mechanics, Volume 6, Springer, pp. 157–162.

[30] Samad, W. A., and Rowlands, R. E., 2014, "Hybrid thermoelastic analysis of an unsymmetrically-loaded structure containing an arbitrarily-shaped cutout," Residual Stress, Thermomechanics & Infrared Imaging, Hybrid Techniques and Inverse Problems, Volume 8, Springer, pp. 51–57.

[31] Kurunthottikkal Philip, S., and Rowlands, R. E., 2016, "Hybrid full-field atress analysis of loaded perforated asymmetrical plate," Residual Stress, Thermomechanics & Infrared Imaging, Hybrid Techniques and Inverse Problems, Volume 9: Proceedings of the 2015 Annual Conference on Experimental and Applied Mechanics, S. Bossuyt, G. Schajer, and A. Carpinteri, eds., Springer International Publishing, Cham, pp. 235–241.

[32] Alshaya, A., Shuai, X., and Rowlands, R., 2016, "Thermoelastic stress analysis of a finite orthotropic composite containing an elliptical hole," Exp. Mech., **56**(8), pp. 1373–1384.

[33] Alshaya, A., and Rowlands, R., 2016, "Determination of stress concentrations in orthotropic composites using mapping collocation techniques," The Plastics Conference, The Society of Plastics Engineers, Indianapolis, IN, pp. 384–391.

[34] Alshaya, A., Shuai, X., and Rowlands, R., 2017, "Stress analysis of a finite orthotropic plate containing an elliptical hole from recorded temperature data," Residual Stress, Thermomechanics & Infrared Imaging, Hybrid Techniques and Inverse Problems, Volume 9: Proceedings of the 2016 Annual Conference on Experimental and Applied Mechanics, S. Quinn, and X. Balandraud, eds., Springer International Publishing, Cham, pp. 47–56.

[35] Correlated Solutions, CSI Application Note AN-525.

[36] Correlated Solutions, "Principle of Digital Image Correlation" [Online]. Available: http://www.correlatedsolutions.com/index.php/principle-of-digital-image-correlation.

[37] Khaja, A. A., Matthys, D. R., and Rowlands, R. E., 2014, "Determining all displacements, strains and stresses full-field from measured values of a single displacement component," Exp. Mech., **54**(3), pp. 443–455.

[38] Samad, W., and Rowlands, R., 2012, "Nondestructive full-field stress analysis of a finite structure containing an elliptical hole using digital image correlation."

[39] Paneerselvam, S., 2014, "Full-field stress analysis of perforated asymmetrical structures from record values of a single displacement component," Master Thesis, University of Wisconsin-Madison.

[40] McConnell, K. G., and Riley, W. E., 1993, "Strain-gage Instrumentation and Data Analysis," Handbook on Experimental Mechanics, A.S. Kobayashi, VCH, pp. 79–117.

[41] Lin, S. J., Quinn, S., Boyce, B. R., and Rowlands, R. E., 2011, "Non-destructive 3-D determination of interior stresses," Applied Mechanics and Materials, Trans Tech Publ, pp. 476–481.

[42] Baek, T. H., and Rowlands, R. E., 1999, "Experimental determination of stress concentrations in orthotropic composites," J. Strain Anal. Eng. Des., **34**(2), pp. 69–81.

[43] Baek, T., and Rowlands, R., 2001, "Hybrid stress analysis of perforated composites using strain gages," Exp. Mech., **41**(2), pp. 195–203.

[44] Foust, B. E., 2003, "Individuals stress determination in inverse problems by combining experimental methods and airy stress functions," Master Thesis, University of Wisconsin-Madison.

[45] Baek, T., and Rudolphi, T., 2010, "A hybrid stress measurement using only x-displacements by phase shifting method with fourier transform (PSM/FT) in laser speckle interferometry and least squares method," Int. J. Precis. Eng. Manuf., **11**(1), pp. 49–54.

[46] Khaja, A. A., 2012, "Experimentally determined full-field stress, strain and displacement analyses of perforated finite members," PhD Thesis, University of Wisconsin-Madison.

[47] Soutas-Little, R. W., 1999, Elasticity, Dover Publications, Mineola, NY.

[48] Lin, S. J., Matthys, D. R., Samad, W. A., Khaja, A. A., Boyce, B. R., and Rowlands, R. E., 2012, "Infrared stress analysis of unsymmetrically-loaded perforated member," ISEM-ACEM-SEM-7th ISEM'12, Taipei, Taiwan.

[49] Kurunthottikkal Philip, S., 2015, "Stress analysis of a finite structure containing an asymmetrical, arbitrarily-shaped cutout based on recorded temperature data," Master Thesis, University of Wisconsin - Madison.

[50] Lekhnitskii, S. G., 1968, Anisotropic Plates, Gordon & Breach Scientific Publishers, New York.

[51] Sokolnikoff, I. S., 1983, Mathematical Theory of Elasticity, Krieger Pub Co, Malabar, Fla.

[52] Boresi, A., Chong, K., and Lee, J., 2011, Elasticity in Engineering Mechanics, J. Wiley & Sons.

[53] Bisshopp, F., 1983, "Numerical conformal mapping and analytic continuation," Q. Appl. Math., **41**, pp. 125–142.

[54] Challis, N. V., and Burley, D. M., 1982, "A numerical method for conformal mapping," IMA J. Numer. Anal., **2**(2), pp. 169–181.

[55] Lekhnitskii, S. G., 1963, Theory of Elasticity of an Anisotropic Elastic Body, Holden-Day, San Francisco.

[56] Muskhelishvili, N., 1977, Some Basic Problems of the Mathematical Theory of Elasticity, Springer, Leyden.

[57] Savin, G. N., 1961, Stress Concentration Around Holes, Pergamon Press.

[58] Churchill, R. V., Brown, J. W., and Verhey, R. E., 1974, Complex Variables and Applications, McGraw-Hill.

[59] Huang, Y. M., and Rowlands, R. E., 1991, "Quantitative stress analysis based on the measured trace of the stress tensor," J. Strain Anal. Eng. Des., **26**(1), pp. 55–63.

[60] Baek, T. H., Chung, T. J., and Panganiban, H., 2008, "Full-field stress determination around circular discontinuity in a tensile-loaded plate using x-displacements only," J. Solid Mech. Mater. Eng., **2**(6), pp. 756–762.

[61] Chen, H. C., 1995, "Stress analysis of laminates with holes by special finite element," Compos. Struct., **31**(2), pp. 99–106.

[62] Rhee, J., and Rowlands, R. E., 1996, "Stresses around extremely large or interacting multiple holes in orthotropic composites," Comput. Struct., **61**(5), pp. 935–950.

[63] Lin, S. T., Feng, Z., and Rowlands, R. E., 1997, "Thermoelastic determination of stress intensity factors in orthotropic composites using the J-integral," Eng. Fract. Mech., **56**(4), pp. 579–592.

[64] Tan, S. C., 1987, "Laminated composites containing an elliptical opening. I. Approximate stress analyses and fracture models," J. Compos. Mater., **21**(10), pp. 925–948.

[65] Tan, S. C., 1994, Stress Concentrations in Laminated Composites, CRC Press, Lancaster, Pa.

[66] Stanley, P., and Chan, W. K., 1988, "The application of thermoelastic stress analysis techniques to composite materials," J. Strain Anal. Eng. Des., **23**(3), pp. 137–143.

[67] Kageyama, K., Ueki, K., and Kikuchi, M., 1987, "Application of thermoelastic stress analysis to FRP," Tokyo, pp. 52–57.

[68] Kageyama, K., Ueki, K., and Kikuchi, M., 1988, " 'Thermoelastic technique applied to stress analysis of carbon fiber reinforced composite materials," pp. 931–936.

[69] Wong, A., 1990, "A non-adiabatic thermoelastic theory and use of SPATE on composite laminates," Copenhagen.

[70] Huang, Y.-M., "Determination of individual stresses from thermoelastically measured trace of stress tensor," PhD Thesis, University of Wisconsin-Madison.

[71] Huang, Y. M., Rowlands, R. E., and Lesniak, J. R., 1990, "Simultaneous stress separation, smoothing of measured thermoelastic isopachic information and enhanced boundary data," Exp. Mech., **30**(4), pp. 398–403.

[72] Rhee, J., He, S., and Rowlands, R. E., 1996, "Hybrid moiré-numerical stress analysis around cutouts in loaded composites," Exp. Mech., **36**(4), pp. 379–387.

[73] Cook, R., and Young, W., 1998, Advanced Mechanics of Materials, Prentice Hall, Upper Saddle River, N.J.

[74] Wang, W.-C., Chen, Y.-M., Lin, M.-S., and Wu, C.-P., 2005, "Investigation of the stress field of a near-surface circular hole," Exp. Mech., **45**(3), pp. 244–249.

[75] Vieira, R. B., Kurunthottikkal Philip, S., Gonzáles, G. L. G., Freire, J. L., Yang, B., and Rowlands, R. E., 2016, "Determination of a U-notch stress concentration factor using thermoelasticity," J. Mech. Eng. Autom., **6**, pp. 66–76.

[76] Hawong, J. S., Lin, C. H., Lin, S. T., Rhee, J., and Rowlands, R. E., 1995, "A hybrid method to determine individual stresses in orthotropic composites using only measured isochromatic data," J. Compos. Mater., **29**(18), pp. 2366–2387.

[77] Ashrafi, M., and Tuttle, M. E., 2015, "High strain gradient measurements in notched laminated composite panels by digital image correlation," Composite, Hybrid, and Multifunctional Materials, Volume 4: Proceedings of the 2014 Annual Conference on Experimental and Applied Mechanics, G. Tandon, ed., Springer International Publishing, Cham, pp. 75–81.

[78] Howland, R. C. J., 1930, "On the stresses in the neighbourhood of a circular hole in a strip under tension," Philos. Trans. R. Soc. Lond. Math. Phys. Eng. Sci., **229**(670–680), pp. 49–86.

[79] Howland, R. C. J., 1935, "Stresses in plate containing an infinite row of holes," Proc. R. Soc. Lond. Ser. Math. Phys. Sci., **148**(864), pp. 471–491.

[80] Pilkey, W. D., and Pilkey, D. F., 2008, Peterson's Stress Concentration Factors, Wiley, Hoboken, N.J.

[81] Schulz, K., "On the state of stress in perforated plates," Doctoral Thesis, Thchn. Hochschule.

[82] Heywood, R. B., 1952, Designing by Photoelasticity, Chapman & Hall.

[83] Kosmodamiansky, A., 1961, "The stress state of an anisotropic plate with two non-identical holes," Akad. Nauk SSSR Izv. Otd. Tekhnicheskikh Nauk, (1), pp. 175–177.

[84] Lin, J.-K., and Ueng, C. E. S., 1987, "Stresses in a laminated composite with two elliptical holes," Compos. Struct., **7**(1), pp. 1–20.

[85] Fan, W., and Wu, J., 1988, "Stress concentration of a laminate weakened by multiple holes," Compos. Struct., **10**(4), pp. 303–319.

[86] Considine, J., Skye, W., Chen, W., Matthys, D., Vahey, D., Turner, K., and Rowlands, R., "Enhancing paper strength by optimizing defect configuration," Proceedings of SEM annual conference and exposition on experimental and applied mechanics, Society for Experimental Mechanics, Inc.

[87] Rhee, J., Cho, H.-K., Marr, D. J., and Rowlands, R. E., 2012, "Local compliance, stress concentrations and strength in orthotropic materials," J. Strain Anal. Eng. Des., **47**(2), pp. 113–128.

[88] 1999, Wood Handbook – Wood as an Engineering Material, US Department of Agriculture, Forest Service. Forest Products Laboratory, Madison, WI.

[89] Cho, H. K., and Rowlands, R. E., 2007, "Reducing tensile stress concentration in perforated hybrid laminate by genetic algorithm," Compos. Sci. Technol., **67**(13), pp. 2877–2883.

[90] Cho, H. K., and Rowlands, R. E., 2009, "Optimizing fiber direction in perforated orthotropic media to reduce stress concentration," J. Compos. Mater., **43**(10), pp. 1177–1198.

[91] Broek, D., 1982, Elementary Engineering Fracture Mechanics, Springer Science & Business Media.

[92] Timoshenko, S., and Goodier, J., 1970, Theory of Elasticity, McGraw-Hill Publishing Company, New York.

[93] Young, W., Budynas, R., and Sadegh, A., 2011, Roark's Formulas for Stress and Strain, McGraw-Hill Education, New York.

[94] Sternberg, E., and Sadowsky, M. A., 1949, "Three-dimensional solution of the stress concentration around a circular hole in a plate with arbitrary thickness," Appl. Mech., (16), pp. 27–38.

[95] Youngdahl, C. K., and Sternberg, E., 1966, "Three-dimensional stress concentration around a cylindrical hole in a semi-infinite elastic body," J. Appl. Mech., **33**(4), pp. 855–865.

[96] Folias, E. S., 1975, "On the three-dimensional theory of cracked plates," J. Appl. Mech., **42**(3), pp. 663–674.

[97] Folias, E. S., 1987, "The 3D stress field at the intersection of a hole and a free surface," Int. J. Fract., **35**(3), pp. 187–194.

[98] Folias, E. S., 1989, "On the three-dimensional bending theory of cracked plates," Int. J. Solids Struct., **25**(5), pp. 497–513.

[99] Folias, E. S., and Wang, J.-J., 1990, "On the three-dimensional stress field around a circular hole in a plate of arbitrary thickness," Comput. Mech., **6**(5–6), pp. 379–391.

[100] Kotousov, A., and Wang, C. H., 2002, "Fundamental solutions for the generalised plane strain theory," Int. J. Eng. Sci., **40**(15), pp. 1775–1790.

[101] Kotousov, A., and Wang, C. H., 2002, "Three-dimensional stress constraint in an elastic plate with a notch," Int. J. Solids Struct., **39**(16), pp. 4311–4326.

[102] Kotousov, A., and Wang, C. H., 2002, "Three-dimensional solutions for transversally isotropic composite plates," Compos. Struct., **57**(1–4), pp. 445–452.

[103] Kotousov, A., and Tan, P. J., 2004, "Effect of the plate thickness on the out-of-plane displacement field of a cracked elastic plate loaded in mode I," Int. J. Fract., **127**(1), pp. L97–L103.

[104] Yang, Z., Kim, C.-B., Cho, C., and Beom, H. G., 2008, "The concentration of stress and strain in finite thickness elastic plate containing a circular hole," Int. J. Solids Struct., **45**(3–4), pp. 713–731.

[105] Dai, L., and Gong, J., 2013, "The three-dimensional stress field in an arbitrary thichness plate holding a circular hole," Int. J. Mech. Syst. Eng., **3**(2), pp. 75–82.

[106] Daniel, I. M., and Ishai, O., 2005, Engineering Mechanics of Composite Materials, Oxford University Press, New York.

[107] Alshaya, A., Hunt, J., and Rowlands, R., 2016, "Stresses and strains in thick perforated orthotropic plates," J. Eng. Mech., **142**(11), p. 4016082.

[108] Collins, C. J., 2016, "A comprehensive evaluation of methods to determine mechanical properties of long bone," University of Wisconsin-Madison.

[109] "54 Million Americans Affected by Osteoporosis and Low Bone Mass," Natl. Osteoporos. Found. [Online]. Available: https://www.nof.org/news/54-million-americans-affected-by-osteoporosis-and-low-bone-mass/. [Accessed: 20-Nov-2016].

[110] Burgers, T. A., Mason, J., Niebur, G., and Ploeg, H. L., 2008, "Compressive properties of trabecular bone in the distal femur," J. Biomech., **41**(5), pp. 1077–1085.

[111] Aiyangar, A. K., Au, A. G., Crenshaw, T. D., and Ploeg, H.-L., "Recovery of bone strength in young pigs from an induced short-term dietary calcium deficit followed by a calcium replete diet," Med. Eng. Phys., **32**(10), pp. 1116–1123.

[112] Stenström, M., Olander, B., Lehto-Axtelius, D., Erik Madsen, J., Nordsletten, L., and Alm Carlsson, G., 2000, "Bone mineral density and bone structure parameters as predictors of bone strength: an analysis using computerized microtomography and gastrectomy-induced osteopenia in the rat," J. Biomech., **33**(3), pp. 289–297.

[113] Nyman, J. S., Munoz, S., Jadhav, S., Mansour, A., Yoshii, T., Mundy, G. R., and Gutierrez, G. E., 2009, "Quantitative measures of femoral fracture repair in rats derived by micro-computed tomography," J. Biomech., **42**(7), pp. 891–897.

[114] O'Neill, K. R., Stutz, C. M., Mignemi, N. A., Burns, M. C., Murry, M. R., Nyman, J. S., and Schoenecker, J. G., 2012, "Micro-computed tomography assessment of the progression of fracture healing in mice," Bone, **50**(6), pp. 1357–1367.

[115] Taddei, F., Schileo, E., Helgason, B., Cristofolini, L., and Viceconti, M., "The material mapping strategy influences the accuracy of CT-based finite element models of bones: An evaluation against experimental measurements," Med. Eng. Phys., **29**(9), pp. 973–979.

[116] Taddei, F., Cristofolini, L., Martelli, S., Gill, H. S., and Viceconti, M., "Subject-specific finite element models of long bones: An in vitro evaluation of the overall accuracy," J. Biomech., **39**(13), pp. 2457–2467.

[117] Schileo, E., Taddei, F., Malandrino, A., Cristofolini, L., and Viceconti, M., "Subject-specific finite element models can accurately predict strain levels in long bones," J. Biomech., **40**(13), pp. 2982–2989.

[118] Schileo, E., Balistreri, L., Grassi, L., Cristofolini, L., and Taddei, F., "To what extent can linear finite element models of human femora predict failure under stance and fall loading configurations?," J. Biomech., **47**(14), pp. 3531–3538.

[119] F. Taddei, S. Martelli, B. Reggiani, L. Cristofolini, and M. Viceconti, 2006, "Finite-Element Modeling of Bones From CT Data: Sensitivity to Geometry and Material Uncertainties," IEEE Trans. Biomed. Eng., **53**(11), pp. 2194–2200.

[120] Fagan, M. J., Julian, S., and Mohsen, A. M., 2002, "Finite element analysis in spine research," Proc. Inst. Mech. Eng. [H], **216**(5), pp. 281–298.

[121] Cristofolini, L., Schileo, E., Juszczyk, M., Taddei, F., Martelli, S., and Viceconti, M., 2010, "Mechanical testing of bones: the positive synergy of finite–element models and in vitro experiments," Philos. Trans. R. Soc. Math. Phys. Eng. Sci., **368**(1920), p. 2725.

[122] Collins, C. J., Vivanco, J. F., Sokn, S. A., Williams, B. O., Burgers, T. A., and Ploeg, H.-L., "Fracture healing in mice lacking Pten in osteoblasts: a micro-computed tomography image-based analysis of the mechanical properties of the femur," J. Biomech., **48**(2), pp. 310–317.

[123] Taylor, W. R., Roland, E., Ploeg, H., Hertig, D., Klabunde, R., Warner, M. D., Hobatho, M. C., Rakotomanana, L., and Clift, S. E., 2002, "Determination of orthotropic bone elastic constants using FEA and modal analysis," J. Biomech., **35**(6), pp. 767–773.

[124] Brault, R., Germaneau, A., Dupré, J. C., Doumalin, P., Mistou, S., and Fazzini, M., 2013, "In-situ analysis of laminated composite materials by X-ray micro-computed tomography and digital volume correlation," Exp. Mech., **53**(7), pp. 1143–1151.

[125] Germaneau, A., Doumalin, P., and Dupré, J.-C., 2007, "3D strain field measurement by correlation of volume images using scattered light: recording of images and choice of marks," Strain, **43**(3), pp. 207–218.

[126] Bouterf, A., Roux, S., Hild, F., Adrien, J., Maire, E., and Meille, S., 2014, "Digital Volume Correlation Applied to X-ray Tomography Images from Spherical Indentation Tests on Light-weight Gypsum," Strain, **50**(5), pp. 444–453.

[127] Chen, Y., Yang, D., Ma, Y., Tan, X., Shi, Z., Li, T., and Si, H., 2015, "Experimental Investigation on the Mechanical Behavior of Bovine Bone Using Digital Image Correlation Technique," Appl. Bionics Biomech., **2015**, p. 609132.

[128] Forsberg, F., Sjödahl, M., Mooser, R., Hack, E., and Wyss, P., 2010, "Full Three-Dimensional Strain Measurements on Wood Exposed to Three-Point Bending: Analysis by Use of Digital Volume Correlation Applied to Synchrotron Radiation Micro-Computed Tomography Image Data," Strain, **46**(1), pp. 47–60.

[129] Ekeland, A., Engesæter, L. B., and Langeland, N., 1981, "Mechanical properties of fractured and intact rat femora evaluated by bending, torsional and tensile tests," Acta Orthop. Scand., **52**(6), pp. 605–613.

[130] Herman, I. P., 2007, Physics of the Human Body, Springer Science & Business Media.

[131] Vashishth, D., 2008, "Small Animal Bone Biomechanics," Bone, **43**(5), pp. 794–797.

[132] Beaupied, H., Lespessailles, E., and Benhamou, C.-L., 2007, "Evaluation of macrostructural bone biomechanics," Joint Bone Spine, **74**(3), pp. 233–239.

[133] Schriefer, J. L., Robling, A. G., Warden, S. J., Fournier, A. J., Mason, J. J., and Turner, C. H., 2005, "A comparison of mechanical properties derived from multiple skeletal sites in mice," J. Biomech., **38**(3), pp. 467–475.

[134] Brodt, M. D., Ellis, C. B., and Silva, M. J., 1999, "Growing C57Bl/6 mice increase whole bone mechanical properties by increasing geometric and material properties," J. Bone Miner. Res., **14**(12), pp. 2159–2166.

[135] "Advanced Laser Materials," Adv. Laser Mater. - Eng. Mater. Rapid Manuf. [Online]. Available: http://alm-llc.com/. [Accessed: 27-Nov-2016].